

Development of Microneedle Devices for Drug Delivery

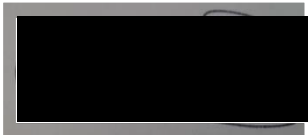


Submitted to Swansea University in fulfilment of the
requirements for the degree of Doctor of Philosophy

Swansea University 2021

DECLARATION

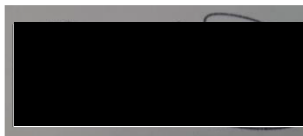
This work has not previously been accepted in substance for any degree and is not being concurrently submitted in candidature for any degree.

Signed  (candidate)

Date28/ 03/ 2021.....

STATEMENT 1


This thesis is the result of my own investigations, except where otherwise stated. Other sources are acknowledged by footnotes giving explicit references. A bibliography is appended.

Signed  (candidate)

Date28/ 03/ 2021.....

STATEMENT 2

I hereby give consent for my thesis, if accepted, to be available for photocopying and for inter-library loan **after expiry of a bar on access approved by Swansea University.**

Signed  (candidate)

Date28/ 03/ 2021.....



Ysgoloriaethau Sgiliau Economi Gwybodaeth
Knowledge Economy Skills Scholarships



Ysgoloriaeth Sgiliau Economi Gwybodaeth (KESS) yn Gymru gyfan sgiliau lefel uwch yn fenter a arweinir gan Brifysgol Bangor ar ran y sector AU yng Nghymru. Fe'i cyllidir yn rhannol gan Gronfeydd Cymdeithasol Ewropeaidd (ESF) cydgyfeirio ar gyfer Gorllewin Cymru a'r Cymoedd.

Knowledge Economy Skills Scholarships (KESS) is a pan-Wales higher level skills initiative led by Bangor University on behalf of the HE sector in Wales. It is part funded by the Welsh Government's European Social Fund (ESF) convergence programme for West Wales and the Valleys.

This work is part funded by the Welsh Government's European Social Fund (ESF) convergence programme for West Wales and the Valleys.

Acknowledgments

Firstly, I would like to thank my Supervisors, **Professor Owen Guy**, and **Dr Sanjiv Sharma** for entrusting a non-engineer in an engineering world and granting me the freedom to explore my ideas and guidance to succeed in them. I learnt a lot thank you.

I would like to thank my funding body KESS II, for without their funding opportunities this project could not have reached its goal. In addition, SPTS technologies and BioMems technologies for their continued collaborations.

All my thanks go towards the technical team who help run and maintain the labs, with a very special thank you to my valued friend **Dr Gareth Blayney**, for taking me under his wing and teaching me everything I know about fabrication and being a magician at fixing everything I broke (including my car).

To my colleagues and now friends, for keeping the fun and laughter in everyday, the copious amount of cake and completing every crossword in the paper. In particular, **Natasha Rajendran**, **Alex Bulpitt** and **Mike Williams** for keeping me sane while writing during the COVID-19 pandemic with virtual real estate, fishing, hunting and net fights.

A special thank you goes to **Ryan Bigham**, for the silly times, the cooked dinners and continuously pulling me out of the quicksand and encouraging me to continue.

To my best friend, **Fiona John**, for housing me, feeding me, putting up with my grumpy stress head and always being ready with a gin and a takeaway after a hard day.

To my partner, **Ellys Gwilliam** who met me halfway through the PhD process and was not deterred by the stressy, crazy mess, but was silly enough to stick by me and provide unconditional love and support.

My biggest thanks go to my Family, **my parents**, **grandparents** and **sister** for the lifelong support and belief that I can succeed. Especially my father **Richard Howells**, for reading Every. Single. Word of my thesis over and over and teaching me how to write and turn sentences around.

My final thanks go to someone very special who unfortunately is no longer with us, my greatest supporter my Bampy **Colin Richards**. He always knew exactly what to say and introduced me to the wonders of the world and encouraged me to be me.

To my parents and grandparents

Abstract

There are numerous modes of therapeutic administration, of which oral delivery is the most convenient and conventional as it involves administration of therapeutics in the form of liquids or solid capsules and tablets. However, this mode encounters several challenges, such as chemical processes within the gastrointestinal track and first pass metabolism which subsequently reduce the efficacy of the therapeutic drugs. To overcome these issues, transdermal drug administration in the form of hypodermic needles, topical creams, and transdermal patches have been employed. However, the effect of transdermal administration is limited due the *stratum corneum* layer of the skin, which acts as a lipophilic and hydrophobic barrier preventing external molecules from entering the skin. Therefore, hypodermic needles are used due to their sharp tip facilitating penetration through the *stratum corneum* to deposit the drug formulation into the skin, subcutaneous fat, or muscles layers. However, these needles induce needle-phobia and reduce patient compliance due to the complexity with administration and pain associated with injection.

Microneedle devices have been developed to avoid these issues and provide enhanced transdermal therapeutic drug delivery in a minimally invasive manner to eliminate the first-pass metabolism and provide a sustained release. Unlike hypodermic needles injection, they do not cause pain and related fear or phobia in individuals, thereby improving compliance to the prescribed dosage regime. Till now different types of microneedles have been fabricated. These include, solid, coated, hollow and dissolvable, where each type has its own advantages and unique properties and designs.

In this thesis, two novel methods utilising silicon etching processes, for the fabrication of both out-of-plane and in-plane silicon microneedles are presented. Hollow out-of-plane microneedles are manufactured through deep reactive-ion etching (DRIE) technology. The patented three-step process flow has been developed to produce multiple arrays of sharp bevelled tipped, hollow microneedles which facilitate easy insertion and controlled fluid injection into excised skin samples.

The in-plane microneedles have been fabricated from simultaneous wet KOH etching of the front and reverse of (100) orientated silicon wafers. The characteristic 54.7° sidewall etch angle was utilised to form a sharp six-sided microneedle tip and hexagonal shaped shaft. Employing this method allowed fabrication of both solid and hollow microneedles

with different geometries i.e., widths and heights of several μm , to determine the optimal MN height and width for effective penetration and transdermal drug delivery.

All microneedles fabricated during the PhD studentship tenure have been characterised through histology, fluorescent studies, and delivery into ex-vivo porcine and human skin tissue (research ethics committee reference 08/WSE03/55) to demonstrate effective microneedle based transdermal therapeutic drug delivery. The transdermal delivery of insulin and hyaluronic acid has been successfully demonstrated by employing a simple poke and patch application technique, presenting a clinical improvement over traditional application such as creams and ointments.

Contents

Abbreviations.....	xi
Units.....	xii
List of Figures.....	xiii
List of Tables.....	xxvii
Publications.....	xxix
Conferences.....	xxix
Awards.....	xxix
Part 1 Introduction and literature review.....	1
Chapter 1 Thesis outline.....	2
Chapter 2 Introduction to transdermal drug delivery.....	3
2.1 Drug delivery.....	3
2.2 Skin anatomy	4
2.2.1 The epidermis.....	5
2.2.2 The dermis.....	7
2.3 Routes of transdermal drug delivery.....	7
2.4 Factors affecting transdermal drug delivery.....	8
2.5 History of transdermal drug delivery	9
2.6 Enhancing transdermal drug delivery.....	11
Chapter 3 Microneedles.....	13
3.1 Introduction.....	13
3.2 Advantages and disadvantages of MNs.....	14
3.3 MN classification.....	15
3.3.1 Solid MNs.....	16
3.3.2 Coated MNs.....	18
3.3.3 Dissolving MNs.....	20

3.3.4 Hollow MNs.....	21
3.3.5 Hydrogel-forming MNs.....	25
3.4 MN structure.....	27
Chapter 4 Silicon microneedle manufacture methods.....	31
4.1 Introduction.....	31
4.2 Silicon.....	31
4.3 Silicon MN manufacturing methods.....	32
4.3.1 Photolithography.....	32
4.3.2 Thin-film deposition.....	34
4.3.3 Silicon etching.....	34
4.4 Silicon MNs in the literature.....	36
Chapter 5 Microneedle applications.....	41
5.1 Introduction.....	41
5.2 Diabetes.....	41
5.3 Vaccines.....	42
5.4 Cancer.....	45
5.5 Obesity.....	45
5.6 Cosmetics.....	46
5.7 Other MN applications.....	48
5.7.1 Patient monitoring, diagnostics and theranostics.....	48
5.7.2 Ocular delivery.....	49
5..7.3 Gastrointestinal delivery.....	50
5.8 Conclusions.....	51
Part 2 Experimental methodology.....	52
Chapter 6 Experimental instrumentation and materials for fabrication methods. 53	
6.1 Photolithography.....	53
6.1.1 Spin coater.....	53
6.1.2 Spray coater.....	53

6.1.3 Mask aligner.....	54
6.2 Silicon dioxide deposition- Chemical vapour deposition.....	55
6.3 Ellipsometry.....	55
6.4 Inductively coupled plasma.....	55
6.5 Etching materials – Potassium Hydroxide.....	56
Chapter 7 Experimental equipment and materials used for characterisation and analytical methods.....	57
7.1 Imaging techniques	57
7.1.1 Scanning electron microscopy.....	57
7.1.2 Optical microscopy.....	58
7.1.3 Fluorescence microscopy.....	58
7.1.4 Optical coherence tomography.....	59
7.2 Mechanical testing.....	59
7.3 Skin preparation.....	60
7.3.1 Porcine skin preparation	60
7.3.2 Histological sectioning.....	60
7.3.3 Transepidermal electrical resistance.....	61
7.4 Drug delivery.....	61
7.4.1 Franz cell <i>in vitro</i> assay.....	61
7.4.2 Franz cell flux rate	68
7.4.3 Tape stripping	69
7.4.4 Skin homogenisation.....	69
7.5 Sample analysis.....	70
7.5.1 Fluorescent spectrometry.....	70
Part 3 Microneedle fabrication.....	71
Chapter 8 Out-of-plane MN fabrication.....	72
8.1 Introduction.....	72
8.2 MN proof of concept designs.....	72
8.3 Bevel photolithography.....	75

8.3.1 Photoresist Az125nxt thickness optimisation.....	77
8.4 Bevel DRIE etching.....	80
8.5 Bore fabrication optimisation.....	81
8.6 Bore DRIE etching.....	90
8.7 Shaft fabrication.....	93
8.8 Shaft DRIE etching.....	97
8.9 Shaft etch optimisation.....	100
8.9.1 Alignment marks.....	100
8.9.2 Removing the wall between the MNs.....	107
8.9.3 Smoothing the bevel surface.....	113
8.9.4 Optimisation of NLOF2070 for shaft patterning.....	114
Chapter 9 In-plane MN fabrication.....	121
9.1 Introduction.....	121
9.2 MN proof of concept experiments.....	123
9.2.1 Using a resist mask.....	123
9.2.2 Using a silicon oxide mask.....	128
9.3 In-plane MN primary mask design.....	133
9.3.1 Alignment marks.....	134
9.4 Resist spin coating optimisation.....	135
9.5 Resist photolithography optimisation.....	139
9.6 In-plane MN fabrication process flow.....	146
9.7 KOH MN etch optimisation.....	148
9.7.1 SEM analysis of fully optimised MNs.....	152
9.8 Optimising MN height.....	156
9.9 Optimising MN width.....	163
9.10 Optimising MN pitch.....	172
9.11 Conclusion.....	173

Chapter 10 Fabrication of hollow in-plane MNs.....	175
10.1 Introduction.....	175
10.2 KOH MN channel etch optimisation.....	179
10.3 Hollow MN tip optimisation.....	182
10.4 Hollow MN channel optimisation.....	185
10.5 Fabricating a closed Hollow channel.....	190
10.6 Conclusion.....	193
10.7 Comparison of out-of-plane and in-plane MNs.....	194
Chapter 11 Fabrication of MN syringe adaptors.....	195
11.1 Introduction.....	195
11.2 Out-of-plane MN adaptor.....	195
11.2.1 Out-of-plane adaptor optimisation.....	197
11.3 In-plane MN adaptor.....	200
11.4 Conclusion.....	202
Part 4 Microneedle characterisation.....	203
Introduction to characterisation.....	204
Chapter 12 Dye staining.....	205
12.1 Introduction.....	205
12.2 Out-of-plane MN methyl blue staining MN.....	206
12.3 In-plane MN methyl blue staining.....	207
12.3.1 In-plane MN pitch.....	207
12.3.2 In-plane MN width.....	208
12.3.3 In-plane MN height.....	209
12.3.4 In-plane MN arrays with varying heights on the same array.....	211
12.4 Polycarbonate MN methyl blue staining.....	212
12.5 Summary.....	213

Chapter 13 MN applicator.....	214
13.1 Introduction.....	214
13.2 MN applicator device.....	215
13.3 Silicon out-of-plane MN applicator testing.....	216
13.4 Polycarbonate MN applicator testing.....	217
13.4.1 MN analysis post application.....	219
13.5 Conclusion and future experiments.....	220
Chapter 14 Optical coherence tomography.....	221
14.1 Introduction.....	221
14.2 OCT optimisation.....	221
14.3 Out-of-plane MNs.....	223
14.4 In-plane MNs.....	226
14.4.1 In-plane MN pitch.....	226
14.4.2 In-plane MN width.....	227
14.4.3 In-plane MN height.....	229
14.5 Polycarbonate MNs.....	232
14.5.1 Polycarbonate MN with applicator.....	233
14.6 Conclusion.....	234
Chapter 15 Mechanical characterisation.....	235
15.1 Introduction.....	235
15.2 Out-of-plane MNs.....	236
15.3 In-plane MNs.....	237
15.3.1 In-plane MN pitch.....	237
15.3.2 In-plane MN width.....	240
15.3.3 In-plane MN height.....	242
15.3.4 In-plane MN conclusion.....	245
15.4 Polycarbonate MNs.....	245

Chapter 16 Hollow MN injection.....	247
16.1 Introduction.....	247
16.2 Hollow out-of-plane MNs.....	247
16.2.1 Syringe adaptor.....	247
16.2.2 Controlled MN injection into skin.....	248
16.3 Hollow in-plane MNs.....	250
16.4 Hollow polycarbonate MNs.....	252
16.4.1 Hollow polycarbonate conclusion.....	254
Part 5 <i>In vitro</i> microneedle drug delivery.....	255
Chapter 17 Optimisation of <i>in vitro</i> Franz cell assay.....	256
17.1 Introduction.....	256
17.2 Transdermal test membranes.....	256
17.3 Porcine skin preparation.....	258
17.4 Summary of guidelines.....	259
17.5 Skin integrity.....	260
17.5.1 Method.....	261
17.5.2 Results.....	262
17.6 Tape strip protocol.....	263
17.6.1 Optimisation of method.....	264
17.6.2 Results.....	264
17.6.3 Conclusion.....	265
17.7 Skin homogenisation.....	265
17.7.1 Mechanical homogenisation.....	266
17.7.2 Enzymatic homogenisation.....	267
17.7.2.1 Method.....	268
17.7.2.2 Results.....	269
17.8 Franz cell analysis optimisation.....	271
17.8.1 Method.....	271
17.8.2 Results.....	271

17.9 Skin thickness optimisation.....	274
17.9.1 Methods.....	275
17.9.2 Results.....	275
17.10 Conclusion.....	278
Chapter 18 Calcein transdermal delivery.....	280
18.1 Introduction.....	280
18.2 Aims and objectives.....	280
18.3 Methods.....	280
18.4 Results.....	281
18.5 Conclusion.....	285
Chapter 19 Transdermal delivery of Insulin and Hyaluronic acid.....	287
19.1 Introduction.....	287
19.2 Aims and objectives.....	288
19.3 Methods.....	289
19.4 Results.....	289
19.4.1 Hyaluronic acid.....	289
19.4.2 Insulin.....	293
19.5 Conclusion.....	296
Chapter 20 Conclusions and future work.....	298
References	300

Abbreviations

ADME	Absorption, Distribution, Metabolism, Elimination
AKA	Also Known As
APC	Antigen Presenting Cells
BAT	Brown Adipose Tissue
BSA	Bovine Serum Albumin
CAD	Computer Aided Design
CVD	Chemical Vapour Deposition
dH₂O	Deionized Water
DRIE	Deep Reactive Ion Etching
DSiV	Deep Silicon Via
EGDMA	Ethylene Glycol Dimethacrylate
FDA	Food and Drug Administration
FITC	Fluorescein Isothiocyanate
GI	Gastrointestinal Tract
GTN	Nitro-glycerine
HA	Hyaluronic Acid
HEMA	2-Hydroxyethyl Methacrylate
HPV	Human papillomavirus
ICP	Inductively Coupled Plasma
ISF	Interstitial Fluid
IP	In-plane
KOH	Potassium Hydroxide
LUMI	Liminal Unfolding Microneedle Injector
MA	Mask Aligner
MB	Methylene Blue
MN	Microneedle
MNs	Microneedles
OCT	Optical Coherence Tomography

OOP	Out-of-Plane
PBS	Potassium Buffered Saline
PC	Polycarbonate
PDMS	Polydimethylsiloxane
PEG	Poly(ethyleneglycol)
PLA	Polylactic Acid
PLGA	Poly(lactic-co-glycolic acid)
PMVE/MA	Polymethyl Vinyl Ether-alt-maleic Anhydride
PTH	Parathyroid Hormone
PVA	Polyvinyl Alcohol
RIE	Reactive Ion Etching
RPM	Rotations Per Minute
SC	Stratum Corneum
SCS	Suprachoroidal Space
SEM	Scanning Electron Microscope
SiO₂	Silicon Dioxide
TEER	Transepithelial/transendothelial electrical resistance
TEWL	Transepidermal Water Loss
TSV	Through Silicon Via
UV	Ultraviolet
WAT	White Adipose Tissue
WHO	World Health Organisation

Units

µm	Micrometre
µl	Microliter
ml	Millilitre
mg	Milligram
J	Flux

List of figures

Figure 2.1 The structure of the skin.....	5
Figure 2.2 The structure of the <i>stratum corneum</i>	6
Figure 2.3 Transdermal drug delivery method of enhancement.....	11
Figure 3.1 Year wise (from 2000-2019) trend in MN array-based research.....	13
Figure 3.2 Schematic diagram of MN application methods to the skin to enhance transdermal delivery * <i>stratum corneum</i> **epidermic (A) MN (B) coated MN (C) dissolving MN (D) hollow MN (E) hydrogel-forming MN.....	15
Figure 3.3 Examples of different shaped solid MNs fabricated from silicon, metal, and polymer.....	17
Figure 3.4 Zosono MN patch with applicator device.....	19
Figure 3.5 Hollow MNs with side opened bores, changes in process flow enable (A) full shaft length bore (B) half shaft length bores or (C) Cylindrical shafts.....	22
Figure 3.6 Hollow glass MNs.....	23
Figure 3.7 Hollow silicon MNs marketed as MicroJet™ from NanoPass.....	24
Figure 3.8 Commercial hollow MN devices (A) 3M (B) Soluvia MicroJect (C) DebioJect.....	25
Figure 3.9 Schematic diagram of hydrogel forming MN (A) demonstrating how the MN patch is arranged (B) application of MN into skin and ISF moving into the MNs (C) MN swelling and releasing drug into the skin.....	26
Figure 3.10 Schematic diagram of (A) OOP MNs and (B) IN-plane MN.....	27
Figure 3.11 MNs fabricated in in-plane orientations and stacked together to produce OOP characteristics.....	28
Figure 3.12 in-plane hollow MNs (A) DRIE etching (B) DRIE and wet etching (C) Wet etching to produce 6 different designs (D) DRIE and wet etching.....	30
Figure 4.1 Schematic diagram of positive and negative photoresist after UV exposure.....	33
Figure 4.2 Schematic diagram isotropic and anisotropic wet chemical etching.....	35
Figure 4.3 SEM image of TSV fabricated from BOSCH etch processes.....	36
Figure 4.4 SEM image of MNs fabricated from RIE techniques.....	36
Figure 4.5 (A) Schematic fabrication process of silicon hollow MN arrays from dry etching (B) SEM image of resulting MN.....	37
Figure 4.6 (A) Process flow of side-opened bore MNs (B) SEM image of MN.....	38

Figure 4.7 (A) Process flow of wet etched MNs (B) SEM image of resulting MN.....	39
Figure 6.1 Schematic diagram demonstrating the spray coating method.....	54
Figure 7.1 Schematic representation of SEM apparatus.....	57
Figure 7.2 Schematic representation of fluorescent microscope.....	58
Figure 7.3 Schematic representation of optical coherence tomography.....	59
Figure 7.4 Franz cell apparatus.....	61
Figure 7.5 Exemplar calibration curve showing fluorescence measurements of different concentrations of calcein.....	64
Figure 7.6 Cumulative concentration graph of exemplar data	68
Figure 8.1 Schematic process flow for hollow silicon MN production. Silicon (grey), with photoresist masks (red) and silicon oxide (blue), respectively.....	73
Figure 8.2 Schematic drawings and AutoCAD mask designs demonstrating how the three masks are used in sequence to fabricate hollow MNs. (A) Rectangular resist mask (red) isotopically undercut to create a bevelled MN tip; (B) 100µm circular bore, etched from the reverse (blue) of the wafer through to the bevelled surface; (C) MN tip and shaft design aligned over the central bore, to etch around the resist (red) and create cylindrical shafts with a pointed tip.....	74
Figure 8.3 SEM image of AZ125nxt resist, after spinning, to measure a thickness of 42µm.....	76
Figure 8.4 Schematic diagram showing contact between the edge bead and the mask. Silicon wafers are represented in Grey, Resist represented in red and glass mask represented in black. (A) wafer spun with edge beads (blue arrows) (B) Chuck ascends towards mask (C) thick edge bead touches mask first (D) continued ascending, shows edge bead being compressed (yellow arrows) against mask, until the thinnest resist area is contacted for the MA to evaluate the surface.....	77
Figure 8.5 SEM analysis of Az125nxt resist spun at speeds of (A) 1000rpm (B) 3000rpm (C) 4000rpm and (D) EDX analysis of 4000rpm showing resist in red and the silicon wafer in green.....	78
Figure 8.6 Graph to show relationship between Az125nxt resist thickness and spin speed.....	79
Figure 8.7 SEM image of Az125nxt resist spun at 3800rpm to create a resist thickness of 20µm.....	79
Figure 8.8 (A) SEM image showing DRIE etched bevel measuring 17.6°.....	81
Figure 8.9 Schematic process flow showing the bore etch step from the reverse (green arrow) side of the silicon wafer. Silicon wafers are represented in grey, with photoresist masks and silicon oxide shown in red and blue, respectively.....	82

Figure 8.10 Schematic process flow showing (A) the bevel etched wafer is flipped, and mounted onto a carrier wafer by the flat tops (green arrow) (B) Etching the bores through the wafer with no back stop (C) etchant gasses (purple dots) pass into the bevelled space to etch available silicon on the bevel (D) Silicon oxide back stop layer (blue) is used to protect the bevels from etchant gasses.....	83
Figure 8.11 SEM image of bevelled surface with ~8µm of silicon dioxide deposited onto the surface (darker grey area on the perimeter)...	84
Figure 8.12 4-inch bevel etched wafer with a blue adhesive dicing tape layer acting as an aid to provide a vacuum seal.....	85
Figure 8.13 SEM image of bore mask pattern showing a resist thickness of 69µm.....	86
Figure 8.14 SEM image of resist measuring 35µm, after a spin speed of 2500rpm.....	86
Figure 8.15 SEM images of bore pattern development in P1316 developer after (A) 3 minutes (B) 5 minute (C) 7 minutes (D) 9 minutes (E) 11 minutes.....	87
Figure 8.16 Cross section SEM images of bore pattern developed into the resist after (A) 3 minutes (B) 5 minute (C) 7 minutes. Yellow arrow shows the undeveloped curved resist, Green arrow indicates the slanted underdeveloped side wall profile..	89
Figure 8.17 Schematic diagram of 3-phase switched etch, illustrated step-by-step. (1) silicon wafer with resist pattern (2) C ₄ F ₈ deposition protection (3) SF ₆ / O ₂ Plasma etch 1, selectively opening the base area (4) SF ₆ Anisotropic plasma etch 2, creating a single scallop, steps 2-4 are repeated in steps 5,6,7 and 8 to etch deeper into the silicon.....	91
Figure 8.18 SEM images of TSV measuring (A) 1157µm deep and (B) 96µm wide, created by 3-phase (C) scallop etches.....	92
Figure 8.19 (A) SEM images of etched bore from back side of wafer, on flat surface (B) SEM cross section of bore etched through the wafer, emerging on the bevelled surface (C) Microscope image of five bores (yellow arrows) along bevelled surface (red outline depicts bevelled sides, while dashed line highlights the top of the bevels).....	93
Figure 8.20 Schematic process flow showing the shaft reveal etch around the bore. Silicon wafers are represented in grey, with photoresist masks and silicon oxide shown in red and blue, respectively.....	94
Figure 8.21 Schematic diagram demonstrating the spray coating method, of atomising the resist to form droplets that once sprayed onto the silicon wafer, come together to form a uniform layer.....	95
Figure 8.22 SEM image of bevelled surface with spray coated resist layer measuring between 12 - 20µm.....	96
Figure 8.23 Microscope from above bevel surface, with shaft design patterned in resist.....	97
Figure 8.24 SEM images of shaft etching on a flat surface (A) sidewall profile narrows towards the base (B) sidewall profile is >89°	98

Figure 8.25 SEM images shaft pattern on bevelled surface showing (A) side profile of MN (B) front profile of MNs and (C) back profile of MN. Demonstrating the etched wall connecting between MNs. Yellow arrow indicates the original bevel flat top..... 99

Figure 8.26 Diagram to show original alignment marks on (A) the bevel mask (B) bore mask (C) shaft mask and (D) how the cross-alignment marks B and C align to the bevel mask A..... 101

Figure 8.27 Mask aligner optical images of alignment marks that are (A) over developed and (B) underdeveloped..... 102

Figure 8.28 Schematic of bevelled surface (blue) with the alignment of the shaft mask pattern (red) at different positions on the bevel (A) perfect alignment at sharpest bevel point (B) alignment over the flat top of the bevel (yellow arrow) (C) and (D) alignment further towards the base of the bevel creating a shallower angled tipped MN. The green outline depicts the angle of the MN bevel tip created from that alignment..... 103

Figure 8.29, Mask aligner microscope images of shaft mask (outline in red dash box) aligned over a bevel wafer (A) the flat top reflecting light (green arrows) can be observed through the open mask areas (B) the red line showing alignment of the bevel flat to exactly the tip of the MN shaft pattern, while the yellow line shows extended alignment further down the bevel..... 104

Figure 8.30, Microscope images of MN shaft pattern alignment, where the yellow arrow highlights the flat top of the bevels (A) shaft aligned exactly to the top of the bevel, actually patterns onto the flat area, indicated by the orange arrow (B) shaft alignment extended away from the top of the bevel showing correct alignment in the top down orientation (C) orientating the microscope to view the full bevel, shows the shaft pattern from image B is not aligned to the steepest part of the bevel, the red arrows shows the spacing between the MN pattern and the bevel flat top..... 105

Figure 8.31 Schematic diagram of (A) square alignment marks (B) corresponding cross alignment marks C) alignment of how the cross and square marks are paired..... 106

Figure 8.32 SEM image of etched 1 x 5 MN array created from new alignment marks..... 106

Figure 8.33 Schematic diagram of silicon bevelled surface (blue) undergoing etching. The red arrows represent the etchant gasses and yellow area highlights the vertical bevel top. (A) Gasses etching in single direction unable to etch the resist to form the MN shaft (B) Gases etching in multiple directions to target the yellow area (C) if shaft etched out, the multiple etch directions would attach the unprotected silicon below the resist (black). 107

Figure 8.34 SEM images of shaft etching demonstrating the narrow trench (yellow arrow) created along the back of the MNs, from the non-etched steep bevel on either side..... 108

Figure 8.35 SEM images of bevel surface (A) not undercutting the resist mask to create a flat top (B) new design undercutting the resist mask to remove flat area..... 109

Figure 8.36 SEM image of etched MN shaft demonstrating the remaining wall (yellow arrow) and grass produced (red arrow)..... 110

Figure 8.37 SEM image of etched MN shafts, showing SiO ₂ still on the tips (red arrows).....	111
Figure 8.38 Schematic diagram of shaft patterning onto the bevel. The red symbolises the resist shaft pattern after development and should be the only resist to remain on the bevel.....	111
Figure 8.39 SEM image of etched MN shaft demonstrating the remaining wall (yellow arrow) and grass produced (red arrow).....	113
Figure 8.40 SEM images of bevel (A) before and (B) after smoothing process.....	114
Figure 8.41 SEM image of MN shaft etch from a flat wafer, demonstrating the top of the shaft has a rough perimeter due to resist failure (yellow arrow).....	115
Figure 8.42 Microscope image of shaft resist pattern on bevelled surface, demonstrating the centre of the resist is darker than the perimeter.....	116
Figure 8.43 SEM images of NLOF2070 resist on bevelled surface demonstrating concaved resist undercut at (A) 168x and (B) 1.04K magnification.....	116
Figure 8.44 NLOF2070 sidewall response to varying UV dosage and post exposure temperature.....	117
Figure 8.45 SEM images of resist shaft mask patterned onto bevel surface under varying UV exposure dose (A) 600mJ/cm ² (B) 700mJ/cm ² (C) 800mJ/cm ² . Yellow arrow shows resist undercut, red highlights residual rest after development.....	118
Figure 8.46 SEM image of shaft pattern on bevel surface with an exposure dosage of 800mJ/cm ² and development time of 6 minutes showing the resist has undercut sidewall (yellow brace)	119
Figure 8.47 SEM image of shaft pattern on bevel surface with a development time of (A) 3 minutes (B) 5 minutes and (C) 7 minutes.....	120
Figure 9.1 Orientation of silicon crystal planes, cut in (100), (110) and (111) directions.....	122
Figure 9.2 Schematic diagram of KOH etched silicon (a) Characteristic 54.7 ° angle of silicon <100>, (b) Anisotropic etched out-of-plane pyramid MN (14), (c) In-plane MN etched from both sides of silicon wafer. Grey area represents a silicon wafer, black indicates the top and underside of wafer, red dashed line show where 54.7 ° is located and blue demonstrates photoresist.....	123
Figure 9.3 Square mask patterned onto silicon wafer in Az125nxT_10A resist, a proof of concept etch.....	124
Figure 9.4 Image (A) showing reverse alignment marks on the mask being overlaid by the alignment marks on the wafer (good alignment) while (B) shows two pairs of alignment marks misaligned with each other.....	125
Figure 9.5 Cross section microscope image of the silicon wafer with aligned square resist pattern on the front and reverse. The resist has a thickness of 112µm. The red dashed line	

represents where the KOH double-sided etch would ultimately produce the 54.7° angled MN tip.....	126
Figure 9.6 (A) Concentration and temperature dependent etching rate of (100) and (110) plane of crystalline silicon in KOH. The pink line marks which temperature to select for a 44% KOH concentration and 1µm/min etch rate. (B) the concentration and temperature dependent selectivity of (100) silicon with SiO ₂ etched in KOH. Orange line represents 44% KOH selectivity to SiO ₂	127
Figure 9.7 Cross section image of silicon wafer post KOH etch, showing no resist left on the surface and a thickness of 100µm.....	128
Figure 9.8 Ellipsometry results of silicon wafer post CVD oxygen plasma, showing a SiO ₂ thickness of 20304.13A, or 2.04µm.....	129
Figure 9.9 Silicon wafer with a patterned SiO ₂ hard mask. The darker grey areas represent the intact SiO ₂ layer, while the lighter grey is the revealed silicon wafer where square windows in the SiO ₂ layer have been etched.....	130
Figure 9.10 KOH etching of 100 Silicon in 45% KOH solution, pink line indicates that a temperature of 70° etches at approximately 30µm/hour.....	131
Figure 9.11 (A) Cross section of resist mask (red arrows) before SiO ₂ etch (B) cross section of silicon wafer post KOH etch showing misaligned 54° angles (C) Side 1 of wafer that was exposed to the surface showing intact SiO ₂ (D) side 2 of wafer that was submerged in KOH showing the SiO ₂ has been completely etched to expose the silicon wafer beneath (contrasts from the rainbow colours of SiO ₂ and the grey silicon).....	132
Figure 9.12 (A) AutoCAD design of solid MN mask on a 4-inch wafer (B) AutoCAD image of two different MN shapes, blunt tips (left) and pointed tips (right).....	133
Figure 9.13 (A) Cross alignment marks on mask 1 measuring 377, 315, 175 and 140µm (B) corresponding square alignment marks on side 2 (C) alignment of how the cross and square marks are paired.....	134
Figure 9.14 spin parameters of test 1(A) thickness of NLOF2070 resist across a 4-inch wafer measured by ellipsometry (B) image of 4-inch wafer showing strike marks upon spinning.....	136
Figure 9.15 Spin parameter results of test 2 (A) thickness of NLOF2070 resist across a 4" wafer measured by ellipsometry (B) image of 4-inch wafer showing reduced strike marks.....	137
Figure 9.16 Spin parameter results of test 3 (A) thickness of NLOF2070 resist across a 4" wafer measured by ellipsometry (B) image of wafer showing near no strike marks...	138
Figure 9.17 Spin parameter results of test 4 (A) thickness of NLOF2070 resist across a 4" wafer measured by ellipsometry (B) image of 4-inch wafer showing no strike marks..	139
Figure 9.18 4-inch silicon wafer demonstrating resist removal upon development.....	140
Figure 9.19 Schematic diagram of in plane MN photolithography optimisation.....	142

Figure 9.20 development optimisation of alignment marks (A) 10 minute (B) 1.5 minutes (C) 2 minutes (D) 2.5 minutes and (E) 3 minutes.....	145
Figure 9.21 Full optimised wafer, showing MN mask pattern in resist and SiO ₂ between devices.....	145
Figure 9.22 Schematic diagram of a KOH etched MN process flow from the cross section of the shaft of the MN (A) p type double sided polished silicon wafer (B) Silicon dioxide deposition onto both sides (red) (C) photolithography used to pattern device mask on side 1 (blue) (D) device pattern transferred into silicon dioxide hard mask using ICP (E) wafer flipped (F) photolithography used to pattern devices onto backside using alignment marks (G) device pattern transferred into silicon dioxide hard mark using ICP (H) wafer submerged into KOH solution for etching, green dashed lines depicts etching process (I) devices removed from KOH solution once silicon has been etched through.....	147
Figure 9.23 KOH etch of in plane MN at 1-hour intervals for pointed (left) and blunt (right) MN mask designs. A-B 1 hour, C-D 2 hours, E-F 3 hours, G-H 4 hours, I - J 6 hours. Red star indicates where the 80° angle is measured.....	149
Figure 9.24 KOH etched 4-inch MN wafer, held together by connected devices to an outer ring.....	151
Figure 9.25 proof of concept MNs post KOH (A) (100) orientated view of MN measuring height and width at 500µm and 540µm respectively, red outline shows original CAD MN mask (B) proof of angle concept, showing sides of MNs etch to 54.7° (C) wafer cross-section from tip view of MN showing hexagonal etched shape of MN shaft, sides 1 and 4 show the (100) plane from the original CAD mask, while sides 2, 3, 5, and 6 are etched from the (110) planes (D) Schematic images of MNs, blue lines represent original CAD design where the dashed line shows how the tip etch undercuts the mask. Red lines show final etched MN design and how the KOH etches to increase the width and reduce the height from etching the (111) and (100) planes. The numbers correspond to the hexagonal sides of image C. The green area highlights the (110) angled etch, to create a triangle form the 90° sides.....	153
Figure 9.26 SEM images of pointed tipped MN post KOH etching for 4 hours and 40 minutes (A) In-plane view of MN measuring full height at 447µm and width at 505µm. (B) cross section image of MN, demonstrating hexagonal shape and 330µm wafer thickness.....	154
Figure 9.27 KOH etch of blunt MN (A) 5 hours (B) 5.5 hours (C) 6 hours and pointed tip MN (D) 5.5 hours (E) 6 hours.	155
Figure 9.28 Results of variable SiO ₂ mask thickness of KOH etching (A) cross section of MN with two different SiO ₂ thickness on either side of the wafer, the red arrow shows a full protective SiO ₂ coverage, while the blue arrow shows too little coverage and an over etched MN (B) rotating the MN to view the less covered side, shows the etched craters in the device, yellow arrow, due to insufficient SiO ₂ coverage.....	156
Figure 9.29. CAD mask designs of in plane KOH solid MNs of various heights. A-E depict MN arrays where all the MN on a single device are the same height, e.g.	

(A)1500 μ m, (B) 900 μ m (C) 700 μ m, (D) 500 μ m, (E) 300 μ m. F-G show MN arrays where the MN on each device vary in height, (F) MN descend in 100 μ m increments from 1200 μ m to 800 μ m (G) MN descend in 100 μ m increments from 700-300 μ m..... 158

Figure 9.30 SEM images of solid in-plane MN starting at different mask heights after KOH etching (A) mask height of 1500 μ m, KOH height 860 μ m. Blue line shows original CAD MN mask, while green outlines new MN shape (B) mask height of 900 μ m, KOH height 730 μ m, (C) mask height of 700 μ m, KOH height 534 μ m (D) mask height of 500 μ m KOH height 311 μ m, (E) mask height of 300 μ m KOH height 134 μ m (F) tip measuring at an angle of 60°..... 159

Figure 9.31 Schematic diagram of MN devices with different heights penetrating the uneven skin surface to account for body contouring and skin depth differences..... 160

Figure 9.32 Solid KOH etched in plane MNs in descending order from 1200 μ m to 300 μ m, in 100 μ m increments..... 161

Figure 9.33 Relationship between CAD mask MN height design and final KOH etched height163

Figure 9.34 Solid KOH CAD mask designs of MN devices where the arrays are all the same widths (A)100 μ m, (B)200 μ m, (C)300 μ m, (D)400 μ m and MN devices where the arrays decrease either in 100 μ m increments (E)700-300 μ m, or by half (F) 200-25 μ m. 165

Figure 9.35 Solid KOH etched in plane MNs in descending width order from 700, 600, 500, 400, 300, 200, 100, 50, 25 μ m..... 166

Figure 9.36 relationship between CAD mask MN height design and final KOH etched width..... 168

Figure 9.37 Schematic images of MNs with different mask widths (outlined in blue), demonstrating how the (110) planes (outlined in red) intersect to create the tip (yellow star) at different (100) orientated angles (green wedge)..... 168

Figure 9.38 SEM images of MN tip angles, highlighted by green wedge, with varying MN width (A) 700 μ m (B) 600 μ m (C) 500 μ m (D) 400 μ m (E) 300 μ m (F)200 μ m (G) 100 μ m (H) 50 μ m (I) 25 μ m..... 169

Figure 9.39 SEM images of MN showing how MN width influences tip angle (A) 200 μ m width, (B)500 μ m width, (C-D) show schematic images of MNs with increasing widths (outlined in blue), and how the (110) planes (outlined in red) undercut the mask in a convex formation to create a curved corner on wider MN masks..... 171

Figure 9.40 CAD design of MN devices, where the MN pitch spacing varied (A) 500 μ m, (B) 1200 μ m, (C) 1400 μ m, (D) 1700 μ m (E) 2300 μ m..... 173

Figure 10.1 Schematic image of first hollow MN demonstrated by L. Lin and A. Pisano et. al..... 176

Figure 10.2 (A) SEM images of jagged silicon MN created from (111) plane etching (B) different mask designs used to etch silicon MN..... 177

Figure 10.3 Schematic diagram of a MN and its process flow for the cross-section A–A (left figures) and B–B (right figures). (a) diagram of a MN; (b) silicon dioxide deposition and patterning on both sides of a wafer; (c) deep silicon etch on the front side of the wafer; (d) deep silicon etch on the back side of the wafer.....	178
Figure 10.4 AutoCAD designs of solid in-plane MN and (B) Hollow in-plane MN, demonstrating the hollow channel (yellow arrow)	179
Figure 10.5 Schematic diagram showing the characteristics of KOH etching corners when (a) the etch is concaved and (b) the etch is convex.....	180
Figure 10.6 Schematic diagram of hollow channel etched in KOH etch, the shape of the channel is controlled by the width of the photolithography mask design (A) thinner resulting in triangular channels (B) wider mask designs producing trapezoid shaped channels. The red and yellow lines demonstrate how the fixed 54.7° side walls would etch.	181
Figure 10.7 Schematic diagram of KOH etched channel with the rules of trigonometry applied to calculate etch characteristics.....	182
Figure 10.8 autoCAD designs of hollow KOH MNs where the channel measures (A) 100µm wide and 200µm form the MN top (B) 200µm wide and 200µm form the MN top (C) 100µm wide and 100µm form the MN top. (D) demonstrates a whole MN device.....	183
Figure 10.9 Schematic diagram of KOH etching of silicon with a smaller width channel (A) start of etch creating 54.7° (111) side walls undercutting the mask (B) continuation of etch vertically deeper into the silicon (C) final V shaped channel created from 54.7° (111) side walls.....	184
Figure 10.10 SEM images of hollow MN channel with a starting mask of (A-B) 200µm (C-D) 100µm. (B) and (D) are orientated to view down the channel and examine the KOH etched shape.....	185
Figure 10.11 Schematic diagram of KOH etching of silicon with a larger channel. Resist illustrated in (blue). (A) shows the beginning of the 54.7° degree (111) side walls and simultaneous (100) etch. (B) further etching shows expansion in both the (111) and 100) planes, the red dashed line depicts where the previous etch lies to illustrate the difference. (C) continuation of etch deeper into the silicon (D) completion of etch to form a V shaped groove.....	186
Figure 10.12 Schematic diagram of KOH etching of silicon with a smaller width channel (A) start of etch creating 54.7° (111) side walls undercutting the mask (B) continuation of etch vertically deeper into the silicon (C) final V shaped channel created from 54.7° (111) side walls.....	187
Figure 10.13 Schematic diagram of the influence of surface area on KOH etching of silicon with (A) larger channels or (B) smaller channels. Red arrows show (111) plane etching while blue arrows show (100) plane etching. The larger channel in (A) shows that a larger surface area is available for etching compared to (B).....	188

Figure 10.14 SEM images of the end of the MN device demonstrating (110) etched planes creating a funnel at the 90° corners (A) whole device view (V) top-down (10) plane view, yellow and red illustrate the two (110) planes rounding the corners (C) magnification on the (110) etch planes.....	189
Figure 10.15 Schematic diagrams of MN cross section demonstrating (A) a single hollow MN (B) A double hollow MN.....	190
Figure 10.16 Schematic diagrams of closed channel MN ideas (A) cross section of a MN bonded to a piece of silicon creating a single closed channel (B) cross section of two MN devices forming a larger channel (C) view of MN showing the piece of silicon would not form a closed channel on the shaft of the MN (D) view of MN showing two MN bonded together to form a double tipped MN with the channel in the centre.....	191
Figure 10.17 2D (A) and 3D (B) microscope images of MN device surface after KOH etching.....	192
Figure 11.1 (A) Autodesk representation of OOP syringe adaptor, demonstrating the inside hollow tube and funnel connections to direct fluid through the MN (B) OOP syringe adaptor with a 1x5 MN array glued to the top platform.....	196
Figure 11.2 (A) Autodesk diagram looking from the top down the MN, showing the opening to the hollow instead and gluing platform in yellow (B) Autodesk diagram of MN device (grey box) on platform, where the yellow lines show gluing around the device (C) SEM image of MN immersed in glue, attached to platform.....	197
Figure 11.3 Autodesk designs of new out of plane MN adaptor showing (A) the ledge the device is placed upon (B) the 300µm depth connecting to the funnel, blue line.....	198
Figure 11.4 3D printed COC adaptor after heat gun application at 283 degree. The polymer has not moulded around the MN device but instead caused the adaptor to bow and loose its rectangular shape.	198
Figure 11.5 MN adaptor influenced by solder iron heat either (A) to the perimeter of the MN, causing the plastic to turn tacky or (B) applying the heat directly to the MN causing the device to sink into the adaptor. Arrow indicates areas the solder iron touched.....	199
Figure 11.6 (A-B) MN glued to full 3D printed adaptor (C) SEM image magnifying perimeter around MN device with glue application, the red arrow shows the ledge the MN are placed upon, while the yellow shows the opening to allow fluid flow. However, glue has sealed it. (D) SEM image showing MN device not obstructed by adaptor.....	200
Figure 11.7 comparison of (A) out-of-plane MN device (B) IN-plane device base size, demonstrating the surface area available for glue application, yellow arrows.....	201
Figure 11.8 In-plane MN adaptor (A) Autodesk design highlighting the slot in blue (B) top-down view of Autodesk design, demonstrating the opening through the funnel (C) 3D printed adaptor top-down view showing funnel opening (D) Autodesk design showing slot and funnel connection (E) In-plane MN inserted into slot, where top of base and MN protrude upwards.	202
Figure 12.1 Porcine skin with visible skin damage	205

Figure 12.2 methyl blue staining of porcine skin after application of (A) positive control, scalpel showing dye staining (B) adaptor negative control with no MN device bonded, showing no dye staining.	206
Figure 12.3 methyl blue staining of porcine skin upon application of (A) 6x6 silicon out-of-plane MN (B) 1x5 out-of-plane, 5 consecutive times.	207
Figure 12.4 (A) Auto CAD image of MN design measuring 300 μ m wide (yellow arrow) (B) SEM image of MN post KOH etching demonstrating original mask width (yellow arrow) and new larger 460 μ m width (red arrow)	209
Figure 12.5 (A) Auto CAD image of MN design measuring 900 μ m in length (yellow arrow) (B) SEM image of MN post KOH etching demonstrating original mask length (yellow arrow) and new shorter 549 μ m length (red arrow)	210
Figure 12.6 SEM images of MN devices with different height on the same array (A) x2 784 μ m and x2 549 μ m (B) Heights decreasing from 784, 696, 616, 549, 470 μ m post KOH etching.....	211
Figure 12.7 Methyl blue staining of PC MN arrays with (A) 64 MN in 4 (4x4) orientation (B) 16 MNs in 4x4 orientation (C) 1x4 MN rows, with 2mm spacing between.....	212
Figure 13.1 MN applicator device controls the velocity and force by adjusting the pin. Image Courtesy: Joseph Wheeler.....	215
Figure 13.2 SEM images of OOP silicon MN (A) before insertion and after insertion into porcine skin with an applicator force of 4 N and velocity (A) 2357 mm/sec (B) 3367 mm/sec.....	217
Figure 13.3 SEM images of PC MN (A) before testing and after MN applicator device showing tip deformation (B) 4N, 3367 mm/sec (C) 7N, 2862 mm/sec (D) 9N, 1515 mm/sec (E) 9N, 2525 mm/sec (F) 13N, 1683 mm/sec.....	219
Figure 14.1 OCT images of A) human breast skin and B) porcine torso skin without MN treatment. (a) stratum corneum (b) epidermis (c) rete papillary junction (d) dermis (e) cork board (yellow box) hair follicles (blue box) blood vessel.....	222
Figure 14.2 (A-B) OCT images of out-of-plane MNs inserted in human breast skin measuring approximately 400 μ m deep and 189 μ m wide. Yellow box highlights light artifacts, which are not part of the microchannel.	224
Figure 14.3 OCT image of 1 x 5 OOP MN showing all 5 MN have penetrated.....	225
Figure 14.4 OCT image of (A) 6 x 6 OOP MN (B) Broken OOP MN.....	225
Figure 14.5 OCT image of in-plane MNs inserted into porcine skin with pitch spacing of (A) 297 μ m (B) 1019 μ m (C) 1238 μ m (D) 1521 μ m (E) 2086 μ m.....	226
Figure 14.6 OCT image of in-plane MNs inserted into porcine skin with MN width measuring (A) 665 μ m (B) 1586 μ m (C) 460 μ m (D) 378 μ m (E) 295 μ m (F) 252 μ m (G) 225 μ m. Schematic diagram MN with wider (H) and thinner (I) MNs inserted into skin. Red arrow highlight indentation, blue arrows show penetration into the skin.....	228

Figure 14.7 OCT image of in-plane MNs inserted into porcine skin with heights spacing of (A) 1150 μ m (B) 784 μ m (C) 549 μ m (D) 392 μ m (E) 245 μ m (F) 66 μ m.....	230
Figure 14.8 Schematic diagram of (A) short MNs penetrating the skin effectively (B) longer MNs penetrating the skin, but causing the skin to compress between the shafts (shown in orange) (C) longer MNs with larger pitch spacing, reducing skin compression issues.....	231
Figure 14.9 OCT images of PC MN (A-B) in a 4 x 4 array, showing inconsistent indentation (C) 1 x 4 array showing 50% penetration.....	233
Figure 14.10 OCT images of PC MN in situ after insertion with an applicator. Red arrow demonstrates skin between each MN.....	234
Figure 15.1 (A) Graph of out-of-plane MN compression at 0.45mm/sec showing a single MN (orange) 1 x 5 array (black) and 6 x 6 array (green. SEM images of single MN after compression at (B) 10N (C) 20N (D) 100N.....	236
Figure 15.2 Graph to show compression of in-plane MN up to 50N with varying pitch measurements (Blue) 500 μ m (Green) 1200 μ m (Grey) 1400 μ m (Yellow) 1700 μ m (Red) 2300 μ m.....	238
Figure 15.3 SEM image of an exemplar MN, demonstrating that a compression distance of 270 μ m (yellow line) correlates to the MN tip fracturing.....	239
Figure 15.4 Graph showing compression of in-plane MN up to 50N with varying width measurements (Blue) 100 μ m (Grey) 200 μ m (Yellow) 300 μ m (Red) 400 μ m.....	241
Figure 15.5 Graph to show compression of in-plane MN up to 50N, with varying heights of (Blue) 500 μ m (green) 700 μ m (grey) 900 μ m (yellow) 1200 μ m (red) 1500 μ m.....	243
Figure 15.6 Graph to show compression of 4(4 x 4) and 4 x 4 polycarbonate MNs up to 100N of force.....	245
Figure 15.7 SEM images of polycarbonate MN after compression of (A) 10N (B) 50N.....	246
Figure 16.1 1 x 5 MN array bonded to a syringe adaptor showing injection of FITC-insulin.....	247
Figure 16.2 syringe pump and micrometre workstation to aid drug delivery parameters.....	248
Figure 16.3 Fluorescent microscope image of OOP MN microchannel, injected with DIL dye (A) perfect representation image and (B) histological sectioning imperfect	250
Figure 16.4 MB syringe injection through in-plane MNs with (A) single open channel (B) double MN with closed channel.....	250
Figure 16.5 Fluorescent microscopy images of FITC-insulin, injected into porcine skin with (A) closed MN channel (B) single open MN channel (C) Control.....	251

Figure 16.6 SEM images of PC MNs drilled with a 400 μ m drill bit showing (A) misalignment and (B) deformation.....	252
Figure 16.7 SEM images of PC MNs bores created with a computer numerical control tool to show (A) double bore design (B) channel drilled down the side of the MN to direct fluids.....	253
Figure 16.8 images of porcine skin treated with hollow PC MNs to deliver calcein solution (A) before MN removal (B) after MN removal, circles indicating calcein pooling on surface.....	253
Figure 16.9, Schematic diagram of PC MN inserted into porcine skin, indicating that 67% penetration leaves a gap between the MN baseplate and the skin(A) 400 μ m drill bit (red box) used to create a bore (in black) subsequently cuts onto the baseplate. The yellow arrows demonstrate calcein delivery and how it pools into the gap (B) smaller drill bit used, showing how an enclosed bore, closer to the tip of the MN could be formed....	257
Figure 17.1 Schematic diagram of a skin cross section, demonstrating the components of split-thickness and full-thickness skin.....	258
Figure 17.2 Franz cell integrity test set up, demonstrating how resistant probes 1 and 2 enter the donor and receptor chambers, to measure TEER.....	262
Figure 17.3 Bar graph to verify reduction in resistance readings with larger skin manipulation of the SC barrier.....	263
Figure 17.4 Bar chart demonstrating the concentration of calcein obtained from tape strips of Franz cells skin samples after 4 hours, with and without calcein application.....	265
Figure 17.5 demonstrates still intact pig skin after mechanical homogenising using (A) TissueRaptor and (B) GentleMACS methods.....	267
Figure 17.6 Calibration curve of calcein concentration against fluorescence.....	270
Figure 17.7 Cumulative concentration of calcein permeability through porcine skin into a Franz cell receptor.....	272
Figure 17.8 (A) diagram from Zsiko et.al demonstrating drug transport across the skin (B) diagram to show how the stacked bar chart colours align with the permeation profile and the OCED guidelines.....	273
Figure 17.9 Permeation profile of calcein through positive and negative controls.....	274
Figure 17.10 permeation profile of calcein through skin with different thicknesses, with no needle treatment. i.e., negative control.	276
Figure 17.11 Permeation profile of calcein through skin of different thicknesses, that have undergone treatment with a hypodermic needle i.e., positive control.....	277
Figure 17.12 permeation profile of calcein through skin of different thickness's, that have undergone treatment with a polycarbonate MN.....	278
Figure 18.1 Exemplar standard curve used in quantitative analysis of calcein permeation (n=3).....	282

Figure 18.2 Cumulative concentration of calcein permeated through porcine skin without MN treatment control (black) and with treatment of MNs with varying heights of either 300 μ m (blue) or 600 μ m (red).....	283
Figure 18.3 stacked bar graph showing the calcein permeation profile through porcine skin with and without MN treatments of 300 and 600 μ m in length.....	284
Figure 19.1 Standard curve used in quantitative analysis of FITC-HA permeation (n=3).....	290
Figure 19.2 Cumulative concentration of FITC-HA permeated through porcine skin without MN treatment control (black) and with MN treatment (orange).....	291
Figure 19.3 stacked bar graph showing the FITC-HA permeation profile through porcine skin with and without MN treatment.....	291
Figure 19.4 Standard curve used in quantitative analysis of FITC-Insulin permeation.	293
Figure 19.5 Cumulative concentration of FITC-insulin permeated through porcine skin without MN treatment control (black) and with MN treatment (orange).....	294
Figure 19.6 stacked bar graph showing the FITC-insulin permeation profile through porcine skin with and without MN treatment.	295

List of tables

Table 3.1 Advantages and disadvantages to MNs.....	14
Table 7.1: Exemplar raw fluorescent data.....	63
Table 7.2: Dilution factor	63
Table 7.3: Exemplar calibration curve data.....	64
Table 7.4: Subtracting the background fluorescence from raw data provided.....	65
Table 7.5: Calculating the sample concentration from the calibration curve equation...	65
Table 7.6: Calculating the sample concentration by the dilution factor	66
Table 7.7: Calculating the concentration difference between consecutive samples.....	67
Table 7.8 Adding the concentration difference of consecutive samples to form a cumulation curve.....	67
Table 7.9: Flux rate calculations.....	69
Table 8.1. Original photolithography parameters for bevel development.....	75
Table 8.2. Optimised photolithography parameters for bevel development.....	80
Table 8.3. Original photolithography parameters for bore development.....	85
Table 8.4. Optimised photolithography parameters for bore development.....	89
Table 8.5. Original photolithography parameters for resist spray coating.....	95
Table 9.1. Manufacturer’s photolithography parameters for Az125nxt_10A.....	124
Table 9.2 CVD SiO ₂ deposition parameters.....	128
Table 9.3 ICP etch parameters.....	129
Table 9.4 photolithography parameters for NLOF2070.....	139
Table 9.5 Summary of result from in plane MN photolithography optimisation.....	143
Table 9.6 optimised photolithography method for NLOF2070 resist to fabricate in-plane MNs.....	146
Table 9.7 Comparison of KOH MN etch height in relation to starting mask design.....	162
Table 9.8 Comparison of KOH MN etch height in relation to starting mask design.....	167
Table 9.9 Analysis of tip angle with MN of increasing widths.....	170
Table 12.1 Methyl blue staining of MN arrays with varying pitch dimensions.....	207
Table 12.2 Methyl blue staining of MN arrays with varying width dimensions.....	209
Table 12.3 Methyl blue staining of MN arrays with varying height dimensions.....	210

Table 12.4 Methyl blue staining of MN arrays with varying height dimensions on the same array.....	212
Table 12.5 Summary of in-plane MN methyl blue staining results.....	216
Table 13.1 Methyl blue staining of OOP MN arrays aided by applicator insertion.....	216
Table 13.2 Methyl blue staining of PC MN arrays aided by applicator insertion.....	218
Table 14.1 OCT analysis of in-plane MN pitch penetration.....	227
Table 14.2 OCT analysis of in-plane MN with varying width.....	229
Table 14.3 OCT analysis of in-plane MN height penetration.....	229
Table 15.1 SEM images of In-plane MNs of different pitch subjected to forces of 10, 20 and 50N.....	240
Table 15.2 SEM images of In-plane MNs of different widths exerted to forces of 10, 20 and 50N.....	242
Table 15.3 SEM images of In-plane MNs of different heights exerted to forces of 10, 20 and 50N.....	244
Table 17.1 Time dependent digestion of porcine skin samples using enzymes collagenase and papain.....	269

Publications

Olivia Howells, Natasha Rajendran, Sarah McIntyre, Sara Amini-Asl, Pauline Henri, Yufei Liu, Owen Guy, Anthony E. G. Cass, May C. Morris, Sanjiv Sharma. Microneedle Array-Based Platforms for Future Theranostic Applications *ChemBioChem* 2019 **20** (17) <https://doi.org/10.1002/cbic.201900112>

Chris J. W. Bolton, **Olivia Howells**, Gareth J. Blayney, Pey F. Eng, James C. Birchall, Benedetta Gualeni, Kerry Roberts, Huma Ashraf and Owen J. Guy. Hollow Silicon Microneedle Fabrication using Advanced Plasma Etch Technologies for Applications in Transdermal Drug Delivery *LabOnAChip* 2020 **20** (15) DOI: 10.1039/d0lc00567c

Olivia Howells, Gareth J. Blayney, Benedetta Gualeni, James C. Birchall, Pey F. Eng, Huma Ashraf, Sanjiv Sharma, Owen J. Guy Design, fabrication, and characterisation of a silicon microneedle array for transdermal therapeutic delivery using a single step wet etch process *Pharmaceutics and Biopharmaceutics* 2021 Accepted for publication.

Conferences

Hollow Silicon Microneedles for Transdermal Delivery of Insulin. *Microneedles Conference* Poster Presentation 2018. <https://www.microneedles2018.org/>

Awards

Winner: “Outstanding contribution to public engagement” Swansea University 2019

Winner: KESS II “Making Waves” research image competition 2017

Part 1

Introduction and literature review

Chapter 1

Thesis outline

This work describes the fabrication of two novel microneedles with the intention of applying them to transdermal drug delivery. Silicon was the chosen substrate for fabrication due to the ease and cost-effective mass production potential and physical properties meaning it can be easily manipulated into various shapes and sizes. The results of this work are divided into five parts, which are each divided into their subsequent chapters. The thesis layout is as follows:

Part 1- Introduction and literature review

Part 1 is composed of four chapters which review and discuss the relevant literature in terms of transdermal drug delivery, classifying microneedles, the methods used to fabricate silicon microneedles and the applications for which microneedles are currently used.

Part 2- Experimental methodology

This part describes the equipment used and the methods optimised to fabricate and characterise the microneedles ability to penetrate and deliver compounds into skin.

Part 3- Microneedle fabrication

Part 3 describes the fabrication and optimisation of two silicon microneedles from wet and dry etching to form out-of-plane and in-plane microneedles.

Part 4- Characterisation

Microneedles are characterised on their ability to penetrate through the *stratum corneum* and maintain their structure in doing so.

Part 5- *In vitro* drug delivery

Part 5 demonstrates the ability of in-plane microneedles to deliver therapeutic compounds transdermally and outline areas of potential future work.

Chapter 2

Introduction to transdermal drug delivery

2.1 Drug delivery

Transporting a pharmaceutical compound into the body requires a delivery system that enables the therapeutic substance to reach the site of action without stimulating adverse side-effects. Existing therapeutic drug delivery systems aim to administer drugs through different anatomical routes, such as, oral, ocular, nasal, transdermal, sublingual, and pulmonary. Of these the most common route is oral delivery, which represents more than 50% of the market, followed by transmucosal (26.2%) and transdermal (12%) [1].

Although oral delivery is the preferred route of administration due to its non-invasive nature, its ease of use and cost effectiveness, challenges arise with its biocompatibility throughout the gastrointestinal (GI) tract. As the drug moves through various organ environments, i.e. the stomach and intestines, the difference in pH, solubility, membrane permeability and chemical and/or enzymatic degradation, all affect the stability of the drug, reducing its bioavailability before it reaches the targeted site of action [2]. In pharmacokinetic studies, the disposition of a pharmaceutical compound within the body is termed ADME - the absorption, distribution, metabolization and excretion of a molecule [3].

- Absorption: to enable a drug to reach the tissue of interest it must be taken into the bloodstream to transport around the body. However, the factors indicated above, that affect absorption abilities reduce the compounds bioavailability.
- Distribution: ideally 100% of the drug compound would be delivered to the tissue of interest. However, to reach this, the drugs travel through organs, muscles and fats which all subject the drug to numerous distribution processes that consequently lowers the resulting dosage concentration.
- Metabolism: as soon as a foreign substance enters the body, compounds such as liver enzymes, notably cytochromes 450, begin to break down the compounds into metabolites [4] such as, first pass metabolism, whereby the concentration of drug is reduced before it reaches the systemic circulation, which further reduces its bioavailability. However, breaking down the compound into metabolites can

sometimes inactivate the parent drug reducing its effects, while other metabolites can become pharmacologically active, thereby relying on the process of metabolism to increase the compounds effects.

- Excretion: metabolites are removed from the body via excretion through the kidneys (urine), faeces or lungs. The rate of excretion is measured as the amount of substance removed from the plasma per unit of time and is termed clearance. Clearance calculations are used to determine the dose a patient requires, as different patients have difference metabolism and excretion rates, which effect the final bioavailability [5].

As the drug is affected by so many factors, orally administering 100% of the dosage to the site of interest is difficult and often onset of action is slow. Alternative routes of administration, such as, transdermal, or nasal delivery will still undergo metabolism and elimination but will bypass the challenges with the GI tract to administer the compound directly into the systemic circulation to increase bioavailability and onset times.

Transdermal application is favourable for paediatric patients or unconscious and vomiting patients where oral administration is difficult. If the delivery application is via a patch system, the patch is favourable over oral administration in the event of adverse reactions [6] as it can be removed immediately to stop absorption and place the individual in control.

To understand transdermal drug delivery, it is necessary to appreciate how the skin anatomy functions to restrict percutaneous absorption of exogenously administered compounds.

2.2 Skin anatomy

The skin is the most accessible and largest organ of the body with a surface area of approximately 1.7m^2 , comprising 16% of the total body mass of an average person [7]. Its role is to serve as a protective barrier between the external environment and the body against UV radiation, chemicals, dehydration, and allergens or microorganisms that may cause disease and illness. Additionally, it regulates body temperature and communicates the sensations of heat, cold, touch, pressure and pain to the central nervous system, thereby making the skin one of the most complex organs of the body [8]. The structure of the skin is divided into three main sections outlined in figure 2.1 [9], these include:

the outermost layer the epidermis which includes the *stratum corneum* (SC), the middle layer termed the dermis and the most inner layer, the hypodermis, composed of subcutaneous fat.

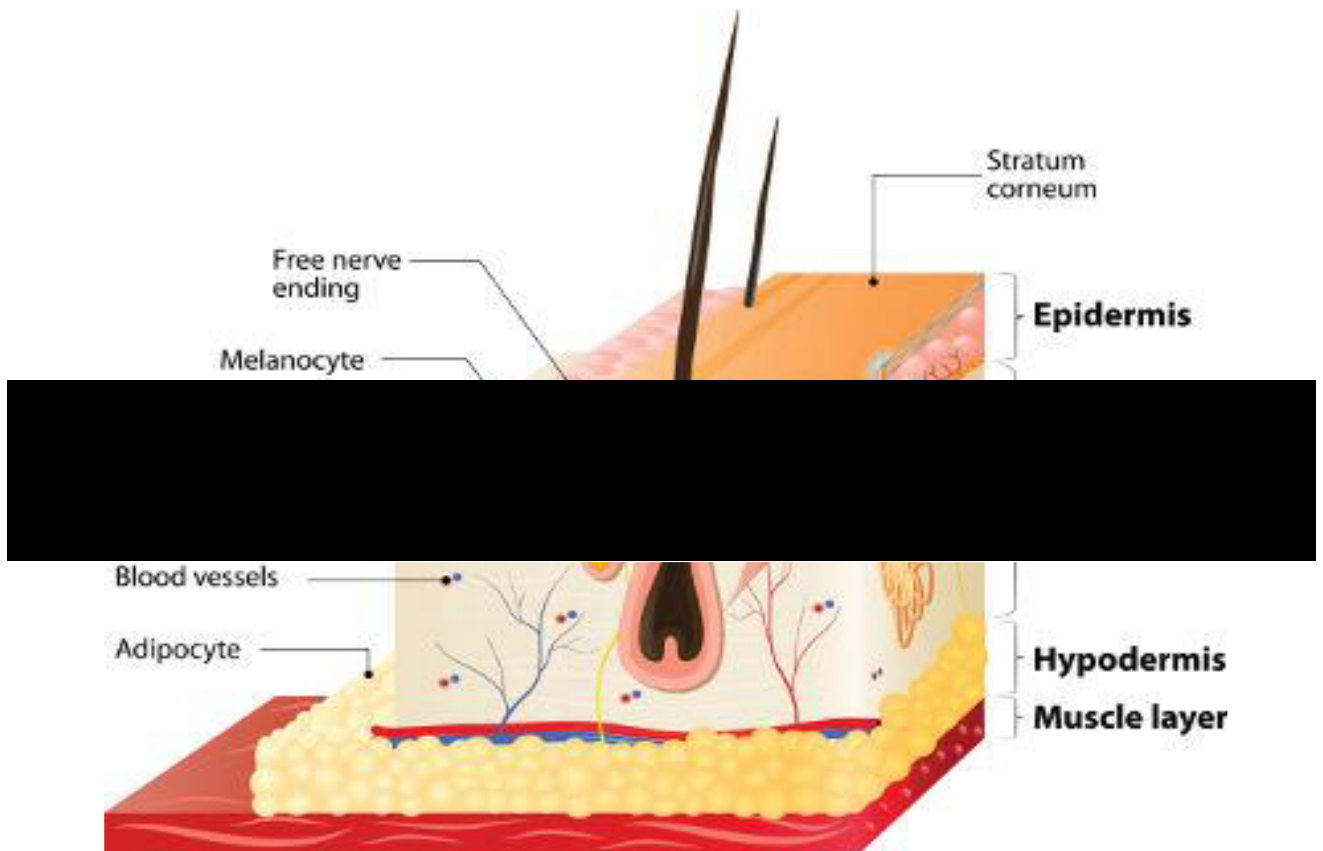


Figure 2.1 The structure of the skin

2.2.1 The epidermis

The epidermis is the outermost layer of the skin and measures approximately 50-800 μ m thick dependent on the anatomical location e.g., eye lids or the palms and soles of the hands and feet. It is comprised of two regions termed the viable and non-viable epidermis; the non-viable regions refer to the SC and the viable region to the layers beneath the SC. The cellular makeup of the epidermis consists predominately of keratinocytes (95%) with other cells including melanocytes, Langerhans cells and Merkel cells [7], [10], [11]. The epidermis is formed from continuous renewal of the keratinocytes maturing and ascending towards the surface. The stages of maturation form the distinct sublayers of the epidermis (figure 2.2 [12]):

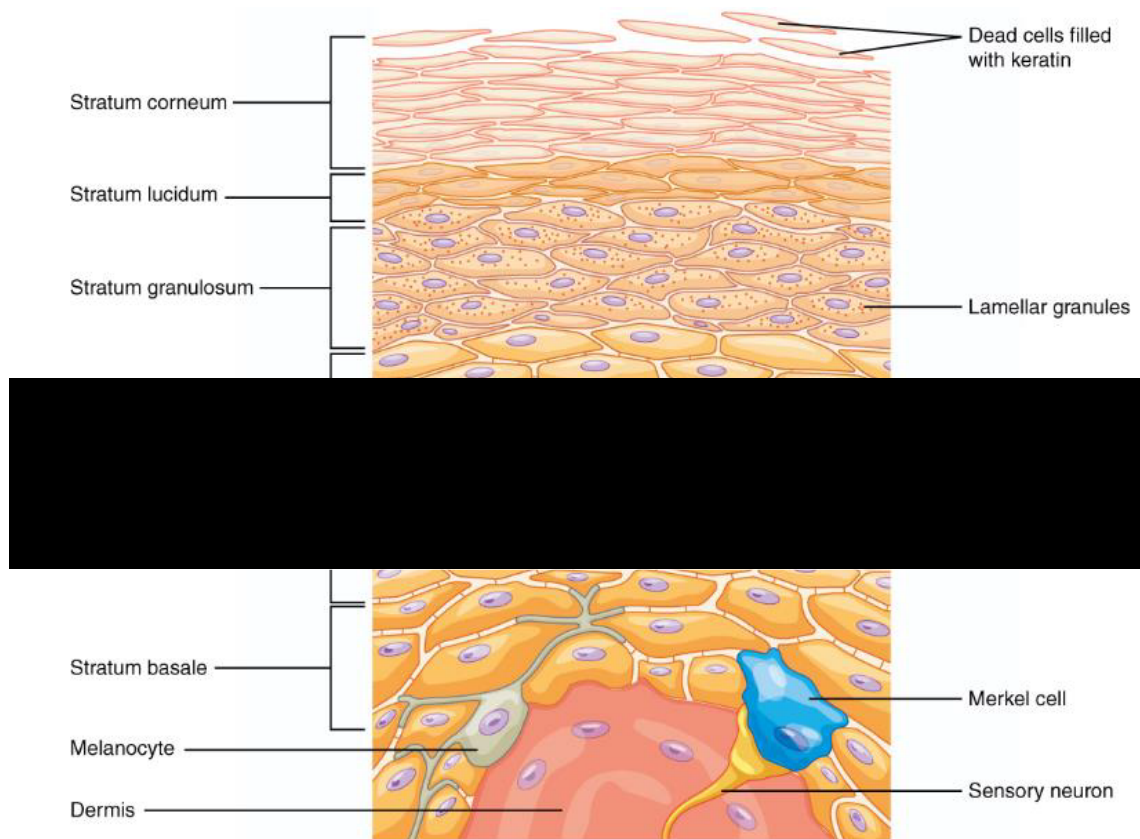


Figure 2.2 The structure of the stratum corneum

- ~ *Stratum Basale*: The deepest layer is composed of a single layer of basal cells that generate keratinocytes; melanocytes, that provide pigmentation are also located here [11].
- ~ *Stratum spinosum*: 10 to 20 layers of newly formed “prickly” shaped keratinocytes.
- ~ *Stratum granulosum*: As the cells mature, they undergo keratinisation, a process that degenerates cell organelles, such as, the nuclei and mitochondria by filling the cells with keratin fibres. Consequently, the cells begin to lose moisture and change shape to become flatter and rounder, contributing to the next 2-4 layers. [13].
- ~ *Stratum lucidum*: Layer of keratinocytes found only in thicker skin areas such as the palms and soles. The cells are densely packed and transparent in appearance [14].
- ~ *Stratum corneum*: the outermost layer is formed from the fully mature dried and harden keratinocytes, now termed corneocytes, that pack together to generate the

barrier function of the skin. These cells are non-viable (non-living) and are constantly renewed from maturation of cells in the lower layers. The cells are packed together to create a “brick and mortar” appearance, where the corneocytes are referred to as the brick, and the lipid by-layer that surrounds the cells is the mortar [15], thereby, making it impermeable to water and hydrophilic substances and prevents desiccation of the underlying tissues [11].

A healthy epidermis asserts a balance between the process of proliferation of keratinocytes and desquamation, that results in a complete epidermal renewal every 28 days [16].

2.2.2 The dermis

The dermis provides the structural support and elasticity to the skin layers and is composed of two regions - the upper papillary layer and the lower reticular layer. The papillary layer, also known as the epidermal dermal junction, segregates the dermis from the epidermis. It is composed of a loose connective tissue that houses nerve fibres and capillaries that provide nutrients to both the epidermis and dermal layers [7]. The lower reticular layer constitutes of a thicker and denser connective tissue, with fewer capillaries and nerve fibres. Overall, the dermis is relatively more hydrophilic than the epidermis, enabling hydrophilic molecules to pass through easily while preventing lipophilic molecules to pass through [17].

Skin appendages such as, hair follicles, sebaceous (oil) glands and sweat glands are located throughout the dermis. The sebaceous glands play a role in lubricating the skins surface and maintaining an acidic pH of ~5; this is termed the acid mantle and acts as a barrier against bacteria, viruses and other contaminants [18].

2.3 Routes of transdermal drug delivery

It is well established that the SC is the principal barrier to the transdermal absorption of exogenous substances, however, there are several routes by which a compound can bypass the SC to gain access into the viable skin layers beneath and thus the systemic circulation. These are either the intracellular route, in which the compound is transported through the corneocytes and keratinocytes cells or the transcellular route,

where the compound moves around the cells through the lipid matrix. The trans-appendageal route involves the passage of compounds via hair follicles and sweat glands. The pathway chosen depends on the physiochemical properties of the permeating compound, with lipophilic and non-polar compounds favouring the transcellular route and hydrophilic and polar compounds favouring the intracellular route [7], [11], [17]. Although this seems simple and each route accommodates most physiochemical properties, crossing the skin barrier is a challenge as each layer of the skin is comprised of different environmental conditions. Thus, a crossing molecule must adhere to each condition in order to partition into multiple hydrophobic and hydrophilic regions.

2.4 Factors affecting transdermal drug delivery

Factors such as age, temperature, ethnicity, disease, skin hydration and application site all cause variation in drug absorbance through the skin.

Age – As skin ages the structure of the skin becomes less robust and the hydration level decreases, losing the moisture content of the skin making it dry and inhabitable for some compounds [19]. Additionally, the blood flow to the skin reduces and lower blood flow in older people suggests that the clearance rates of drugs will be slower which has a negative impact of the drug flux gradient [20].

Temperature – The movement of molecules across the skin is a passive process, thus when the temperature increases, it results in a rise in kinetic energy to the molecule, causing it to move faster [20].

Ethnicity – Transdermal formulations are generally designed for the general population; however, several studies have investigated how skin ethnicity affects drug delivery and identified that permeation across afro-Caribbean skin is often lower compared to Caucasian. It was found that this was due to a lower water content and a greater number of keratinocytes layers within the SC [21]–[26].

Disease – Skin diseases compromise the natural skin barrier of the SC, for example, common diseases such as impetigo, dermatitis and eczema all enhance the permeability of drugs through the layers stimulating an inflammatory response [27] and UV radiation can cause skin burns which reduces the effectiveness of the skin barrier [28].

Anatomical location – The structure of the skin varies between different anatomical sites of the body; thicker skin is found on the soles and palms, due to an additional layer termed the *stratum lucidum*, which makes the skin 13 times thicker in comparison the skin on the eyelids. Whilst it is theorised that thinner skin should enable molecules to permeate easier this is not always the case as some studies have identified similar permeation profiles between different SC thickness and different permeation profile where the SC thickness is similar [29]. Other studies have indeed shown that the permeability does vary between anatomical sites [30], [31]. A hierarchy of permeability for different anatomical location is formed where the genital region is said to have the highest permeability followed by the skin on the head and neck, the chest, stomach and back and lastly the arms then legs [28], [32].

The variation in percutaneous delivery described in this subchapter means experimental analysis must be considerate of the external and internal factors that may inadvertently affect the results. Therefore, to maintain consistency throughout this thesis, all experiments will be conducted in the same manner, to minimise these factors.

2.5 History of transdermal drug delivery

There is evidence that topical remedies have been used for many centuries with practices becoming evident through written records such as clay tablets used by the Sumerians c. 4100-1750 BCE [33] [34], showing use for healing, protective and cosmetic reasons. The advancement of transdermal delivery is also documented in the *Papyrus Ebers* (1550 BC), an Egyptian medical record that documents over 800 prescriptions and 700 drugs for treating skin conditions including burns, blisters, and wounds. One such recipe notes one of the first transdermal delivery of drugs aimed at the systemic circulation; the topical application of frankincense to remove head pain [34]. A whole millennium later, the Greek physician Claudius Galenus, introduced the concept of combining herbal drugs and developed a formula for a cold cream which is similarly used today [35]. An advanced concept that certain drugs can cross the skin barrier was coined by Ibn Dina (980 -1037 AD), a Persian physician known as Avicenna within the western world. His works “The canon of medicine” documents that topical drugs have two states – soft and hard, where the soft part penetrates the skin, and the hard part does not. He further suggested that dermally applied drugs not only

provide local effect but also affect tissues immediately beneath the skin, including the joints and the systemic circulation [36] [37]. Avicenna provided the first physical approach to pharmaceutical knowledge and development in topical and transdermal delivery. Our understanding of transdermal delivery has evolved from topical applications of available compounds to creating new compounds by mixing these together. However, further knowledge has developed through understanding how the skin structure works and how these compounds move to treat illness.

The observation that the skin is relatively permeable to lipid-soluble substances but not to water was discussed by Schwenkenbecker in 1904 [34], which initiated a plethora of research on transdermal delivery of many compounds such as testosterone [38], follicular hormone [39] and nitro-glycerine [40], [41]. From this, in 1907, a US company, Alza Corporation, registered the first patent describing transdermal delivery systems for motion sickness that delivered scopolamine, nitro-glycerine and nicotine [35]. These delivery systems, in the form of a patch, offered several advantages, such as, overcoming the limitation of oral delivery with low bioavailability and vomiting and acted as a non-invasive, reliable means to maintain a constant blood level for over 24 to 72 hrs. Additionally, the patch could be removed at any time which consequently ceases administration quickly. Ten years later, nicotine patches were approved to the market, raising the profile of transdermal delivery in medicine. Now, the growth forecast for the global transdermal market is set to reach \$18 Billion by 2026 [42].

The largest challenge for transdermal delivery is that a limited number of drugs are amenable to administration via this route. Currently there are less than 20 approved transdermal delivery systems for drugs such as oestradiol, lidocaine and testosterone or combination patches that contain more than one drug for contraception and hormone replacement applications [43]. Drug candidates that utilise this route are restricted by their physiochemical properties; Lipinski et al [44] identified that transdermal drug products share physiochemical properties, commonly known as Lipinski's rules, in order to bypass the skin layers; the molecules need to be <500Da in molecular mass, exhibit an octane-water partition of $\log P = 1-3$ to favour lipophilic properties, with a high potency that's enables less than milligrams to be delivered per day [45]–[47]. Therefore, the transdermal administration of hydrophilic and/or large molecular weight compounds such as peptides, provide challenges that need the assistance of penetration enhancement technologies.

2.6 Enhancing transdermal drug delivery

The primary goal of transdermal delivery is to effectively overcome the barrier properties of the SC as this controls what can and cannot pass through the skin.

Technologies that modify the barrier properties of the SC have been trailed; these can be divided into either passive or active methodologies (figure 2.3).

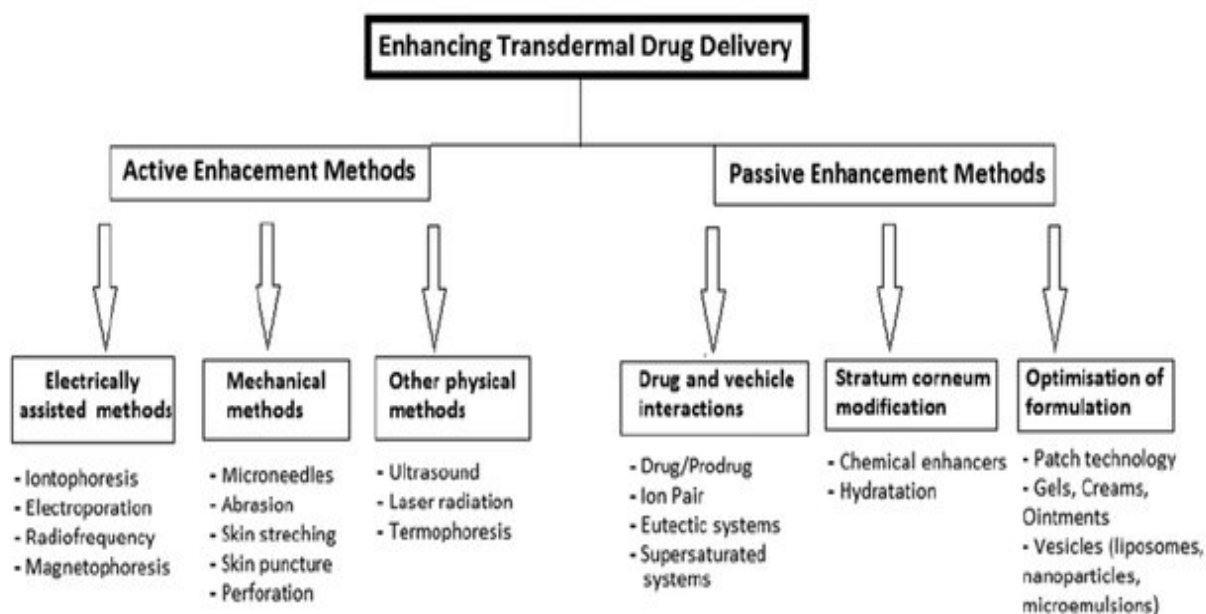


Figure 2.3 Transdermal drug delivery methods of enhancement

Passive methods include the use of chemical enhancers such as carrier vehicles or formulation excipients to either dissolve the SC or increase the solubility of the drug itself. Active methods include a physical driving force to create a pathway, including thermal or electrical assistance and mechanical aids such as, hypodermic needles, tape stripping and microneedles (MNs) [7], [35], [48].

The subject of this thesis focuses on mechanical approaches to enhancing transdermal drug delivery. Traditionally, hypodermic needles are the conventional method of avoiding oral drug administration and utilising the skin to deliver a drug into the body. However injections are painful, can cause bruising and bleeding and in some cases creates needle-phobia in patients, which correlate with non-compliance and avoidance of treatments [49].

Early needle and syringes were originally a single piece of metal that injected the drug via a leather strap. However, these needles were reused and difficult to sanitise.

Therefore, hypodermic needles have evolved into a 2-part disposable device with the syringe composed of plastic and the needle made of stainless steel [50]. The needles come in a range of lengths and gauges that enable delivery into different body compartments, e.g. intramuscular, subcutaneous, and intradermal e.g. the smallest needles available measure 30 gauge and are largely used for insulin administration [50]. To administer hypodermic needles staff require appropriate training and correct disposal measures to ensure that needle-stick injuries, which could cause infection or transmit diseases, are minimised [51].

Microneedles (MNs), the subject of this thesis, are an advancing alternative for pain-free and patient friendly transdermal delivery. A MN is a minimally invasive, micron sized needle like projection, supported on a solid base or patch, that penetrate through the SC [52]. They generally range from 25 μ m to 2000 μ m in height and 50 μ m to 700 μ m base width and are various shapes and designs formed from a variety of fabrication methods. Due to their shorter length in comparison to hypodermic needles, they avoid stimulation of nerves and pressure receptors found in the dermal skin layers and create open microchannels to allow therapeutic compounds to diffuse through without stimulating pain, bleeding or bruising [7].

Chapter 3

Microneedles

3.1 Introduction

Microneedles (MNs) were conceptualised in the 1970's by Gerstel and Place from Alza Corporation, as described in the 1976 US patent [53]. However, the first silicon fabricated MN arrays were reported by Hashmi et al., and inserted intracellular to increase molecular uptake and gene transfection [54]. Shortly after this work, MNs were developed for transdermal delivery applications with the first transdermal proof of concept study published in 1998 by Henry et al. [55]. Due the expansion of fabrication capabilities the authors were able to fabricate a solid silicon MN that increased the permeability of calcein in cadaver skin by a magnitude of four orders. Since then, the trend in MN development for drug delivery application has increased tremendously; a literature search using the key words “microneedle” “transdermal” and “drug delivery” resulted in 753 published papers in the last 5 years alone, figure 3.1 [56].

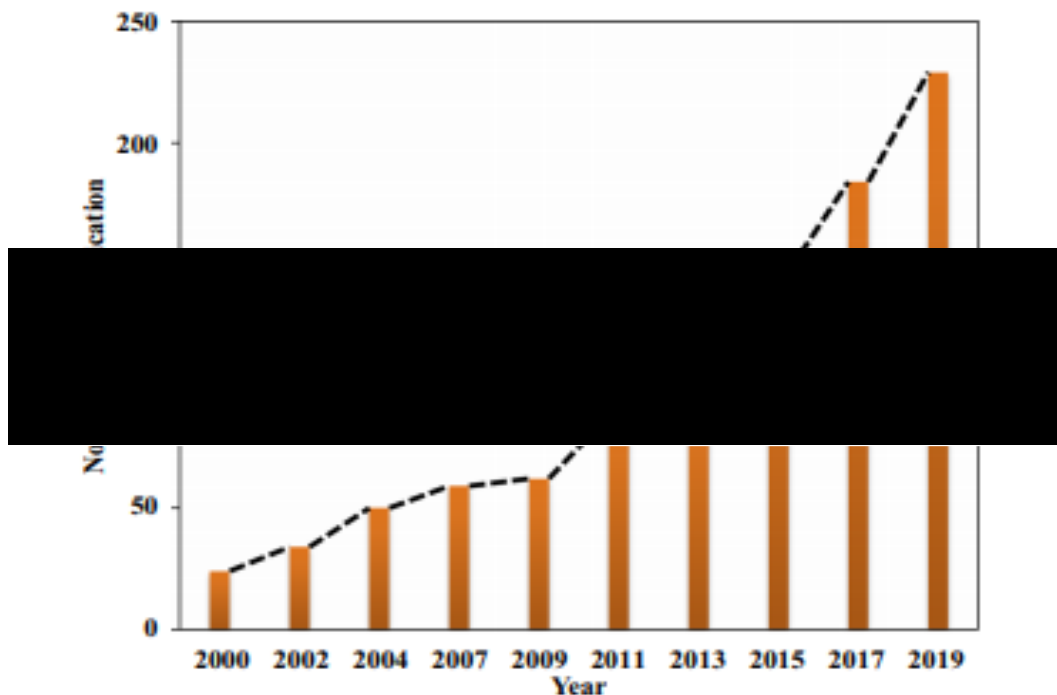


Figure 3.1 Year wise (from 2000- 2019) trend in MN array-based research

3.2 Advantages and disadvantages of microneedles

The advantages of MN's are well established, however it is recognised that there still some drawbacks; table 3.1 provides a summary of the main advantages and disadvantages [48], [50].

Table 3.1 Advantages and disadvantages to microneedles

Advantages	Disadvantages
Painless and non-invasive administration	Dose accuracy maybe less than with an hypodermic needle for larger volumes which require deeper penetration
Administration of large and small molecules	Thickness of SC and other skin layers vary between individuals, so penetration depth could differ
Avoidance of first-pass metabolism	External conditions, such as temperature and hydrate can affect delivery
Injection site healing more rapid than hypodermic injection	Breakage of non-skin-compatible materials left in the skin upon MN removal
Avoids needle phobia and increases patient compliance	Local inflammation or skin irritation could result in sensitive skin
Targeted delivery to specific skin depths and active sites	MNs must be applied to individual instructions, as different MNs have different administration techniques e.g., solid, dissolving, and hollow.
Ease of administration that does not rely on trained personnel, removing a clinical setting	
Targeted drug delivery consequently enhances the drug dosage available for therapeutic action, thus increasing the drugs efficacy. This can result in a dose reduction	
Rate of drug delivery can be controlled	
Reduced dosing frequency for compounds with short half-lives	
Avoids sharp disposal and ability to re-use devices	

3.3 Microneedle classification

MN's are classified according to their function into one of five different types: solid, coated, hollow, dissolving and hydrogel-forming (Figure 3.2 [57]) where each category will have its own advantages and disadvantages.

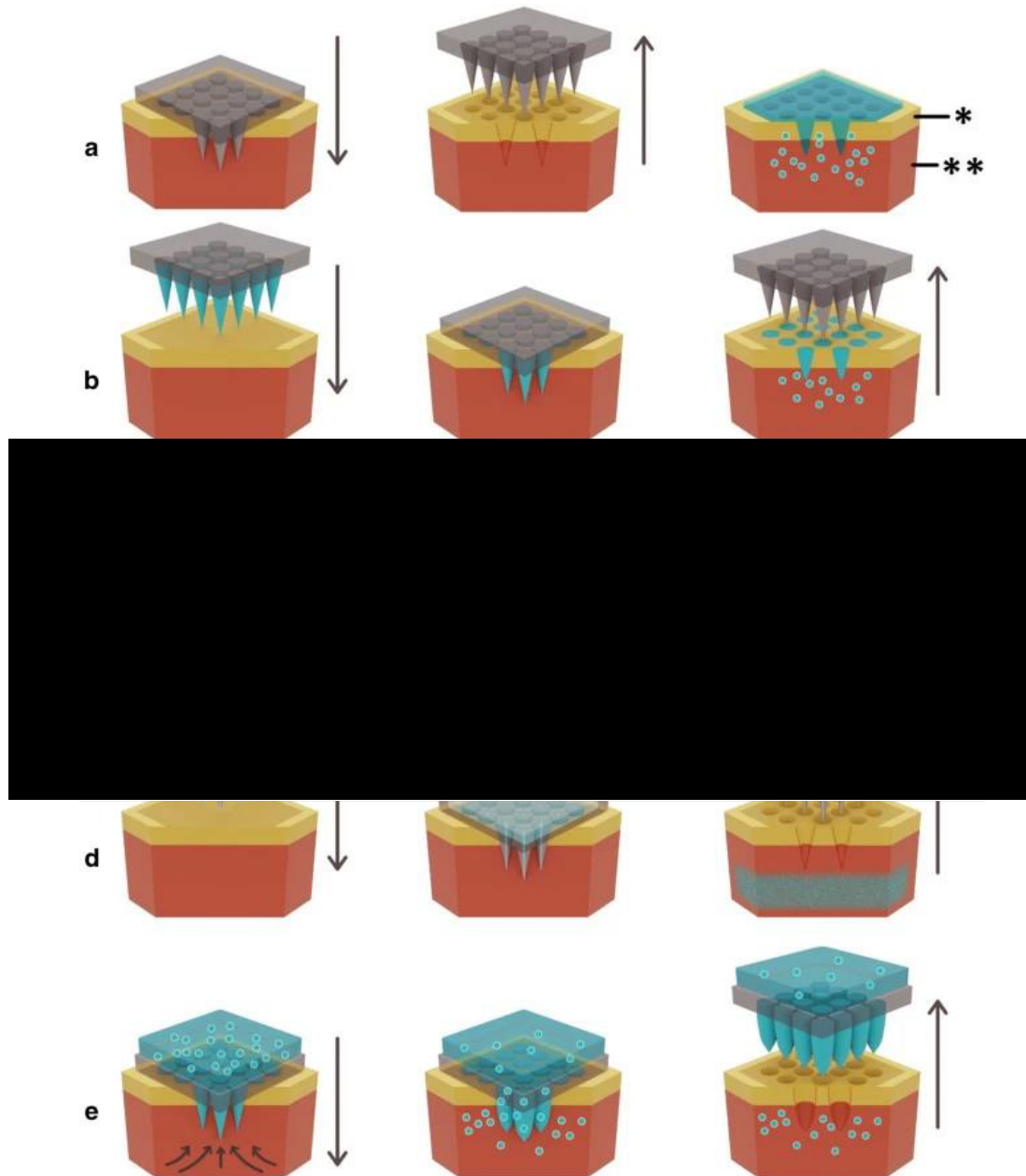


Figure 3.2 Schematic diagram of MN application methods to the skin to enhance transdermal delivery, * SC ** epidermis (A) Solid MNs (B) Coated MNs (C) Dissolving MNs (D) Hollow MNs (E) Hydrogel-forming MNs

3.3.1 Solid MNs

Solid MNs rely upon their structure to transdermally deliver therapeutic compounds. This form of administration is termed “poke and patch”, where the MNs are applied to the skin as a pre-treatment to create pores in the SC, and the drug formulation (patch, gel, or cream) is applied over the pores. Permeation through the pores occurs via passive diffusion to transport the drug into the dermis or systemic circulation [58].

The first transdermal MN study, discussed previously, was conducted using solid silicon MN to investigate the permeability of calcein before and after MN poke and patch treatment. In a follow up study, McAllister et al. [59] introduced a range of compounds including insulin, BSA (bovine serum albumin) and latex nanoparticles measuring 100µm in diameter. These studies were significant as they demonstrated that using MNs the permeability of the skin can be increased by several orders of magnitude to deliver compounds across the SC barrier. However, it was Mohammed et al. [60] who established a link between the molecular weight of the compound and its ability to permeate through the skin. Using a range of cosmetically relevant peptides, Mohammed demonstrated that lower molecular weight compounds showed the greatest transdermal enhancement.

Beyond the fabrication of solid MNs from silicon etching, other technologies have been developed to fabricate solid MNs from other materials such as glass [61], metals [62], [63], maltose [64], and polymers including 3-D printed plastics [65] or polycarbonate [66], to create MNs of various sizes and shapes, that range from octagonal [67], cylindrical [68], rectangular [69], pyramidal [70], conical [71] and quadrangular [64] figure 3.3 [72].

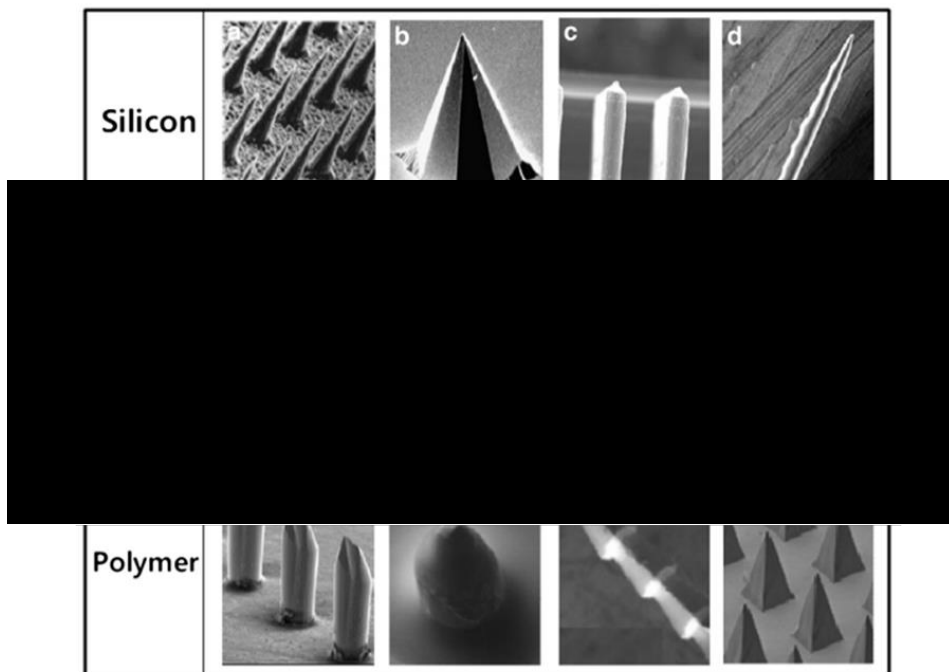


Figure 3.3 Examples of different shaped solid MNs fabricated from silicon, metal and polymer

It is to be expected that the design of the MN used for skin pre-treatment will affect the permeability of the drug compound being tested, for example, Yan et al. [73] studied the effects of MN length (100 – 1100 μ m) and density (400 – 11900 MN/cm²) of solid silicon MNs to deliver acyclovir across the epidermis. There was an approximate 2 – 8-fold increase in acyclovir flux reported with MN lengths of <600 μ m and a 50 – 100-fold increase with longer MNs. Maintaining a MN length of 400 μ m but increasing the density from 200 to 5,625 needles/cm² consequently lowered the enhancement of drug flux across the epidermis. The authors suggested that by applying the same application force to a higher density array then less force will be exerted upon each individual MN resulting in the “bed of nails” effect and a negative impact on penetration abilities.

The first study in humans using solid stainless-steel MNs as a pre-treatment was conducted by Wermeling et al in 2007 [74], to administer 12.6mg/day of naltrexone acting as a model drug. The MN patch was composed of 50 stainless steel MNs with dimensions of 620 μ m in length and a base width of 160 μ m with a tip radius of <1 μ m and applied to six healthy volunteers followed by the drug patch. The results showed that increased plasma concentrations were obtained within 2 hours and maintained over 48 hours. Interestingly, this study also demonstrated that upon administering 12.6

mg/day of naltrexone using the MNs was actually a quarter of the dose administered in an oral tablet and achieved similar plasma levels. This indicated that MN application can significantly improve the delivery of low molecular weight compounds into the systemic circulation without the application of large dosage to compensate for the loss of drug through ADME [74].

Although poke and patch is a simple and easy form of application, it has been reported that the barrier properties of the SC can restore within 2 hours preventing further drug diffusion [75]. To improve delivery occlusive barriers such as, patches or tape have proven to extend the length of time that the pores remain open [76], however, this also leaves the pores more susceptible to infection risk [77]. As research into MN transdermal delivery progressed the need for a two-step application method, pre-treating the skin with MNs and then applying the drug formulation, was considered impractical for patient use so a more straightforward single step application would improve MN efficiency while improving patient adherence.

3.3.2 Coated MNs

To utilise the solid MN and eliminate the two-step application method, a new method approach termed “coat and poke” was created, whereby the surface of the MN was coated with a drug formulation that is released upon skin insertion. This form of application offered a better controlled and efficient route of transdermal delivery than solid MNs alone and had an advantage of a prolonged shelf-life. For example, coating desmopressin (a synthetic peptide hormone) onto MNs maintained a 98% integrity rate after 6 months of storage under nitrogen at ambient conditions [78]. Depending on the formulation used to coat the MNs, different coatings can encapsulate different molecules that vary in physicochemical properties such as, molecular weight, solubility and polarity etc. thereby lending itself to better deliver larger molecular weight compounds [79]. However, the drug dosage coated on the MNs is limited to the surface area of the MN shaft and tip and any coating on the array base is wasted [80]. A solution would be to increase the thickness of the coating on the MN enabling more to be carried into the skin, however, a thicker coating could potentially blunt the tip of the MN and influence its ability to penetrate the skin effectively [81]. Therefore, to use a coated MN, it is important to consider the quality, quantity, uniformity, and

reproducibility of the coating process. Despite this challenge, coated MNs have shown great efficiency for potent therapeutic applications such as vaccinations, where a small dosage is required, for example, Koutsonanos et al. [82] demonstrated that to vaccinate mice with an influenza virus only nano or micrograms were required to trigger an antigen immune response [82][68] [127].

Zosano Pharma, a clinical-stage pharmaceutical company, has developed the first successfully commercially available transdermal MN patch (figure 3.4) composed of titanium micro projections that are dry-coated with a drug formulation which, according to the company, offers “rapid onset, consistent drug delivery, improved ease of use and room-temperature stability” [83]. Its first MN trial tested the delivery of parathyroid hormone (PTH), where patches coated with 30 μ g PTH were applied to various sites of the body, including the abdomen, upper forearm, or thigh, in 30 healthy individuals aged 40 - 85 years old. Encouragingly, irrespective of application site, the patch resulted in rapid peak plasma levels that were achieved three times faster than administration through subcutaneous injection [84]. In phase II, doses of 20, 30 and 40 μ g of PTH were administered to post-menopausal women with osteoporosis and also showed an increase in plasma concentration. Additionally, this study revealed that 98% of the of the formulation remained stable over two years at a consistent temperature of 25°C, [85].



Figure 3.4 Zosano MN patch with applicator device

3.3.3 Dissolving MNs

The structure of a dissolving MN is composed from materials that dissolve upon interaction with the skin's interstitial fluid (ISF). The MNs are inserted into the skin and dissolve away to release the drug compound that is encapsulated within the MNs structure. On completion, it leaves only the base for disposal, avoiding sharps waste and reducing needle stick injuries [58]. Incorporating the drug directly into the MN allows the release rate of the active ingredient to be tailored and modified to suit the application. To date, dissolvable MNs have been produced from a variety of synthetic or natural materials including PLGA poly(lactic-co-glycolic acid) [86], polyvinylpyrrolidone [87], carboxymethylcellulose [88], amylopectin [88], dextrin [89], galactose [90] and maltose [90]. One of the earliest reported dissolvable MN utilises PLGA, an FDA-approved biodegradable polymer, to encapsulate CMC or PLA microparticles that contained calcein or BSA. This study demonstrated successful controlled drug release that ranged from hours to months. However, the authors did note a slight loss of protein activity due to the elevated temperatures required throughout processing [86]. In a follow-up study, processing conditions were revised to prepare MNs from amylopectin and CMC that instead maintained the stability of a model drug through a milder process and *in vitro* drug delivery experiments, even after 2 months of storage at room temperature [91].

One notable research group from Belfast University, under the supervision of Ryan Donnelly, investigated the transdermal delivery possibilities of dissolvable MNs. His group designed and developed a novel water soluble, dissolvable MN from poly(methyl vinyl ether-co-maleic anhydride) known as Gantrez AN®, through micromoulding techniques [92]. The co-polymer was extensively characterised to demonstrate successful skin insertion capabilities and mechanical strength [92], [93], to deliver a variety of hydrophilic, low molecular weight drugs including, caffeine, lidocaine, theophylline and metronidazole [94], [95]. In the case of theophylline for example, the MN demonstrated delivery of 83% of the total dosage through *in vitro* skin testing, over a period of 24 hours. In comparison to a control patch formulation, it demonstrated a detectable level after 5 minutes, rather than 4 hours [92]. To investigate the delivery capabilities for larger molecular weight compounds, the same MN formulation was analysed to deliver Insulin *in vivo* to rat models. The results demonstrated a dose-dependent hypoglycaemic effect and highlighted the challenges of macromolecular

delivery, for example, the administration dose is restricted to the loading capabilities of the MN [96].

3.3.4 Hollow MNs

By mimicking hypodermic needles, a hollow MN administers a drug formulation through a bore, once the MN has been inserted into the skin; this approach is termed “poke and flow”. As the drug formulation is administered after MN insertion, this method enables a more rapid rate of delivery that does not require the drug formulation to be adapted or altered such as, for coated MNs. However, fabricating hollow MNs relies on a complex, multi-step method [7]; to deliver the drug formulation the MN must be attached to a drug reservoir, where passive diffusion enables the formulation to move into the skin tissue. However, as the bore opening diameter is small, diffusivity into dense tissue is slow and impractical for rapid treatments or administration of larger dosage loads. To control the rate of drug delivery the MNs can be attached to other reservoirs that actively push the drug into the skin at controlled rates, such as, a syringe or micropump [97].

Hollow MN have an inherently weaker structure, in comparison to solid MNs, as a portion of the MN is removed from the shaft to accommodate the hollow bore. Additionally, the placement of the bore on the MN influences tip sharpness, for example, a cone shaped MN with a central bore means the sharp tip could be removed influencing penetration abilities. To overcome this Griss et al, [98] designed several different MNs where the bore opened along the sides of the shaft enabling the tip to stay intact and remain sharp (figure 3.5 A and B [98]). However, penetration experiments were not fruitful, leading the authors to redesign the MN shaft into a cylindrical column rather than square (figure 3.5 C); this created a new ultra-sharp tip that successfully produced penetration results into human skin. However, upon testing liquid delivery leakage onto the skin was observed, due to the high flow rates and only small amounts of liquid could be delivered suggesting further studies on flow are required.

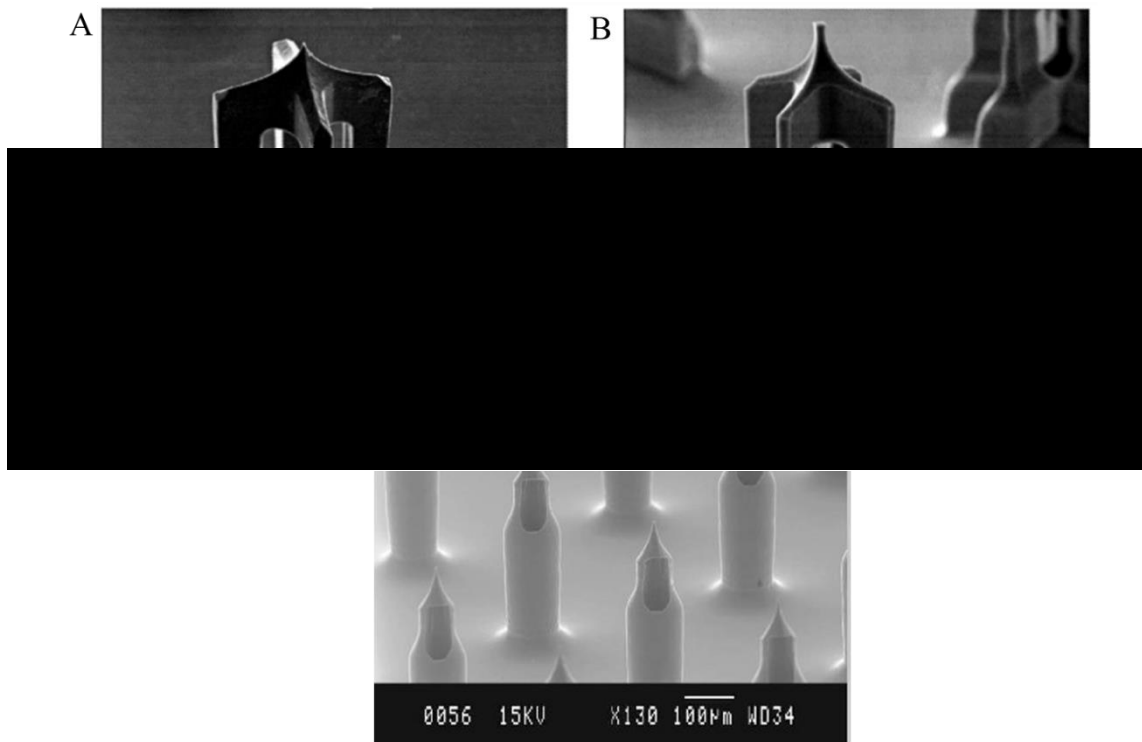


Figure 3.5 Hollow microneedles with side opened bores, changes in process flow enable (A) full shaft length bore (B) half shaft length bores or (C) Cylindrical shafts

Glass MNs (figure 3.6), were analysed in a study by Maranto et al. [99] to establish the rate-limiting barriers to hollow MN flow where the bore was slightly off the tip of the MN. Sulforhodamine was used as a model drug and inserted into cadaver skin; initially the study determined a slow flow rate of 15-96 μ l/h and suggested the dense dermal tissue was compressing during MN insertion and blocking the bore opening. To resolve this, once the MN was fully inserted, the MN was partially retracted to controlled distances to relieve the compression forces and allow the fluid to flow into the open cavity. This increased the flow rate 11.6-fold. To confirm that it was tissue compression that prevented the flow, they also injected the enzyme hyaluronidase alongside sulforhodamine into skin tissue. Hyaluronidase works by breaking down hyaluronic acids within the skin collagen fibres, therefore, if the skin was causing a blockage and preventing the flow rate, hyaluronidase would remove this tissue and open a cavity for the formulation to flow into. Including hyaluronidase into the injection formulation further increased the flow rate x7, supporting the hypothesis that the dense tissue limited the flow.

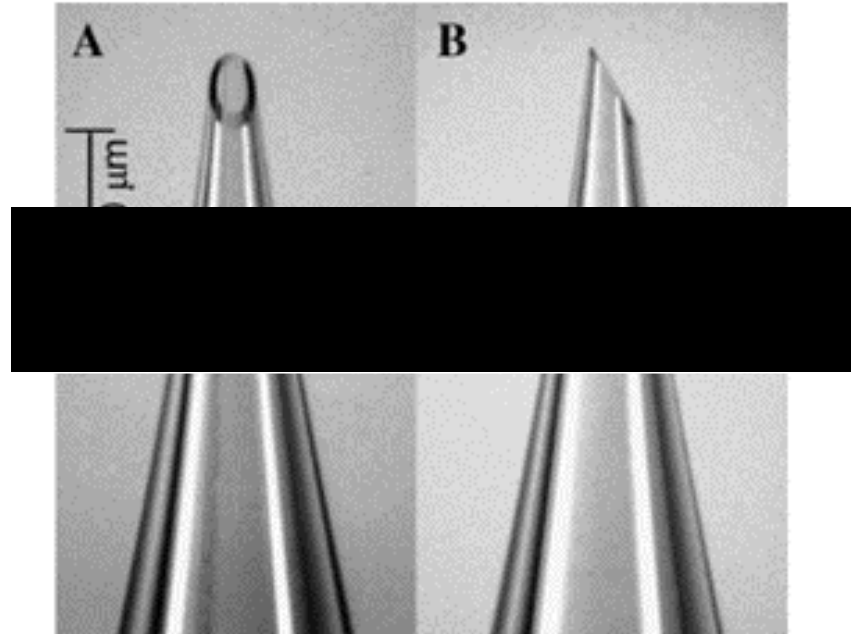


Figure 3.6 Hollow glass microneedles

Despite the potential issues of clogging, hollow MNs have shown promising results to deliver a variety of substances, for example, Vinaya Kumar et al. [100] developed a 300 μ m long hollow stainless-steel MN to deliver insulin into diabetic rats. By attaching the MN to a peristaltic pump, insulin was successfully diffused into the skin to decrease blood glucose level to normal level after 5 hours. This was also reported by McAllister et al, where they delivered of up to 32 μ l of insulin into diabetic rats over a 30 minute period using the glass MNs, again, producing a drop in blood glucose levels over a 5 hour period [45].

Another study by Pamornpathomkil et al. [102] demonstrated the use of hollow silicon MNs fabricated from NanoPass technologies, and marketed as MicronJet™ (figure 3.7 [103]), for the delivery of nanocarriers filled with plasmid DNA vaccine coding ovalbumin for skin immunisation. It concluded that the MNs were able to enhance the permeation of plasmid DNA vaccine coding ovalbumin into skin to induce a strong immunoglobulin G immune response without causing infection or pinpoint bleeding.



Figure 3.7 Hollow silicon MNs marketed as MicroJet™ from NanoPass

Although hollow MN infusion has been demonstrated in the microlitre range, the MNs fabricated by 3M are designed to infuse larger volumes up to 1.5mls [99]. The fully-integrated device was designed for patient self-application and consists of twelve 1500µm polymeric MNs, that are attached to a glass vial which holds the drug formulation (figure 3.8 A [104]). The MN device has shown promise in delivering a range of materials such as, small molecule salt protein models and model monoclonal antibodies and established its pharmacokinetic profiles and bioavailability to be similar to that of subcutaneous injections [45]. The 3M MN design has caught much attention and is undergoing clinical trials with several partners, for instance, Radius Health Inc is trialling the 3M hMTS device for novel biotherapeutics such as, abaloparatide, a parathyroid hormone-related protein analogue drug, for the treating post-menopausal women with osteoporosis [105]. In addition, Panacea Pharmaceuticals is investigating a therapeutic cancer vaccine with the aim to deliver 1ml directly into the dermis [106]. Many other hollow MN devices on the market replicate hypodermic needle applications rather than a MN patch, as a single MN is injected at the end of a loaded reservoir, for example, BD Soluvia (figure 3.8 B [107]) for the administration of influenza vaccinations and the DebioJect (Figure 3.8 C [108]), the commercial product of the MNs in figure 3.8 C.

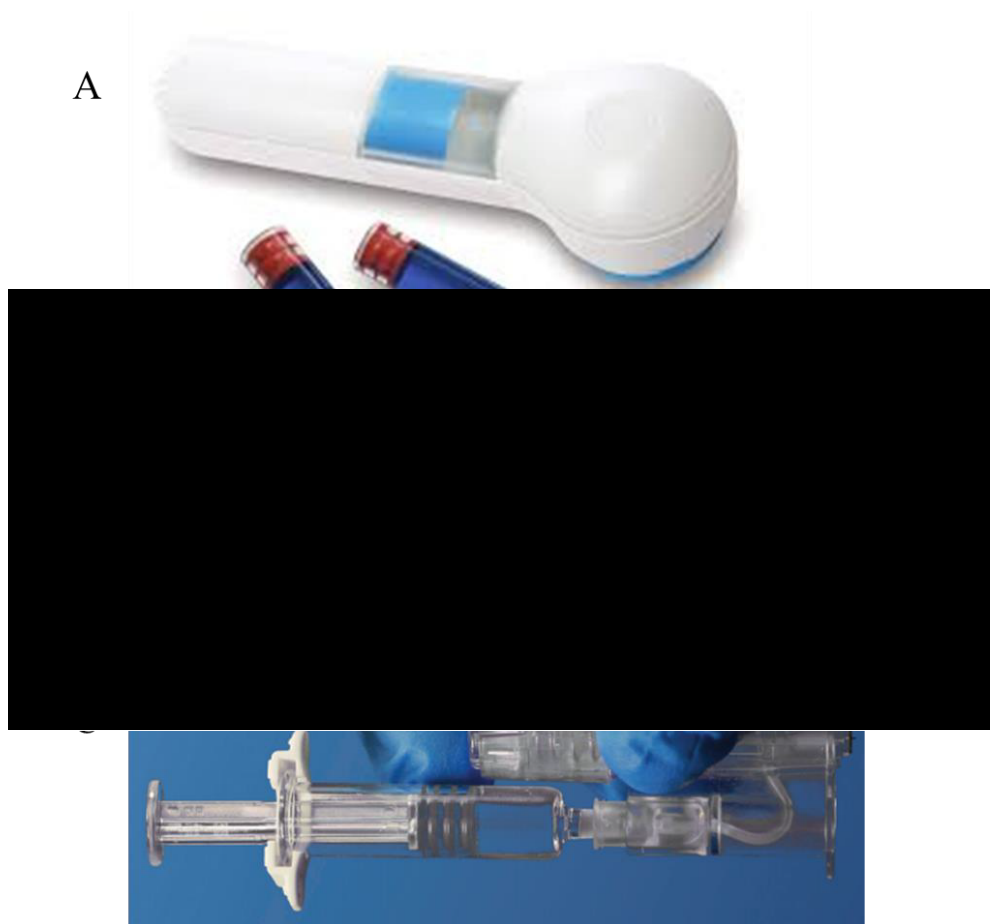


Figure 3.8 Commercial hollow MN devices (A) 3M (B) Soluvia MicroJect (C) DebioJect

3.3.5 Hydrogel-forming MNs

Hydrogel-forming MNs were established by Donnelly et al in 2012 [109]. The concept involves a MN fabricated from a hydrogel polymer, that in the dry state forms a sharp, robust tip and shaft that can penetrate through the SC. Upon penetration, the hydrogel swells and opens the polymer crosslinks within the structure, enabling any drug formulation either encapsulated within or in a separate drug reservoir, to be released at a controlled rate [110]. A key important feature to hydrogel delivery is that upon removal the MN leaves no polymer residue within the skin and the MNs cannot be reused, removing challenges with pin prick injuries and contamination. Additionally, these MN can be easily sterilised and resist problems with hole closure as the MNs stay in place throughout delivery [111].

The first hydrogel MNs were manufactured from heating two aqueous polymers namely PMVE/MA and poly(ethyleneglycol) (PEG), to induce esterification and form crosslinks between the chains [109]. To deliver the drug, a drug loaded adhesive patch

was placed on the reverse of the patch, that upon insertion, enables the drug to move through the opened crosslinks and into the skin (figure 3.9 [109]).

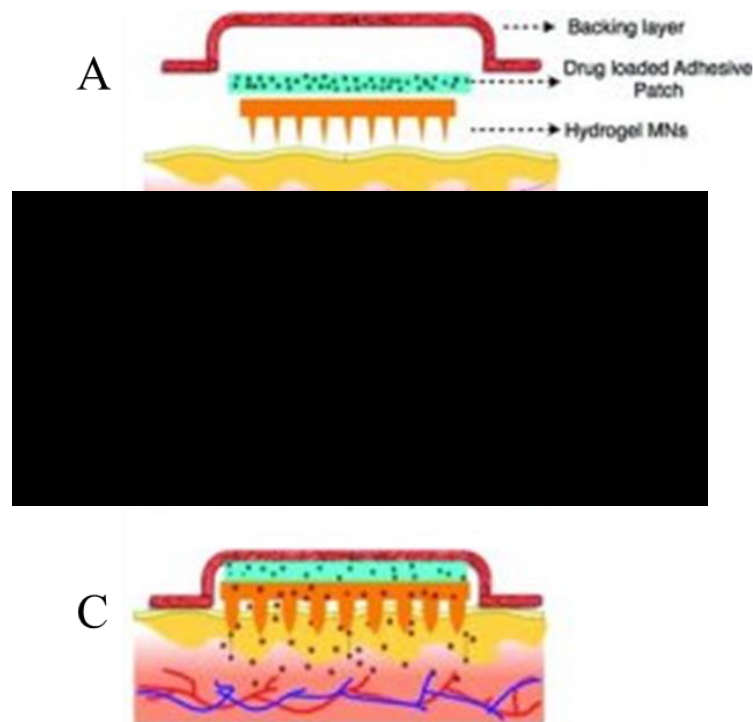


Figure 3.9 Schematic diagram of hydrogel forming MN (A) demonstrating how the MN patch is arranged (B) application of MN into skin and ISF moving into the MNs (C) MN swelling and releasing drug into the skin

Since the first report in 2012, other hydrogel based MNs have been created, which instead of a drug reservoir, incorporated the drug within the MN structure itself. For example Yang et al. [112] created a MN patch from polyvinyl alcohol (PVA) solution, dextran and CMC, that incorporated the drug in the tip of the MN and was cross-linked and solidified by a freeze-thawing processes. To examine the release kinetics, *in vitro* Franz cell analysis of insulin release was conducted. The test concluded that 30% of the insulin load was released within the initial 30 seconds, followed by an additional 26% within 4 hours of application, successfully demonstrating the feasibility of PVA hydrogel MNs. Although these results are promising, as the drug is impregnated within the hydrogel MN structure rather than an external reservoir, there is a limit to the dosage of drug that can be administered as this depends on the loading capacity of the MN patch.

Hydrogel MNs have shown to successfully deliver a number of molecules that vary in molecular weight and hydrophilicity, such as, small molecules like caffeine, theophylline, metronidazole [109], methotrexate [113], esketamine [114] and metformin hydrochloride [115] or larger molecules such as peptides and proteins including insulin, vancomycin [116] and fluorescein isothiocyanate labelled BSA [109]. The first high molecular weight molecule to be delivered in hydrogel formed MNs, was published by Courtenay et al. [117] for the delivery of a therapeutic monoclonal antibody Avastin®, for the treatment of cancer. However, due to its high molecular weight, a large volume of drug was trapped within the cross-linked network of the hydrogel. Administering Avastin® *in vivo*, also found it drained into the lymphatic system, thereby suggesting that hydrogel MNs could be used to target cancer metastases within the lymphatic system.

3.4 Microneedle structure

In addition to being classified by their drug delivery method, MNs can be further categorised into out-of-plane (OOP) or in-plane orientation, depending on the fabrication method. OOP MNs are fabricated so their shaft lengths are perpendicular to the substrate, (figure 3.10 A [118]), while in-plane MNs shaft lengths are in parallel to the substrate (figure 3.10 B [118]).

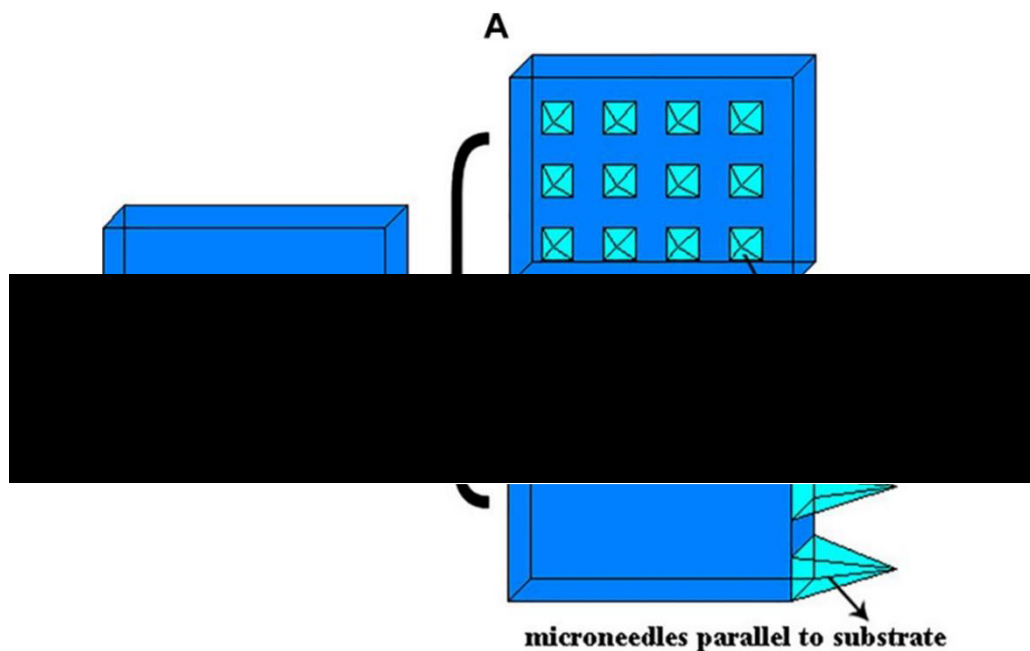


Figure 3.10 Schematic diagram of (A) OOP MNs and (B) IN-plane MN

OOP is the most common fabrication orientation, as manufacturing steps are simple and cost effective, however, fabrication in this orientation places a restriction on the aspect ratios i.e., the length and width of the MNs that can be created. In comparison in-plane MN fabrication is not restricted by aspect ratios and can be easily fabricated to any aspect ratio and incorporated into microfluidic chips. However, in-plane MN's fabrication is constrained by the density of the MN array i.e. the number of MNs that can be supplied onto a single device [118]. To increase the density of the array in-plane MNs can be stacked together to incorporate both in-plane and OOP properties as shown in figure 3.11 [119].

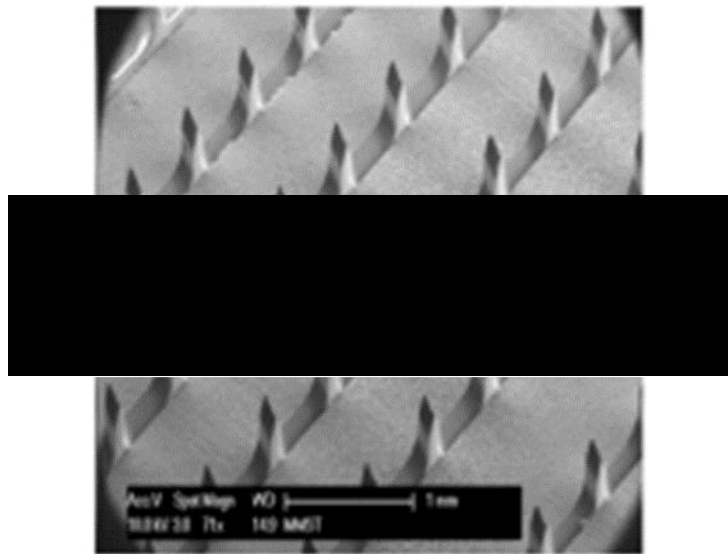


Figure 3.11 MNs fabricated in in-plane orientations and stacked together to produce OOP characteristics.

Koutsonanos et al. [120] demonstrated that solid in-plane metal MNs could improve the delivery of an inactivated influenza vaccine labelled with a fluorescent dye into mice, to stimulate a broad spectrum of immune responses in the spleen, lungs and draining lymph node that induced the production of virus-specific memory B-cells. In addition, MNs immunisation showed a dose-sparing effect when compared to intramuscular immunisation. Although solid MN have shown promising results, as discussed, hollow MNs offer more advantages for transdermal drug delivery, however, their fabrication methods are more complex.

To transform in-plane MNs from solid to hollow, Seung-Joon Paik et.al [121] used silicon wafers to create buried microchannels through anisotropic DRIE (deep reactive

ion etching), sidewall passivation and isotropic etching, while the MN shafts were etched in two steps via deep silicon etching (figure 3.12 A). The devices were then combined with a microfluidic chip to demonstrate fluid flow with rhodamine B into rabbit ear skin. The same research group later published an improved hollow in-plane MN fabrication method [122], this time simplifying the process and lowering costs with wet etching potassium hydroxide (KOH) (figure 3.12 B). Firstly, a 10 μ m wide, 50 μ m deep microchannel was DRIE etched along the shaft of the MN and into a microfluidic chip interface, then the second step created the MN around the microchannel to establish a single bevelled 200 μ m wide and 2000 μ m long MN, that aligned to the vertical (110) silicon plane. A further paper was published on a fully optimised KOH only process that used a six step process to produce six solid MNs with geometrically different MN tips (figure 3.12 C), and a nine step process to integrate a microfluidic channel using simultaneous front and back side silicon (110) KOH etching [123] that simplified the fabrication process and avoided the costs of DRIE etching. However, due to the vertical (111) side wall profile, the tips of the MNs were not sharp and instead produced blunt “ledges” measuring the thickness of the wafer.

The latest in-plane MN technologies were fabricated from Yan Li et.al in 2019 from DRIE etching to produce an open capillary microfluidic network rather than delivery. Nonetheless, the resulting wedged shape MN (figure 3.12 D) was not sharp enough to penetrate the skin and therefore, including a second wet etching process was incorporated to sharpen the tip to successfully penetrate porcine skin [124].

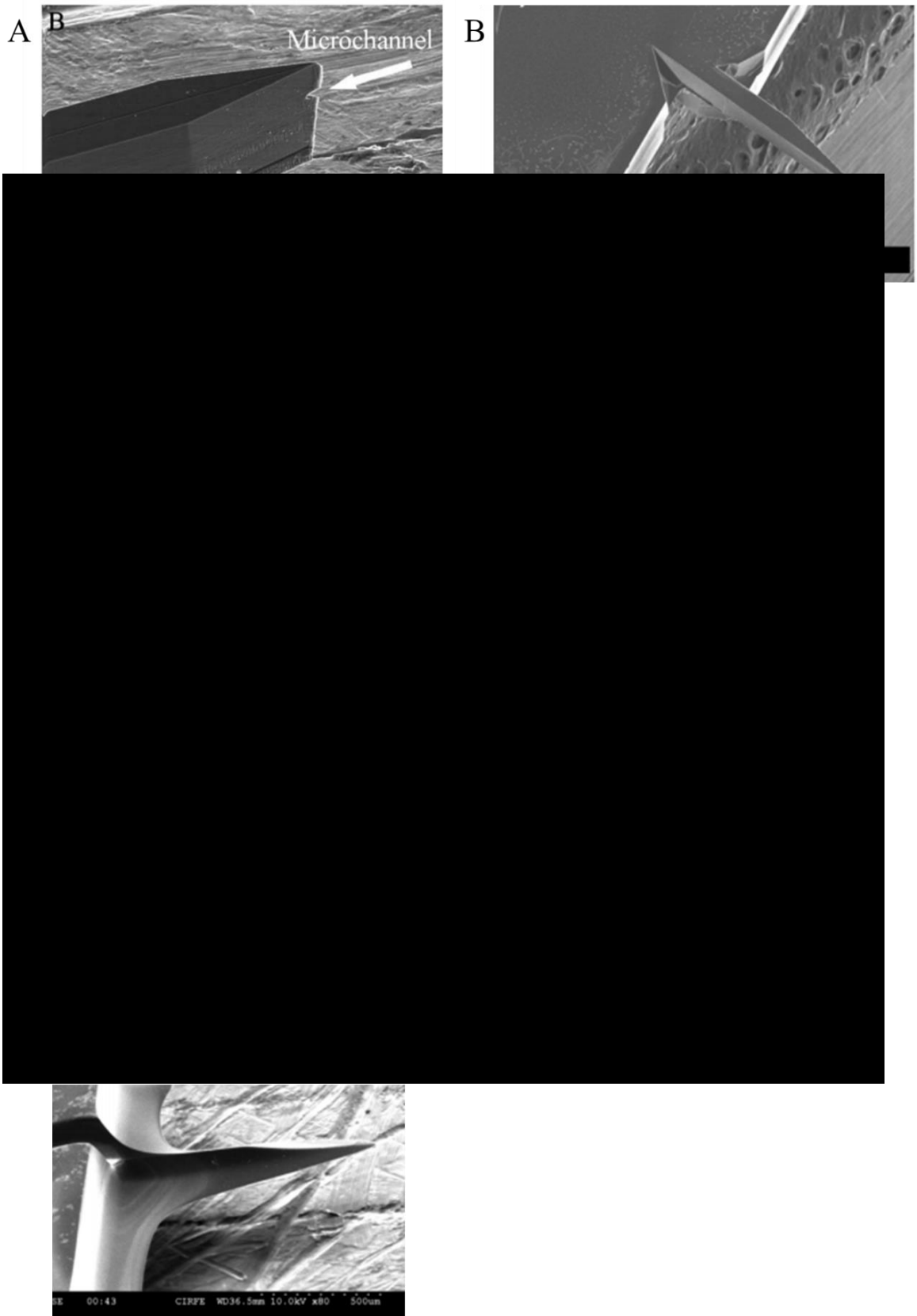


Figure 3.12 in-plane hollow MNs (A) DRIE etching (B) DRIE and wet etching (C) Wet etching to produce 6 different designs (D) DRIE and wet etching

Chapter 4

Silicon microneedle manufacture methods

4.1 Introduction

With the advancement of the latest microfabrication technologies, MNs can now be fabricated in a range of designs from a variety of materials such as silicon, metals, glass, ceramics, sugars, and polymers etc. However, the fabrication of MNs using silicon wafers is the main focus of this thesis and thus will be discussed in the following chapter.

4.2 Silicon

The first MN created was fabricated from silicon in the 1990s to produce OOP anisotropic pyramids [55]. The metalloid properties of silicon makes it a desirable material in the field of microstructures and microelectromechanical systems (MEMS) for its natural semiconductor nature [125]. The crystalline structure of silicon is similar to that of a diamond lattice where 8 atoms form a repeating cubic lattice pattern. Dependent on the orientation at which the silicon lattice is cut, different planes can be exposed which occupy different properties; common orientations are (111), (100), and (110) and are defined by the Miller index [126]. A further in-depth description can be found in chapter 9, with in-plane MN fabrication.

The versatile monocrystalline or polycrystalline structure of silicon enables various shaped and sized MN to be fabricated along a batch production line, however, the fabrication cost is high with multiple manufacturing processes and there are concerns over its biocompatibility. In addition, as silicon is a brittle material there are concerns with the MN breaking upon insertion and leaving silicon fragments in the skin [125]. Although, owing to the normal turnover of the epidermis, any broken fragments are likely to be removed naturally within four weeks [127].

4.3 Silicon MN manufacturing methods

Silicon MNs are primarily fabricated using MEMS (micro-electromechanical system) technology which was originally designed to create integrated circuits, however, its ability to form small 3-D structures in the sub-micrometre range made it attractive for MN production. A MEMS process involves three basic techniques: photolithography mask patterning, deposition of thin films on the substrate and selective etching of the films to produce the mask into the substrate.

4.3.1 Photolithography

Photolithography is a technique used to transfer a pattern in the form of a mask onto the silicon wafer substrate using photosensitive resist coatings. The process was originally adapted from traditional lithography ink printing, but instead uses an UV light source to change the properties of a photoresist coating that acts as a mask. A photoresist is composed of:

- ~ the polymer, a solid organic material that changes its solubility upon exposure to UV light,
- ~ a solvent used to thin the photoresist to the desired thickness,
- ~ sensitisers

and

- ~ additives used to control the reaction of the resist under UV light.

Varying the dosage of UV light will adjust the solubility of the resist which affects the final mask design [128]. The type of resist used will also determine if a reverse mask can be produced, these include positive or negative photoresists (figure 4.1). Upon exposure to UV light the chemical bonds within the positive photoresist are weakened, causing the resist to become soluble and any exposed areas will be removed in the development stage thereby, forming an exact copy of the mask on the silicon substrate. A negative photoresist is simply the reverse, where the UV exposed areas become less soluble and the chemical bonds strengthen making it more difficult to remove the exposed areas in comparison to the non-exposed. Upon development the resulting substrate image is the inverse of the original [129].

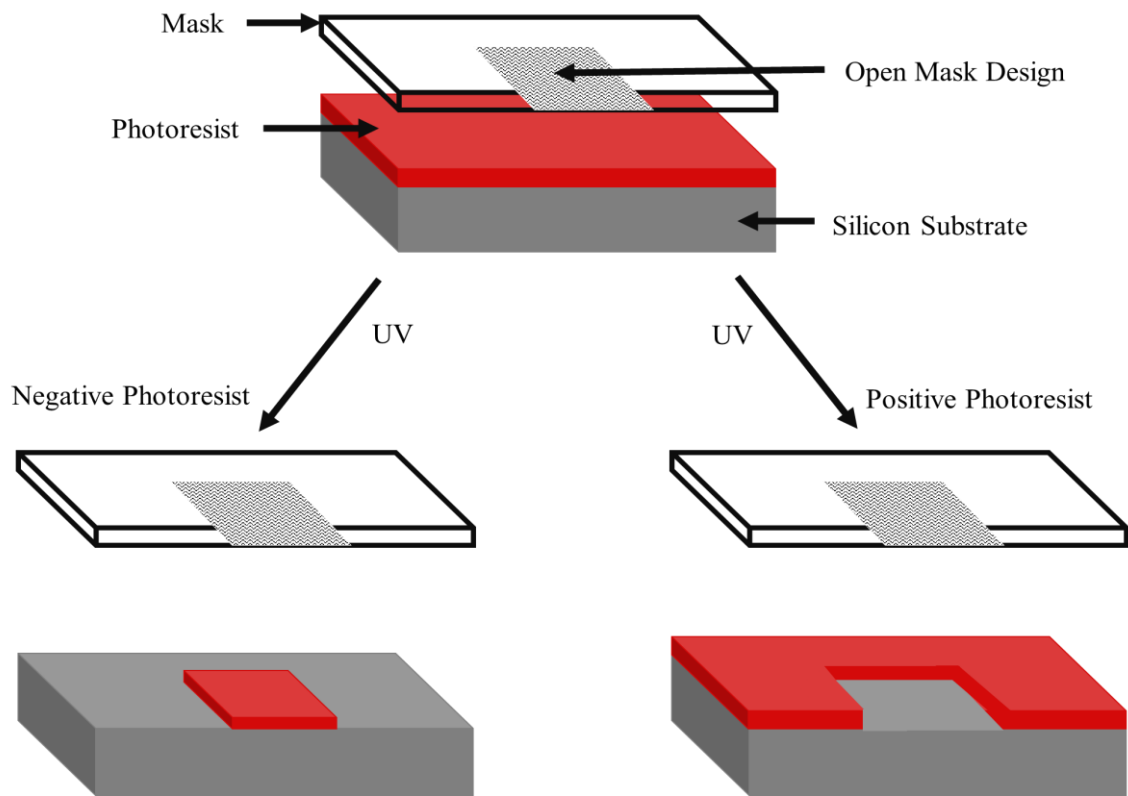


Figure 4.1 Schematic diagram of positive and negative photoresist after UV exposure

To apply the resist onto the silicon substrate and form a uniform coating two techniques can be used, either spin coating or spray coating. Spin coating is used when the substrate is a flat uniform surface; the photoresist is dispensed onto the substrate and spun at high speeds and the centripetal force and surface tension of the resist drive the resist to spread evenly over the substrate. The depth of the final resist coating can be modified by altering the speed i.e. the faster the spin speed then the thinner the coating produced and vice versa [130]. If the surface of the substrate is non-uniform, then applying the resist via spin coating would not allow a uniform layer to form.

Alternatively, the spray coating method coats the substrate by atomising the photoresist into a fine spray, with droplet sizes in the μm range, that land on the substrate and amalgamate into a film. To cover the substrate the spray coater arm scans over the substrate back and forth, this can be programmed to modify the final thickness of the photoresist layer [131], this is discussed further in chapter 8.6 table 8.5.

4.3.2 Thin-film deposition

Thin-film deposition is the process of applying a very thin layer of material, typically a few nanometres to micrometres, onto the surface of a substrate. These films can then be patterned using photolithography techniques. Common films include silicon dioxide and nitride oxide and present a higher etching selectivity in comparison to resist films [132]. This means that as the silicon wafer is etched into the design patterned from the mask, the film layer will protect the silicon beneath by only etching a small portion in comparison to any silicon exposed. These films are termed “hard masks”. Alternatively, a “soft mask” is described when the mask design is patterned into the resist alone. Resist has a lower selectivity in comparison to oxide or nitride, meaning that the resist will etch away faster than the subsequent hard masks.

To deposit the film, two categories of systems can be used, either chemical vapour deposition (CVD) or physical vapour deposition (PVD). The distinguishing feature between each is the composition of the deposition vapour. With PVD the vapour is constructed of atoms and molecules that simply condense onto the substrate within a vacuum and thickens over time. The CVD vapour undergoes a chemical reaction between the vapour and the substrate to form the film layer on the sample surface; the chemical composition of the reaction and physical structure can be tailored by regulating the process parameters such as temperature, input concentration, pressure, and gas flow rates [133].

4.3.3 Silicon etching

Following photolithography, the substrate undergoes etching processes to form the final MN shape. In general, there are two etching processes termed wet and dry etching. To wet etch the substrate is immersed into a liquid bath of the chemical etchant and left until the process is complete. The concentration, temperature and volume of the solution all control the speed of etching. However, the final MN shape is controlled by the mask design and the orientation of the silicon wafer.

Dependant on the etchant chemical used, the substrate can undergo either isotropic or anisotropic etching. An isotropic etch is when the chemical etchant attacks the substrate at the same rate from all directions [134]. This means the etchant can undercut the mask design as demonstrated in figure 4.2. Alternatively, anisotropic wet etching etches the silicon substrate at different rates due to the different index planes, for example, silicon (100) etches at an angle of 54.7° from the surface to expose the (111) planes which have a different electron density than the (100) planes, and thus etch at a different rate, additionally avoiding any undercutting of the mask, figure 4.2. Etchants used for isotropic etching include hydrofluoric and nitric acids while potassium hydroxide (KOH) or tetramethyl ammonium hydroxide (TMAH) is used for anisotropic etching [134].

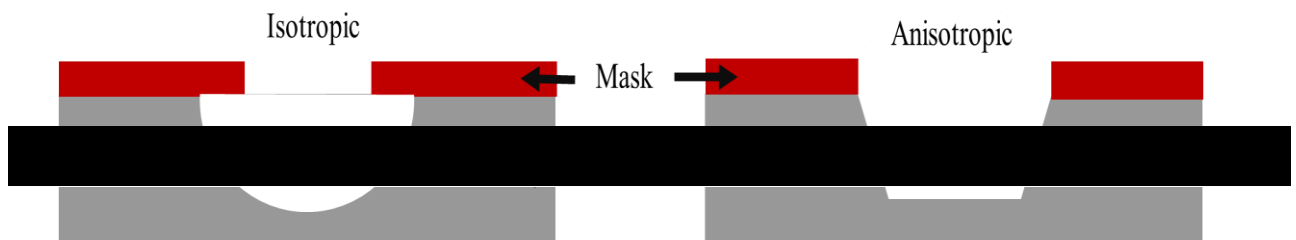


Figure 4.2 Schematic diagram isotropic and anisotropic wet chemical etching

Dry etching is a physical process which utilises gases pumped into a vacuum chamber. This thesis uses dry etching in the form of reactive ion etching (RIE); here a plasma is formed over the substrate and is accelerated towards it using a potential difference. The plasma particles bombard the sample surface causing it to selectively react with the silicon to form a waste product that is pumped away. The etching process can be tailored to etch isotropically or anisotropically by fine tuning the parameters of the equipment used, demonstrated in the OOP fabrication chapter 8. However, to create MN bores or TSV (through silicon vias) through the wafer, deep RIE (DRIE) processes which combine CVD and RIE are applied. This type of etch is termed a BOSCH etch and can form completely anisotropic tunnels as demonstrated in figure 4.3 [135] through thick silicon wafers. Further explanation is found in the OOP fabrication chapter 9.

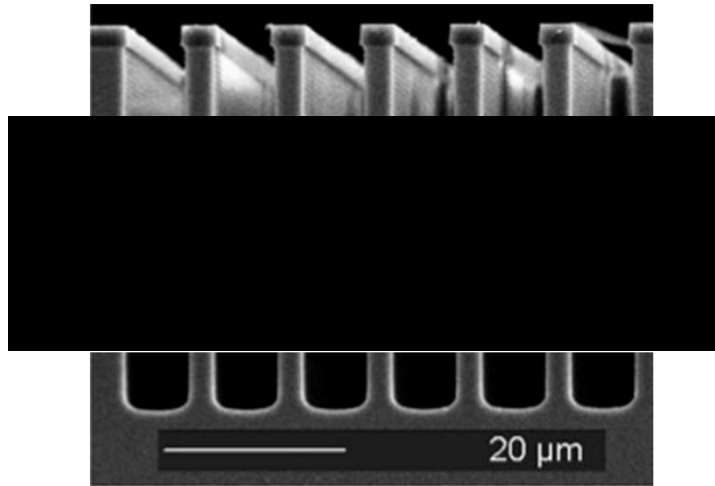


Figure 4.3 SEM image of TSV fabricated from BOSCH etch processes

4.4 Silicon MNs in the literature

Mark Prausnitz's research group, at the Georgia Institute of Technology, Atlanta, USA, was the first research group to publish the fabrication of solid silicon MN using RIE dry etch processes protected by a chromium layer that had been patterned with dots, to protect the silicon below and form MN spears (figure 4.4 [136]). Under experimental analysis they found that the MN tips were very sharp from measuring $<1\mu\text{m}$ in diameter and upon human skin penetration tests, 95% of the MN array successfully pierced to increase the permeability of calcein by four orders of magnitude [136].

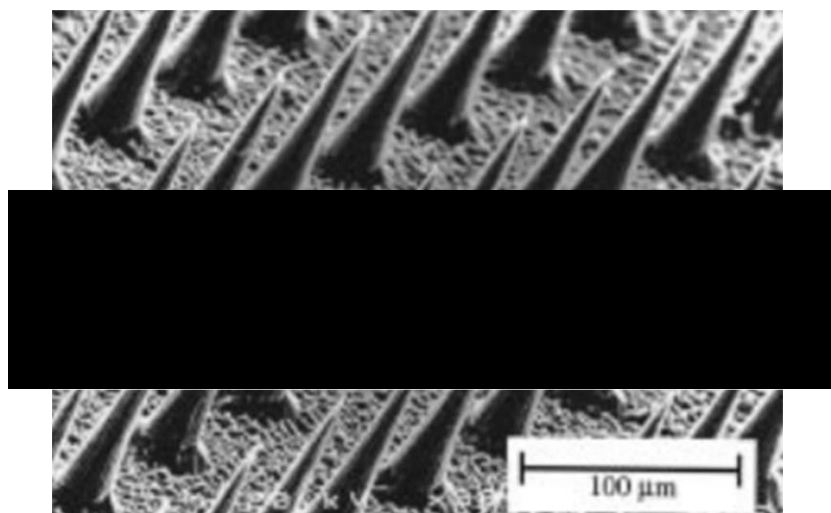


Figure 4.4 SEM image of MNs fabricated from RIE techniques

Several research groups have since adopted and adapted Prausnitz microfabrication methods to create MNs of different shapes and sizes with various delivery methods. For example, Li et al [137], adapted the solid MNs above into hollow MNs by including a BOSCH etch through the reverse of the wafer (figure 4.5 A); next the wafer is flipped and an anisotropic etch was used to create a pillar around the hollow bore. To sharpen the tip of the MN and open the bore, isotropic etching was used to produce the final MN shown in figure 4.5 B.

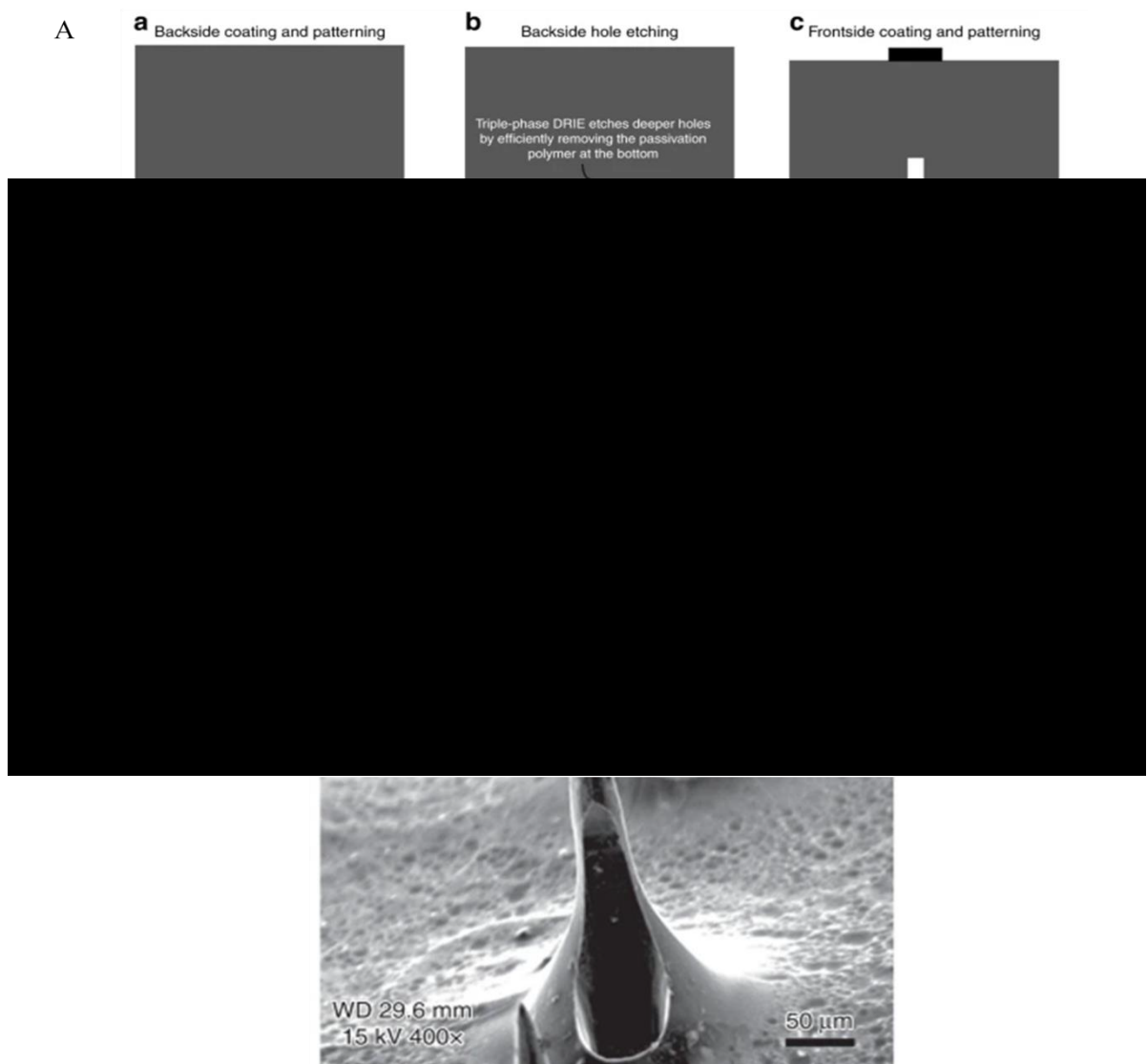


Figure 4.5 (A) Schematic fabrication process of silicon hollow MN arrays from dry etching (B) SEM image of resulting MN

A more complex fabrication process was demonstrated by Roxhets group from the Royal Institute of Technology, Sweden [138], which changed the overall shape of the hollow MN. Again, the BOSCH etch was applied first to etch the hollow bore through the reverse of the wafer, followed by the MN shape etched around the bore from the front side of the wafer. A combination of isotropic and anisotropic dry etching was used to create the tip and shaft separately, while increasing the length of the MN (figure 4.6 [138], [139]).

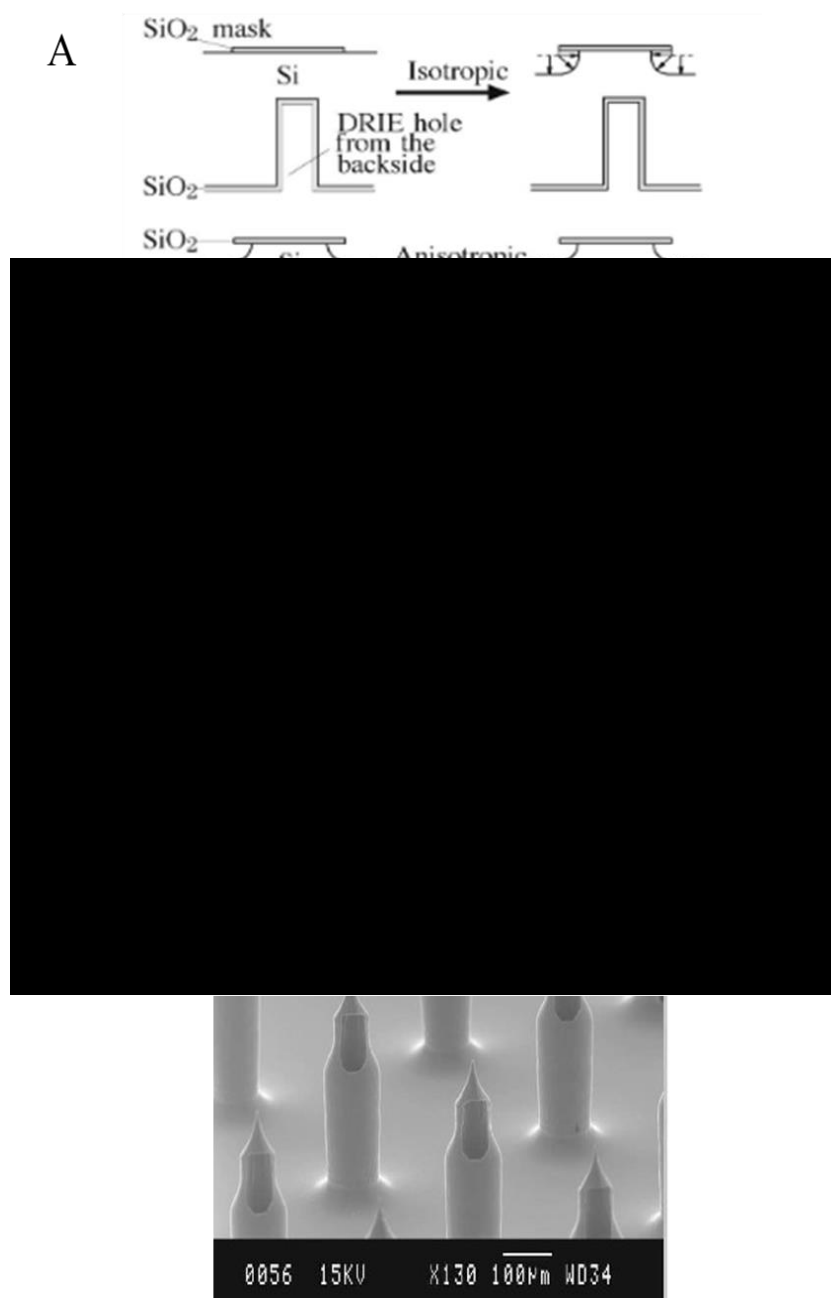




Figure 4.6 (A) Process flow of side-opened bore MNs (B) SEM image of MN

As dry etching can be an expensive fabrication method, wet etching can be used as an alternative, however, the MNs produced are much simpler in structure. Morrissey's research group at the Tyndall National Institute in Cork, Ireland fabricated solid silicon MN using wet etching processes (figure 4.7 A) [140].

A

	Side View	Process step
1		LPCVD, 350Å pad oxide and 1000Å nitride double layer on silicon
2		Plasma etch to pattern mask

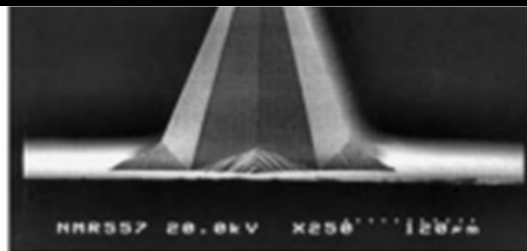
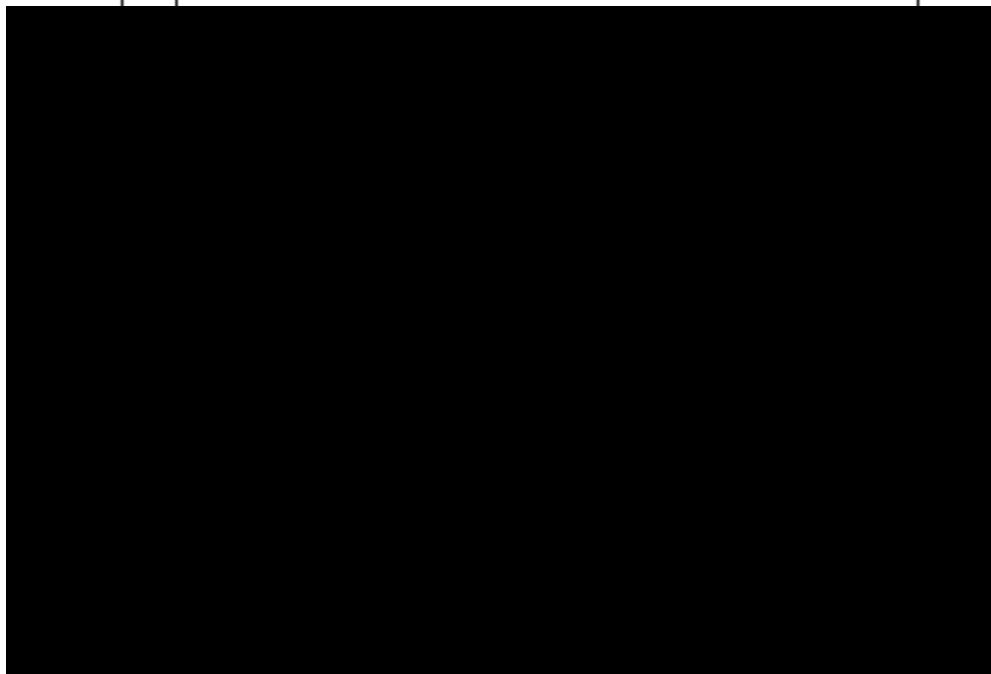


Figure 4.7 (A) Process flow of wet etched MNs (B) SEM image of resulting MN

In order to control the MN morphology, the etch was based on the crystal structure of silicon and its resulting etch characteristics in KOH. The process relied on precise alignment of the mask design with the crystal planes prior to KOH exposure. The anisotropic characteristics then undercut the mask to create convex corners in the form of an octagonal prism (figure 4.7 B) and the tip of the MN was formed where the convex corners met.

The fabrication of MNs from a silicon substrate through either dry or wet processes remains one of the dominant techniques due to the excellent mechanical strength, electrical and flexible properties of silicon enabling a number of different MN designs to be processed through wet and dry etching and integrating circuits and microfluidic chips onto a device.

Chapter 5

Microneedle applications

5.1 Introduction

The wide variety of methods discussed above reflects the extensive amount of research that has been conducted to improve transdermal drug delivery with MNs. The various mechanisms in which the drug can be administered e.g., poke and patch, poke and flow etc, also show how researchers are applying each MN design to specific and tailored drugs or molecules to enhance the way they work. The next section reviews the possible applications for MN technology with the caveat that it is constantly expanding.

5.2 Diabetes

The most common studied MN application is for the administration of insulin to manage diabetes. Delivery of insulin is considered to be difficult as the molecule is too large to permeate the SC independently [141] and oral methods encounter degradation of the medication before it is effective. Therefore, currently, diabetics regularly inject themselves with insulin through a hypodermic needle, but this is painful [142]. Hence, MNs have been developed to breach the SC barrier and administer insulin into deeper skin layers without causing pain.

Martanto et al [143], demonstrated that delivering insulin *in vivo* through solid stainless steel MN poke and patch application, reduced blood glucose levels in diabetic rat models by 47-80%, when 0.05-0.5 units of insulin were delivered over a period of 4 hours. To improve this and offer the advantage of a single one-step application process, dissolvable gelatine MNs encapsulated with 0.2 units of insulin were prepared by Chen et al [144]. The dissolvable MNs demonstrated a maximum 70% decrease in glucose plasma levels after 3 hours, while the hypodermic injection group observed an 80% decrease, showing MNs can effectively control blood sugar levels and are a promising alternative to hypodermic injection.

Whilst effective there was still a need to improve the onset of action time and increase the concentration of insulin units that could be delivered in one application. Therefore hollow metal MNs were designed by Davies et al [145], with a glass chamber adhered

to the base of the array which served as an insulin reservoir. Through passive-diffusion the insulin was delivered into diabetic rats; this test reported a blood glucose concentration reduction of 54% over 4 hours and which remained constant for 4 hours post-delivery. However, this process relies on passive diffusion which is a slow method of delivery. Recognising this, Roxhed et al [146], created the first MN based transdermal patch that integrated an active dispensing function to increase the rate of onset of action. The electrically controlled system consisted of a low-cost dosing and actuation unit capable of controlling the release of liquid in the microliter range at low flow rates. The side opened silicon MNs previously discussed in figure 4.6 [139], successfully demonstrated delivery of an insulin concentration 5 times greater in 3 hours compared to passive diffusion and resulted in a significant decrease in blood glucose levels in diabetic rats. Moving the testing to human subjects, for the first time Gupta et al [147] assessed the effect of syringe pumped hollow MNs on two adult participants with type 1 diabetes in comparison to catheter infusion. The results showed that a MN inserted 1mm into the skin led to rapid insulin absorption and a faster reduction in glucose levels in comparison to the subcutaneous catheter-based delivery system.

It has been shown that delivering insulin transdermally through multiple different MN designs are successful in decreasing the concentration of glucose suggesting that MNs could be a new effective approach for the treatment of diabetes. However, some MNs are not so effective, for example Ye et al [148], investigated the possibility of delivering pancreatic beta cell capsules through MNs, to sense blood level and secrete insulin when low, but found the patch did not work as effectively.

5.3 Vaccines

A vaccine is a biological preparation, using a dead or weakened form of a disease causing micro-organism that stimulates an active acquired immunity response without initiating illness and protects against future encounters [148]. Hypodermic needles create biohazardous sharps waste which rely on careful disposal to prevent contamination through reusing the needles, whether accidental or intentionally. The WHO estimates that 1.5 million children die each year from vaccine-preventable diseases, with a high frequency found in developing countries. To administer a vaccine,

a needle and syringe is required, which can only be administered by trained personnel for safe administration and to avoid needle stick injury. However, the lack of trained health care providers in developing countries provides a significant barrier to attaining high vaccination rates. Additionally, vaccines must be maintained at the correct temperatures during storage (usually refrigerated), distribution and vaccine reconstitution, otherwise the biological material can degrade. The resulting need for a cold chain to protect the vaccines can be difficult to maintain due to the limited infrastructure in developing countries. Additionally, some vaccines require reconstitution where trained experts and sterile conditions are required on top of the extra consumables that need to be stored correctly [149].

The viable skin is an ideal target for vaccine delivery as it contains a large network of immunologically active cells and antigen-presenting cells (APC), which are responsible for initiating an adaptive immune response. Additionally, skin vaccination presents a dose-sparing effect when compared to conventional intramuscular injections; this effect is due to the larger amount of APC present in the skin, leading to the induction of a stronger immune response with lower antigen concentration [150].

MNs which are administered into the skin do not require highly trained personnel and offer the possibility of better self-administration with the smaller size of a MN patch requiring simpler storage solutions. Some MNs such as, coated and dissolving designs, encapsulate the drug, meaning dried vaccine formulations and suitable excipients could be added to the MN formulation to generate thermostable options that eliminate the need for cold chain storage or vaccine reconstitution. As MNs are a few hundred microns tall and only require thumb pressure application into the skin, casual contact with the MN is unlikely to result in accidental penetration into the skin, thereby reducing the associated needle stick risk and contamination issues [149]. Overall utilising a MN for vaccine applications can reduce costs, increase patient uptake and enable a greater proportion of the population to be vaccinated.

Initial studies by Prausnitz's research groups from Atlanta USA, described the vaccination of influenza using a dissolvable polymer MN to target the APC [151]. The MNs incorporated 3µg of lyophilized vaccine to avoid reconstitution. After applying the MNs with thumb pressure into mice the MNs dissolved within minutes, eliminating any issues with sharps. The results concluded that dissolvable MNs could induce a robust

humoral and cellular immune response after a single immunisation with a low antigen dose and that MN technology could provide a simpler and safer vaccination.

The Bouwstra research group has focused its work on vaccine delivery through hollow MNs and in a series of linked experiments [152]–[154], recording the delivery of inactivated poliovirus vaccine into rats. Hollow MNs were fabricated from wet etched fused silica capillaries and tested on *in vivo* skin. Overall, administration with hollow MNs induced a higher and stronger immune response compared to intramuscular and subcutaneous injection. Another study by Siddhapura et al [155], compared the delivery efficacy of tetanus toxoid loaded chitosan nanoparticles through hollow and solid MNs. Both MNs elicited IgG and IgG1 antibody reaction in *in vivo* mouse models, however, the hollow MNs induced a higher level. The authors concluded that the hollow MNs should be favoured over solid MNs as the hollow MN application induced both hormonal and cellular immune responses through better administration accuracy and precision.

At the time of writing this thesis, on March 11th, 2020, a novel coronavirus, SARS-CoV-2 (COVID-19) became an international pandemic. Fortunately, the genome sequence was rapidly released enabling scientists to begin constructing a vaccination. The first MN COVID-19 paper published in Lancet by Kim et al [156], demonstrated the rapid development of COVID-19 subunit vaccines and their promising immunogenicity in mice. A dissolvable CMC MN was fabricated by PDMS moulds to incorporate a number of COVID-19 spike proteins such as SARS-CoV-2-S1fRS09, were administered to mice models against a negative control of no protein or a subcutaneous injection. Over the course of a week, various serum samples were taken until a booster vaccine was given 2 weeks later and antibody concentrations were tested through the immunoassays. The results indicated that all proteins vaccines tested generated a higher level of antigen-specific antibodies beyond the controls samples. Although much more work is required, this study suggested that it may be possible to rapidly produce clinically translatable vaccine against novel pathogen for human testing and subsequent global distribution in time to significantly impact the spread of the disease.

In addition, another team of researchers at Swansea University are developing self-administrable patch fabricated from either polycarbonate or silicon MN arrays for

vaccine delivery against the SARS-Cov-2 virus. The silicon MNs developed throughout this PhD studentship were repurposed for the vaccine patches [157].

5.4 Cancer

Cancer remains one of the leading health problems worldwide despite the tremendous effort put in by research groups to find a treatment. Currently, chemotherapy and radiotherapy alongside anticancer therapeutics provide sub-optimal efficacies with only 0.7% of the administered dose reaching the tumour site [158], leading to acute toxicity and side-effects as well as tumour reoccurrence. In cancer therapy MN applications have been explored to trigger anticancer immunological responses or to deliver anticancer compounds while lowering side effects and increasing patient comfort.

Bhatnagar et al [159], reported a dissolvable polymeric MN for co-delivery of 522 μ g of doxorubicin HCL and 227 μ g of docetaxel for the chemotherapy treatment of breast cancer in mice. A control of injecting the mixture directly into the tumour was used as a comparison. The injection results revealed significant toxicity and a reduction in body weight in all mice, followed by death after 9 days with a two-dose administration. Alternatively, MN administration demonstrated a significantly greater survival rate (100%) after 16 days with 4 doses and a reduction in tumour volume and weight.

Another dissolvable MN combined with a thermal-sensitive solid lipid nanoparticle for the treatment of melanoma tumours was presented by Qin et al [160]. Paclitaxel and photothermal agent IR-780 were encapsulated into nanoparticles and concentrated into the tips of dissolvable MNs and directly inserted into the tumour site *in vivo* and irradiated with near-infrared light; the nanoparticles underwent a phased transition to release paclitaxel into the tumour. Thirty days after treatment, the primary tumours were completely eradicated, with the highest survival rate of 66.67% after 100 days of treatment.

5.5 Obesity

In the human body there are two types of adipose (fat) tissues known as brown adipose tissue (BAT) and white adipose tissue (WAT). BAT plays a crucial role in producing heat and consequently increasing energy exposure, whereas WAT stores exceeded

energy resulting in weight gain. Where too much WAT is stored the individual becomes obese which will likely lead to further complications such as stroke, diabetes, heart disease and cancers [161]. According to the WHO at least 2.8 million people die worldwide each year as a result from being obese [162]. The FDA list of approved drugs to battle obesity include oral drugs Lorcaserin and Orlistat, however, the former causes headaches and depression, while the latter has serious gastric side effects. Than et al [162], fabricated a dissolvable MN that slowly delivered anti-obesity compounds β 3-adrenoceptor agonist and thyroid hormone T. The results showed that MNs effectively promoted WAT browning and suppressed weight gain in mice, without the daily need of administration. A further study by Zhang et al, [161], demonstrated a similar approach, however, the mice models also had type 2 diabetes. Therefore, this study not only examined the MNs ability to deliver medication to brown WAT and increase whole body energy expenditure but reduce type-2 diabetes. The degradable MN patches consisted of nanoparticles loaded with rosiglitazone, an antagonist for adipose tissue transformation, glucose oxidase to provide an acidic environment and catalase to consume undesired H_2O_2 . The results concluded that the MNs were able to deliver the drugs that stimulated local browning of WAT to prevent potential side effects in other organs. It further demonstrated that by increasing energy expenditure and fatty acid oxidation, it improved insulin selectivity thus suggesting an alternative drug administration strategy for the treatment of obesity and its comorbidities.

5.6 Cosmetics

Cosmetic applications with MNs are gaining in importance as individuals seek a cost effect way to reduce scars, acne, blemishes, and signs of aging. Current skin routines include the use of topical creams or gels; however, the SC barrier is effective at preventing these penetrating successfully. The concept of “microneedling” was pioneered in 1995 when Orentreich and Orentreich reported the use of needles in the treatment of acne scars [163]. Their approach involved pricking or puncturing the skin and then scarifying the dermis with a needle to build up connective tissue beneath the scars. Following this, in 1997 Camirand and Doucet used a tattoo pistol to “needle abrade” scars [164]. However, this would have been slow and laborious when working on large areas of skin. To improve on this concept, Fernandes [165] designed a drum-

shaped device with 192 protruding needles and initiated a new technological approach termed microneedling.

The principle behind microneedling is to break the collagen strands within the skin which tether the scar to the dermis. By using MNs the breakdown can be controlled to small sections that instead of causing more scarring stimulated angiogenesis and collagenases to heal the breaks and improve the appearance of the scar tissue [166]. A study by El-Domyati et al [167], applied six sessions of microneedling treatment on 10 patients with different types of atrophic acne scars over 3 months. The results found that with MN treatment rolling for boxcar scars their appearance significantly improved while ice-pick scars only moderately improved. However, treatment over a longer period of time may be able to achieve further improvement as the deposition of new collagen takes place gradually.

A randomised 6-month clinical trial by Afra et al [168], compared the efficacy of topical tazarotene gel, 0.1% in combination with microneedling for the management of atrophic acne scars. Thirty-six patients were selected to receive microneedling with a derma roller on one side of the face and topical tazarotene therapy on either side, for 4 sessions over a period of 3 months. The results indicated comparable improvement and patient satisfaction for both treatments.

As microneedling alone has shown only moderate improvement to scarring the cosmetic improvement business has turned to dissolving MNs where the treatment application is simpler, and the treatment can be directly inserted into the affected skin area. For example, Janh et al [169] fabricated dissolvable MNs from high or low molecular weight HA, that used encapsulated adenosine for wrinkle improvement. Over the 12-week period, it was found that high molecular weight HA showed skin improvement with regard to skin wrinkling, elasticity and dermal density. Another group [170], tested the daily application of dissolvable MNs with either retinyl-retinoate or ascorbic acid on the left or right eye to treat crow's feet wrinkles. Both MNs dissolved fully within 6 hours of application and resulted in an overall improved skin look, with ascorbic acid providing better results in smoothness depth and retinyl-retinoate improving skin roughness.

The original MN concept designed by Fernandes is known commercially as a Dermaroller® manufactured by Deutschland GmbH and FDA registered as a class I

medical device. The lengths of the MNs protruding from the drum are designed with the type of treatment in mind, for example lengths of 1500-2000 μ m are employed for acne and scars, while 500-1000 μ m needle lengths are used to treat skin aging and wrinkles [171].

The Dermapen, is an automated microneedling device with 9-12 MNs arranged in rows that are disposable. The pen operates in a stamp like manner to insert the MNs into narrow regions of the face such as the nose, around the eyes and lips. The pen is battery rechargeable and performs in two modes, high (700 cycles/min) and low (412 cycles/min). This technology has been designed to prevent accidental pin pricks, by withdrawing the MN tips inside the pen when not in use and overcomes application issues of varying pressure or penetration depth in an automated mode; thereby making it less painful [171].

5.7 Other MN applications

It is clear that MNs improve the delivery of many different drugs and molecules across the SC barrier of the skin to facilitate better treatment of various diseases and ailments. In light of this, several research groups have begun investigating the use of MNs for other applications beyond drug delivery and the skin.

5.7.1 Patient monitoring, diagnostics and theranostics

Therapeutic monitoring refers to an analytical system aimed at detecting and quantifying drugs or endogenous markers primarily in the serum or plasma and is used extensively as a rapid diagnostic tool for many disease states. The tools can be used as point of care monitors by extracting ISF samples for quantification. However, the next stage would be to combine the monitoring system with a treatment system that reacts upon stimulus detection to release the therapy; this is termed theranostic systems.

The first MN extraction system was based on capillary action of ISF, however, novel strategies now involve the use of more complex extraction mechanisms such as, vacuums or osmotic pressures [172]. Glucose monitoring is a popular application for MN use; hollow glass MN fabricated by Wang et al [173], were used to extract ISF from hairless rats and human volunteers using a vacuum over 2 and 10 minutes. The

results from electrochemical measurements in the lumen of MNs found that the concentrations of glucose found in the extracted ISF correlated to that of the blood glucose.

Alternatively, electrochemical sensors could be used to continuously monitor metabolites such as, glucose or lactate [174] or drugs such as, theophylline and penicillin [175] in real time and eliminate the need to extract fluids from the skin. This can be done by either entrapping the molecular recognition element (for example, in the case of a glucose sensors: the enzyme glucose oxidase) either in a thin polymer such as, electropolymerised polyphenol, or in hydrogels on platinum or graphene coated MN arrays [176]. A collaboration between Swansea University and University of Montpellier France, has shown the potential of a MN array to assess intracellular cyclin-dependent kinase 4 (CDK4) using specific peptide substrates [177], in both cultured cells and frozen skin samples onto which they were applied. Western blot analyses revealed that CDK4 was found on the MN array following insertion into A375 melanoma cells grown on petri dishes establishing MNs as sampling devices for screening of skin melanoma. Another research group, Mohan et al [178], demonstrated a hollow MN based electrochemical sensor, where the device consisted of a hollow MN array integrated with a platinum and silver wire. The MN sensor was successfully used to monitor continuous real-time alcohol content from the ISF of *ex vivo* mouse skin.

Combining a diagnostic and therapeutic device while moving away from transdermal applications, Yuan et al [179], reported a MN that combined OCT (optical coherence tomography) imaging for fast ultrahigh resolution deep-brain imaging with an efficient near-infrared laser for ablation of abnormal tissue. The ability of a dual-functioning MN may be useful for future understanding and management of deep-seated brain diseases as characterisation and assessment can be performed simultaneously over-coming potential challenges with invasive brain procedures.

5.7.2 Ocular delivery

Ocular drug delivery presents an interesting area of research, as current therapies such as topical eye drops are inefficient with a bioavailability of <5%, due to the non-associable, intricate, and delicate nature of the ocular tissues that form a barrier against

drug delivery. Whilst hypodermic needles can be used to inject the treatment directly to the target tissues, this is a highly invasive procedure and causes significant tissue damage, pain, extreme discomfort and a number of side effects [180]. The minimally invasive and painless nature of a MN makes it an attractive model for ocular drug delivery.

Mark Prausnitz's group was the first to demonstrate that stainless steel MNs coated in the model drug sodium fluorescein can successfully deliver into the eye and achieved a 60-fold increase in delivery when compared to topical application [181]. Another study by the same group demonstrated ocular delivery using hollow glass MNs to inject the model drug sulforhodamine and micro/nanoparticle formulations [182]. To create an injection flow, the MNs were inserted to a depth of 700-1080 μ m and then retracted in 60 μ m increments. This increased the overall flow rate from 10 to 35 μ l, however incorporating hyaluronidase and collagenase enzymes into the injection solution, stimulated the breakdown of ocular tissue to increase the size of the opening through which the fluid flowed.

However, due to the complex structure of the eye, with different layers and pathways, ocular delivery is complex. The above studies both focused on anterior, intrastromal and intrascleral injections, however, Patel et al [183], was the first to investigate the possibility of injecting into the posterior suprachoroidal space (SCS), that surrounds the eye, using similar glass hollow MNs. The study suggested that particles measuring 20 and 100nm could spread within the sclera as well as the SCS whereas particles of 500 and 100nm localised exclusively in the SCS.

5.7.3 Gastrointestinal delivery

Oral drug delivery is a quick and patient friendly mode of delivering therapeutics, however, the first pass hepatic clearance makes it incompatible for some molecules. To overcome these challenges Traverso et al, [184] incorporated MN technology into an oral delivery system to deliver insulin into the gastrointestinal (GI) tract and compared its bioavailability to a subcutaneous injection. The delivery system consisted of a cylindrical MN pill in a pH responsive coating; once the pill was in contact with the GI tract the coating dissolved to reveal the MNs that penetrated the intestinal tissue. Two types of MNs were tested, hollow and solid MNs. In the case of the hollow MNs, the

drug would be delivered through compression of the pill via peristalsis movement, while the solid MNs contained the drug formulation on the MN structure. *In vivo* proof of concept studies in pigs found that GI MN delivery improved pharmacokinetic effects and bioavailability. In addition, the onset of hypoglycaemic effects was faster and the whole process in comparison to multiple injections was simplified.

Following on from this, in 2019 the same group later improved the MN pill design to incorporate a spin actuator that propelled the MNs into the GI track, termed the liminal unfolding MN injector (LUMI) [185]. Once the MNs were expelled, the arms of the LUMI pressed the MN patches into the intestinal epithelial, where they dissolved and released the encapsulated drugs. The remaining capsule then breaks apart and biodegrades before being eliminated from the body. Using this method, administering insulin to pigs showed similar pharmacokinetic and blood glucose pharmacodynamics similar to those following subcutaneous injection.

5.8 Conclusion

These chapters introduce the pathways of drug delivery highlighting the challenges and benefits of each and the reasons why transdermal drug delivery is favourable. The barrier effects of the SC show that topical applications have low bioavailability and only a select number of compounds that possess the appropriate physiochemical properties can permeate through it. These challenges have promoted an advancement in research focused on methods to by-pass this barrier, of which, MN show promising results.

The initial MN concept included simple solid steel MNs for poke and patch applications, however, new generations of MNs can now be formulated from a range of materials, including metals, polymers, and carbohydrates, in varying geometries to deliver through hollow, coated or dissolvable methods, and all have their advantages depending on their application and use.

Initially, MNs were theorised for transdermal drug delivery for cosmetic and immunisation purposes however, the potential for use in diagnostic monitoring and drug delivery to other tissues such as ocular and GI, shows the versatility, acceptability, and potential for MNs to become an everyday clinical importance.

Part 2
Experimental methodology

Chapter 6

Experimental instrumentation and materials for fabrication methods

This chapter discusses the instrumentation and materials employed for the fabrication of both out-of-plane and in-plane silicon MNs.

6.1 Photolithography

6.1.1 Spin coater

A Laurell WS-650 spin coater was used to coat 4" silicon wafers with a uniform and controlled thickness of resist. Unless stated otherwise Az125nxt and Nlof2070 negative resists were used to pattern the out-of-plane (OOP) MN bevel and bore and the in-plane MN respectively. The spin speeds and run parameters are discussed in both OOP fabrication and in-plane MN fabrication chapters, per optimisation results.

6.1.2 Spray coater

A SUSS MicroTec AS8 spray coater was used to deposit Nlof2070 photoresist onto the OOP MN bevel surface to create the shaft pattern. The resist used for spray coating (Nlof2070), has a high viscosity, therefore, to modify it into a sprayable liquid, the resist is diluted in acetone in a ratio of 1:8, enabling the resist to be atomised on to the wafer. The atomised particles then amalgamate together to form a uniform layer. The vacuum chuck was heated to 70°C and a flow rate of 1.5ml/min and arm motor speed of 120 was programmed to scans over the wafer 12 consecutive times (figure 6.1 [186]) to create a uniform film to a final resist thickness of 14µm.

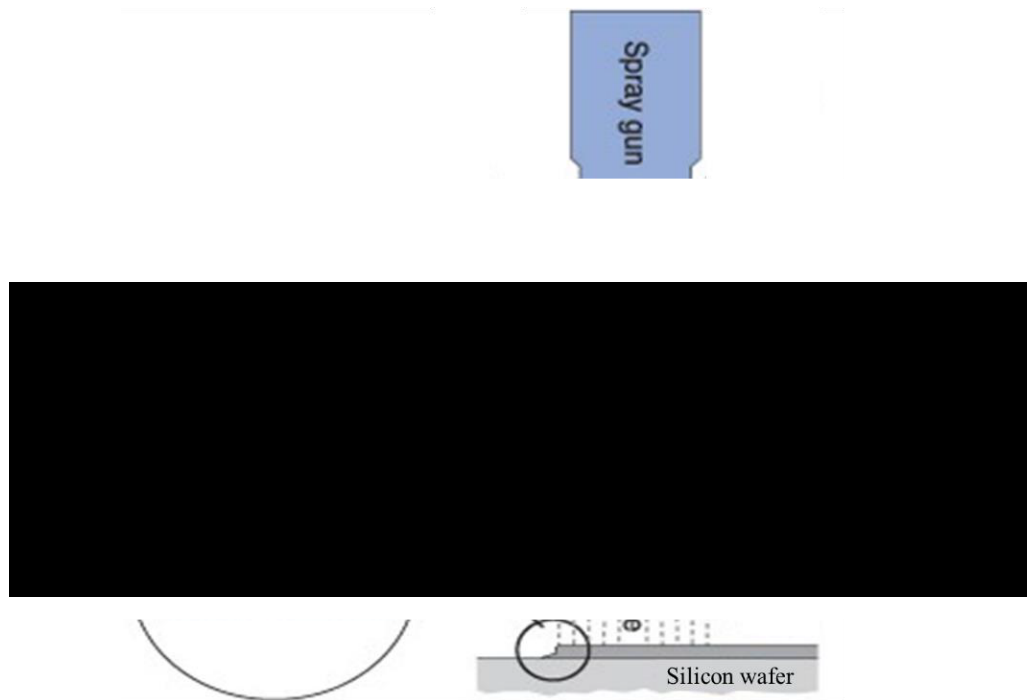


Figure 6.1 Schematic diagram demonstrating the spray coating method

6.1.3 Mask aligner

To transfer MN mask designs onto the resist, a SUSS MicroTec MA8 UV mask aligner (MA) was used. As explained in chapter 4.3.1, the areas of photoresist exposed to UV light will either become more or less soluble dependent on if the resist tone. In this case AZ125nxt and NLoF2070 are both negative tone resists, meaning that the exposed areas will become insoluble and will not be removed upon development with AZ MIF 726.

All wafers once coated in resist were placed on the sample stage and secured with a vacuum. A film mask, designed in AutoCAD, patterned with the MN design was inserted into the mask holder and held in place via a vacuum. The mask holder was then inserted into the MA and again secured through a vacuum. To align the mask and wafer, the alignment marks were visualised through top side and back side alignment features and the sample stage could be moved left, right or up and down to an alignment accuracy of $<0.5\mu\text{m}$. Once in place, the sample stage rose slowly, bringing the mask and wafer into soft contact, this analyses the wafer angle and adjust the wafer if it was not parallel with the mask. Following this, the wafer was exposed to a 1000W mercury arc lamp, perpendicular from an overhead bulb shining the UV light through the mask design. The exposure time is dependent on the UV dosage required and is calculated by the tool; UV dosages are discussed in each MNs respective fabrication chapter. Once

exposed, samples were either baked or placed straight into AZ MIF 726 developer for their respective optimised times, to remove the soluble regions of photoresist. Optimisation can be found in chapter 8 for OOP MN or chapter 9 for in-plane MNs.

6.2 Silicon dioxide deposition- Chemical vapour deposition

To protect the OOP bevels from etching and form a hard mask for the in-plane MN fabrication, a layer of silicon dioxide (SiO_2) was deposited onto the wafers using an SPTS plasma enhanced chemical vapour deposition (PECVD) system. A conventional CVD system uses higher temperatures to induce a reaction at the wafers surface with the input gases, instead, the PECVD uses the energy created by a plasma to induce the reactions at the wafer surface thereby lowering the temperatures required [187].

6.3 Ellipsometry

An ellipsometer (J. A. Woollam M-2000) was used to measure the thickness of SiO_2 . Ellipsometry is an optical technique that measures the change in polarised light as it reflects or transmits from the wafers surface, the thickness of the film can then be determined by using the refractive index [188].

Once the CVD had deposited SiO_2 onto the silicon wafers surface, polarised light was fired over the wafer to calculate an average film thickness and to determine whether some areas were thicker or thinner than the average. Ellipsometry results are found in chapter 9 and were used to optimise the in-plane MN fabrication method.

6.4 Inductively coupled plasma

The SPTS inductively coupled plasma etcher (ICP) was used to selectively etch through the SiO_2 film on the in-plane MNs to reveal the silicon wafer beneath, in the design of the mask pattern. Gases were inserted through the shower head at the top of the vacuum chamber and a plasma was formed around the edges of the chamber due to the radial coil power source surrounding the chamber. A platen, located beneath the wafer, creates a potential difference between the wafer and the plasma, thus drawing the plasma ions towards the wafer to facilitate etching.

To control the etch shape and depth the platen power could be adjusted, for example, an increase in the platen power would increase the potential difference between the plasma and wafer, which would accelerate the particles towards the wafer, causing the particles to “hit” the wafers surface with increased energy and cause a reaction. Gases used in the SiO₂ etching process were O₂, C₄F₈, and CF₄.

6.5 Etching materials- Potassium Hydroxide

Potassium hydroxide (KOH) was used as the wet etchant for in-plane MN fabrication. KOH etches silicon wafers preferentially in the (100) plane producing the characteristic anisotropic V-shaped etch with (111) sidewalls that form at a 54.7° angle to the surface. To etch the wafer, 200mls of KOH was heated to 70°C and the wafer was submerged for approximately 5 hours, full protocol optimisation is found in chapter 9.7. It is important to note that KOH is hazardous and can cause severe burns in liquid and vapour states, therefore correct PPE and lids are required during etching.

Chapter 7

Experimental equipment and materials used for characterisation and analytical methods

The equipment discussed in this chapter was used to image each MN structure and analyse each MN mechanical strength, penetration ability and drug delivery abilities.

7.1 Imaging techniques

7.1.1 Scanning electron microscopy

MN imaging was performed using a Hitachi S-4800 ultra-high-resolution scanning electron microscope (SEM) that can magnify a sample up to $\times 1,000K$ to a high resolution of 1nm. The system has a cold emission electron source that forms a beam of high energy electrons targeted at the samples surface (figure 7.1 [189]). Detection of the electron back scatter then forms an image of the samples surface. Additionally, the SEM is equipped with an X-ray detector for elemental analysis (EDX) to differentiate between the silicon wafer and the resist or SiO_2 coatings, for precise and accurate measurements.

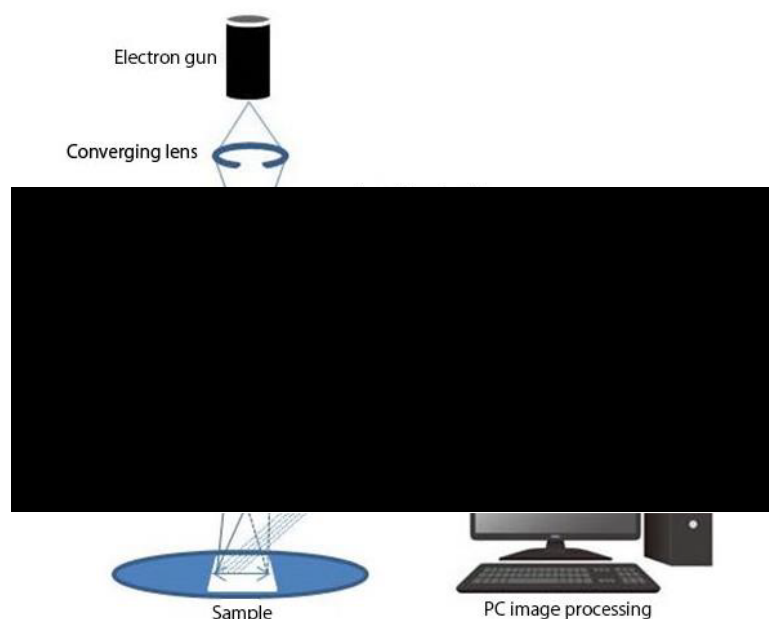


Figure 7.1 Schematic representation of SEM apparatus

7.1.2 Optical microscopy

The Keyence VHX-950F series optical microscope was used to optically examine the MN wafers throughout the fabrication optimisation steps. In comparison to a standard microscope, the Keyence has the ability to take angled measurements up to x 5,000 magnification and enables the user to analyse the data with a computer application that enables editing functions, such as, false colourisation and 3D imaging.

7.1.3 Fluorescence microscopy

A Zeiss Fluorescence microscope (figure 7.2 [190]) was used to visualise histological slides of porcine skin samples after hollow MN injection with fluorescently tagged molecules such as, FITC-Insulin. A fluorescence microscope uses a xenon or mercury bulb to produce ultraviolet light; this light shines into a dichroic mirror that separates the wavelengths ranges to allow only a specified range to pass through and illuminate the sample. Any fluorescence within the samples at these wavelengths will be excited and detected to form the final image.

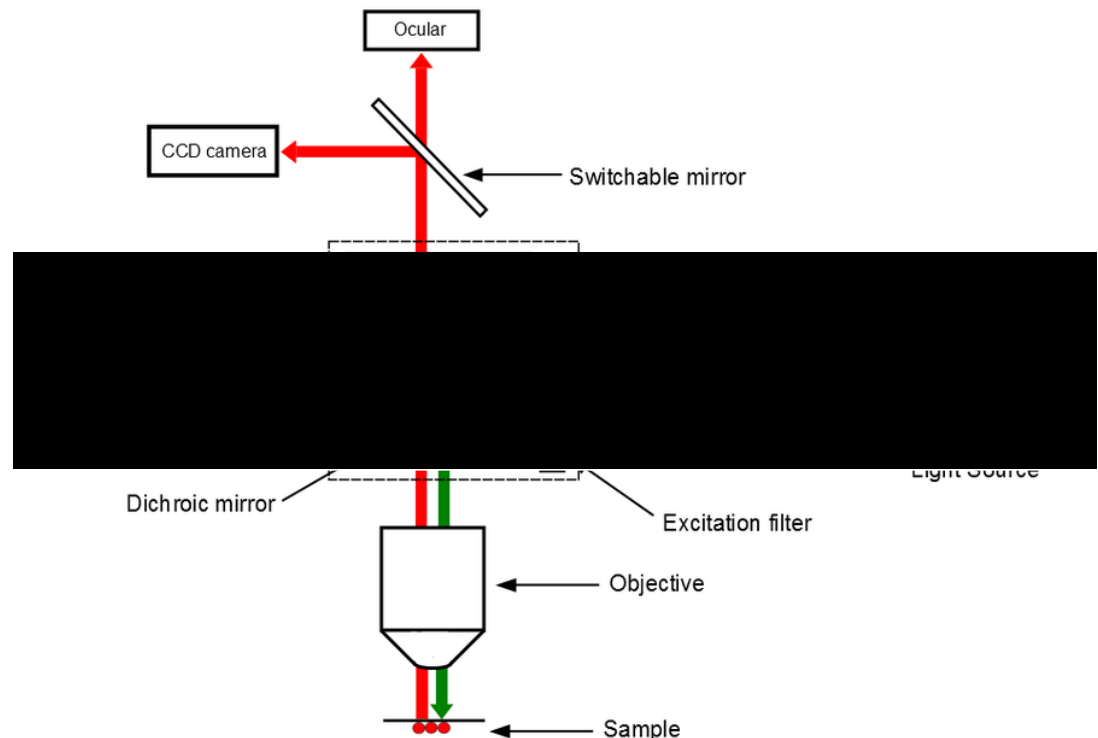


Figure 7.2 Schematic representation of fluorescent microscope

7.1.4 Optical coherence tomography

Optical coherence tomography (OCT) is a non-invasive *in vivo* imaging technique that uses light waves to visualise cross sections of tissues such as the retina of the eye and skin (figure 7.3 [191]). Here the OCT was employed to visualise microchannels created by MNs in *ex vivo* human skin samples immediately after application. OCT was carried out at Cardiff University on human breast tissue under local Research and Ethics Committee reference 08/WSE03/55. Both OOP and IN-plane MNs were inserted into skin samples and scanned with the OCT probe immediately after removal. The probe was laterally placed over the skin surface to detect reflective light waves from different depths inside the tissue, enabling the OCT to reconstruct the depth-profile of the skins structure. OCT analysis and image clarification can be found in chapter 14.2.

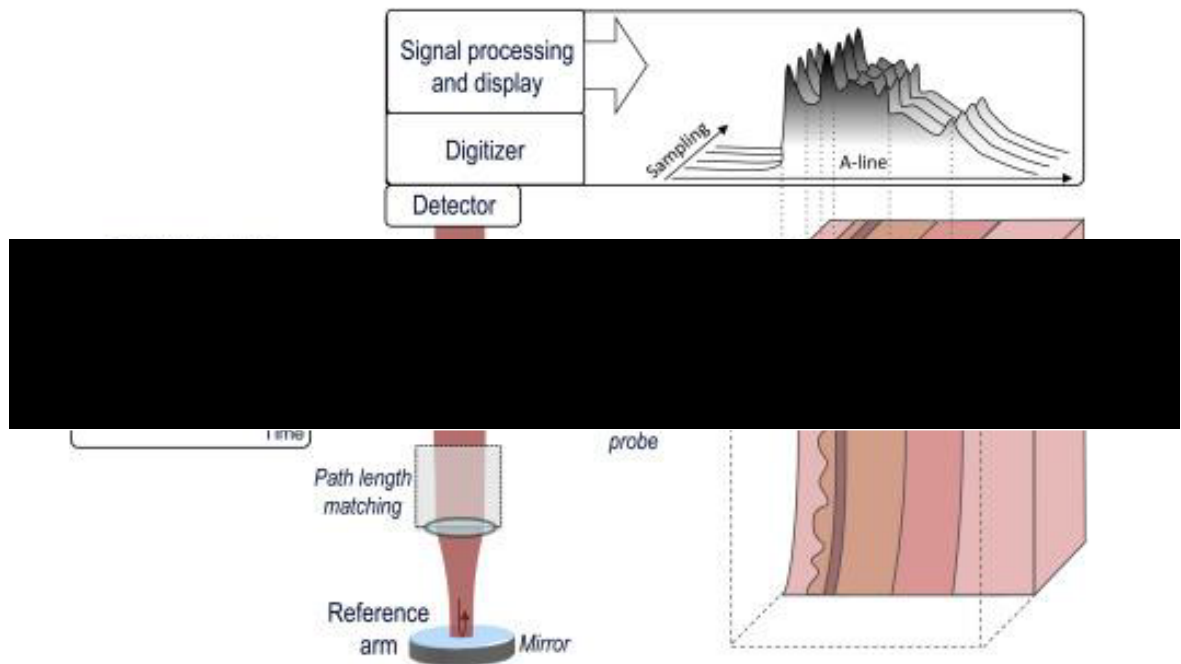


Figure 7.3 Schematic representation of optical coherence tomography

7.2 Mechanical testing

Axial compression tests were performed with a Hounsfield/Tinius Olsen compressions analyser (model H1-KS) to test the mechanical strength of the MNs. The Hounsfield has a positional accuracy of $1\mu\text{m}$ with an interchangeable load cell capacity.

MN arrays were secured to the sample stage and a 100N load cell was programmed to 10N, 20N, 50N and 100N forces. The force of a downward compressing platform was

gradually increased at a constant rate of 4.5mm/second, onto the MNs until the desired force was reached. The force and displacement measurements were continuously recorded to identify the level of force and the point along its length at which the MN broke. The force started at 0N until the tip of the MN was reached where, upon contact, the force was gradually increased. When the MN breaks e.g., at 15N, this will be illustrated on the force / displacement graph as a decrease in force. Each test was run in triplicate with the average data plotted; each demonstrating the full compression profile of the MN with increasing force. Post exposure SEM images were taken at forces of 10N, 20N, 50N and 100N to examine if the applied forces caused the MN's fracture and / or bend.

7.3 Skin preparation

7.3.1 Porcine skin preparation

To prepare skin samples for testing, full thickness porcine skin was purchased from Wetlab Ltd. Warwick. The pig was euthanised in the morning of delivery to maintain freshness and delivered on ice. Once received the pig was defrosted and any muscle or fat removed. For experiments that required full thickness skin, the skin was sectioned into smaller pieces and wrapped in foil and frozen at -20°. Drug delivery experiments using Franz cells required thinner skin, a thickness between 100 and 1000µm, hence an electric dermatome (Pagett®) was used for its ability to adjust the thickness settings of the skin to be shaved. Once cut, the skin was wrapped in foil and frozen at -20°.

7.3.2 Histological sectioning

A Leica cryostat was used to create histological skin cross sections to visualise MN microchannels. Porcine skin samples, once injected with dyes through hollow MNs, were immediately frozen in liquid nitrogen and kept on dry ice until cutting. O.C.T. embedding medium purchased from Sigma, was used to stabilise the skin samples, and adhere the samples to the stage. The cryostat was maintained at a cold temperature between -15 and -20°. The sample stage was inserted into the cryostat and the cutting blade brought forward until it came into contact with the sample. By rotating the handle,

the blade vertically sliced through the sample to create 8µm thick skin slices that were mounted onto glass slides.

7.3.3 Transepidermal electrical resistance

Transepidermal electrical resistance (TEER) was used to assess the barrier function of porcine skin before Franz cell delivery experiments. TEER works by measuring the flow or electrical resistance across the skin membrane. The theory is that the electrical resistance across the skin membrane will not change if the SC barrier is intact; however, if the SC has been broken the electrical resistance across the membrane will change and result in a variance of resistance. Full optimisation of this method is documented in chapter 17.5.

7.4 Drug delivery

7.4.1 Franz cell *in vitro* assay

A Franz cell is a glass diffusion cell composed of two stacked chambers that are separated by a membrane in which the diffusion is being tested, in this case porcine skin was used (figure 7.4).

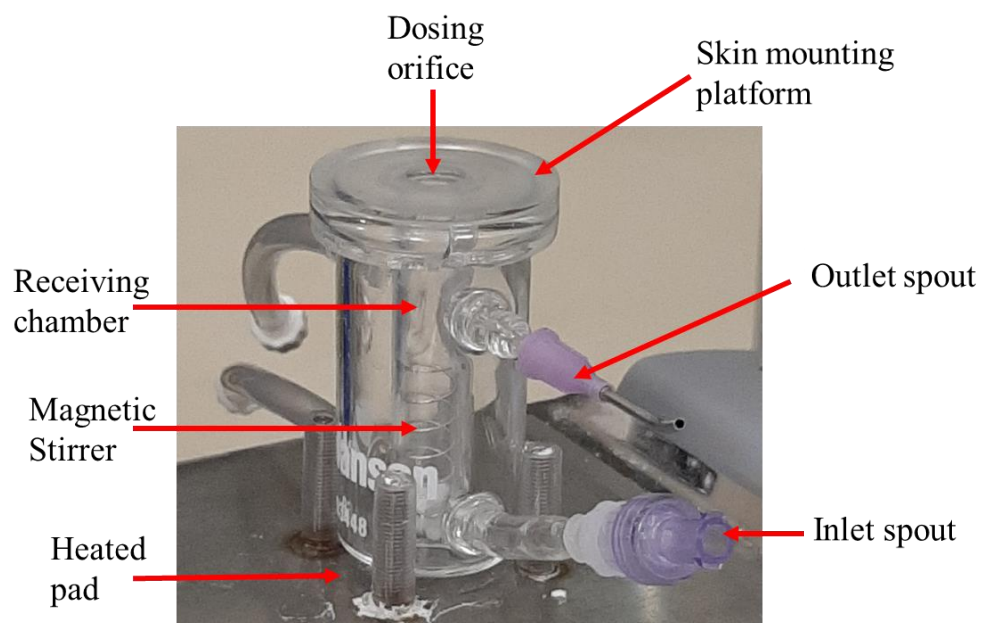


Figure 7.4 Franz cell apparatus

The top chamber is termed the dosing chamber, as this is where the drug sample is administered. The lower chamber is termed the receiving chamber, as this is where the drug pools if it diffuses across the membrane.

However, for poke and patch MN studies the dosing chamber was not required and omitted, leaving the porcine skin, SC side up, available to the air to mimic MN application.

The receiving chamber was filled with 4mls of 0.1M PBS to simulate the solubility and pH of the deeper dermal skin compartment and placed on a heated magnetic stirring pad and set to 32°C, to represent skin surface temperature. A magnetic stirrer was placed at the base of the chamber to maintain a homogeneous mixture. The skin membrane to be tested was stretched over the skin mounting platform and held in place with a clamp. Any drug molecules that diffused into the receiving chamber would move through the dosing orifice into the open chamber below. To collect samples from the receiving chamber, two spouts, equipped with bubble traps, protrude from the side of the chamber. The bottom spout, known as the inlet, was used to inject 400µls of 0.1M PBS and the top spout was used to collect the solution that had been displaced. In all Franz cell experiments, 11 samples were collected at time points of 5 minutes, 15 minutes, 30 minutes and 1, 2, 4, 6, 8, 10, 12 and 24 hours and the results used to form a cumulative concentration curve.

The samples were analysed against a calibration curve of known concentrations to calculate the concentration of drug. In total, all samples tested were repeated in at least triplicate to provide statistical evaluation. Each time a sample was removed from the receiving chamber to be analysed, 400µls of fresh PBS was injected into the chamber, diluting the concentration. To factor in the dilution and calculate the total drug concentration the following calculations were used: For clarification, example fluorescent spectroscopy data of a control and MN results are provided in table 7.1, the dilution factor calculations are provided in table 7.2 and an example calibration curve is presented in table 7.3 and in figure 7.5 which calculates an R value of 0.991 and an M values of 24301.

Table 7.1: Exemplar raw fluorescent data

Time (hrs)	Fluorescence	
	Control	MN
0	205	2991
0	205	6625
1	199	6849
1	198	5078
2	185	4450
4	192	3735
6	209	3359
8	219	2674
10	228	2423
12	296	2057
24	260	1844

Table 7.2: Dilution factor

Time (hrs)	Dilution Factor	Factor (f)
0.25	400/4000	0.1
0.5	800/4000	0.2
1	1200/4000	0.3
2	1600/4000	0.4
4	2000/4000	0.5
6	2400/4000	0.6
8	2800/4000	0.7
10	3200/4000	0.8
12	3600/4000	0.9
24	4000/4000	1

Table 7.3: Exemplar calibration curve data

Calibration curve	
Concentration $\mu\text{g/ml}$	Fluorescence
2.50	61761
1.25	28985
0.63	14390
0.31	6928
0.16	3396
0.08	1732
0.04	927
0.02	529
0.01	342
0.00	292
0.00	262

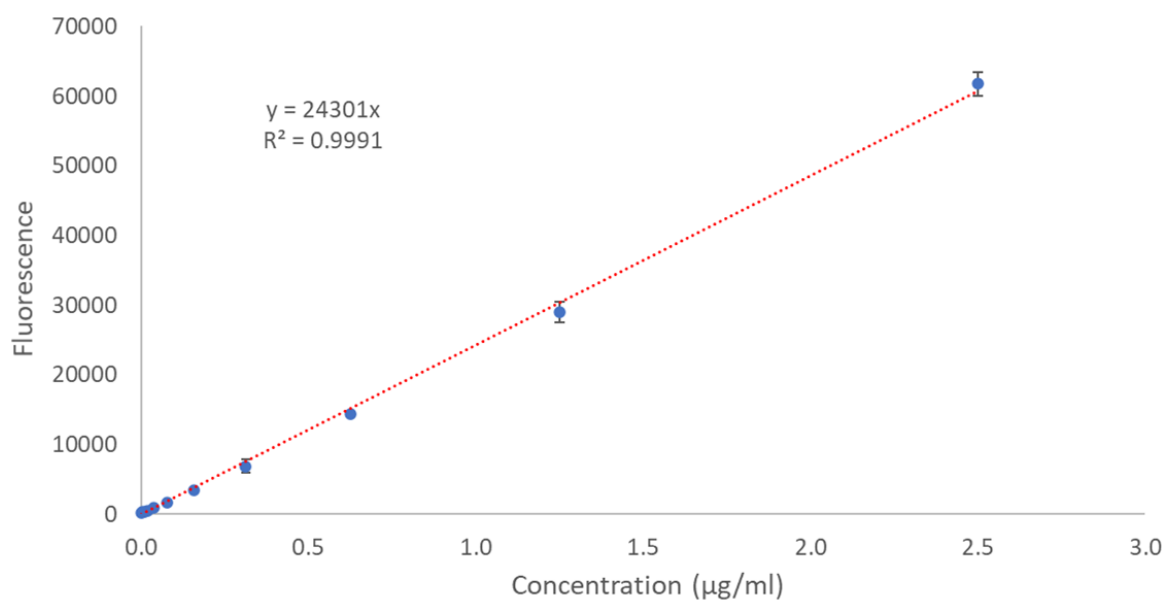


Figure 7.5 Exemplar calibration curve showing fluorescence measurements of different concentrations of calcein

Step 1: Subtract any background fluorescence from the PBS control from each sample (table 7.4), the PBS only sample found on calibration curve as 262.

Table 7.4: Subtracting the background fluorescence from raw data provided

	Fluorescence	
Time (hrs)	Control	MN
0.08	-57	2729
0.25	-57	6363
0.5	-63	6587
1	-64	4816
2	-77	4188
4	-70	3473
6	-53	3097
8	-43	2412
10	-34	2161
12	34	1795
24	-2	1582

Step 2: Using the calibration curve, the concentration of each sample was calculated using the $y = mx + c$ equation, which was rearranged to find x .

Where c (the intercept) = 0, and $m = 24,301$.

Therefore, an example equation looks like $x = y / 24,301$ (table 7.5).

Table 7.5: Calculating the sample concentration from the calibration curve equation

	Concentration $\mu\text{g/ml}$	
Time (hrs)	Control	MN
0.08	0.0	0.13
0.25	0.0	0.29
0.5	0.0	0.30
1	0.0	0.22
2	0.0	0.19
4	0.0	0.16
6	0.0	0.15
8	0.0	0.12
10	0.0	0.10
12	0.0	0.09
24	0.0	0.08

Step 3: To remove the influence of dilution, each sample was multiplied by their respective timepoint dilution factor calculated in table 7.2, this calculated the concentration of the drug in the receiving chamber at that time point (table 7.6).

For example, the time point at 2 hours has a dilution factor of 0.4 as 4 samples have been drawn from the Franz cell, accumulating 1600µls.

Thus, $1600\mu\text{l} / 4000\mu\text{l}$ (Franz cell volume) = 0.4

Also, it is important to note the first time point does not have a dilution factor as the first timed sample was taken straight from the original 4mls and was not diluted, however, the following samples were then all subsequently diluted.

Therefore, for the time point of 2 hours, a concentration of 0.19µg/ml multiplied by the dilution factor 0.4 equals an undiluted concentration of 0.08µg/ml.

Table 7.6: Calculating the sample concentration by the dilution factor

Time (hrs)	Concentration µg/ml	
	Control	MN
0.08	0.0	0.13
0.25	0.0	0.03
0.5	0.0	0.06
1	0.0	0.07
2	0.0	0.08
4	0.0	0.08
6	0.0	0.09
8	0.0	0.08
10	0.0	0.08
12	0.0	0.08
24	0.0	0.08

Step 4: To create a cumulative concentration curve, the concentration difference between each time point and the time point before it was calculated (Table 7.7) and added together (Table 7.8).

For example, time point 2 hours equals the difference between time point 1 hours (0.07 μ g/ml) and time point 2 hours (0.08 μ g/ml) which calculates 0.01 μ g/ml.

Table 7.7: Calculating the concentration difference between consecutive samples

Time (hrs)	Concentration μ g/ml			
	Control	MN	Control Difference	MN Difference
0.08	0.0	0.13	0.0	0.00
0.25	0.0	0.03	0.0	0.10
0.5	0.0	0.06	0.0	0.03
1	0.0	0.07	0.0	0.01
2	0.0	0.08	0.0	0.01
4	0.0	0.08	0.0	0.00
6	0.0	0.09	0.0	0.01
8	0.0	0.08	0.0	0.01
10	0.0	0.08	0.0	0.00
12	0.0	0.08	0.0	0.00
24	0.0	0.08	0.0	0.00

The final MN concentrations in table 7.8 was plotted onto a concentration / time graph to form the cumulative concentration curve in figure 7.6. These equations were applied to every Franz cell experiment in this thesis.

Table 7.8 Adding the concentration difference of consecutive samples to form a cumulation curve

Time (hrs)	Concentration μ g/ml	
	Control	MN
0.08	0.00	0.00
0.25	0.01	0.10
0.5	0.01	0.13
1	0.01	0.14
2	0.01	0.15
4	0.01	0.15
6	0.01	0.16
8	0.01	0.17
10	0.02	0.17
12	0.02	0.17
24	0.02	0.17

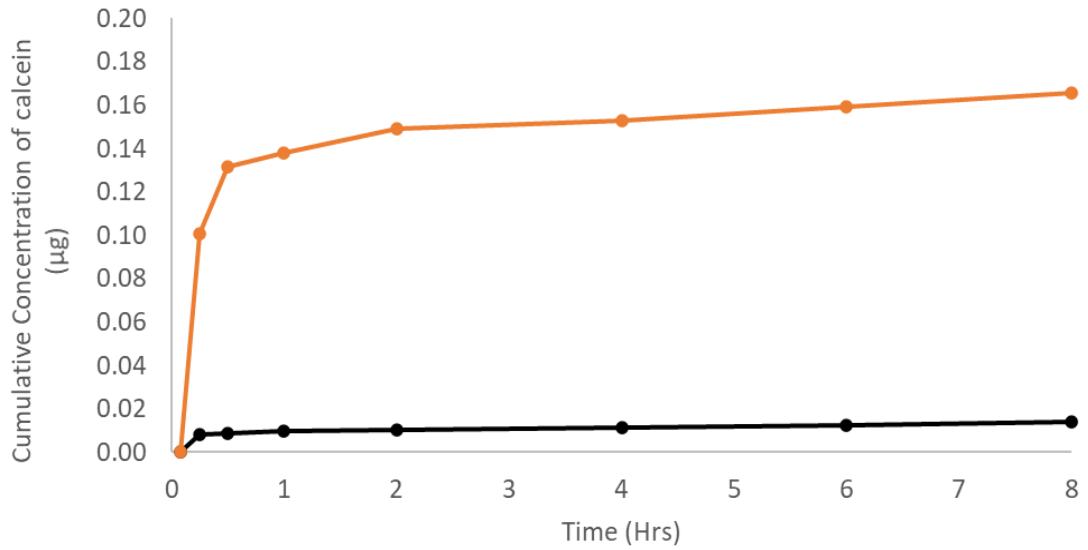


Figure 7.6 Cumulative concentration graph of exemplar data

7.4.2 Franz cell flux rate

To calculate the flux rate i.e., the rate at which the drug samples flow into the receptor chamber, the concentration was divided by the Franz cell orifice area (the size of the aperture that the drug diffuses through) and the sample corresponding time point (hours).

The Franz cell orifice is circular with a radius of 0.45mm, thus, using the surface area of a circle equation πR^2 , the surface calculated as 0.63585mm.

Therefore, the flux was calculated as: sample concentration / 0.63585/ time point ($\mu\text{g}/\text{cm}^2/\text{h}$), which is demonstrated in table 7.9 using the previous example data.

Table 7.9: Flux rate calculations

Time (hrs)	Flux Js ($\mu\text{g}/\text{cm}^2/\text{h}$)	
	Control	MN
0.08	0.00	0.00
0.25	0.05	0.63
0.5	0.03	0.41
1	0.02	0.22
2	0.01	0.12
4	0.00	0.06
6	0.00	0.04
8	0.00	0.03
10	0.00	0.03
12	0.00	0.02
24	0.00	0.01

7.4.3 Tape stripping

To calculate the concentration of drug that had remained either on the skins surface or partitioned into the SC after Franz cell analysis, the tape strip method was applied. Adhesive tape strips cut to 4cm^2 sized strips were manually applied to the skin, SC side up. At a consistent rate, the strips were removed from the skin and placed into PBS. In total 10 tape strips were applied, where the first strip was isolated in PBS to analyse the amount of drug found on the SC, while the following 9 strips were pooled together to calculate the amount that had partitioned into the SC. Overnight the tape strips were rotated on a roller mixed to resuspend any drug from the tape strips into the solution.

7.4.4 Skin homogenisation

To calculate the concentration of drug that had partitioned into the epidermis, after tape stripping skin samples were homogenised in either papain or collagenase enzymes to break down the skin structure and release any drug that has accumulated.

Collagenase enzymes degrades the helical peptide bonds found in collagen that form the

skin epithelial and connective tissues. Collagenase was diluted in PBS at concentrations of between 1mg/ml - 20/mg.

Papain is a proteolytic enzyme extracted from the fruit of a papaya plant and functions by cleaving peptide bonds rich in leucine or glycine amino acids [192]. However, when digesting active ingredients that are protein based, collagenase is alternatively used. Papain was diluted to 2mg/ml in activation buffer consisting of 20mM Sodium Acetate, 1mM EDTA (Ethylenediaminetetraacetic acid) and 2mM DTT (Dithiothreitol) to a pH of 6.8.

7.5 Sample analysis

7.5.1 Fluorescent spectrometry

Fluorescence spectrometry is the measurement of the fluorescence emitted by a substance while it is exposed to electromagnetic radiation at the correct wavelength. The FLUOstar® Omega spectrophotometer was used for its multi-mode microplate reader with a variety of UV/vis and fluorescent filters.

To analyse the concentration of the drug compound from the Franz cell receptor chamber samples, fluorescent spectrometry was used. For ease of analysis, all drugs and model drugs tested in this thesis were fluorescently tagged. Therefore, the fluorescent signal detected is proportional to the concentration of the drug.

A 96 well plate was used to analysis the samples whereby, 100µl of each sample was pipetted into three wells (totalling 300µl per sample), for triplicate statistical analysis. The 96 well plate was inserted into the plate reader and programmed to the corresponding drugs fluorescent wavelength. The plate reader then shone the correct wavelength of light at each individual sample well and the detector converted the emitted light into a reading, which was compared to a calibration curve of known fluorescent concentration readings.

Part 3
Microneedle fabrication

Chapter 8

Out-of-plane MN fabrication

8.1 Introduction

The Out-of-plane microneedle (OOP MN) fabrication work was initiated through a collaboration between Swansea University and SPTS Technologies (Newport, UK) in 2010, in which the following patent was created EP3415465A1. This patent covers the unique bevel design of the MN constructed from deep reactive ion etching (DRIE) of silicon. At the start of my PhD studies in 2017, the initial MN proof of concept designs and MN prototypes had been tested to show encouraging and successful skin penetration results. However, further optimisation of the photolithography process and etch steps was required to resolve some of the remaining design and fabrication issues which are discussed throughout this chapter. Through a continued collaboration, photolithography development was undertaken at Swansea University, while the DRIE etching optimisation was completed at SPTS technologies by Chris Bolton. The results of this chapter are published in *Lab on a chip* (<https://doi.org/10.1039/D0LC00567C>).

8.2 MN proof of concept designs

The fabrication concept for hollow MNs is outlined in figure 8.1, and consists of three main phases:

- A. formation of a bevel for the sharp angled MN tip (steps a to c)
- B. etching of the central bore, which can be used to transport fluid (steps d to f)
- C. formation of the MN shaft (steps g to i)

Although this process is designed for the manufacture of hollow MNs, by omitting step (B), solid MNs can also be fabricated.

As the MNs are in out-of-plane (OOP) orientation, the thickness of the silicon wafer will determine the maximum length of the MN. Therefore, to create MNs of 700 μm length and maintain a stable base for mechanical support, 1.2mm thick silicon wafers were used.

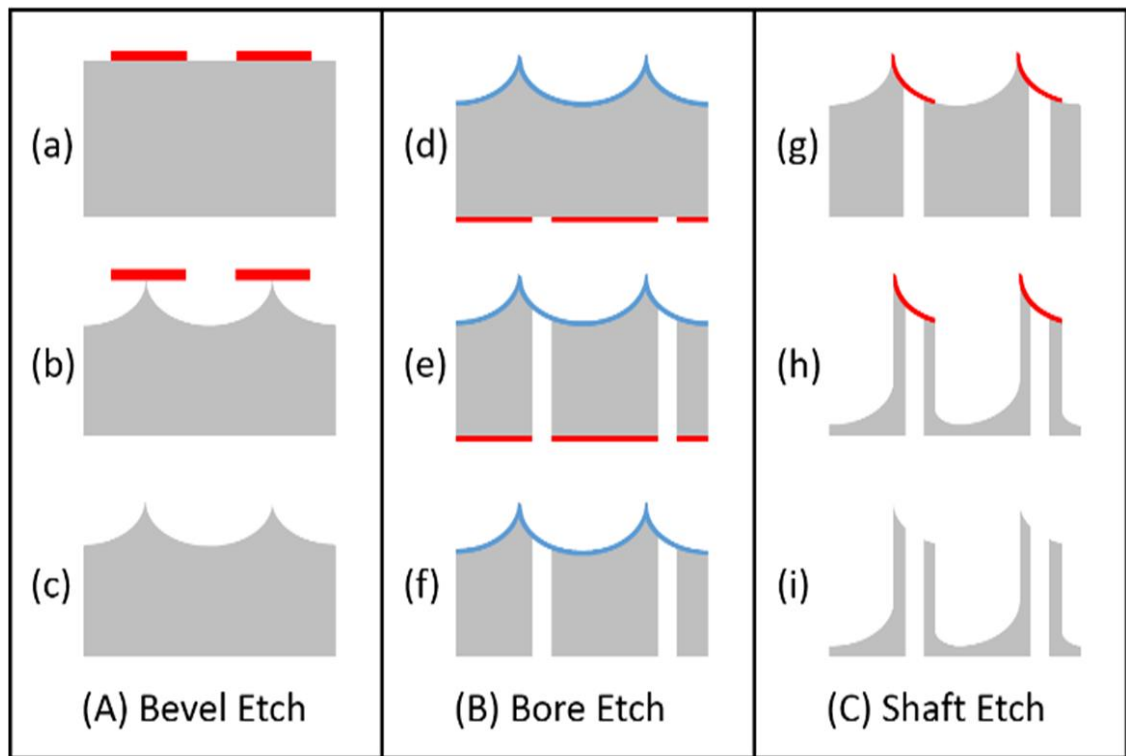


Figure 8.1 Schematic process flow for hollow silicon MN production. Silicon (grey), with photoresist masks (red) and silicon oxide (blue), respectively.

To perform each fabrication step, unique mask patterns were designed to guide subsequent anisotropic and isotropic DRIE etching into the required shape. Although further detail on each step will be addressed in the following subchapters, for clarity, figure 8.2 shows how these masks are used in sequence to create the OOP silicon MNs. The first mask (figure 8.2A) is designed as a simple rectangle ($950\mu\text{m} \times 700\mu\text{m}$), with a pitch spacing of $700\mu\text{m}$ between subsequent rectangles. Here an isotropic etch is used to undercut the rectangular mask and form the MN bevelled tip surface. To create the bore i.e. the hollow channel that runs centrally and vertically through the MN (out of the plane of the wafer), a mask consisting of $100\mu\text{m}$ circular windows is created on the reverse of the wafer, which are aligned to the centre of the bevel (blue shading in figure 8.2B). A BOSCH etch process is utilised to etch from the reverse side of the wafer, through the circular windows and completely through the wafer until the oxide etch stop on the bevelled surface is reached. The final etch mask is used to construct the overall shape of the MN (figure 8.2C), by combining the bevelled tip to a $300\mu\text{m}$ diameter cylindrical shaft. When incorporating the $100\mu\text{m}$ diameter bore for hollow MN

fabrication, aligned centrally within the 300 μ m shaft generates a final MN shaft wall thickness of 100 μ m.

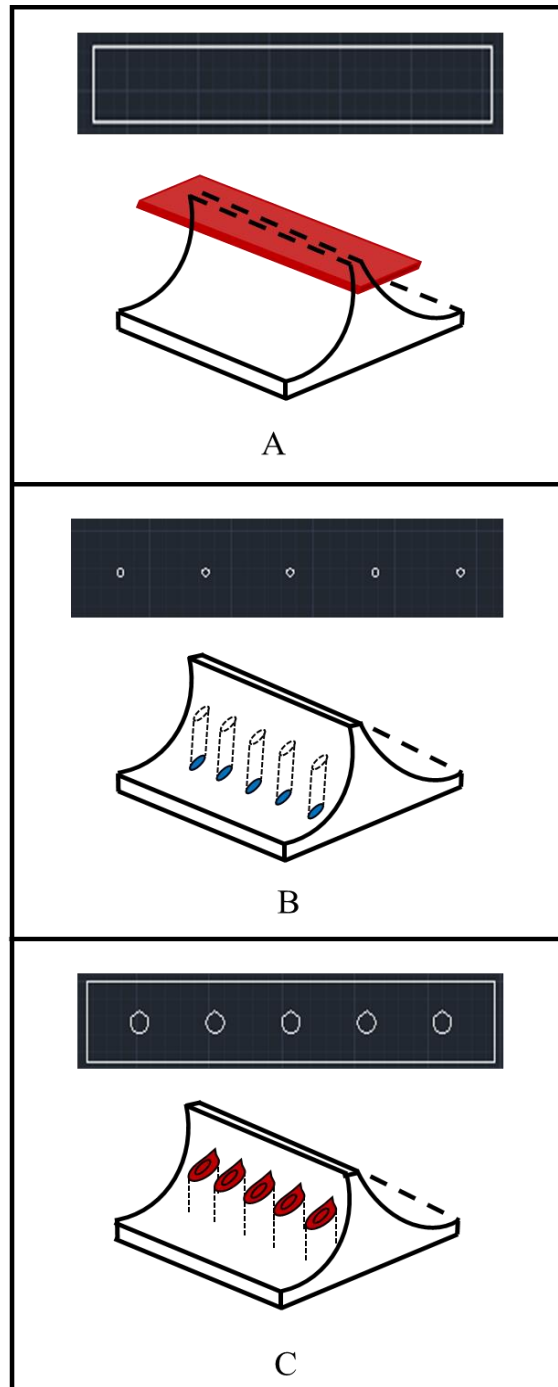


Figure 8.2 Schematic drawings and AutoCAD mask designs demonstrating how the three masks are used in sequence to fabricate hollow microneedles. (A) Rectangular resist mask (red) isotropically undercut to create a bevelled MN tip; (B) 100 μ m circular bore, etched from the reverse (blue) of the wafer through to the bevelled surface; (C) MN tip and shaft design aligned over the central bore, to etch around the resist (red) and create cylindrical shafts with a pointed tip.

8.3 Bevel photolithography

The first step (A) in the process flow (figures 8.1 and 8.2) is the photolithography mask patterning of the bevel design onto the surface of a silicon wafer. The mask design (figure 8.2) is patterned using negative resist Az125nXT_10A, to the spin coating parameters in table 8.1, this should produce a resist mask thickness of 34 μ m.

Table 8.1. Original photolithography parameters for bevel development

Wafer cleaning procedure	10 minutes in acetone bath 5 minutes in IPA bath Dry with nitrogen gas Bake for 10 minutes at 150°C
Spin parameters	Spin at 300rpm for 10 seconds at an acceleration of 150rpm Spin at 2000rpm for 30 seconds at an acceleration of 300rpm
Soft bake parameters	130°C for 5 minutes
UV Exposure parameters	Dosage of 1500mJ / cm ²
Post exposure bake	100°C for 1 minute
Development parameters	Az726 for 2 minutes

These spin parameters in table 8.1 were developed before the start of this PhD in 2017 and were an inherited method process. However, upon patterning the wafer with this method several issues were identified; these included an increased soft bake time from 5 minutes to 60 minutes, leaving the resist wet and sticky rather than the required dry and smooth state for processing. While aligning the wafer in the MA, the chuck is levelled by an automated process of gently pressing the wafer to the mask. However, the sticky state of the resist consequently caused the wafer to stick to the mask which then had to be manually removed thus damaging the resist layer. The thickness of the final spun resist measured 42 μ m (figure 8.3) rather than the required 34 μ m and developing the resist for 2 minutes left areas of the wafer undeveloped and patchy.

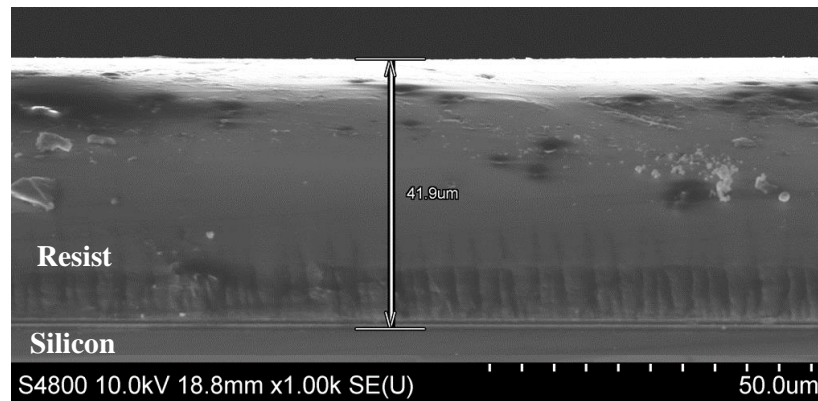


Figure 8.3 SEM image of AZI25nxt resist, after spinning, to measure a thickness of 42µm

To address these issues initially, any wafers spun using these parameters, the following parameters such as bake times and development times were instinctively adjusted until the resist was suitable for use. However, the full optimisation process is outlined in section 8.3.1, to create a reliable and repeatable spin method.

It was determined that the increased resist thickness was the source of several issues, for instance; a bake time of originally thought 5 minutes was intuitively increased to over 60 minutes in order to bake (harden) the resist sufficiently to avoid it sticking to the glass mask in the MA. In addition, it was found that upon exposing the resist to UV via the MA, the thicker resist layer was not uniformly crosslinked and caused uneven development. Thus, to enable the UV wavelengths to penetrate deeper into the thicker resist and initiate cross-linking, either a longer UV exposure times and/or a higher exposure dose is required.

Issues observed from the spin parameters itself, detected an edge bead (a thicker area of resist) formed around the circumference of the wafer; this was due to the acceleration spin speed reaching the desired RPM too quickly (figure 8.4A) thereby pushing the resist outwards. Consequently, this edge bead exacerbated the resist / mask sticking issue when the chuck levelling process was carried out in the MA. To understand how, figure 8.4 illustrates the chuck levelling method. As this is an automated process to ensure the mask and resist align parallelly, this cannot be manually modified. Therefore, as the chuck is raised, if the edge bead is thicker than the resist in the centre of the wafer, it will become increasingly compressed against the glass mask until the whole resist layer is in contact with the mask. Thereby damaging both the resist and the mask.

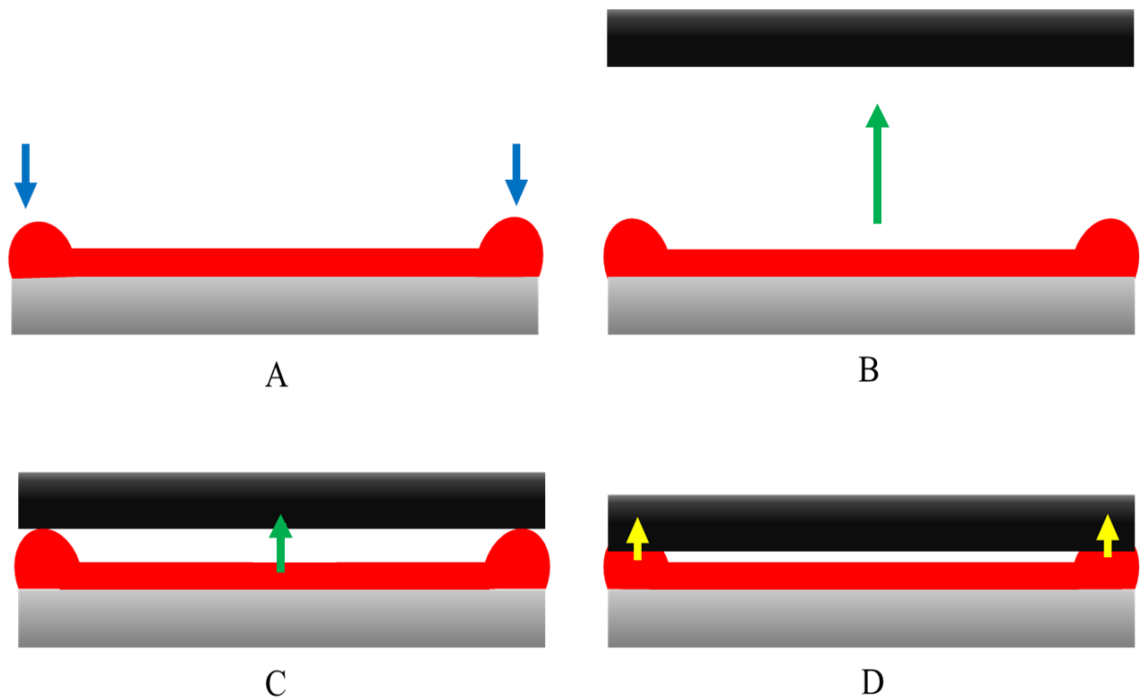


Figure 8.4 Schematic diagram showing contact between the edge bead and the mask. Silicon wafers are represented in Grey, Resist represented in red and glass mask represented in black. (A) wafer spun with edge beads (blue arrows) (B) Chuck ascends towards mask (C) thick edge bead touches mask first (D) continued ascending, shows edge bead being compressed (yellow arrows) against mask, until the thinnest resist area is contacted for the MA to evaluate the surface.

To resolve the aforementioned issues, a thinner more uniform resist thickness is required, which is still suitable to withstand the isotropic bevel etch and achieve an approximate depth of $500\mu\text{m}$.

Etching experiments identified a resist etch selectivity of 1:50 (resist: silicon) for Az125nxt, meaning a resist thickness of approximately $20\mu\text{m}$ would be suitable to withstand the DRIE etching processes.

8.3.1 Photoresist Az125nxt thickness optimisation

To begin optimisation, the previous spin recipe was used as a guideline and each parameter was changed independently to analysis its effects. Primarily, the first parameter to change is the thickness of the resist, from $42\mu\text{m}$ to $20\mu\text{m}$. Therefore, initial experiments were performed by varying the spin speed of the second step (annotated as a an ?), to create a resist thickness of $20\mu\text{m}$.

- Spin parameters
 - ~ Step 1: Spin at 300rpm for 10 seconds at an acceleration of 150rpm
 - ~ Step 2: Spin at ? rpm for 30 seconds at an acceleration of 300rpm

Spin speeds tested were 1000, 3000 and 4000rpm (2000rpm was already known to generate a thickness of 42 μ m). The resist thickness after MA exposure were examined through SEM and EDX analysis (figure 8.5) with the thickness results plotted on a graph (figure 8.6). All other parameters i.e., bake times etc remained the same, with the exception of the PEB, which upon consulting the MicroChemicals technical data sheets for Az125nxT resist, is not necessary and was thus removed.

The SEM images (figure 8.5) show resist thicknesses of 68 μ m, 27 μ m and 19 μ m for spin speeds 1000, 3000 and 4000 rpm, respectively. Figure 8.5D shows the EDX chemical mapping of resist and silicon layers for a spin speed 4000 rpm, where the carbon-based resist is highlighted in red and the silicon wafer in green enabling a clear distinction between the two.

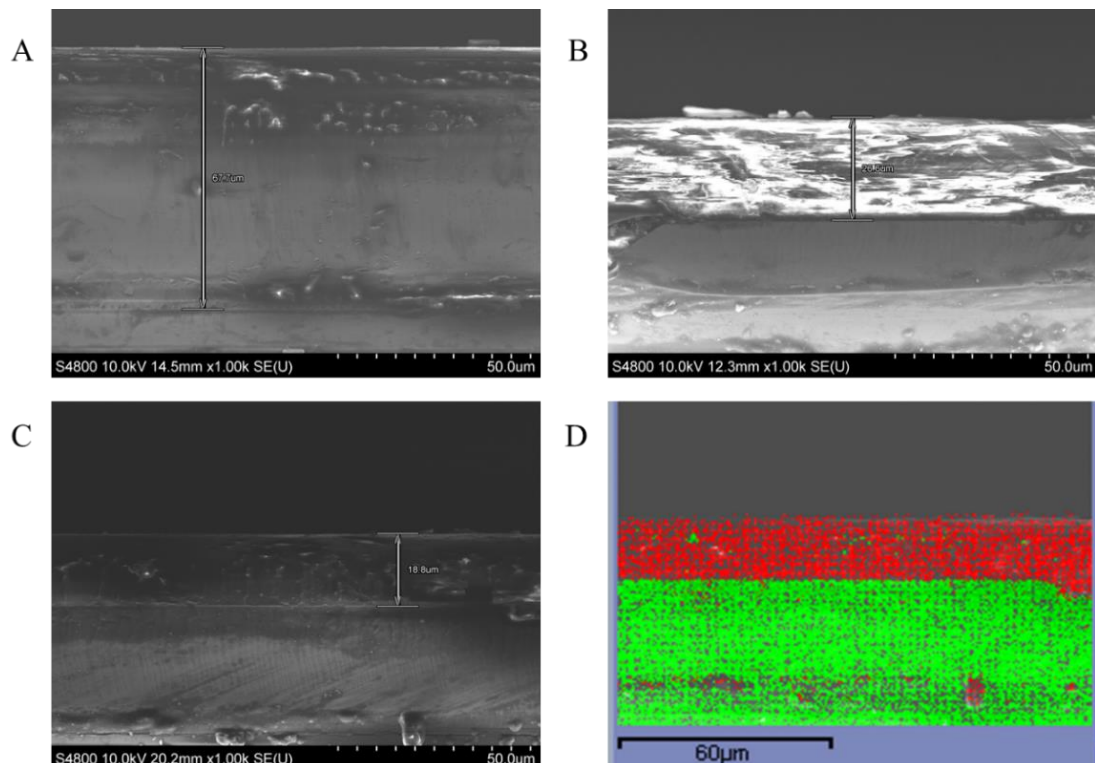


Figure 8.5 SEM analysis of Az125nxT resist spun at speeds of (A) 1000rpm (B) 3000rpm (C) 4000rpm and (D) EDX analysis of 4000rpm showing resist in red and the silicon wafer in green.

The thickness results (figure 8.6) were plotted as a function of spin speed and a fitted quadratic equation was used to calculate the required spin speed for a desired thickness. For the bevel etch, a resist thickness of 20µm is required; a spin speed of 4000rpm created a resist thickness of 19µm, therefore, the precise speed would be slightly slower as it is seen that faster speeds create thinner resist.

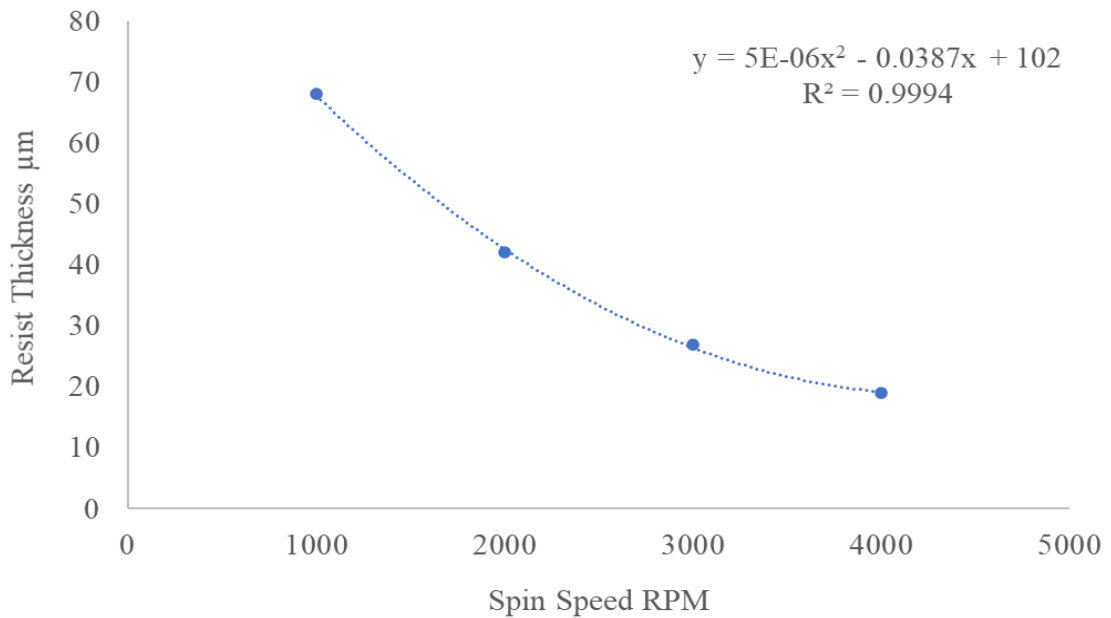


Figure 8.6 Graph to show relationship between Az125next resist thickness and spin speed

To find the spin speed (x) for a thickness (y) of 20µm, the quadratic equation in figure 8.6 was rearranged to find x, which calculated 3800 rpm. Therefore, the next test substituted 3800rpm into the second spin step and found that 3800rpm creates a resist thickness of 20µm (figure 8.7), suitable for bevel etching.

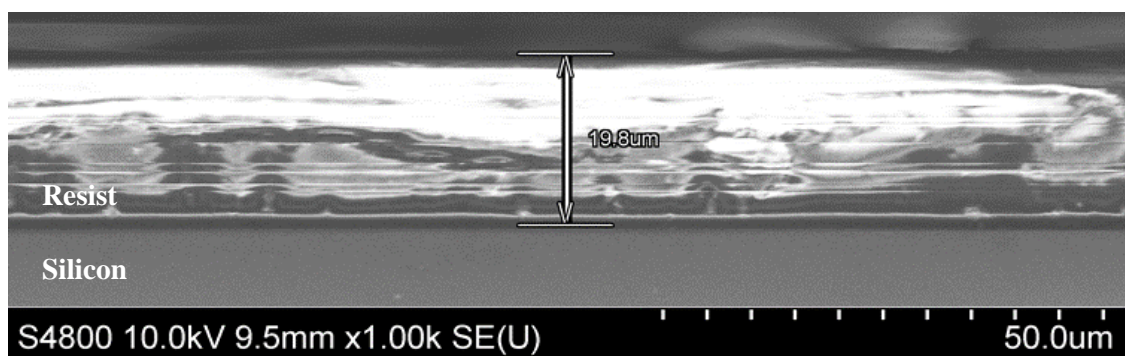


Figure 8. 7 SEM image of Az125next resist spun at 3800rpm to create a resist thickness of 20µm

Maintaining all other parameters proved successful in creating a uniform resist thickness of 20 μ m that was not sticky after baking and developed in 2 minutes. Therefore, the new method for bevel mask patterning and development is as follows (table 8.2).

Table 8.2. Optimised photolithography parameters for bevel development

Wafer cleaning procedure	10 minutes in acetone bath 5 minutes in IPA bath Dry with nitrogen gas Bake for 10 minutes at 150°C
Spin parameters	Spin at 300rpm for 10 seconds at an acceleration of 150rpm Spin at 3800rpm for 30 seconds at an acceleration of 300rpm
Soft bake parameters	130°C for 5 minutes
UV Exposure parameters	Dosage of 1500mJ / cm ²
Post exposure bake	100°C for 1 minute
Development parameters	Az726 for 2 minutes

8.4 Bevel DRIE etching

To create the bevelled tip of the MN an SPTS deep silicon etch (DSiV) tool was used at SPTS labs; the isotropic etch undercuts the rectangular resist mask to create a sloped surface either side of a flat top (figure 8.8). To achieve this, a single step etch was optimised at SPTS, whereby vertical and lateral etching took place in conjunction with a simultaneous passivation step to direct the ion bombardment to the base surface of the feature and form the isotropic bevel. This partial directionality during the isotropic etch enabled the bevel angle to be tuned. For instance a maximum MN tip angle of 20° was used as a guide to create sharp and robust MN tips that requires little applied force for skin penetration [193]. By tuning the following etch parameters, a subsequent bevelled slope measuring 17.6° was created, sufficient for the shape for the MN [194].

Gases	SF ₆ : C ₄ F ₈ : O ₂	In flow ratio of 6:1:1
Chamber pressure	70mTorr	
RF Coil Power	2500W	
RF Bias Platen	40W	

The two opposite bevels created are purposely not etched to completion to form an intersecting point, but instead a flat area between the MNs is left. This flat bevel top is required in the next step, as a support platform for wafer bonding. Post etching, the wafers were transported to Swansea university to be cleaned with designated resist stripper and IPA, to remove residual resist and etch debris.

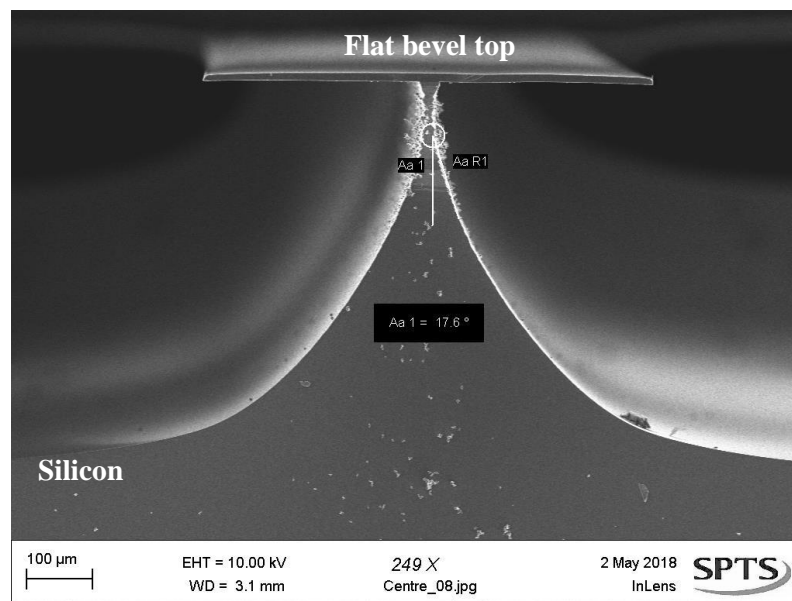


Figure 8.8 (A) SEM image showing DRIE etched bevel measuring 17.6°

8.5 Bore fabrication optimisation

The next step in hollow MN fabrication, was to etch the MN bore from the reverse of the wafer, through to the front, steps d and e from figure 8.1, reproduced in figure 8.9.

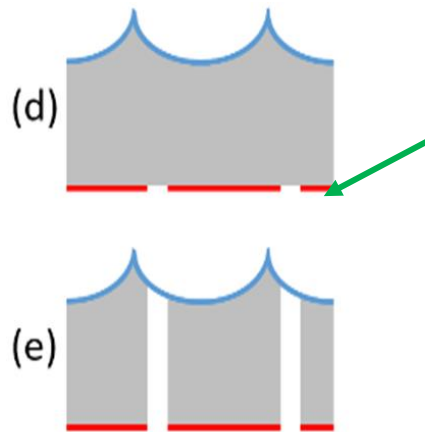


Figure 8.9 Schematic process flow showing the (d) bore mask patterned onto the backside of the wafer (green arrow) and (e) etched from the reverse of the wafer. Silicon wafers are represented in grey, with photoresist masks and silicon oxide shown in red and blue, respectively.

To pattern the bore mask onto the reverse of the wafer, the wafer was flipped and mounted onto a silicon oxide coated carrier substrate; supported by the flat tops of the etched bevels (figure 8.10A). However, before the wafer can be mounted onto the carrier, the bevelled slopes on the front of the wafer need to be protected from the DRIE bore etch step (figure 8.9e), otherwise once the hollow bore has etched through the wafer (figure 8.10B), it would create an opening through which the etchant gasses would flow and subsequently etch the available silicon on the front of the wafer, consequently damaging the bevel features (figure 8.10C). Therefore, to protect the bevels, a silicon oxide hard mask was deposited on the bevelled surface before etching to act as an etch stop (figure 8.10D).

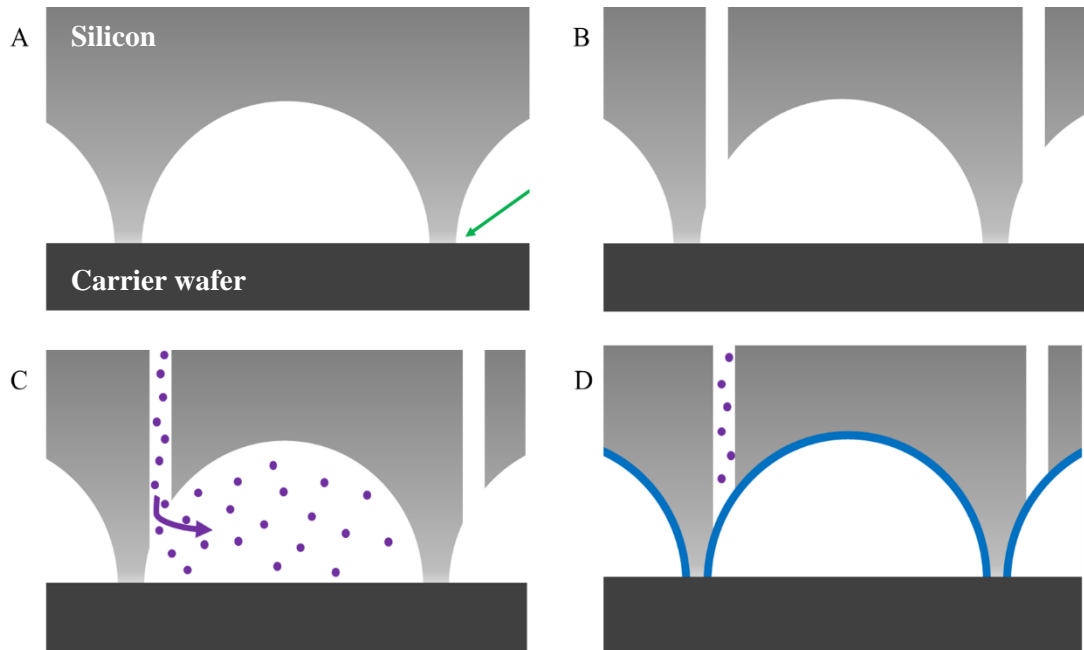


Figure 8.10 Schematic process flow showing (A) the bevel etched wafer is flipped, and mounted onto a carrier wafer by the flat tops (green arrow) (B) Etching the bores through the wafer with no back stop (C) etchant gasses (purple dots) pass into the bevelled space to etch available silicon on the bevel (D) Silicon oxide back stop layer (blue) is used to protect the bevels from etchant gasses

The etch selectivity between silicon and silicon dioxide is considerably higher than resist selectivity, at >100:1, meaning that for every 100 μm of silicon only 1 μm of silicon dioxide is etched [195]. The amount of silicon dioxide required will thus depend on the wafer thickness and the etch depth required for the bore. Calculations determined that 8 μm of silicon dioxide would be sufficient to etch an 800 μm bore whilst protecting the bevels from etch damage.

An SPTS PECVD system was used to deposit 8 μm silicon dioxide (figure 8.11), using the following in-house recipe:

Gases and flows	SIH ₄	3000
	N ₂ O	105
HF generator power	540	
Process time	7 Minutes	



Figure 8.11 SEM image of bevelled surface with $\sim 8\mu\text{m}$ of silicon dioxide deposited onto the surface (darker grey area on the perimeter)

Following silicon dioxide deposition, the next step is to spin coat resist onto the flat surface of the backside of the wafer for bore mask patterning. This requires the bevelled surface to be placed facing the chuck which forms the vacuum and holds the wafer in place. However, as the bevelled surface is not uniform, the chuck cannot form a vacuum to seal to the surface and the wafer would not remain in place upon spinning. To fix this, transparent dicing tape that is adhesive on one side, was cut to the shape of the wafer and applied to the bevelled surface (figure 8.12). The adhesive side of the tape adheres to the flat tops between each bevel to create a uniform flat layer that forms a vacuum seal with the chuck; thus, upon spinning the wafer remains in place.

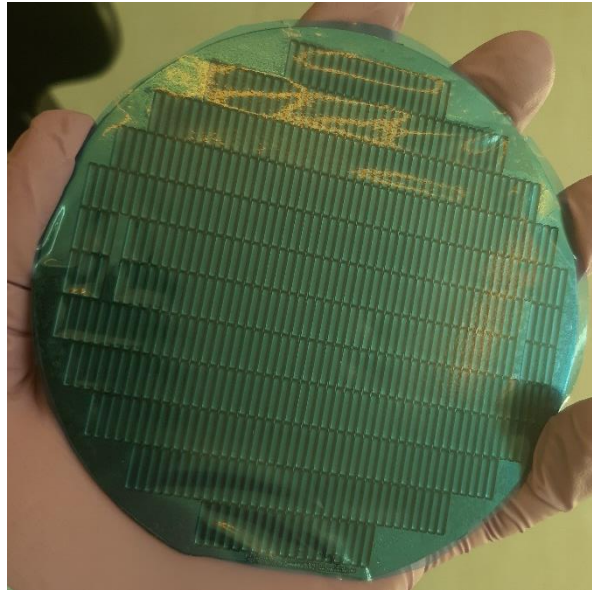


Figure 8.12 4-inch bevel etched wafer with a blue adhesive dicing tape layer acting as an aid to provide a vacuum seal.

Next, the wafer was placed in the spin coater, dicing tape side down, and spun to the following recipe in table 8.3, to coat Az125nxt resist to a thickness of 35 μ m suitable for the bore mask design.

Table 8.3. Original photolithography parameters for bore development

Wafer cleaning procedure	10 minutes in acetone bath 5 minutes in IPA bath Dry with nitrogen gas Bake for 10 minutes at 150°C
Spin parameters	Spin at 300rpm for 10 seconds at an acceleration of 150rpm Spin at 1000rpm for 30 seconds at an acceleration of 300rpm
Soft bake parameters	130°C for 14 minutes
UV Exposure parameters	Dosage of 2500mJ / cm ²
Post exposure bake	110°C for 2 minutes
Development parameters	Az726 for 15 minutes

However, the recipe in table 8.3 was once again an inherited recipe and was found not to be fully optimised. For instance, the spin speed of 1000rpm has already been confirmed in the graph in figure 8.6, to create a resist thickness of 68 μm (figure 8.5A), which is 28 μm thicker than the thickness required for bore etching. SEM imaging of the bore pattern using the spin parameters above, confirmed a resist thickness of 69 μm , (figure 8.13) which created the same issues as discussed in section 8.2.1.

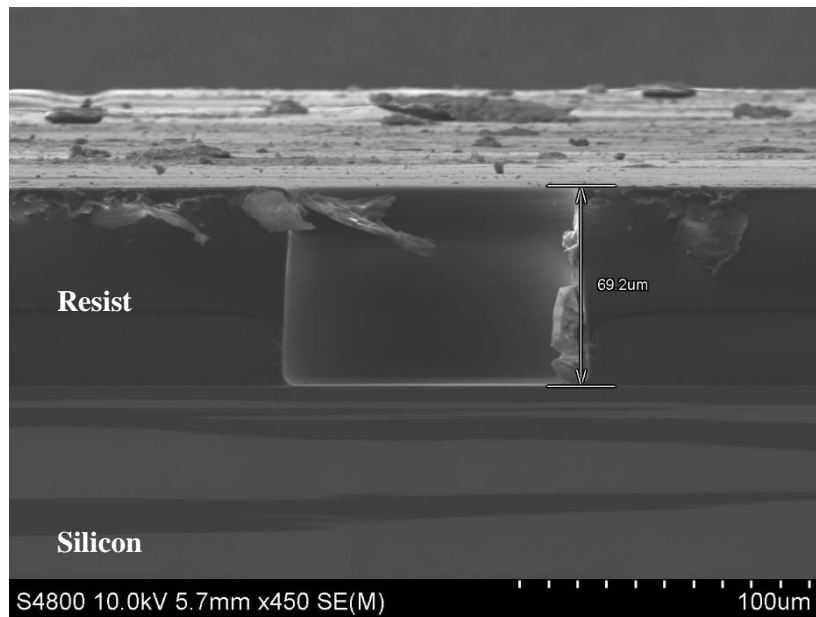


Figure 8.13 SEM image of bore mask pattern showing a resist thickness of 69 μm

The quadratic equation from figure 8.6, was used to find the spin speed (y) for a resist thickness (x) of 35 μm ; this calculated a spin speed of 2500rpm. Substituting 2500rpm into the spin method in table 8.3, successfully created a resist thickness of 35 μm (figure 8.14), which was used for all subsequent bore patterning.

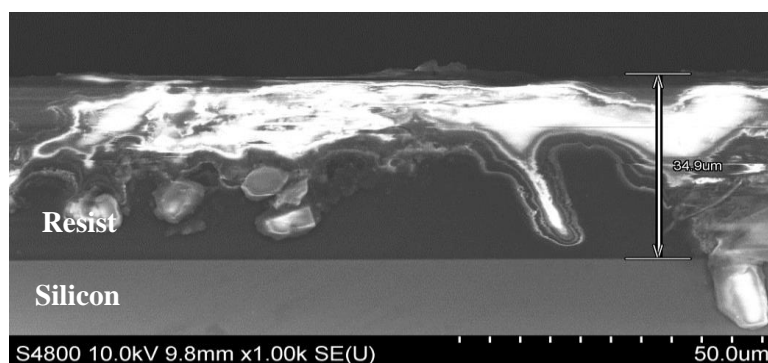


Figure 8.14 SEM image of resist measuring 35 μm , after a spin speed of 2500rpm

Due to the new resist thickness, other parameters such as bake, and development times were re-evaluated to ensure the optimal method was established. The original method developed before this PhD, again included a post exposure bake, however with guidance from the MicroChemicals data sheets, this was removed [196]. The original resist development time for a 69 μm thickness was 15 minutes. However, as the thinner 35 μm resist is ~half the thickness, 15 minutes may over develop the resist pattern.

To optimise the development time a bore patterned wafer was diced into five portions, with each piece submerged in P1316 developer for either 3, 5, 7, 9, or 11 minutes, respectively. The SEM images in figure 8.15, show a top-down view of the bores after each development time to assess how the circular bore opening had formed.

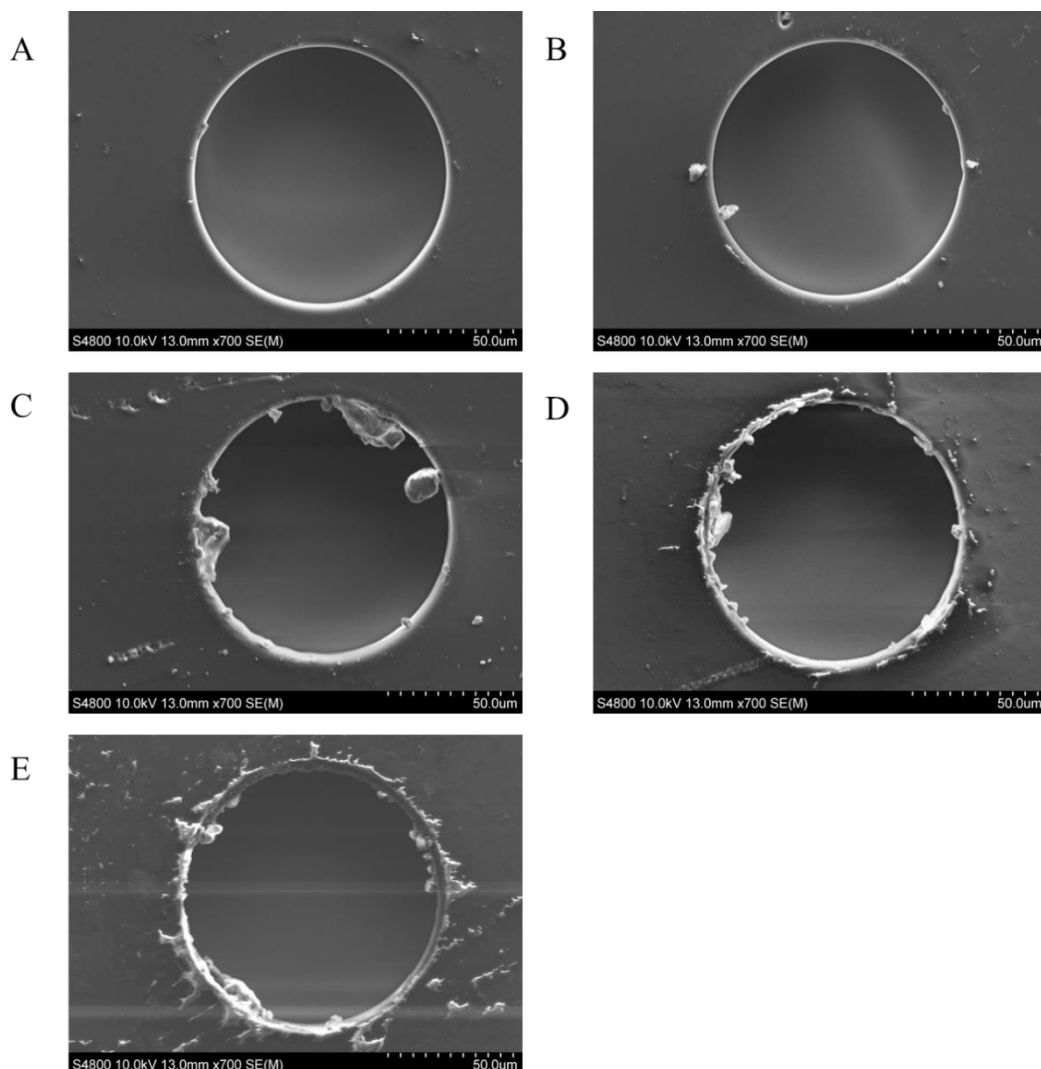


Figure 8.15 SEM images of bore pattern development in P1316 developer after (A) 3 minutes (B) 5 minute (C) 7 minutes (D) 9 minutes (E) 11 minutes

At the development times of 3 and 5 minutes the circular form of the bore is uniform, clean and seems to be fully developed. Increasing the development to 7 minutes shows the edge of the bore start to roughen, with resist debris depositing around the circumference of the circular openings in the resist layer. At 9 and 11 minutes it is clear that the edge of the bore is extremely rough and has lost uniformity, indicating overdevelopment. Therefore, the top-down SEM images indicate a development time of between 3 and 5 minutes is optimal and developing longer than 5 minutes may produce sub-optimal lithography which then translates to imperfect cylindrical bore side walls, which may disrupt uniform fluid flow through the subsequent fabricated MN.

However, as the thickness of the resist is $35\mu\text{m}$, the shape of the resist opening needs to be fully developed for the whole depth of the resist to transfer the profile shape to the wafer during etching. To determine if the resist opening was fully developed, wafer pieces with development times 3, 5 and 7 minutes respectively, were diced to visualise the cross section of the resist on the wafer (figure 8.16). At 3 minutes development it is clear that the resist has not fully developed through the full resist thickness, as the remaining resist has forming a curved profile at the base of the opening, indicating that the silicon wafer has not yet been exposed (figure 8.16A). After a development time of 5 minutes the resist has completely developed, exposing the silicon wafer beneath (figure 8.16B). However, the side walls are slanted inwards, meaning the base of the opening is smaller than the top; if this profile were to be etched then the resulting bore would be smaller in diameter than the required mask design. Increasing the development time to 7 minutes (figure 8.16C) again shows a clear fully developed opening in the resist, however the extra 2 minutes of development have enabled the sidewalls to become vertical, mirroring the mask design.

Although originally images viewed from a top-down orientation (figure 8.15) proposed a development time of <5 minutes for bore development, the cross-section analysis revealed that the sidewalls of the resist pattern were not vertical and thus required a longer development time of 7 minutes to mirror the resist mask.

The starting resist thickness measured $68\mu\text{m}$ and was intended to develop within 15 minutes. This work indicates that a new thinner resist mask layer of $35\mu\text{m}$, approximately half the thickness, develops in less than half the time (7 mins).

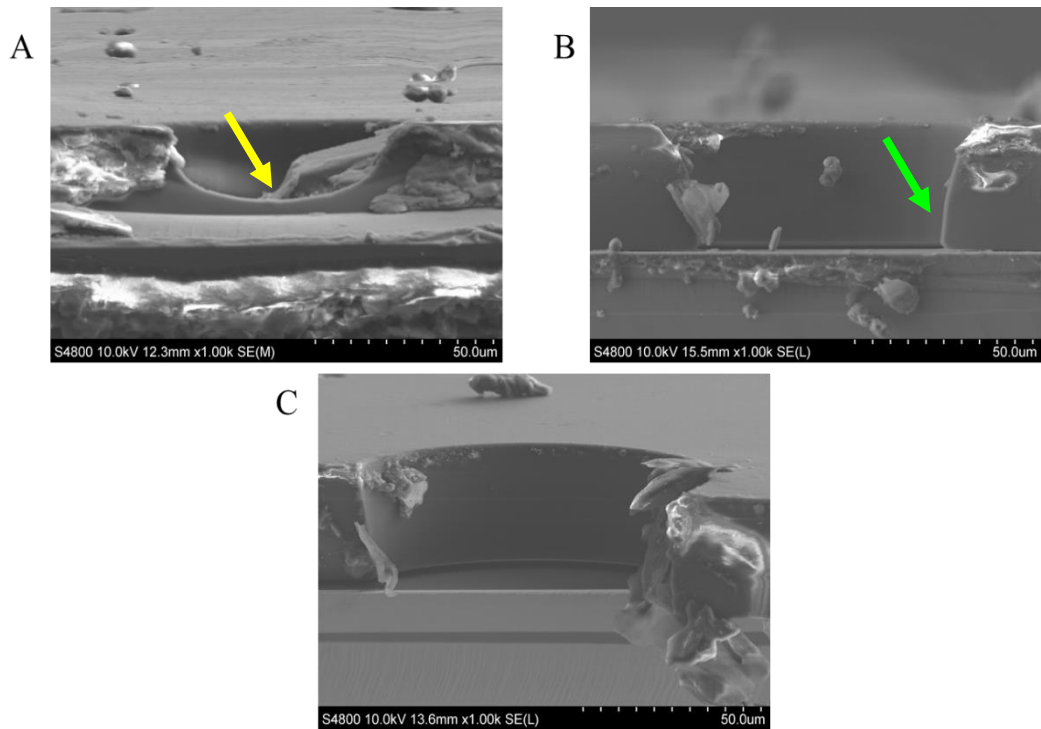


Figure 8.16 Cross section SEM images of bore pattern developed into the resist after (A) 3 minutes (B) 5 minute (C) 7 minutes. Yellow arrow shows the undeveloped curved resist, Green arrow indicates the slanted underdeveloped side wall profile

The optimised parameters for bore photolithography are outlined in table 8.4.

Table 8.4. Optimised photolithography parameters for bore development

Wafer cleaning procedure	10 minutes in acetone bath 5 minutes in IPA bath Dry with nitrogen gas Bake for 10 minutes at 150°C
Spin parameters	Spin at 300rpm for 10 seconds at an acceleration of 150rpm Spin at 2500rpm for 30 seconds at an acceleration of 300rpm
Soft bake parameters	130°C for 14 minutes
UV Exposure parameters	Dosage of 2500mJ / cm ²
Post exposure bake	110°C for 2 minutes
Development parameters	Az726 for 7 minutes

8.6 Bore DRIE etching

To etch a bore vertically through the silicon wafer, a traditional switched etch process was used where the two switching steps consisted of a polymer deposition coating (typically using C_4F_8), followed by an anisotropic etch. This iterative sequence is commonly known as the BOSCH etch and is used to specifically etch bores through silicon wafers without etching the surrounding material. The deposition step forms a protective coating over the side walls of the etch feature, so that during the anisotropic etch, the etch molecules preferentially etch the base of the feature [197]. By only etching the base the etch proceeds vertically into the silicon to create a through silicon via (TSV); each anisotropic etch can be distinguished by the “scallop” on the via sidewall, therefore one complete etch sequence creates a single scallop, while increasing the depth of the etch into the silicon, increases the number of scallops.

More recent etching techniques combine the BOSCH etch with an additional etching process step to create a 3-phase switch etch [194]. The additional step selectively etches into the polymer deposition layer at the base of the via to expose the silicon only at the base of the feature (figure 8.17. panel 3). This effectively allows the silicon to be etched faster to increase the overall process etch rate. Figure 8.17, panels 2-4 illustrates the overall deposition (450sccm C_4F_8), etch 1 (200/100sccm O_2/SF_6) and etch 2 (720sccm SF_6) sequence, with the subsequent panels illustrating the repeated steps to achieve depth etching.

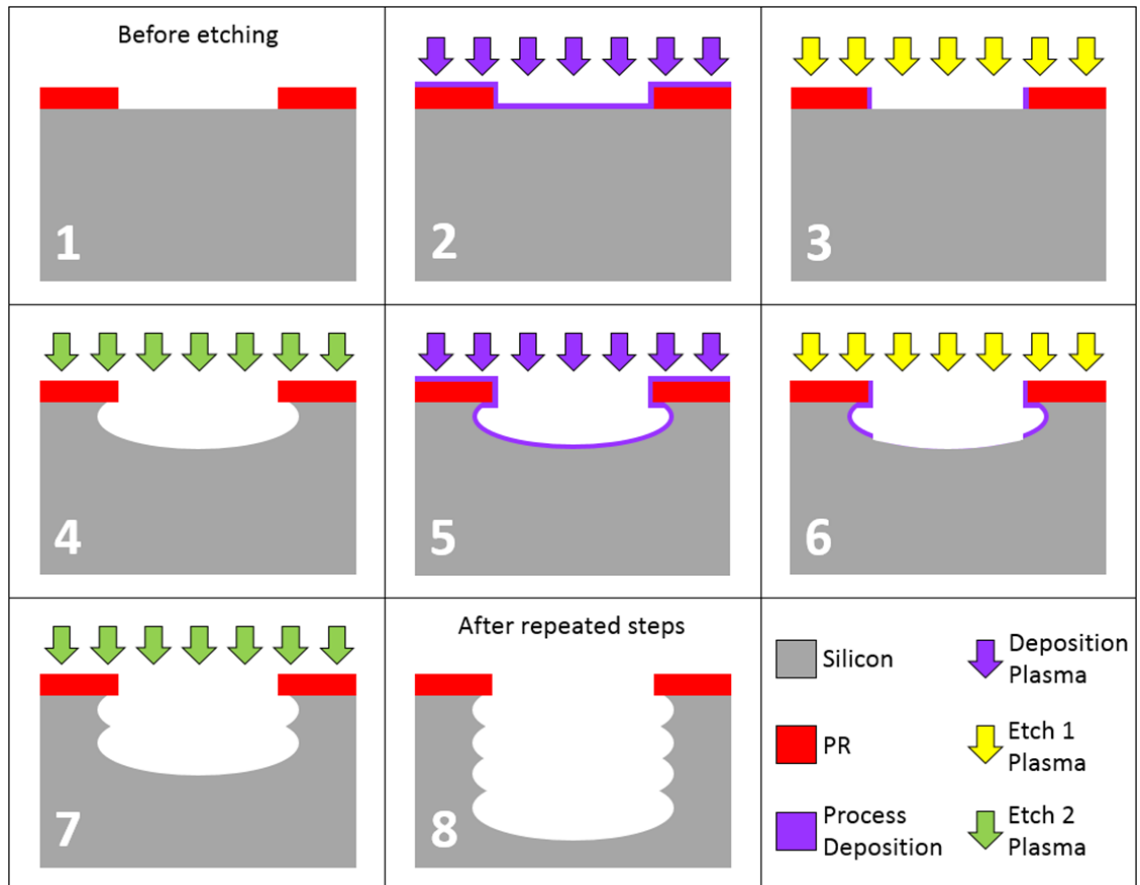


Figure 8.17 Schematic diagram of 3-phase switched etch, illustrated step-by-step. (1) silicon wafer with resist pattern (2) C_4F_8 deposition protection (3) SF_6 / O_2 Plasma etch 1, selectively opening the base area (4) SF_6 Anisotropic plasma etch 2, creating a single scallop, steps 2-4 are repeated in steps 5,6,7 and 8 to etch deeper into the silicon

Figure 8.18 shows a test TSV structure, etched into a silicon wafer, with a via depth of $1257\mu m$ and diameter of $96\mu m$, from using a 3-step switch etch. A higher magnification image (figure 8.18C) shows the scalloped effect of the etch on the via sidewalls.

The optimised photolithography resist thickness ($35\mu m$) was sufficient to withstand and protect the surrounding silicon throughout the via etch process, to create a TSV which is deeper than that required for hollow MN applications.

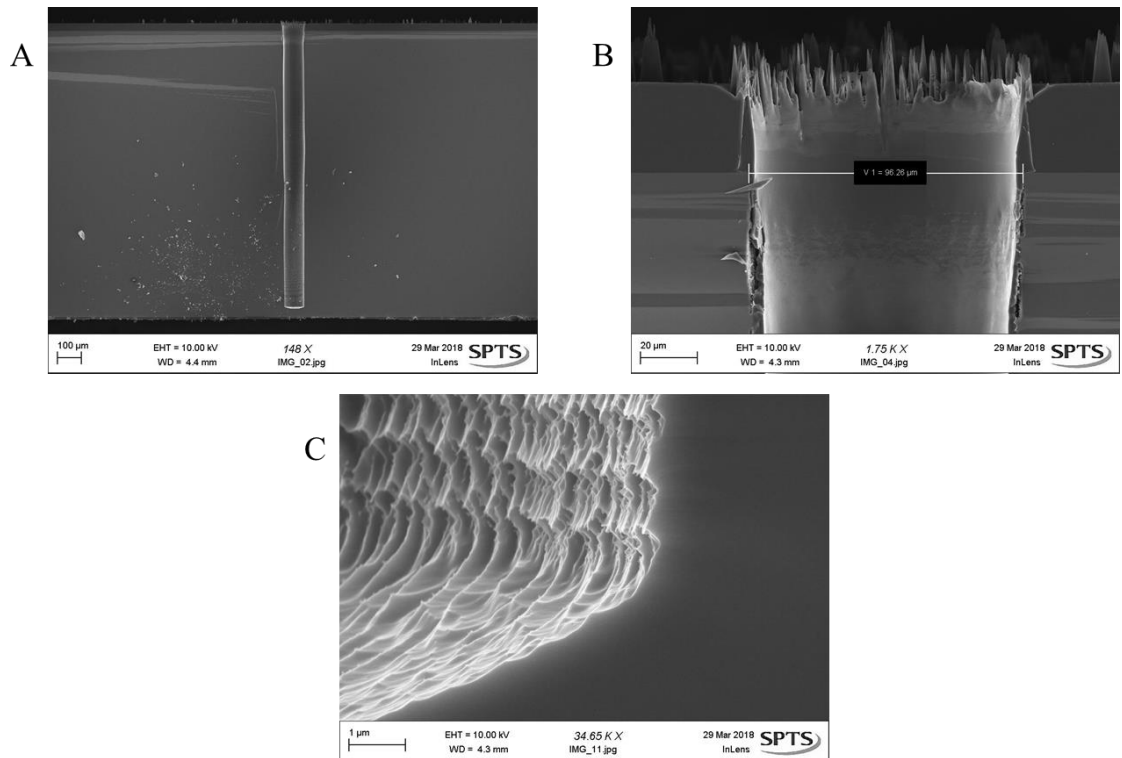


Figure 8.18 SEM images of TSV measuring (A) 1157µm deep and (B) 96µm wide, created by 3-phase (C) scallop etches

The next step was to translate the bore etch from a flat surface wafer and onto the bevelled wafer. After photolithography patterning the bore mask onto the reverse of the wafer, the wafer was wax bonded to a carrier substrate, bevel-side down. When bonded in this configuration, the bevels are protected from damage by the flat tops of the bevels supporting the weight of the wafer (described previously in section 8.5).

The images in figure 8.19, demonstrate that the bore has translated onto the bevel surface without any etching complications. From the reverse of the wafer (figure 8.19A) it is clear the shape of the bore has remained circular and measures ~100µm, the same as the starting mask design. On the bevelled surface the bores are aligned approximately halfway down the bevel, (figure 8.19B). The microscope image (figure 8.19C) reveals that the 1 x 5 MN bore has etched uniformly along the full length of the bevel to create the array (outline in red).

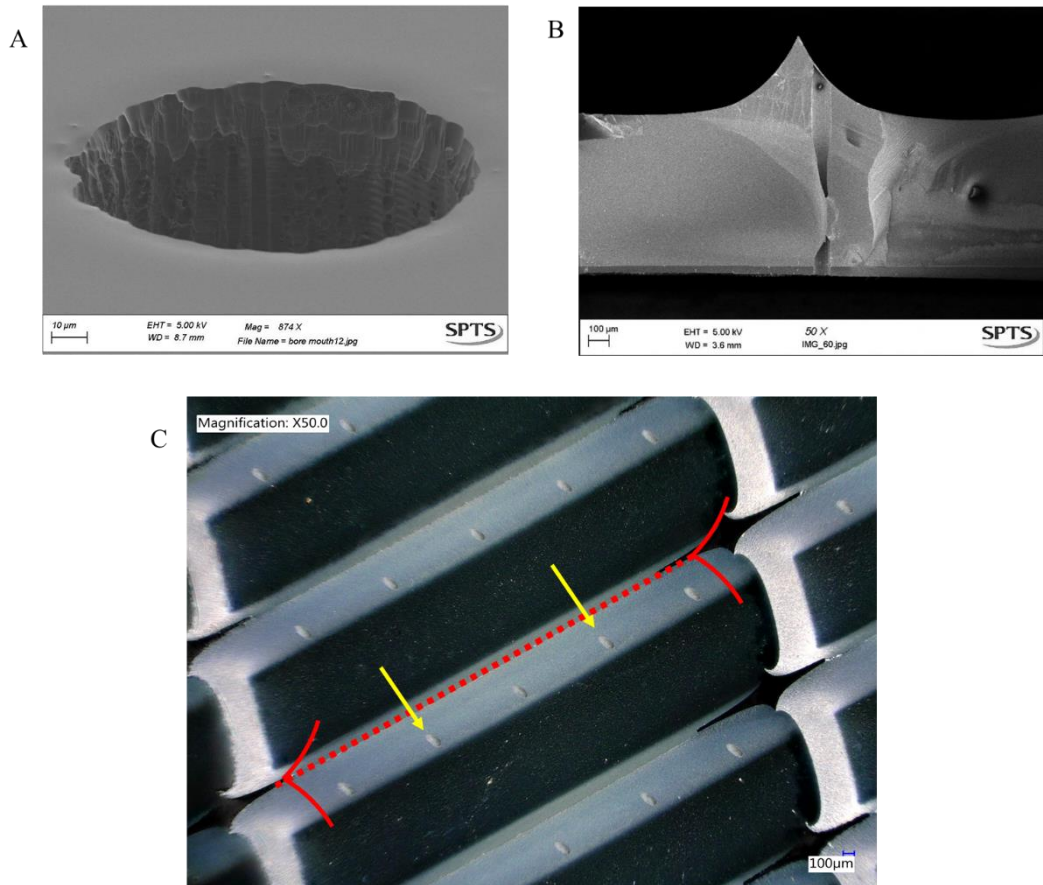


Figure 8.19 (A) SEM images of etched bore from back side of wafer, on flat surface (B) SEM cross section of bore etched through the wafer, emerging on the bevelled surface (C) Microscope image of five bores (yellow arrows) along bevelled surface (red outline depicts bevelled sides, while dashed line highlights the top of the bevels)

8.7 Shaft fabrication

The final step in the MN fabrication process was to pattern the shaft mask design onto the bevel and etch the MN shaft shape with the bore centrally located within (figure 8.20 - a reproduction of figure 8.1). The shaft resist pattern (figure 8.20 g) selectively protects the silicon beneath, whilst the unprotected silicon is etched to reveal the hollow shaft in the form of a column (figure 8.20 h and i). To fabricate solid MNs, the bore step in section 2.5 is omitted, and the shaft process can be patterned straight onto the bevelled surface.

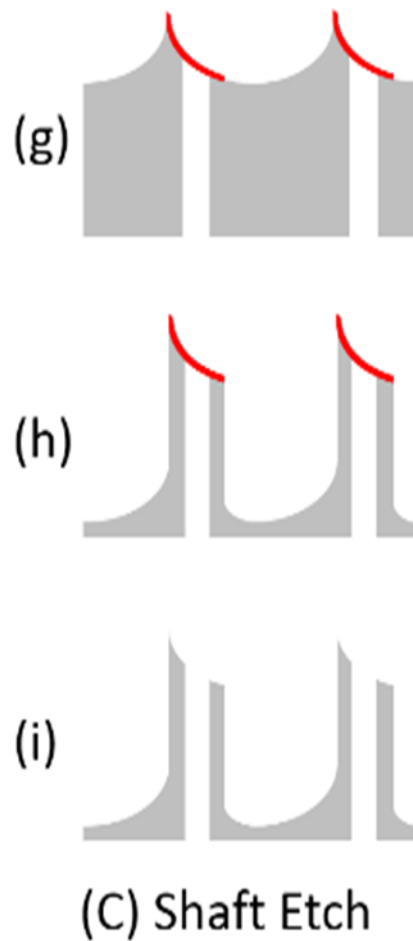


Figure 8.20 Schematic process flow showing the shaft reveal etch around the bore. Silicon wafers are represented in grey, with photoresist masks and silicon oxide shown in red and blue, respectively.

As the wafer surface is now bevelled, spin coating the resist layer onto the wafer would be ineffective as the surface is uneven and the resist would pool at the base of the bevels. To overcome this a spray coating method, optimised prior this PhD, was used. Here a spray coater arm moves over the bevels at a fixed rate and atomises the resist onto the surface to create a uniform film, as described in section 6.1.2 (figure 8.21 [186]).

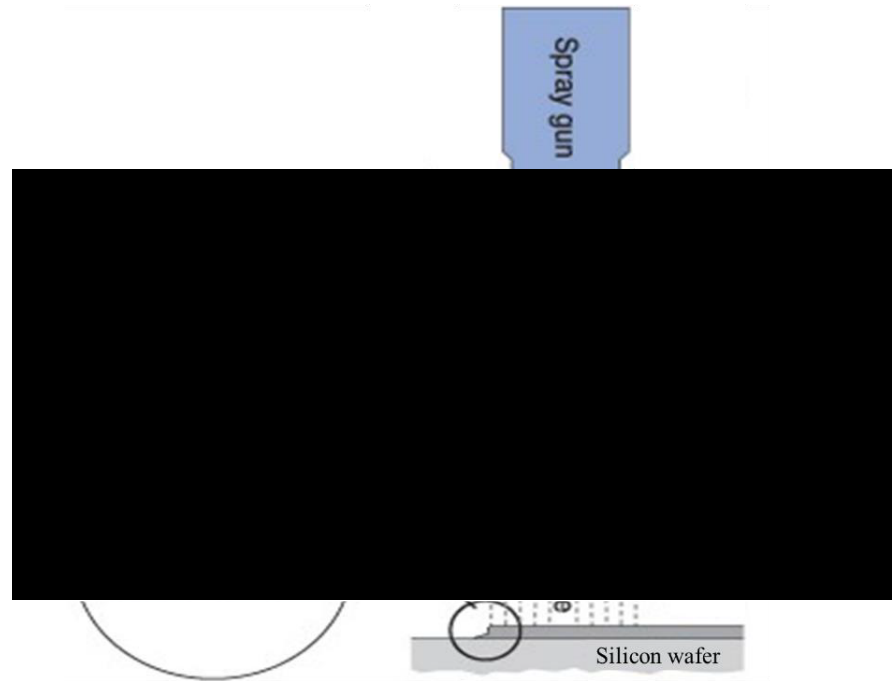


Figure 8.21 Schematic diagram demonstrating the spray coating method, of atomising the resist to form droplets that once sprayed onto the silicon wafer, come together to form a uniform layer

The resist used for spray coating (Nlof2070), has a high viscosity, therefore, to modify it into a sprayable liquid, the resist is diluted in acetone in a ratio of 1:8, enabling the resist to be sprayed on to the wafer to create a conformal resist coating on the bevelled surface. A final thickness of 14 μ m was used as this thickness can withstand a silicon etch of up to 900 μ m in depth. The spray coater recipe is outlined in table 8.5.

Table 8.5. Original photolithography parameters for resist spray coating

Spray Parameters	Arm speed 120 Scans 12 Dry with nitrogen gas Nitrogen flow 18L/ minute Chuck temperature 70 °C Resist flow rate 1.5ml/min
Soft bake parameters	90°C for 1.5 minutes
UV Exposure parameters	Dosage of 500mJ / cm ²
Post exposure bake	110°C for 2 minutes
Development parameters	Az726 for 10 minutes

However, analysis of the resist layer after spray coating showed a non-uniform resist thickness that ranged from 12-20 μm on the surface of the bevel (figure 8.22). A thickness of $\sim 20\mu\text{m}$ was measured along the centre of the bevel (dark blue), while the top and bottom of the bevel was coated in a thinner resist layer of $\sim 12\mu\text{m}$ (lighter blue). Although, initially it was deemed that a resist thickness of $14\mu\text{m}$ was required to create the shaft pattern, as the shaft pattern is aligned centrally onto the bevel, the top and bottom areas of the bevel measuring a resist thickness of $\sim 12\mu\text{m}$ will be developed away and exposed to etching. Therefore, optimising these areas to $14\mu\text{m}$ is not necessary and a $\sim 20\mu\text{m}$ thickness is suitable.

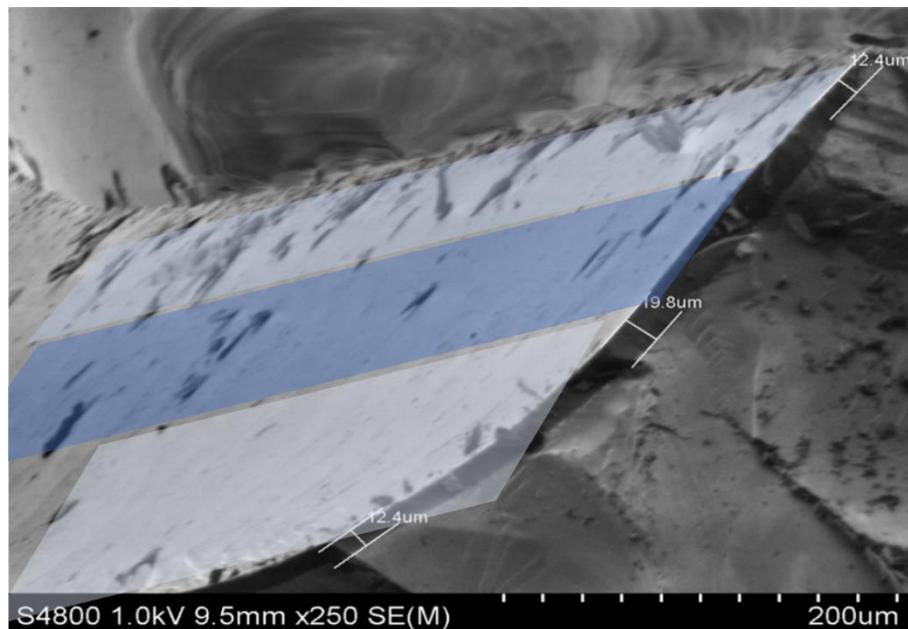


Figure 8.22 SEM image of bevelled surface with spray coated resist layer measuring between 12 - 20 μm

After spray coating, the wafers were patterned with the shaft mask design and developed for 10 minutes to produce the final resist pattern on the bevelled surface (figure 8.23). As this is a top-down view, the bevels are viewed from above, therefore, to clarify the image the bevel is marked in red and each feature labelled.

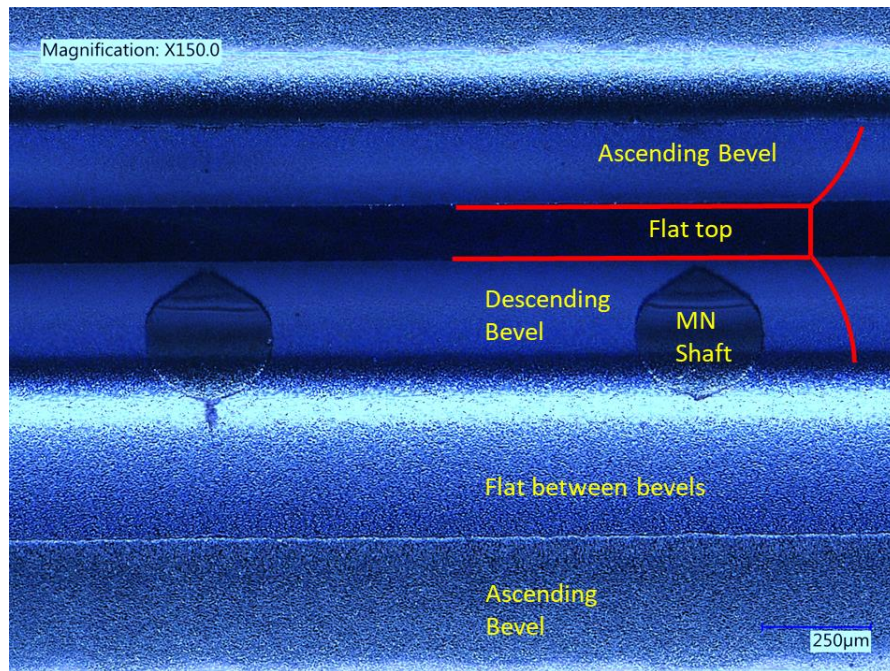


Figure 8.23 Microscope from above bevel surface, with shaft design patterned in resist

8.8 Shaft DRIE etching

To create the shaft of the MN, a vertical DRIE etch was used to remove the exposed silicon from around the resist shaft pattern (as described in section 8.5); the etch process used, created a straight sidewall, to form a uniform cylindrical silicon column. This profile shape is key to maintaining mechanical rigidity of the MN; if the sidewall angle is inverted, narrowing the column towards the base, figure 8.24A, the MN shaft can become too narrow and prone to potential fracture near the base [198]. If the sidewalls angle outward excessively, the MN base diameter can become too wide and prevent the entire length of the MN shaft from penetrating into skin.

To optimise the shaft-etch, a flat prime wafer was patterned with the shaft design. An initial etch test produced a side wall profile angled inwards towards the base of the MN, which meant that the columns fractured easily when mechanically tested. The etch was optimised at SPTS, so that the final result produced a column with a sidewall angle of $>89^\circ$ etched to a depth of $\sim 864\mu\text{m}$ (figure 8.24B).

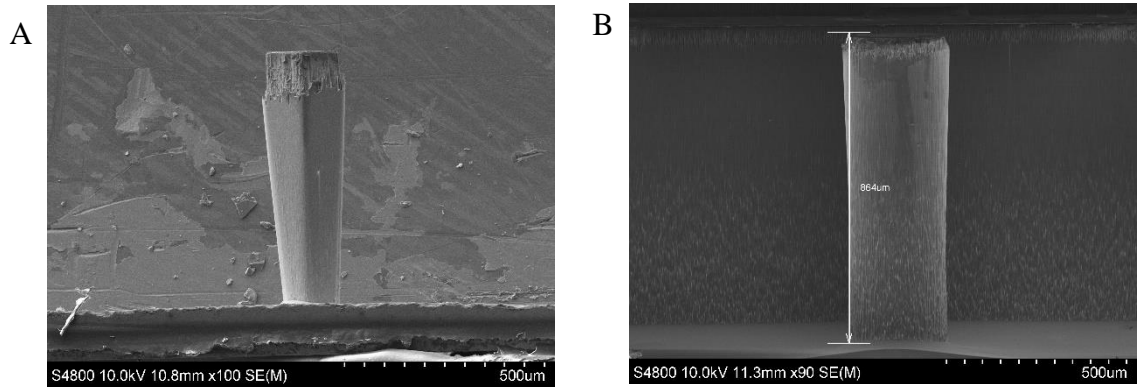


Figure 8.24 SEM images of shaft etching on a flat surface (A) sidewall profile narrows towards the base (B) sidewall profile is $>89^\circ$

The optimised etch consisted of three steps; deposition (Dep), etch1 (E1) and etch2 (E2), which all used medium source RF powers and low chamber pressures. The gas flows comprised 360 sccm C_4F_8 , 320 sccm SF_6 and 315 sccm SF_6 for Dep, E1 and E2 respectively. To maintain the vertical wall profile the platen RF Bias applied was 112W during E1 and 36W during E2.

Transferring the shaft etch onto the bevelled surface introduced new and unique challenges to create the final MN shaft shape. It can be seen in figure 8.25, that upon etching, the shafts of each MN are no longer separated, but are joined together via a wall along the back of the shafts. The wall measures $\sim 350\mu m$ in height, approximately half the overall MN height, meaning it would impede the MNs ability to penetrate the skin entirely.

Additionally, the shaft itself was not smooth towards the top of the column, indicating that the resist failed to protect the silicon throughout the whole etch process, enabling undesired etching of the exposed silicon.

Lastly, it is observed that the flat area at the top of the two connecting bevels, have not etched to the same depths as the other flat areas of the wafer. As this flat area is surrounded by subsequent created silicon wall, it is thought that the wall prevents the etchant gasses from accessing the area as readily as the open space, thus preventing the silicon from being etched away (indicated by the yellow arrow in figure 8.25).

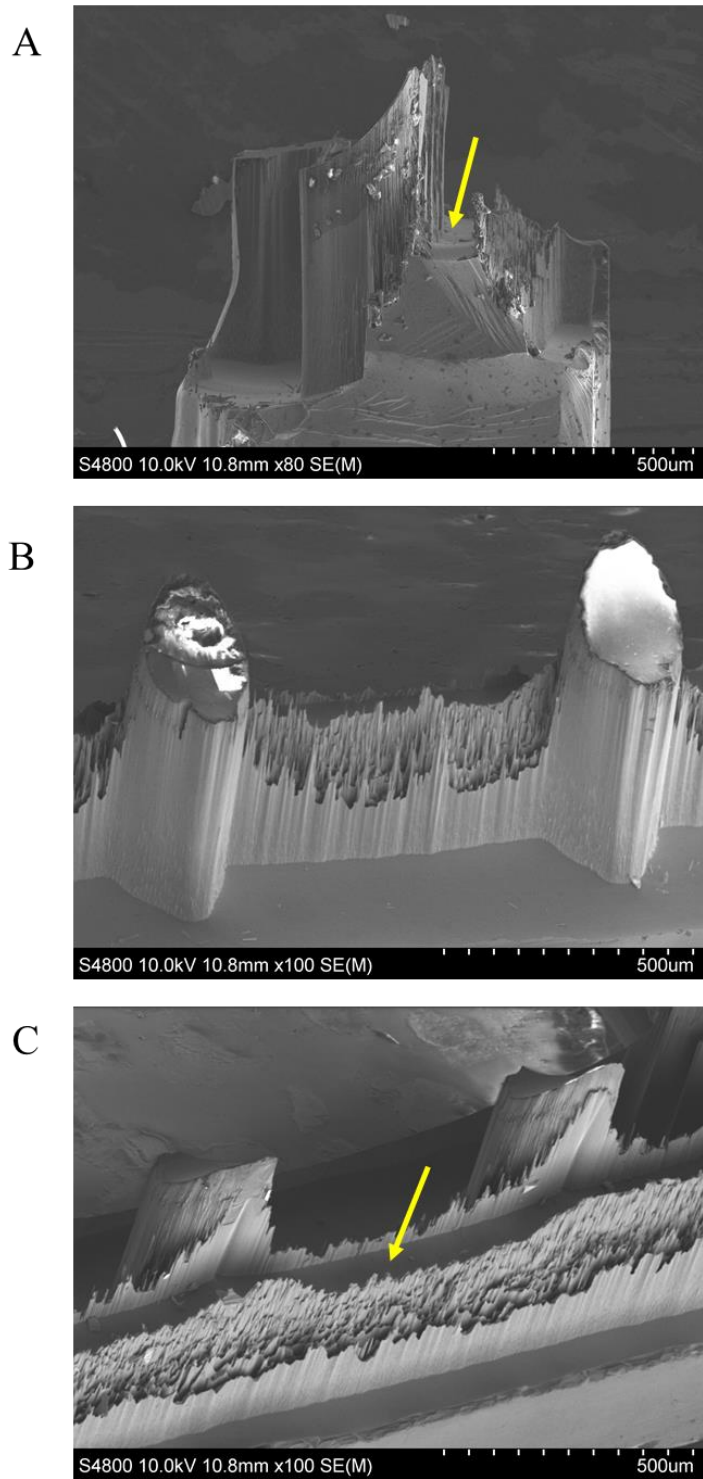


Figure 8.25 SEM images shaft pattern on bevelled surface showing (A) side profile of MN (B) front profile of MNs and (C) back profile of MN. Demonstrating the etched wall connecting between MNs. Yellow arrow indicates the original bevel flat top

Further shaft optimisation was required in relation to all mask and photolithography processes to eliminate the silicon wall and prevent thinning of the resist. Each challenge is individually addressed in the following sections; however, each step should not be considered in isolation but rather, one step has an effect on another and all need to be optimised to improve the quality of the MN. The following challenges will be discussed.

- Alignment marks used to align masks
- Removal of the wall between MNs
- Smoothing of the shaft surface
- Optimisation of the resist thickness

8.9 Shaft etch optimisation

8.9.1 Alignment marks

When a process involves several photolithography masks to create a design, alignment marks are created as distinctive patterns that when aligned will ensure that the mask steps align accurately. If these images do not align then the wafer can be misaligned, and the photolithography processes will not produce high resolution features. Typically, two alignment marks are created either side of the mask to correct the x and y translations; however more marks can be placed across the wafer to increase the accuracy of alignment.

The MA used throughout this thesis was a SUSS MicroTec MA8 UV MA that has back-side alignment capabilities. This means there are two microscope lenses, one above and one below the wafer that allow alignment of a mask to the reverse (back-side) of the wafer, which is necessary for the bore alignment steps.

The alignment marks designed before this thesis and used to develop the MN structures detailed in the previous sections are illustrated in figure 8.26, where each design is reproduced on the left- and right-hand side of the wafers. The cross marks designed should align into their corresponding square marks. The rectangular design (figure 8.26A) is patterned onto the wafer via the first mask (bevel), while the two cross alignment marks are patterned prior to the bore etch (figure 8.26B) and shaft etch

(figure 8.26C) respectively. Alignment of the crosses within the square alignment marks should ensure that the bevel, bore and shaft of the MN all align correctly. However, several issues arose with these alignment marks due to the similarities in the cross designs B and C; for example, misalignment occurs due to mistakenly using cross B when cross C was required, or *vice versa*. In this case, the whole wafer would be misaligned, which would not be made apparent until the wafer was developed.

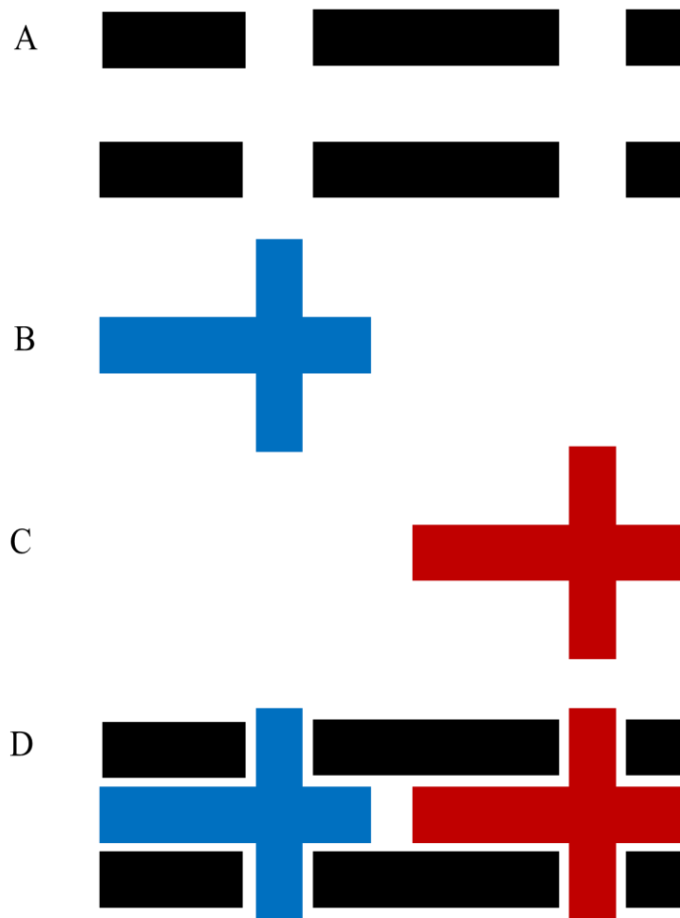


Figure 8.26 Diagram to show original alignment marks on (A) the bevel mask (B) bore mask (C) shaft mask and (D) how the cross-alignment marks B and C align to the bevel mask A.

After etching using the first mask design, it also became apparent that the development of the alignment mark etch was not consistent i.e., sometimes the alignment marks would be over developed (figure 8.27A) or under-developed (figure 8.27B). Creating a visual challenge for aligning the crosses accurately.

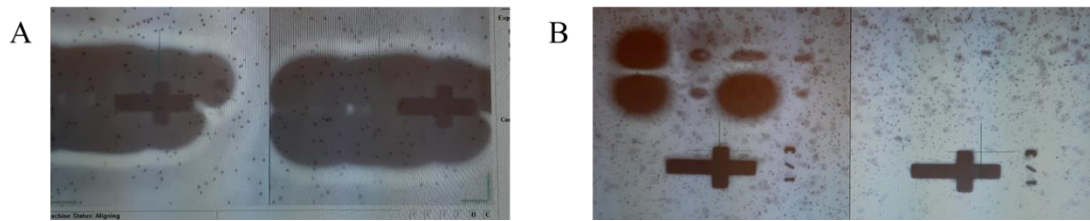


Figure 8.27 Mask aligner optical images of alignment marks that are (A) over developed and (B) underdeveloped

To overcome the alignment issues, the wafers were aligned to the mask design by eye. However, due to the difficulties with aligning the bore mask and ongoing alignment issues, alternatively solid MNs were produced as the bore alignment step is omitted, until the issues were rectified.

Manual alignment of the shaft pattern onto the etched bevels to create solid MNs alternatively utilised the overhead microscope lenses. However, the focal range of the lenses meant that only one design could be viewed at a time, (either the mask pattern or the bevelled wafer below), and therefore, the focus was continuously adjusted to visual the alignment marks on each and ensure correct alignment.

As the surface of the wafer is bevelled a new challenge was identified where, adjusting the focus to a sloped surface did not allow the full bevel to be viewed simultaneously. In addition, the steepest part of the bevel is near vertical and therefore could not be observed through the top-down orientation of the microscope. This proved difficult upon aligning the shaft mask pattern, as the shaft must be placed at the steepest bevel angle to create a sharp tip, figure 8.28A.

If the mask patterns were misaligned too high up the bevel towards the flat area, the tips of the MN would overlap onto the flat area between the bevels (figure 8.28B) and create a flat tipped MN that is incapable of penetration. If the mask were aligned towards the lower end of the bevel, where the microscope was able to focus, the shaft pattern would align to the end of the bevel curve where the slope is gentler (figures 8.28C and 8.28D) creating a MN with a shallow angled tip which could penetrate less effectively.

Therefore, it is imperative that the alignment of the shaft is precise and accurate, as in figure 8.28A.

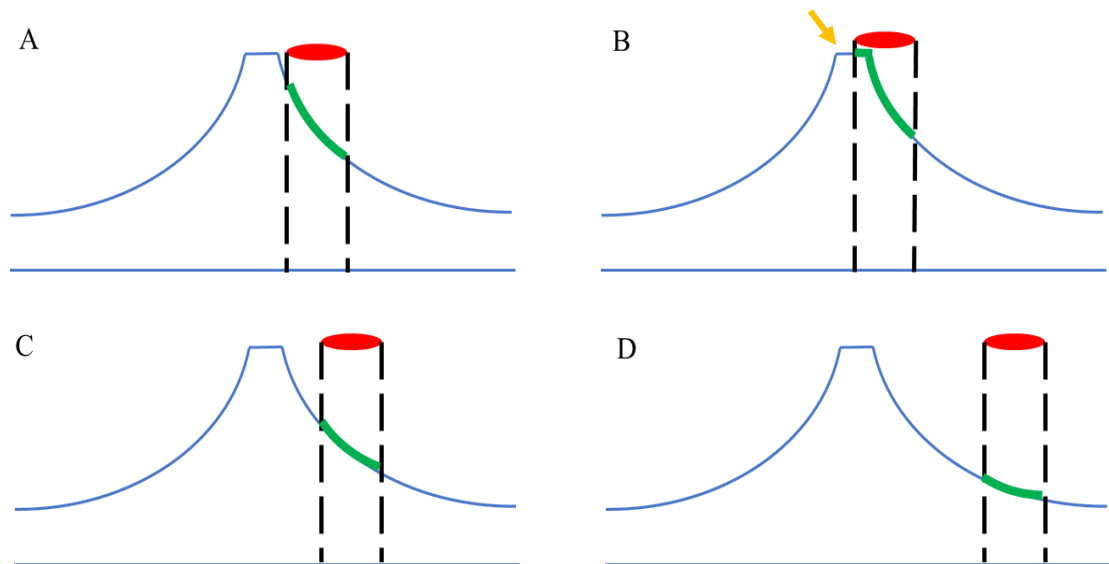


Figure 8.28 Schematic of bevelled surface (blue) with the alignment of the shaft mask pattern (red) at different positions on the bevel (A) perfect alignment at sharpest bevel point (B) alignment over the flat top of the bevel (yellow arrow) (C) and (D) alignment further towards the base of the bevel creating a shallower angled tipped MN. The green outline depicts the angle of the MN bevel tip created from that alignment.

To overcome the issue with the microscope not being able to observe the steepest part of the bevel during the alignment process, the flat area between the bevels reflected the microscope light to produce an optical effect in the form of a white line that can be visualised on the microscope image; this line was used as a marker to guide the mask alignment to the bevels (figure 8.29A). However, as the reflected line is not an accurate or clear representation of the bevel and is only a guide, true alignment of the mask onto the sharpest part of the bevel is still difficult to judge, therefore figure 8.29B demonstrated how two mask configurations were tested to help visualise how the shaft mask pattern onto a sloped surface. First the red line shows how the reflected bevel was aligned exactly to the tip of the MN mask, which was assumed to be the steepest part of the bevel, while the yellow line shows the alignment slightly further away from the MN tip mask, to factor in the inaccuracies with microscope focus.

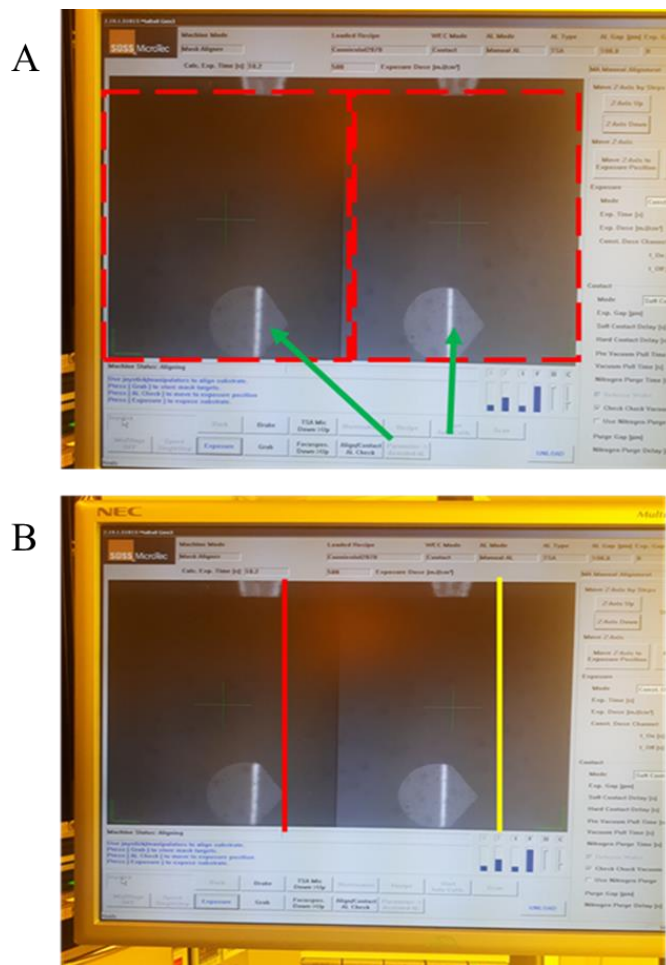


Figure 8.29 Mask aligner microscope images of shaft mask (outline in red dash box) aligned over a bevel wafer (A) the flat top reflecting light (green arrows) can be observed through the open mask areas (B) the red line showing alignment of the bevel flat to exactly the tip of the MN shaft pattern, while the yellow line shows extended alignment further down the bevel.

After alignment, the wafers were developed using the method described in section 8.7 and analysed under the microscope. The wafer which was thought to have been aligned exactly to the tip of the MN shaft pattern, actually saw the tip of the shaft extend over the flat area (orange arrow in figure 8.30A). This would subsequently cause the MN tip to be blunt after shaft etching and is therefore unsuitable for future testing. However, the second wafer that had been aligned with the resist patterned further away from the tip, was thought to have demonstrated precise alignment of the tip with the shaft pattern at the steepest part of the bevel alignment precisely with the tip of the MN shaft pattern (figure 8.30B). However, altering the microscope angle to visualise the bevel surface clearer, shows the mask shaft pattern had not actually aligned to the steepest part of the

bevel and has, in fact, patterned towards the centre (figure 8.30C). This demonstrates how difficult accurate alignment is without clear alignment marks.

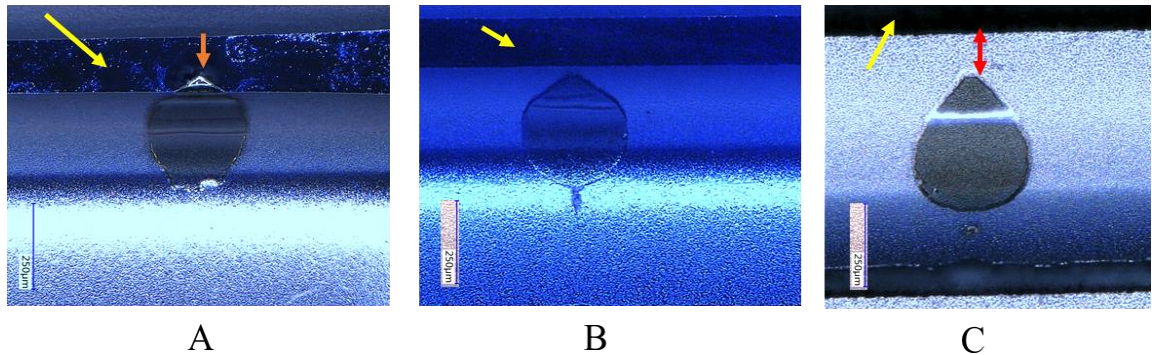


Figure 8.30 Microscope images of MN shaft pattern alignment, where the yellow arrow highlights the flat top of the bevels (A) shaft aligned exactly to the top of the bevel, actually patterns onto the flat area, indicated by the orange arrow (B) shaft alignment extended away from the top of the bevel showing correct alignment in the top down orientation (C) orientating the microscope to view the full bevel, shows the shaft pattern from image B is not aligned to the steepest part of the bevel, the red arrows shows the spacing between the MN pattern and the bevel flat top.

To resolve the alignment issues, new simpler alignment marks were designed which can be interpreted easily by other researchers in the group without explanation, to produce sharp and steep MN tips every time. The new mask design included four crosses in decreasing size from 377 μm , 315 μm , 175 μm and 140 μm , which were configured in a square arrangement (figure 8.31A). Next, blocks with dimensions congruent with the spaces between the arms of each cross, were aligned between the arms of the crosses in the matching descending feature size block configurations (figure 8.31B). Thus, when these marks are overlaid, they create a completed square (figure 8.31C). The first mask used to create the bevels included the square pattern, while the second and third masks, to create the bores and shaft were designed with the crosses, to both align to squares on mask 1.

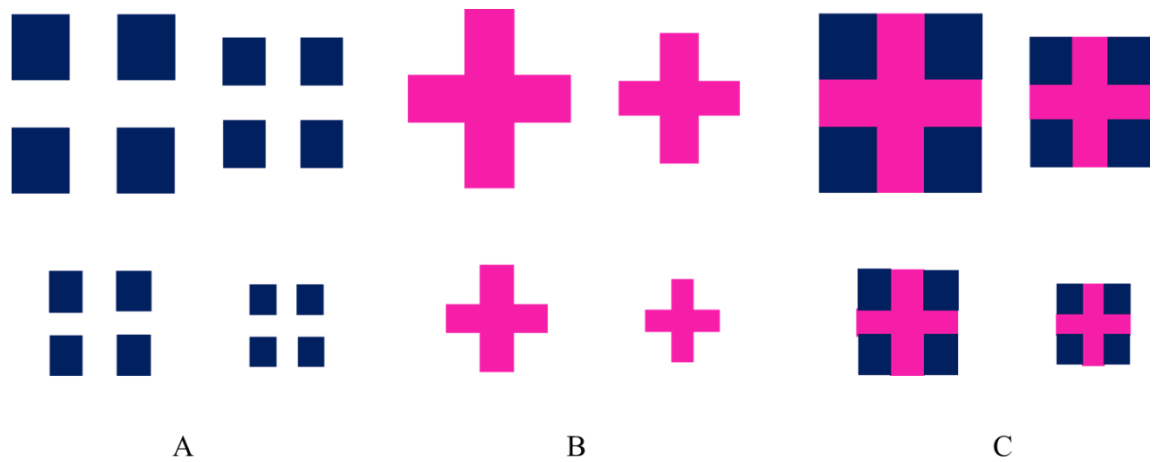


Figure 8.31 Schematic diagram of (A) square alignment marks (B) corresponding cross alignment marks (C) alignment of how the cross and square marks are paired

Although the new mask design produced new improved sharp MNs where the tip of the shaft mask aligned perfectly to the steepest part of the bevel (figure 8.32), the wall between the MNs was still prominent and had not decreased in height or size. Meaning the wall was not produced from issues with alignment but is instead related to etching or photolithography processes. Therefore, removing the wall is the next challenge to be addressed in order to create individual MNs that can penetrate to their full potential.

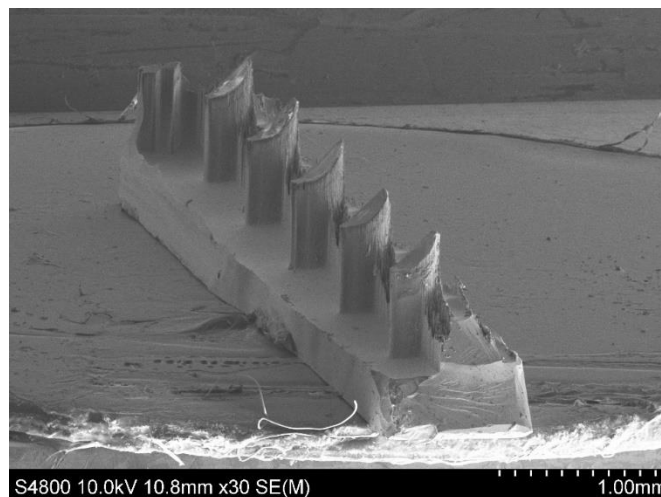


Figure 8.32 SEM image of etched 1 x 5 MN array created from new alignment marks

8.9.2 Removing the wall between the MNs

As previously described, upon etching the shaft, a silicon wall measuring $\sim 350\mu\text{m}$ in height was created between individual MNs connecting the array together. If left on the array the wall would prevent complete MN penetration into the skin and therefore needs to be removed. The wall was created from insufficient etching at the steepest part of the bevel (highlighted in yellow in figure 8.33). This is explained whereby inside the etching chamber the etchant gasses are accelerating towards the silicon in a uniform vertical direction (figure 8.33A), however as the angle of the top of the bevel is near vertical, the gasses are unable to make contact with the silicon in order to facilitate etching. Therefore, to etch this area, the gasses would need to accelerate towards the silicon with less directionality, in a more isotropic etch - as seen with wet etching techniques (figure 8.33B). However, this could cause problems further into the etch upon forming the MN shaft. To create the shaft a vertical etch is required as the resist mask protects the silicon beneath to create the columnar shaft structure. If the gasses etch the silicon from multiple directions, the gasses will undercut the shaft beneath the resist pattern (figure 8.33C), creating either an undesirable deformed shaft shape or completely etching the MN shaft away.

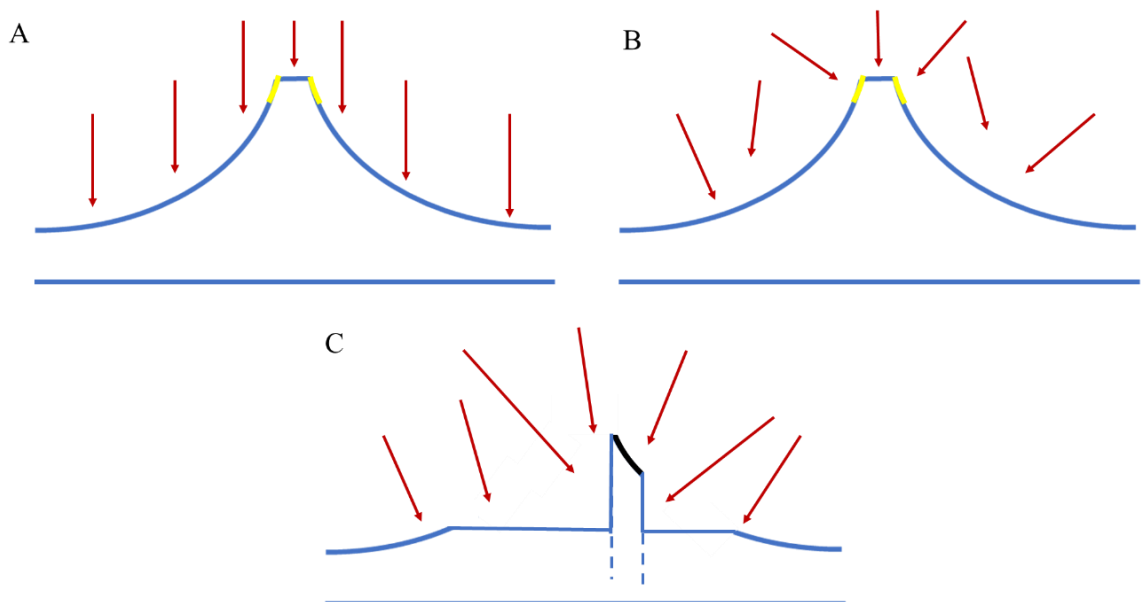


Figure 8.33 Schematic diagram of silicon bevelled surface (blue) undergoing etching. The red arrows represent the etchant gasses and yellow area highlights the vertical bevel top. (A) Gasses etching in single direction unable to etch the resist to form the MN shaft (B) Gases etching in multiple directions to target the yellow area (C) if shaft etched out, the multiple etch directions would attach the unprotected silicon below the resist (black)

One approach to etch the inaccessible part of the bevel, would be to reduce the steep bevel angle to a degree that enables the gases to come into contact with the bevel, however this would affect the sharpness of the MN and its penetration abilities.

A previously mentioned further challenge that also needs to be addressed, is the inability of the flat area between the bevel to completely etch away. Usually, all flat surfaces are directionally etched, and we would assume the flat would also etch. However, the inability of the steep bevel to etch this, instead forms a wall either side of the bevel, which instead forces the etch gases into a narrow trench along the back of the MNs (figure 8.34). The narrow gap prevents the gasses from entering and leaving at the constant required etch rate, thereby slowing down the etch rate and thus preventing the MNs from being individually etched out.

To overcome this, the etch process could be “ramped up” halfway through to increase the etching rate; however, this would speed up the etch all over the wafer and is likely to be counterproductive. Another solution could be widening the width of the flat top, this would subsequently widen the trench formed allowing more etchant gasses to access the back of the MNs to remove the wall, however, this would not remove the wall issues between each individual MNs.

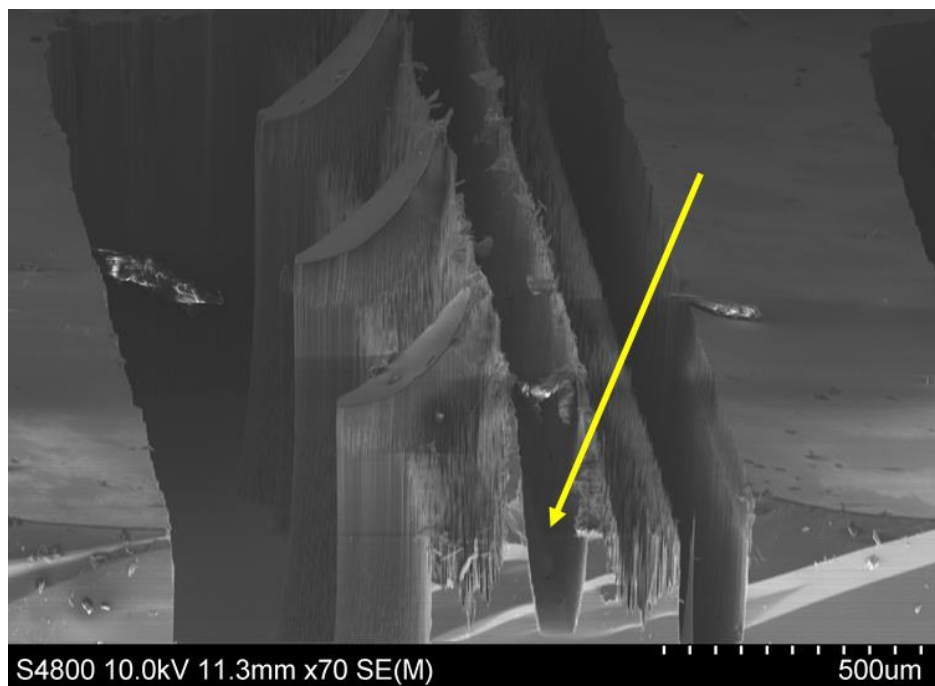


Figure 8.34 SEM images of shaft etching demonstrating the narrow trench (yellow arrow) created along the back of the MNs, from the non-etched steep bevel on either side

To resolve both problems, it was decided that the flat area between the bevels was to be omitted by continuing the bevel isotropic etch in step 1, until it undercuts the resist mask completely (figure 8.35A); creating two bevels that intersect to produce a pointed angled top (figure 8.35B).

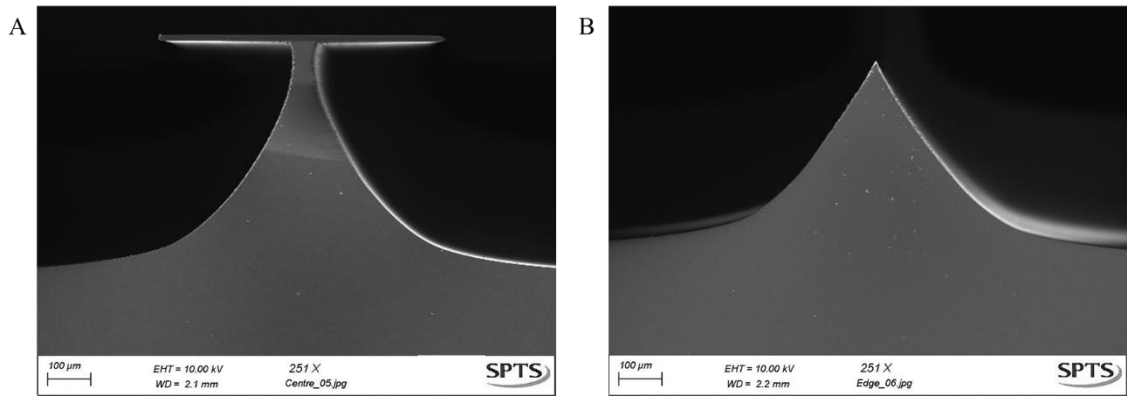


Figure 8.35 SEM images of bevel surface (A) not undercutting the resist mask to create a flat top (B) new design undercutting the resist mask to remove flat area

Using the improved alignment marks, aligning the tip of the MN shaft mask to the top of the new bevel was straightforward and repeatable and did not require rigorous manual alignment.

However, upon etching the shafts, the resulting etch observed similar trench issues as previously described, figure 8.36 demonstrates that although the flat area between the bevels was omitted, the wall between individual MNs still exists but has instead etched into a shallower trench (yellow arrow).

Additionally, grass (sharp spikes of silicon) was observed on both sides of the bevel, which would prevent effective penetration into the skin. As the wall and grass features are observed on both sides, this could still be due to the steep angle of the bevel preventing the etchant gasses from etching this area consistently.

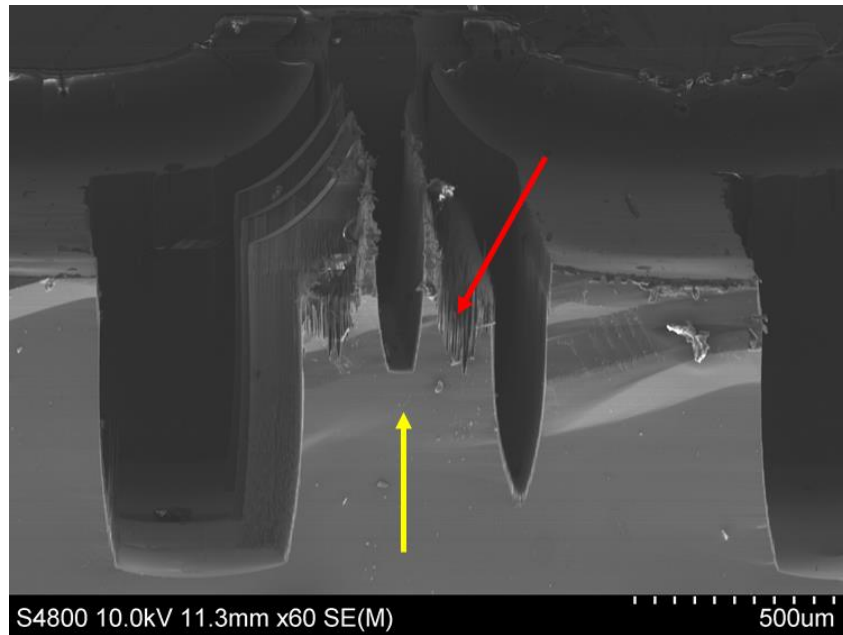


Figure 8.36 SEM image of etched MN shaft demonstrating the remaining wall (yellow arrow) and grass produced (red arrow)

An alternative origin for the grass may be from residual SiO_2 on the bevel that is acting as a micro mask and protecting the silicon beneath from etching (SiO_2 was deposited on the bevel in the previous step to act as an etch stop during bore etching section 8.6). After the bore etch, the SiO_2 etch stop is intentionally not removed as it is expected that it would be etched away through the shaft etch process. However, to pattern the shaft onto the bevel, the next step was to spray coat the bevels with resist and develop the shaft pattern for etching. This means that any remaining SiO_2 located where the shaft mask is patterned would also be covered in resist and inherently protected from etching. This is evident by the shiny SiO_2 layer observed on the MN tips after shaft etching (figure 8.37).

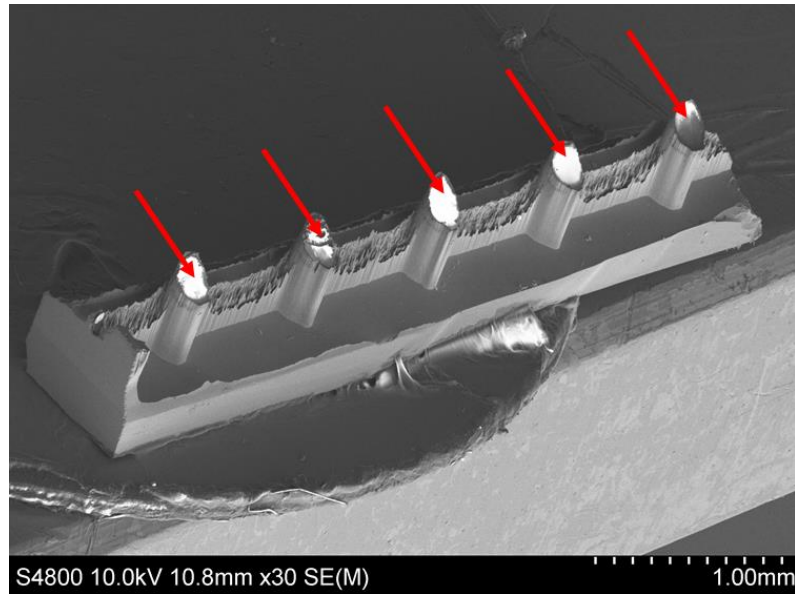


Figure 8.37 SEM image of etched MN shafts, showing SiO₂ still on the tips (red arrows)

However, if the shaft resist pattern is fully developed i.e., the unwanted resist is removed, the only resist that would remain on the bevel should be in the design of the shaft and therefore, should not contribute to the grass and wall problems (figure 8.38).

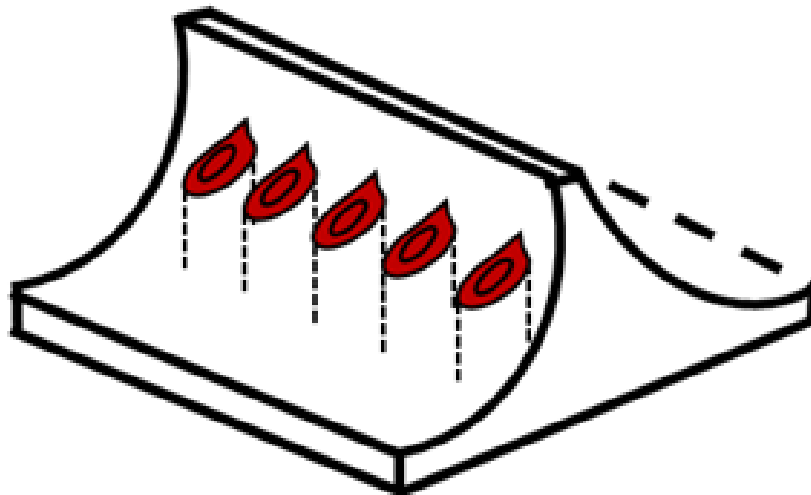


Figure 8.38 Schematic diagram of shaft patterning onto the bevel. The red symbolises the resist shaft pattern after development and should be the only resist to remain on the bevel

It was suggested that the grass area observed in figure 8.36, was alternatively a result of the steepest part of the bevel not being accessible to the etchant gasses, which consequently means any remaining SiO₂ in this location was not uniformly etched away and instead acted as a mask to protect the silicon and contribute to grass production. Originally the SiO₂ layer acted as an etch stop to protect the bevelled surface from the bore etch (explained in chapter 8.6). However, as the oxide proved difficult to remove from the steeper areas of the bevel due to the directional etch, a resist etch stop was instead suggested due to its readiness to be removed post processing using designated strippers.

To apply the resist etch stop to the bevels, the previously optimised spray coating recipe table 8.5 section 8.7 used to pattern the shaft mask on the bevels, was re-used. This method created a resist layer measuring between 12-20µm, with a 20µm thickness located in the centre of the bevel and 12µm at the top of the bevel (as shown previously in figure 8.22). Although all thicknesses will protect the bevel surface from the bore etch, having a thinner layer at the top of the bevel where the etchant gasses have difficulty accessing, will assist the subsequent resist development step and help prevent the creation of grass upon silicon etching.

Figure 8.39 demonstrates the results of a MN shaft etch, where a resist backstop had been used. It is clear that the wall behind the MN (yellow arrow) has been etched considerably lower, to a height of ~200µm. However, the red arrow indicates that silicon grass is still produced, potentially meaning the alternative resist backstop is also not being fully removed from the steepest part of the bevel before the shaft etch step and is subsequently still micro-masking the silicon to create grass.

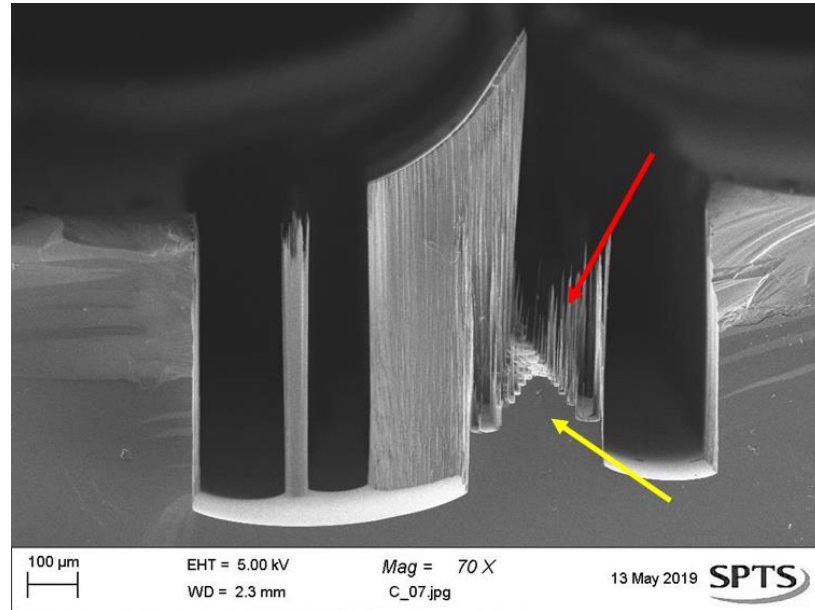


Figure 8.39 SEM image of etched MN shaft demonstrating the remaining wall (yellow arrow) and grass produced (red arrow)

8.9.3 Smoothing the bevel surface

On closer inspection of the etched bevel (figure 8.40A), it was observed that the surface of the bevel after etching is rough and comprised of pockets and pits. It was believed that these pockets and pits could harbour residual resist, which was then difficult to remove during development and washing, especially on the steepest part of the bevel. It was thought that if these areas are not fully cleared of resist, the resist remains on the surface and acts as a mask to mask the underlying silicon from etching, consequently contributing to the formation of grass and walls as established in figure 8.39.

To resolve this issue, a silicon smoothing process developed by SPTS technologies (as part of Roland Mumford's PhD research) was used to modify the silicon MN bevel surface and remove the roughness. Although this process was not initially optimised for MN fabrication, the method could be used to smooth the bevels prior to spray coating (figure 8.40B). Thereby removing the possibility for resist to pool in any pits or pockets.

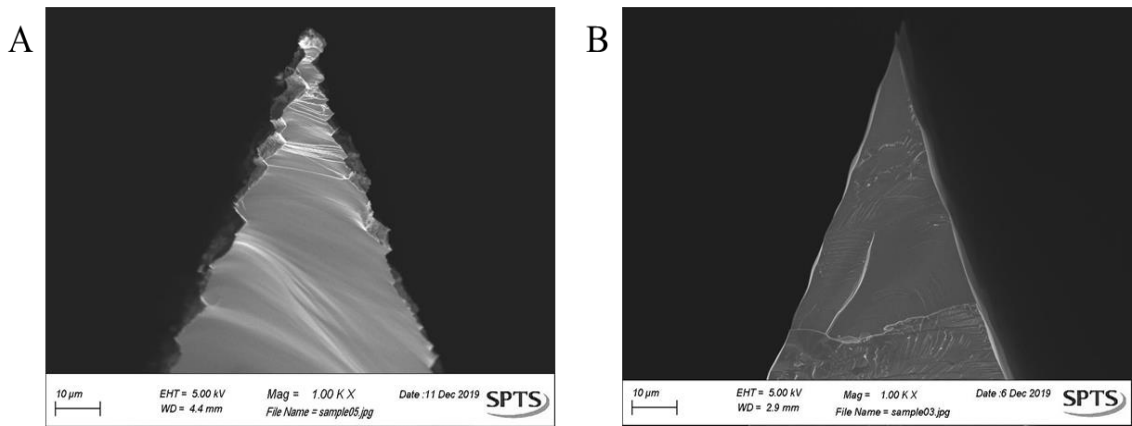


Figure 8.40 SEM images of bevel (A) before and (B) after smoothing process

At this point, further process optimisation was undertaken by the MN research group at Swansea University due to the natural end of the PhD timeframe. Future steps advised were to spray the new smoothed bevel with the shaft resist pattern and subjecting the wafer to etching to observe if a wall or grass is still produced.

8.9.4 Optimisation of NLOF2070 for shaft patterning

Subchapters 8.8 and 8.9, discussed the process of etching the shaft of the MN and identified challenges with smoothness towards the top of the MN. It presented the possibility that this could be due to the resist thickness failing during the etch at the perimeter of the shaft design or inadequate resist development. To resolve this problem, optimisation of the resist was initially conducted on a flat wafer to eliminate any issues as a result from the steep angle of the bore and focus solely on the characteristics of the resist.

To keep the method consistent, the spray coating method optimised for the shaft patterning on the bevel was used to spray a resist layer uniformly over a flat wafer, however due to the planar surface this consequently created a thicker resist layer of 155 μ m, rather than 20 μ m measure on a bevelled surface. As to not alter the process, this thickness was used to pattern the shaft pattern onto the flat surface, and the bake and development parameters were adjusted accordingly. As the resist thickness has increased it is thought that any issues with the resist failing during the etch, should be resolved as 155 μ m is more than thick enough to protect the shaft shape to an etch depth

of at least 900 μm . Therefore, upon etching it was expected to observe a shaft that was uniformly etched and smooth along the whole length.

However, figure 8.41 demonstrates that even on a flat surface, with a substantially thicker resist layer the top of the MN shaft is rougher compared to the lower part of the shaft. Suggesting that the resist could still either be failing to protect the perimeter of the shaft column, or the photolithography needs further optimisation.

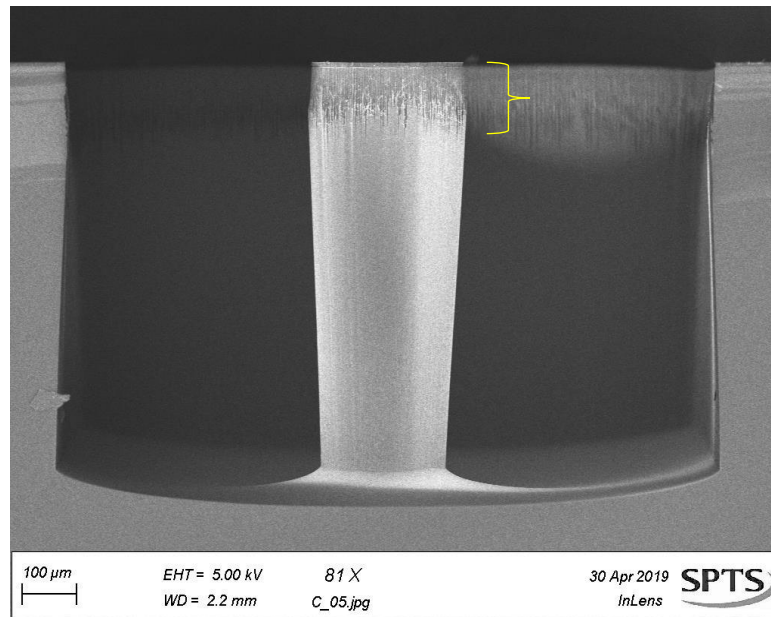


Figure 8.41 SEM image of MN shaft etch from a flat wafer, demonstrating the top of the shaft has a rough perimeter due to resist failure (yellow arrow)

To identify why this is happening, the shaft resist mask was re-patterned onto a bevelled wafer and observed under the microscope. Figure 8.42 demonstrates that a clear “tear-drop” resist shape was produced in line with the MN shaft mask.

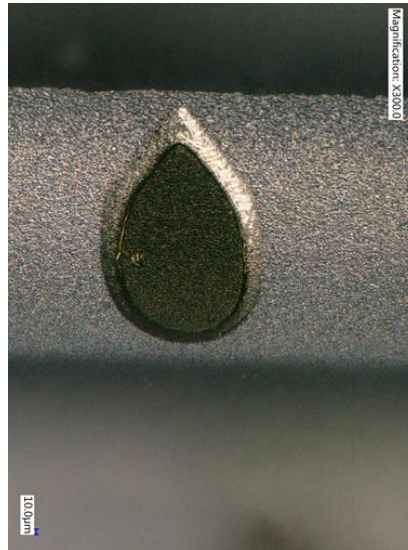


Figure 8.42 Microscope image of shaft resist pattern on bevelled surface, demonstrating the centre of the resist is darker than the perimeter

However, the centre of the teardrop shape is a darker shade than the perimeter indicating that the resist is thicker in the centre. To confirm this, the shaft resist pattern was analysed using SEM, which revealed that at the perimeter (edge) of the resist, the profile was concaved, which consequently causes the resist to thin (figure 8.43). This confirmed that during the etching process the resist around the perimeter of the pattern is etched away quicker than the resist in the centre and thus does not protect the silicon beneath, thereby exposing the silicon to the etchant gasses causing the edges of the shaft to etch and become rough.

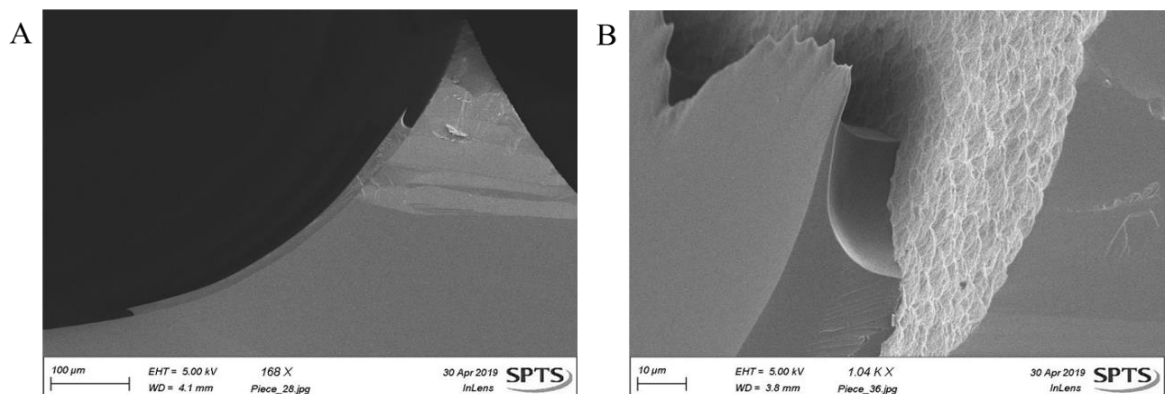


Figure 8.43 SEM images of NLOF2070 resist on bevelled surface demonstrating concaved resist undercut at (A) 168x and (B) 1.04K magnification

The resist used for spray coating was selected and optimised before this PhD commenced, for its negative ability for the UV exposed portion to become insoluble and thus create the tear drop shaft shape. However, NLOF2070 is predominately applied to lift off processes where the resist is removed post processing. Here the concaved edges aid the resist to “lift off” from the substrate i.e., it can be removed by acting as entry points for the developing solution to get underneath.

However, for MN shaft patterning, a lift off resist is not needed as the resist is not removed post etching and instead a more uniform thickness over the whole tear drop shape is required. To improve the uniformity two options are presented:

1. Improve the angle of the NLOF2070 sidewall from concaved to straight, through extended bake and UV exposure times
2. Change the resist type and restart optimisation

Using the NLOF2070 data sheets provided by MicroChemicals, varying the UV exposure dosage and increasing the PEB temperature and times straightens the side walls to reduce the lift off properties, figure 8.44[199].

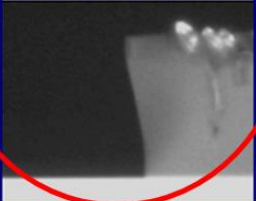

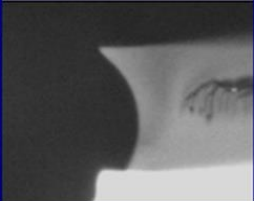
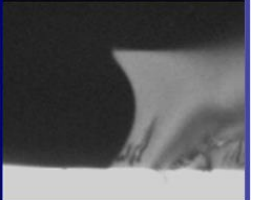
Exposure Dose:	500 mJ/cm ² i-line	500 mJ/cm ² i-line	1.000 mJ/cm ² i-line	1.000 mJ/cm ² i-line
PEB	110°C 2 minutes	130°C 2 minutes	110°C 2 minutes	130°C 2 minutes
Development	4 min AZ [®] 826mif	7 min AZ [®] 826mif	4 min AZ [®] 826mif	9 min AZ [®] 826mif
After through-development				

Figure 8.44 NLOF2070 sidewall response to varying UV dosage and post exposure temperature

However, the current photolithography recipe used already utilises the UV and PEB parameters for the straightest sidewall, circled in figure 8.44. However, as seen in the previous figure 8.43, applying this recipe actually creates the opposite effect.

In an attempt to improve the sidewall angle, the PEB temperature and UV exposure dosages were further increased beyond the MicroChemicals guidelines. The original UV exposure dosage was set at 500mJ/cm² and PEB at 140°C, therefore these parameters

were increased in increments to determine their effect on the resist sidewall; all other parameters remained the same. The first tests increased the UV exposure dosage from $500\text{mJ}/\text{cm}^2$ to $600\text{mJ}/\text{cm}^2$, $700\text{mJ}/\text{cm}^2$, and $800\text{mJ}/\text{cm}^2$, while the PEB was maintained at 110°C (figure 8.45). Increasing the UV dosage increases the length of time the resist is exposed to the UV; longer exposures enables the UV wavelengths to penetrate further through the resist layer to stimulate crosslinking and harden the resist [200], which should prevent it from forming undercut sidewalls. However, the undercut did not change with increasing UV dose and instead, due to the hardened resist profile, the amount of undeveloped resist remaining on the bevel after development increased, as it was more difficult to remove in the 3-minute development time.

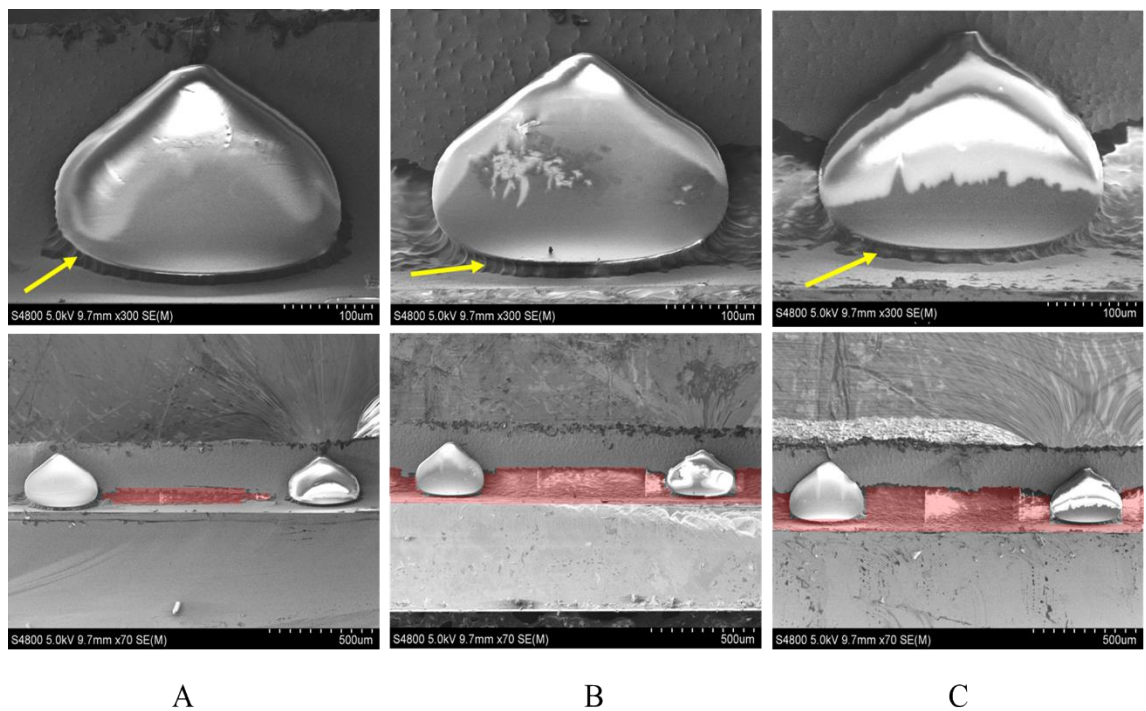


Figure 8.45 SEM images of resist shaft mask patterned onto bevel surface under varying UV exposure dose (A) $600\text{mJ}/\text{cm}^2$ (B) $700\text{mJ}/\text{cm}^2$ (C) $800\text{mJ}/\text{cm}^2$. Yellow arrow shows resist undercut, red highlights residual resist after development

To detect the time required for the residual resist to be removed from the bevel surface, the development time was increased until the resist was visually removed; this was found to be 6 minutes. However, the increased development time was counterproductive, as the angle of the resist side wall subsequently became more undercut and thinned, due to the extended time in the developer, figure 8.46.

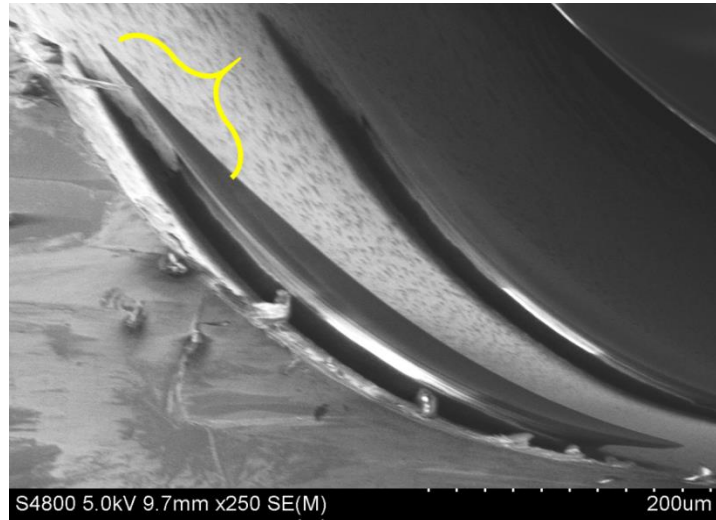


Figure 8.46 SEM image of shaft pattern on bevel surface with an exposure dosage of 800mJ/cm² and development time of 6 minutes showing the resist has undercut sidewall (yellow brace)

Adjusting the UV exposure dosage also did not straighten the sidewall, but again made it more difficult to remove the residual resist from the bevelled surface. Therefore, even though the side wall is still undercut, the original dosage of 500mJ/cm² enabled the resist to be removed the easiest and therefore, this exposure dose was applied to the next stages.

The next test increased the PEB time, in an attempt to harden the UV exposed resist without hardening the unexposed resist; all other parameters remained the same. The original PEB was 2 minutes at 110°C, therefore the PEB time was increased to 3, 5 and 7 minutes.

Figure 8.47 shows the results of the shaft pattern after developing the samples for 3 minutes. All PEB times observed no removal of the resist from the bevel surface. Therefore, in an attempt to develop the resist, the development time was visually

monitored until the resist was removed; however, after 10 minutes no difference was observed and the resist still remained difficult to remove from the bevel.

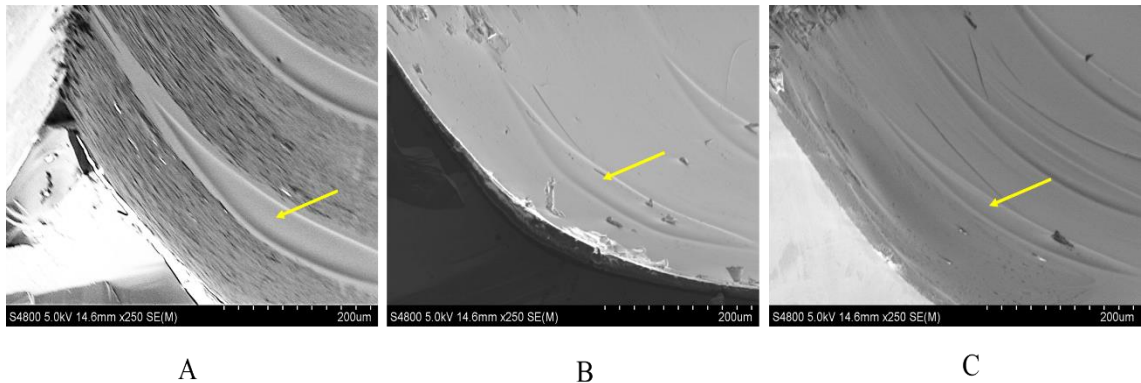


Figure 8.47 SEM image of shaft pattern on bevel surface with a development time of (A) 3 minutes (B) 5 minutes and (C) 7 minutes

Increasing the UV exposure dose and PEB baking time did not straighten the sidewalls of the shaft mask design, but instead exacerbated the issue. Therefore, as the optimisation of NLOF2070 was not fruitful, the next option was to change the resist type.

MicroChemicals was contacted for advice and guidance to determine an appropriate resist for shaft patterning, and it was suggested that AZ4999 would be appropriate. AZ4999 is a tailored spray coating resist that can produce a resist thickness from 0.5µm to 20µm with a uniform thickness coating on non-planar features such as the bevelled surface [201]. The optimisation of spray coating AZ4999 onto the bevelled surface for the MN shaft patterning has been allocated as future work for the MN research group beyond this PhD thesis.

Chapter 9

In-plane microneedle fabrication

9.1 Introduction

This chapter describes a simple 6-step MN fabrication method using a single KOH wet etch to produce the first solid, and hollow double-sided bevelled MN, where the tip is formed from the (111) planes of (100) orientated silicon simultaneously etched from both sides of the wafer to intersect in the centre. The method utilises a KOH anisotropic etch to fabricate MN using a low-cost process which can be completed in just a few hours. This method also demonstrates the first MN array where different aspect ratios (height: width) MNs can be fabricated on the same device for various delivery depths for diagnostic and theragnostic applications. The results of this chapter has been accepted by the journal of pharmaceutics and biopharmaceutics for publication.

Chapter 8 demonstrated how the DRIE process can be employed to fabricate hollow OOP MNs. Although DRIE enables greater control over the etching process, the fabrication requires proprietary complex photolithography and deep silicon etch DRIE steps [202]. Alternatively, MNs can be fabricated using a wet etch process with KOH (potassium hydroxide) or a combination of both DRIE and wet etching, which, although provides less control, does not require such expensive infrastructure. However, KOH etching still presents challenges as the etch parameters depend on the selectivity between the high index crystal planes found in the silicon [203] and therefore, an intricate design of the mask is required to utilise these characteristics to create a suitable MN shape.

The structure of silicon is described as a crystalline, diamond shaped lattice, due to its ability to form four covalent bonds with subsequent silicon atoms [204]. The orientation of this diamond lattice, defined by the Miller index, must be taken into account when preparing silicon, as multiple crystalline orientations can be produced [205]. The three most used atomic orientations include (111), (110) and (100) planes, which are demonstrated in figure 9.1 [206].

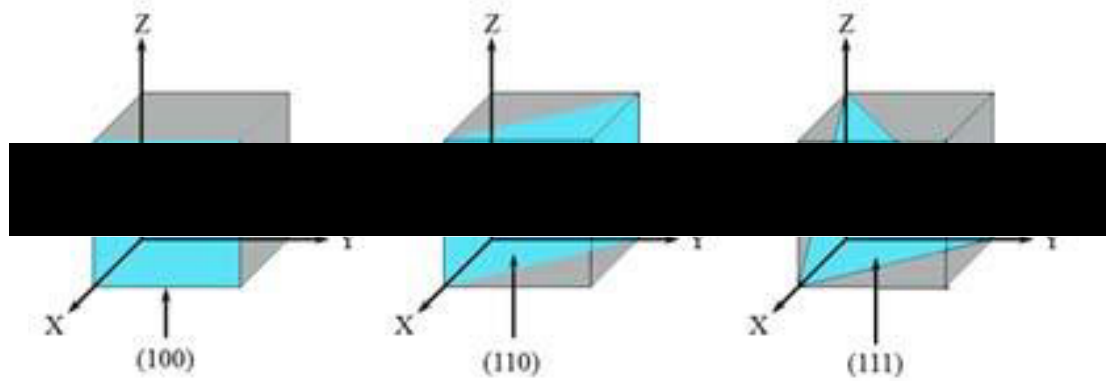


Figure 9.1 Orientation of silicon crystal planes, cut in (100), (110) and (111) directions

The orientation of the lattice influences the properties of silicon in regard to charge carrier mobility or, wet etch rates. Upon KOH etching, silicon demonstrates anisotropic properties, with different crystal orientations having different etch rates and etch angles. If the exposed surface is (110) orientation the etch exhibits the slowest etch rate to produce structures with smooth vertical (111) sidewalls [207]. Alternatively, etching silicon with the (100) surface exposed, produces (111) side walls with an angle of 54.7° respectively, to create an inverted triangle [208], figure 9.2 a. To utilise KOH etching for MN fabrication, a published method is to use photolithography to pattern a square photoresist design onto a (100) orientated wafer [209]. This enables the KOH to undercut the mask at 57.4° to produce an out-of-plane 8-sided octagonal cone, outlined in figure 9.2b. However, this process only allows fabrication of cones with low height-pitch ratios, as the crystallographic properties and thickness of the silicon wafer restrict the size and shape of the silicon microstructure created.

The literature review in chapter 4 reported that KOH etching is predominantly used to etch OOP MNs. However, simple photolithography and KOH etching, can be alternatively used to produce much greater aspect ratio MNs with shaft lengths not limited by the wafer thickness (as in OOP MNs). The MNs can be designed with a sharp tip, in the in-plane direction by simultaneously etching an (100) orientated silicon wafer from the front and reverse. This produces characteristic 54.7° (111) side walls which intersect from either side of the wafers to produce a symmetrical point that can function as the MN tip, (figure 9.2).

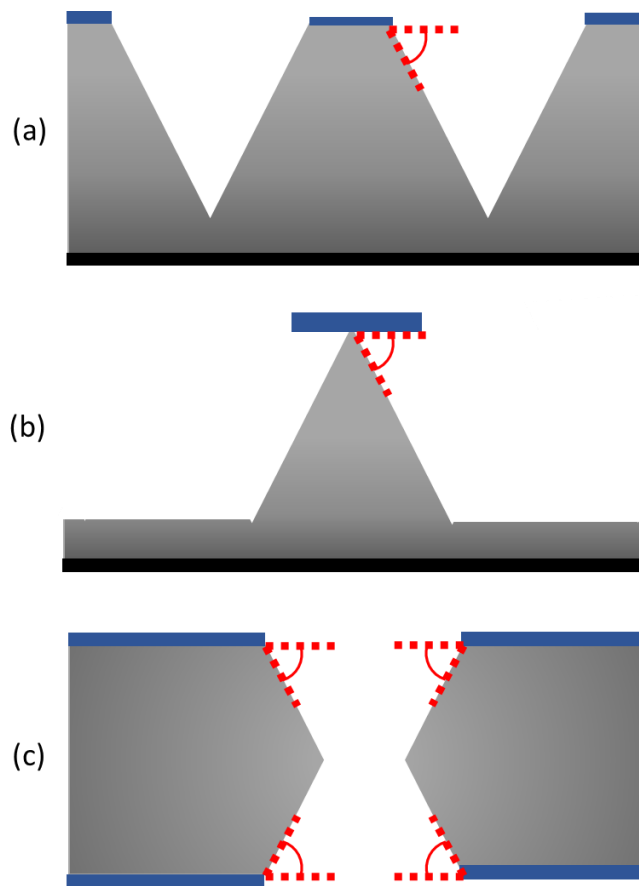


Figure 9.2 Schematic diagram of KOH etched silicon (a) Characteristic 54.7° angle of silicon (100), (b) Anisotropic etched out-of-plane pyramid MN (14), (c) In-plane MN etched from both sides of silicon wafer. Grey area represents a silicon wafer, black indicates the top and underside of wafer, red dashed line show where 54.7° is located and blue demonstrates photoresist.

9.2 MN proof of concept experiments

9.2.1 Using a resist mask

To optimise simultaneous KOH etching of the front and reverse sides of a wafer, a mask constructed of a repeating square pattern was used as a proof of concept, to observe if the etched sidewalls can meet at a point. A $300\mu\text{m}$ thick, double-side polished, 4-inch diameter (100) silicon wafer was patterned with negative resist Az125nxT_10A (figure 9.4). According to the technical data sheets provided by MicroChemicals GmbH, $100\mu\text{m}$ thickness Az125nxT_10A resists can withstand a KOH etch until the exposed silicon has etched to an approximate depth of $100\text{--}120\mu\text{m}$. To etch completely through the wafer, the KOH etch must penetrate to a depth of $150\mu\text{m}$ into the silicon wafer from each side, which requires a resist thickness of greater than $100\mu\text{m}$ on each side.

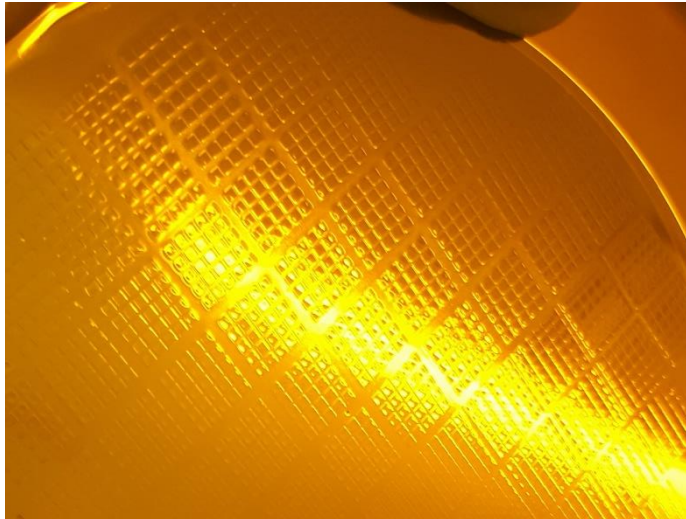


Figure 9.3 Square mask patterned onto silicon wafer in Az125nxT_10A resist, a proof of concept etch

Lithography conditions were adopted from the manufacturer's (MicroChemicals) recommended processes. The lithography process flow is outlined in table 9.1:

Table 9.1. Manufacturers photolithography parameters for Az125nxT_10A

Wafer cleaning procedure	10 minutes in acetone bath 5 minutes in IPA bath Dry with nitrogen gas Bake for 10 minutes at 150°C
Spin parameters	Acceleration of 1000rpm Spin at 300rpm for 5 seconds Spin at 1100rpm for 2 seconds Spin at 620rpm for 12 seconds
Soft bake parameters	135°C for 25 minutes
UV Exposure parameters	Dosage of 3000mJ / cm ²
Development parameters	Az726 for 6 minutes

The above lithography process was conducted on the front side of the wafer and once developed, the wafer was flipped, and the same process repeated on the reverse side. To ensure correct alignment of resists masks on both sides of the wafer, the reverse side alignment was conducted on the mask aligner using the alignment marks (figure 9.4) and backside alignment. If the squares and rectangles are mis-aligned, the double-sided simultaneous etch will not intersect in the middle, and the resulting MN will be imperfect.

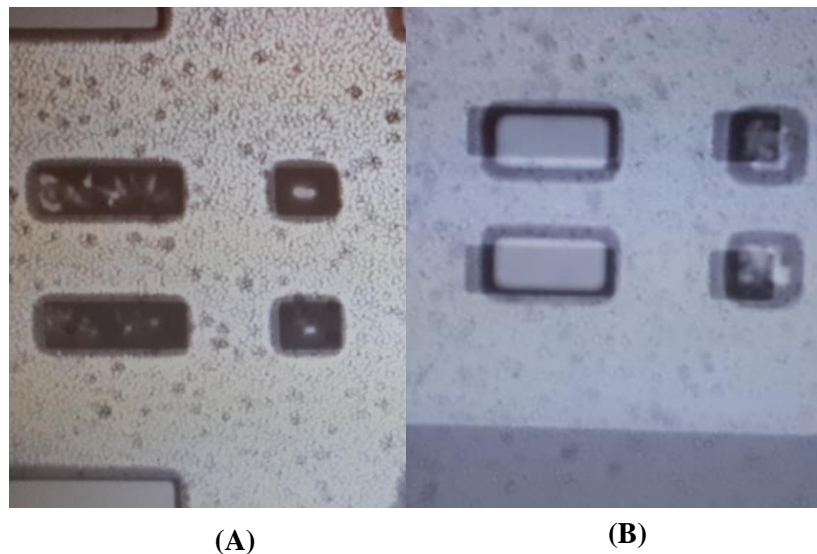


Figure 9.4 Image (A) showing reverse alignment marks on the mask being overlaid by the alignment marks on the wafer (good alignment) while (B) shows two pairs of alignment marks misaligned with each other.

Upon patterning the reverse side of the wafer, two challenges were identified:

- 1) Firstly, to hold the wafer onto the spin coater chuck and within the mask aligner, a vacuum is generated on the underside of the wafer. Usually, resist is not placed on both sides of a wafer, therefore, the vacuum suction would not have any detrimental effect on the silicon wafer. However, when patterning both sides of the wafer with resist the strong vacuum of the spin coater could potentially damage the resist on the reverse side of the wafer, as it comes into contact with the chuck.
- 2) Secondly, when the reverse side of the wafer undergoes development, the front side, which has already been developed, would be placed back into the developer. This extra development time could begin to over-develop the resist on the front, potentially losing pattern integrity or pattern resolution.

To overcome this, the front side could undergo partial development, enough to harden the resist and prevent deformities, but not too much that once placed back into the developer for the reverse side development, it would not over-develop. Thus, both sides are developed together.

Initially, to determine if there were any vacuum issues, each side of the wafer was developed independently. Once the reverse had been developed, the wafer was cleaved and placed under the microscope to examine whether the resist on the front had been over etched or altered in anyway, figure 9.5.

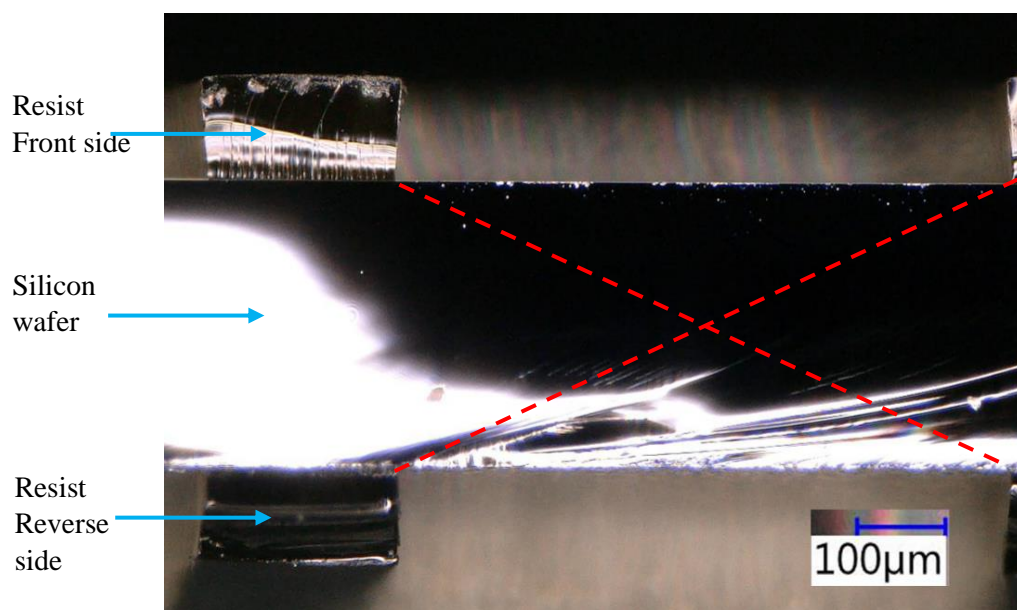


Figure 9.5 Cross section microscope image of the silicon wafer with aligned square resist pattern on the front and reverse. The resist has a thickness of 112µm. The red dashed line represents where the KOH double-sided etch would ultimately produce the 54.7° angled MN tip.

Figure 9.5 shows no visible damage to the resist on the front, either from contact with the vacuum chuck or from overdevelopment, and the square resist patterns on both sides are precisely aligned. The thickness of the resist measures 112µm, which should be suitable to withstand the KOH etch and selectively protect the masked areas of the silicon wafer. The red dashed lines represent the KOH (111) etch plane, at 54.7° angle, which will ultimately reveal the MN tip. To prevent over etching, and predict the required KOH etch time to etch through 150µm silicon, an etch rate prediction model, figure 9.6 [210] (from MicroChemicals) was used to estimate the KOH etch time at the

specific KOH concentrations and temperatures used; determined to be 80°C for 44% KOH at an etch rate of 1µm/min.

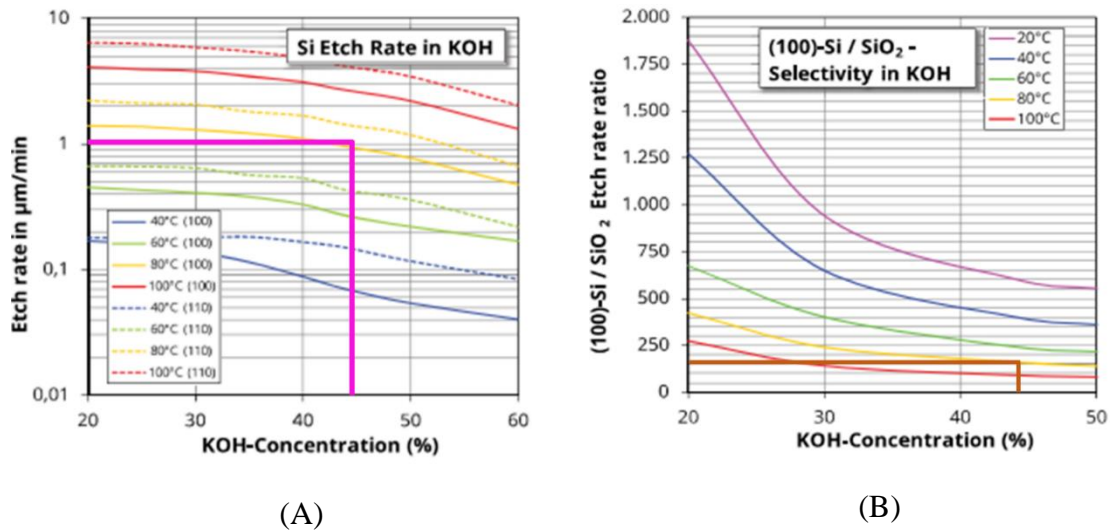


Figure 9.6 (A) Concentration and temperature dependent etching rate of (100) and (110) plane of crystalline silicon in KOH. The pink line marks which temperature to select for a 44% KOH concentration and 1µm/min etch rate. (B) the concentration and temperature dependent selectivity of (100) silicon with SiO₂ etched in KOH. Orange line represents 44% KOH selectivity to SiO₂.

The KOH concentration used was w/w 44%. Although the etch rate is highest at elevated temperatures such as 100°C, a steady etch rate of 1µm/min is easier to maintain control with a lower temperature of 80°C. The wafer was placed in 200ml of 44% KOH solution and left for 2.5 hours. Post etch, the wafer was removed, rinsed thoroughly in dH₂O and cross-sectionally examined under an optical microscope.

Figure 9.7 shows a cross-sectional image of the silicon wafer after 2.5 hours of etching. The remaining silicon has etched to a uniform thickness of 100µm and has not produced any (111) angles to create the 57.4° V shape. This means the resist had failed, i.e., had been etched completely away and thus was unable to protect the silicon beneath. This could be due to the characteristics of KOH, usually, if the concentration of an etching substrate is diluted, the etch rate slows down. However, the reverse happens for KOH. Therefore, as the silicon is deposited into the KOH solution upon etching lowering the KOH concentration, the etch rate is increasing and consequently over etches the wafer. To avoid this, a harder mask which can more greatly withstand KOH etching was sourced.

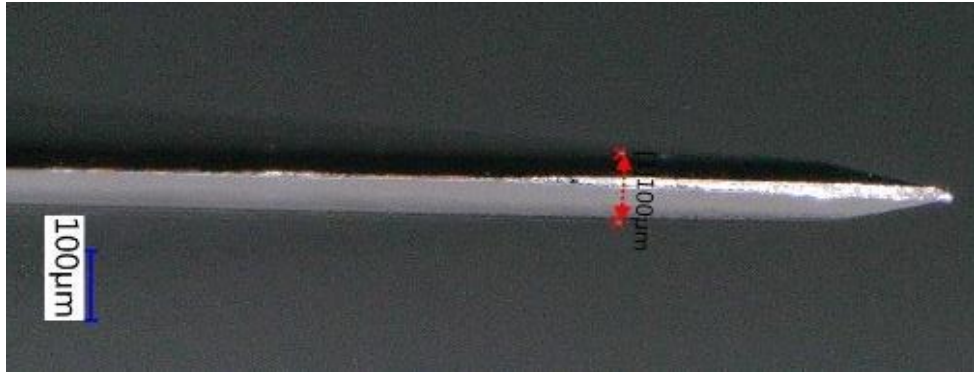


Figure 9.7 Cross section image of silicon wafer post KOH etch, showing no resist left on the surface and a thickness of 100µm

9.2.2 Using a silicon oxide mask

To protect silicon from KOH etching, a hard mask with higher selectivity such as silicon oxide (SiO_2), can be used as an alternative to the photoresist mask. SiO_2 has a selectivity ratio of $>1:150$ to silicon in 44% KOH, (figure 9.6, [210]). This means for every 1µm of SiO_2 that is etched, 150µm of silicon is etched. However, to ensure adequate masking during etching, 2µm of SiO_2 was deposited onto the surface of a 4-inch, double-side polished wafer, using the below CVD recipe (table 9.2).

Table 9.2: CVD SiO_2 deposition parameters

	2 µm SiO_2 Deposition
Power	HF Generator 540W LF Generator 0
Pressure	1800 mTorr
Gas Flow	N_2O 3000 SCCM SiH_4 105 SCCM
Temperature	Lower Electrode 300°C Upper Electrode 250°C Chamber 45°C
Process Time	420 seconds

To optimise the time required for the 2µm CVD oxide deposition, at time intervals the wafer was removed from the CVD chamber and the oxide layer thickness was measured via ellipsometry until a 2µm deposition thickness was achieved (figure 9.8).

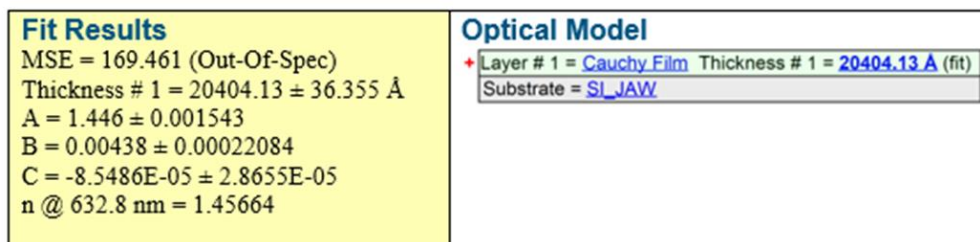


Figure 9.8 Ellipsometry results of silicon wafer post CVD oxygen plasma, showing a SiO₂ thickness of 20304.13Å, or 2.04µm

Next, the resist photolithography process from section 9.2.1 was repeated to pattern the square mask design onto the front of the oxide coated wafer. To transfer the mask pattern into the SiO₂ layer, ICP DRIE etching was used (table 9.3) to etch the oxide and expose the silicon wafer. Note that the resist mask was not processed onto the reverse of the wafer at this point, as placing a wafer with resist on the reverse into the ICP would cause it to come into contact with the vacuum chuck and as the ICP chuck is heated this is likely to affect the resist layer and cause contamination in the tool. To avoid this, the front and reverse of the wafer were processed independently.

Table 9.3: ICP etch parameters

	Oxygen Plasma descum	SiO ₂ etch
Power	800 W Coil, 25 W Platen	800 W coil, 300 W Platen
Pressure	20 mTorr	5 mTorr
Gas Flow	100 SCCM O ₂	- 32 SCCM C ₄ F ₈ - 8 SCCM CF ₄ - 40 SCCM H ₂
Process Time	20 seconds	Dependent on etch rate calculated on the day.

To calculate the time required to etch through the SiO₂, a test wafer with a layer of deposited SiO₂, was measured via ellipsometry before and after a specific etch time. The difference between the original SiO₂ thickness and the post etch thickness is used to calculate the etch rate e.g., the oxide thickness of a test piece of SiO₂ silicon wafer measured at 7641nm prior etching and 6901nm post etching, thus yields an etch rate of:

Thickness difference / Time (seconds) = $740/120 = 6.2\text{nm/second}$ etch rate. Using an etch rate of 6.2nm/second would etch through $2\mu\text{m}$ of silicon dioxide in 5.37minutes. After etching, the wafer is washed in acetone and IPA, to remove any residual resist. The reverse side of the wafer is photolithography processed in the same way as the front, and the mask patterns aligned using the backside alignment function of the MA (figure 9.9).

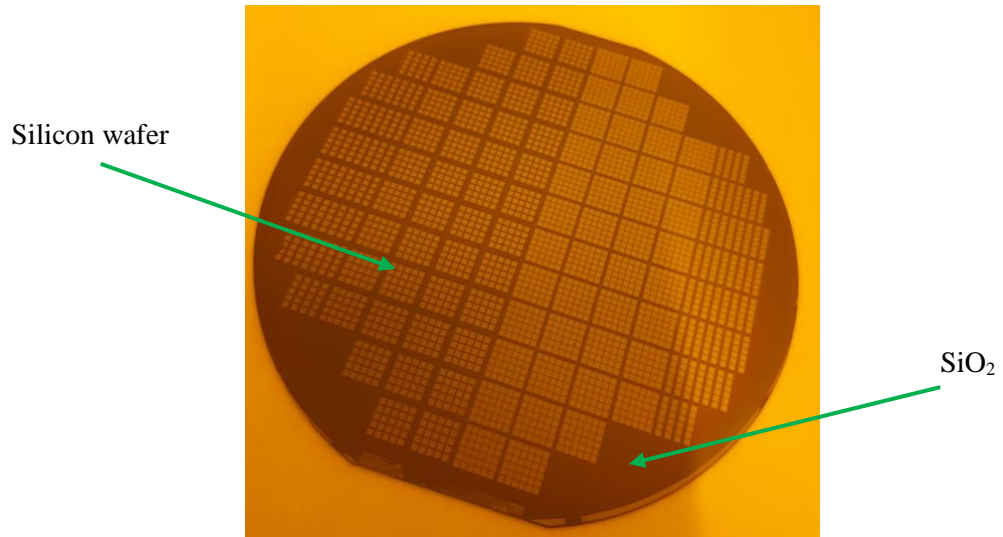


Figure 9.9 Silicon wafer with a patterned SiO₂ hard mask. The darker grey areas represent the intact SiO₂ layer, while the lighter grey is the revealed silicon wafer where square windows in the SiO₂ layer have been etched.

Once the SiO₂ on both sides of the wafer are etched, the wafer was then submerged in 200 ml of 44% KOH solution. The previous temperature of 80°C produced an over etch in the 2.5 hour etch process. Therefore, the temperature was reduced to 70°C to obtain greater control and monitoring of the etch process. Figure 9.10 [211] shows a specific etch rate guide for 45% KOH solution. At 70°C the etch rate is approximately $30\mu\text{m/hr}$, meaning a $150\mu\text{m}$ thickness etch would take approximately 5 hours.

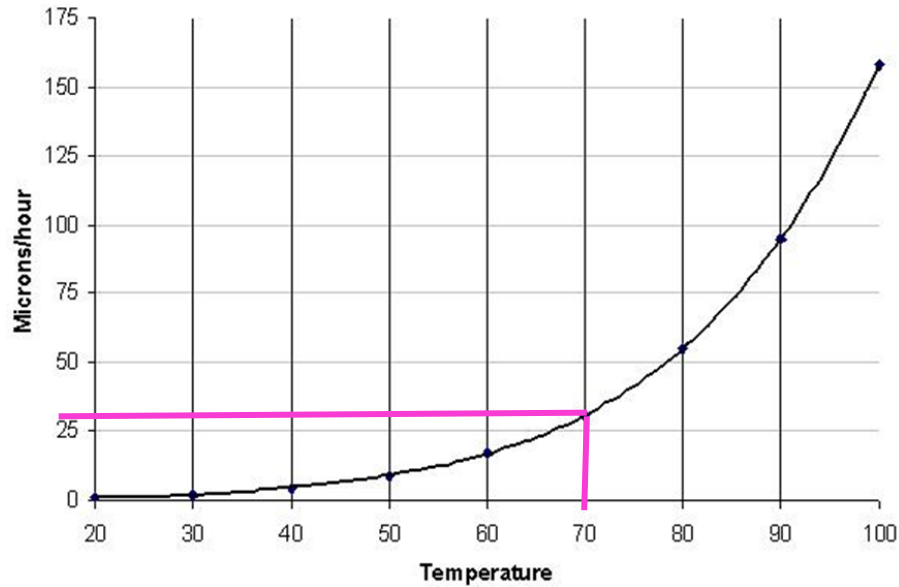


Figure 9.10 KOH etching of 100 Silicon in 45% KOH solution, pink line indicates that a temperature of 70° etches at approximately 30 μ m/hour

The KOH etch was monitored and after 6 hours the wafer was removed from the etch solution and rinsed thoroughly in deionised H₂O. Although misaligned, (due to issues with the alignment marks on the mask) the cross-section analysis in figure 9.11A-B, shows the silicon has etched at a 54.7° angle and if correctly aligned, the (111) sidewalls would intersect to form a pointed tip. During the etching, it was observed that one side of the wafer had etched to a greater extent than the other, (Figures 9.11 C-D). It was noted that when the wafer was placed in KOH it began to float, and thus, one side of the wafer was not fully submerged in the KOH and resulted in the etch rate on this side being lower than the submerged side. To prevent this, a KOH resistant weight can be placed on top of the wafer once within the KOH to maintain total KOH exposure of the silicon.

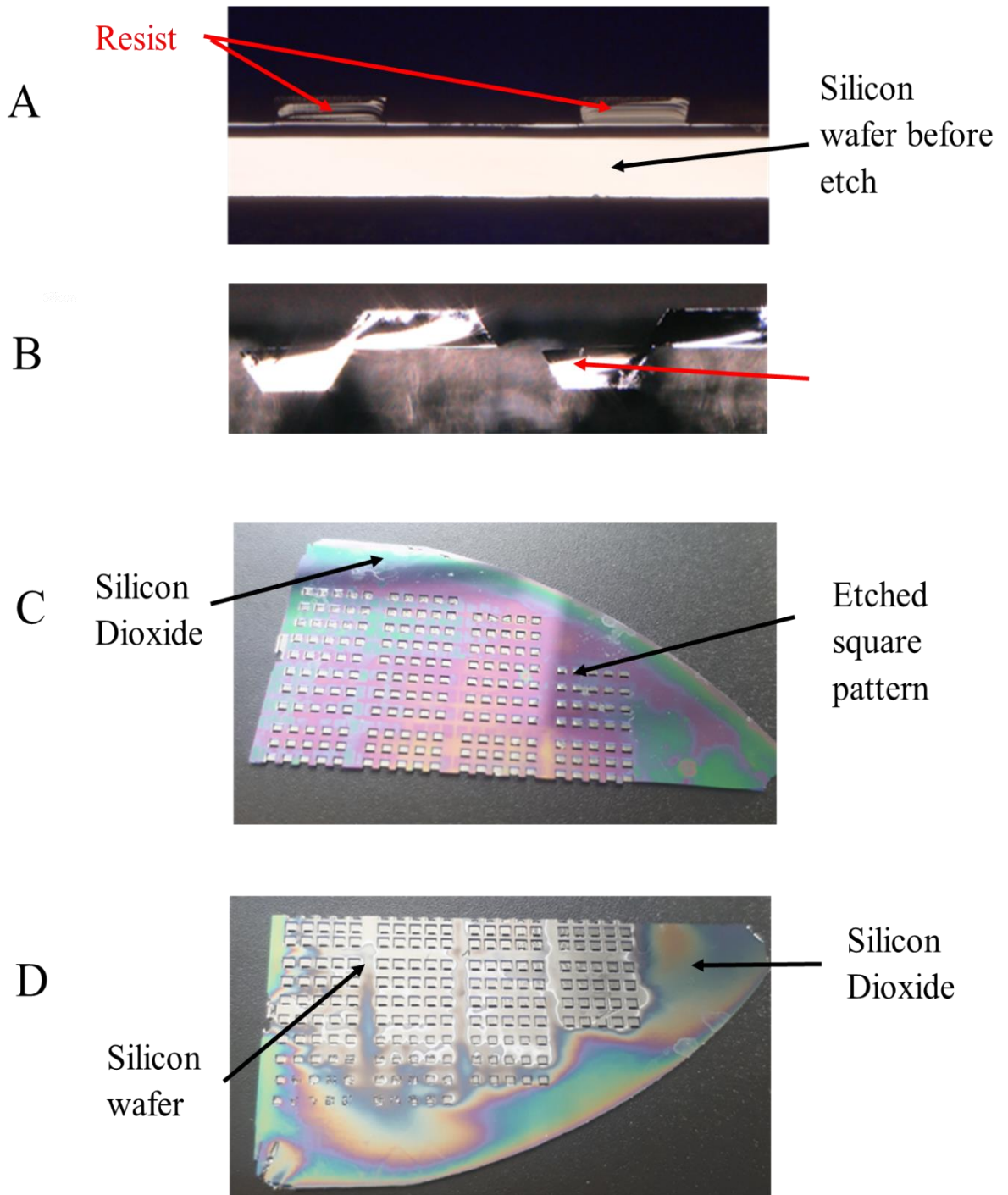


Figure 9.11 (A) Cross section of resist mask (red arrows) before SiO_2 etch (B) cross section of silicon wafer post KOH etch showing misaligned 54° angles (C) Side 1 of wafer that was exposed to the surface showing intact SiO_2 (D) side 2 of wafer that was submerged in KOH showing the SiO_2 has been completely etched to expose the silicon wafer beneath (contrasts from the rainbow colours of SiO_2 and the grey silicon)

9.3 In plane MN primary mask design

As simultaneous double-side etching was proven to be successful, a photolithography MN mask outline was designed in AutoCAD for a 4-inch wafer. The thickness of the MN is determined by the thickness of the wafer, therefore a 300 μm thick wafer was used as the starting point. Each MN device is designed with a 1 x 5 MN array, with individual MNs with dimensions 700 μm in height and 300 μm in width. The body of the device measures 20 mm in length and 5mm height, which includes two extended wings either side (Figure 9.12B); which provide extra surface area for bonding attachment to the MN adaptor. For ease of production and further processing each device is connected to the next, with the outside devices being connected to an outer ring; these structures are protected during KOH etching, allowing all the devices to remain intact, while the surrounding areas etch away leaving open cavities, figure 9.12A.

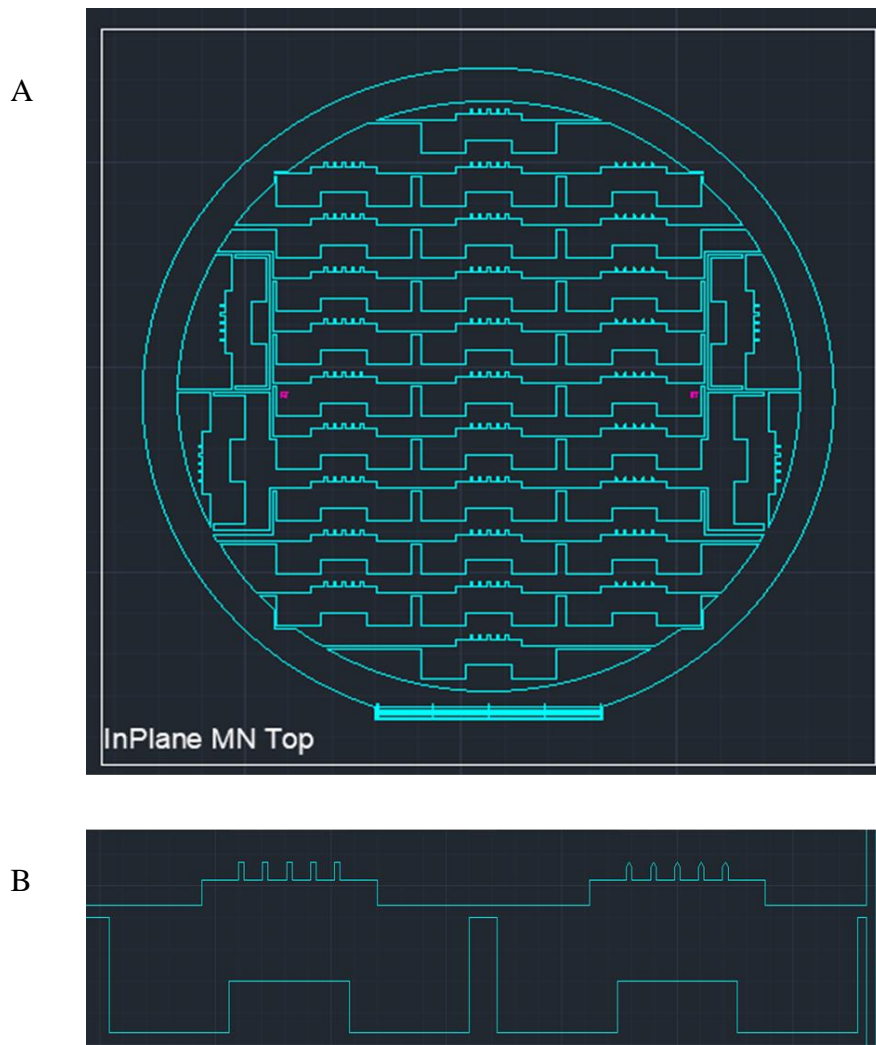


Figure 9.12 (A) AutoCAD design of solid MN mask on a 4-inch wafer (B) AutoCAD image of two different MN shapes, flat tips (left) and pointed tips (right)

To test the performance of the etch and how the MNs are created, two separate MN tip shapes were designed (figure 9.12B). Firstly, a “flat tip”, where the tip of the MN was not drawn, and the MN mask remained as a rectangle; this enabled the KOH to create the MN tip from front and reverse etching. Secondly a “pointed” tip design, with the MN tip patterned onto the wafer before the etch, allowing for more control and precision over the final tip design. For future reference, all MNs produced from the rectangular design are termed “flat tips” and the pointed mask design are termed “pointed tips”; the etch results are discussed in chapter 9.9 Currently a single wafer produces 33 devices which can be increased upon optimisation.

9.3.1 Alignment marks

As the previous test wafer was misaligned the alignment marks used to match the front and reverse patterns were re-designed. Mask one contained four crosses in descending size from 377, 315, 175 and 140 μm , which were designed in a square arrangement, (figure 9. 13A). Squares can be aligned between the arms of the crosses in the matching descending order, figure 9.13B. Thus, when these marks are paired, they produce perfect alignment in figure 9.13C.

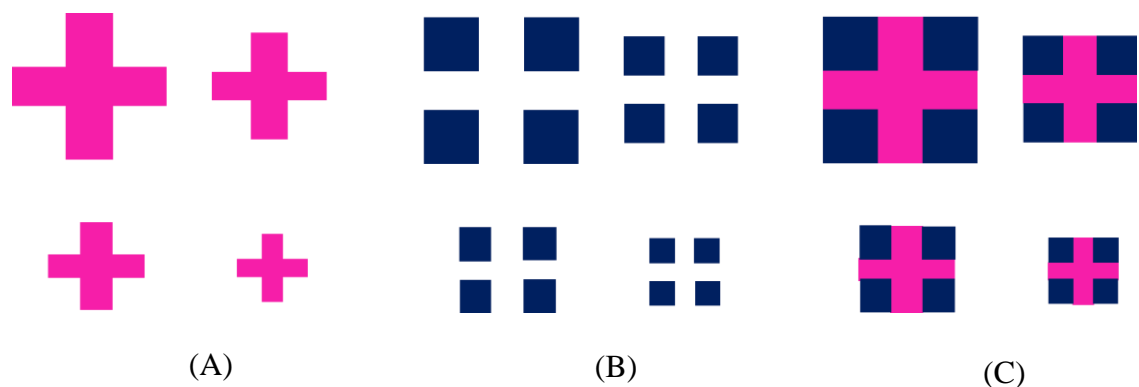


Figure 9.13 (A) Cross alignment marks on mask 1 measuring 377, 315, 175 and 140 μm (B) corresponding square alignment marks on side 2 (C) alignment of how the cross and square marks are paired

9.4 Resist spin coating optimisation

Previously, negative resist AZnxt10A was used as a mask due to its ability to spin to a thickness of $>100\mu\text{m}$ and protect the silicon from a $150\mu\text{m}$ etch depth. However, as a resist mask for KOH etching is no longer being used to protect the silicon, the resist is now only used to transfer the mask design into the SiO_2 mask and thus is only required to survive the ICP etch. Therefore, this new resist mask does not need to be excessively thick. To reduce waste and decrease the process time thinner resists such as NLOF2070, NLOF2035 or NLOF2020 which according to the MicroChemicals work sheets spin to thickness's of $7\mu\text{m}$, $3.5\mu\text{m}$ and $2\mu\text{m}$ respectively, can be applied. As the resist etches much more quickly than the SiO_2 , to withstand the ICP etch resist thickness of $>4\mu\text{m}$ is required, therefore NLOF2070 was selected for optimisation. According to the NLOF2000 series data sheet from MicroChemicals, NLOF2070 spun at 4000rpm will spin to a thickness of $5.5\mu\text{m}$, using a spin process recipe of:

- Pre-bake at 120° for 10 minutes to dehydrate the wafer
- Spin parameters
 - ~ Spin at 4000rpm for 40 seconds
 - ~ Accelerate at 1000rpm

However, the MicroChemicals spin graph for NLOF2070 only shows results up to a spin speed of 4,000rpm which results in a thickness of $5.5\mu\text{m}$. Although $4\mu\text{m}$ is required a spin speed of 4,000rpm was used as a starting point.

- Soft bake parameters
 - ~ 100°C for 5.5 minutes

Bake times are calculated as 1 minute per μm of resist, e.g. $5.5\mu\text{m} = 5.5$ minutes

- UV Exposure parameters
 - ~ Dosage of $300\text{mJ} / \text{cm}^2$
- Post exposure bake parameters
 - ~ 110° for 1 minute

This step is necessary to cross link and harden the resist post exposure.

- Development parameters
 - ~ AZ726 for 3 minutes

Using ellipsometry, the thickness of the resist from the previous recipe, measured 6.4 - 6.7 μm across the wafer, with the addition of strike marks seen in figure 9.14. The strike marks are a result of the spin speed and/or acceleration settings of the spin coater being too high; in this instance, the wafer is moving from 0rpm to 4000rpm in a single second, producing strain on the resist. Although a faster spin is needed to create a thinner coating, the spin speed needs to be increased gradually to avoid stress and strike marks.

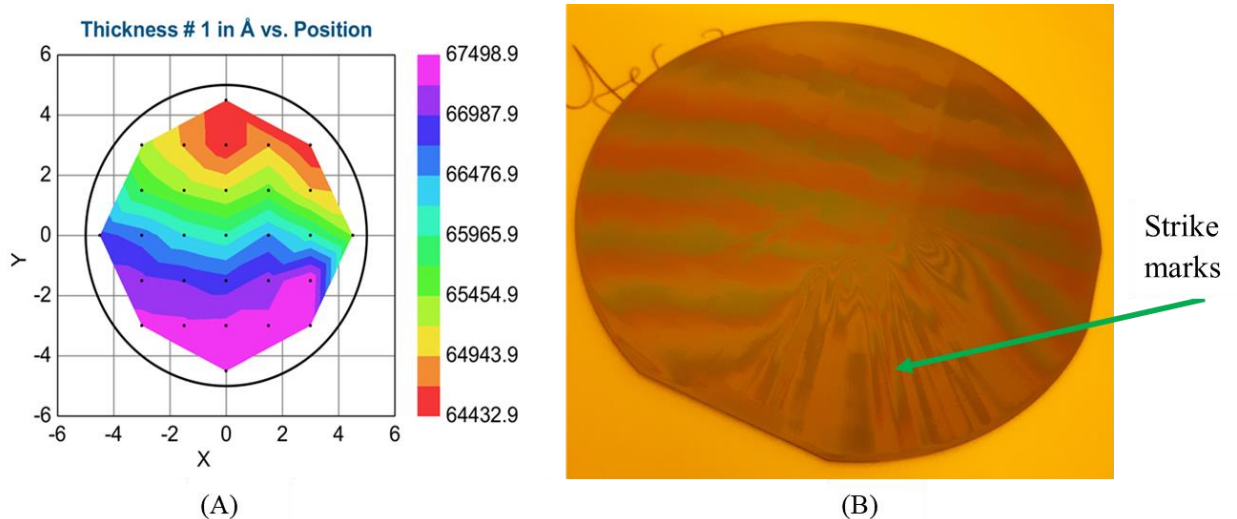


Figure 9.14 spin parameters of test 1(A) thickness of NLOF2070 resist across a 4-inch wafer measured by ellipsometry (B) image of 4-inch wafer showing strike marks upon spinning

To remove the strike marks and create a uniform thickness across the wafer, additional steps were inserted to create a 3-step process.

- The first spin step gradually accelerated towards the desired final spin speed, to evenly spread the resist across the wafer and off the edge, ensuring the whole wafer is covered.
- The second step maintained a constant spin speed to achieve the required coating thickness.
- The third step required a gradual deceleration to prevent abrupt jolting of the resist.

This new 3 step spin method was used for all optimisation spins, where the length of the second spin was adjusted to determine the optimal resist thickness.

- Spin parameters of test 2

1 = 2000rpm, 10 seconds, 200 accelerations

2 = 4000rpm, 15 seconds, 1000 accelerations

3 = 0 rpm, 8 seconds, 500 accelerations

Figure 9.15 shows the result of spin test 2 using the 3-step process (method 2). The resist thickness measures 6.9-7.2 μm and is still not completely uniform. However, the strike marks have reduced demonstrating that the multi-step process is not as traumatic as method 1.

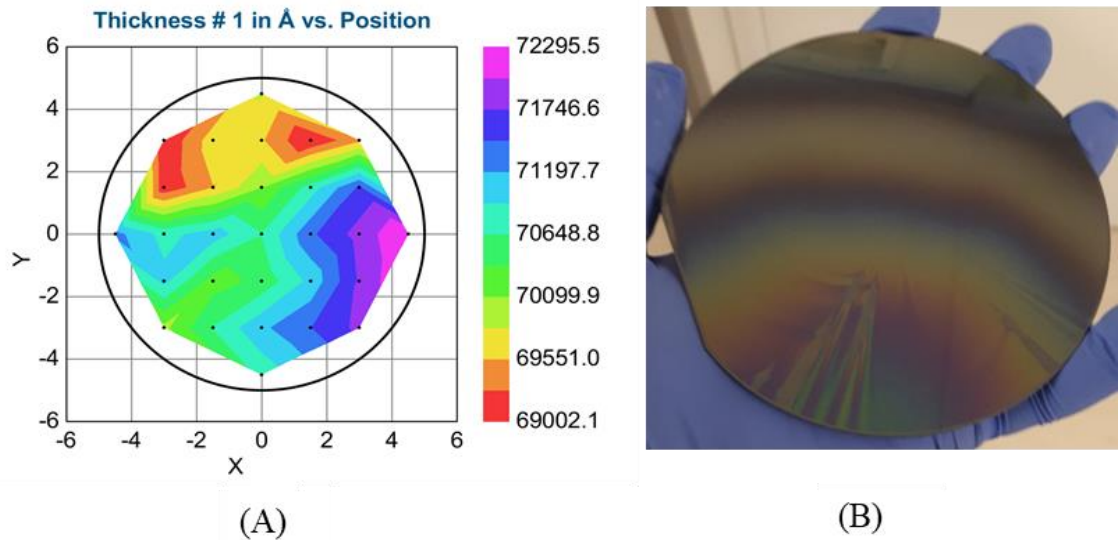


Figure 9.15 Spin parameter results of test 2 (A) thickness of NLOF2070 resist across a 4" wafer measured by ellipsometry (B) image of 4-inch wafer showing reduced strike marks

As the results of this method produced an improved uniformity, the subsequent process increased the spin time of step 2, as it is anticipated that a longer spin time will reduce the thickness of the final resist. The initial spin time of 15 seconds produced a thickness of approximately 7 μm , therefore the time was increased to 45 seconds for test 3.

- Spin parameters test 3.

1 = 2000rpm, 10 seconds, 200 accelerations

2 = 4000rpm, 45 seconds, 1000 accelerations

3 = 0 rpm, 8 seconds, 500 accelerations

Spin test 3 resulted with near zero strike marks and a thickness of between approx. 7-7.2 μm , (figure 9.16), which shows a greater uniformity than the previous spin test of 6.9- 7.2 μm .

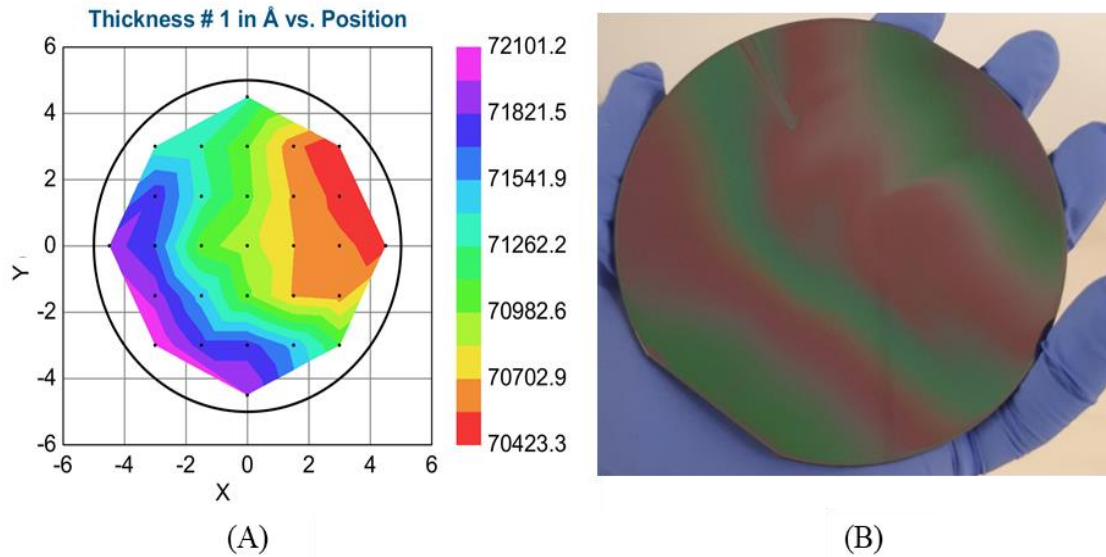
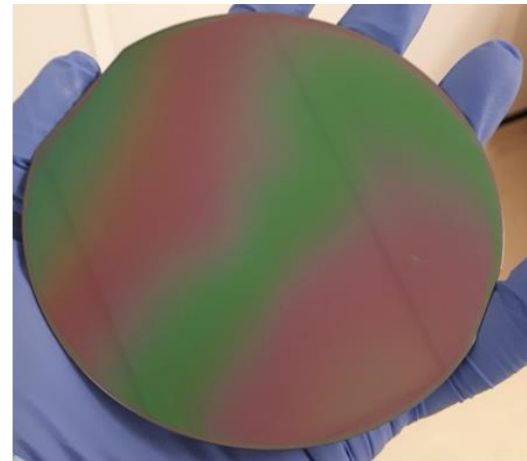
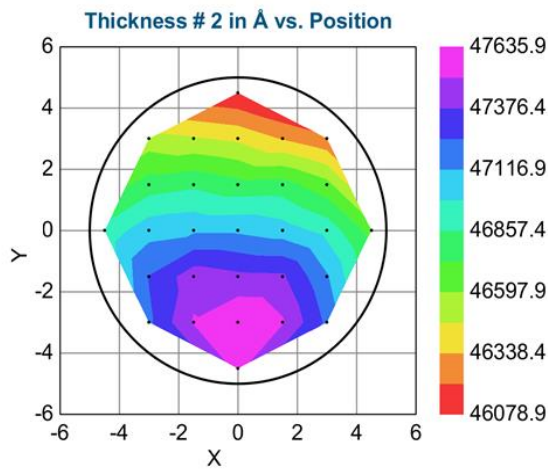


Figure 9.16 Spin parameter results of test 3 (A) thickness of NLOF2070 resist across a 4" wafer measured by ellipsometry (B) image of wafer showing near no strike marks

As a thickness of $4\mu\text{m}$ is required and it is known that increasing the spin time does not thin the resist any further, then increasing the spin speed at step 2 to 5500rpm and reducing the time back to 15 seconds was tested as test 4.

- Spin parameters test 4
 - 1 = 2000rpm, 10 seconds, 200 accelerations
 - 2 = 5500rpm, 15 seconds, 1000 accelerations
 - 3 = 0 rpm, 8 seconds, 500 accelerations

Figure 9.17A demonstrates that adjusting the parameters to the max speed of the second spin to 5500rpm for 15 seconds reduced the resist thickness to $4.6 - 4.7\mu\text{m}$, reaching as close to the $4\mu\text{m}$ target as possible, while additionally improving the uniformity across the wafer. Figure 9.17B shows no strike marks, indicating that the parameters used in test 4 provided were appropriate to use for all subsequent resist spin times for MN manufacture.



(A)

(B)

Figure 9.17 Spin parameter results of test 4 (A) thickness of NLOF2070 resist across a 4" wafer measured by ellipsometry (B) image of 4-inch wafer showing no strike marks

9.5 Resist photolithography optimisation

Using the MicroChemicals data sheets and the new spin coating parameters the following recipe (table 9.4) was used to coat wafers in NLOF2070 to a thickness of 4.6 μ m.

Table 9.4 photolithography parameters for NLOF2070

Wafer cleaning procedure	10 minutes in acetone bath 5 minutes in IPA bath Dry with nitrogen gas Bake for 10 minutes at 150°C
Spin parameters	Spin at 2000rpm, 10 seconds, 200 acceleration Spin at 5500rpm, 15 seconds, 1000 acceleration Spin at 0rpm, 8 seconds, 500 acceleration
Soft bake parameters	100°C for 7 minutes
UV exposure parameters	Dosage of 300mJ / cm ²
Post exposure back parameters	110°C for 11 minutes
Development parameters	Az726 for 3 minutes

Although the method of MicroChemicals data sheets had been followed to produce the above recipe, upon resist development at 45 seconds the resist began to peel (Figure 9.18).

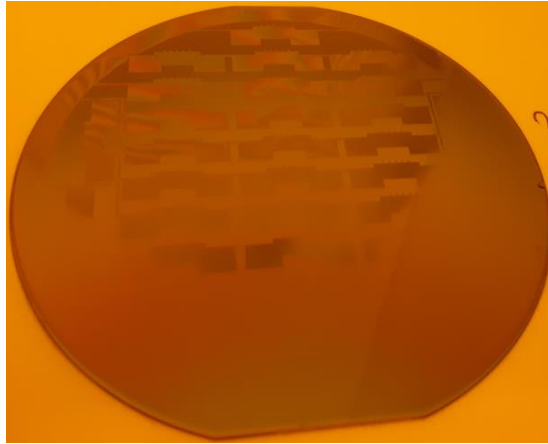


Figure 9.18 4-inch silicon wafer demonstrating resist removal upon development.

Further optimisation to enhance the resist adhesion to the SiO_2 was required. Potential parameters considered were bake times, MA UV dosage and the addition of adhesion promoters, such as, Ti Prime.

Discussion with the MN team who had experience with NLOF2070, lead to the following parameter changes.

- Wafer cleaning procedure
 - ~ 10 minutes in acetone bath
 - ~ 5 minutes in IPA bath
 - ~ Dry with nitrogen gas
 - ~ Bake for 10 minutes at 150°C

Emphasis was placed on the cleaning procedure and pre-bake to ensure no impurities affected the resists contact to the SiO_2 .

- Pre-bake = 140° for 10 minutes

The temperature was increased to ensure dehydration

- Allow to cool to room temperature
- Ti Prime spin parameters
 - ~ 1 = 4000rpm, 20 seconds, 1000 acceleration

Ti Prime is an adhesion promotor applied to the wafer via spin coat application prior to resist application, the spin parameters were followed from the MicroChemicals worksheets.

- Soft bake parameters
 - ~ 120°C for 2 minutes
- Resist spin parameters (as previously optimised)
 1. 2000rpm, 10 seconds, 200 accelerations
 2. 5500rpm, 15 seconds, 1000 accelerations
 3. 0 rpm, 8 seconds, 500 accelerations
- Rest wafer for 5.5 minutes

Resting the wafer allows for the resist to stabilise to its final form

- Soft bake parameters
 - ~ 100°C for 5.5 minutes

Bake minutes are calculated per μm of resist thickness. The new thickness is between $4.5\mu\text{m}$ - $5\mu\text{m}$, therefore, 5.5 minutes was selected to ensure the full thickness was baked.

- Allow to cool
- UV Exposure parameters
 - ~ Dosage of $300\text{mJ} / \text{cm}^2$ and $500\text{mJ} / \text{cm}^2$ tested

Higher UV dosages enabled the wavelengths to penetrate the entire resist film thickness to harden the full thickness of the exposed areas. Lower dosages hardened the top of the resist only, with incomplete adhesion of the resist to the wafer, enabling it to be easily removed.

- Post exposure bake parameters
 - ~ 110° for 3 minutes

This step is necessary for the cross-link reaction of the resist, prolonging the exposure beyond the original 1 minute should maximise crosslinking reactions.

- Development parameters
 - ~ Az726

The wafer was monitored during development and removed once the mask pattern was visible, and the unwanted resist had cleared. Two different wafers were examined one with, and one without the use of an adhesion promoter, Ti Prime, as outlined in figure 9.19.

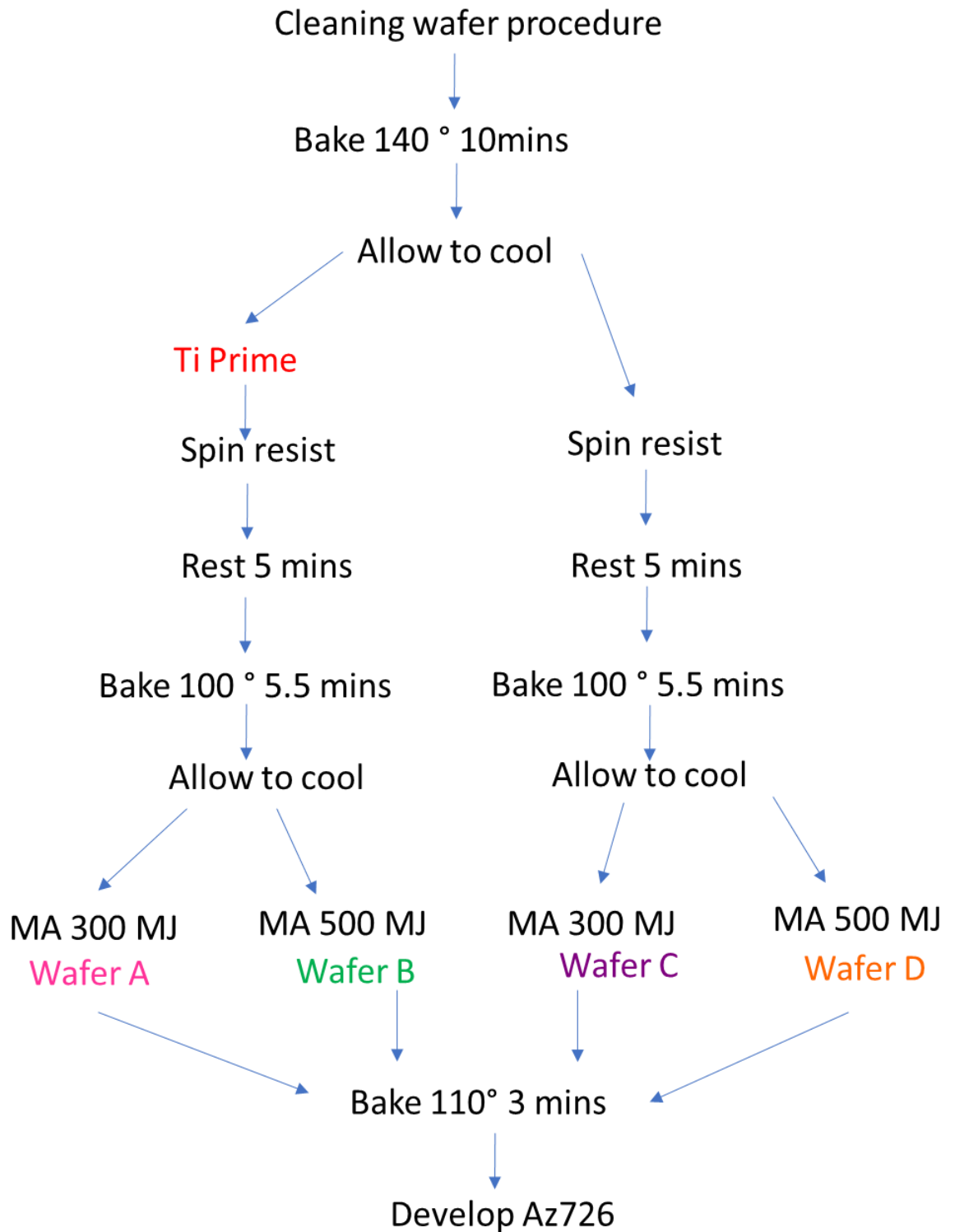


Figure 9.19 Schematic diagram of in plane MN photolithography optimisation

Results of the in-plane photolithography optimisation are summarised in table 9.5; all four processes saw no resist de-lamination upon development. However, wafers A and B saw longer development times compared to those of C and D. The method for wafers A and V differed with the use of the adhesion promotor, Ti prime, at the start of method A. This resulted in the development time of wafer B being 4 minutes longer than wafer A, this was due to the extra hold TI prime provided to the resist on the silicon wafer, which takes longer to remove through developing. Adjusting the UV dosage between 300mJ or 500mJ, observed no difference in the final photolithography results from wafers that had and had not been treated with Ti prime. The resist had hardened through the full thickness of the resist, which consequently prevented the resist from delamination. This demonstrated that the adhesion promoter, Ti Prime, only increased the method process time due to the additional step and development time compared to methods without it. The method used to develop wafer C was considered the optimal process for MN fabrication, as it possessed the least number of steps and shortest development time compared to the other methods.

Observations throughout the optimisation tests identified that the temperature and humidity of the cleanroom can affect the photolithography process. A high level of humidity during the resist dehydration step meant that less solvent was baked out of the resist, and that during the rest period water was reabsorbed. Both factors affect the resist development and integrity during KOH etching. Fluctuations in temperature conditions can also affect results; the temperature in the cleanroom varied from $>5^{\circ}$ - $<20^{\circ}$ dependent upon the weather and this may also affect the final formation. To overcome this, wafers were processed under similar, consistent cleanroom conditions.

Table 9.5 Summary of result from in plane MN photolithography optimisation

Wafer	Ti Prime	MA Dosage mJ	Development time of devices	Comments
A	Yes	300	6 minutes	Resist did not delaminate.
B	Yes	500	>10 Minutes	Resist did not delaminate. Took longest to develop.
C	No	300	1 minute 45 seconds	Resist did not delaminate. Shortest development time.
D	No	500	3 minutes	Resist did not delaminate.

As previously shown, the development time of the MN devices without resist delamination was optimised to <2 minutes. However, in this development time, the alignment marks were not completely developed. As alignment marks are crucial for precise wafer alignment, the length of the development time needed amendment. Using the method for wafer C, wafers were fabricated and removed from the developer in 30 second intervals to microscopically analyse the alignment marks (figure 9.20). The longer the wafer remained in developer the more pronounced the alignment marks became, until a point was reached at which the marks began to over-etch. The larger alignment marks developed faster than the smaller ones potentially due to their larger surface area and ease of resist removal. At 1-minute, (figure 9.20A), the smaller marks had only developed in the centre to produce small circles, in comparison, the larger marks were identified as crosses, although not fully developed on the arms. At 1.5 and 2 minutes (figure 9.20B and C), the arms of the large marks began to fill out and the smaller cross shape started to be revealed. By 2.5 minutes, (figure 9.20D), all four crosses were fully developed. Developing the wafer for 3 minutes, (figure 9.20E), caused over developed the alignment marks, with crosses developing rounded edges. The smaller crosses expanded into a circle with overdevelopment. These results suggest that the optimal development time for alignment marks is at 2.5 minutes.

During reverse alignment processes, alignment of the top two larger crosses was sufficient to produce precise and repeatable alignment of the front and reverse wafer masks. Therefore, for future mask development only the two larger crosses are required as alignment marks. Thus 2-minute development time can be used, as device features are already developed at this time. The final optimised wafer is shown in figure 9.21 ready for the next oxide ICP etch step.

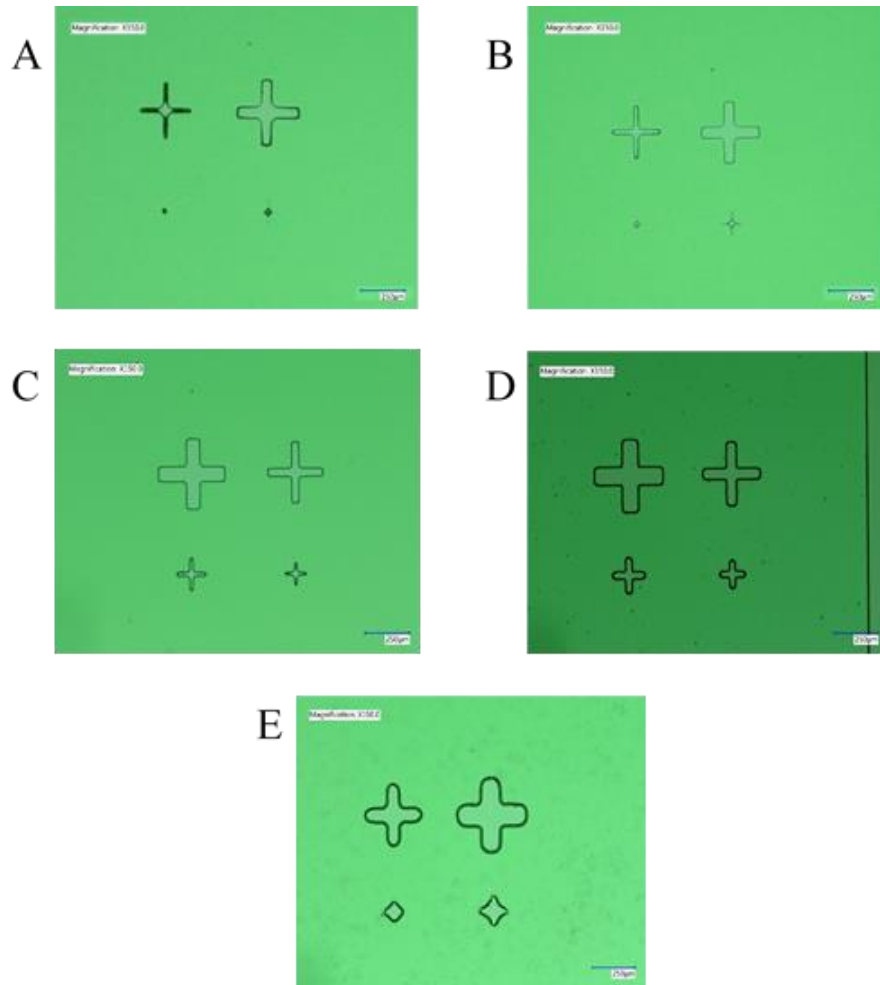


Figure 9.20 development optimisation of alignment marks (A) 10 minute (B) 1.5 minutes (C) 2 minutes (D) 2.5 minutes and (E) 3 minutes

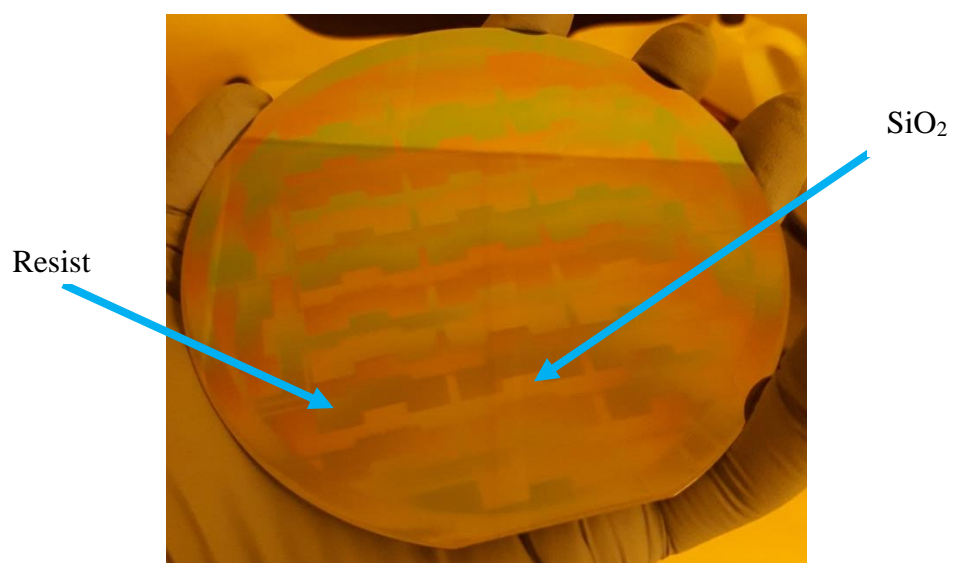


Figure 9.21 Full optimised wafer, showing MN mask pattern in resist and SiO₂ between devices

9.6 In-plane MN fabrication process flow

The finalised in-plane MN photolithography fabrication process is as follows (table 9.6);

Table 9.6 optimised photolithography method for NLOF2070 resist to fabricate in-plane MNs

Wafer cleaning procedure	10 minutes in acetone bath 5 minutes in IPA bath Dry with nitrogen gas Bake for 10 minutes at 140°C
Spin parameters	Spin at 2000rpm, 10 seconds, 200 acceleration Spin at 5500rpm, 15 seconds, 1000 acceleration Spin at 0rpm, 8 seconds, 500 acceleration Rest wafer for 5.5 minutes
Soft bake parameters	100°C for 5 minutes
UV exposure parameters	Dosage of 300mJ / cm ²
Post exposure bake parameters	110°C for 3 minutes
Development parameters	Az726 for 2 minutes

After photolithography, the SiO₂ is etched to replicate the resist mask in the ICP and the wafer is flipped, and the same lithography process repeated on the reverse side of the wafer, subsequently followed by ICP etch of the SiO₂. Figure 9.22 shows a schematic of the wafer cross section of the in-plane double sided lithography, SiO₂ etch and subsequent KOH processes.

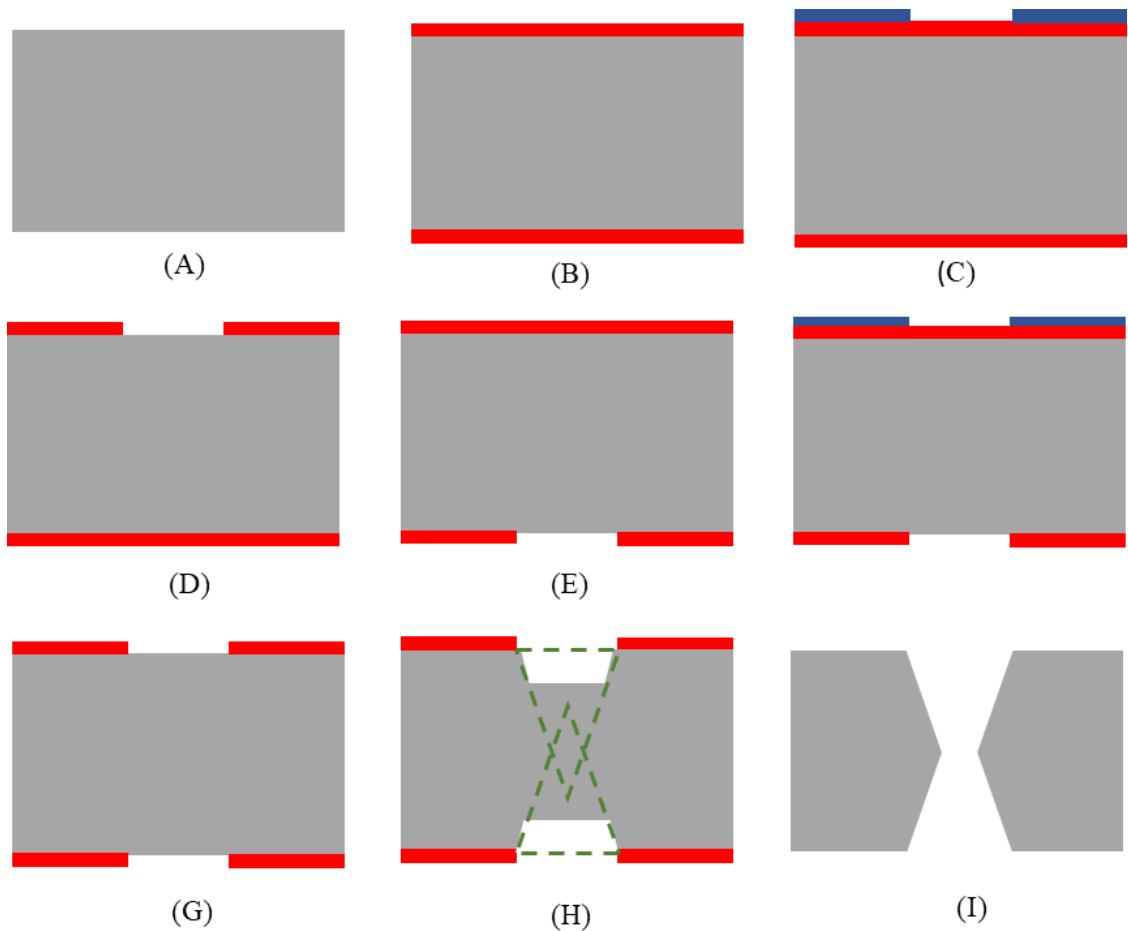


Figure 9.22 Schematic diagram of a KOH etched microneedle process flow from the cross section of the shaft of the microneedle

(A) p type double sided polished silicon wafer

(B) Silicon dioxide deposition onto both sides (red)

(C) photolithography used to pattern device mask on side 1 (blue)

(D) device pattern transferred into silicon dioxide hard mask using ICP

(E) wafer flipped

(F) photolithography used to pattern devices onto backside using alignment marks

(G) device pattern transferred into silicon dioxide hard mark using ICP

(H) wafer submerged into KOH solution for etching, green dashed lines depicts etching process

(I) devices removed from KOH solution once silicon has been etched through

9.7 KOH MN etch optimisation

Following optimisation of the photolithography and ICP etching steps, the final step is to etch the MNs out of the silicon wafer in one simultaneous KOH etch step. Previous data in section 9.2.2 determined that the etch process takes approximately 5 hours, however, this depends on the volume and concentration of KOH used. Larger volumes and higher concentrations of KOH means more KOH is available to etch the silicon wafer, which speeds up the reaction rate. To maintain a consistent and repeatable process all etching is undertaken with a 200ml volume of 44% KOH. However, during silicon etching KOH is consumed, in most circumstances where the concentration of an etchant decreases then the reaction rate slows, however, for KOH this was the reverse. As the concentration of KOH decreased, the etch rate increased, demonstrated previously in the graph of KOH concentration against etch rate (figure 9.6A) so, as the silicon wafer is etched and released into the solution, the etch rate increases and the time to etch completion decreases (the etch rate accelerates) [210].

The size of the silicon wafer or piece to be etched also affects the etch outcome; smaller diameter wafers or pieces have less material to etch through, resulting in a lower quantity of silicon dissolved into the KOH solution. The KOH solution, therefore, maintains a higher concentration in comparison to a larger piece. This means that smaller pieces of silicon will etch slower than larger pieces in the same volume of KOH due to the rate of concentration change.

To monitor the etch rate and estimate the time for a full wafer to etch to completion, 4-inch wafers were placed in separate beakers containing 200ml of 44% KOH heated to 70°C. At 1-hour intervals the wafers were removed from solution, washed in deionised H₂O and observed under the microscope.

Figure 9.23 shows the MNs produced after KOH etching from the top of the wafer in the (100) plane; the left-hand side images (A,C,E,G,I) started with the pointed tipped MN mask, while the right hand-side images (B,D,F,H,J) began with a flat mask (figure 9.12B).

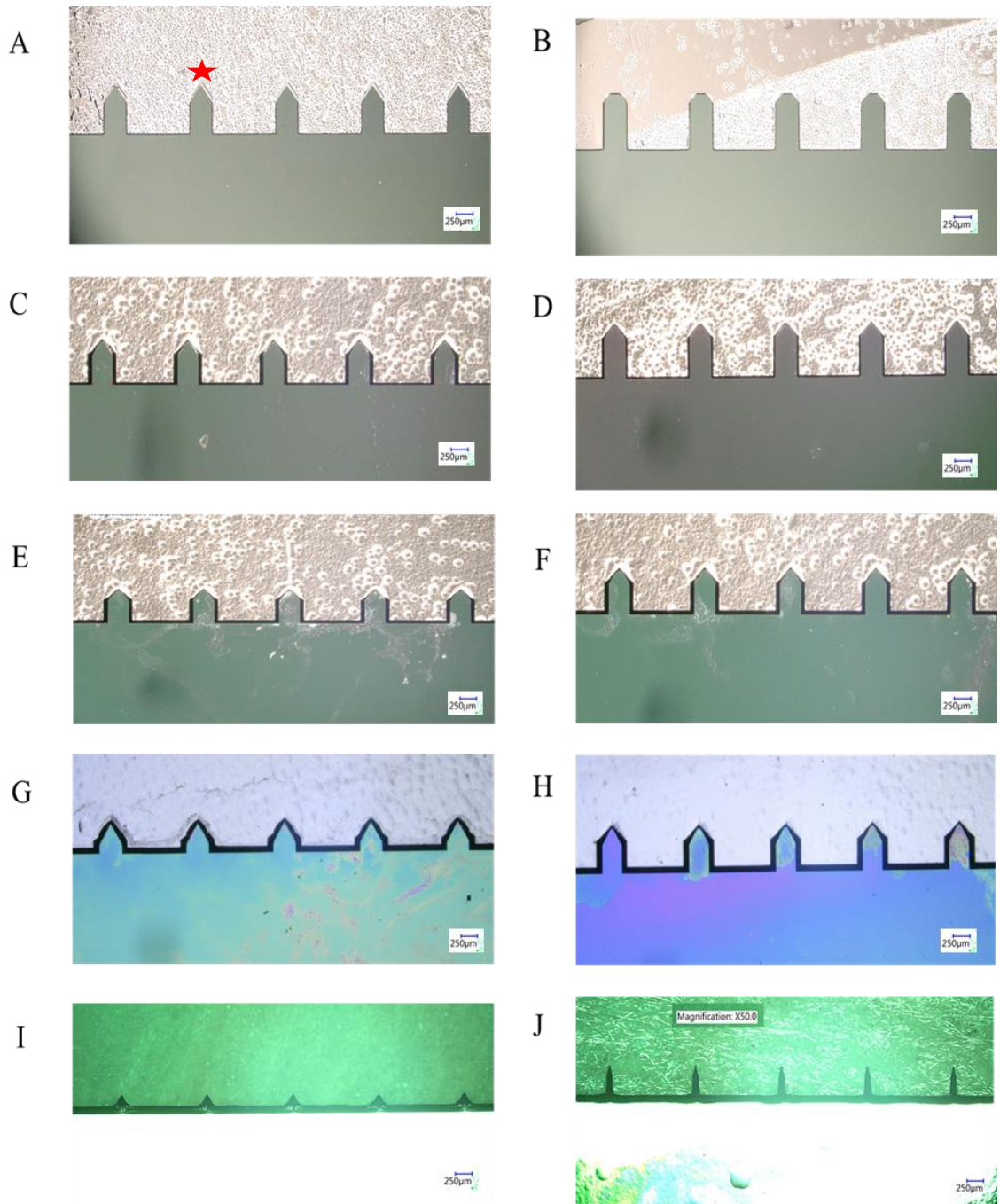


Figure 9.23 KOH etch of in-plane MN at 1-hour intervals for pointed (left) and flat (right) MN mask designs. A-B 1 hour, C-D 2 hours, E-F 3 hours, G-H 4 hours, I-J 6 hours. Red star indicates where the 80° angle is measured

Pointed mask designs:

After 1 hour of etching the mask pattern had translated into the silicon wafer. The average height of the MNs measured $672\mu\text{m}$ while the average width measured $338\mu\text{m}$, with an 80° -pointed tip in the (100) orientation, marked by the red star (figure 9.23A), therefore all MNs correlated with the starting mask dimensions. As the etch continued, at 2 hours the MN heights reduced to $546\mu\text{m}$ while the width remained at $335\mu\text{m}$, figure 9.23C. An additional observation was made where the black outline around the MN, began to thicken; it was believed that the edges of the MN's shafts were also etching into 54.7° (111) sidewalls. After 3 and 4 hours the wafer was still intact, (figure 9.23E and G), but the MN heights have reduced further to $473\mu\text{m}$ and $413\mu\text{m}$ respectively but maintained the (100) orientated 80° tip angle. Continuing the process for 6 hours to etch completely through the wafer, resulted in the MN losing all shaft height, leaving only the pointed tip protruding from the device edge, (figure 9.23I). This process shows that using a mask design where the tip is already designed on the MN shaft, results in a significant decrease in the final MN height upon completion of the wafer etch.

Flat mask design:

The MNs created from a mask design where the tip is omitted, "flat", (figure 9.23B) observed that after 1 hour of etching the tip has begun to form via the 90° corners of the rectangle mask, etching in what's known as "corner rounding", where the (110) silicon planes are exposed, the newly created angle has changed from 90° and now measures 133° , figure 9.23B. After 2 hours, the (110) planes have etched further inwards and intersect to form a 94° -point that is the beginning of the MN tip, (figure 9.23D); the height measures approximately $653\mu\text{m}$ and width measures approximately $346\mu\text{m}$. After 3 and 4 hours, the heights of the MNs reduce to $613\mu\text{m}$ and $593\mu\text{m}$ while the width is maintained at $349\mu\text{m}$, respectively (figures 9.23F and 9.23H). Leaving the wafer to continue etching for 6 hours saw a large reduction in the MN height, from $593\mu\text{m}$ to $403\mu\text{m}$ and the width reduce from $346\mu\text{m}$ to $113\mu\text{m}$ (figure 9.23J). At this time point the MNs are clearly over-etched, and the shape has deformed into a thin spike; the KOH had not only etched through the $300\mu\text{m}$ wafer to create the MNs but had continued to etch away the SiO_2 mask that protected the silicon from etching. This consequently exposes a larger surface area of the silicon wafer from beneath the mask to

the KOH expediting the etching to all over the MNs. Overall, the height and width of the final MN is primarily reliant on the time it takes for the KOH to completely etch through the 300 μm wafer, beyond this, further etching will continue to etch the MNs until the SiO_2 mask is completely removed to expose the silicon beneath, making it susceptible to the etch.

After 4 hours of etching, the heights of the MNs produced by the flat tipped mask are approximately 180 μm longer than the pointed mask, while the widths of both increased to 335-350 μm . Designing the mask with flat tips prevents exposure of the (110) planes straight away, which ultimately forms the tip. Enabling the KOH solution to create the (110) planes requires more time, which prevents the KOH from etching in the (110) orientation from the start of the etch, thereby preserving the height of the MN.

Designing the MN mask with a pointed tip, enabled the tips of the MN to be fabricated faster by the KOH as it was not reliant on the KOH to form the tip shape from the (110) planes. Therefore, as the shape of the tip takes less time to fabricate, once created, the (110) planes are exposed to the KOH longer and thus will be continuously etched until the full 300 μm wafer thickness is etched though. This continued etching of the (110) planes continues to removes silicon from the height of the MN, making it shorter in comparison to the flat tipped masked MNs. Figure 9.24 shows a silicon wafer fully etched through after 4 hours and 40 minutes in KOH solution, the MN devices are still intact, enabling further processing or can be cut away from the outer ring.

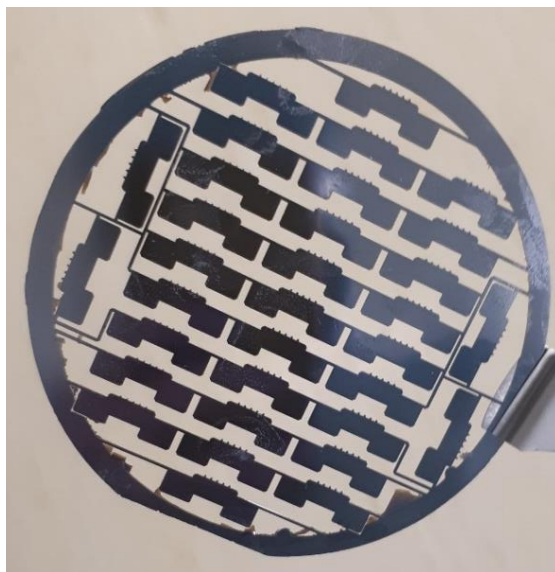


Figure 9.24 KOH etched 4-inch MN wafer, held together by connected devices to an outer ring

9.7.1 Analysis of optimised solid MN

Etch optimisation concluded that after 4 hours and 40 minutes the KOH had completely etched through the 300 μm wafer to reveal the final MN design of flat and pointed mask designs. The KOH etching of the flat masked MNs, produced MNs that measured approximately 500 μm in height and 540 μm in width, figure 9.25A. This indicated that the height of the MN decreased by 200 μm and the width increased by 240 μm from the original mask design. The tip of the MN has formed from the corners of the rectangular mask convex etching in the (110) planes from the front and reverse side of the wafer. The two-original masked (100) planes and the four new (110) planes all intersect to create a 6-sided pyramidal tip, seen in figure 9.25C. To establish the tip and etch through a 300 μm wafer, approximately 200 μm of the designed MN height was sacrificed due to the 90° corners of the mask exposing the (110) planes to form the tip (original mask illustrated as the red dashed line in figure 9.25A). Figure 9.25B shows a cross-section of the MN tip confirming the 54.7° angle produced from simultaneous front and reverse etching. Figure 9.25C views the MN from the apex of the tip looking down the shaft; this shows that the sides of the MN shaft has etched in the (111) axis (sides 2, 3, 5, and 6) creating an 54.7° sidewall from the front and back of the wafer. These new sides join with the original (100) masked sides 1 and 4 to result in a hexagonal shaped MN shaft. Therefore, two widths can be measured, the first being the original width from the CAD mask, which still measures approximately 300 μm , and the new width, which includes the etched (111) sides, measuring 537 μm : an additional 119 μm each side, figure 9.25A.

Every straight edge designed on the MN CAD mask will produce a 54.7° (111) side wall angle upon KOH etching, that ultimately intersects from the front and reverse etching, and is why the width of the MN increases. However, any designed 90° corners, such as the original rectangle corners, will etch in the (110) plane to create an angled or “rounded” convex corner. These angle edges are used to create the MN tip in the (100) and (110) orientations; in the (100) plane, the corners of the original rectangle mask, etches inwards, undercutting the mask to eventually meet in the middle and form a triangle (highlighted in green in image 29.5.D). In the (110) orientation the planes etch at 54.7° to create four additional sides, which join to the original two (100), creating a six-sided pyramidal MN tip.

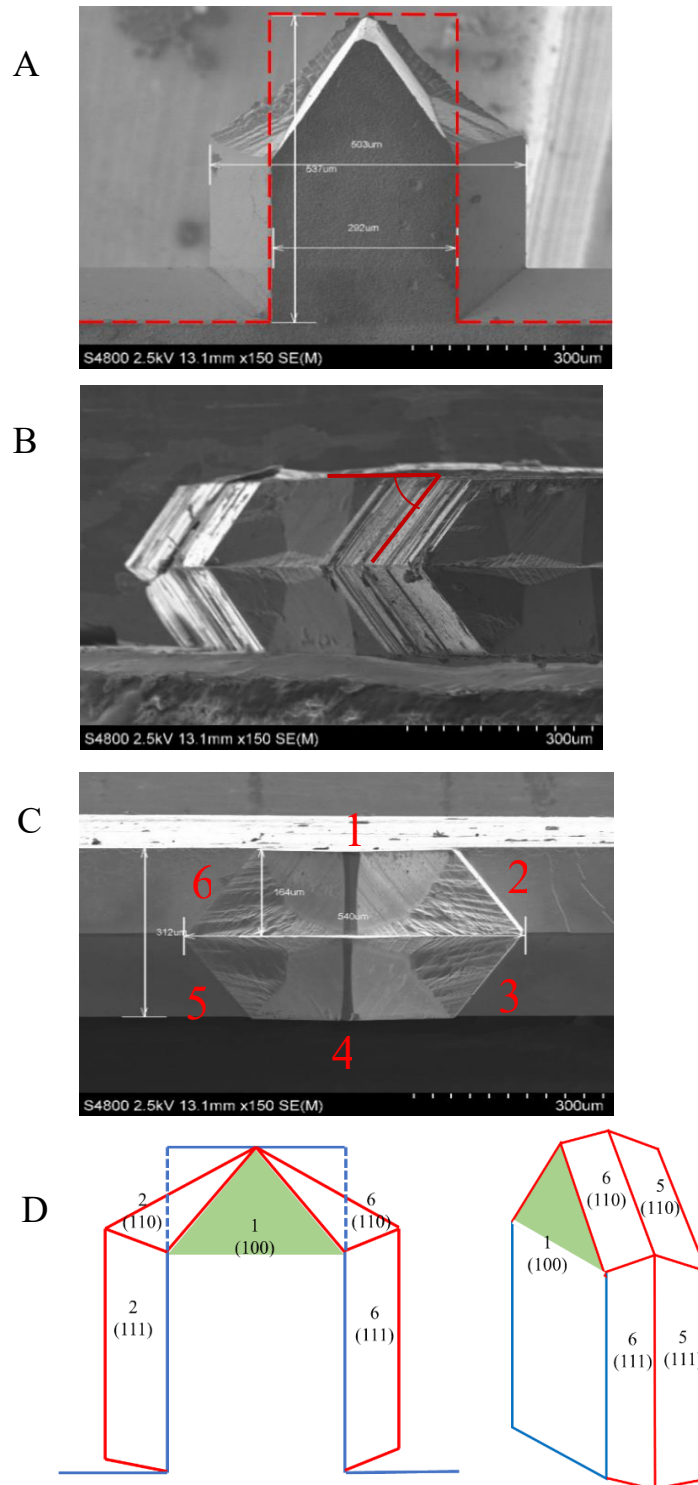


Figure 9.25 proof of concept MNs post KOH (A) (100) orientated view of MN measuring height and width at $500\mu\text{m}$ and $540\mu\text{m}$ respectively, red outline shows original CAD MN mask (B) proof of angle concept, showing sides of MNs etch to 54.7° (C) wafer cross-section from tip view of MN showing hexagonal etched shape of MN shaft, sides 1 and 4 show the (100) plane from the original CAD mask, while sides 2, 3, 5, and 6 are etched from the (110) planes (D) Schematic images of MNs, blue lines represent original CAD design where the dashed line shows how the tip etch undercuts the mask. Red lines show final etched MN design and how the KOH etches to increase the width and reduce the height from etching the (111) and (100) planes. The numbers correspond to the hexagonal sides of image C. The green area highlights the (110) angled etch, to create a triangle from the 90° sides

It has already been demonstrated that MNs that started as pointed mask designs suffer a larger reduction in height through KOH etching than the flat masked MNs. Through SEM analysis (figure 9.26), the pointed masked MNs after 4 hours and 40 minutes of etching, measured a height of $447\mu\text{m}$ and width $505\mu\text{m}$; a height difference of approximately $150\mu\text{m}$ and width difference of approximately $200\mu\text{m}$ from the original masked design (red dashed outline figure 9.26A). It is also observed that the shaft of the MN has completely etched away (top of shaft outlined in yellow in figure 9.26A), leaving mostly the triangular tip of the MN protruding from the device edge.

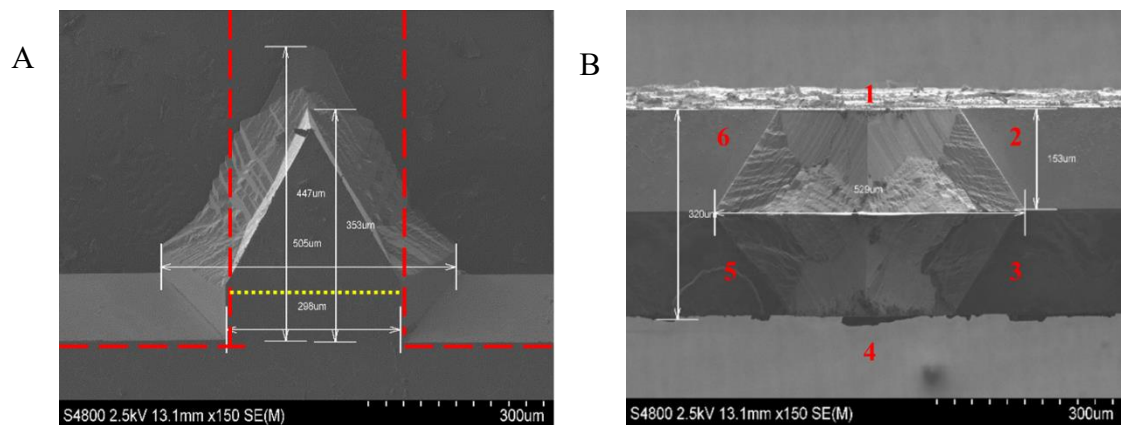


Figure 9.26 SEM images of pointed tipped MN post KOH etching for 4 hours and 40 minutes (A) (100) orientated view of MN, showing etched height at $447\mu\text{m}$ and width at $505\mu\text{m}$. Original mask design is outlined in red, while the yellow line indicates where the shaft of the MN starts (B) cross section image of MN tip, demonstrating hexagonal shaft shape created from two (100) planes, sides 1 and 4, and four (110) planes, sides 2, 3, 5 and 6.

To observe further changes to the MNs upon continued etching, flat topped MNs after 5 hours, 5.5 hours and 6 hours were examined using SEM (figure 9.27). After 5 hours the original flat topped MNs began to lose their hexagonal shape as the (111) sides continue to undercut the SiO_2 mask, this reduced the original (100) plane width from $300\mu\text{m}$ to $229\mu\text{m}$. Continuing the etch for 5.5 hours sees the original width reduced further to $30\mu\text{m}$, and the SiO_2 mask is etched away. After 6 hours the original (100) width was completely etched away enabling the four (111) sides to join into a diamond shaped shaft, that resembles a sword, figure 9.27C.

The same process was observed with the original pointed tip MN, design where at 5.5 hours the original mask width was reduced to approximately $60\mu\text{m}$, and upon continued etching, eventually, only the diamond shaped tip, protruding from the device edge remains, figures 9.27 D and E.

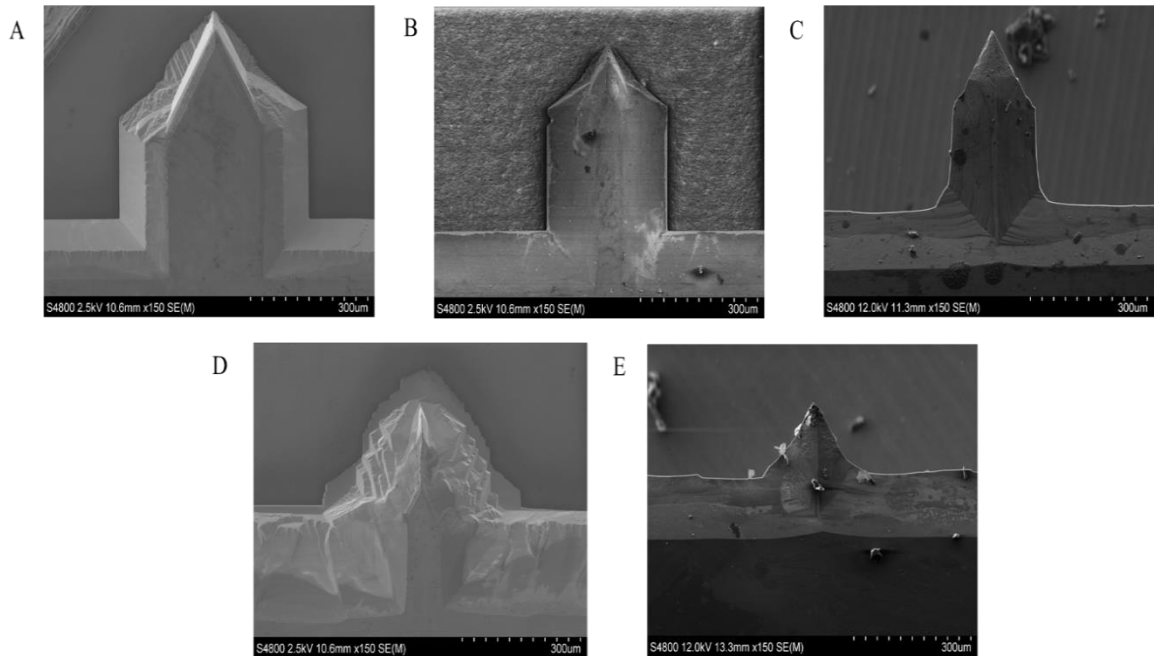


Figure 9.27 KOH etch of flat MN (A) 5 hours (B) 5.5 hours (C) 6 hours and pointed tip MN (D) 5.5 hours (E) 6 hours

In both flat and pointed mask designs some of the MNs were observed with “pits” etched out of the side of the shafts, figure 9.28. Some wafers had more SiO_2 deposited on the surface of one side compared to the other e.g., $1.99\text{-}2.3\mu\text{m}$ which was due to the variability of the chemical vapour deposition (CVD) even after deposition rate tests. The side with less SiO_2 protection was more susceptible to etching than that with a thicker SiO_2 layer, resulting in a MN where one side had over etched while the other side was protected. The image in figure 9.28A shows a cross section of a MN where side one (red arrow), had sufficient SiO_2 protection, whilst side two (blue arrow) had a thinner SiO_2 mask that had consequently over etched to produce a smaller (100) plane width. Rotating the needle to view side 2, with the thinner SiO_2 mask, figure 9.28B shows areas where the SiO_2 had failed and the KOH had etched into the silicon wafer to produce 54.7° concave craters, (shown by yellow arrow). These craters create weak spots that could cause the device to break during skin insertion. To prevent insufficient

SiO₂ mask deposition, all future SiO₂ coatings were increased from 2μm to 2.3μm, allowing for variation in CVD deposition thicknesses and etch rates.

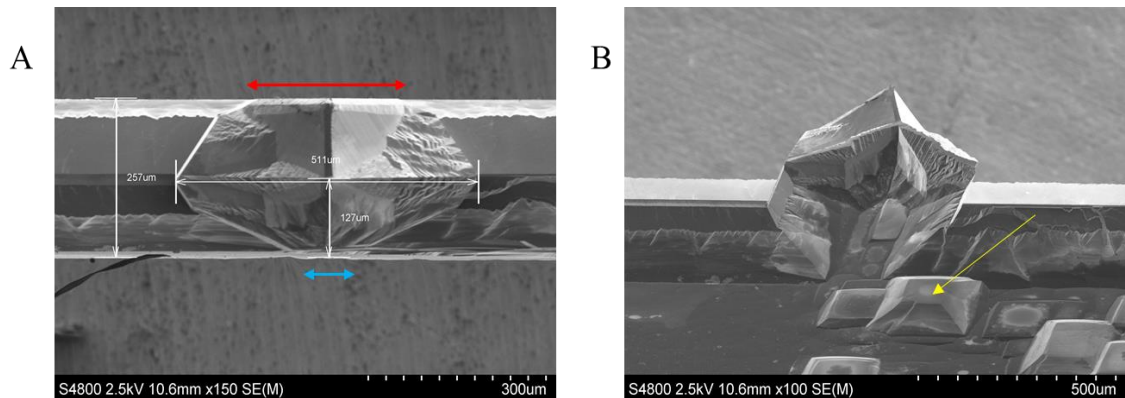


Figure 9.28 Results of variable SiO₂ mask thickness of KOH etching (A) cross section of MN with two different SiO₂ thickness on either side of the wafer, the red arrow shows a full protective SiO₂ coverage, while the blue arrow shows too little coverage and an over etched MN (B) rotating the MN to view the less covered side, shows the etched craters in the device, yellow arrow, due to insufficient SiO₂ coverage.

9.8 Optimising MN height

The above proof of concept studies demonstrates that MNs fabricated from “pointed” tip mask designs have tips which etch faster than those designed without, and thus resulted in the MN shaft etching impractically short. To compensate for this, the original CAD mask would need to be designed longer, however, this would take up more room on the wafer and reduce the overall MN yield. As the tips produced from either design are practically identical, therefore, to maintain the yield, all future MNs were designed using the “flat” mask.

The original mask height was designed to 700μm, however after KOH etching the new height measured approximately 500μm. To understand fully how the etch influenced the height of the MN, several masks were designed to produce MNs of variable heights. The height of the MN needs to be optimised for specific application e.g. for cosmetic application the MN height will range between 200-500μm, while for therapeutic API delivery, e.g. for Insulin injection, a height of >600μm is desirable [212].

The MN device arrays were designed in two formations either:

1. all the MNs on the same device measure the same height
2. the MNs on the same device had different heights

Design 1

Arrays of 1 x 5 MNs were created where all the MN's on the device were the same height i.e., all 1500, all 900, all 700, all 500 and all 300 μ m figure 9.29A-E.

Design 2

Arrays of 1 x 5 MNs were created where the MN's on the same array possessed different heights i.e.,

Figure 9.29F = 1 x 5 array measuring 1200-800 μ m in descending 100 μ m increments,

Figure 9.29G = 1 x 5 array measuring 700-300 μ m in descending 100 μ m increments,

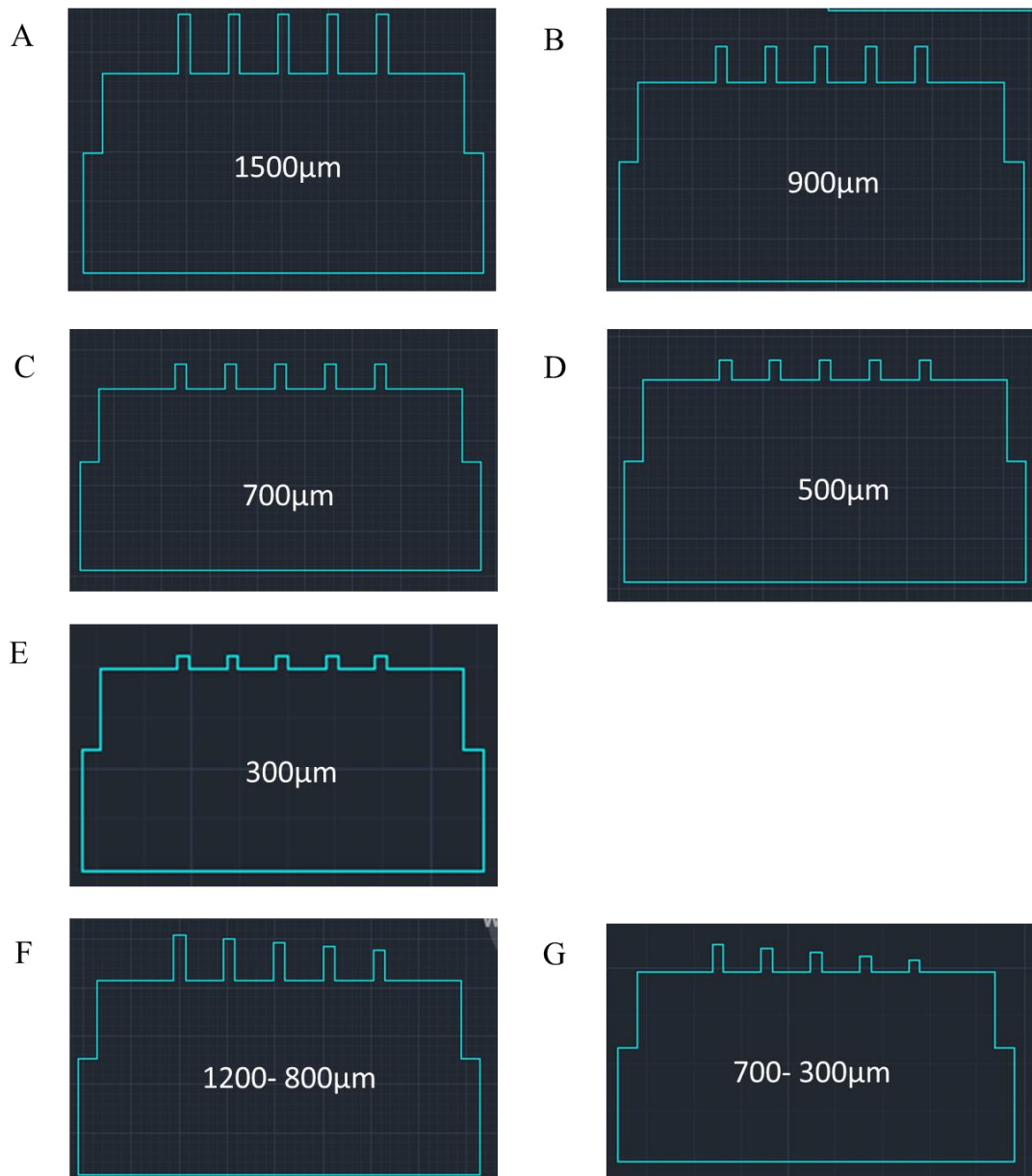


Figure 9.29. CAD mask designs of in plane KOH solid MNs of various heights. A-E depict MN arrays where all the MN on a single device are the same height, e.g. (A)1500µm, (B) 900µm (C) 700µm, (D) 500µm, (E) 300µm. F-G show MN arrays where the MN on each device vary in height, (F) MN descend in 100µm increments from 1200µm to 800µm (G) MN descend in 100µm increments from 700-300µm.

The use of a connecting ring to hold the devices together post etching, was not required to produce solid MNs as no extra processing is required after etching, therefore the omission of the ring enables the MNs to completely etch out of the wafer for immediate use. Additionally, removing the ring reduces the device size, meaning more MNs could be designed on each wafer. The previous mask design in figure 9.24 showed that a maximum of 33 MN devices connected to the ring could be produced from a 4” wafer.

In contrast, the new mask design increased this to 82 MN devices per wafer. Following KOH etching, MNs were examined using SEM to determine their etched height. Figure 9.30 shows the results of mask design 1, where the MN array heights began at either 1500, 900, 700, 500 or 300 μm . Initial obvious observations were that the shorter the original mask design, the shorter the resulting MN. However, the ratio in which the MN height reduced compared to the original mask design height was not consistent, for example a mask height of 1500 μm etched to 860 μm , a difference of 640 μm . While a MN mask height of 500 μm etched to 311 μm , a difference of 189 μm . However, the angle at which the tip was created in the (100) plane remained constant at 60°.

Devices fabricated from design 2, where the MNs on each individual array measured different heights, were produced to address challenges such as skin contours.

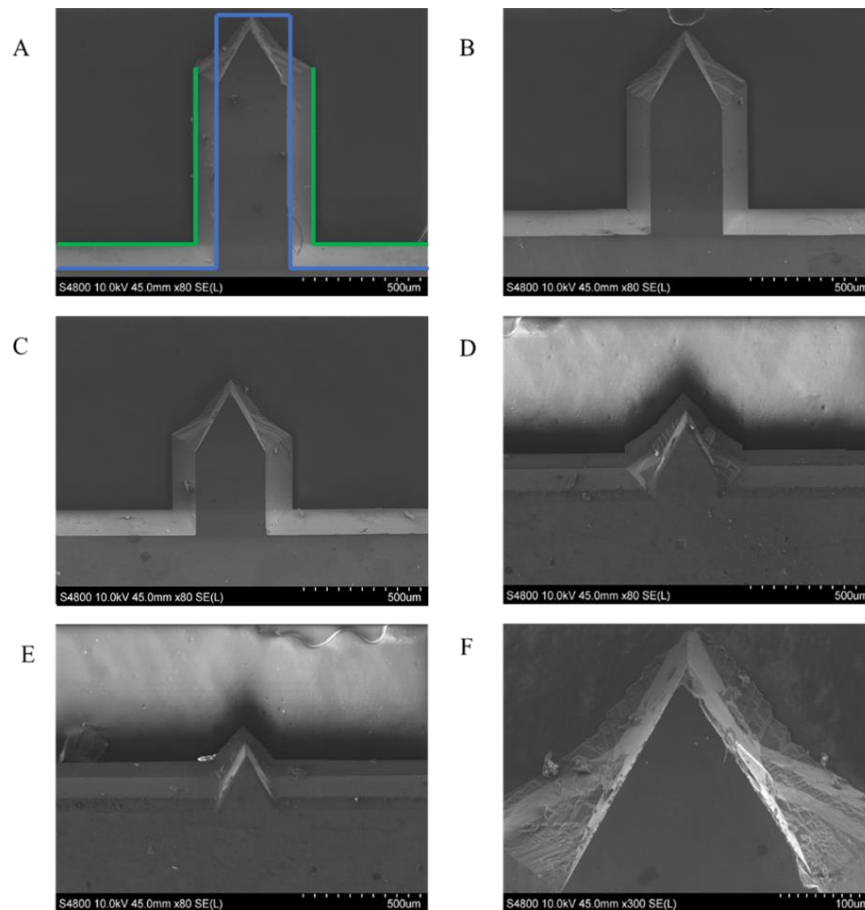


Figure 9.30 SEM images of solid in-plane MN starting at different mask heights after KOH etching (A) mask height of 1500 μm , KOH height 860 μm . Blue line shows original CAD MN mask, while green outlines new MN shape (B) mask height of 900 μm , KOH height 730 μm , (C) mask height of 700 μm , KOH height 534 μm (D) mask height of 500 μm KOH height 311 μm , (E) mask height of 300 μm KOH height 134 μm (F) tip measuring at an angle of 60°.

In terms of contouring, as the skin forms a protective layer around the body the application site is not necessarily always uniformly flat. Additionally, different areas of the body comprise of thicker or thinner skin layers; such as the palms of the hands and bottom of feet or the thinner layers such as, facial skin and eyelids [213]. Therefore, the fabrication process allows MNs to be created with flexible lengths, to achieve different penetration depths, (figure 9.31). Using MNs in arrays with different heights can overcome challenges such as, skin contours and thicker or thinner skin.

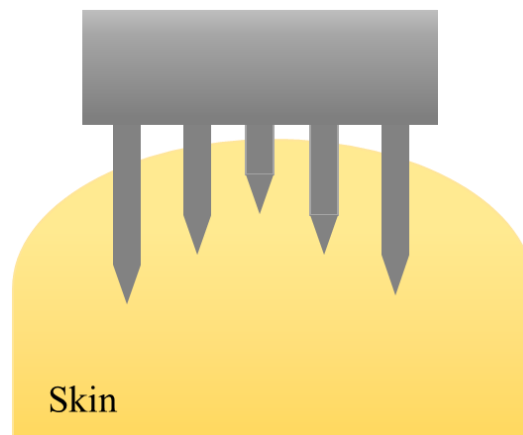


Figure 9.31 Schematic diagram of MN devices with different heights penetrating the uneven skin surface to account for body contouring and skin depth differences.

So far, we have determined that the final etched height and shape of the MN is influenced by the etching time and the thickness of the SiO₂ mask.

To mathematically analyse the post KOH etching MN height, in comparison to the specifications of the starting mask design, the MNs of different design heights (1200, 1100, 1000, 900, 800, 700, 600, 500, 400, 300 μ m) were examined in figure 9.32. Each height is measured using ImageJ, with the results listed in table 9.7 and interpreted in figure 9.33.

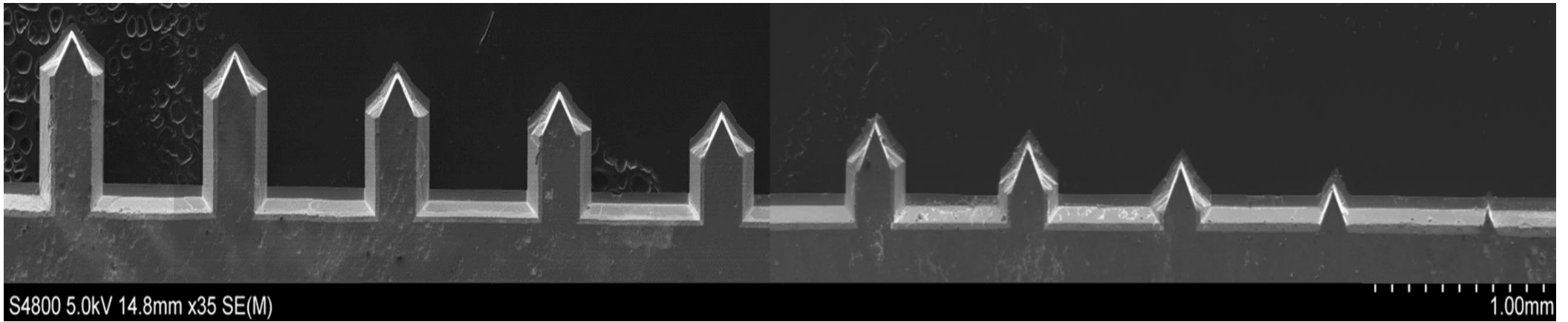


Figure 9.32 Solid KOH etched in plane MNs in descending order from 1200 μm to 300 μm , in 100 μm increments

Table 9.7 shows that as the CAD mask height decreases the KOH etched height also decreases, on average by $313\mu\text{m} \pm 70$. However greater height differences of 350-416 μm are observed with the larger MN i.e., mask designs 1200, 1100, 1000 and 900 μm , while shorter mask designs of 800-300 μm see a height decrease of 230-330 μm post etching. Plotting the results on a scatter graph, (figure 9.33) and calculating the linear regression produces the equation $y = 0.7644 x - 139.62$ with a R^2 value of 0.9973. For a result to be significant the R^2 needs to be >0.98 . A value of 0.9973 shows that the results fit closely to the regression line and the equation $y = m x + c$ can be applied as a statistical means of estimating the mask design height measurements required to KOH etch a MN and vice versa.

Table 9.7 Comparison of KOH MN etch height in relation to starting mask design

MN CAD mask design height (μm)	KOH etched MN height (μm)	Difference between CAD design height and KOH etched height (μm)
1200	784	416
1100	696	404
1000	616	384
900	549	351
800	470	330
700	392	308
600	333	267
500	245	255
400	186	214
300	66	234

For example, if a final MN length of 600 μm is required then inputting the numbers into the equation gives:

$$y = 0.7644 x - 139.62$$

$$600 = 0.7644 * x - 139.62$$

Rearranged

$$x = (600 - -139.62) / 0.7644$$

$$x = 968\mu\text{m}$$

Therefore, a MN mask design height of $968\mu\text{m}$ is needed to produce a KOH etched MN of $600\mu\text{m}$.

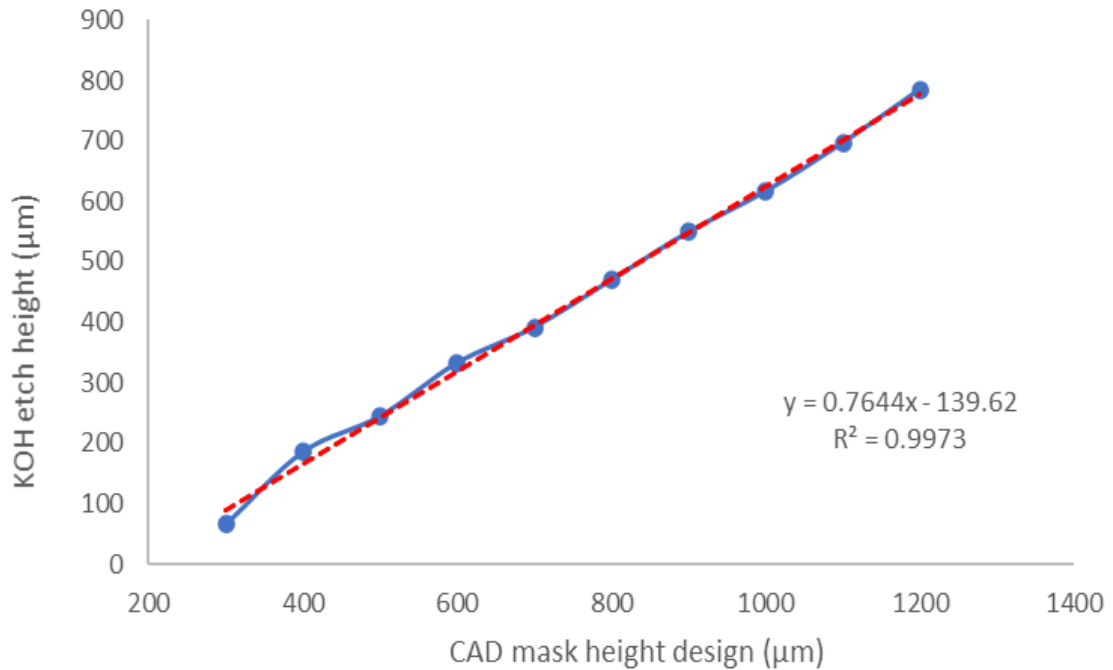


Figure 9.33 Relationship between CAD mask MN height design and final KOH etched height

9.9 Optimisation MN width

As previously described, the final width of the MN is related to the 54.7° (111) planes undercutting the mask. The width of the MN is a significant parameter and needs to be optimised; if the MN is too wide it will not penetrate through the skin. Conversely, if the MN is too thin it could fracture and break either through handling, upon insertion, or after insertion into skin. To prevent these issues, a MN width that has sufficient robustness to prevent breaking upon usage but is narrow enough to penetrate through the skin effectively, is essential. Additionally, the surface area of the MN is important for applications in drug delivery and diagnostics applications. For example, if a drug formulation is to be coated onto the MN surface, a larger surface area will enable a

greater drug dose to be coated on to the MN. While diagnostic MNs, using electrochemical detection, require a surface area large enough to produce a signal response [214].

In section 9.7.1 it was determined that the MN width increased, due to the new hexagonal shape, from a mask design of 300 μm to 540 μm after KOH etching. Thus, to validate how the etch fully affects the MN width parameters and how these parameters influence skin penetration, new masks were designed where either:

Design 1:

All MNs on an individual device array measured the same height but various widths. These included widths of 100, 200, 400, and 500 μm , respectively figure 9.34 A-D.

Design 2:

Each MNs on an individual device had a different design width, from 700-300 μm wide in descending 100 μm increments (Figure 9.34 E) or from 200, 100, 50, 25 μm wide, (figure 9.34 F).

All MNs were designed with a mask design starting height of 700 μm .

MN arrays were imaged using SEM after KOH etching (figure 9.35). Each MN width was measured using ImageJ software and the data tabulated in table 9.8 and plotted in figure 9.36. Figure 9.36 shows a linear regression analysis of the MN width data, which displays the direct correlation between the starting MN design width and the MN width after KOH etching.

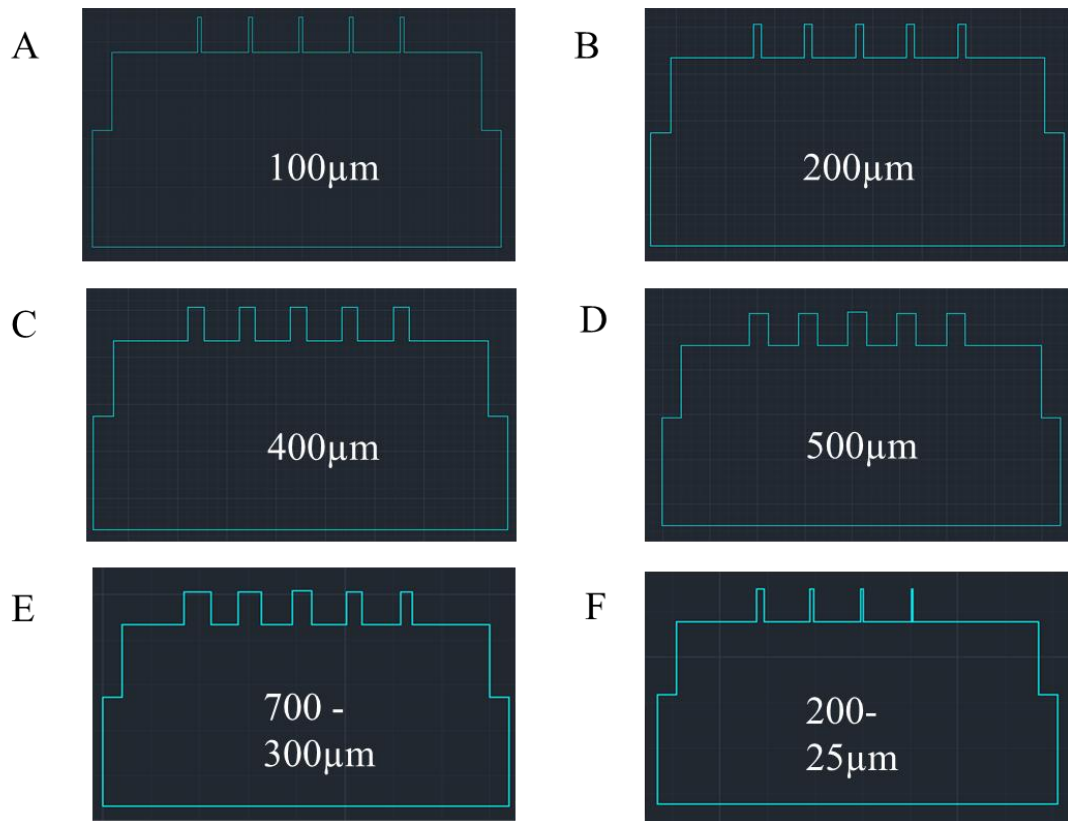


Figure 9.34 Solid KOH CAD mask designs of MN devices where the arrays are all the same widths (A) 100 μm , (B) 200 μm , (C) 300 μm , (D) 400 μm and MN devices where the arrays decrease either in 100 μm increments (E) 700-300 μm , or by half (F) 200-25 μm

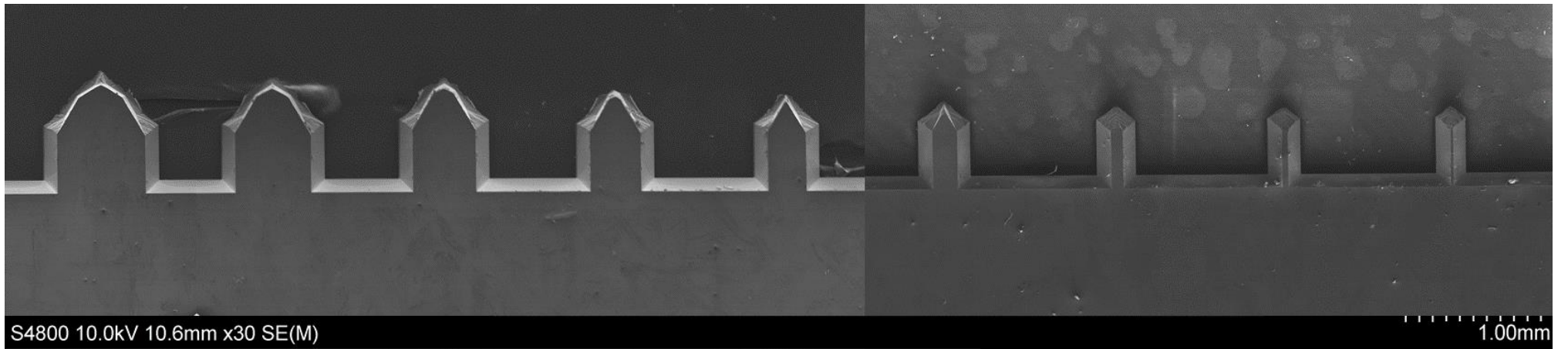


Figure 9.35 Solid KOH etched in plane MNs in descending width order from 700, 600, 500, 400, 300, 200, 100, 50, 25 μ m

Table 9.8 shows that the width of the KOH etched MN is on average $179\mu\text{m} \pm 18\mu\text{m}$ wider than the original mask design width.

Table 9.8 Comparison of KOH MN etch height in relation to starting mask design

MN CAD mask width design (μm)	KOH etched MN width (μm)	Difference between CAD design width and KOH etched width (μm)
700	865	165
600	757	157
500	665	165
400	586	184
300	460	160
200	378	178
100	297	197
50	252	202
25	225	200

To determine the precise width increase, plotting the data on a graph (figure 9.36) calculates a linear regression equation of $y = 0.9395x + 198.2$ and an R^2 value of 0.9981.

Using this equation, we can predict the dimensions required for the mask design to create a MN of a known width.

e.g., a MN of $350\mu\text{m}$ is required for testing. Inputting 350 into the above equations gives:

$$350 = 0.9395 * x - 198.2$$

Rearranged

$$x = (350 - -198.2) / 0.9395$$

$x = 161.6 \mu\text{m}$ Thus, a mask design where the MN width measures $161.6\mu\text{m}$ will produce a MN $350\mu\text{m}$ wide.

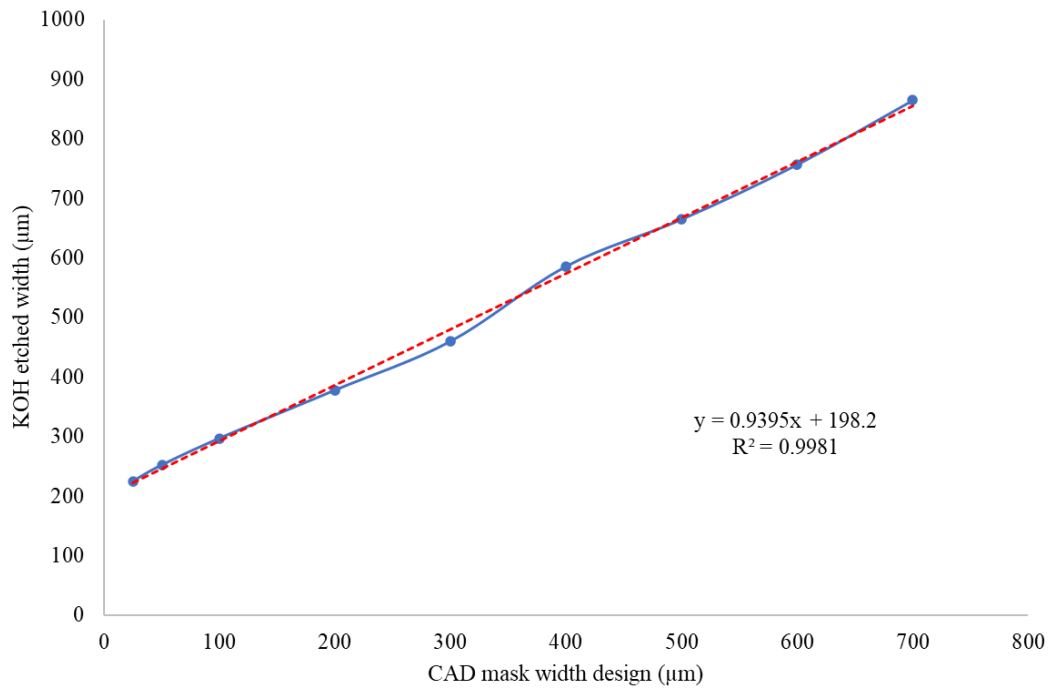


Figure 9.36 relationship between CAD mask MN height design and final KOH etched width

Closer observations of the MN tips in figure 9.38, demonstrate that as the MN width increased, the angle in which the (110) planes intersect in the (100) orientation, also increases. This is due to the consistent 54.7° etch angle, directing the (110) planes to intersect at the same point (represented as the star in figure 9.38). With different distances between the to (110) starting points (blue MN width outline), the angle in which the (100) planes (represented in red) intersect becomes larger, illustrated in figure 9.37.

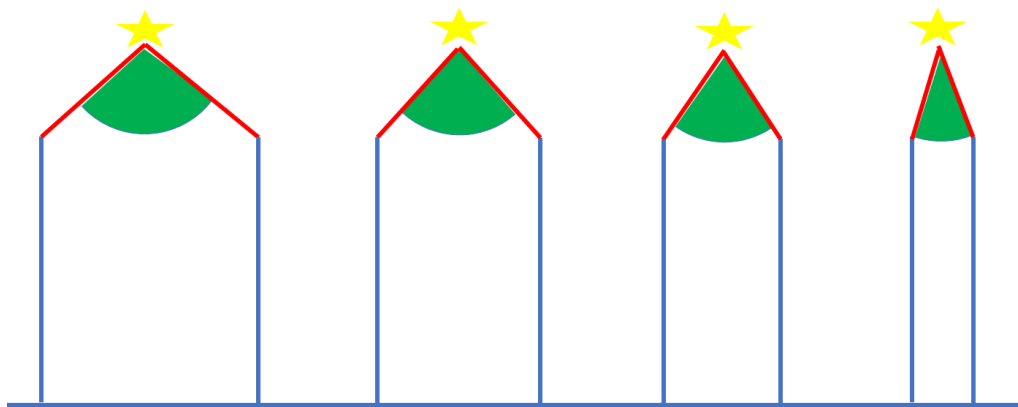


Figure 9.37 Schematic images of MNs with different mask widths (outlined in blue), demonstrating how the (110) planes (outlined in red) intersect to create the tip (yellow star) at different (100) orientated angles (green wedge)

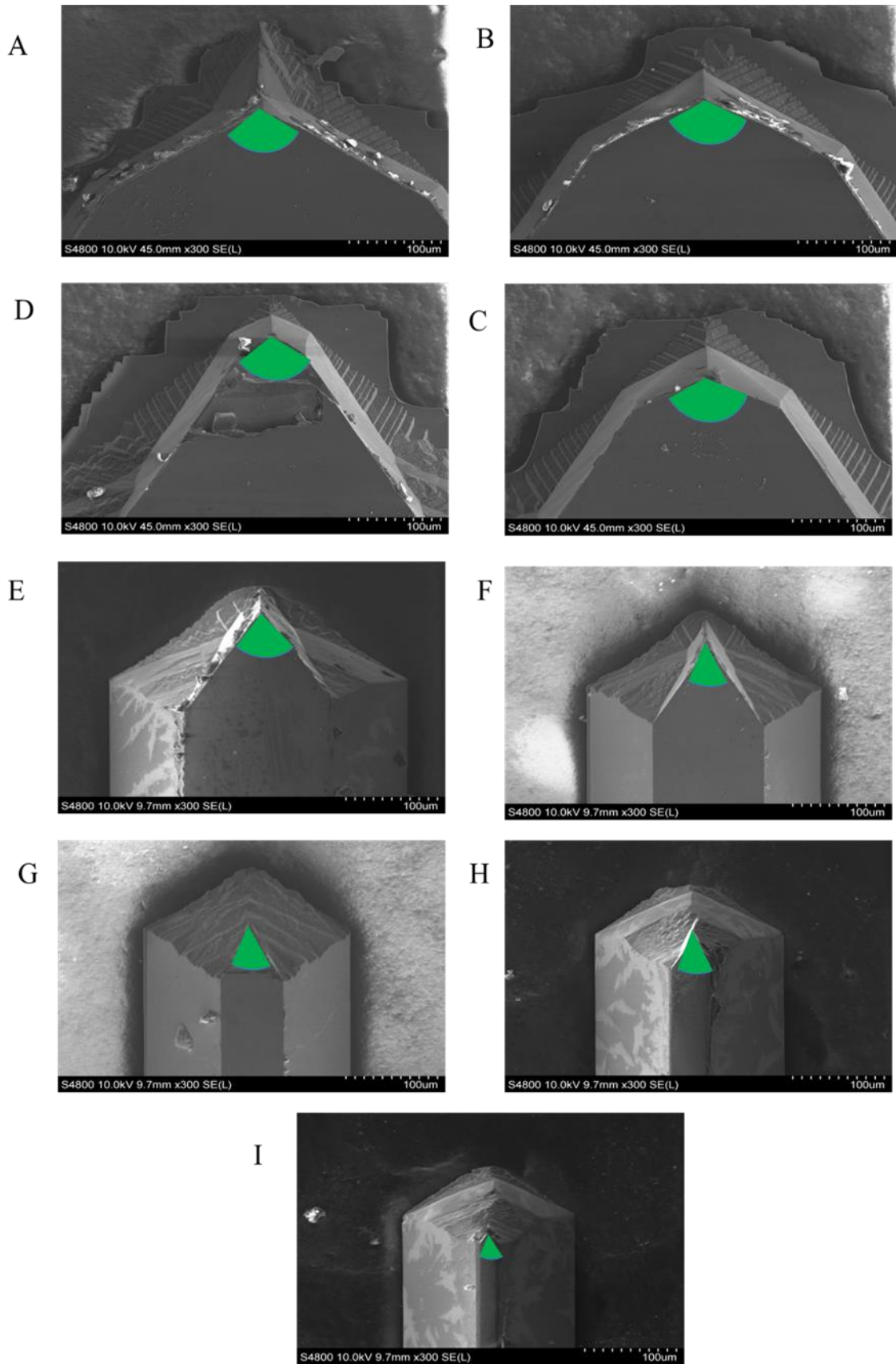


Figure 9.38 SEM images of MN tip angles, highlighted by green wedge, with varying MN width (A) 700 μm (B) 600 μm (C) 500 μm (D) 400 μm (E) 300 μm (F) 200 μm (G) 100 μm (H) 50 μm (I) 25 μm

The tip angle measurements are outlined in table 9.9; as the width of the MN increases from 25 to 100 μm the tip angle is almost constant 53-60°. In contrast, widths above 400 μm result in a larger angle of between 117-123°.

Table 9.9 analysis of tip angle with MN of increasing widths

MN CAD mask width design (μm)	KOH etched MN Angle (μm)
700	117
600	123
500	122
400	73
300	60
200	57
100	51
50	53
25	57

The explanation lies with the crystalline structure of silicon and how the (110) planes etch at 90° angles. Previously it was discussed that any 90° masked corners will etch to expose the (110) planes and consequently “round” the corner. However, it is observed at larger MN dimensions (>400 μm) the tip is no longer created from two intersecting (110) sides, illustrated by the red outline in figure 9.39A. Instead, the tip is created from several different (110) planes on each MN side, highlighted in green and blue in figure 9.39B. The schematic illustrations in figure 39C-F demonstrate how with increased width, the 90° corners expose more (110) planes that subsequently round the corner further and will eventually join to form a larger angled MN tip. The smaller width MNs do not form convex corners, as the widths are too thin to enable rounding to occur. Instead, as previously observed two (110) planes are formed which join to create the triangular shaped tip.

Consequently, MNs with larger widths will produce larger tipped MNs, which reduces the sharpness of the tip and thus, may not produce effective skin penetration in drug

delivery applications. Moreover, a blunt tip may cause pain on insertion. The study by Romgens, et.al recommended a tip diameter of $15\mu\text{m}$ for controlled penetration as larger tip diameters require a higher insertion forces to achieve skin penetration [215].

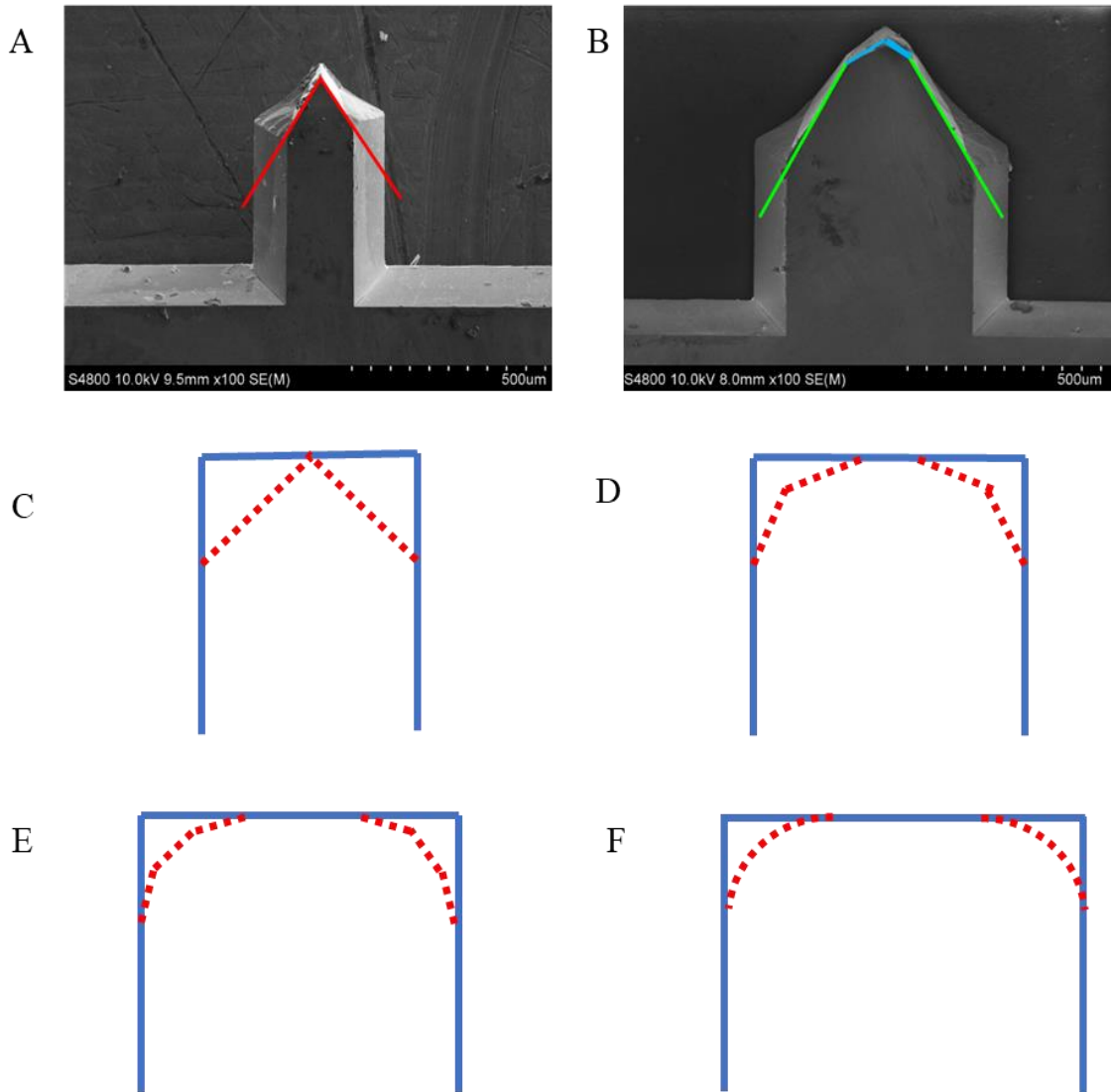


Figure 9.39 SEM images of MN showing how MN width influences tip angle (A) $200\mu\text{m}$ width, (B) $500\mu\text{m}$ width, (C-D) show schematic images of MNs with increasing widths (outlined in blue), and how the (110) planes (outlined in red) undercut the mask in a convex formation to create a curved corner on wider MN masks

9.10 Optimising MN pitch

Fabricating MNs of different widths emphasised the importance of pitch, i.e., the spacing between individual MNs. As the width of the needles increased, the spacing between each decreased, which could potentially influence penetration. If the MNs, regardless of width, are fabricated too close together then the force applied on insertion is distributed across the array, resulting in a potential inability to overcome the skin elasticity and thus an inability to penetrate the skin [216]. To focus the insertion force on each individual MN of the array and enable all MNs to penetrate the skin, the MNs need to be distributed further apart on the array. Published data about MN pitch design indicates that patch arrays can exhibit a bed of nails affect, where the insertion force is equally distributed over the arrays and prevents the MNs from effectively penetrating [217].

An advantage of fabricating the MNs in the in-plane orientation means they can be etched out in single line arrays, as opposed to a 2D patch type arrangement. Whilst this removes the bed of nails affect for an array, the distance between each MN on the single linear array still needs to be optimised. All previous MN production has been fabricated as 1 x 5 arrays with a pitch spacing of 1000 μm , however, as previously demonstrated, due to the 54.7° etch increasing the MN width by approximately 200 μm , the pitch distance is reduced.

To explore and validate the effect of the pitch on KOH etched in-plane MNs, 5 masks were designed where each MN remained the same height and width but the distance between each MN increased from 500, 1200, 1400, 1700 and 2300 μm (figure 9.40). After KOH etching the MN pitches reduced to 297, 1019, 1238, 1521 and 2086 μm , respectively.

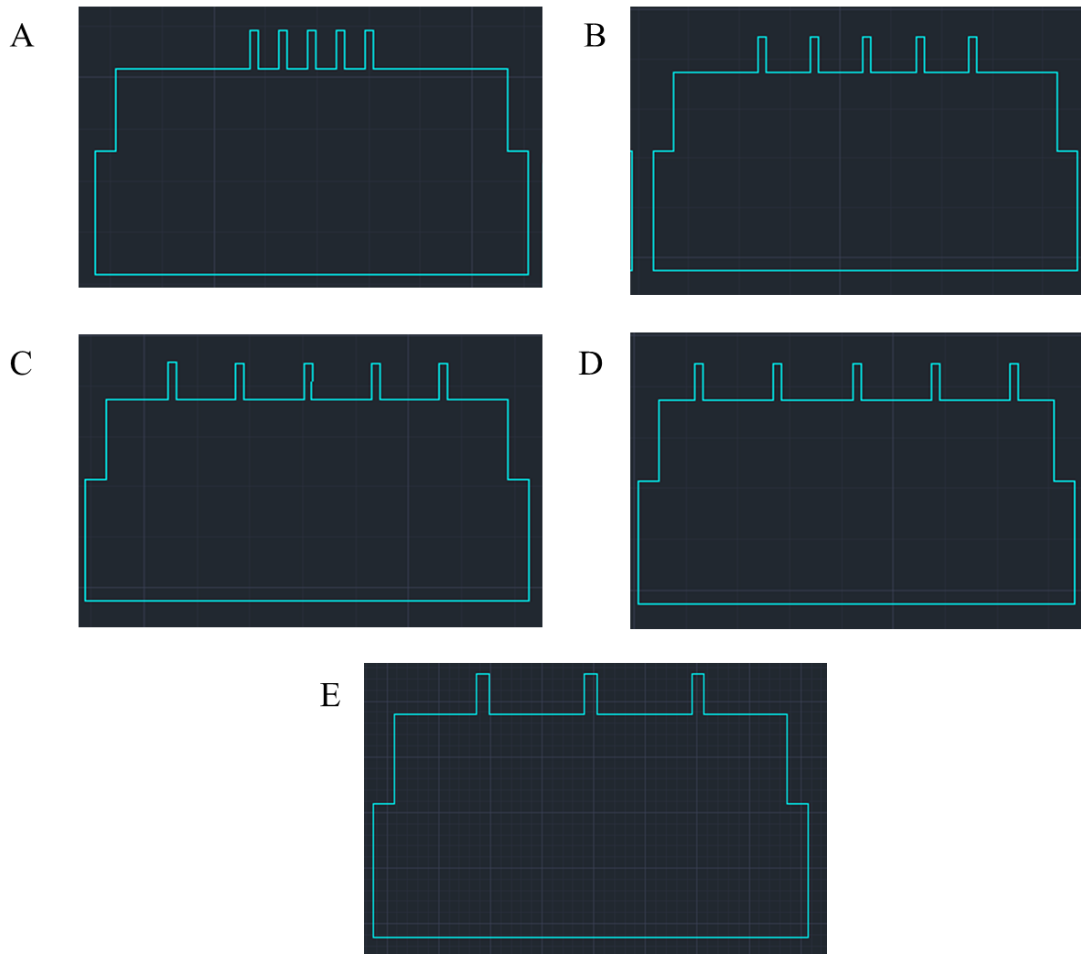


Figure 9.40 CAD design of MN devices, where the MN pitch spacing varied (A) 500 μm , (B) 1200 μm , (C) 1400 μm , (D) 1700 μm (E) 2300 μm .

9.11 Conclusion

The focus of this chapter was to fabricate the first in-plane solid MNs from simultaneous front and reverse etching of a silicon wafer in KOH, utilising the (111), (110) and (100) planes to etch the silicon at a 54.7° angle and create a tip. It was demonstrated that different aspect ratio MNs can be fabricated to create a hexagonal shaped shaft where the tip is constructed from a “flat” mask design to formulate 6 silicon planes that come together in a pyramidal arrangement. As the whole wafer is submerged in KOH the devices etch out completely in a single etch step. The optimisation of this etch led to MN arrays where the design of the MN can be easily adapted by a simple change of the mask. MNs of various height, widths and pitch can be fabricated either on separate arrays or on the same array for different applications and for maintaining uniform penetration over body contours.

Using KOH as the etchant simplifies the MN fabrication process by reducing the number of process steps required, which means that the MN can be fabricated and ready for use in the same day. The process is scalable and can be performed with reduced infrastructure costs.

The next chapter will focus on utilising the wet etch process to fabricate hollow MNs from modified CAD designs. These designs can then be used to deliver increased drug dosages or for diagnostic wicking.

Chapter 10

Fabrication of hollow in-plane MN

10.1 Introduction

Injections using a hypodermic needle can rapidly deliver large doses of drugs into the body, however, penetration through the skin stimulates pain and requires trained personnel to administer the medication [212]. As an alternative hollow MN's can provide painless injection and produce sustainable and adaptable delivery rates, that when compared to other MN types such as coated drug delivery, the hollow MN's enable larger drug dosages to be delivered [218]. Additionally, the hollow bore can also serve as a sampling port for point of care diagnostic / monitoring systems.

In 1993 at the 7th international conference on solid-state sensors and actuators, the first concept of hollow microhypodermic needles were demonstrated by L. Lin and A. Pisano et. al [219] and who later published their paper in 1999 [220]. The needles were fabricated from a silicon substrate encased in a silicon nitride shell; HF wet etching and DRIE plasma etching processes were used to fabricate a fully enclosed channel for the transport of liquids or gases (figure 10.1). Furthermore, electrodes could be directly patterned along the length of the needle or connected to an integrated electronic and/or fluidic chip for diagnostic measurements. Although the needles produced were in the in-plane orientation, the needles were not minimally invasive due to fabrication lengths of 1-6mm, with the fluid channels only occupying a small interior volume. This resulted in a small fluid carrying capacity, only capable of delivering at a low fluid injection rate of $<0.1\mu\text{l}/\text{sec}$, which, unfortunately, is insufficient for many therapeutic injections, such as insulin, which require large volumes such as 0.3ml, 0.5 or 1ml to be injected quickly [221].

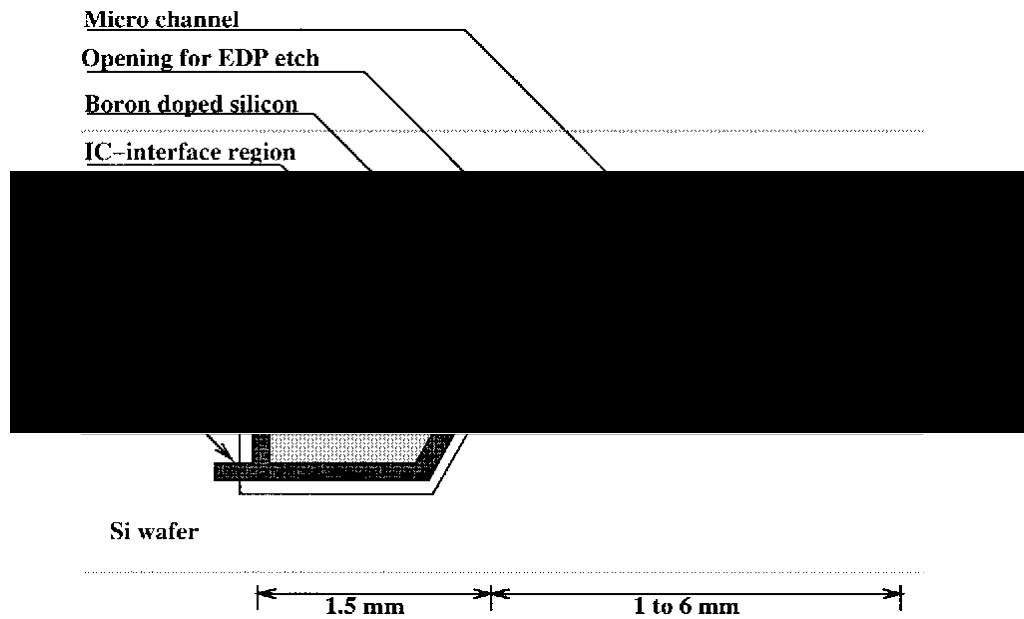


Figure 10.1 Schematic image of first hollow MN demonstrated by L. Lin and A. Pisano et. al

Similar MN designs were fabricated by Brazzle et. al [222] using metal micromachined processes on the surface of a silicon substrate. Their studies showed shorter MNs had advantages over previous forms of MN such as, precise control of penetration depth, reduced trauma at the penetration site, greater freedom of patient movement and practically pain free drug delivery. Additionally, fabricating MN arrays in the in-plane orientation enabled the array density to be altered by stacking the MNs into an adaptor. Here, the combined fluid volume capabilities of 625 MNs (25 x 25 array) were comparable to that of a hypodermic needle.

Another, but different shaped in-plane silicon MN device was developed by Oka et al., [223] to collect trace amounts of blood by mimicking the shape of a mosquito proboscis with a highly jagged edge (figure 10.2A). The steps required to process the jagged edge rely on the formation of the (111) planes of silicon by anisotropic etching, using a mask that varies in pattern size figure 10.2B).

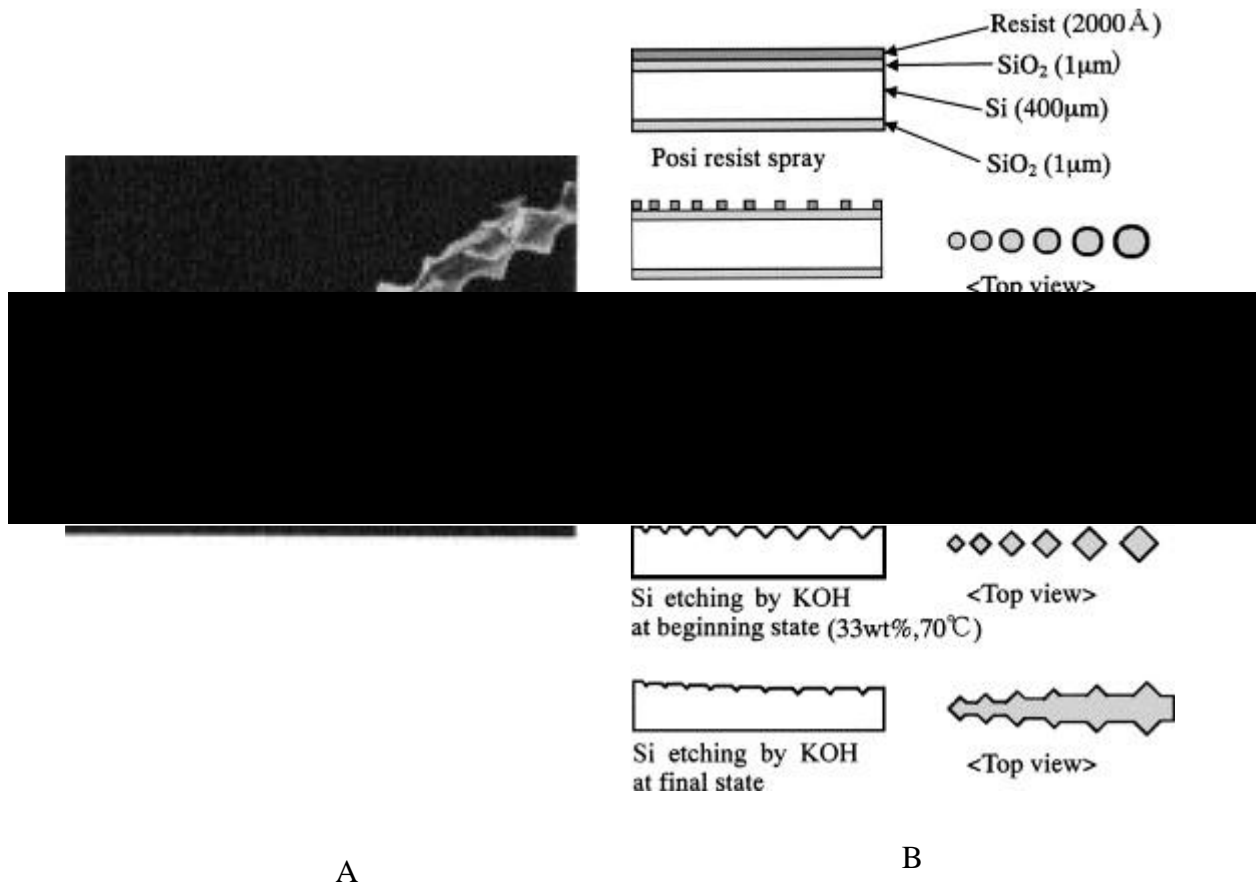


Figure 10.2 (A) SEM images of jagged silicon MN created from (111) plane etching (B) different mask designs used to etch silicon MN

Paik et al, [121] published a method of processing in-plane hollow silicon MNs that included a buried channel within the silicon substrate and along the MN shaft. Instead of using several different substrate designs, as previously seen with those designed by Lin, Brazzle and Oka etc., Paik used a combination of anisotropic dry etching, sidewall passivation, isotropic dry etching, and trench refilling with polysilicon as the main components figure 10.3.

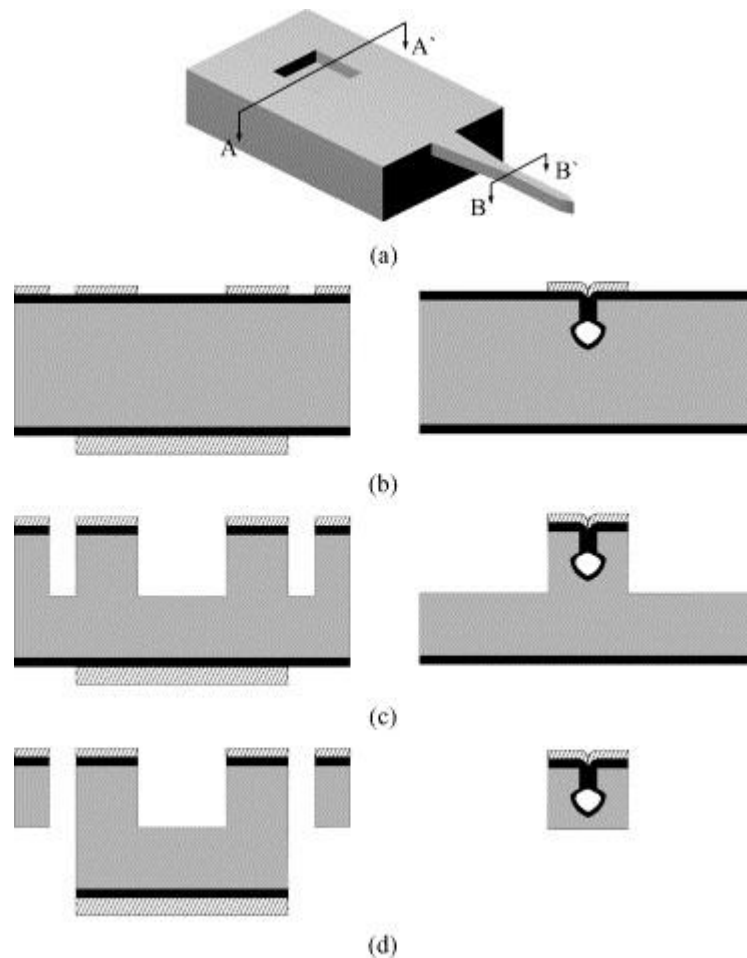


Figure 10.3 Schematic diagram of a microneedle and its process flow for the cross-section A–A (left figures) and B–B (right figures). (a) diagram of a MN; (b) silicon dioxide deposition and patterning on both sides of a wafer; (c) deep silicon etch on the front side of the wafer; (d) deep silicon etch on the back side of the wafer

It is clear that to produce an in-plane MN with a hollow channel presents a more challenging, multi-step fabrication method than that of a solid MN fabrication. Chapter 9.7 demonstrated the fabrication of a solid in-plane KOH etch MN, with simple cost-effective photolithography steps that utilise the advantages of the in-plane fabrication methods. These MN's can be further optimised to incorporate an open or closed bore through the shaft of the MN to enable delivery and/or analyte sampling, with a few relatively simple additional process steps.

10.2 KOH MN channel etch optimisation

Chapters 9.7 – 9.10 discussed the optimisation process to fabricate multiple in-plane solid MNs from a single KOH etch. Using the same process, but with a modified mask that incorporates a channel along the MN shaft and through the device, a hollow in-plane KOH MN can also be created from the same single etch step (figure 10.4).

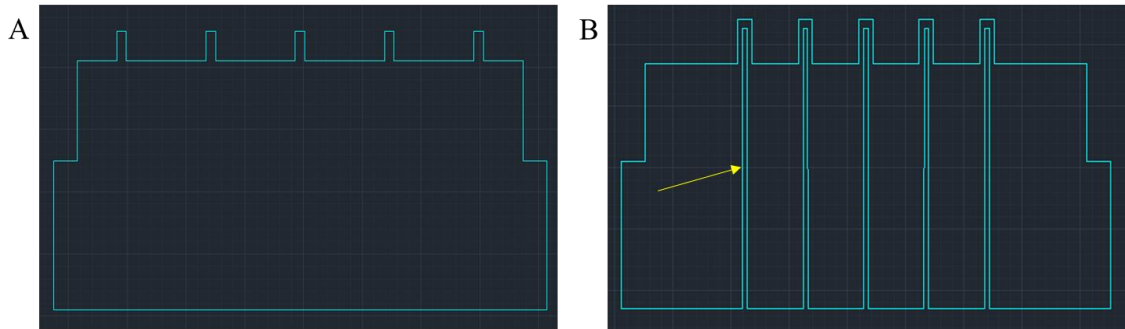


Figure 10.4 AutoCAD designs of solid in-plane MN and (B) Hollow in-plane MN, hollow channel (yellow arrow)

The previous chapters demonstrated how the MN tip and shaft side walls were created from the 54.7° KOH etch angle, etching in the convex formation. However, the new mask design incorporates a channel that runs centrally along the MN shaft. This channel will not be photolithography coated with resist, instead leaving it open and available for KOH silicon etching. This opening allows the KOH to etch at the 54.7° angle, however rather than a convex sidewall be produced, the side walls will etch inwards or concaved to form the a groove for the channel, figure 10.5 [224].

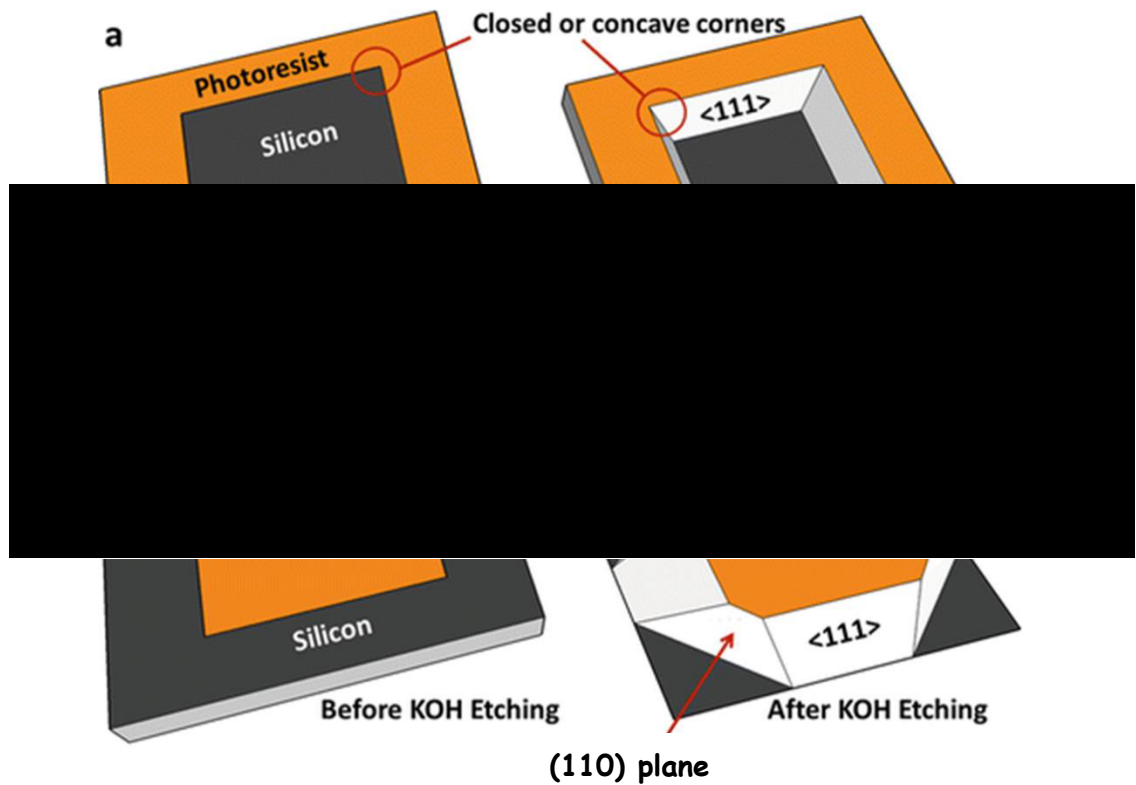


Figure 10.5 Schematic diagram showing the characteristics of KOH etching corners when (a) the etch is concaved and (b) the etch is convex

In order for the concave side walls to etch deep enough into the silicon and create a channel that can retain solution, the width of the channel mask design needs to be optimised so that during the etch time of the MN fabrication, the channel simultaneously etches to the correct depth from a single KOH etch. The red and yellow lines in figure 10.6 highlight the importance of hollow channel width and the subsequent shape of the channel created. The diagram shows that for the same etching time, if the width of the channel is designed thinner, the subsequent (111) planes would etch into an intersected V shaped groove (10.3a), while the (111) planes of a wider channel would not intersect and instead produce a channel with a flat (100) plane base to form a trapezoidal shaped groove. If this etch time were to continue, eventually the (111) planes would intersect to create a larger volumed V shaped groove to that of the thinner mask design. The shape of the channel is important in terms of the injection rate, pressure, and volume. For larger channels, a larger volume can be delivered faster with a lower pressure build up, which could cause pain or blockage during injection into the skin.

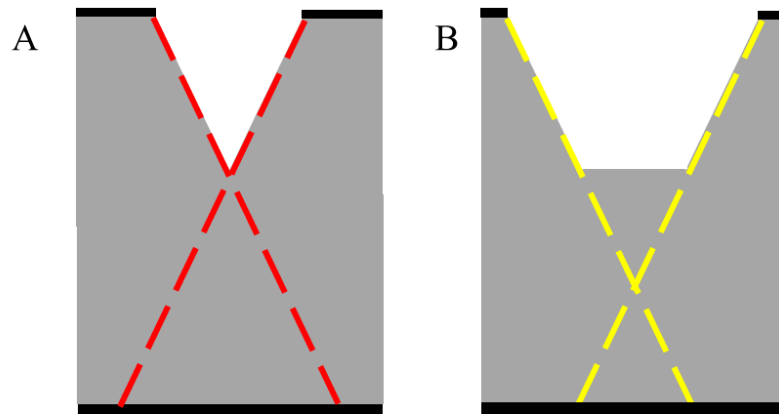


Figure 10.6 Schematic diagram of hollow channel etched in KOH etch, the shape of the channel is controlled by the width of the photolithography mask design (A) thinner resulting in triangular channels (B) wider mask designs producing trapezoid shaped channels. The red and yellow lines demonstrate how the fixed 54.7° side walls would etch.

Understanding the etch mechanics enables the channel shape to be predicted before any etching takes place. Using simple trigonometry, the width of the mask channel required for a maximum channel depth of 150µm (half the thickness of the wafer) can be calculated (figure 10.7). For instance, KOH etches at an angle of 54.7° and we need a depth of 150µm represented by line C in figure 10.4. Therefore, the length of the “adjacent” side of the triangle, represented by B can be calculate using equation:

$$\tan \vartheta = \text{opposite} \div \text{adjacent}.$$

$$\text{This gives: } \tan 54.7^\circ = B / 150\mu\text{m}$$

$$\text{Rearranged to find } B = \tan 54.7^\circ * 150\mu\text{m}$$

$$B = 106\mu\text{m}.$$

As B is half the length of the channel width then the full mask channel width A is 212µm. The two (111) sides thus meet, with an angle of 70°, to creates a V shaped groove. Channel design widths larger than 212µm would not intersect at an etch depth of 150µm, leaving the base of the channel flat as illustrated in figure 10.7B. A width smaller than 212µm would produce a shallower V shaped channel.

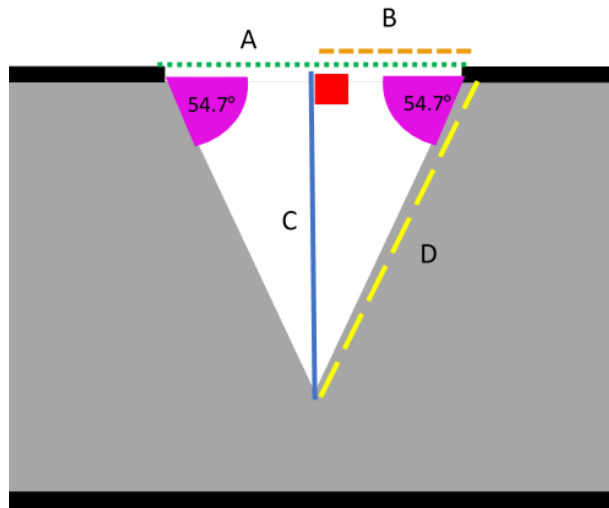


Figure 10.7 Schematic diagram of KOH etched channel with the rules of trigonometry applied to calculate etch characteristics

10.3 Hollow MN tip optimisation

A series of MNs with different channel designs, created using autoCAD, have been fabricated. All MN's measured $900\mu\text{m}$ in height and $300\mu\text{m}$ in width and were photolithography patterned either on a single wafer side, or both wafer sides, using the previously optimised KOH wet etch method described in chapter 9.7. Figure 10.8A shows a MN mask design with a channel measuring $100\mu\text{m}$ wide and the “gap size” or distance from the top of the MN design to where the channel starts, measures $200\mu\text{m}$, the gap is shown by the arrows.

Chapter 9.8 demonstrated that when creating the MN tip, the height of the shaft will reduce by approximately $200\mu\text{m}$, therefore, the MN channel will be designed to start at $200\mu\text{m}$ from the top to allow the tip to form around the channel without interference. The width of the channel was selected to produce a smaller V shaped channel at one third of the width of the whole MN. As the channel etches out a significant proportion of the shaft, concerns were raised about the strength of the MN structure to withstand pressure on insertion. To review the MN strength, the second MN in figure 10.8B had a larger channel width of $200\mu\text{m}$ with a $200\mu\text{m}$ gap from the top. Widening the channel to two thirds of the MN width should produce a deeper etched V shaped channel that removes more of the shaft structure; however, a larger channel would accommodate a larger delivery volume and faster flow rates. The final channel shown in figure 10.8C

measures $100\mu\text{m}$ wide with a $100\mu\text{m}$ gap; $100\mu\text{m}$ from the top was selected to visualise how the KOH tip etch and the channel etch interact, as one etch is in the concaved orientation and the other in the convex.

To connect the channels to the syringe and enable solutions to be pumped through, the channels are patterned along the whole length of the device, with the ends left open to act as injection inlets.

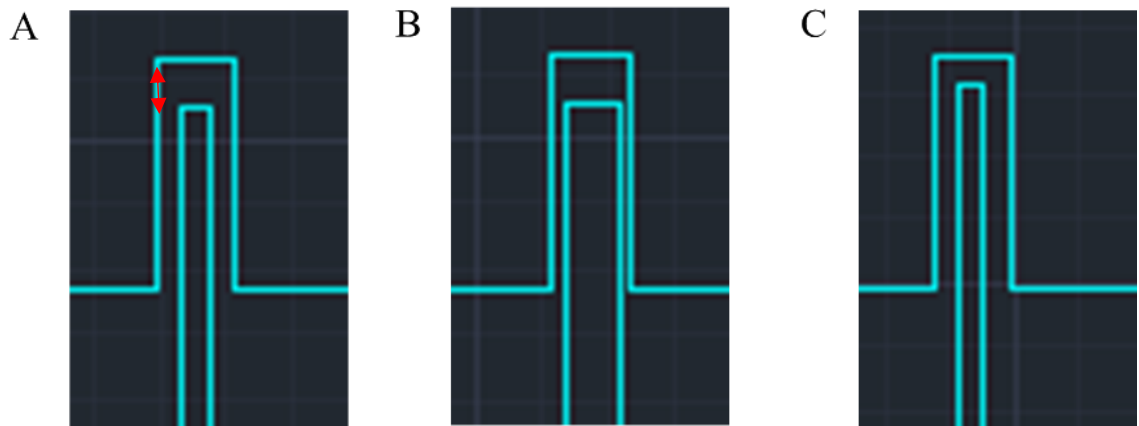


Figure 10.8 autoCAD designs of hollow KOH MNs where the channel measures (A) $100\mu\text{m}$ wide and $200\mu\text{m}$ form the MN top (B) $200\mu\text{m}$ wide and $200\mu\text{m}$ form the MN top (C) $100\mu\text{m}$ wide and $100\mu\text{m}$ form the MN top. (D) demonstrates a whole MN device

Post KOH etching, the MN tip was analysed using SEM to verify its formation. Figure 10.8 reveals that a MN channel with a $200\mu\text{m}$ gap from the top of the mask design was not affected by the subsequent (110) tip etch, and therefore both features have etched independently. The gap between the designs was protected by a SiO_2 mask and thus was not etched away from the formation of the tip (110) convex planes or the concave (111) channel etch. However, protection has resulted in a block structure forming between the channel and the tip, highlighted by the red arrow in figure 10.6B. Here the flow of solutions through the channel would be affected by the abrupt stop wall and create difficulties delivering liquids into the skin. As the skin is composed of dense tissue any blockage preventing the flow of fluid could result in a build-up of pressure causing the fluid to leak out of the skin. While, on the other hand, reducing the flow rate could enable more time for the fluids to diffuse into the skin tissue.

Decreasing the gap between the channel design and the top of the MN design to $100\mu\text{m}$ saw the convex (110) tip and the concaved (111) planes merge to form a single connecting MN channel and tip, figures 10.9 C-D. This new combination produced an unobstructed free-flowing channel that can direct the solution right through to the MN tip.

Simultaneous etching has enabled both the tip and channel designs to merge without detrimentally influencing each other's function, i.e., the sharpness of the tip is preserved whilst the channel can direct the solutions through the MN tip. Previous literature reviews have discussed that in order to create a sharp tip on a hollow MN to prevent tip blunting and clogging then the bore must be designed separately on the side of the MN [194]. As the hollow channel is etched open along the MN shaft this prevents clogging problems seen with closed bores [225]. From these results, optimised future hollow MN autoCAD masks will be designed with the MN channel $100\mu\text{m}$ from the top of the MN mask.

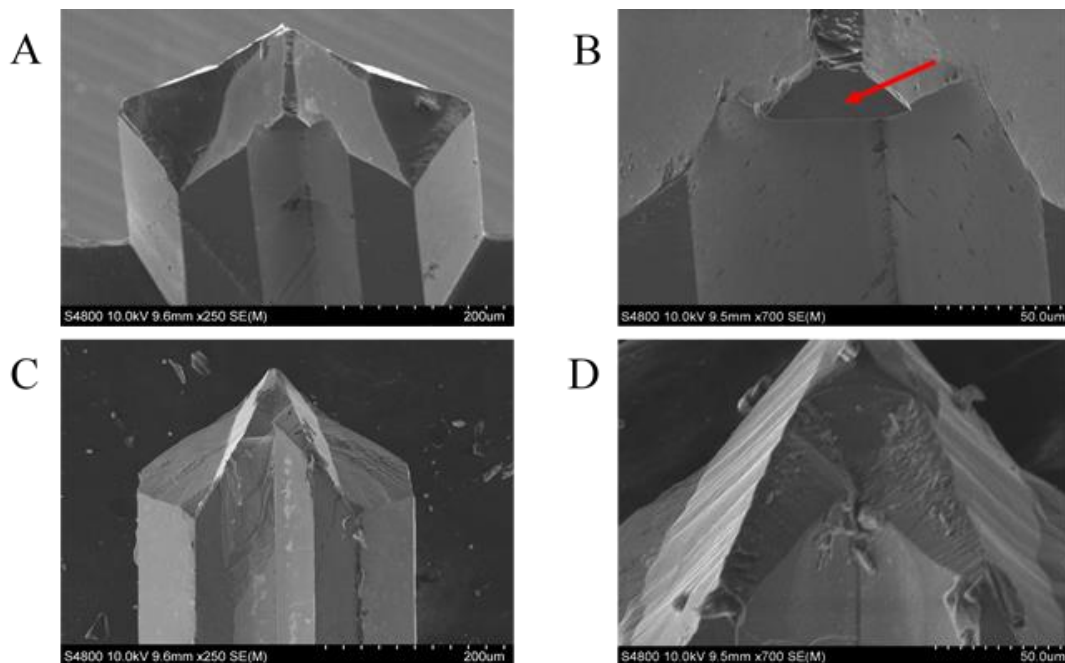


Figure 10.9 SEM analysis of KOH Hollow MN where the hollow channel is design (A-B) $200\mu\text{m}$ from the top edge and (C-D) $100\mu\text{m}$ from the top edge. The red arrow in (B) demonstrates where the KOH has not etched between the channel and MN tip forming a wall.

10.4 Hollow MN channel optimisation

Shifting the focus to the shape of the etched channel, figures 10.10 A-B demonstrate that a MN mask channel design width of $200\mu\text{m}$ created an etched channel width of $231\mu\text{m}$ and depth of $67\mu\text{m}$ along the shaft of the MN, in a trapezoid shape.

In comparison the $100\mu\text{m}$ mask design in figures 10.10 C-D, shows a channel measuring $134\mu\text{m}$ wide and $88\mu\text{m}$ deep along the whole length of the MN shaft and into the device. This time the (111) side walls intersect to create a V shaped channel.

Overall, both channels have etched wider than their starting mask designs, with the $200\mu\text{m}$ mask etching shallower than expected.

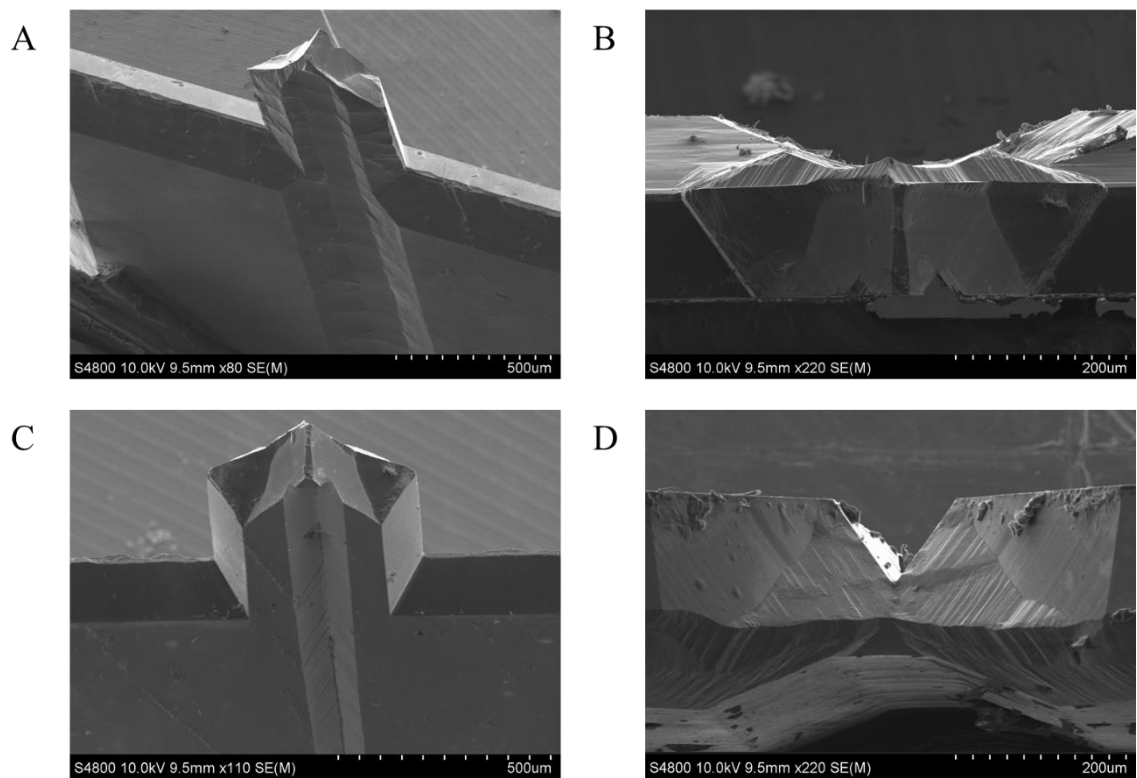


Figure 10.10 SEM images of hollow microneedle channel with a starting mask of (A-B) $200\mu\text{m}$ (C-D) $100\mu\text{m}$. (B) and (D) are orientated to view down the channel and examine the KOH etched shape

Previous calculations demonstrated that to etch a depth of 150 μm , a mask design of 216 μm would be suitable, however, a design of 200 μm only etched 67 μm deep. This difference is explained by the way the etch progresses for different size etch windows. Figure 10.11 illustrates a series of etching steps undertaken by the KOH. Figure 10.11A shows that the etch begins by etching in both the vertical (100) and (111) planes, to undercut the mask design and produce 54.7° side walls that connect to a (100) flat base creating a trapezoid shape. Figure 10.11B, shows that next, the (111) side walls continue to expand, further undercutting the mask while simultaneously etching deeper in the (100) plane; the red dotted line outlines the previous etch shape. Figure 10.11C demonstrates that further etching deepens the V shape into the wafer, whilst retaining the 54.7° wall angle. In figure 10.11D the 54.7° (111) side walls are etched deep enough to intersect and produce a V shape channel.

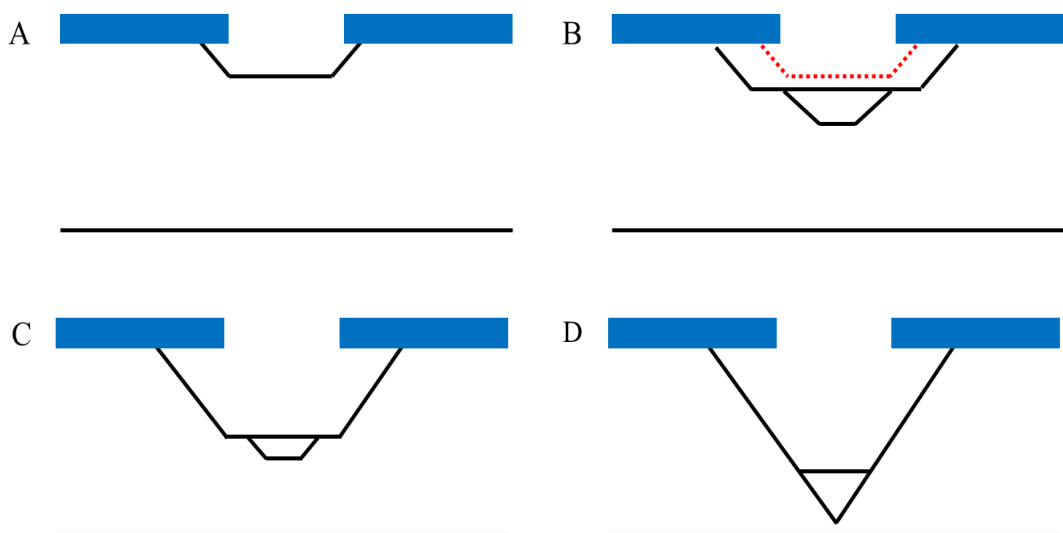


Figure 10.11 Schematic diagram of KOH etching of silicon with a larger channel. Resist illustrated in (blue). (A) shows the beginning of the 54.7° degree (111) side walls and simultaneous (100) etch. (B) further etching shows expansion in both the (111) and 100) planes, the red dashed line depicts where the previous etch lies to illustrate the difference. (C) continuation of etch deeper into the silicon (D) completion of etch to form a V shaped groove.

Designing a mask channel width of 100 μm exposes a smaller opening to the KOH etchant, as illustrated in figure 10.12. The etch process follows the same etching steps as in figure 10.11; the etch begins by under cutting the mask in the (111) planes while simultaneously etching in the (100) plane. However, the smaller undercut created means

the (111) side walls are closer together, meaning they come together to form a V shaped channel sooner (figures 10.12C), and not as deep into the silicon as seen with the wider opening.

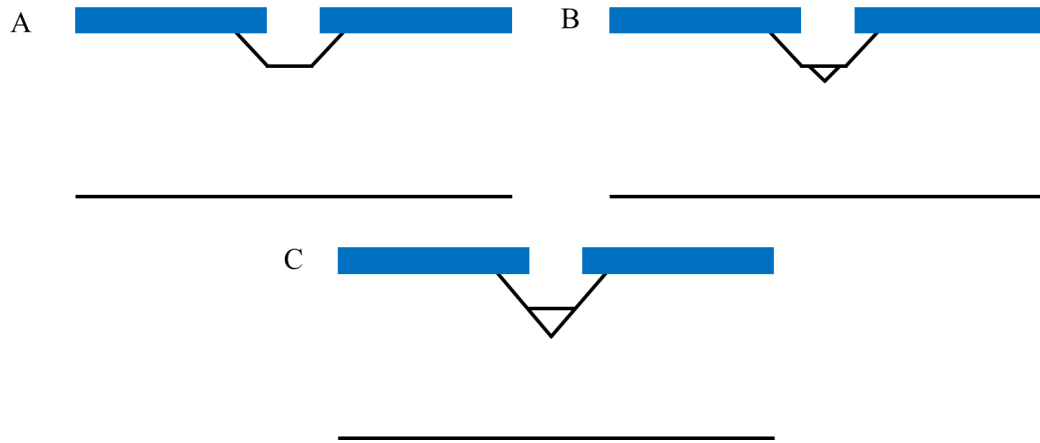


Figure 10.12 Schematic diagram of KOH etching of silicon with a smaller width channel (A) start of etch creating 54.7° (111) side walls undercutting the mask (B) continuation of etch vertically deeper into the silicon (C) final V shaped channel created from 54.7° (111) side walls

These results demonstrate that changing the width of the channel opening, limits how much silicon is exposed to the KOH and thus controls the etch rate and the resulting channel shape. A wider channel opening enables more KOH ions to enter the open area, react with the silicon and form etch products that are removed quickly by the solution, figure 10.13A. Additionally, as the surface area of the two (111) side walls is larger than the (100) flat plane, more silicon in the (111) axis is exposed to the KOH for etching. Thus, the (111) planes etch quicker than the (100) planes, resulting in the channel widening faster than becoming deeper, to form a shallow and wide trapezoid shape.

A smaller channel opening, such as, the 100 μm channel, does not expose as much silicon to the KOH for etching, figure 10.13B. This means fewer KOH ions can react with the silicon and the etch particles cannot be removed as easily, consequently reducing the reaction rate [226], [227]. The slower rate and the lower surface area simultaneously reduces the degree of mask undercutting, explaining why the 100 μm channel only increased by 34 μm , while the 200 μm channel increased by 228 μm .

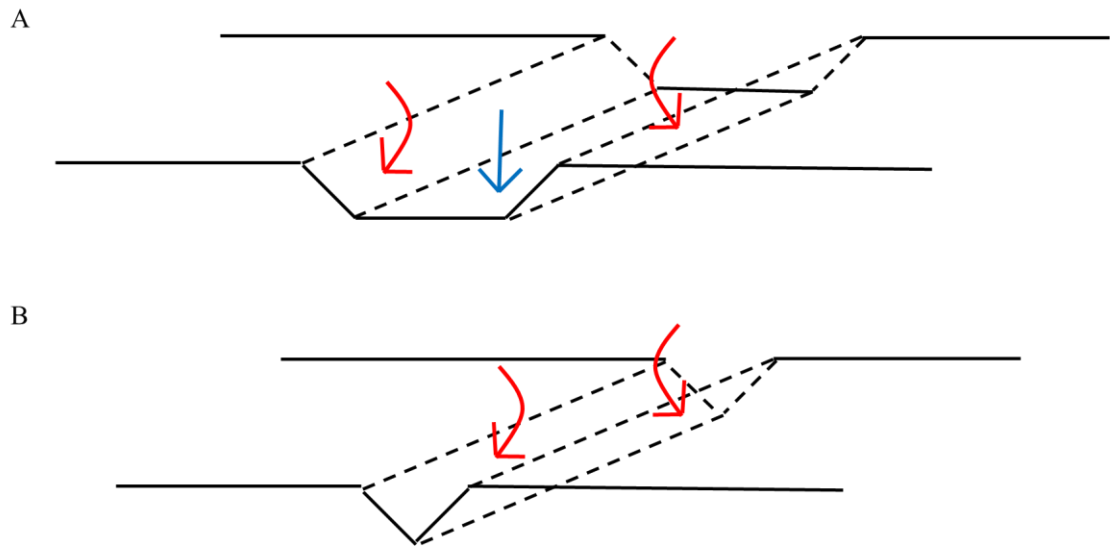


Figure 10.13 Schematic diagram of the influence of surface area on KOH etching of silicon with (A) larger channels or (B) smaller channels. Red arrows show (111) plane etching while blue arrows show (100) plane etching. The larger channel in (A) shows that a larger surface area is available for etching compared to (B).

The CAD mask design in figure 10.4 shows that the hollow channels are designed along the full length of the device but do not close at the end, instead connect with the perimeter design on the device to create two 90° angles. This opening allows the fluids to be directed along the channel to the MN tip.

Due to the “rounding” of 90° corners during KOH etching, the openings at the base of the device have also etched to expose two (110) planes (highlighted in red and yellow in figure 10.14 B) and rounded into a convex funnel shape, figure 10.14A-C. This shape could be beneficial as it can act as a guide-to-guide fluids into the channels and through the MNs.

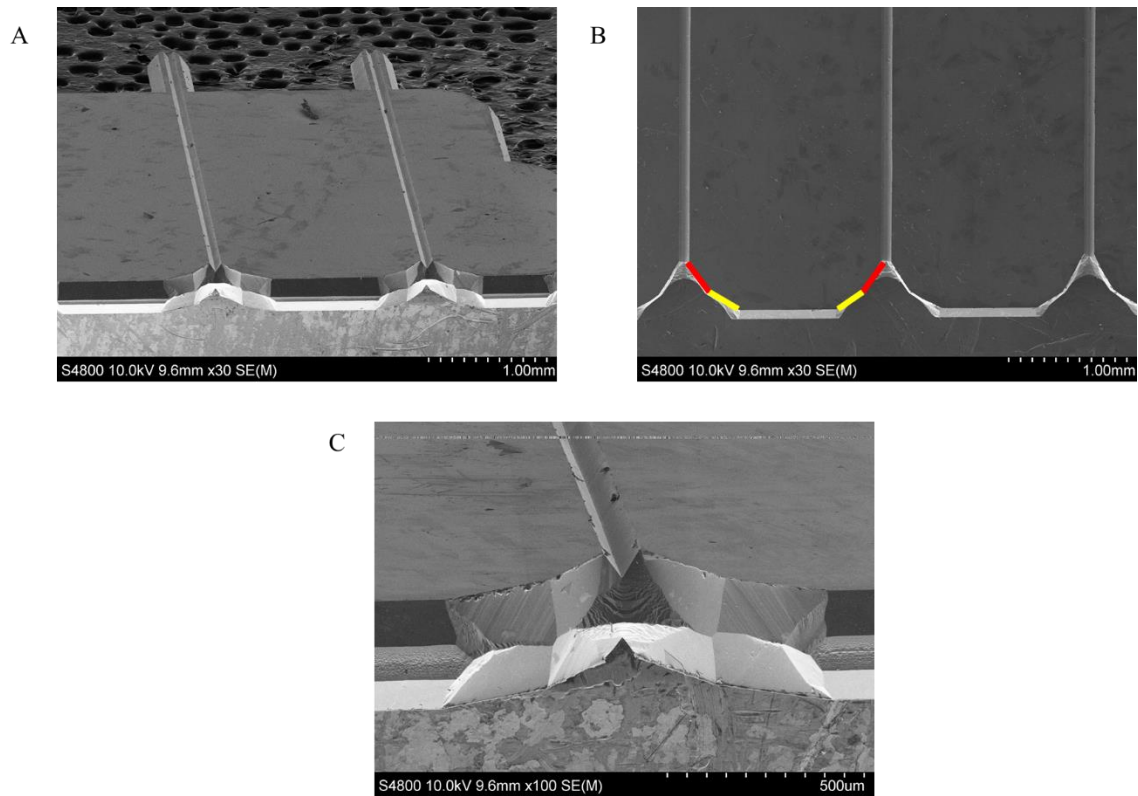


Figure 10.14 SEM images of the end of the MN device demonstrating (110) etched planes creating a funnel at the 90° corners (A) whole device view (V) top-down (10) plane view, yellow and red illustrate the two (110) planes rounding the corners (C) magnification on the (110) etch planes

MN devices can be fabricated with either one side (figure 10.15A) of the device with a hollow channel, or both sides (figure 10.15B). Where only one side is patterned, the corresponding reverse alignment mask would not include channels. A two-sided hollow MN allows double the volume of fluid to be delivered at the same rate. To incorporate two channels additional silicon is removed from the shaft of the MN and the main structure of the device, consequently, mechanically weakening the MN in these areas. This weakness was observed upon handling of the devices, as the devices were easily snapped upon bonding of the MN to the adaptor. Therefore, until an optimised precise handling procedure is developed, all future hollow MNs have been fabricated as single sided hollow channels to maintain stability.

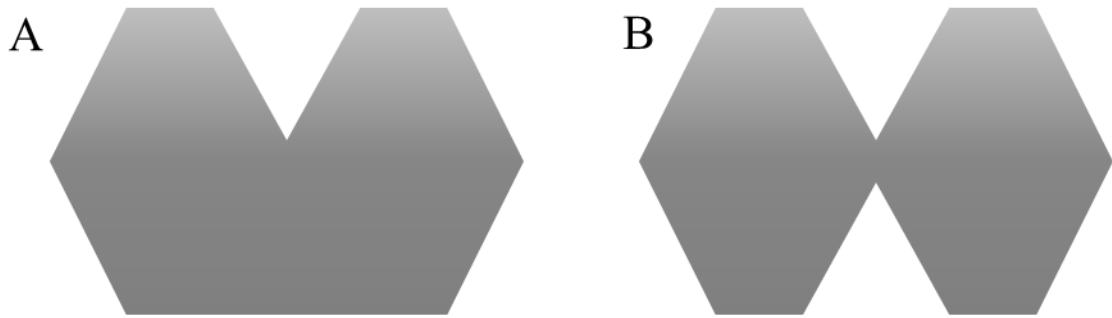


Figure 10.15 Schematic diagrams of MN cross section demonstrating (A) a single hollow MN (B) A double hollow MN

10.5 Fabricating a closed hollow channel

So far, all hollow MNs have been fabricated with open channels extending down the shaft of the MN. However, to improve the transdermal fluid transport efficacy and control the fluid direction, the channels can be sealed. To seal the channel and fabricate a MN with a closed hollow bore there are two main methods, either:

1. A piece of silicon cut to the dimensions of MN device can be bonded to the base of MN device, without hindering the MN, figure 10.16 A and C.
2. Two MN devices can be aligned together to create a double tipped MN with the bore encapsulated between them, figure 10.16 B and D.

Each channel type is examined in chapter 16 to verify that whilst a closed channel improves directional injection and prevent any leakage, could a double tip be too thick to penetrate through the skin? or could the skin become wedged between the tips to clog the bore?

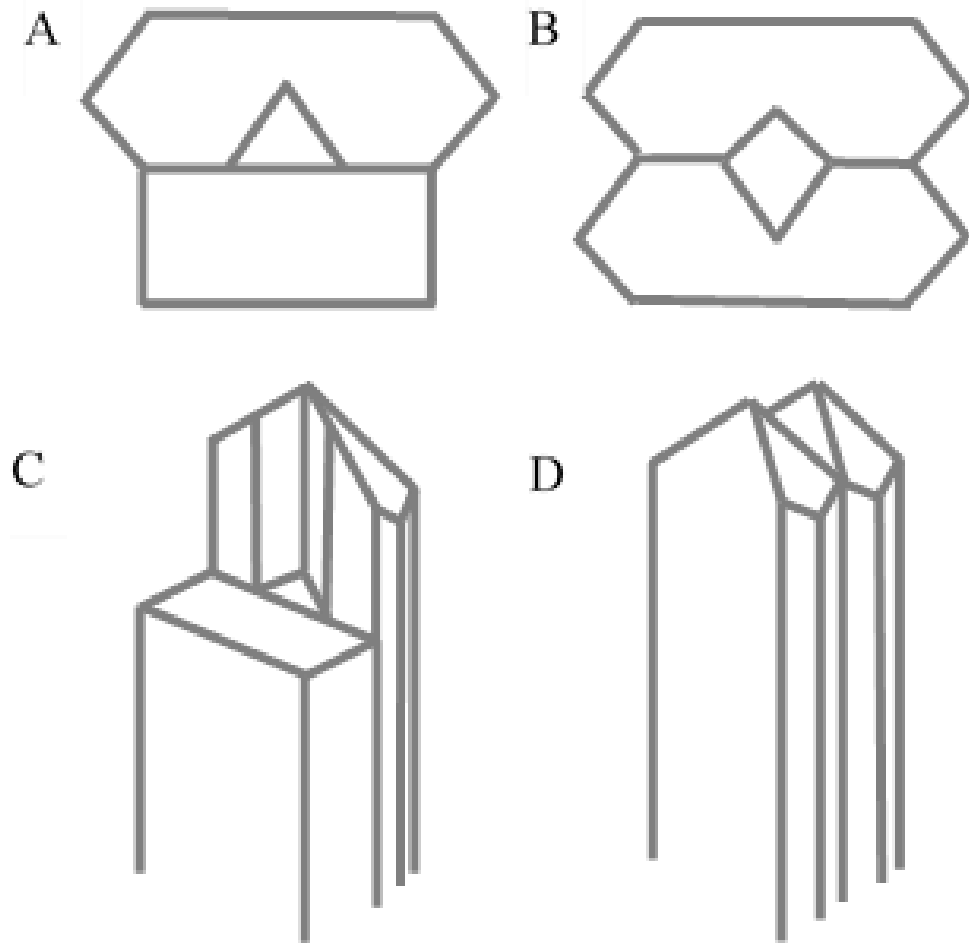


Figure 10.16 Schematic diagrams of closed channel MN ideas (A) cross section of a MN bonded to a piece of silicon creating a single closed channel (B) cross section of two MN devices forming a larger channel (C) view of MN showing the piece of silicon would not form a closed channel on the shaft of the MN (D) view of MN showing two MN bonded together to form a double tipped MN with the channel in the centre

To fabricate a closed hollow channel, two pieces of silicon, either in the form of MN devices or plain silicon, could be bonded together via a process termed “fusion” or “molecular bonding”. Direct binding of silicon wafers was first reported by M. Shimbo et al.[228] and J. B. Lasky et al. [229], where both groups demonstrated the ability to bond silicon at room temperature followed by high temperature annealing to create covalent bonds across the bonding interfaces. However, direct bonding can only take place if the surface of the wafers is smooth, flat, and immaculately clean to enable a wide contact area for effective bonding. To assess the surface of the MN devices, post KOH etching, a three-dimensional surface measurement was taken using an Elite K optical microscope, by a Bruker engineer.

The microscope images in figure 10.17, clearly demonstrate that although the wafer surface is protected by SiO₂, the surface of the device has been damaged by KOH on the nm scale, to produce a non-uniform, rough exterior that would prevent the silicon wafers from bonding. Therefore, adhering two MN device together by direct silicon bonding would be unsuccessful.

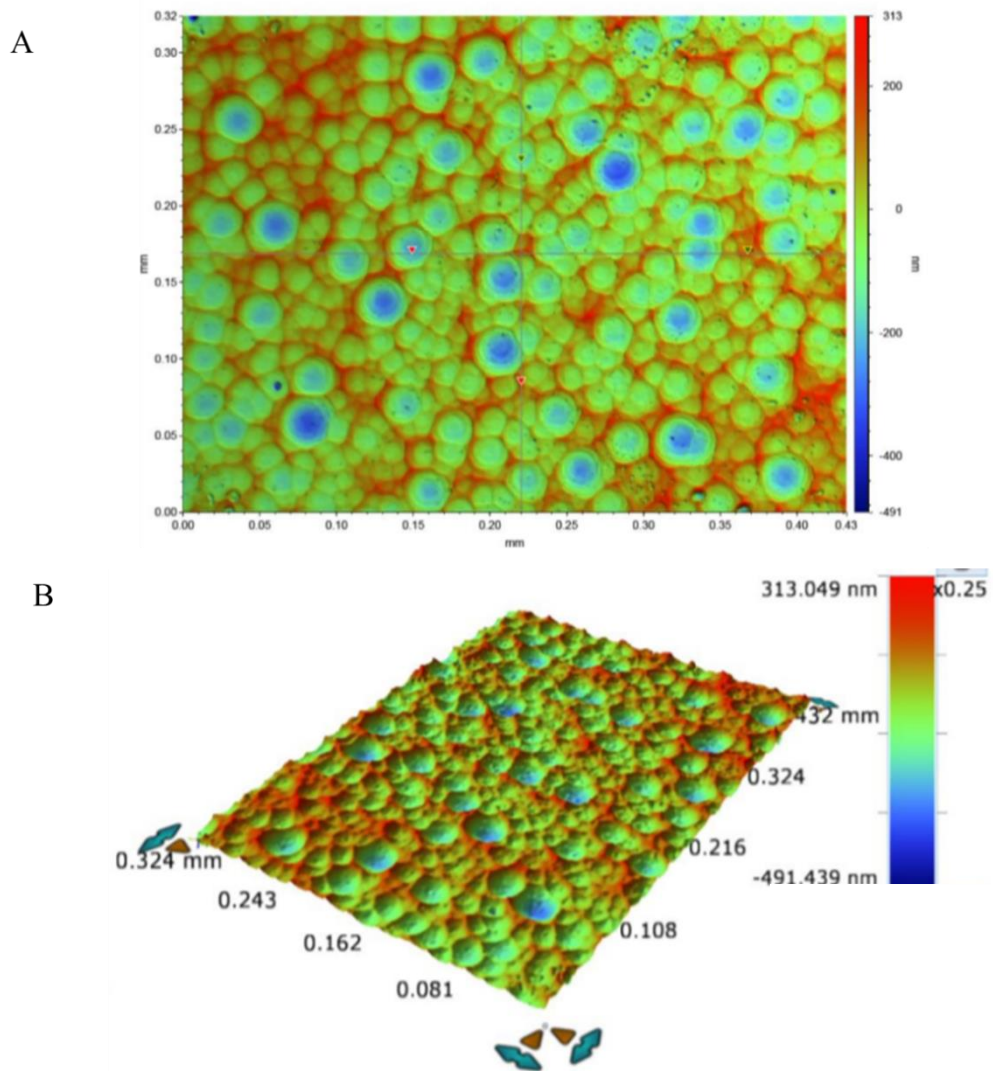


Figure 10.17 2D (A) and 3D (B) microscope images of MN device surface after KOH etching.

For a quick and simple resolution, UV curable, biomedical grade glue called DYMAX, was applied to bond the devices together. A 100 μ m nozzle attached to a syringe was used as a guide for precise application. Although this process was adequate to bond a MN device to a plane piece of silicon to seal the channels, when adhering two devices,

the alignment of the two channels and the MNs proved more difficult. To improve this a mould could be produced to hold the two devices in place, that upon contact are precisely aligned.

10.6 Conclusion

This chapter demonstrates that a hollow in-plane MN can be fabricated using a single KOH etch step. The design utilised the etch characteristics of KOH to etch silicon along its crystalline planes to produce a concave (111) plane etched hollow channel and a convex (110) etched tip, that simultaneously enables fluid injection while maintaining tip sharpness.

Two MN channel designs were fabricated where either the channel is etched onto a single MN (100) side, or both front and reverse (100) sides. However, the two-sided hollow MN requires a delicate handling procedure due to the increased fragility of the etched MN shaft. In addition, the channels can be fabricated as “open” channels or “closed” bores by bonding two devices together. “Open” channels would lower the injection pressure and removes the potential issue of tissue clogging, whilst a “closed” channel would improve injection accuracy and direction and provides extra structural support to the MN, albeit further optimisation is required to correct alignment and bonding methods.

The shape of the MN channel was also explored where different shapes were etched, and larger channels created a larger surface area for improved drug delivery and diagnostic purposes. The depth and width of the channel varied dependent upon the initial width of the channels mask design and etching of either triangular or trapezoid grooves.

Future experiments with hollow MN will examine if and how they inject solutions into the skin and if the channels shapes affect delivery, chapter 16.

10.7 Comparison of out-of-plane and in-plane MNs

Throughout chapters 9 and 10 the fabrication of two MNs were optimised by etching a silicon wafer either in the OOP or in-plane orientation using DRIE or wet etching, respectively. However, each MN has its own advantages and disadvantages compared to the other. Each MN orientation can be fabricated in either solid or hollow designs for a variety of applications for example, solid MNs are recognised for more cosmetic application where the MN does not need to penetrate the skin to deeper skin depths past the epidermis and the treatment can be distributed across a larger skin surface, whereas hollow microneedles can be facilitated for larger drug volumes and a more targeted delivery approach.

In addition to the MN design, the physical orientation on the MN, i.e., in-plane or OOP does not have an effect on which applications can be used as either are exchangeable, for example both solid in-plane and out-of-plane can be used for cosmetic applications, or either hollow MN could be used for delivery through injection. Rather than looking at the orientation of the MN to compare each, instead how the MN is fabricated could decide which MN to apply. For instance, the in-plane MN was fabricated through a simple one step wet etch method, which consequently reduces costs and fabrication time in comparison to DRIE methods. In addition, the in-plane orientation allows the fabrication of MNs with different geometries (heights and length) by simply changing the mask design in the photolithography step, and the etch method remains the same. Although out-of-plane MN fabrication has less flexibility in altering the MNs dimensions, the angle of the MN tip can be adjusted by modifying the etch at the bevel step i.e., by creating a shallower bevel the tip subsequently becomes larger and less sharp and vice versa. In comparison, the tip of the in-plane MNs cannot be altered as the etching of silicon is restricted but the characteristic etch angle of 54.7° of silicon etching in KOH solution; a smaller tip angle is desirable to facilitate a more pain free delivery method and ease of penetration through the SC.

While the in-plane MN fabrication is more simplistic, etching in the OOP orientation enables the hollow bore to be etched within the MN structure to create a closed channel, whereas the in-plane hollow bore is located along the outside of the MN shaft. Thus, injection through the in-plane MN could be susceptible to leakage if the MN is not fully inserted. Therefore, the out-of-plane MN is more reliable for direct and complete drug delivery in targeting the deeper skin layers.

Chapter 11

Fabrication of MN syringe adaptors

11.1 Introduction

Nanopass Technologies developed the first FDA approved intradermal MN injection system, MicronJet®; where a <500µm hollow silicon MN attached to a plastic device connects the MN to any conventional syringe, via a Leur-lock and Leur-slip connection [230]. Other approved products include the dermal roller for cosmetic applications such as improving skin texture. MicroHyal® a dissolving MN patch to treat wrinkles and Soluvia®, a single 1.5mm long hollow MN attached to a prefilled syringe marketed for the flu injections [231] [232].

As the MNs fabricated in this thesis are to be employed to into a variety of different delivery applications, it is important that the adaptor is compatible with various standard syringes, to increase its potential, as in the case of the MicronJet®. Therefore, this chapter describes the design and development of a MN adaptor compatible with standard syringes.

11.2 Out-of-plane MN adaptor

The original OOP syringe adaptor was developed by Connie Pey Eng before this PhD work commenced in 2017. The 3D printed adaptors included both a Leur-lock and Leur-slip at the base for syringe attachment. The Leur-slip is constructed of a hollow tube that connects to a hollow protruding platform via a funnel; this continuous hollow compartment enables fluid to flow through and be directed into the MN bores that are attached to the platform, figure 11.1.

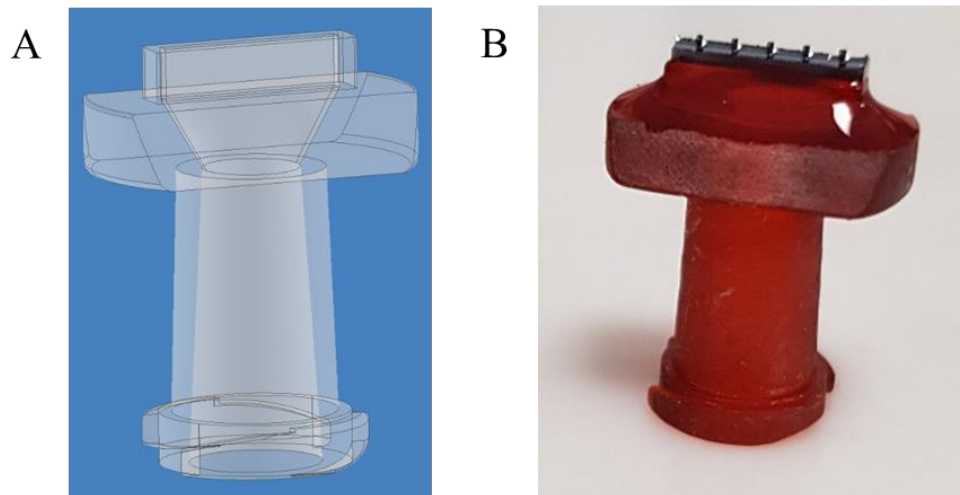


Figure 11.1 (A) Autodesk representation of OOP syringe adaptor, demonstrating the inside hollow tube and funnel connections to direct fluid through the MN (B) OOP syringe adaptor with a 1x5 MN array glued to the top platform

In order to attach the MNs to the hollow platform, the ledge of the platform, outlined in yellow in figure 11.2A, is coated in a biomedical grade glue (Dymax) using a 100 μ m nozzle. The MNs are then carefully and accurately lowered onto the platform to align with the funnel below and cured using a UV lamp. This step needs a steady hand as the devices are only 1mm long and any glue flowing onto the back of the MN device may flow into the bores and block the hollow MN. Once the glue is cured on the platform the perimeter of the device is also coated in glue, extending down the sides of the platform, depicted in yellow in figure 11.2B. This technique immerses the whole of the base of the MN in glue enabling it to be attached to the larger surface area of the platform and preventing it from detaching from the adaptor, figure 11.2C.

Upon MN penetration testing, it was confirmed that some of the glue had flowed over onto the base of the device, where the MNs are aligned. This subsequently submerged either the whole MN or part of the MN shaft in glue, reducing its penetration ability. In addition, insertion testing found that some of the MNs came off the adaptors as the glue beneath the device was still wet and the MN had not bonded to the adaptor. It was found that the UV light was unable to penetrate through the silicon or the adaptor plastic, resulting in the glue not being fully cured between the MN and the platform. In addition, covering the platform in glue only produced a thin layer around the base which is not strong enough to hold the device onto the platform.

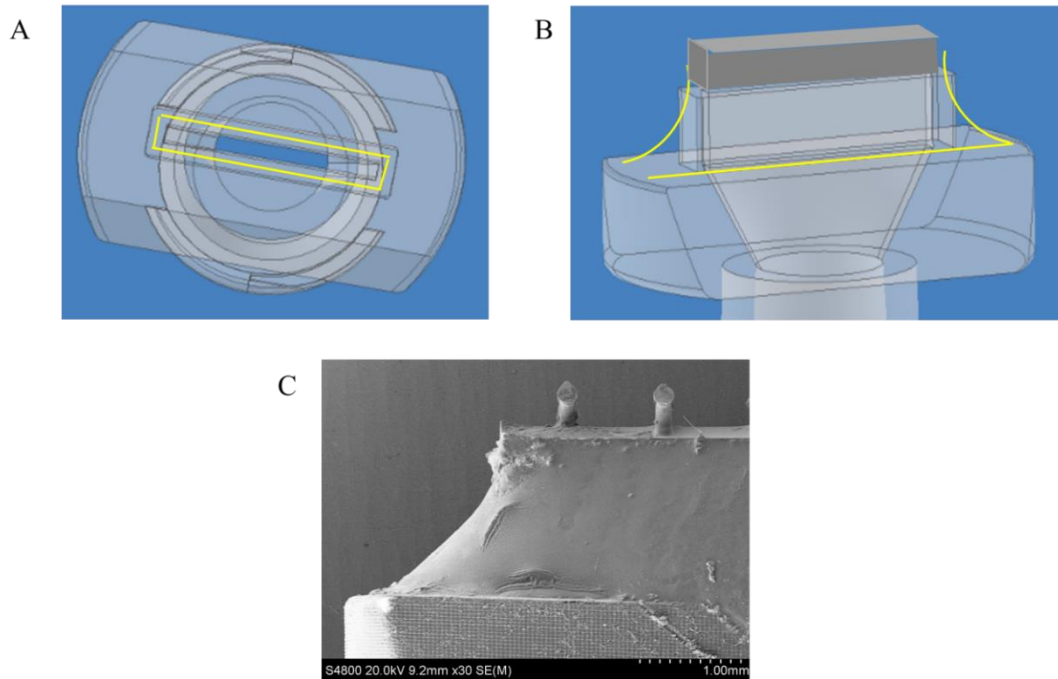


Figure 11.2 (A) Autodesk diagram looking from the top down the MN, showing the opening to the hollow instead and gluing platform in yellow (B) Autodesk diagram of MN device (grey box) on platform, where the yellow lines show gluing around the device (C) SEM image of MN immersed in glue, attached to platform

11.2.1 Out-of-plane adaptor optimisation

To improve the process a new MN adaptor was designed in Autodesk and 3D printed using a dolomite fluidic factory and cyclin olefin copolymer (COC). Instead of attaching the MN to the top of a protruding platform, the MN device was designed to be embedded within the adaptor. For proof-of-concept purposes, only the top of the MN adaptor was 3D printed; the design incorporated a rectangular prism of a width of 5500 μm : length of 11000 μm : thickness of 2500 μm , with a recessed rectangle hole measuring a width of 9000: length of 2000 and thickness 300 μm as seen in figure 11.3. A connecting funnel is designed to direct fluid through the adaptor and into the MNs, meaning the top of the shaft is not solid, and incorporates a small ledge on which to allow the MN to sit with the opening aligned to the back of the MN bores, shown by the red arrows in figure 11.3A. As the device measures 1000: 8000: 400 μm , it should fit comfortably, while leaving a perimeter around the MN available for glue application. Additionally, only 300 μm of the 400 μm base is embedded within the adaptor to prevent overflow of the glue onto the surface of the MN device, as shown by the blue line in figure 11.3B.

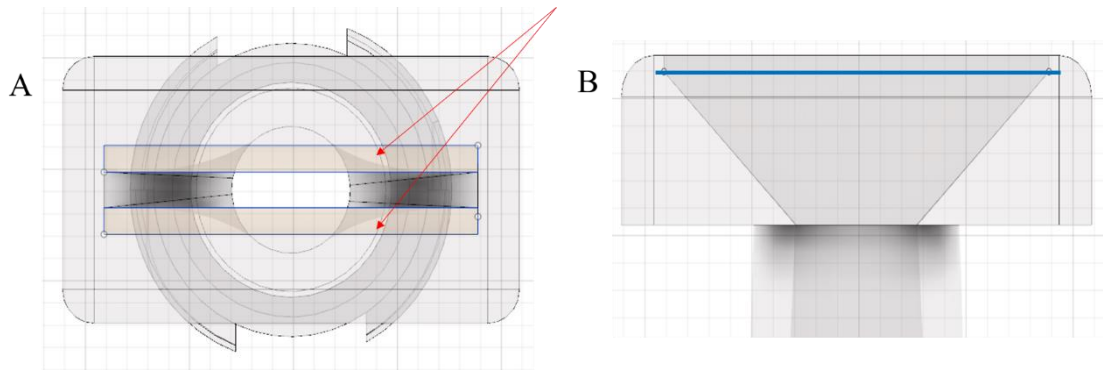


Figure 11.3 Autodesk designs of new out of plane MN adaptor showing (A) the ledge the device is placed upon (B) the 300µm depth connecting to the funnel, blue line

Rather than gluing the device into the adaptor, initial testing tried to mould the adaptor plastic around the device, as omitting the glue would remove any glue channel clogging issues. The first test was completed using a heat gun where the MNs were held with a crocodile clip and treated with a directional jet of hot air from a 1mm nozzle to direct heat to a precise area of the adaptor. The melting point of COC is 240 degrees; therefore 260 degrees was first tested. First observations saw little movement of the plastic, so the heat was increased to 280 degrees. Here the polymer began to melt unevenly around the adaptor and caused the adaptor to bow, figure 11.4. Placing the adaptor on a flat surface and then applying the heat still did not fix this problem but continued to melt the plastic around the crocodile clip. Upon heat application the plastic was unable to reach a fluidic state that could be moulded around the MN and remain upon cooling, but instead remained as solid and putty textured.



Figure 11.4 3D printed COC adaptor after heat gun application at 283 degree. The polymer has not moulded around the MN device but instead caused the adaptor to bow and loose its rectangular shape.

An additional observation found that the nozzle of the heat gun measured 1mm, which was too large to apply heat to only the perimeter of MN leading to the whole adaptor deforming. To correct this a soldering iron was used as the heated tip of the iron can directly touch the areas that need to be melted. Firstly, the iron was targeted on the plastic that surrounded the MN. However, instead of the plastic flowing it again turned tacky and stuck to the iron; the iron indentations can be seen in figure 11.5A.

Next, as the MNs are composed of silicon which can conduct heat, it was thought that applying the heat directly to the MNs instead of the plastic, would enable the heat to transfer through the MN and into the immediate plastic surrounding the device, causing it to flow around it and encapsulate the MN base. However, instead, the heat transferred to the bottom of the device, heating the ledge upon which the MN was placed, causing this to melt and the MN to sink further into the adaptor, figure 11.5B.

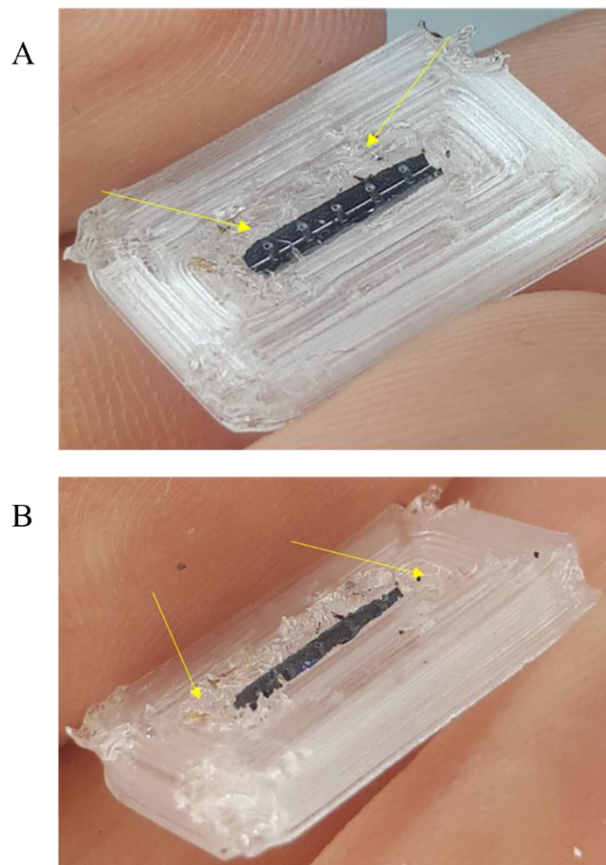


Figure 11.5 MN adaptor influenced by solder iron heat either (A) to the perimeter of the MN, causing the plastic to turn tacky or (B) applying the heat directly to the MN causing the device to sink into the adaptor. Arrow indicates areas the solder iron touched

Due to the challenges of heat treatment, manual glue application was re-visited for the new design. The new 300 μm deep perimeter helped guide the glue nozzle around the MN device preventing the glue from running over the top of the device and instead resulted in a thick glue wall, figure 11.6. Upon insertion testing, the MNs remained within the adaptor and its penetration ability was not obstructed.

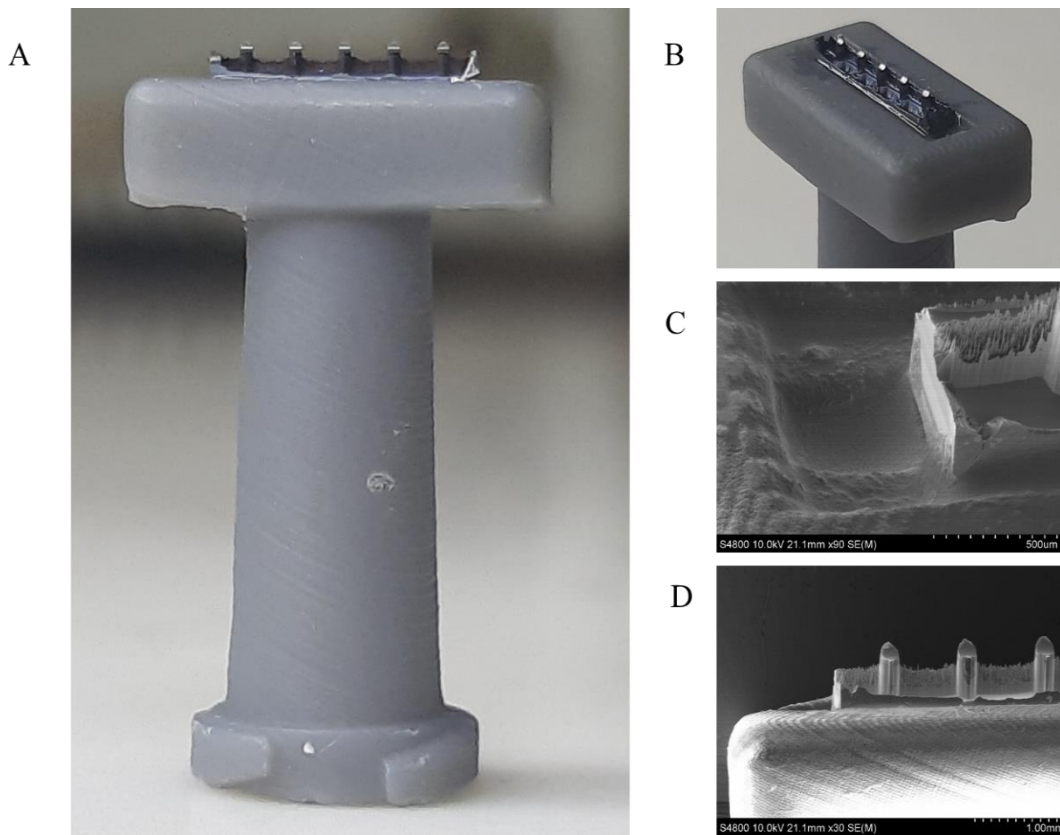


Figure 11.6 (A-B) MN glued to full 3D printed adaptor (C) SEM image magnifying perimeter around MN device with glue application, the red arrow shows the ledge the MN are placed upon, while the yellow shows the opening to allow fluid flow. However, glue has sealed it. (D) SEM image showing MN device not obstructed by adaptor.

11.3 In-plane MN adaptor

The in-plane MN adaptor was designed in Autodesk and 3D printed in resin from 3D hubs (UK). The base of the in-plane MN measures approximately 300: 10500: 3000 μm , in width: length: thickness respectively, in comparison to the out-of-plane device measuring 1000: 8000: 400 μm , figure 11.7. Due to the orientation of in-plane MNs,

devices can be fabricated in larger sizes for handling purposes, where the greater surface area can act as a superior platform for glue application to the adaptor.

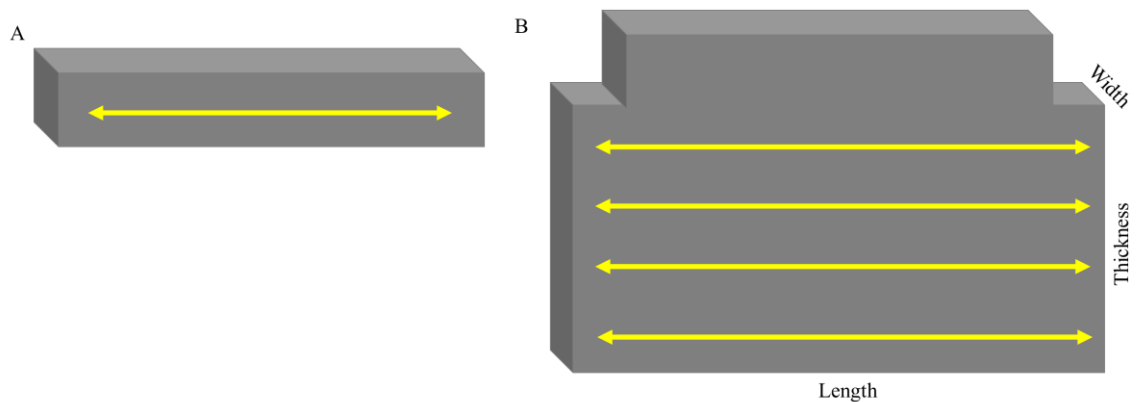


Figure 11.7 comparison of (A) out-of-plane MN device (B) IN-plane device base size, demonstrating the surface area available for glue application, yellow arrows.

The new adaptor design for in-plane MNs included a large insertion area in the form of a slot, outlined in blue in figure 11.8A, that opens at the base to access the funnel, figure 11.8B-C. Here the MNs do not need to be handled as precisely, as the larger area allows straightforward insertion of the device into the slot, with no alignment onto a ledge. The new adaptor design measurements 3000: 13000: 4000 μm , with a slot of 500: 12000: 3000 μm , figure 11.8D. By inserting only the lower part of the MN device into the adaptor slot, this enables the MNs to protrude out of the adaptor (figure 11.8E), to prevent any glue coming into contact with the MNs and remains inside the device slot for a stronger hold. This design was validated as upon penetration testing the MNs did not break out of the adaptor nor did the adaptor inhibit penetration. In addition, the base of the adaptor can incorporate into the leur-lock and leur-slip design to create a universal syringe adaptor.

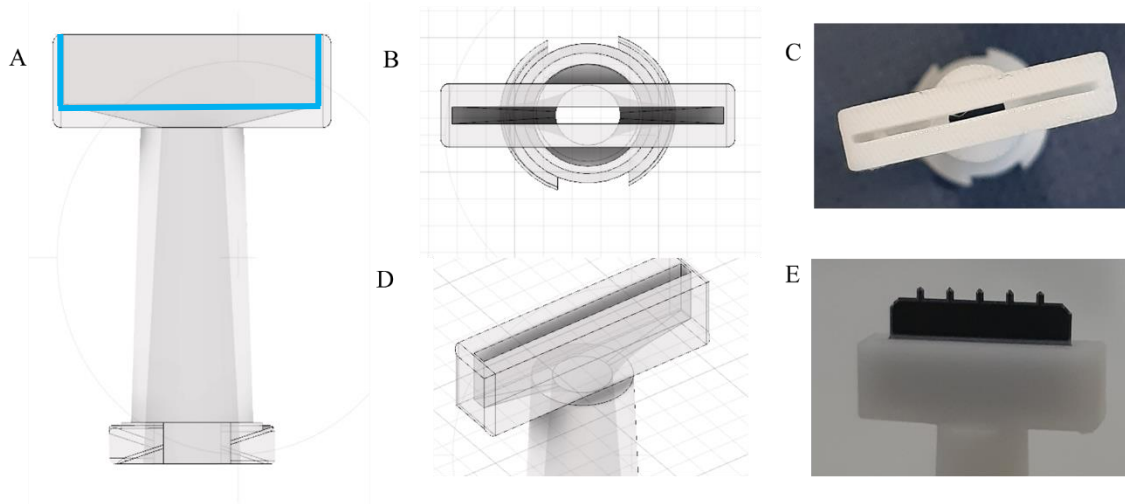


Figure 11.8 In-plane MN adaptor (A) Autodesk design highlighting the slot in blue (B) top-down view of Autodesk design, demonstrating the opening through the funnel (C) 3D printed adaptor top down view showing funnel opening (D) Autodesk design showing slot and funnel connection (E) In-plane MN inserted into slot, where top of base and MN protrude upwards.

11.4 Conclusion

The original out-of-plane device adaptor design was found to be unsuitable as the MN devices were too fragile, broke easily and were too small for precise placement onto the edge of the platform.

For OOP MNs various methods were used to reduce the reliance on the glue-based methods including using a heat gun and solder iron, but these proved cumbersome and ineffective and melted the plastic adaptor instead of the surrounding MN. Therefore, a glue-based approach was revisited. To improve MN strength and handling ability, embedding the devices within the adaptor provided a larger surface area for glue application and as the MNs did not need to be aligned onto an edge, simply placing the device into an accurately printed hole, automatically aligned it over the funnel. It was found that the new adaptor design enabled the glue to be applied with precision and did not affect the MN structure or cause the device to become detached.

For in-plane MNs the larger surface area of the device base makes it easier for glue application and handling to insert the device into a slot. Additionally, as the MN protrudes out from the device and above the adaptor, this prevents any penetration interference from the glue overflow or the adaptor. Therefore, all future MNs will be placed in 3D resin printed adaptors that embeds the MN device.

Part 4

Microneedle characterisation

Introduction to characterisation

Part 3 discussed the fabrication of MNs with varying aspect ratios including MNs with different height, width, and pitch parameters. Next, characterisation experiments were conducted to identify the optimal aspect ratio for successful penetrations where potential unsuitable choice of either pitch, width or height could lead to insufficient or painful penetration into the skin. If the pitch spacing between the MNs is too small a MN array may be subject to the “bed of nails” effect where the applied insertion force is distributed across the array and results in the failure of the MNs to overcome the elasticity of the epidermis and have difficulty in penetrating the skin [233]. If the width of the MN is decreased to overcome this, the MN may become too slender and prone to breaking due to insufficient structural mechanical support. Alternatively, if the MN is too wide then the angle of the tip increases, reducing its sharpness and ability to penetrate without additional force [234]–[237]. The height of the MN, also referred to as the length of the MN, needs to be accurately controlled; too long a length can penetrate into the deeper epidermis/dermis and stimulate the pain receptors located there, while, conversely, a too short a length will not be able to penetrate through the skin [238]. There is no guide to determine the exact lengths of a MN to avoid these challenges; it is important to note that the penetration depth does not directly represent the physical length of the MN, as the penetration depth is subjective to how the shape of the MN preforms [239]. To determine the optimal MN aspect ratio, each factor is interdependent, Davis et.al [240] discussed that the insertion force depends not only on the MN pitch but also the MN length. Additionally, Davidson [239] contended that longer, larger and more densely packed MNs results in less significant and ineffective skin penetration in comparison to less dense and shorter MNs [224][225][7]. However, the results would depend on the tensile strength of the material used, as harder materials can withstand greater forces than softer materials and is proportional to the pressure used upon insertion. The aims of the following chapters are to understand the relationship between MN pitch, height, and width in order to optimise a MN with successfully penetrates skin with a low insertion force and maintains its structure upon compression force testing. The OOP MN results throughout this part are published in *Lab on a chip* (<https://doi.org/10.1039/D0LC00567C>), while the in-plane MN characterisation results have been accepted for publication by the journal of *pharmaceutics and biopharmaceutics*.

Chapter 12

Dye staining

12.1 Introduction

Basic enface characterisation such as dye staining with trypan blue [241], [242] or methyl blue (MB) [243], [244] can be employed to visualise successful MN skin penetration, as the dyes selectively stain viable (living) cells, which are located in the epidermis and not within the skin barrier layer, the *stratum corneum* (SC), enabling accurate identification of any created microchannels [245]. Porcine skin was used for the following experiments due to its accessibility and similarities to human skin. Full thickness sections measuring approx. 1mm, were shaved with an electric shaver and diced into sections, any part of the skin that had warts or visible skin damage were discarded, (figure 12.1)



Figure 12.1 Porcine skin with visible surface damage

Control experiments using a scalpel and the MN adaptor, were conducted to demonstrate positive dye staining and to rule out the possibility of the MN adaptor influencing penetration. Figure 12.2A shows MB staining of porcine skin after treatment with a scalpel; it is clear that after washing with alcohol wipes only the areas which were cut with the scalpel have stained blue. Figure 12.2B shows skin treatment with a MN adaptor without any MNs bonded to it; after staining there is no blue dye detectable within the application area. However, indentation of the applicator can be seen confirming the applicator did not break the SC, resulting in no MB skin staining.

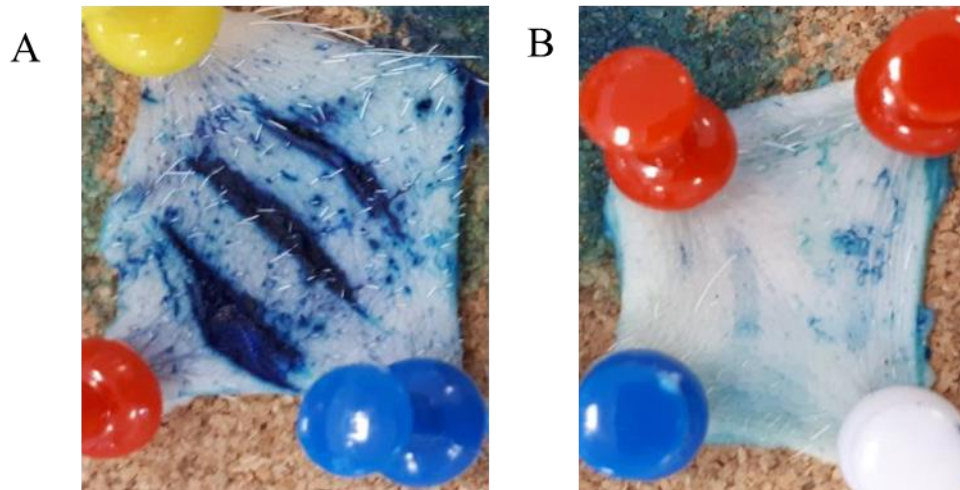


Figure 12.2 Methyl blue staining of porcine skin after application of (A) positive control, scalpel showing dye staining (B) adaptor negative control with no MN device bonded, showing no dye staining.

12.2 Out-of-plane MN methyl blue staining

To calculate skin penetration efficiency (PE), the percentage of MB spots against the total number of MN's was calculated e.g. (total number of MB spots produced / total number of MNs) x 100 [246]. Silicon OOP 1 x 5 and 6 x 6 MN arrays were inserted into full thickness pig skin, of approximately 3cm x 3cm, using thumb pressure and stained with MB (thumb pressure is defined as approximately 10N [66]). Solid 1 x 5 and 6 x 6 MN arrays consist of MNs pitch: width: height of 1000 μ m: 240 μ m: 720 μ m. Each MN array demonstrated a degree of effective penetration through the SC to create small circular blue stained dots. The 6 x 6 array (figure 12.3A) demonstrated a PE of 81%, with a lack of penetration in the centre of the array, potentially due to the bed of nails affect; to prevent this from happening the pitch spacing between MNs would need to be increased. The 1 x 5 MN array of the same measurements saw 100% PE (figure 12.3B) which was reproduced upon applying the same method with a 1 x 5 MN arrays on 5 consecutive occasions. As the array only consists of a single row of 1 x 5 MNs there was no bed of nails affect as the same thumb pressure force was distributed across fewer MNs, resulting in a more uniform application with each MN penetrating through the SC.

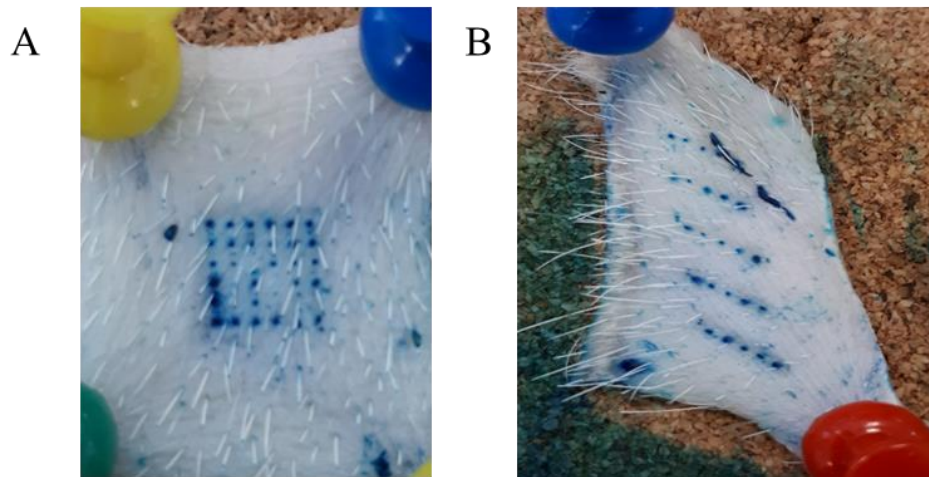


Figure 12.3 methyl blue staining of porcine skin upon application of (A) 6x6 silicon out-of-plane MN (B) 1x5 out-of-plane, 5 consecutive times.


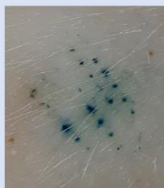
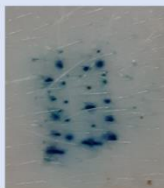
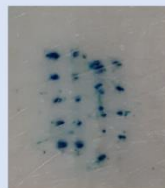
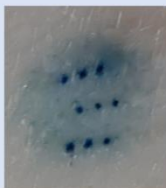
12.3 In-plane MN methyl blue staining

In-plane silicon MNs were fabricated in a variety of aspect ratios to examine which MN dimensions penetrated the skin more effectively and to determine the optimal ratios. Each MN array was inserted repeatedly into full thickness pig skin via thumb pressure, stained with MB and washed with an ethanol wipe.

12.3.1 In-plane MN pitch

To examine and optimise the pitch spacing for efficient MN penetration MN masks were designed with pitch dimensions of 500, 1200, 1400, 1700 and 2300 μm . Each MN was inserted into porcine skin four consecutive times (note three times for 2300 μm), to create a 100% PE of 20 MB stains- the post etched dimensions and resulting MB stains are outlined in table 12.1.

Table 12.1 Methyl blue staining of MN arrays with varying pitch dimensions

Mask pitch dimensions	500 μm	1200 μm	1400 μm	1700 μm	2300 μm
Post etch pitch	297 μm	1019 μm	1238 μm	1521 μm	2086 μm
Methyl Blue Stain					

The results established that a MN array with pitch space of $297\mu\text{m}$ post KOH etching did not allow for effective MN penetration; the MB dots created were small and non-uniform, showing minimal penetration. Increasing the pitch to $1019\mu\text{m}$ showed a PE of 80%, however, the MB dots created were smaller in comparison to the larger pitches. Pitches 1238 , 1521 and $2086\mu\text{m}$ all demonstrated complete, repeatable 100% PE. To note, due to the large mask pitch dimension of $2300\mu\text{m}$ only a 1×3 MN array could be fabricated on a device of the same size used with other dimensions. Therefore, to retain a 1×5 MN array and maximise the number of MNs that penetrate in one application, while spacing the MN as far apart as possible, mask designs with a pitch spacing of $1700\mu\text{m}$ provided the optimal result.

12.3.2 In-plane MN width

As discussed in the fabrication chapter 9.9, the width of the MN after KOH etching increases on average by $179\mu\text{m}$ irrespective of the original mask design. To reiterate figure 12.4 shows a mask design of $300\mu\text{m}$ represented by the shorter yellow arrow, and the subsequent etched MN with an increased width of $460\mu\text{m}$ signified by the longer red arrow.

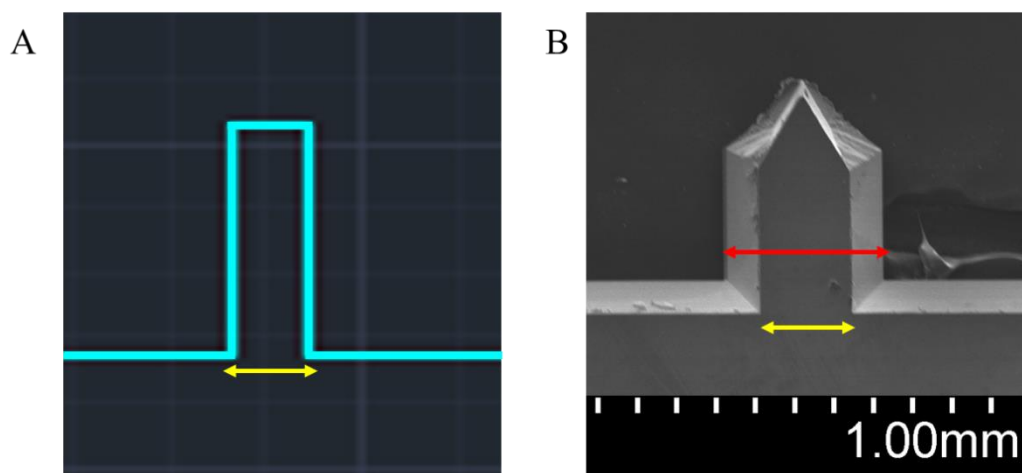
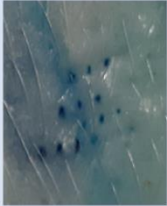
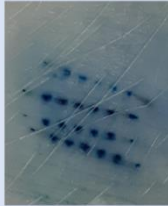
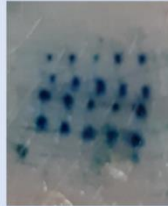
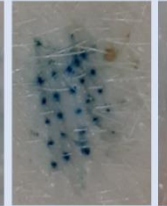
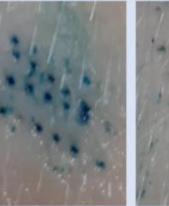
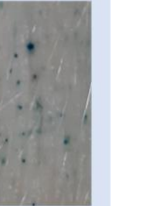


Figure 12.4 (A) Auto CAD image of MN design measuring $300\mu\text{m}$ wide (yellow arrow) (B) SEM image of MN post KOH etching demonstrating original mask width (yellow arrow) and new larger $460\mu\text{m}$ width (red arrow)

To avoid ineffective penetration of larger widths or MN breakage if the MNs are too thin, MNs measuring 900 μm in height but varying width dimensions of 500, 400, 300, 200, 100, 50, 25 μm , were tested. The post KOH etched widths and MB results are shown in table 12.2.

Table 12.2 Methyl blue staining of MN arrays with varying width dimensions

Mask design width	25 + 50 μm	100 μm	200 μm	300 μm	400 μm	500 μm
Post etch width	225 + 252 μm	297 μm	378 μm	460 μm	586 μm	665 μm
Methyl Blue Stain						

The thinnest MN widths of 25 - 50 μm show a PE of 60%, while MN widths 100 – 300 μm all successfully produced clear 100% PE profiles, where all 5 MNs created reproducible MB staining. A larger MN width of 400 μm achieved a lower PE of 85%, suggesting the MNs are becoming too wide to penetrate. A width of 500 μm showed very little MB staining, not only producing fewer MB dots, but also producing smaller diameter dots when compared to the smallest width MNs. As discussed in chapter 9.9, a wider MN consequently widens the MN tip and although the tip maintains its 57.4° angle in the <111> orientation, the thicker tip loses its sharpness in the <100> axis preventing it from penetrating through the SC. Furthermore, although MNs of widths 25 μm and 50 μm successfully penetrated the skin, difficulty was found with handling due to their fragility and common breakage before and during insertion. Therefore, overall MN widths of 200 and 300 μm yielded the best results as the MNs did not break on handling and saw successful penetration of the SC.

12.3.3 In-plane MN height

As discussed in chapter 9.8, the original mask designed height of the MN decreases post etching due to the creation of the MN tip (figure 12.5) – the amount of reduction varies depending on the starting mask design.

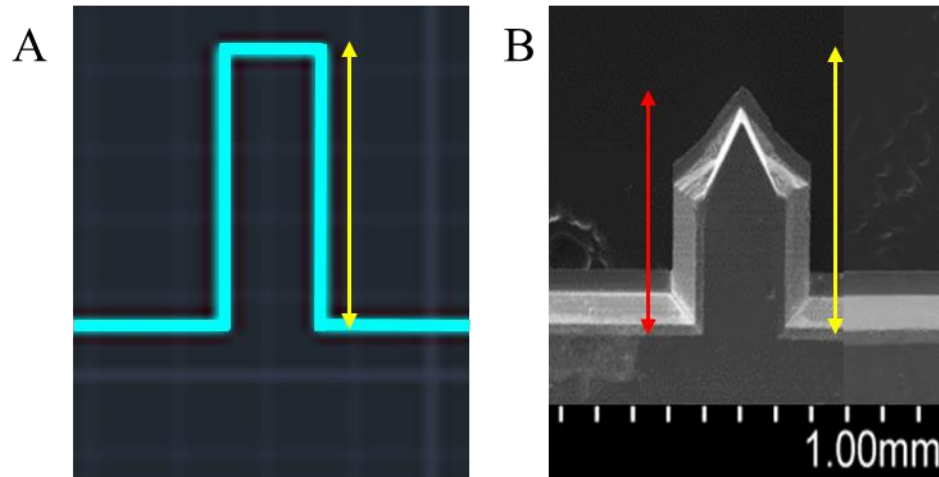


Figure 12.5 (A) Auto CAD image of MN design measuring 900µm in length (yellow arrow) (B) SEM image of MN post KOH etching demonstrating original mask length (yellow arrow) and new shorter 549µm length (red arrow)

The mask designed heights tested were 300, 500, 700, 900, 1200 and 1500µm which subsequently measured 66, 245, 392, 548, 784 and 1150µm post KOH etching.

The results illustrated in table 12.3, demonstrate that the longer the MN, the greater penetration as more MB staining is observed. The MNs with design heights of 300µm decreased to 66µm post etch which were not long enough to penetrate through the SC. Increasing the design heights to 500 and 700µm, created MN of heights 245 and 392µm, respectively, post etch. Although some MB-stained dots were produced using these MNs, the MN penetration is inconsistent and unreliable. MN design heights of 900 and 1200µm gave an ideal MB penetration profile displaying large circular MN dots characteristic of the MN shape and all MNs repeats gave 100% PE. Increasing the height to 1500µm, however created an indistinguishable PE% due to the MB stain bleed within the tissues, indicating excessive penetration that caused a larger area to stain.

Table 12.3 Methyl blue staining of MN arrays with varying height dimensions

Mask Height Dimensions	300µm	500µm	700µm	900µm	1200µm	1500µm
Post Etch Height	66µm	245µm	392µm	549µm	784µm	1150µm
Methyl Blue Stain						

12.3.4 In-plane MN arrays with varying heights on the same array

To factor in the flexibility of the skin and for use in theranostic applications, two MN arrays were designed with different MN heights on the same array, figure 12.6.

- A. Device containing mask heights of x2 1200 μm height MNs and x2 900 μm heights MNs
- B. Array decreasing in mask height from 1200 - 800 μm , in 100 μm increments.

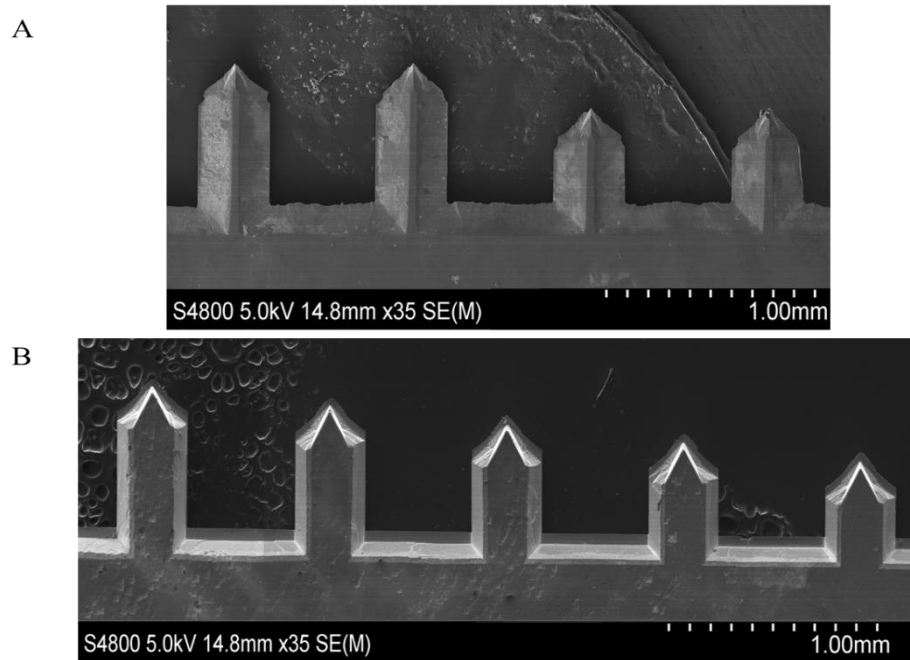
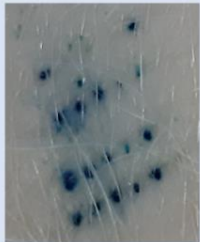
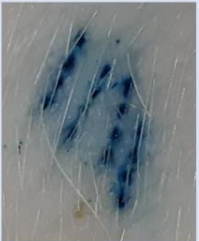


Figure 12.6 SEM images of MN devices with different height on the same array (A) x2 784 μm and x2 549 μm (B) Heights decreasing from 784, 696, 616, 549, 470 μm post KOH etching

The results presented in table 12.4 reflect the MB results in the previous chapter, for example, device design A contained MNs which after KOH etching measured between 748 - 470 μm ; the two longer 738 μm produced successful MD stains while the two smaller MNs show non-uniform, inconsistent penetration. Device B was designed with heights that all measured above 549 μm after KOH etching, but each individual MN varied by approximately 100 μm from the next; these MNs demonstrated efficient and reproducible MB penetration with all MN heights. Overall, these results established that irrespective of the neighbouring MN height, each MN will still penetrate to its individual potential.

Table 12.4 Methyl blue staining of MN arrays with varying height dimensions on the same array

Array Design	1	2
Post Etch Height	784 - 470 μ m	784 - 549 μ m
Methyl Blue Stain		

12.4 Polycarbonate MN methyl blue staining

The fabrication of polycarbonate (PC) MNs results in either 4 x (4 x 4), 1 x (4 x 4), or 1 x (1 x 4) MN arrays, with 64, 16 and 4 MNs per array, respectively. To assess the PE all arrays were subjected to the same thumb pressure force and inserted into porcine skin for MB staining (figure 12.7).

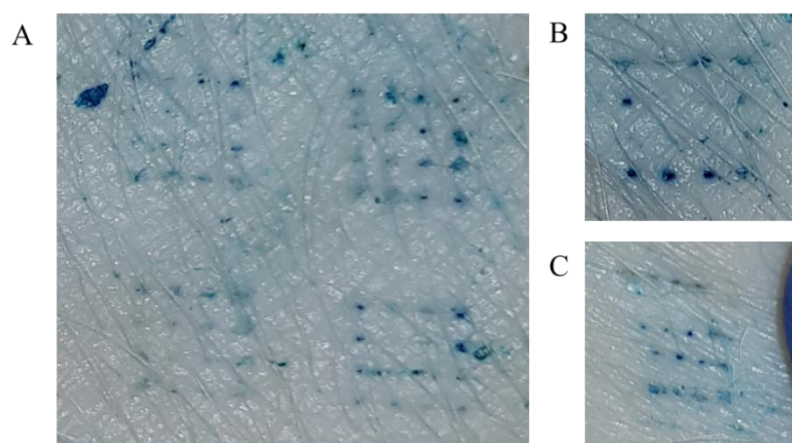


Figure 12.7 Methyl blue staining of PC MN arrays with (A) 64 MN in 4 (4x4) orientation (B) 16 MNs in 4x4 orientation (C) 1x4 MN rows, with 2mm spacing between

Figure 12.7A demonstrates the staining results for 4 (4 x 4) MN arrays, with a low PE of 22%, indentations of where the MNs met the skin can be observed, with small, inconsistent MB dots, possibly meaning the MNs did not penetrate through the SC successfully. Reducing the array to 16 MN, figure 12.7B, still showed very little

penetration through the SC, although there was an increase of PE to 44%. The 4 x 4 array was diced into quarters to produce four 1 x 4 rows of MNs, each row was then placed 2mm apart from the next to create parallel MN rows with larger pitch spacing. The results seen in figure 12.7C again observed MN indentations on the skin surface, with minimal MB staining. As the PC MNs are larger (base width of 700µm, height of 700µm) than the silicon MNs, they might have been expected to produce larger micro channels in skin that would be observable by greater MB staining. However, this was not the case, suggesting that penetration of the PC MNs was less effective than silicon MNs. To improve the PE of PC MNs then either a higher force needs to be exerted upon insertion or the MN shape (tip sharpness and MN width) needs to be adjusted.

12.5 Summary

Table 12.5 summarises the MB results throughout this chapter for the in-plane MNs. It demonstrates that MN pitches greater than 1400µm penetrate effectively, in addition to heights of 900µm. However, heights greater than 1200µm become restricted by the pitch of the MNs, which is discussed in chapter 14. The width of the MNs, except for 500µm, all observed some penetration, however the smallest MNs were not robust enough to maintain penetration. MNs larger than 500µm saw an ineffective penetration which is evaluated more thoroughly in chapter 14, with the aid of OCT analysis.

Table 12.5 Summary of in-plane MN methyl blue staining results

In-plane Microneedle			PE (%)
Pitch (µm)	Width (µm)	Height (µm)	
500			-
1200			80
1400			100
1700			100
2300			100
	25 + 50		60
	100		100
	200		100
	300		100
	400		85
	500		-
		300	-
		500	-
		700	-
		900	100
		1200	100
		1500	-

Chapter 13

Microneedle applicator

13.1 Introduction

PC MN's were fabricated at Glasgow University using injection moulding techniques and transported to Swansea University for testing. However, issues during transportation and storage saw the tips of the MNs blunt or become damaged, which consequently affected the MNs ability to penetrate the SC with thumb pressure application alone. The triangular shape of the PC MNs measured 1000 μ m in height with a 700 μ m base width in a 4 (4 x 4) array that contained 64 MNs densely packed with 1000 μ m spacing between each. To improve the PE of high-density MN arrays and control reproducible and reliable self-application MNs can be applied with the help of an applicator device.

The study by Maaden et. al [246], tested an applicator to aid insertion of high density silicon MNs (576 MN on a 5 x 5 cm backplate) that measured 200 μ m in height. Forces from 3.43N – 22.1N were tested by applying weighted rods onto the insertion device for manual application. It was observed that increasing the applied force up to 7.36N with a constant application time of 10 seconds, greatly improved the penetration ability.

Increasing the force further or extending the application time only increased the PE minimally, however, improved reproducibility. Instructing people with no MN experience to test the MNs with and without the applicator saw a successful increase in the PE with aid of the applicator. Although, this result showed that using an applicator was essential for effective and reproducible penetration of high-density MN arrays, the applicator used did not provide precise control over pressing force or impact velocity.

The study by Leone et.al [247] developed a digitally controlled MN applicator that regulated the insertion parameters (velocity and force) and evaluated the optimal conditions for reproducible penetration. The applicator tested six different MN arrays from various companies (Bosch, My Life Technologies (MLT) and Tyndall National Institute), that varied in shape, geometries, densities, and material to assess PE. It was shown that, although each MN had different optimal application parameters, all MN used produced a reproducible PE close to 100%, in *ex vivo* human skin, with applicator-controlled force and velocity. This is key as MN designs varied from Bosch's narrow

tetrahedral cones that presented the smallest tip diameters, to MLT nanoporous alumina MNs which possessed the largest tip diameters. This showed that regardless of MN shape all MNs can produce 100% PE with the aid of an applicator. The following section reports the use of an applicator to enhance MN penetration for controllable and repeatable penetration.

13.2 MN applicator device

A universal MN applicator that controls force and velocity of MN insertion was fabricated by Joe Wheeler as part of his master's degree project and tested using OOP 6 x 6 silicon MN arrays and PC MNs. The applicator was fabricated using a 3D printer to incorporate a two-part piston which, on adjustment of a simple threaded pin locking system, can vary the force and velocity of a spring-loaded piston. It is to be noted that upon pin adjustment, in order to change only the force, the velocity will have a slight variation, for example, changing the force from 4N to 9N alters the velocity from 2357mm/sec to 2525mm/sec. As this is not a significant change then direct comparison between the forces can still be made. Adhesive was placed on the back of the MN array base to attach the MNs to the piston impact face. The surrounding cone simultaneously protects the MNs from damage while aligning the piston to the skins surface for accurate and consistent insertion height, figure 13.1.

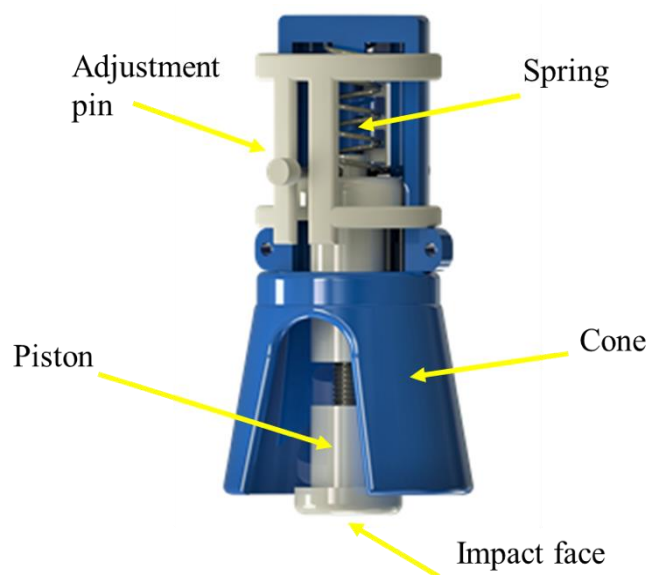



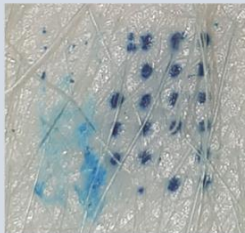

Figure 13.1 MN applicator device controls the velocity and force by adjusting the pin. Image Courtesy: Joseph Wheeler

13.3 Silicon out-of-plane MN applicator testing

Previously it was determined that the central MNs of the 6 x 6 silicon OOP MN array did not penetrate the skin upon thumb pressure application. To improve this, the array was subjected to application at different velocities and forces (detailed in table 13.1) via the adjustment of the applicator pin. Moderate thumb pressure is defined as approximately 10N, therefore, initial tests were conducted with insertion forces below 10N but with variable velocities, to determine whether the speed of application could improve penetration alone. The first run tested a force of 4N and velocity of 2357mm/second; this produced a PE of 36%, much less than the 81% recorded with thumb pressure alone. Increasing the velocity to 3367mm/second but maintaining 4N, saw a PE increase to 55%. From this it was considered that a force of 4N was not suitable for 100% PE. The force was increased to 9N and the velocity reduced to 2525mm/sec, however, upon insertion the MNs fractured and broke off into the skin. This meant that either the force applied had exceeded the strength of the MNs, as the brittle properties of silicon were exacerbated due to the MN shape, or the introduction of velocity increased the impact force. As the silicon MNs are sharp and robust enough to penetrate the skin with little force and lower speeds, optimal PE results were found with thumb pressure alone, confirming that an insertion aid was not required.

SEM images of silicon OOP MN arrays after 4N applicator tests reveal no deformation and very little fractures to one or two MNs in either array used (figure 13.2). Each array was able to withstand velocities of 2357 and 3367 mm/sec even though the array did not completely penetrate.

Table 13.1 Methyl blue staining of OOP MN arrays aided by applicator insertion

Applicator Force	4N	4N	9N
Applicator Velocity	2357 mm/sec	3367 mm/sec	2525 mm/sec
Methyl Blue Stain			

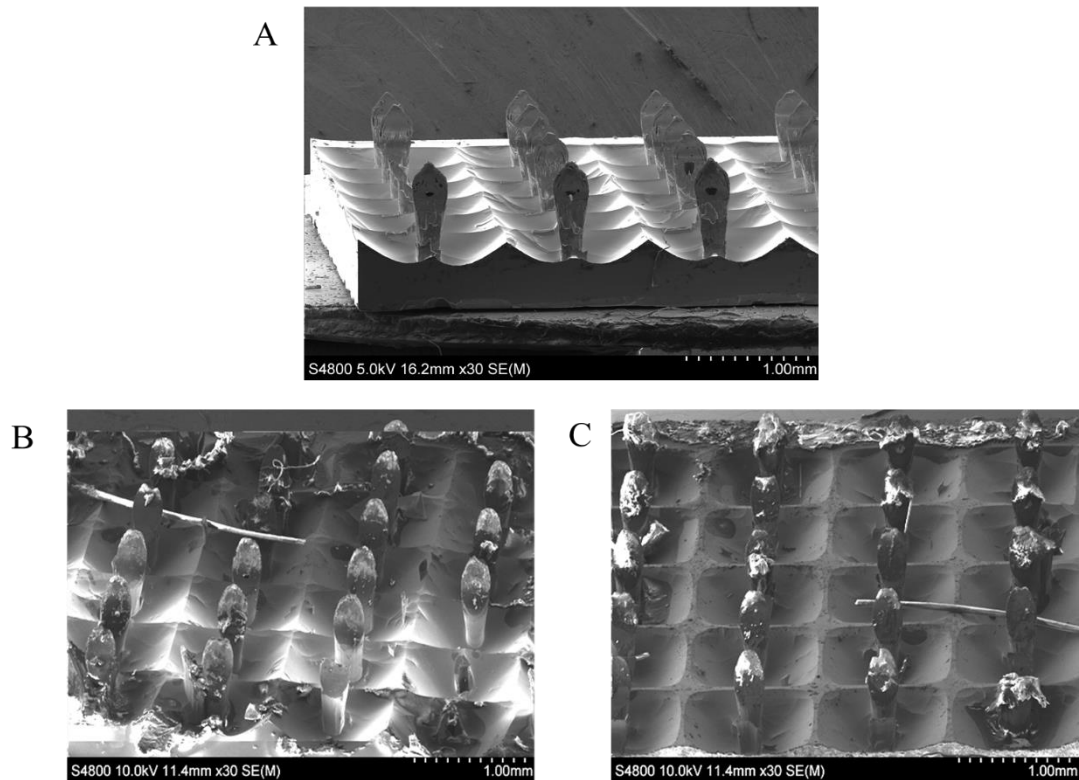


Figure 13.2 SEM images of OOP silicon MN (A) before insertion and after insertion into porcine skin with an applicator force of 4 N and velocity (A) 2357 mm/sec (B) 3367 mm/sec

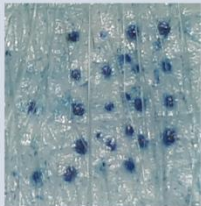
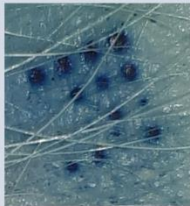
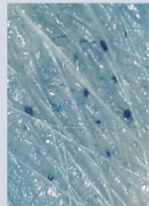
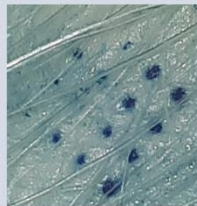
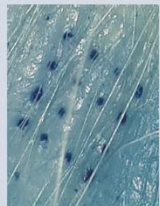
13.4 Polycarbonate MN applicator testing

In an attempt to improve the PE from 44% with thumb pressure application, 4 x 4 PC MNs arrays were inserted into porcine skin via the applicator, using a range of forces from 4N to 13N at low and high velocities.

The first test was run at 4N at a velocity of 3367mm/sec as this was the optimal result found for OOP silicon MN. The results show positive MB penetration; however, the PE was calculated as 137%. Even though the array had successfully penetrated, two separate insertion sites were observed. This was a result of a rebound action from the piston interacting with the skins elastic surface, causing the piston to bounce back upon itself, losing velocity and reinserting the MN array a second time, however, this time with a reduced PE. To remove the recoil action the velocity was decreased to 2,862 mm/sec which due to the pin adjustment subsequently increased the force to 7N. This time no rebound MB penetration was seen; however, larger round MB spots were produced generating a PE of 75%, a vast difference to thumb pressure application which

had a PE of 44%. To improve the PE further the applicator force was increased to 9N and tested on velocities of 1,515 mm/sec and 2,525 mm/sec with the purpose of analysing the difference in velocity used for the same force. Table 13.2 shows that the lower velocity generated overall provides the lowest PE of approximately 31%, where the MB stains are small and difficult to identify. Alternatively, the larger velocity produced significant MB staining and a PE of 75%. This is interesting as the second test also reached a PE of 75%, but at a lower force of 7N whilst the velocity used for both differed by only 337mm/sec. To substantiate this a final test was set to a velocity of 1,683 mm/sec and a force of 13N, the PE calculated as 93%, with only one MN not penetrating.

Table 13.2 Methyl blue staining of PC MN arrays aided by applicator insertion.

Applicator Force	4N	7N	9N	9N	13N
Applicator Velocity	3365 mm/sec	2862 mm/sec	1515 mm/sec	2525 mm/sec	1683 mm/sec
Methyl Blue Stain					

Hence, the relationship between the velocity and force of the applicator may be described as:

1. If the velocity is low, a higher force is required to create a successful PE, shown by the difference in tests 3 and 5
2. If the velocity is too high and the force is too low to control the insertion, the MN will rebound upon hitting the skin, test 1.

Therefore, for successful use of an adaptor, outcomes 1 and 2 need to be considered to obtain successful penetration through the SC.

13.4.1 MN analysis post application

SEM images of PC MNs after skin insertion aided by an applicator show tip deformation on all MN regardless of force and velocity. Notably, the MNs that rebound in test 1, figure 13.3B, shows the greatest deformation; this explains why the second rebound PE is less efficient than the first, as the blunted tips prevent further successful penetrations, instead a second penetration only blunts the tips further.

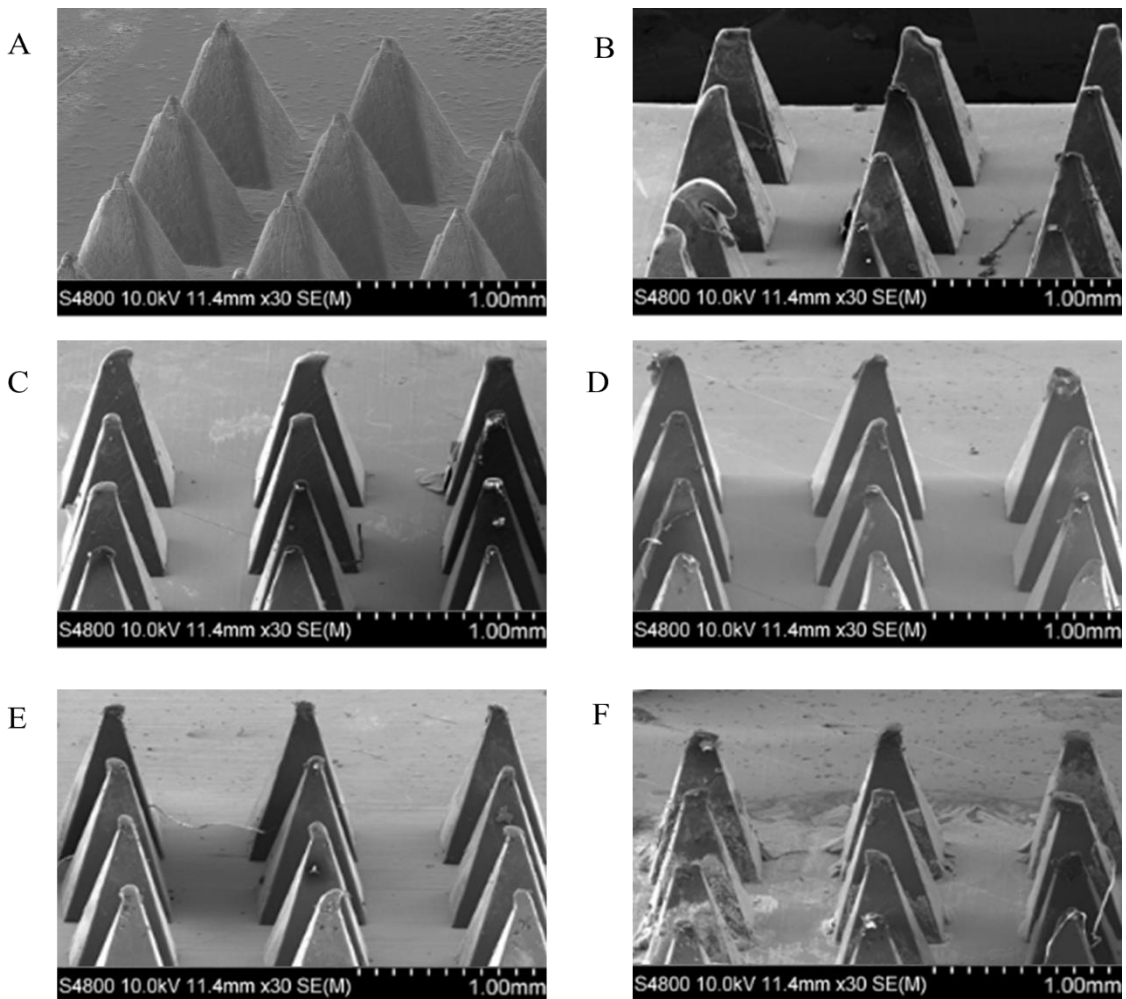


Figure 13.3 SEM images of PC MN (A) before testing and after MN applicator device showing tip deformation (B) 4N, 3367 mm/sec (C) 7N, 2862 mm/sec (D) 9N, 1515 mm/sec (E) 9N, 2525 mm/sec (F) 13N, 1683 mm/sec.

13.5 Conclusion and future experiments

This chapter quantified MN penetration in porcine skin using MB staining. Evidence of microchannel shape, size and depth are limited due to the lateral diffusion of dye within the skin, leading to potential overestimation of pore diameters [248]. Differences between successful MN penetration and MN skin indentation can be difficult to distinguish in some samples, as MB dye is capable of pooling in crevices resulting in potential false positive results.

To remove these complications, two approaches can be considered:

1. Maaden et. al [246], demonstrated that tape stripping the area after MB application removes the outer layers of skin and thus any areas that have not stained the underlying layer. However, if MN are $<300\mu\text{m}$, the smaller microchannels created may not be visible after tape stripping, therefore, this technique is only suitable for longer MNs.
2. The MN could be coated or loaded with the dye, so upon insertion, only the precise MN locations are stained removing false results.

Utilising a penetration enhancing applicator improved the PE and insertion reproducibility of the high-density PC MN array, facilitating reliable self-application for people who are not trained in the use of MN's. A force and velocity of 13N at 1683mm/sec demonstrated the highest PE at 93%, as this is significantly larger than with thumb pressure alone (44%), all experiments that involve PC MN penetration, will involve the applicator at these parameters.

The applicator is unlikely to be suitable for silicon MNs due to their fragile structure, which can break when using the higher injection forces and velocities administered. However, silicon MNs have very sharp tips, which allow skin penetration with application of thumb pressure sufficient for manual insertion.

Chapter 14

Optical coherence tomography

14.1 Introduction

While dye studies demonstrate the ability of MNs to breach the SC, information about architectural changes within the skin after MN treatment can be evaluated through optical coherence tomography (OCT) analysis. OCT is a non-invasive real time 3D imaging technique, that utilises light waves to produce *in vivo* micrometre resolution images of biological tissues up to 3mm in depth [249], [250], in-depth description can be found in chapter 7.1.4. OCT is used to visualise the microchannels produced by the MN either after treatment or *in-situ* without the need for tissue pre-treatment [251]. Other techniques to determine penetration depth involve traditional histological sectioning, however, this is a laborious method involving freezing tissue samples and lots of manual handling which potentially destroys or alters the skin structures and influences the final shape and measurements of the microchannels created [251]. Additionally, mechanically slicing the tissue, leaves room for user error, as aligning the blade precisely through the centre of a microchannel without visual aid is difficult and if the results are found inconclusive, then the whole process needs to be repeated.

OCT analysis was conducted at Cardiff University on porcine and excised human breast skin (local research ethics committee reference 08/WSE03/55), that had part of the dermal tissue removed and was supported on a corkboard. The aim of this investigation was to obtain *in vivo* images of pre, and post MN treated porcine and human skin, to obtain information on the morphological changes that are created from MN application. Further, the depth of MN insertion can be calculated to derive whether the length of the MNs is adequate for successfully drug delivery or, with respect to hollow OOP silicon MN, total bore coverage whilst inserted *in situ*.

14.2 OCT optimisation

It is important to be able to interpret the natural morphology of both porcine and human skin tissue from OCT images, in order to identify changes caused by MN insertion. The OCT images of untreated human and porcine skin are analysed in figure 14.1. Although OCT can distinguish between individual components of the skins structure, the images

are not completely defined, meaning all measurements are approximations. Figure 14.1A shows human tissue with the SC appearing as the superior bright band measuring $12\mu\text{m}$ (a), while directly below lies the epidermis, forming the homogeneous $56\mu\text{m}$ light grey band (b). Underneath the epidermis lies a distinctive partitioned line identified as the epidermis-dermis junction (c). Separated by this junction is the dermis (d), skin appendages such as hair (yellow box) and blood vessels (blue box) are visible due to their distinctive densities affecting the wavelength refraction. Overall, the total skin thickness measures $769\mu\text{m}$ and appears smooth and uniform enabling the skin components to be clearly identified.

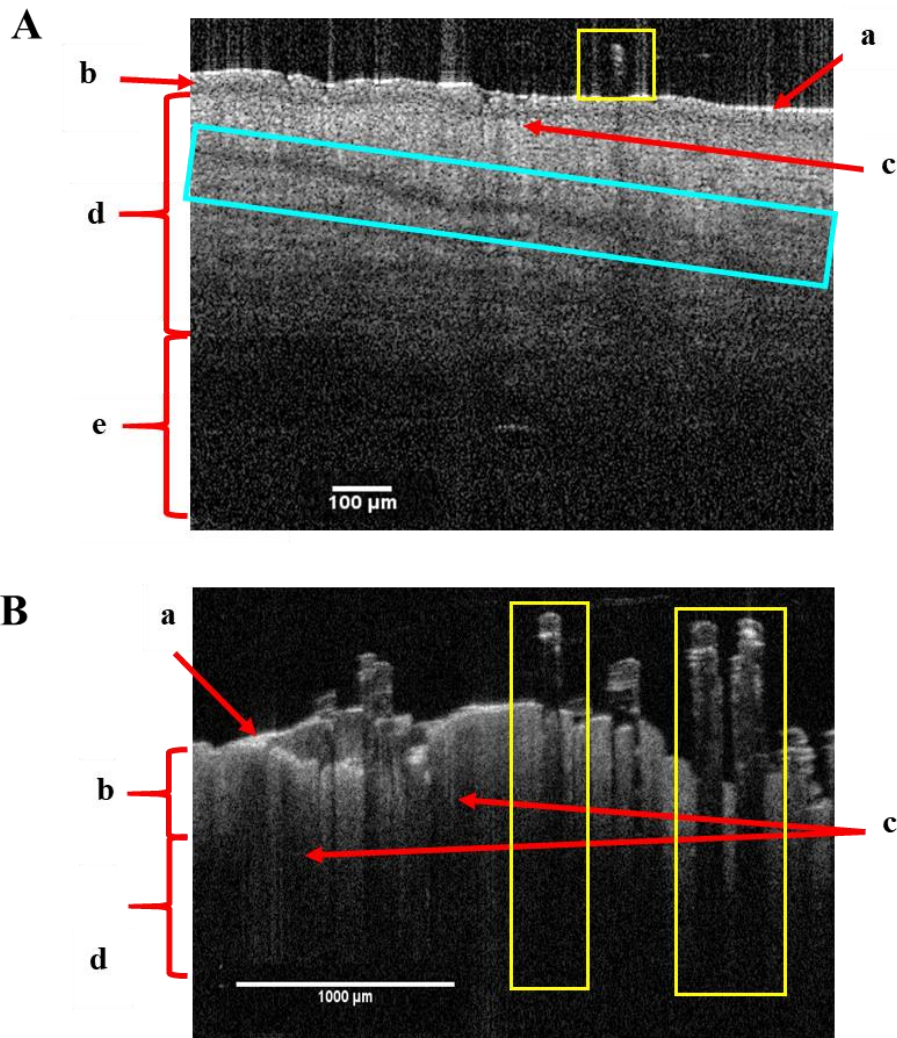


Figure 14.1 OCT images of A) human breast skin and B) porcine torso skin without MN treatment. (a) stratum corneum (b) epidermis (c) rete papillary junction (d) dermis (e) cork board (yellow box) hair follicles (blue box) blood vessel

Although porcine skin is composed of the same layers as human skin (SC, epidermis, dermis), which are represented in the same greyscale contrasts through OCT (figure 14.1B), the main difference is that the depth of each layer is thicker in porcine skin. The SC can still be visualised as the thin white portion measuring approximately $50\mu\text{m}$ (a) at the skin surface, while (b) highlights the epidermis measuring approximately $539\mu\text{m}$. However, the epidermis-dermis junction (c) is not a clear partitioned line as seen in human skin and instead can only be identified by the difference in grey contrast between the epidermis and dermal layers (d). Additionally, these layers are non-uniform (as in human skin), but instead fluctuate in thickness. Another clear difference with human skin is the increased number of hair follicles (outlined in yellow) vertically protruding through the layers to emerge at the top of the skin. Overall, the total thickness of the porcine skin used is $1300\mu\text{m}$. The combination of the thick, non-uniform layers and multiple hair follicles makes it more difficult to distinguish between structures and on occasions a hair follicle exit site, is mistaken for a MN microchannel. Therefore, for clarity and certainly all subsequent MN penetration OCT experiments are conducted using human breast skin. In addition, all OCT images used for analysis in this chapter have been falsely coloured to clarify between the *stratum corneum* (red) and epidermis (green) and identify MN penetration sites.

14.3 Out-of-plane MNs

Figure 14.2 shows evidence of silicon OOP MN penetrating through the SC of human breast skin using thumb pressure. The uniform red line that represents the SC is clearly disrupted and the underlying layers are displaced into a penetration profile that mirrors the characteristic bevelled shape of the MN tip and columnal shaft.

ImageJ measurements of individual microchannels measured on average a depth of $400\mu\text{m}$ from the longest point and a width of $189\mu\text{m}$, corresponding to the fabricated $200\mu\text{m}$ MN width. However, the OOP MNs are fabricated $700\mu\text{m}$ in length, suggesting that only 57% of the total MN length had inserted into the skin. This may present challenges for total bore tissue immersion, which may be required to inject the full drug dosage. As the bore of the MN lies approximately $200\mu\text{m}$ from the tip of the MN, inserting the MN $400\mu\text{m}$ deep should ensure that the bore is submerged into the dermal

tissue. However, the question remains whether this level of depth is sufficient to deliver a full drug dosage without pressure build up or overspill onto the surface of the SC.

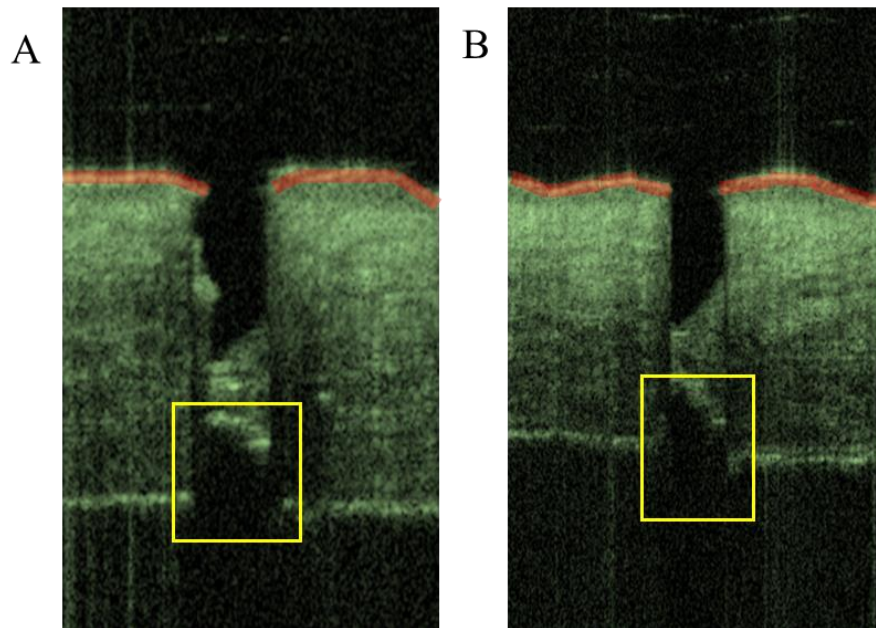


Figure 14.2 (A-B) OCT images of out-of-plane MNs inserted in human breast skin measuring approximately $400\mu\text{m}$ deep and $189\mu\text{m}$ wide. Yellow box highlights light artifacts, which are not part of the microchannel.

As the microchannels are scanned after the OOP Si MNs have been removed from the skin, we can interpret the measurement as a minimum length of penetration as the elastic and retractable abilities of the skin means that once the MNs are removed, the skin is free to bounce back to its original morphology - which is likely to affect the microchannel measurements. This assumption is made for all OCT measurements. Additionally, below each MN insertion a mirror image of the microchannel can be seen, these artefacts are caused by light casting shadows beyond the MN tip and are not to be confused as extended microchannels, represented by the yellow box in figure 14.2. To analyse how all five MNs along the array penetrate with a pitch spacing of $1000\mu\text{m}$, figure 14.3 shows successful penetration with all five MNs, confirming the suitability of a 1×5 OOP silicon MN array.

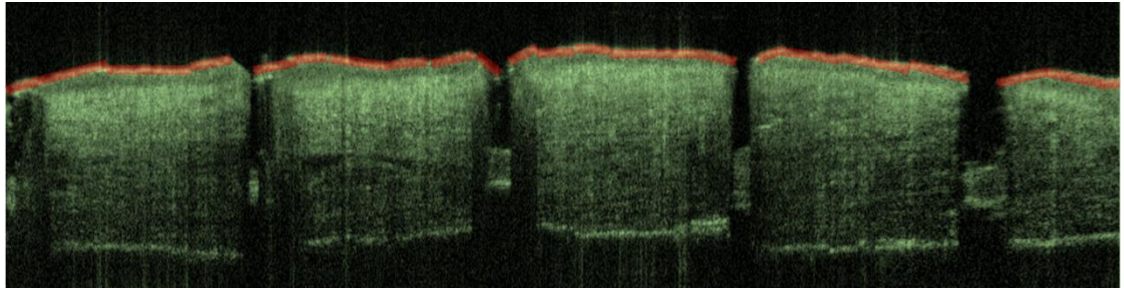


Figure 14.3 OCT image of 1 x 5 OOP MN showing all 5 MN have penetrated.

As a comparison 6 x 6 OOP MN arrays were tested in the same manner to produce the OCT images in figure 14.4A. It is clear that the MNs have not penetrated the skin as successfully as the 1 x 5 MN with the average depth and width measuring $114\mu\text{m}$ and $194\mu\text{m}$ respectively, calculating the depth as on average 29% of the overall MN length.

In an attempt to penetrate deeper, the MNs were pressed into the skin with increased force, however, this proved to be too excessive and some of the silicon MNs broke off into the skin and the baseplate snapped, figure 14.4B. Due to the bed of nails effect, the MN were able to disrupt the SC but could not penetrate to the depths required for total bore coverage.

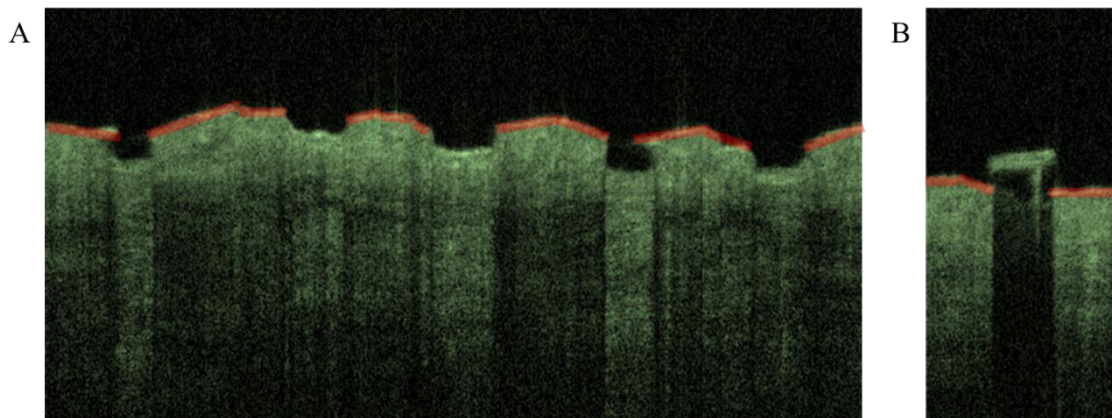


Figure 14.4 OCT image of (A) 6 x 6 OOP MN (B) Broken OOP MN

14.4 In-plane MNs

14.4.1 In-plane MN pitch

To test how pitch spacing affects the penetration ability of in-plane MNs, MNs measuring approximately $549\mu\text{m}$ in height and $350\mu\text{m}$ wide after KOH etching, were designed in 1×5 arrays, where the pitch spacing varied from $297\mu\text{m}$, $1019\mu\text{m}$, $1238\mu\text{m}$, $1521\mu\text{m}$ and $2086\mu\text{m}$. The OCT images in figure 14.5 demonstrated that all MNs arrays designed, irrespective of pitch spacing penetrated through the SC successfully, even though, previously the smaller pitches did not show successful MB staining results. Human skin is softer and smoother in comparison to porcine skin, thus porcine skin makes it harder for the MN to penetrate the tough SC under the same thumb pressure, therefore the smaller pitched MNs, can now easily penetrate through human skin. The above OCT and MB results show that the in-plane MNs are all sharp and robust enough to penetrate through human breast skin and the tougher porcine skin. The average penetration depths and widths of the microchannels created are outline in table 14.1.

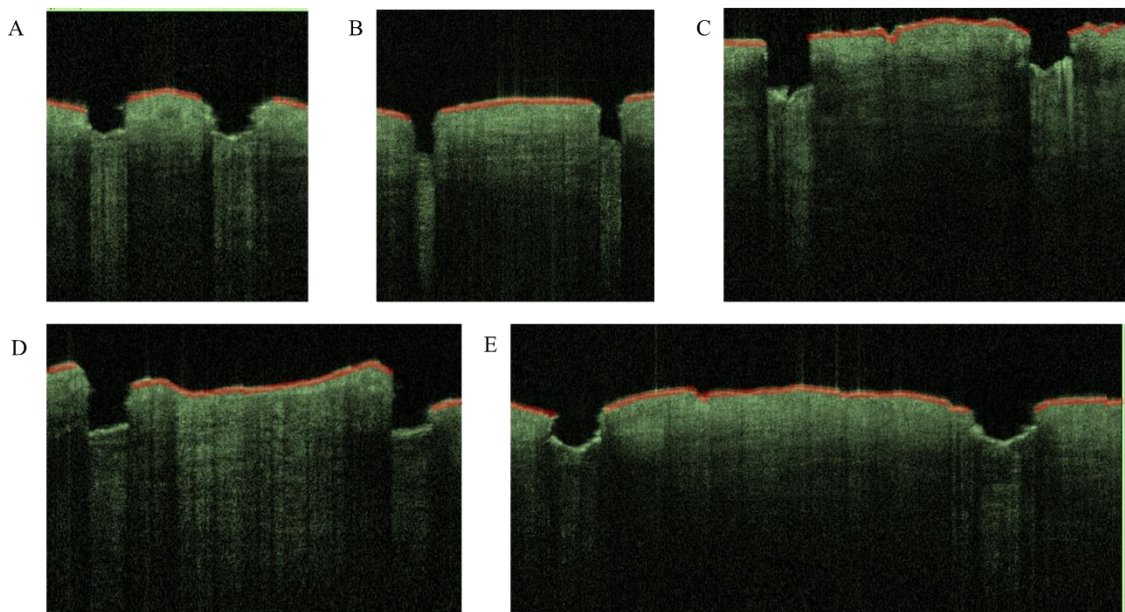


Figure 14.5 OCT image of in-plane MNs inserted into porcine skin with pitch spacing of (A) $297\mu\text{m}$ (B) $1019\mu\text{m}$ (C) $1238\mu\text{m}$ (D) $1521\mu\text{m}$ (E) $2086\mu\text{m}$

Table 14.1 OCT analysis of in-plane MN pitch penetration

Microneedle Pitch (μm)	Average Depth (μm)	Average Width (μm)
297	205	227
1019	318	183
1238	282	283
1521	348	229
2086	306	301
Average	292	245

The figures indicate that on average 53% of the total MN length was inserted into the skin. However, it is still possible that the underlying tissue may have compressed during MN insertion and reformed upon removal, thus resulting in a depth measurement subsequently less than the actual penetration depth. The measurements also show that 70% of the width of the MN has penetrated. This reduced width measurement is indicative of the skins rebound effect after MN removal, as for the MNs to penetrate, the whole width thickness needs to be inserted. However, as the bore of the MN is orientated at the tip of the MN, we can be satisfied that the bore is placed deep into the upper dermis. If the MNs were tested in porcine skin, in line with the MB results, it is likely that the smaller pitch of 297 μm would not have penetrated. However, this result is useful as the MN are fabricated for human use and knowing that their successful human skin penetration is not greatly influenced by pitch size allows for greater flexibility in the numbers of MNs that can be fabricated on a single array in order to maximise drug delivery and minimise cost.

14.4.2 In-plane MN width

To analyse the effects of MN width on skin penetration, the height of all MNs was kept constant at 900 μm which subsequently etched to 549 μm . MN widths tested after KOH etching measured 225 μm , 252 μm , 378 μm , 460 μm , 586 μm ad 665 μm . Figure 14.6 clearly demonstrates that the smaller MN widths penetrated the deepest into the skin. However, widths of 568 μm and 665 μm did not penetrate through the SC, as the OCT image shows that the red SC layer is still intact within the microchannel. As discussed in chapter 9.9, increasing the MN width subsequently increases the angle of the tip in

the $\langle 100 \rangle$ orientation, thus preventing the ability of the MN to penetrate through the SC.

The first MN to successfully puncture the skin had a width of $460\mu\text{m}$, figure 14.6C, which created a microchannel of depth $364\mu\text{m}$ equivalent to 66% of the MN height. However, the width of the microchannel created measured $824\mu\text{m}$, which was 179% wider than the MN itself. This was due to the inability of the MN shaft to fully penetrate and instead, owing to its flexibility, the skin distorted around the MN tip creating a significant indentation (illustrated in figure 14.6H and 14I). MN widths D-G in figure 12 measured 225 , 252 , 295 and $378\mu\text{m}$ using ImageJ, and all showed successful penetration that mirrored the shape of the MN. The depths of the microchannels reached $428\mu\text{m}$, $403\mu\text{m}$ and $411\mu\text{m}$ and $277\mu\text{m}$ respectively, equalling to 78%, 73%, 75% and 50% of the MN length.

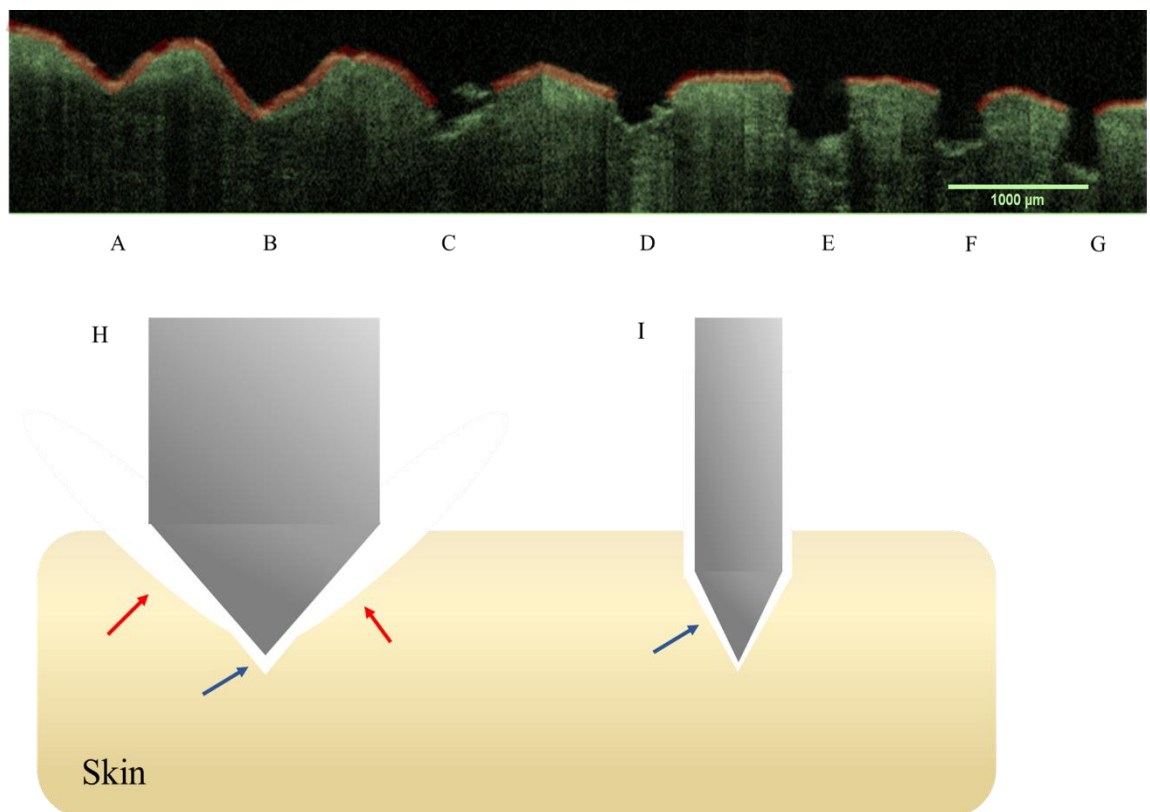


Figure 14.6 OCT image of in-plane MNs inserted into porcine skin with MN width measuring (A) $665\mu\text{m}$ (B) $1586\mu\text{m}$ (C) $460\mu\text{m}$ (D) $378\mu\text{m}$ (E) $295\mu\text{m}$ (F) $252\mu\text{m}$ (G) $225\mu\text{m}$. Schematic diagram MN with wider (H) and thinner (I) MNs inserted into skin. Red arrow highlight indentation, blue arrows show penetration into the skin.

The results summarised in table 14.2, indicate that smaller width MNs can penetrate skin more effectively and form a deeper insertion microchannel that reaches the upper dermis regions. MNs with larger widths do not penetrate reliably, as most tests showed indentation or indentation coupled with shallow epidermal insertion. Therefore, the table records inconclusive penetration results.

Table 14.2 OCT analysis of in-plane MN with varying width

Microneedle Width (μm)	Average depth (μm)	Average Width (μm)
665	-	-
586	-	-
460	364	824
378	277	479
295	428	420
252	403	336
225	411	244

14.4.3 In-plane MN height

To analyse the effect of MN height on penetration depth and determine which heights were suitable for different applications, different MN heights were fabricated that measured 66 μm , 245 μm , 392 μm , 549 μm , 784 μm and 1150 μm after KOH etching (table 14.3). All MNs were fabricated with a mask width of 300 μm which subsequently etched to a width of 460 μm .

Table 14.3 OCT analysis of in-plane MN height penetration

Microneedle Height (μm)	Average Depth (μm)	Average Width (μm)
66	-	-
245	218	630
392	294	529
549	394	453
784	453	579
1150	462	546
Average	364	548

Overall, the results in table 14.3 show that increasing the height of the MN increased the depth of penetration into human skin (figure 14.7), however, as the MN height increases the difference between each MN penetration depth decreases. It was found that longer MNs actually inserted a lower percentage of its MN shaft when compared to smaller MNs. For example, MN lengths of 245, 392, 549, 784, 1150 μm , inserted 89%, 75%, 72%, 58% and 40% of their MN shaft. It was also observed that the smallest height of 66 μm did not break or indent the SC and left no sign of MN application on the OCT in figure 14.7f.

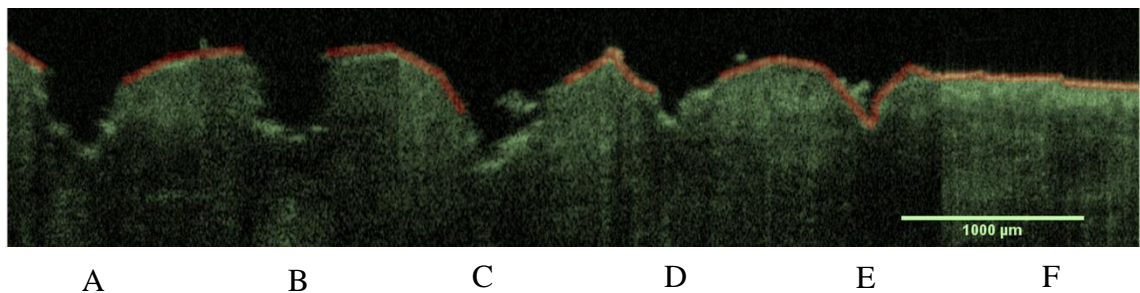


Figure 14.7 OCT image of in-plane MNs inserted into porcine skin with heights spacing of (A) 1150 μm (B) 784 μm (C) 549 μm (D) 392 μm (E) 245 μm (F) 66 μm

As the pitch of the MN arrays were consistent at 1000 μm , this may have been a factor preventing MNs of longer heights from penetrating to their full potential. This was observed previously using MB staining, as on application of the 1150 μm MN the tip penetrated but it was visually identified that the whole length of the MN was unable to submerge into the skin. As illustrated in figure 14.8, the skin may be compacting and clogging between the MN shafts, preventing the MN from being inserted further, thus widening the pitch spacing can relieve the clogging and allow the full length to penetrate.

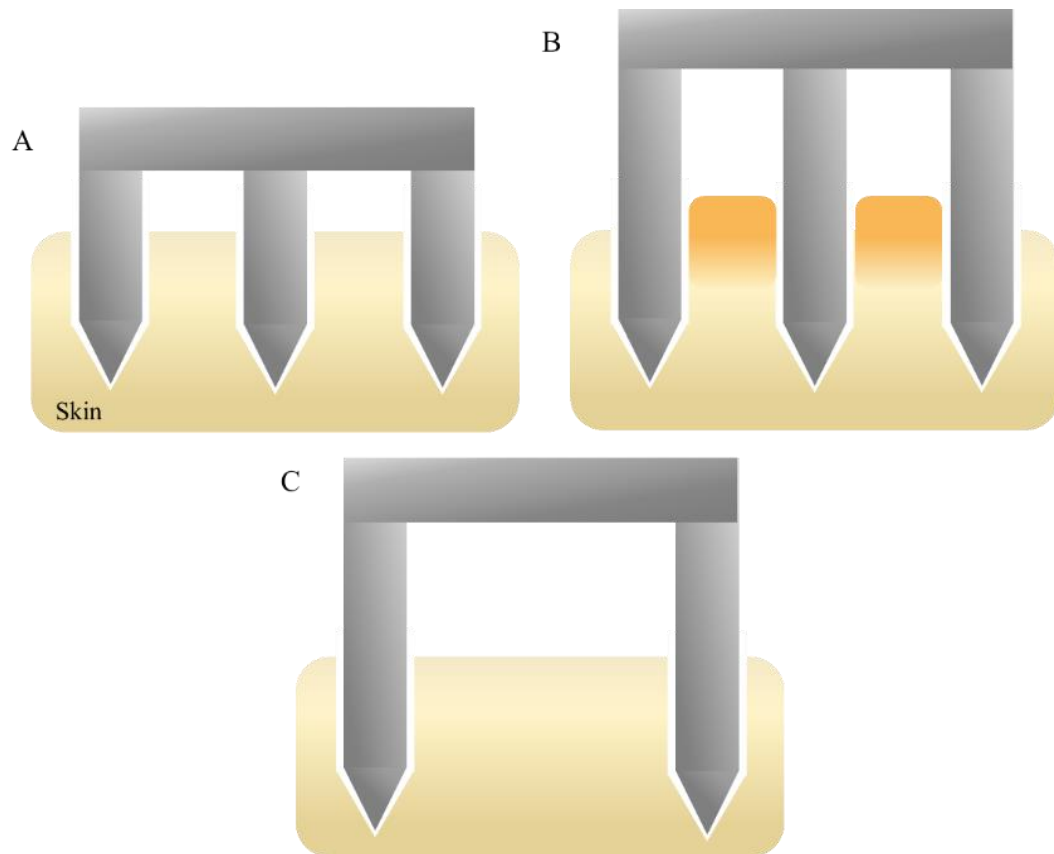


Figure 14.8 Schematic diagram of (A) short MNs penetrating the skin effectively (B) longer MNs penetrating the skin, but causing the skin to compress between the shafts (shown in orange) (C) longer MNs with larger pitch spacing, reducing skin compression issues

Additionally, the shape of the microchannels created provides evidence of how the MN penetrates the skin, i.e., indentation or penetration. Figure 14.7 shows that the longest MNs clearly produce microchannels that mirror the shape of the MN; the microchannels are wide and rectangular toward the skin's surface, while a triangular tip can be seen at the base. Smaller MNs of lengths 392 and 245 μm in figure 14.7D and E show triangular shaped microchannels, as less of the MN shaft is available for penetration, only the tip of the MN has fully penetrated consequently creating a microchannel that mirrors the tip. However, the width of these microchannels has significantly increased from their originally shaft widths of 460 μm to 529 and 630 μm , as the elasticity of the skin has stretched around the MN, revealing indentation rather than penetration, giving the illusion that the microchannel is wider. As there is no distinct microchannel shape apart

from a small tip penetration, it is difficult to determine where the microchannel starts and where the skin is merely indented, therefore penetration results are uncertain.

From this study, it was found that MNs with a <300µm mask design length did not penetrate the skin, while MNs measuring >300µm in mask length all penetrated consistently and reproducibly into human breast skin. Depending on the application, the height of the MN can be fine-tuned to penetrate to exact skin depths and deliver the drug to the necessary skin layer.

14.5 Polycarbonate MN

The penetration characteristics of 4 x 4 (16 MNs) MN arrays were studied by inserting the array into human skin via thumb pressure and removing the MN afterwards. The OCT in figure 14.9, found inconsistent penetration profiles showing no definitive penetration through the SC, although indentations of varying depths were observed. To improve penetration, the MN array was diced into four 1 x 4 arrays to remove the influence of MN pitch and minimise the bed of nails effect. The OCT image in figure 14.9C, shows that penetration was improved by 50% as 2 of the 4 MNs in the array successfully penetrated the SC. However, it was still inadequate for drug delivery purposes.

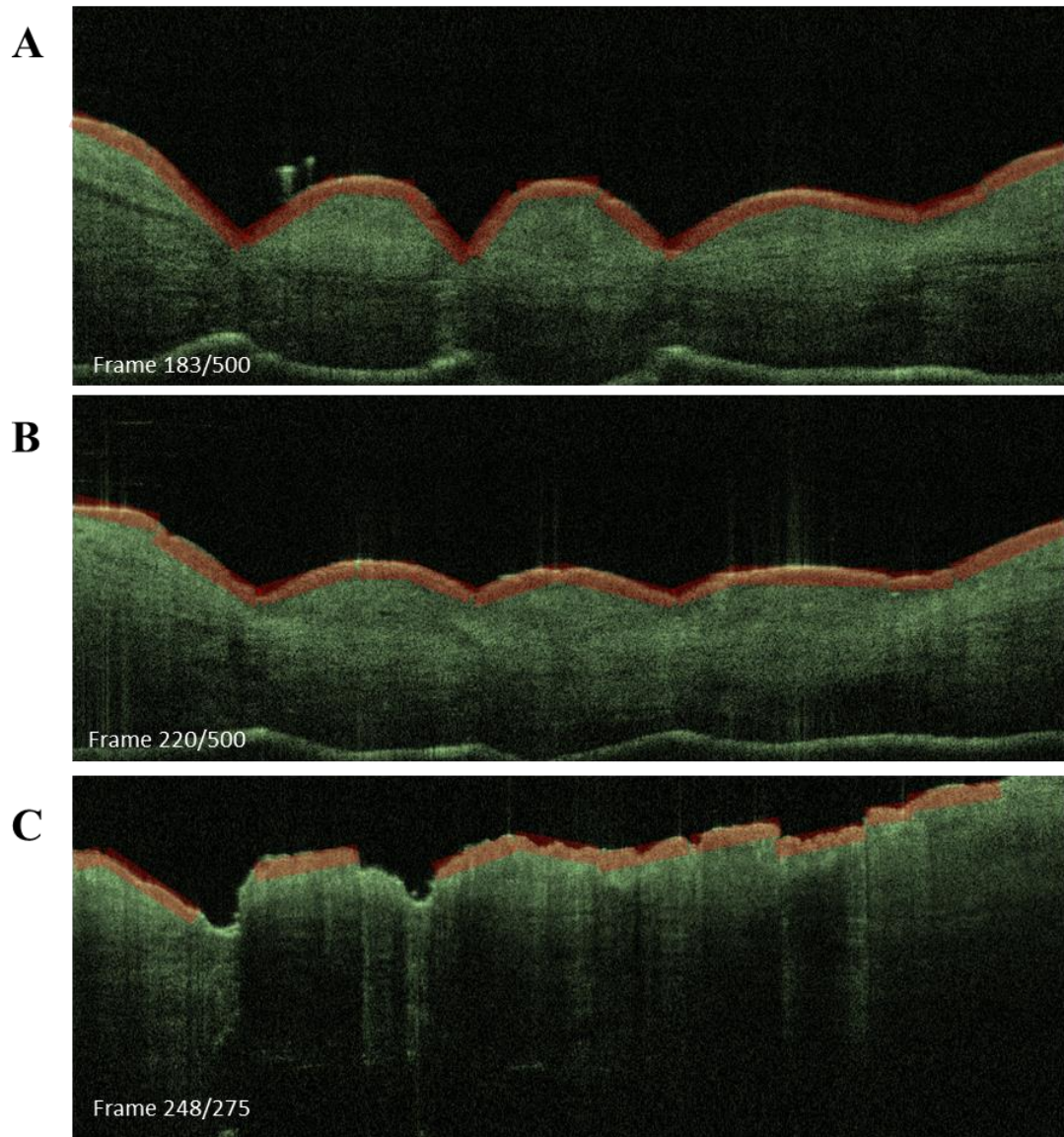


Figure 14.9 OCT images of PC MN (A-B) in a 4 x 4 array, showing inconsistent indentation (C) 1 x 4 array showing 50% penetration

14.5.1 Polycarbonate MN with applicator

As the use of an applicator has been shown to improve PC MN penetration through MB staining studies, utilising the applicator at force 13N and velocity 1,683mm/sec produced the results in figure 14.10. The force of the applicator was sufficient to fully insert the MN into the skin and enable *in situ* measurements to be made. In situ imaging is possible due to the transparent nature of the PC. Using the applicator PC MNs successfully penetrated through the SC and achieved significantly greater penetration depths of 671 μ m, 67% of the MN length. The skin between each MN, demonstrated by

the red arrow, does not bend around the MN shape, but instead forms columns where the tissue has not been compressed by the MN.

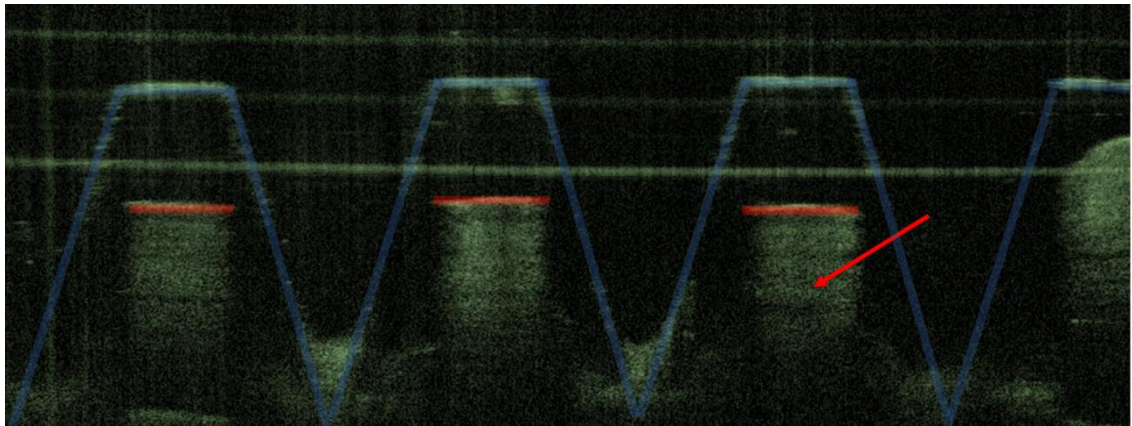


Figure 14.10 OCT images of PC MN in situ after insertion with an applicator. Red arrow demonstrates skin between each MN

14.6 Conclusion

Importantly, these studies have highlighted the significant difference between MN geometry and the morphology of the microchannel insertion profile created. The pitch of the MNs plays a key role in determining the depth to which the MNs are able to penetrate, whereby increasing the pitch facilitates a higher degree of penetration, particularly for longer in-plane MN lengths. OCT is a useful technique that complements MB staining to comprehensively analyse MN geometry and microchannel formation. It was observed that PC MNs do not penetrate the skin without the aid of an applicator. Using an applicator, *in situ* MN measurements were recorded at 67% penetration of the total MN height. In contrast, the applicator was not required for any silicon MNs, and in fact proved counterproductive to MN insertion, as higher velocities caused the OOP MNs to fracture. As silicon is not a transparent material, the OCT light waves were unable to pass through the silicon array base to enable *in situ* visualisation. Consequently, the subsequent microchannels that were created could only be measured as a minimal penetration depth, as the skins natural elasticity makes it recoil upon MN removal. Overall, in-plane MNs of parameters that measure $>66\mu\text{m}$ in height and $<460\mu\text{m}$ in width are suitable for efficient skin penetration, to prevent indentation and can be tailored to penetrate to specific skin depths.

Chapter 15

Mechanical characterisation

15.1 Introduction

As MNs are subjected to a range of forces during insertion and removal into and out of the skin, mechanical testing is a key step to provide quantitative analysis of the required force for penetration into the skin. In addition, upon insertion the MNs need to withstand axial forces to the tip of the MN to avoid fracturing or buckling [252], while, transverse forces will be applied to the MN once embedded within the skin – these are related to the non-uniformity of the skin contours inadvertently causing the MN to break if not fully inserted or due to human movements causing the skin to apply lateral forces [253].

The density of the MN array should also be considered; with a higher density array the applied insertion force is spread across many MNs in comparison to the force applied to a single MN [254]. Further parameters, including the material used, the geometric design of the MN array and the use of different applicators, will also influence how the force is tolerated across each needle. Manual insertion presents more variables as the insertion force differs person to person, while the velocity parameter of an applicator obeys the laws of physics, in that, the faster the compression velocity then the greater the subsequent impact force. Thus, it is important to note that direct comparison between different MNs cannot be made [255], and so, instead, this study will evaluate the fracture force of each type of MN when subjected to a range of forces. As such, we can then define the MN failure force as the maximum force applied directly before fracture [256].

For axial force studies a Hounsfield/Tinius Olsen compression analyser (model H1-KS) was used to compress the MNs at a controlled force and rate. However, during skin insertion studies the force was unable to be recorded due to the inability of the instrument to measure smaller forces precisely on soft, flexible surfaces. Alternatively, to obtain precise measurements to an accuracy of 1µm the MNs were compressed against a solid polymer surface, however, this again is not precisely accurate as it does not simulate movement of the skin during insertion as the force is concentrated at the tip of the MN whereas the skin is flexible and would wrap around the MN tip and distribute

the force over a greater area [245]. Furthermore, the softer skin would allow the MN to penetrate, whilst the solid surface does not allow penetration and instead crushes the MN on continuous force application. Even so, this study is very useful as it verified the physical limitations of each MN and provided data on their corresponding fracture strength, to determine if they can withstand at least 10N of thumb pressure force.

15.2 Out-of-plane MNs

Axial compression tests were performed on a single MN, a 1 x 5 array, and a 6 x 6 array (figure 15.1A). The graph demonstrates that the compression force fluctuates between 3N and 8N for a compression distance of approximately 250 μ m; this suggests the tip of the single MN is partially withstanding the force but also crumbling away, which is confirmed in the SEM images of figure 15.1 B, C, D.

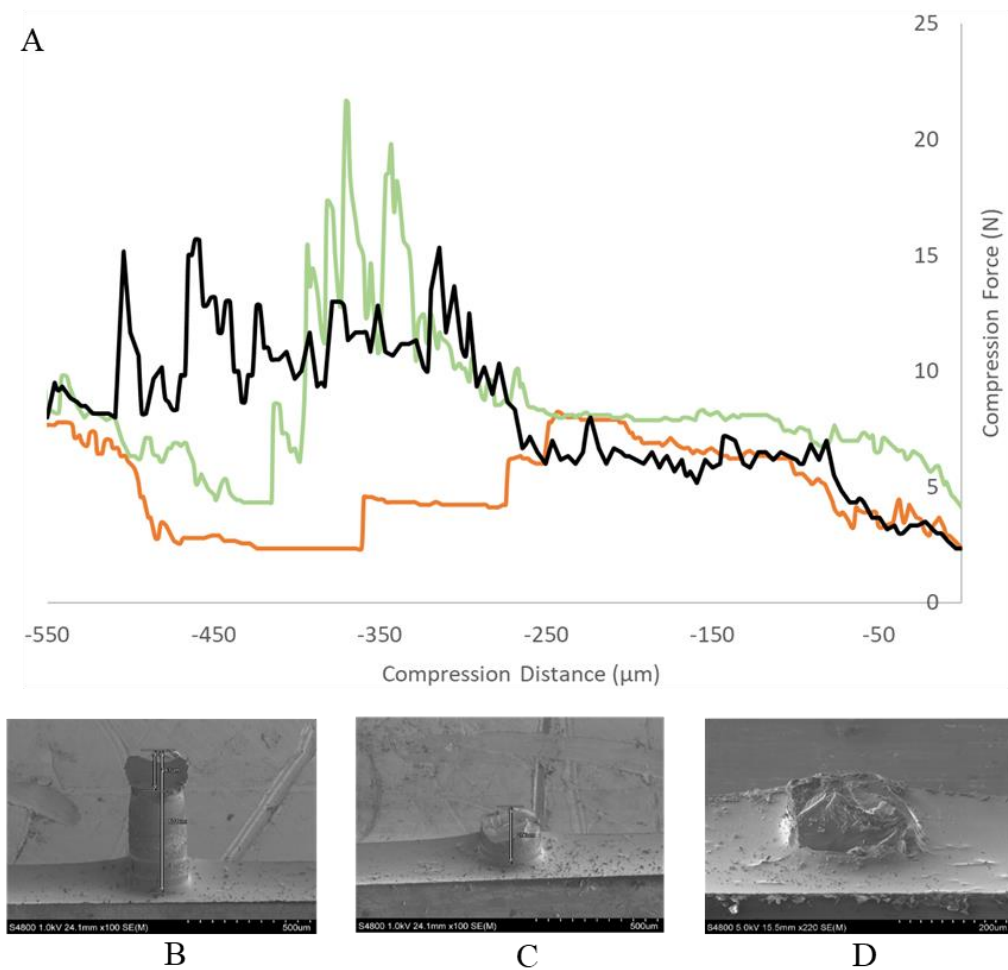


Figure 15.1 (A) Graph of out-of-plane MN compression at 0.45mm/sec showing a single MN (orange) 1 x 5 array (black) and 6 x 6 array (green). SEM images of single MN after compression at (B) 10N (C) 20N (D) 100N

At 250 μm it is seen that the single MN fractured at a maximum force of 8N; however, the analyser continued to descend and comes back into contact with the MN on two further occasions indicating that the MN fractured in 3 separate places. The higher density arrays of 1 x 5 and 6 x 6 are seen to have several fractures, attributable to several MNs breaking over different compression distances. It is seen that the 1 x 5 MN array breaks between 250-400 μm reaching a maximum force of 22N, while the 6 x 6 array breaks over a compression distance of between 250-510 μm and reaches a maximum force of 16N. The MNs that are fractured cannot be distinguished individually as the readings for the continuous fracturing of multiple MNs are captured together to read as an overall result. However, the graph indicates that the 6 x 6 array withstands the force longer than a single MN; it is likely that the force is distributed over the whole array of 36 MNs instead of being focused on a single MN tip. The results indicate that the multi-MN arrays can withstand forces of greater than 10N, whilst a single MN will not. This implies that larger arrays will not fracture upon thumb pressure insertion, which is deemed <10N.

Furthermore, the MNs were compressed against a solid surface with little elasticity or movement, and it is likely that the single MN will be able to withstand a greater force upon penetration through the softer skin.

15.3. In-plane MNs

15.3.1 In-plane pitch

To analyse the effects of pitch spacing on fracture force, each 1 x 5 in-plane MN array with varying pitch designs of 500 μm , 1200 μm , 1400 μm , 1700 μm and 2300 μm as described in chapter 9.10, were subjected to 50N of force to establish their maximum failure force, figure 15.2. For future reference, pitch designs will be referred to as P500, P1200, P1400, P1700 and P2300.

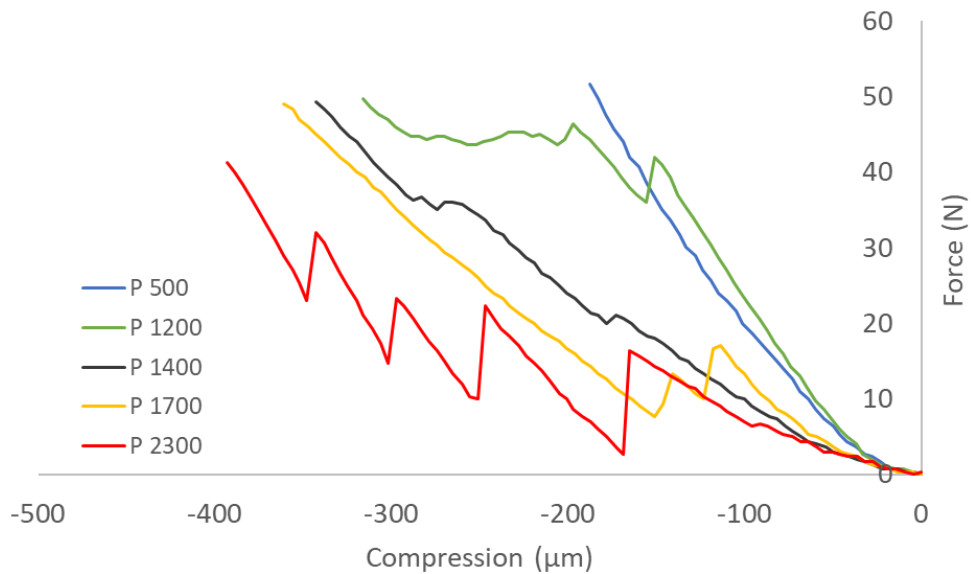


Figure 15.2 Graph to show compression of in-plane MN up to 50N with varying pitch measurements (Blue) 500 μm (Green) 1200 μm (Grey) 1400 μm (Yellow) 1700 μm (Red) 2300 μm .

The MNs show that, in general, all arrays observe some form of fracturing upon force exertion, except for P500; the smallest pitch shows no fracture properties and is capable of withstanding <50N to a compression distance of 188 μm , this means the fracture force for P500 is >50N. This result is due to the bed of nails effect, as the MNs are close together, they combine their strength as if they were one, to withstand a larger force than if individually. Spacing the MNs to P1200 shows an initial fracture at a force of 42N and a second larger force of 45N between compression distances of 130 μm - 200 μm . Increasing the distance further to P1400 again yields two small fractures at the tip of the MN at compression distances of 173 μm and 270 μm equating to 21N and 36N. The larger spacing of P1700 shows two fractures between 100 μm and 150 μm compression measuring 15N and 13N. These results demonstrate that increasing the pitch decreases the amount of force required to fracture the MN as the MNs are further apart the force is dispersed over a wider area. Thus, each MN acts independently of each other resulting in a lower fracture force. Additionally, all arrays show two dominant fractures at maximum and minimum distances of 100 - 270 μm ; illustrating this in figure 15.3, shows that these distances correlate to the tip of the MN. However, as MN array P2300 comprises of a 1 x 3 MN design, (in order to obtain the pitch spacing on the same device size), its results show x5 fracture sites at forces 15N, 22N, 22N, 32N and 4N.

Suggesting that fewer MNs on an array are either enabling individual readings for each MN or the MNs are breaking in more than two points along its length. As the same amount of force is distributed over 3 MNs, not 5, each MN experiences a higher force and thus fractures more easily.

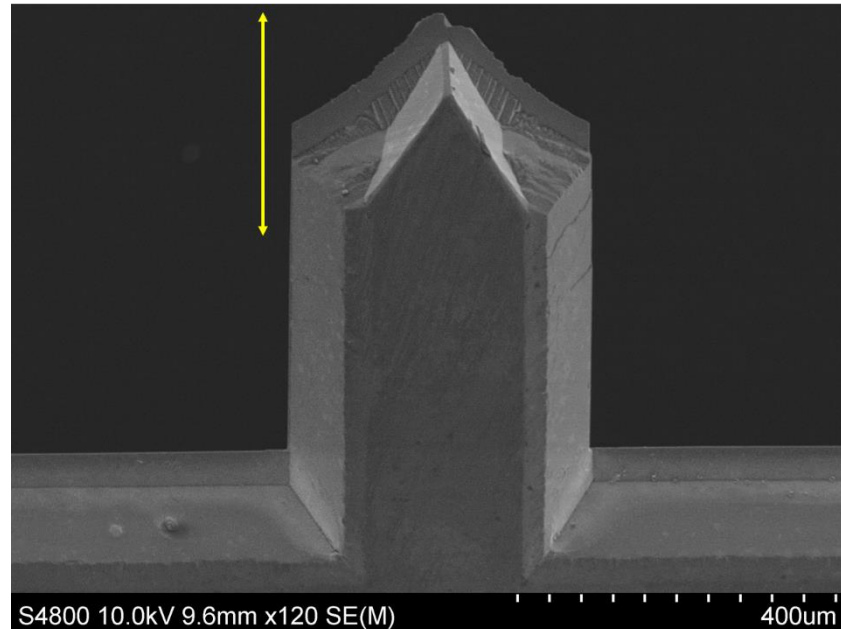
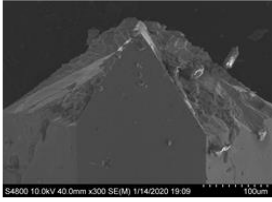
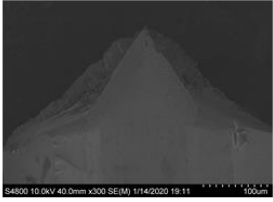

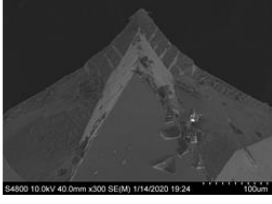
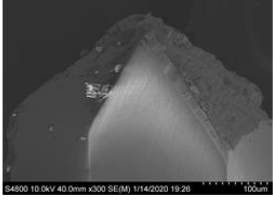
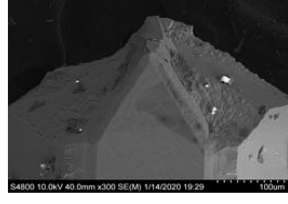
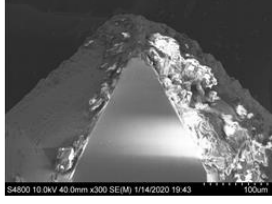
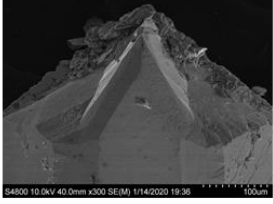
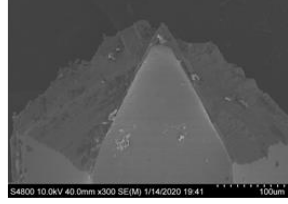


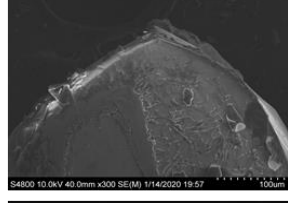
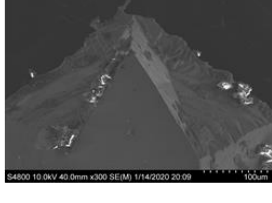
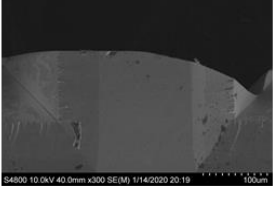
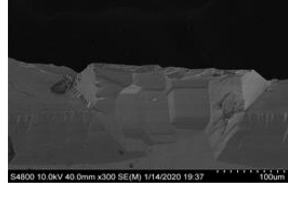


Figure 15.3 SEM image of an exemplar MN, demonstrating that a compression distance of 270µm (yellow line) correlates to the MN tip fracturing

To assess the nature of the fractures, SEM images of the MN tips after testing at 10N, 20N and 50N (table 15.1) were taken. At 10N, it's seen that all MNs maintained their original structure with no significant breakages; there is slight debris on all the MN tips, suggesting the (110) planes are crumbling due to their thinner nature, but overall, all MNs, irrespective of pitch, are capable of withstanding 10N, equivalent to approximate thumb pressure. Increasing the force to 20N again sees minimal damage to MNs P500 - P1700, however, the largest pitch spacing P2300, fractured towards the base of the MN. Increasing the force further to 50N caused MNs P1200 and P1400 to chip towards the tip of the MN. The larger fractures produced with P2300 are a result of the MN completely fracturing at the base of the MN. All MN arrays excluding P2300, can tolerate a force of at least 20N, while at 50N the MN tips begin to chip. This demonstrates that all pitch designs below 2300µm, are suitable to penetrate the skin

without fracturing, as the point of failure force is higher than the 10N force exerted by thumb pressure.

Table 15.1 SEM images of In-plane MNs of different pitch subjected to forces of 10, 20 and 50N

		Force		
		10N	20N	50N
MN Pitch	P500			
	P1200			
	P1400			
	P1700			
	P2300			

15.3.2 In-plane width

To evaluate the effect of MN width on the force required for MN failure, MN arrays of different widths 100 μ m, 200 μ m, 300 μ m and 400 μ m (W100, W200, W300 and W400), but with a constant length of 700 μ m, were subjected to 10N, 20N and 50N of force, figure 15.4 and table 15.2. The smallest width, W100, shows several significant MN

breakages at 10N, 27N and 41N; these fractures are at compression distances of between 87 μ m and 316 μ m corresponding to the tip and shaft of the MN breaking.

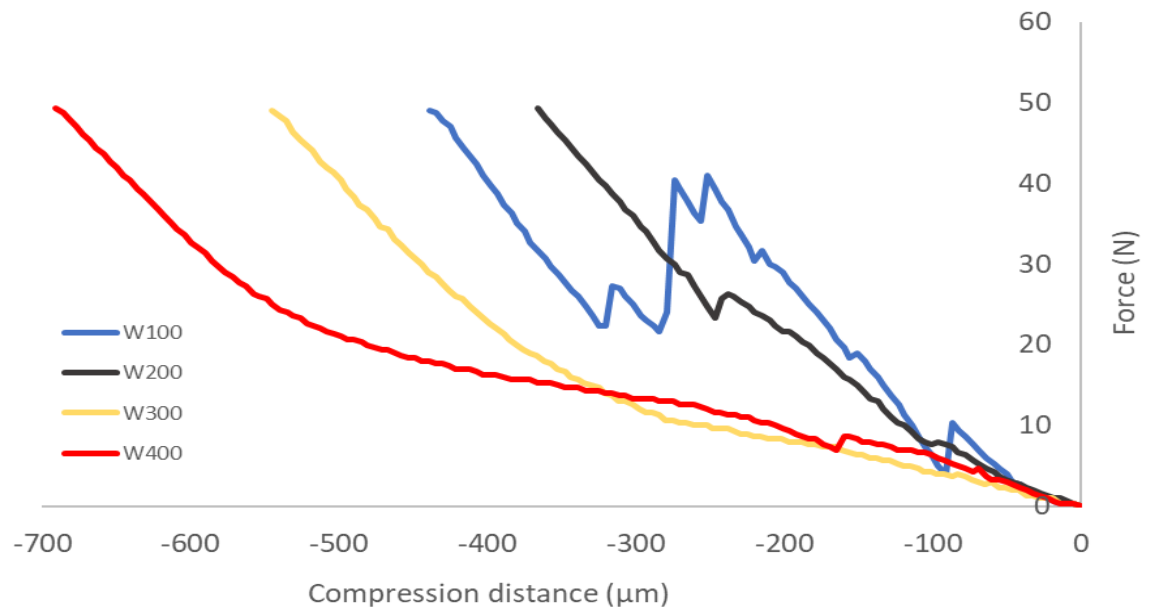
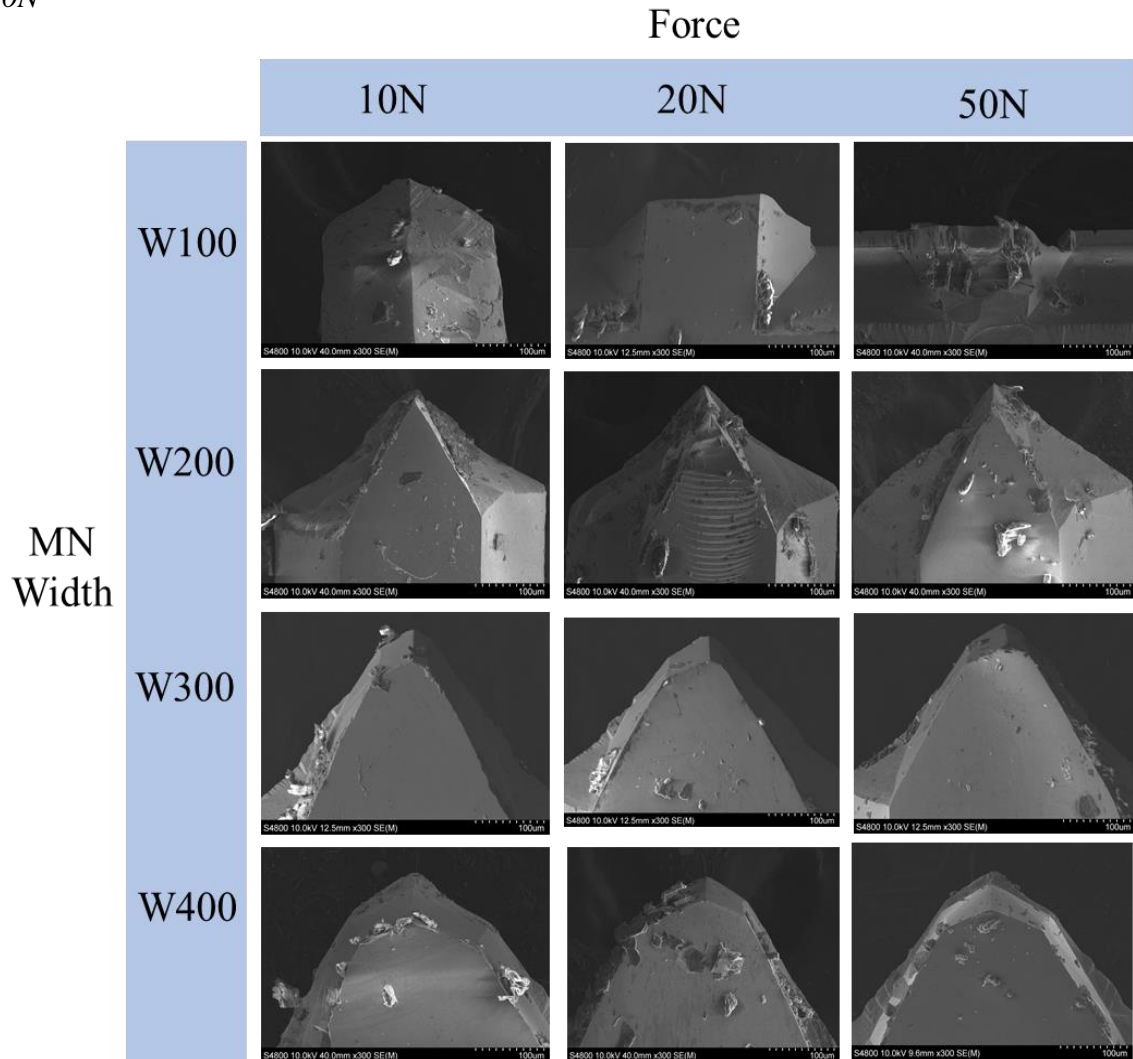


Figure 15.4 Graph showing compression of in-plane MN up to 50N with varying width measurements (Blue) 100 μ m (Grey) 200 μ m (Yellow) 300 μ m (Red) 400 μ m

The SEM images in table 15.2 confirm that W100 breaks in the middle and at the base of its shaft. In comparison W200 shows a single smaller breakage at a compression distance of 237 μ m resulting from 26N of force. SEM images reveal that the smaller fracture is due to tip crumbling as the images show no significant difference in tip structure for all forces tested. Increasing the width to 300 and 400 μ m yielded little to no fractures, which is confirmed through SEM imaging, as no significant tip deformation is observed. The notable debris left on the MN tips demonstrates that the silicon is crumbling somewhat, but overall, both widths endured a force of <50N. The mechanical strength of the MNs was found to increase with increasing width, due to the surface area of the MN becoming larger and thus enabling a larger load force to be tolerated. All MN widths were capable of withstanding at least 10N of thumb pressure force and thus their design is suitable for skin penetration use without fracture.

Table 15.2 SEM images of In-plane MNs of different widths exerted to forces of 10, 20 and 50N



15.3.3 In-plane height

The effects of compression force on MNs of different heights: 500 μm , 700 μm , 900 μm , 1200 μm and 1500 μm are presented in figure 15.5 where corresponding MNs are referred to as H500, H700 etc. Figure 15.5 shows that the smallest MN, H500, exhibits two simultaneous fractures above 10N at compression distance 114 μm and 156 μm . Increasing the heights to 700 μm and 900 μm sees a similar trend where the MNs fracture at 142 μm and 151 μm from a force of 10N and 15N, respectively. As the compression distance is still in the range of the MN tip these fractures are likely due to the tip crumbling or chipping, as previously discussed. Increasing compression force shows no

additional fractures and that MNs can withhold $<50\text{N}$ of force. However, MNs H1200 and H1500 both experience several larger fractures at compression distances $123\mu\text{m}$, $270\mu\text{m}$ and $453\mu\text{m}$ for H1200 and $87\mu\text{m}$ and $298\mu\text{m}$ for H1500, corresponding to 13N , 18N and 37N , and 6N and 29N of force, respectively. As these fractures are large and there is a corresponding large drop in force, it is believed that the shaft of the MN has failed in several places. However, as all MN heights, with the exception of H1500, fractured above 10N , they are all deemed to be suitable to penetrate the skin via thumb pressure.

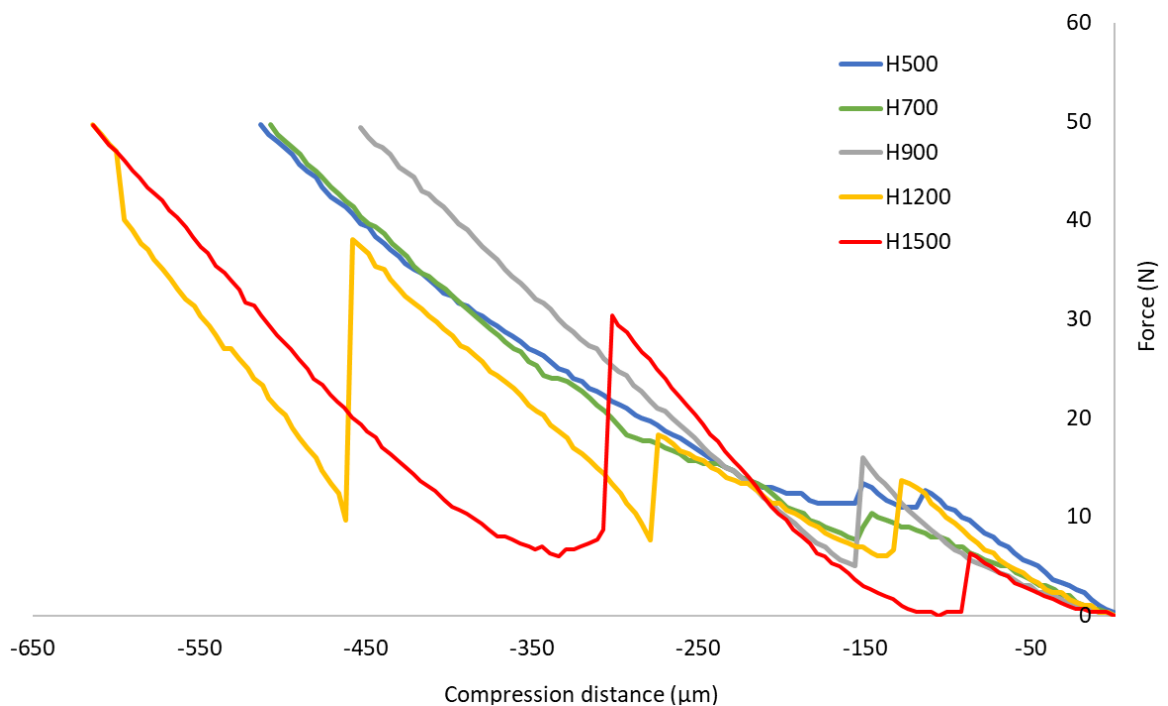
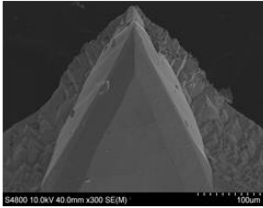
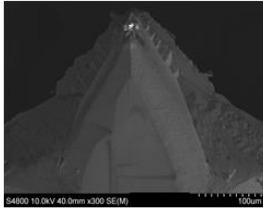
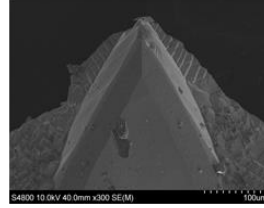

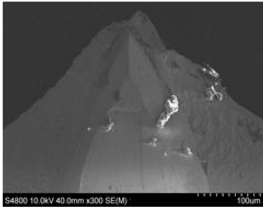
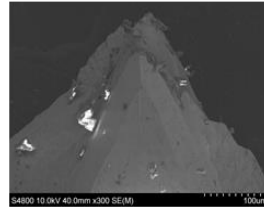
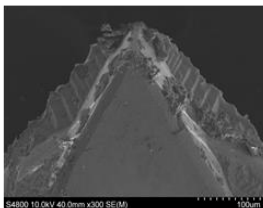
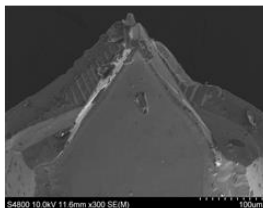
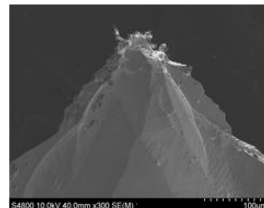
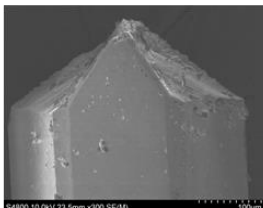
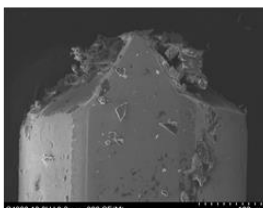
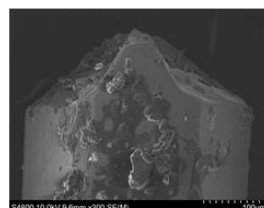

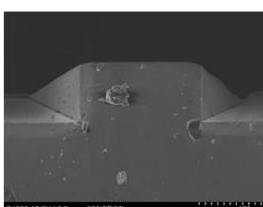
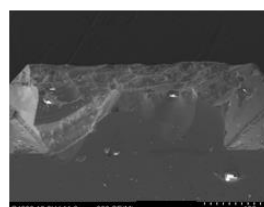


Figure 15.5 Graph to show compression of in-plane MN up to 50N , with varying heights of (Blue) $500\mu\text{m}$ (green) $700\mu\text{m}$ (grey) $900\mu\text{m}$ (yellow) $1200\mu\text{m}$ (red) $1500\mu\text{m}$

SEM images in table 15.3 confirm MN fractures in line with figure 15.5 to determine the mode of failure. 10N of force did not significantly alter the tip structure of any of the MNs apart from H1500, where complete tip removal was observed. Increasing to 20N yielded no change for H500, however, minor chips are created in the (110) plane of H700 and H900. Additionally, the tip of the MN for H1200 has begun to blunt, leaving debris on the shaft of the MN. The longest height H1500 MN has the most significant fracture in the shaft, losing the whole MN structure. Forces of 50N continue to only chip MNs H500, H700 and H900 in the (110) plane, while H1200 continues to blunt and crumble.

Table 15.3 SEM images of In-plane MNs of different heights exerted to forces of 10, 20 and 50N

		Force		
		10N	20N	50N
MN Height	H500			
	H700			
	H900			
	H1200			
	H1500			

As H1500 has already significantly fractured, the base of the MN continues to compress but does not significantly break further. These results demonstrate that the longer the MN the more fractures are likely to result upon exerting higher forces. This can be explained by the fact that centre of mass for a MN is located in the middle of the shaft, thus, for longer MNs this centre is further away from the array base, removing the structural support to prevent any breakages. All but one of the MNs have been shown to withstand a force >10N, the exception being H1500. However, as the tests were

conducted on a solid compression surface it is believed that H1500 could withstand the same penetration forces into softer skin tissue.

15.3.4 In-plane MN conclusion

The primary mechanism of failure for the in-plane MN was compression at the tip of the MN causing it to crumble, chip or blunt. Without the support of a wider MN structure, application of higher forces saw longer MNs and larger pitched MNs fracture at the shaft and the base of the MN. However, all MN geometries were mechanically strong enough to withstand at least 10N of force represented by thumb pressure insertion into skin.

15.4 Polycarbonate MNs

Compression tests were carried out on 4 x (4 x 4) and 1 x (4 x 4) MN arrays equating to 64 and 16 MNs per array, respectively. Each test was performed in triplicate at a rate of 0.05mm/sec with a loading cell programmed to forces of 10N and 50N. Figure 15.6 shows a smooth exponential curve characteristic of bending properties. Thus, both MN arrays can tolerate large forces without fracturing.

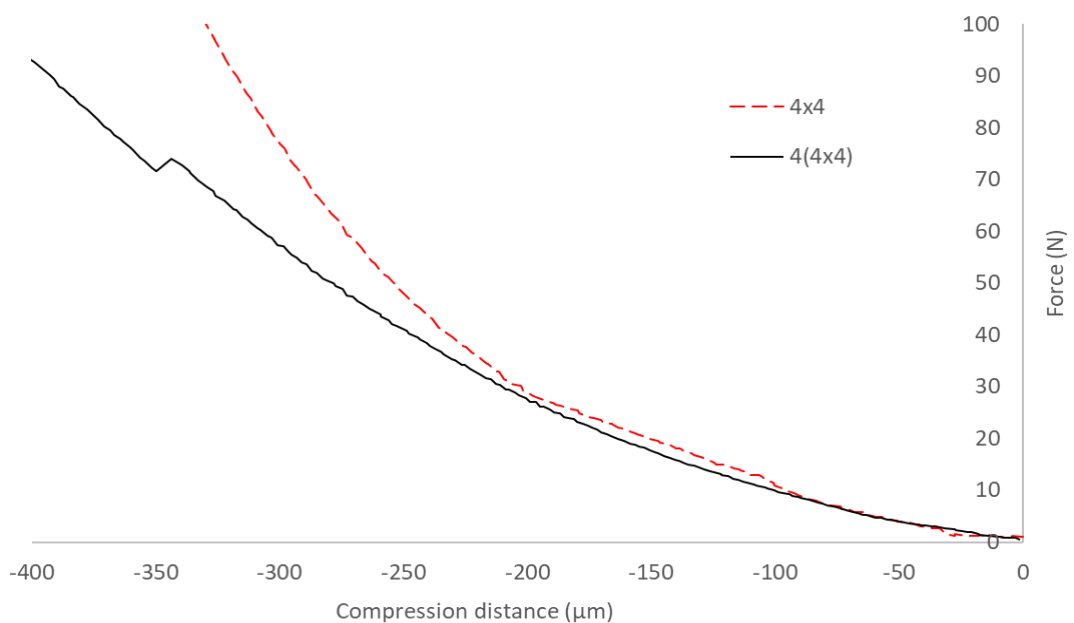


Figure 15.6 Graph to show compression of 4(4 x 4) and 4 x 4 polycarbonate MNs up to 100N of force

SEM images in figure 15.7 demonstrate the bending properties of polycarbonate and that applying 10N of force reduced the MN height from 1000 μ m to 838 μ m converting the tip of the MN into a flat blunt edge. Increasing the force to 50N reduced the MN height further to 782 μ m and exaggerated the tip deformation. PC MN's demonstrate a more favourable failure mechanism when compared to silicon MN due to the propensity of the PC to bend rather than fracture into the skin. However, more importantly, the tip of the MN has become blunt, which could prevent the MN from penetrating effectively. At 10N of force, the tip has blunted upon compression onto the solid polycarbonate surface, rendering it unusable upon thumb pressure application.

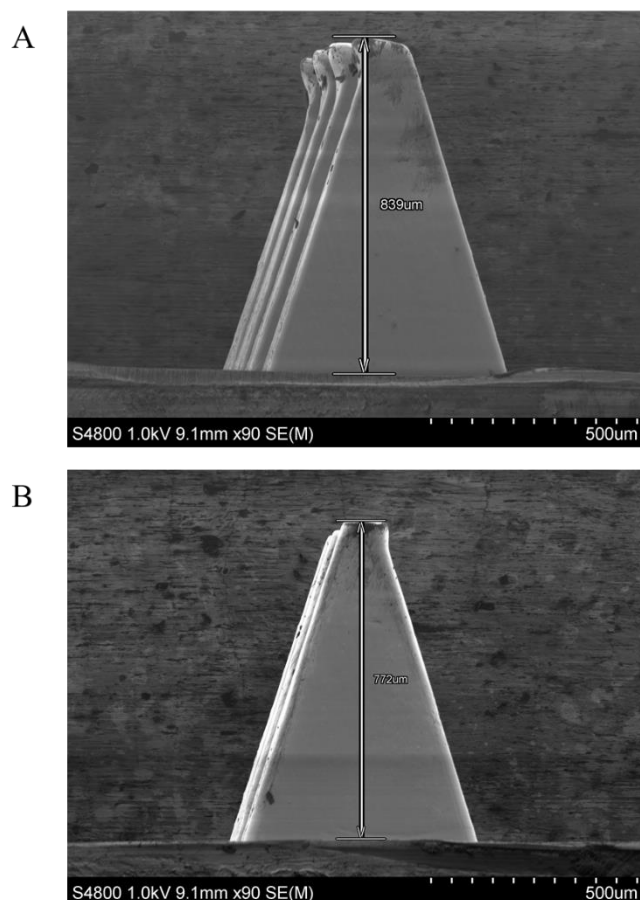


Figure 15.7 SEM images of polycarbonate MN after compression of (A) 10N (B) 50N

Chapter 16

Hollow microneedle injection

16.1 Introduction

The administration of drugs and therapeutic agents explored in this thesis, utilise solid and hollow MN devices fabricated as either OOP or in-plane silicon or PC MN's. Solid MN can be classified as either a two-part delivery system such as “poke and patch”, or a single system by directly coating the MN with the therapeutic agent. In contrast, hollow MNs inject the solution directly into the skin tissues [257], [258]. To validate hollow MNs for drug delivery, the next chapter characterises and optimises syringe adaptable hollow MN designs.

16.2 Hollow Out-of-plane MNs

16.2.1 Syringe adaptor

Chapter 11 describes the fabrication and optimisation of a MN adaptor that connects the MNs to a syringe. To determine if the adaptor is suitable to enable hollow MNs to deliver solutions, 10mls of fluorescent FITC-insulin, to act as a visual aid, was loaded into a syringe and gently injected through the MNs via thumb pressure on the plunger. Figure 16.1 demonstrates that 3 of the 5 MNs produce straight, consistent jets indicating that solutions were able to flow easily through the MNs. Lack of flow through MN 1 and 5 were due to gluing errors blocking the bores of the MNs.



Figure 16.1 1 x 5 MN array bonded to a syringe adaptor showing injection of FITC-insulin

16.2.2 Controlled MN injection into skin

To evaluate the potential for hollow MN to inject into skin, initial tests inserted the MN's into porcine skin and manually injected the insulin using thumb pressure – similar to hypodermic needle injection methods. However, due to the pressure build-up of injected fluid within the skin, the solution over-flowed onto the skin surface. To rectify this, a delivery system was constructed that included a syringe pump to monitor and control the delivery rate and a micrometre that controlled the upward and downward motion of a platform that held the skin. The MNs were connected to a syringe via a system that aligned the MNs perpendicular to the platform and held them stationary. This enabled the platform to be raised towards the MN and permitted precise and adaptable insertion of the MNs into the skin, figure 16.2.

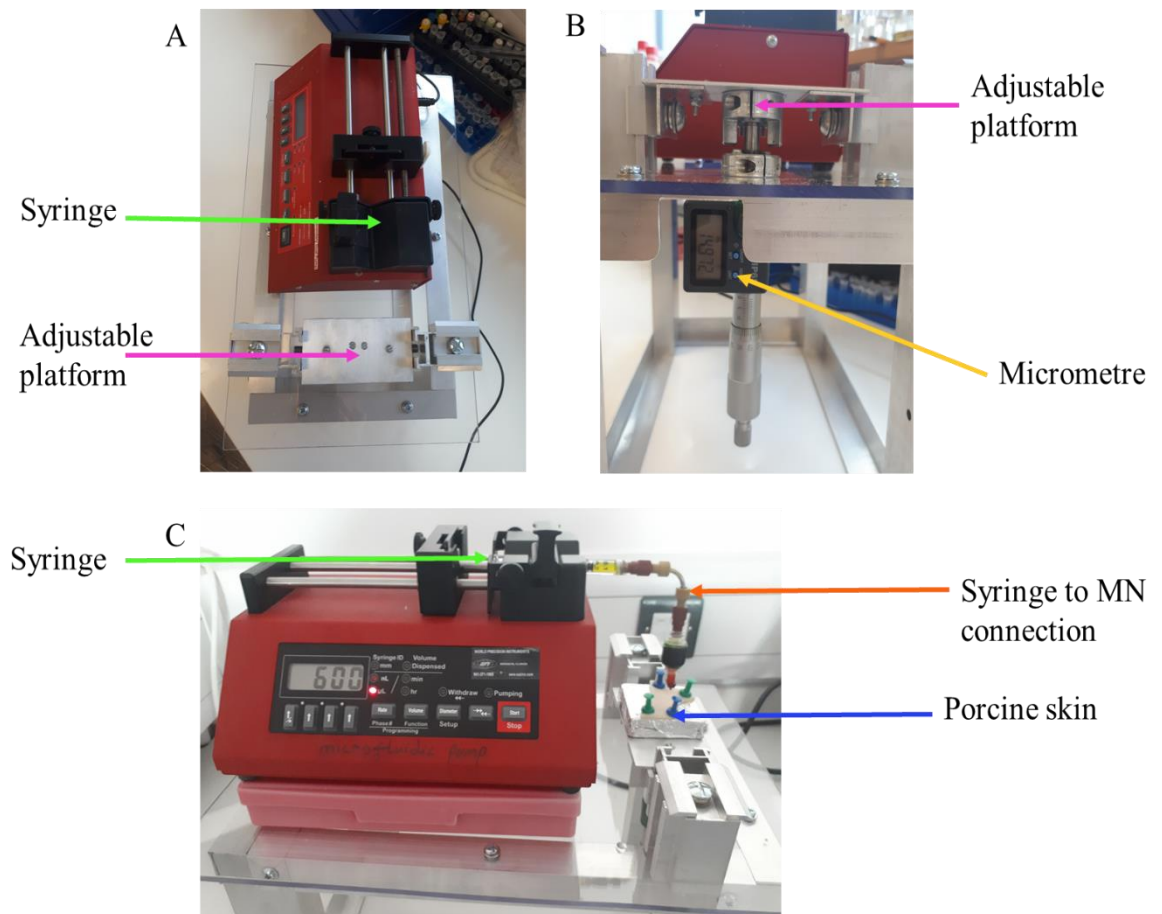


Figure 16.2 syringe pump and micrometre workstation to aid drug delivery parameters

As the MN were 700 μm in height, once the skin came into contact with the MN tip, the micrometre was zeroed, and the platform subsequently raised by 700 μm to insert the MNs into the skin sample. The syringe pump was then programmed to 10 $\mu\text{l}/\text{min}$ and loaded with fluorescent DIL (1,1'-Dioctadecyl-3,3,3',3'-Tetramethylindocarbocyanine Perchlorate) dye. However, even though the delivery rate has decreased significantly, the solution leaked over the surface of the skin, indicating that the pressure was still too high. It was recognised that this was due to the porcine skin tissues compacting, preventing the dye from diffusing away fast enough to enable the full 10 μl to be injected into the space. To reduce pressure build up in the skin, a small opening or pocket beneath the injection location was created, which allowed the dye to be injected. Once the MN is fully inserted, retracting the platform by 100 μm , consequently removes the MN out of the skin by 100 μm but maintains the opening of the microchannel below. Repeating the injection saw no dye leakage onto the skin and full injection of the 10 μl volume. To confirm and visualise that the dye had successfully injected into the skin, the skin was immediately frozen in liquid nitrogen and sectioned vertically to 8 μm using a cryostat, producing histological slides of the skin cross-section to observe the microchannel created.

Fluorescent microscope images (figure 16.3) taken at an absorption wavelength of 538nm, show an OOP MN microchannel. Figure 16.3 A shows a perfect MN microchannel that measures 495 μm deep and 322 μm wide. Additionally, confirmation of DIL injection is indicated by the high concentration of red dye at the base of the microchannel. This demonstrates that the OOP silicon MNs are efficient at delivering small volumes at lower, controlled flow rates. However, image 16.3 B also confirm penetration but due to the uncertainty of histological sectioning cutting the skin directly through the microchannel centre is difficult and sometimes does not yield perfect images. Future experiments will analysis the maximal volume and maximal flow rates for injection to improve delivery aspects.

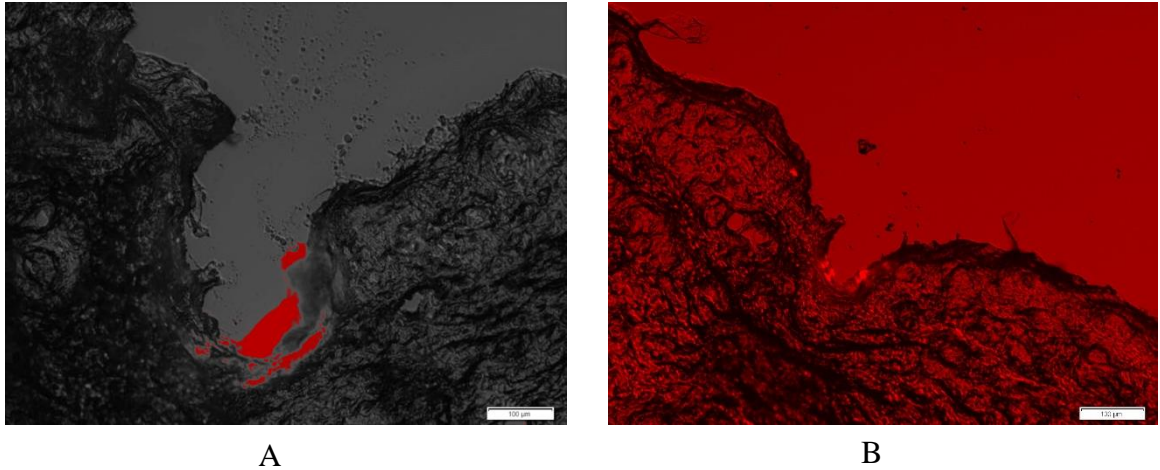


Figure 16.3 Fluorescent microscope image of OOP MN microchannel, injected with DIL dye (A) perfect representation image and (B) histological sectioning imperfect

16.3 Hollow in-plane MNs

Hollow in-plane MNs were fabricated to include open grooves down the shaft of the MN, (chapter 10). Utilising this process, two separate MN designs can be fabricated with either a single MN with the open channel or two MNs bonded together to enclose the channels and form a central channel along the length of the two bonded MN devices. Each MN was inserted into an adaptor and connected to a syringe filled with 10mls of MB dye diluted in water. Figure 16.4A shows injection through a single MN device with an open MN channel. Although the MNs can direct fluid through the channel, the streams produced converge to produce non-uniform flow.

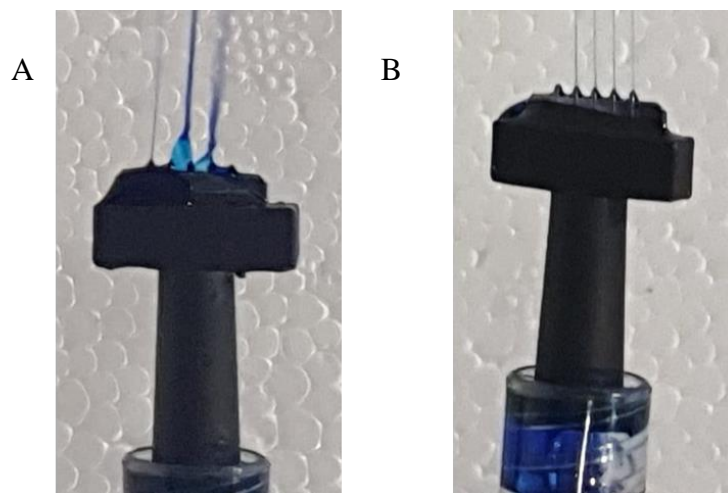


Figure 16.4 MB syringe injection through in-plane MNs with (A) single open channel (B) double MN with closed channel

In contrast figure 16.4B, shows a closed bonded MN channel, which, upon injection directs the fluid in parallel linear streams, enabling a better controlled directional injection.

Fluorescent histological sectioning was conducted (as previously described for OOP MNs) to visualise the microchannels formed in porcine skin after injection of 10 μ l of fluorescent FITC-insulin, figure 16.5. Although the skin shows some green autofluorescence (figure 16.5 C), the indentations in figures 16.5 A and B created from the MN penetrating through the SC, observe a stronger green, fluorescent portion, characteristic of FITC-Insulin, centred near the tip of the microchannel formed. This suggests both open and closed hollow in-plane MNs can successfully inject into porcine skin. Future experiments will be conducted on the maximal volume and flow rates each MN can inject for improved delivery.

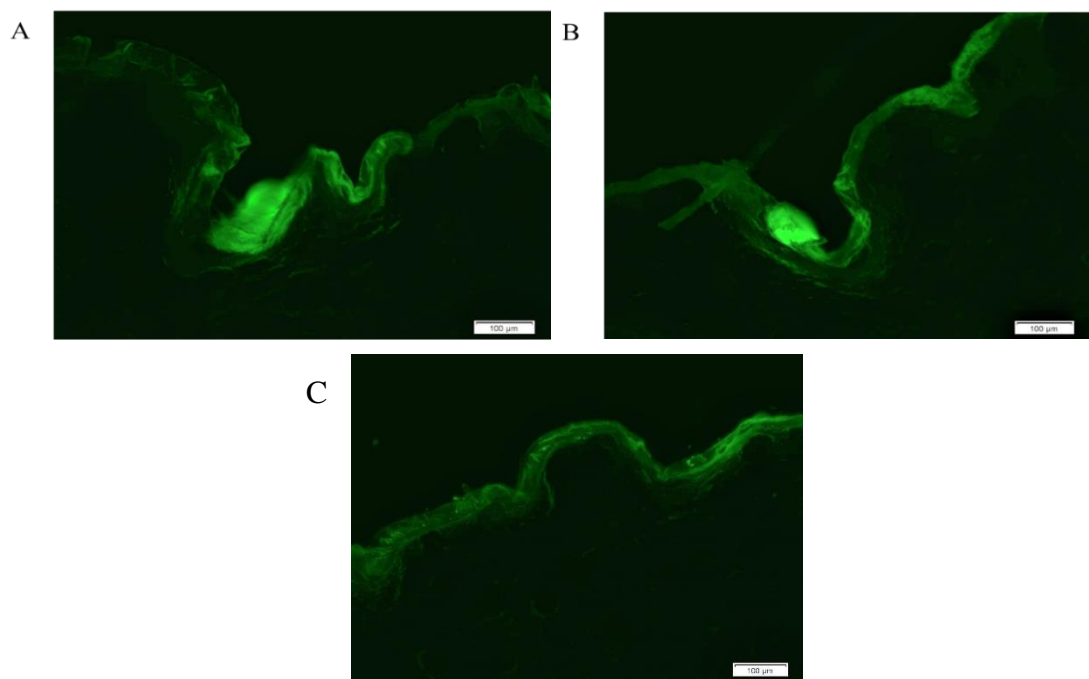


Figure 16.5 Fluorescent microscopy images of FITC-insulin, injected into porcine skin with (A) closed MN channel (B) single open MN channel (C) Control

16.4 Hollow polycarbonate MNS

Polycarbonate MNs were fabricated via injection moulding to produce square based pyramid solid arrays. In order to convert a solid MN into a hollow MN a 400 μ m drill bit was used to manually bore through the back of the baseplate and emerge through the pyramidal body of each MN. To maintain the MN tip the bores were drilled off centre to emerge out of the side of the pyramids (figure 16.6). However, due to the microscale measurements of the MNs and difficulty in seeing through the opaque baseplate, bores could not be aligned precisely to a single pyramid face. This meant that the bore placement was inconsistent for each MN. The pyramid structure of some MNs was deformed to the point where skin penetration was not possible, as MB results demonstrated no porcine skin staining after PC MN application.

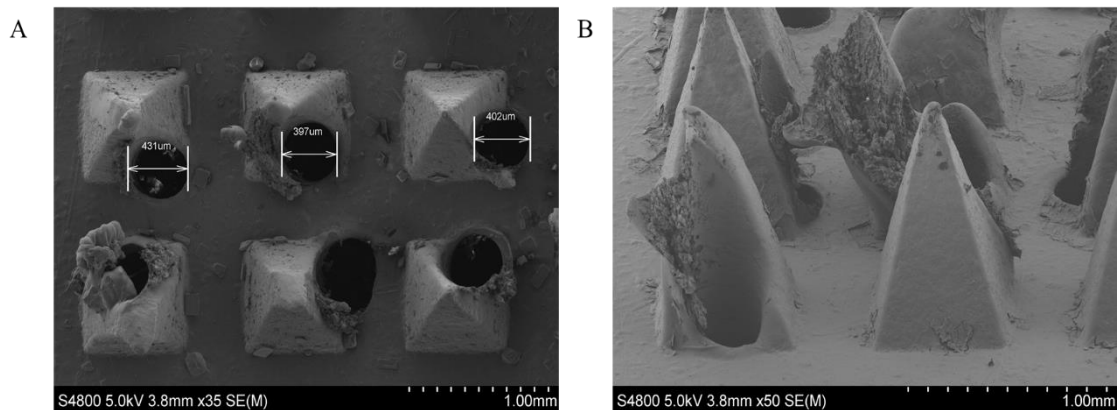


Figure 16.6 SEM images of PC MNs drilled with a 400 μ m drill bit showing (A) misalignment and (B) deformation

To improve the fabrication process Master's student Sara Amini-Asl designed a method where a drill slot bored through the back of the MNs via a computer numerical control tool. To prevent deformities, a method was designed whereby the drill bit slowly drilled in an in-and-out "pecking" movement. The results, demonstrated in figure 16.7, show the new design incorporated two bores either side of the pyramid, with the objective that the solutions would run down the inside of the bore towards the apex of the MN which is embedded within the skin.

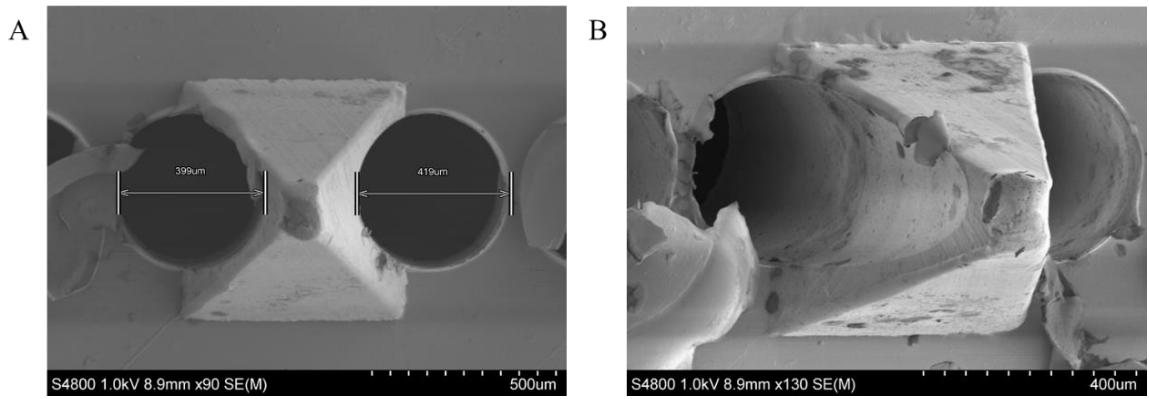


Figure 16.7 SEM images of PC MNs bores created with a computer numerical control tool to show (A) double bore design (B) channel drilled down the side of the MN to direct fluids

To test this theory the MNs were inserted into porcine skin with hard thumb pressure to ensure penetration and held in place using tape and pins. Then 10µl of calcein solution (for histological visual aid) was pipetted into each 4 x 4 well and left to diffuse for 1 minute (figure 16.8A). Primary observations show that calcein had pooled under the base plate of the MNs and dyed the surface of the skin yellow. Upon removal of the tape and MN array there is evidence that the calcein did not deliver into the skin as the solution had pooled on top of the skin, figure 16.8B, therefore further histological sectioning was not completed.

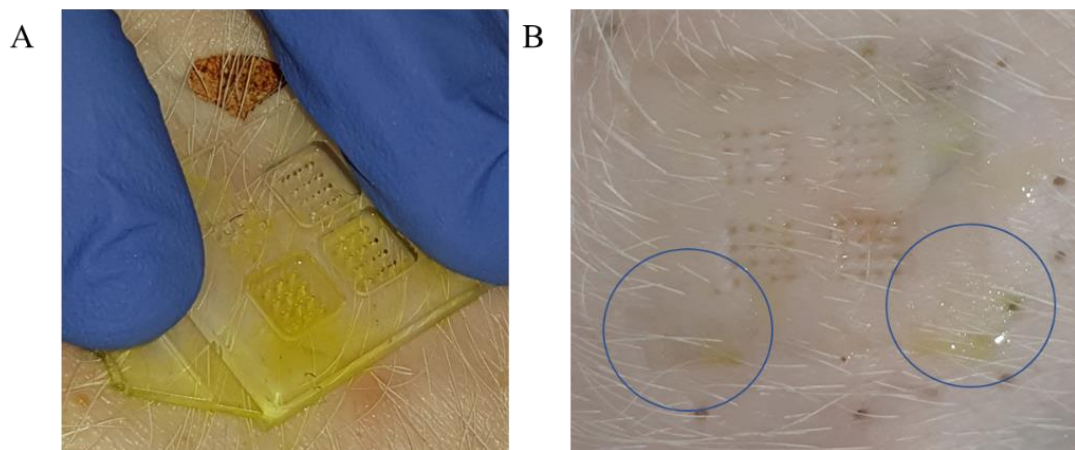


Figure 16.8 images of porcine skin treated with hollow PC MNs to deliver calcein solution (A) before MN removal (B) after MN removal, circles indicating calcein pooling on surface

The OCT results in chapter 14 reported that 67% of the MN penetrated the skin. Figure 16.9 helps explain the reason why the solution is pooling on the surface and not delivering into the skin. As the whole MN is not inserted, a gap is formed between the skin surface and the base of the MN; consequently, as the bore is not sealed or aligned to the tip of the MN, any fluid injected through will enter the gap and sit on top of the skin; proving that this is inefficient at delivering fluids (figure 16.9A). To improve bore delivery, future work will test a smaller drill-bit diameter that can align the whole bore to the top of a single face on the MN pyramid and not cut into the baseplate. This would enable a closed bore aligned close to the MN tip to improve delivery into the deeper skin tissues, figure 16.9B.

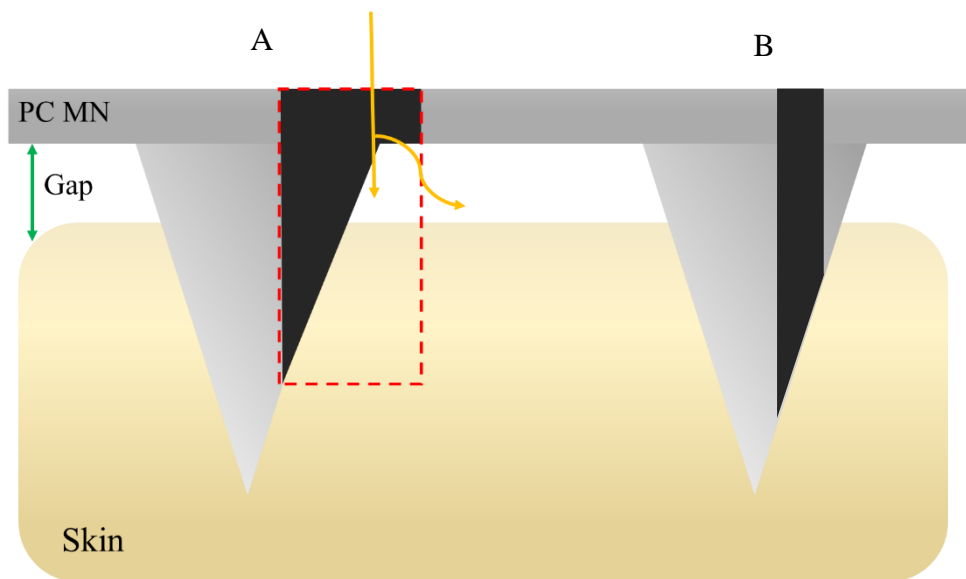


Figure 16.9, Schematic diagram of PC MN inserted into porcine skin, indicating that 67% penetration leaves a gap between the MN baseplate and the skin(A) 400µm drill bit (red box) used to create a bore (in black) subsequently cuts onto the baseplate. The yellow arrows demonstrate calcein delivery and how it pools into the gap (B) smaller drill bit used, showing how an enclosed bore, closer to the tip of the MN could be formed

16.4.1 Hollow polycarbonate conclusion

The attempts to improve the drug delivery parameters of PC MN from solid MNs to hollow were unsuccessful. Techniques required to fabricate more precise hollow MNs, such as, laser cutting, were beyond the current capabilities of the University facilities. Therefore, the current PC MNs are only suitable for “poke and patch” drug delivery.

Part 5

***In vitro* microneedle drug delivery**

Chapter 17

Optimisation of *in vitro* Franz cell assay

17.1 Introduction

In vivo transdermal delivery is the gold standard method to evaluate the drug delivery capabilities of a novel transdermal delivery device, however, there are several drawbacks to this method including high cost, obtaining ethical approval and potential harmful side effects [259]. Alternatively, *ex vivo* human skin can be obtained from cadavers or surgery, with appropriate ethical approval; the skin sourced from the abdomen, breast or back regions are considered the best for use, however, consistency and availability is unreliable at Swansea University as this depends on the frequency of surgeries and agreed donations of cadavers [260] and without ethics approval we cannot practice on human skin. Several *in vitro* drug delivery techniques have been developed to remove the use of living organisms. Typically, the most popular method includes a diffusion Franz cell developed by Thomas J. Franz in 1970 [261]. The Franz cell enables quantification of drug transported across the skin barrier, whether human, animal or other skin model and is composed of either a static or flow-through cell; however, for this work only the static cell will be discussed and implemented, of which the setup is described in chapter 7.4.

17.2 Transdermal test membranes

Due to the difficulty in acquiring human skin, alternative approaches, such as, synthetic membranes are sometimes used to derive reproducible and reliable data that predicts the results of *in vivo* human skin. One such membrane, STRAT-M™ (Merck Millipore, Burlington, Massachusetts, USA), is composed of multiple layers of polyester sulfone that vary in density to mimic the diffusivity of human skin. Although synthetic membranes can be easily stored and reduce the variability associated with biological samples, it is challenging to separate the layers of STRAT-M™ to study the drug permeation through each layer [259]. Additionally, as the synthetic membrane is designed for diffusion studies and not for penetration studies, it does not reflect the

natural elastic properties of skin as the surface is solid and impenetrable, thus, when testing MNs, the silicon MNs broke and the PC MNs were not sharp enough to penetrate the membrane of the STRAT-M. Therefore, synthetic membranes such as STRAT-M™ were not used for MN based permeation studies.

Another alternative skin model is *ex vivo* animal skin. It is important to note that as with human skin, the structure of the skin differs between species, within species (age, colour, sex) and even on the same species (anatomical location), which can all contribute to considerable differences in skin absorption properties, e.g. the thickness of the *stratum corneum* and hydration levels [262]. The degree of skin permeability of commonly used animals in relation to humans can be described as increasing from rabbit >rat >guinea-pig >pig >rhesus monkey >human [263]. Porcine skin is anatomically, physiologically, biochemically and immunologically similar to human skin, for example, they both comprise a similar arrangement of dermal collagen and elastic fibres and have a relatively thick epidermis which mirrors epidermal turnover kinetics [264]. However, in terms of lipid composition, the SC thickness of new-born piglets is considerably thinner than adult pigs and is more reflective of human skin [265]. Due to the ease of availability and acceptance that piglet skin is histologically similar to human skin, freshly excised porcine skin from Wetlab (UK) was utilised for all Franz cell experiments.

Numerous studies have addressed the effects of storage conditions on skin permeability and found that frozen storage can have potential detrimental effects on the SC barrier function, by increasing its permeability [266]–[270]. In light of this, international advisory and regulatory agencies have published recommendation articles for *in vitro* transdermal testing, for example, The Organisation for Economic Cooperation and Development (OECD) guideline 427 [271] suggests skin should not be stored at very low temperatures such as -80°C as this can damage the SC and increase the permeability of the sample, alternatively storing skin at -20°C has shown to yield no change in skin permeability [272] and can be adopted for all skin storage conditions. Additionally, it is inadvisable to refreeze thawed skin specimens as this can also increase permeability [273], hence any samples once defrosted will be used or discarded to prevent any influence on the SC barrier.

17.3 Porcine skin preparation

The correct preparation of porcine skin is essential to replicate the permeation profile of human skin. Preparation of two relevant skin thicknesses include (figure 17.1 [274]):

- ~ *Full-thickness skin*: prepared by removing the subcutaneous fat and parts of the dermal tissue by either heat-separation, chemical or enzymatic preparations, to produce a membrane thickness of approximately 1000 μm . However, it is noted, that any presence of the hydrophilic dermis may limit the movement of lipophilic molecules into the receptor fluid, as lipophilic molecules do not have an affinity for hydrophilic layers and therefore, avoid moving through the layer to access the receptor fluid but would instead remain in the more lipophilic layers of the epidermis.
- ~ *Split-thickness skin*: measuring approximately 200-500 μm , is prepared using a dermatome to separate the SC and epidermis from the rate-limiting dermal layer. Challenges associated with thinner skin membranes include fragility with handling which could lead to tears and overestimations of drug permeation into the receptor fluid of the Franz cell [262], [263].

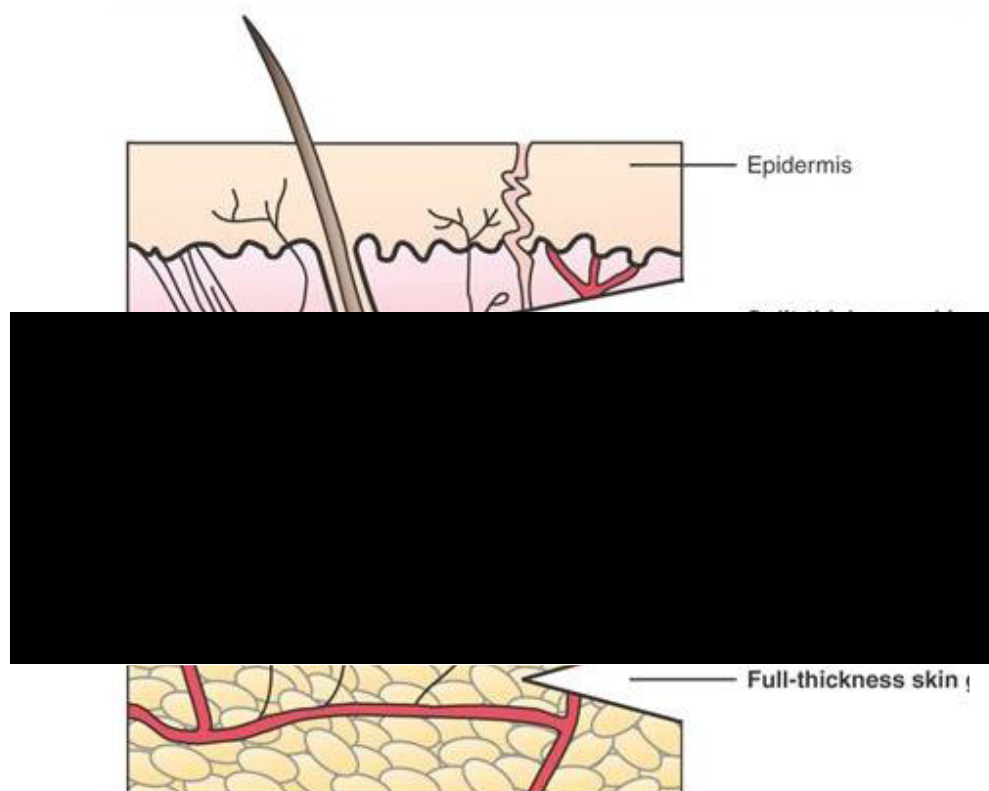


Figure 17.1 Schematic diagram of a skin cross section, demonstrating the components of split-thickness and full-thickness skin

Evaluating the literature to establish an ideal skin thickness for MN Franz cell permeation yielded inconclusive results; there are a number of MN papers that either did not cite a membrane thickness [275]–[278], or only stated that “full-thickness” or “split-thickness” skin was applied [279]–[283]. Publications that did cite a skin thickness measurement, ranged from 350µm [284]–[286], 500µm [287], 550µm [288], [289], 800µm [290], [291] and as thick as 1240µm [292]. Additionally, publications from the same research groups also quoted different thickness 300-500µm [293]–[295] for similar Franz cell studies. Due to conflicting reports and uncertainty between published studies, guidance was sought from the OCED 428 guidelines on “Skin absorption: *in vitro* Method” [271] and *WHO/IPCS* environmental Health Criteria 235: Dermal Absorption [296]. The guidelines state that only where justified should “full-thickness” skin be applied to Franz cells studies, and calculation of flux rates should not be used due to uncertainty in the variability of absorption and instead, “split-thickness” is recommended to avoid these issues. The next chapters demonstrate the analysis of the permeability of different dermatomed porcine skin thicknesses to determine the optimal thickness for the Franz cell experiments within this thesis.

17.4 Summary of guidelines

The OCED 428 guidelines on “Skin absorption: *in vitro* Method” [271] and *WHO/IPCS* environmental Health Criteria 235: Dermal Absorption [296] provide international detailed direction on *in vivo* and *in vitro* absorption experimental methods, to improve consistency of data derivation, presentation and interpretation. Some details included, but are not limited to:

- A sampling period of 24hrs to allow the absorption process to be clearly characterised, in which 6-12 receptor samples are collected.
- At least six repeats of each Franz cell sample, including controls.
- Continuous stirring of the receptor fluid for homogenous sampling.
- As the passive diffusion of molecules is affected by temperature, the Franz cell temperature should be maintained at a constant temperature close to the normal skin temperature of 32°C.
- The barrier integrity of the skin should be examined by either transepidermal water loss (TEWL) or electrical resistance before each experiment.

- The receptor fluid should reflect the molecules solubility properties to remove a rate-limiting step. The pH of the molecule is an important consideration as the molecule's ionisation state at a physiological pH will influence its ability to cross the lipophilic and hydrophobic membrane.

The cumulative amount of drug permeated through the skin is quantified through analysis of the Franz cell receptor fluid samples at dedicated time points. However, the above guidelines emphasize that the original dosage administered needs to be recovered at the end of the experiment.

The permeation value is calculated as a percentage of the original applied dose and the dose recovered in the receptor fluid and any amount retained in the skin. Thus, partitioning layers to quantify the dose found in each creates a more accurate picture of the permeation profile. The OCED 428 guidelines states:

- Dosages retained in the top layers of the SC may be removed by desquamation and therefore may not be absorbed. Therefore, tape strips of the first layers are deemed as non-absorbed.
- Sample dosages found to remain in the skin may be considered unavailable to the systemic circulation, unless the dermal absorption has demonstrated a rate limiting reservoir, then absorption into the systemic circulation is incomplete.

The degree of tape stripping can vary from 10-15 adhesive strips and is used to quantify the percentage in the SC. However, further analysis is required to quantify the remaining percentage in the epidermal layer. The optimisation of these methods is discussed in section 17.6.

17.5 Skin integrity

Before a skin sample can be used, it must be established that it does not already possess any holes or damage that may affect the SC barrier and cause an over-estimation of permeation. To evaluate the integrity of skin samples, two integrity tests, transepidermal water loss (TEWL) and transepidermal electrical resistance (TEER) are compared.

TEWL is a non-invasive technique that measures the loss of water from the epidermis to the surface of the skin [297]. The theory is that if the SC barrier is intact, minimal water will pass through the SC to be detected. However, if the SC is compromised, then water

loss will result. To determine TEWL, the density gradient of water evaporation from the skin is measured by placing a probe perpendicularly to the skin site of interest. The probe applied contains two pairs of sensors that monitor temperature and relative humidity and from this the TEWL measurement is derived [298]. However, a major drawback with TEWL assessment is that it requires a stabilisation period in a controlled environment to prevent temperature and humidity influences as a result of rehydration of samples from frozen storage. Therefore, this method is not practical with studies involving a large number of Franz cells [299]. TEWL measurements were tested on porcine skin over a Franz cell receptor to measure the water loss across the skin. However, pressure from the probe and the small surface of the skin meant water leaked from under the skin which gave misrepresented readings. Therefore, TEWL was not a practical approach.

Alternatively, TEER is considered a sensitive and reliable method that measures the flow of electrical resistance across the skin membrane [300]. The theory is that the electrical resistance across the skin membrane will not change if the SC barrier is intact. However, if the SC has been broken the electrical resistance across the membrane will change and result in a variance of resistance. To measure the change, the Franz cell receptor and donor chambers are filled with two different concentrations of PBS, with the higher concentration in the donor chamber. Between the chambers the skin membrane is inserted and if the SC is intact, it will not allow the movement of the higher PBS concentration into the receptor chamber below to signal a resistance change in comparison to a control. Therefore, due to sensitivity and reliability of TEER testing, the TEER method is applied for all Franz cell skin integrity tests throughout this thesis.

17.5.1 Method

To optimise the skin integrity tests and test a range of skin thickness, 4cm² split-skin skin sections of approximately 400-600µm, were mounted onto a Franz cell receptor chamber that contained 0.01M PBS. The dosing chamber was aligned on top of the receptor chamber to sandwich the skin membrane and was filled with 0.1M PBS; the two chambers were sealed using parafilm to prevent leaks, (figure 17.2). Of the two resistance probes, one was placed through the spout of the receptor chamber, while the other was placed in the dosing chamber. Triplicate readings were taken at 10-minute

intervals to monitor any resistance change due to ion flux through the skin membrane. If the resistance measurement significantly decreased from the original reading over this time then the skin sample was discarded, as the sample enabled the higher concentrated PBS to move into the lower chamber, signifying a compromised SC. This was verified with control skin samples with an intact SC, compared to test samples that had been purposefully disrupted with hypodermic needles and scalpels.

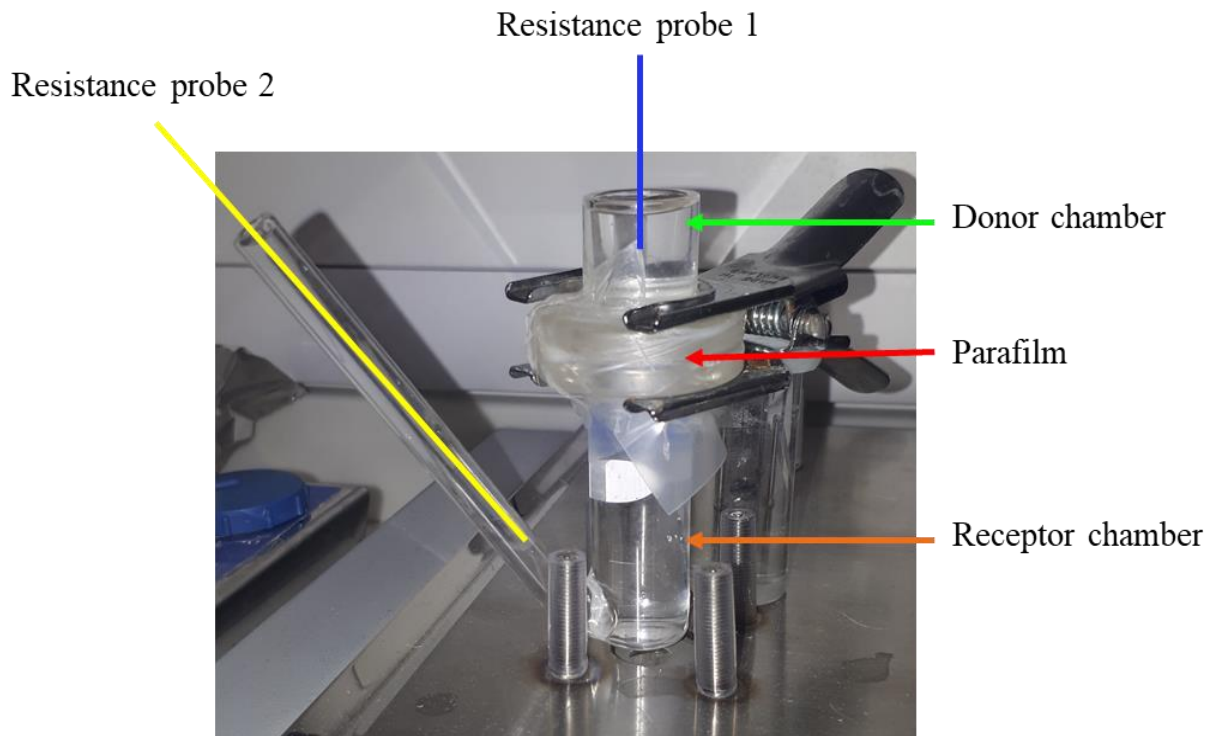


Figure 17.2 Franz cell integrity test set up, demonstrating how resistant probes 1 and 2 enter the donor and receptor chambers, to measure TEER

17.5.2 Results

The bar graph in figure 17.3 confirms that after 30 minutes the resistance measurement decreased in samples that had visible SC damage, that was produced intentionally i.e., a sample sliced with a scalpel read an average resistance of 245Ω , while a single hypodermic needle application measured an average of 325Ω compared to 347Ω of the sample with no damage. Decisions on whether a piece of skin were acceptable for use were taken from the mean and standard deviation of the non-damaged skin, for example the standard deviation gave a resistance variance of 2Ω , while a piece of skin with a single hypodermic puncture read a decrease in resistance of 22Ω therefore if the

resistance decreased by more than 5Ω over 30 minutes the skin was discarded. These results show that TEER can be successfully used to test the skin integrity of Franz cell skin samples.

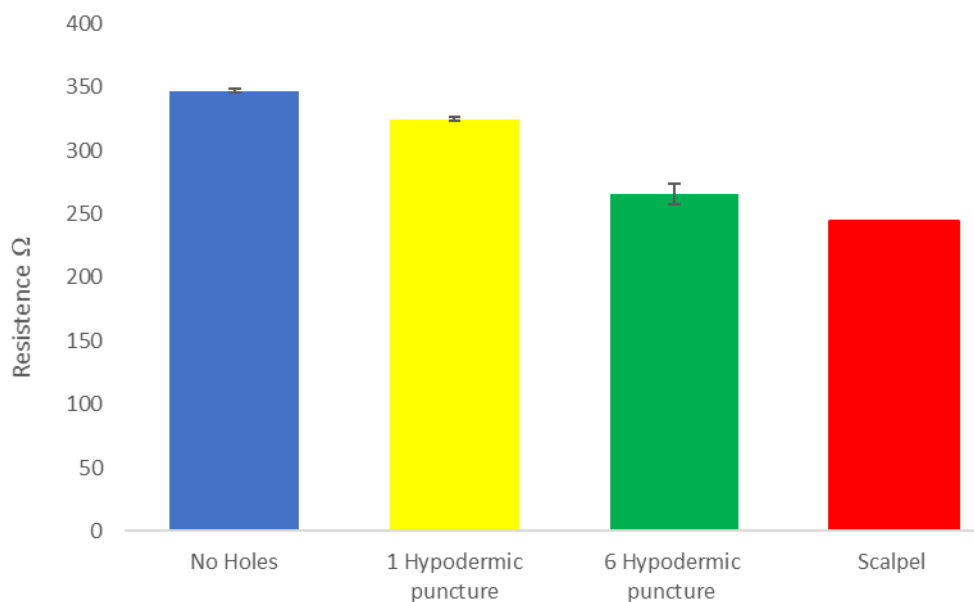


Figure 17.3 Bar graph to verify reduction in resistance readings with larger skin manipulation of the SC barrier

17.6 Tape strip protocol

Tape stripping is a minimally invasive quantitative method used to analyse the concentration of an active ingredient present in the SC. An adhesive tape strip is applied to the skin's surface to remove a layer of the SC and any active ingredient that resides on or within it. It is important that each tape strip is flattened with the same force and removed at the same speed to ensure consistent results e.g., slower removal speeds allow greater adhesion of the SC to the tape, thus increasing the amount of skin removed. Once removed, the active ingredient can then be extracted and analysed using HPLC or spectroscopy techniques such as, fluorescent or mass spectroscopy [301]. The standardised protocol described in chapter 7.4.3 was optimised through the following experiments.

17.6.1 Optimisation of method

An approximate 4cm² porcine skin sample were mounted onto a Franz cell receptor chamber filled with 0.01M PBS. However, in contrast to the previous Franz cell experiment (15.5.1), the donor chamber was omitted. The subsequent Franz cells were set up as described in chapter 7.4.1 with six controls and six repeats.

50µl of 0.2mg/ml calcein was applied to the surface of the skin, while the control experiments received no calcein application to the skin. After 4 hours the skin samples were removed and subjected to tape stripping. Thumb pressure was used to flatten a one-inch tape strip over the whole skin sample; the strips were cut longer than the skin sample to create a tab to provide effective continuous removal. The first tape strip was placed in a 5ml tube and submerged in 4mls of 0.01M PBS while the following 2-10 tape strips were collected and all submerged in 4mls, 0.01M PBS. All tubes were sealed in foil to prevent bleaching of the fluorescence and agitated on the roller mixer overnight to allow any material stuck to the tape to suspend into the PBS. Following the overnight process, triplicate 100µl aliquots of each sample were removed and analysed at fluorescence excitation wavelength 485nm. A standard curve of known calcein concentration versus fluorescence was produced to determine the concentration of calcein extracted from the tape strip samples.

17.6.2 Results

Figure 17.4 shows the concentration of calcein recovered from the tape strips with and without calcein application to the skin surface. The control skin samples with no calcein application show very little fluorescence, which is attributable to the PBS; determining that any additional material pulled from the SC onto the tape strips did not significantly contribute to the fluorescent reading. The Franz cell samples with the addition of calcein measured a calcein recovery of 0.8µg/ml on tape strip 1 and 0.7µg/ml on the consecutive 2 – 10 strips. According to OCED guidelines, tape strip 1 quantifies the amount of calcein found on top of the SC, which was not absorbed into the skin, while tape strips 2 – 10 represent the amount of calcein that has begun to partition into the SC but is still not classified as absorbed material.

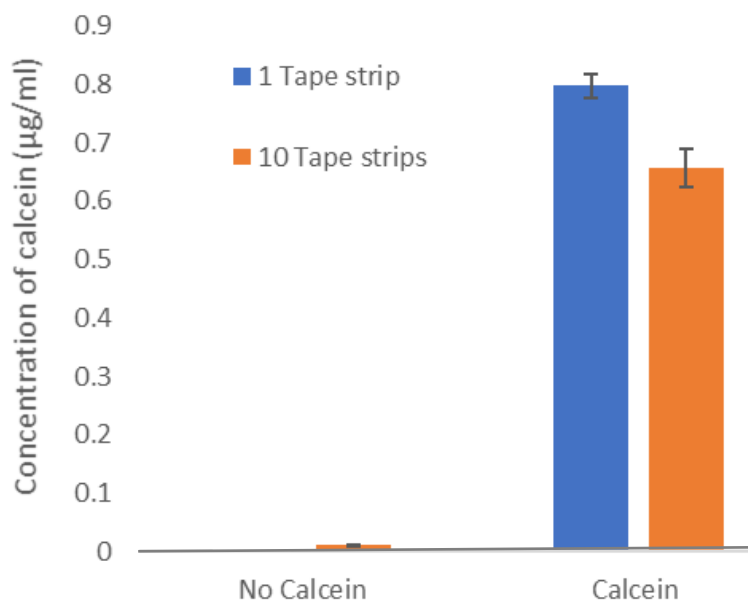


Figure 17.4 Bar chart demonstrating the concentration of calcein obtained from tape strips of Franz cells skin samples after 4 hours, with and without calcein application.

17.6.3 Conclusion

The results show that the tape strip method enables successful quantification of the amount of calcein found on top and within the SC and that other components adhered to the strips do not contribute to background fluorescence. However, the amount of calcein applied to the skin was 2.5µg/ml and only <0.8µg/ml of this was recovered from the tape stripping process. Therefore, to recover the total amount of calcein applied, further quantification of the remaining skin layers and receptor fluid is required.

17.7 Skin homogenisation

Homogenisation is the process of breaking down a tissue structure to form a semi-homogeneous suspension of tissue cellular fragments that can be further isolated [302]. Tissue homogenisation is an important technique used to determine the distribution of an active ingredient throughout the body, facilitating a pharmacokinetic profile that allows quantitative analysis to capture the activity of the ingredient. To characterise the percentage of active ingredient retained within the skin tissue several homogenisation extraction techniques were used, such as, mechanical, and enzymatic digestion. The three main mechanical methods include the use of grinding, rotating blade shearing and

bead beating to homogenise the skin. Selecting the precise technique depends on the size and structure of the tissue and the degree of homogenisation required; for soft tissues, sonication and grinding methods are suitable, however, tougher tissues such as skin, are more challenging and require a more powerful homogenisation technique such as shearing or enzymatic softening [258], [303]. It is also important to select a process that limits the production of heat especially if the analytes of interest are sensitive to thermal degradation e.g. insulin.

Enzymatic digestion can be used as an alternative or addition to mechanical homogenisation as the enzyme, typically a protease, is effective for softening and dissolving large particles and tough and fibrous tissues by breaking down the skins protein components into smaller polypeptides or single amino acids [304]. A further advantage is that the sample can be left unattended to digest, for potential automated procedures that do not require manual intervention, at lower costs [303]. As with all methods, the choice of enzyme is driven by the make-up of the desired tissue to be digested.

17.7.1 Mechanical homogenisation

Primary homogenisation tests examined two types of mechanical techniques, utilising a TissueRuptor or a gentleMACS tool.

The TissueRuptor (Qiagen, UK) is a handheld rotor-stator probe that claims to rapidly disrupt human and plant samples, as porcine skin is similar to human skin, the probe should work as efficiently. A 1cm² sample of porcine skin was cut into smaller segments and placed into an Eppendorf tube; the tube is kept on ice to allow the brittleness induced by freezing to help break up the tissue and keep the tissue cool. Upon blending, it became quickly apparent that the probe created lots of heat and the sample needed to be continuously submerged in ice to prevent thermal influences. In addition, the blades were unable to slice through the skin tissue, even in the already diced smaller sections. Therefore, due to the size of the probe, completion of a full sample was time consuming and largely ineffective, figure 17.5A.

A gentleMACS (Miltenyi Biotec, Germany) is a semi-automated blending tool used to dissociate tissue into single cell suspensions. However, figure 17.5B demonstrates that

the gentleMACS was unable disrupt the skin tissue, which may have been due to the blunt plastic blades, that were not sharp enough to tear through the tissues structure.

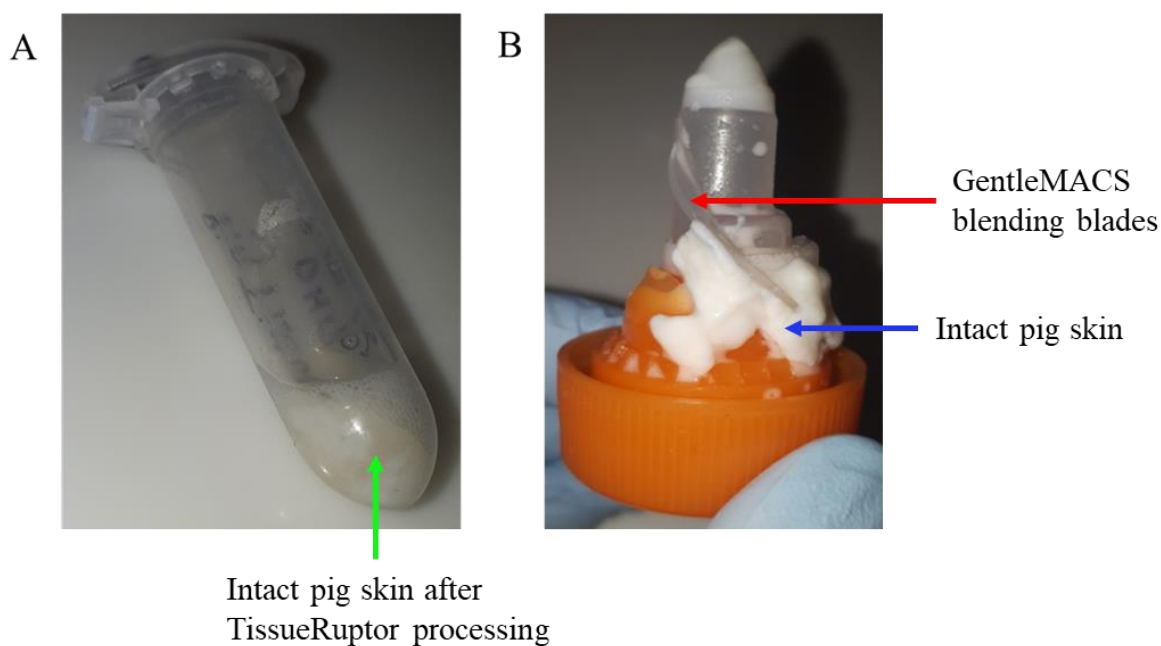


Figure 17.5 demonstrates still intact pig skin after mechanical homogenising using (A) TissueRaptor and (B) GentleMACS methods

17.7.2 Enzymatic homogenisation

The above mechanical methods demonstrated that a more powerful dissociation protocol was required to homogenise porcine skin tissue than mechanical methods alone. Enzymes are powerful biological molecules that act throughout the body to catalyze chemical reactions and can be extracted and manufactured for other precise applications. A literature survey was conducted to identify potential enzymes that can break down skin components without affecting the drug or molecule of interest; two potential enzymes were identified, collagenase and papain.

Since collagen is known to be the most abundant protein found in mammals, it seemed rational to utilise a protease enzyme, such as, collagenase, as this degrades the helical peptide bonds found in collagen that form the skin epithelial and connective tissues. Removing the skins scaffolding dissociates the tissue into a suspension that can be further analysed [305]–[307]. As collagenase has a specific mechanism of action, it can be assumed that the active ingredient would not be targeted for degradation and would be recoverable from the suspension, as long as the drug is not encapsulated within cells.

Papain is a proteolytic enzyme extracted from the fruit of a papaya plant and is commonly used in food (to tenderise meat or clean beer), pharmaceutical (to reduce inflammation, manufacture cosmetic face creams and dental creams) and textile industries (degumming silk and tanning leather) [308]. A study by Stremnitzer et.al [309], demonstrated that papain could disrupt the barrier integrity of the SC and epidermis as well as to breakdown tight junctions, which are responsible for connecting the cellular membranes that form a barrier to prevent free diffusion between different extracellular compartments [310]. Therefore, breaking these connections consequently releases single cells into a suspension. More specifically papain functions by cleaving peptide bonds rich in leucine or glycine amino acids [192]. Therefore, when digesting active ingredients that are protein based, such as insulin, papain would not be recommended as it would also degrade the bonds within the protein of interest, misrepresenting its final quantification. However, for non-protein based active ingredients, papain may be more beneficial than collagenase, therefore, both enzymes were explored.

17.7.2.1 Method

Collagenase was purchased from Sigma Aldrich and stored at -20°C . Concentrations of 2mg/ml, 6mg/ml, 10mg/ml, 15mg/ml, and 20mg/ml were dissolved in 0.01M PBS. An approximate 4cm^2 , $700\mu\text{m}$ thick sample of porcine skin was placed into 4mls of each concentration and left on a roller mixer at room temperature. At timed intervals, the skin samples were visually checked to observe any changes to the porcine skin.

Papain was purchased from Sigma Aldrich and stored at $2-8^{\circ}\text{C}$. An activation buffer consisting of 20mM Sodium Acetate and 1mM EDTA (Ethylenediaminetetraacetic acid) at pH 6.8 was prepared as a stock. On the experiment day 2mg/ml papain and 2mM DTT (Dithiothreitol) were added to the stock to activate papain. A $700\mu\text{m}$ thick, 4cm^2 porcine skin sample was submerged in the solution and heated to 60°C . The digestion was monitored at timed intervals to observe any changes.

To compare the homogenisation results with and without the addition of calcein, two further samples were created; A $700\mu\text{m}$ thick, 4cm^2 porcine skin sample was mounted onto a Franz cell chamber and treated with $100\mu\text{l}$ of 0.2mg/ml calcein; after 4 hours the

samples were removed and either homogenised in 4mls of 20mg/ml collagenase or 2mg/ml papain.

All final homogenised skin samples were spun in a centrifuge at 3300rpm for 10 minutes, to allow the skin debris to form a pellet at the base of the tube. Then, 100µl of the remaining supernatant solution was withdrawn and quantified using fluorescence spectrophotometry at the fluorescent wavelength 485nm. If the homogenisation samples without any calcein fluoresced in the same wavelength range as the active ingredient, this would contribute to the final quantification and therefore, yield an over estimation of active ingredient recovery, therefore it would be necessary to add a purification step such as chromatography, to separate the sample components for individual analysis.

17.7.2.2 Results

To optimise the method for skin homogenisation, several concentrations of each enzyme were tested for their ability to break down a sample of porcine skin i.e. when the skin samples were no longer solid, and the solution had turned clear. Table 17.1 demonstrates that higher concentrations of collagenase break down the sample faster with a concentration of 20mg/ml breaking down the sample in only 1 hour. Only one concentration of papain enzyme was tested, 2mg/ml, as after a 1-hour incubation the whole skin sample was digested.

Table 17.1 Time dependent digestion of porcine skin samples using enzymes collagenase and papain

Enzyme	Concentration (mg/ml)	Time (Hours)				
		1	3	4	6	24
Collagenase	2	x	x	x	x	✓
	6	x	x	x	x	✓
	10	x	x	x	✓	✓
	15	x	✓	✓	✓	✓
	20	✓	✓	✓	✓	✓
Papain	2	✓	✓	✓	✓	✓

To verify whether the homogenisation samples, digested with different concentrations of either collagenase or papain, produced a fluorescent signal before calcein was added, the calibration curve in figure 17.6 was created. Measuring the fluorescence of the homogenised samples with collagenase or papain digestion gave an average result of 1,077 and 631 respectively that did not significantly differ upon enzyme concentration increase. With the addition of calcein in the homogenised samples the fluorescent readings increased to 100,969 for collagenase and 107,815 for papain. This confirms that the background fluorescence of both enzymes, irrespective of concentration, measured negligible results that do not significantly interfere with the fluorescent signal of calcein.

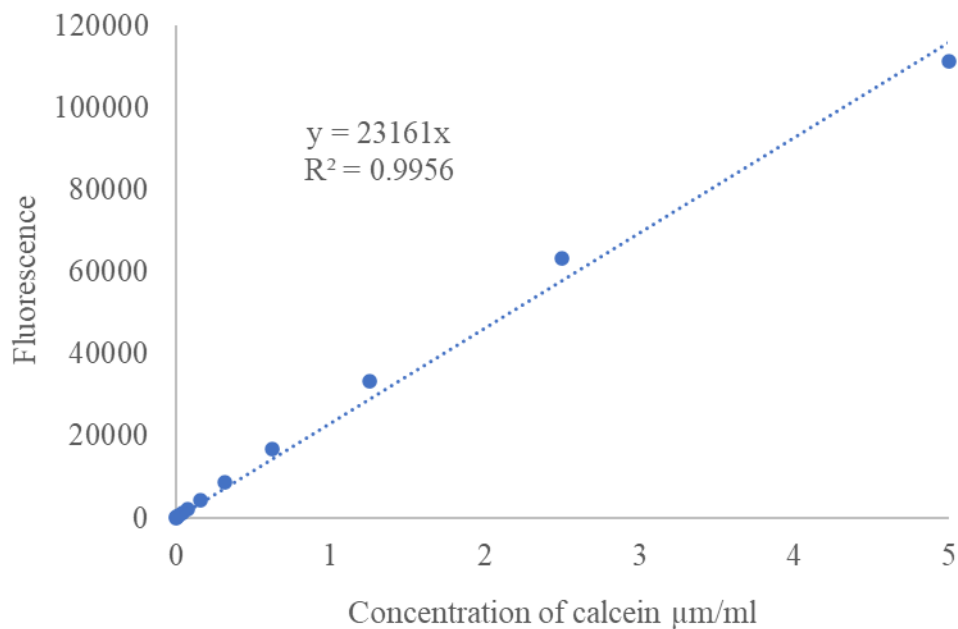


Figure 17.6 Calibration curve of calcein concentration against fluorescence

The recovered concentrations of calcein equate to 4.35μg/ml and 4.65μg/ml for collagenase and papain respectively. As the original dosage administered (100μg of 0.2mg/ml calcein in 4mls of enzyme) equals 5μg/ml, the recovered calcein concentrations calculated as 87% and 93% respectively confirming that calcein can be quantified from the skin through enzyme homogenisation.

17.8 Franz cell analysis optimisation

The previous chapters demonstrate a fully optimised method to recover and quantify the dosage of active ingredient in each skin layer after sample utilisation in Franz cell analysis. To combine these findings, an additional proof of concept experiment was conducted with three control groups to establish whether the sum of the calcein concentration found in the tape strips, homogenisation and Franz cell receptor can be combined to form a full permeation profile:

1. Skin sample with no treatment and no calcein application
2. Skin sample with 50µl of 0.2mg/ml calcein applied to the surface
3. Skin sample with 50µl of 0.2mg/ml calcein applied to the surface and treated with a hypodermic needle to positively breach the SC

17.8.1 Method

Franz cells were set up as described in chapter 7.4.1 and run for 4 hours to collect 6 time points at 5mins, 15mins, 30mins, 1 hour, 2 hours and 4 hours to form a cumulative curve, (figure 17.6). A time course of 4 hours was selected rather than the suggested 24 hours, as this was a proof-of-concept experiment and the results were used only to determine if the methods were viable. Each skin sample measured 4cm² and 700µm thick and was subjected to the previously described TEER examination before the Franz cell experiment, and tape stripping and homogenisation, using 2mg/ml papain, after the experiment.

17.8.2 Results

Figure 17.7 demonstrates that the skin samples treated with a hypodermic needle had a significantly higher concentration of calcein in the Franz cell receptor chamber than the controls without hypodermic treatment, which showed that no calcein was recovered from the receptor chamber.

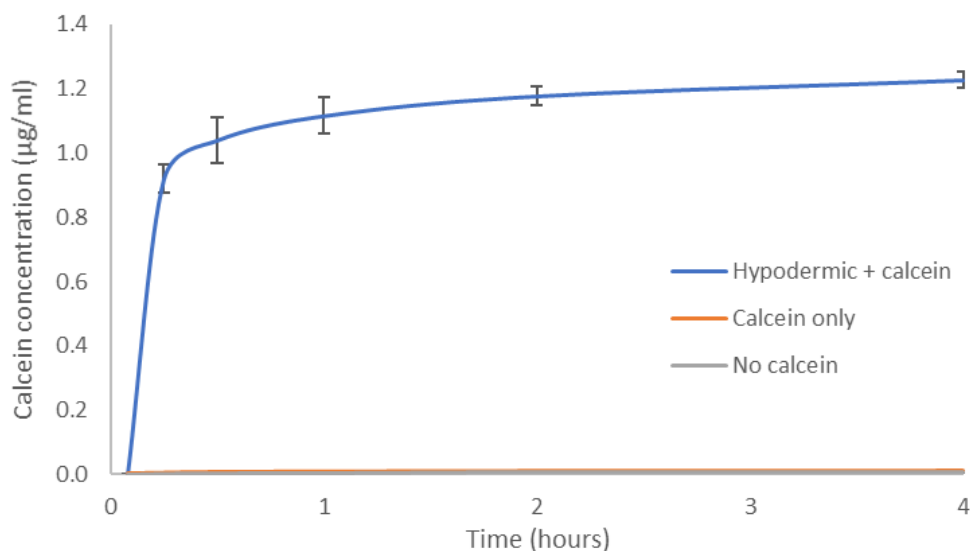


Figure 17.7 Cumulative concentration of calcein permeability through porcine skin into a Franz cell receptor

To quantify where and how the dosage of calcein had permeated through the skin, a stacked bar graph factoring in the final cumulative concentration of the tape strip concentrations and the homogenisation concentration was produced. It is believed that this quantification approach and visual representation has not been reported previously, and thus this permeation profile to show how the drug penetrates through each skin layer is a novel method for quantification of an active molecule in skin.

The stacked bar graph is to be interpreted, according to OCED guidelines in conjunction with the review from Zsiko et.al [261] on “methods used to evaluate skin penetration *in vitro*”, The image in figure 17.8A is reprinted from the review to show how a drug is transported across the skin. Therefore, this information was used to form figure 17.8B and demonstrate how the stack bar analysis aligns with the permeation to form a permeation profile.

- The darkest blue represents the percentage of calcein recovered from the first tape strip and thus the amount that has remained on the skin surface
- The second darkest blue demonstrates the percentage recovered from 2-10 consecutive pooled tape strips, to quantify the amount of calcein that has partitioned into the SC

- The next section represents the percentage of calcein quantified from the homogenisation and thus the amount of calcein that has successfully permeated into the viable epidermis
- The lightest blue shows how much calcein has been recovered from the Franz cell receptor, and thus would be available to the lower epidermis and systemic circulation.

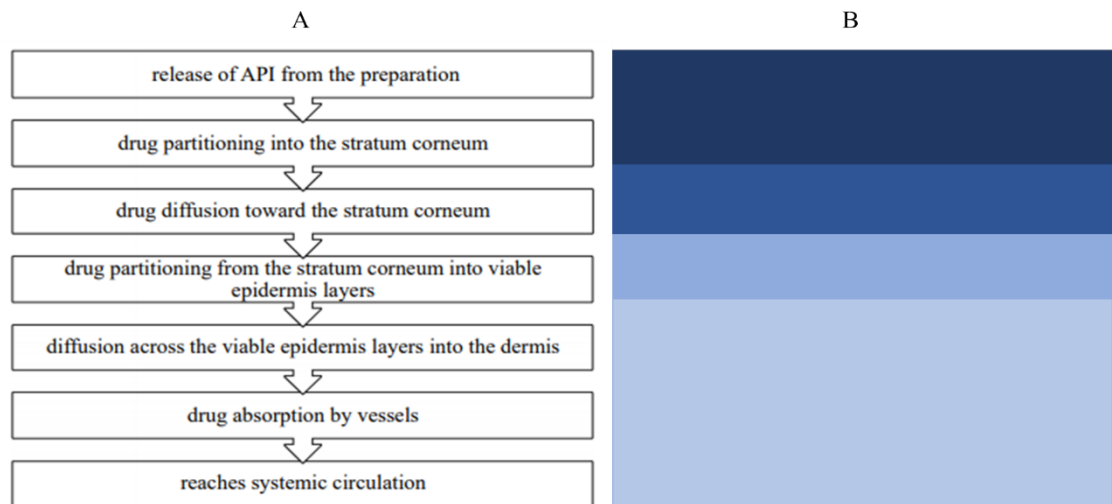


Figure 17.8 (A) diagram from Zsiko et.al demonstrating drug transport across the skin (B) diagram to show how the stacked bar chart colours align with the permeation profile and the OCED guidelines

To compare data between samples the concentration is converted to the percentage of the total calcein recovered from each sample. In some samples the calcein dose recovered may not amount to the full 100% dosage applied to the skin sample. Therefore, comparing these against a sample in which e.g., 50% is recovered will provide a false representation of the permeation profile. The control sample that did not receive any needle or calcein treatment produced an insignificant fluorescent signal that was removed from all samples as background fluorescence. The samples that did receive calcein treatment (figure 17.9) showed that the positive control (using a hypodermic MN to breach the SC) recovered 72% of the calcein from the receptor chamber. In comparison, the negative control (that did not receive any SC influences), recovered 64% of calcein dosage from the first tape strip, this shows that very little calcein was able to cross the SC barrier. Tapes strips 2-10, demonstrated a 12% and 18% recovery respectively, determining that some of the calcein had started to partition

into the SC layers. The homogenisations recovered a percentage concentration of 4% for the positive control and 18% for the negative control, demonstrating that some of the calcein is able to partition into the epidermal layers. The results show that overall, treatment with the hypodermic needle enabled more calcein to permeate through the skin layers and into the receptor via the open channel created, directly connecting the surface of the skin and the Franz cell receptor. The negative control, with no treatment indicated that 82% of the calcein dosage was unable to cross the SC and thus resides on the SC or in the epidermal layers.

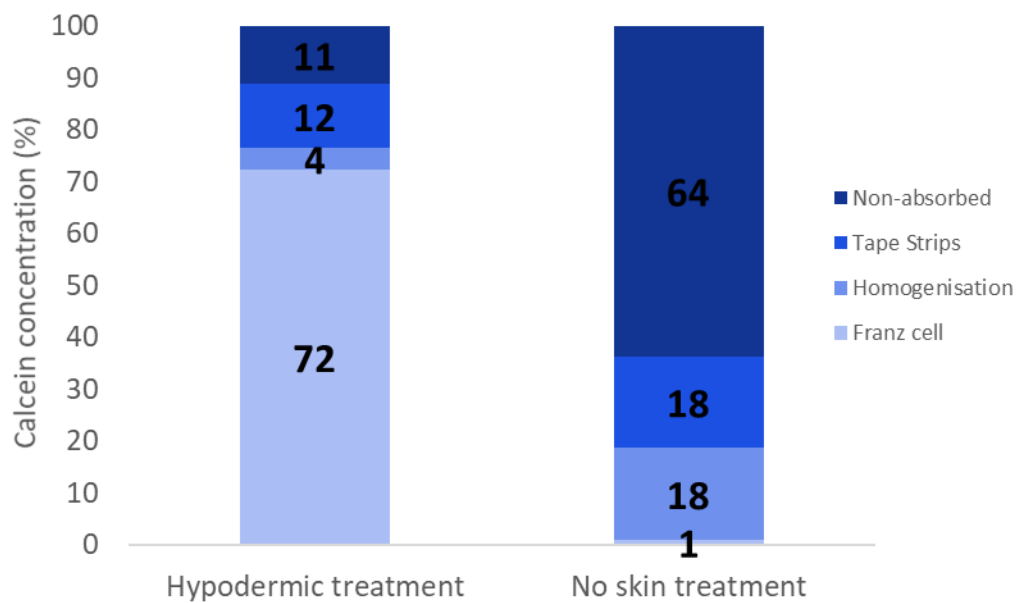


Figure 17.9 Permeation profile of calcein through positive and negative controls

17.9 Skin thickness optimisation

As discussed in chapter 17, the scientific literature, OCED 428 and WHO/IPCS guidelines are contradictory when attempting to determine the ideal skin thickness for Franz cell analysis. Therefore, to analyse the permeability of varying porcine skin thicknesses the Franz cell experiment in 17.8 was repeated to establish permeation profiles, however, application of a PC MN into the skin samples was used as a guide for MN permeation optimisation.

17.9.1 Methods

Franz cells were set up as previously described in 7.4 and run for 24 hours to collect receptor data for samples extracted over 11-time points; 5, 15 and 30 minutes and 1, 2, 4, 6, 8, 10, 12 and 24 hours. Experimental samples were:

- a positive control, where a hypodermic needle punctures completely through the skin to create a channel from the skin surface to the receptor fluid.
- A negative control, where the skin was not treated with any type of needle and
- a PC MN treated sample.

A PC MN was inserted using the applicator discussed in chapter 13.2 and held in the skin for 1 minute. To prepare skin samples with different thicknesses a dermatome was utilised and programmed to cut the skin from 100-1000 μm . However, the precise skin measurements ranged from 66 μm to 993 μm . Each skin sample was cut into 4 cm^2 sections with each being grouped into samples of similar thickness for precise and in-depth analysis of the thickness effect on permeation. The groups included thickness of <200 μm , 300 μm , 500 μm , 700 μm and >900 μm . Each skin samples integrity was tested before being mounted onto the Franz cell and 50 μl of 0.2mg/ml calcein was applied to the surface of each sample after treatment with a hypodermic or PC MN, respectively. The receptor fluid was analysed over an increased time of 24 hours, in line with the above guidelines. After 24 hours the skin samples were subjected to tape stripping and homogenisation with papain, to create a permeation profile. This was repeated 3 times for each skin thickness sample to obtain statistically significant results.

17.9.2 Results

Figures 17.10 to 17.12 show how the thickness of the skin affects the permeation of calcein. These are shown as positive control, negative control, and MN treated samples in the results.

The negative control samples did not receive any needle treatment and therefore, in theory, should only allow negligible calcein permeation. However, it is first noted, that from integrity testing, thinner samples that measure <300 μm , produced decreasing integrity results which is indicative of a compromised SC barrier. Therefore, it is

already known that these samples would not prevent the calcein from permeating into the Franz cell receptor. Figure 17.10 confirms that skin thicknesses of $<200\mu\text{m}$ and $<300\mu\text{m}$, enabled a significant portion 97% and 93% respectively of the calcein concentration into the dermal layer and receptor fluid. This implies that a skin thickness of $<300\mu\text{m}$ were too thin to act as an effective barrier, and calcein was able to diffuse through it easily. This may have been due to the dermatome disrupting the integrity of these thin skin layers, where thinly cut skin, due to its delicate nature, often contained visible defects, such as, tears and clogging of the blade making cutting of these thin layers difficult. Increasing the skin thickness from 500-900 μm , shows that a greater concentration of calcein was recorded on the skin surface and in the epidermis implying that the calcein has not permeated efficiently into the skin. Confirming that thicker skin does prevent a calcein from penetrating into the deeper skin layers and into the Franz cell.

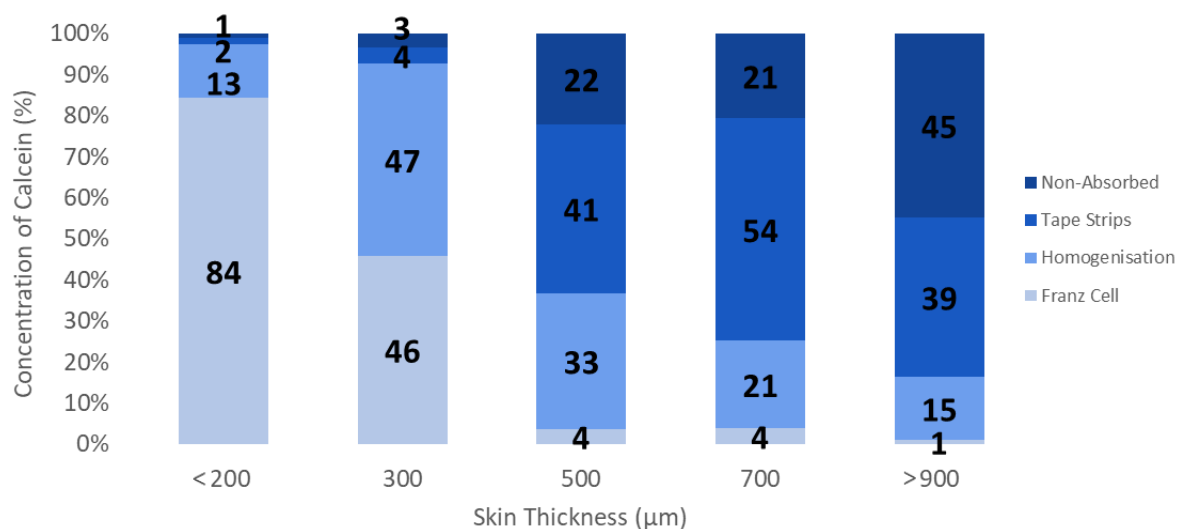


Figure 17.10 permeation profile of calcein through skin with different thicknesses, with no needle treatment. i.e., negative control.

To evaluate the effects of a positive control, a hypodermic needle was used to completely puncture through the skin. The open channel, created by the needle insertion, facilitated the movement of calcein from the surface of the skin into the receptor fluid, mimicking natural hypodermic injection into either the systemic circulation or muscle. The permeation profile in figure 17.11 shows that calcein can penetrate through the skin and into the receptor chamber of all skin samples up to 700 μm thickness. Beyond this thickness the concentration of calcein recovered within

the SC increases, suggesting that calcein permeation through larger thicknesses is significantly reduced. This may be due to two factors

1. The skin's natural flexibility and ability to close any pores or channels created.
- or
2. Thick skin of <900µm retains the hydrophilic dermis which as discussed above, limits the movement of hydrophobic molecules

To prevent either of these factors from occurring, skin thickness's of <700µm are deemed too thick and will be omitted from further studies.

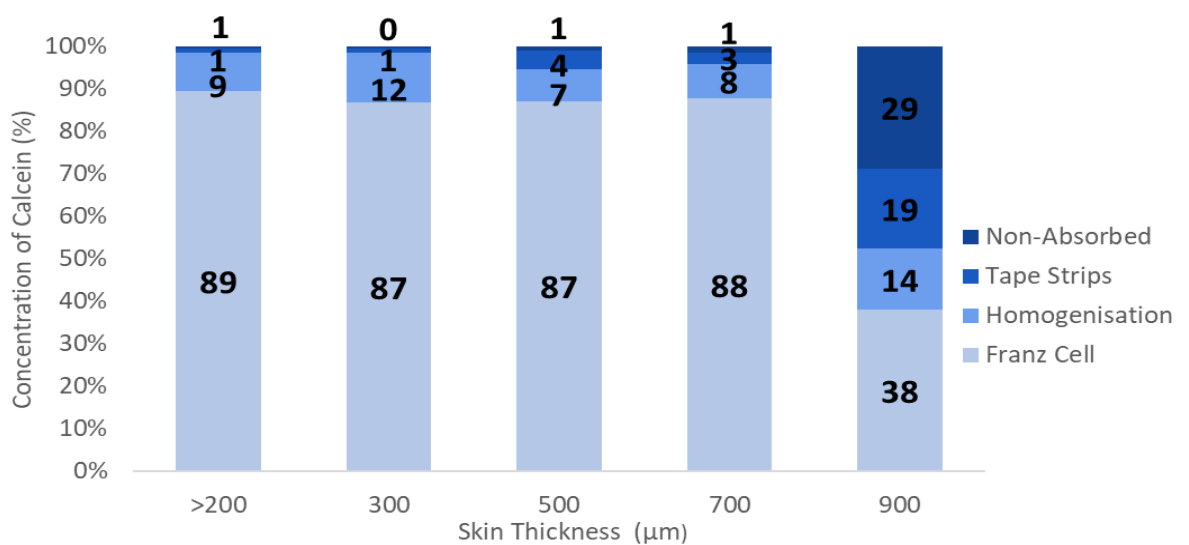


Figure 17.11 Permeation profile of calcein through skin of different thicknesses, that have undergone treatment with a hypodermic needle i.e., positive control.

The results obtained for skin samples treated with PC MNs, figure 17.12 reflects the results of the positive and negative controls above. When using skin thicknesses of less than 300µm a significant concentration of calcein was recovered from the receptor chamber, while for thicker skin samples of >900µm a larger concentration of calcein was recovered from the tape stipes. However, as these thicknesses have already been ruled out, thickness of between 500 - 700µm are to be used for further evaluation. These results present a distributed concentration of calcein in each section of the skin in comparison to the control (without any MN treatment), thereby indicating the MNs facilitate calcein permeation through the skin into the deeper skin layers (beneath the SC) and into the Franz cell receptor compartment. In addition, not all of the calcein has distributed into the receptor fluid, as seen with the hypodermic needle, which may be

due to the application time of the MN into the skin, as it was only held for 1 minute. As previous characterisation results in chapter 13.3 and 13.4 have shown the flexibility of the skin pores to reclose after PC MN insertion without an applicator.

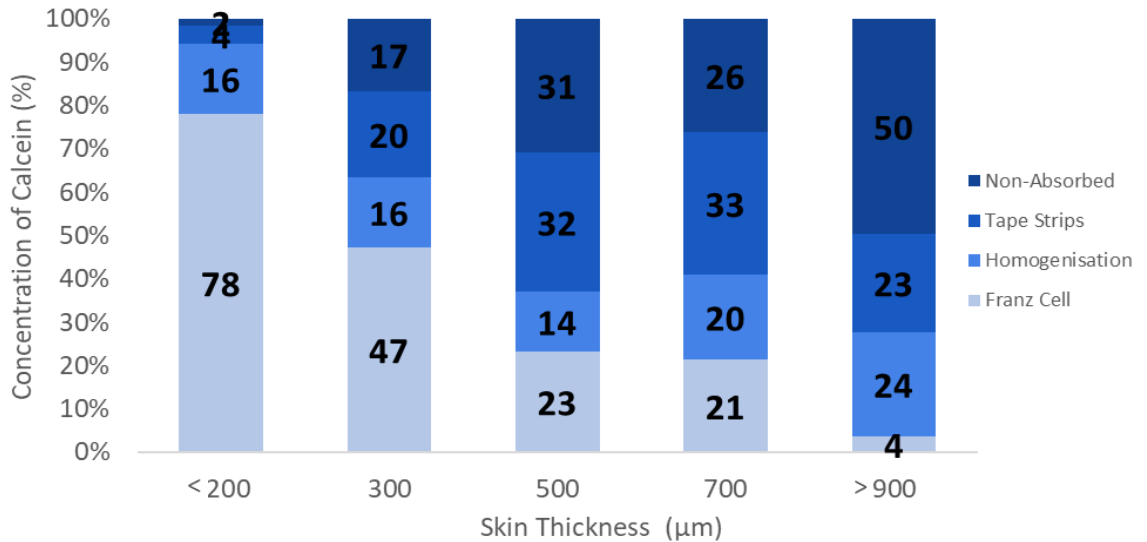


Figure 17.12 permeation profile of calcein through skin of different thicknesses, that have undergone treatment with a polycarbonate microneedle.

At the time of establishing these results PC MNs were easily available, but the silicon MN's were still undergoing fabrication optimisation. Therefore, to compare and confirm whether these results could be used as a universal guideline for all MN types, regardless of material, shape or size, future studies would repeat the above experiments on both OOP and in-plane silicon MNs.

17.10 Conclusion

The aim of this chapter was to optimise a skin permeation Franz cell assay in agreement with international guidelines. The integrity of the skin samples was measured using TEER to observe any changes in electrical resistance. The guidelines state that the active ingredient tested needs to be fully recovered and quantified in each layer of the skin to form a permeation profile. Tape stripping and enzyme homogenisation protocols were optimised to recover active ingredients and characterise their location. The enzymes collagenase and papain were identified and confirmed to be effective at breaking down the skin to release the active ingredient for analysis. Although both

enzymes overall produce the same results, papain works faster to break down proteins in the skin. This also means, active ingredients that are based on proteins e.g. insulin, cannot be homogenised using papain, as the active ingredient would also be broken down, and subsequently unquantifiable.

To create a visually simple, quantification graph that incorporated all quantification methods i.e., tape strips, homogenisation, and the cumulative concentration, the stacked bar graph produced in figure 17.8 provides an easily usable interpretation of the permeation profile of the active ingredient, using coloured banding to visualise the amount of permeation. When the darkest blue band is greater it is immediately obvious that most of the active ingredient has not permeated, whereas if the lightest blue band is greater this shows that most of the active ingredient has permeated into the receptor.

Lastly, the effect of skin thickness for *in vitro* Franz cell testing was optimised. Skin thickness that were less than 300µm, were rendered delicate and prone to defects and tearing and thus too thin for Franz cell analysis, while skin that was too thick, measuring more than 900µm, inhibited permeation of calcein. Calcein is a slightly hydrophilic drug molecule, and therefore, naturally has an affinity for the hydrophilic dermal layer and receptor fluid and thus is the reason it was chosen for optimisation studies. If a hydrophobic molecule were to be used, it would naturally reside in the lipophilic layers of the SC and would have difficulty permeating into the deeper hydrophilic layers, regardless of skin thickness. Experiments conducted with hydrophobic molecules for transdermal delivery are discussed further in this chapter.

Overall, the optimal skin thickness for Franz cell permeation experiments was found to vary between 500-700µm, and thus will be used for all subsequent Franz cell studies.

Chapter 18

Calcein transdermal delivery

18.1 Introduction

As described in chapter 14, the optimal measurements for a solid in-plane MN to effectively penetrate into the epidermis while being mechanically stable, measured a post etch height of above 66 μm and a post etch width of less than 460 μm . However, although the MNs have proven their ability to penetrate the skin, the next step is to determine whether the in-plane MNs can successfully deliver substances across the SC barrier and into the skin to stimulate a therapeutic response.

It was also discussed that depending on the therapeutic application, the height of the MN can be fine-tuned to penetrate to specific skin depths to deliver the compounds to the necessary skin layer for an enhanced response. Therefore, to test this theory two MNs etched to lengths of 300 μm and 600 μm were selected to simultaneously investigate how the effect of MN length affects the depth of compound delivery. The model compound calcein was selected for delivery due to its lipophobic nature preventing it from naturally penetrating through the SC independently [311] and its fluorescence ability for ease of detection in the skin analysis. The results in this chapter from using in-plane MNs for drug delivery of calcein are currently being reviewed by the journal of controlled release for publication.

18.2 Aims and objectives

1. To use *in vitro* proof of concept studies to demonstrate that in-plane MNs can deliver a model drug through porcine skin using
2. To provide a quantitative assessment of *in vitro* delivery with varying MN height.

18.3 Methods

The fabrication of in-plane MNs was discussed in chapter 9 where MN devices were etched to 300 μm wide and either 300 μm or 600 μm in height in an 1 x 5 array. Porcine skin samples were freshly excised from piglets and dermatomed to the optimised

thickness of 500 μm . To test skin integrity electrical resistance tests were completed as discussed in chapter 17.5, any defective skin samples were discarded. The Franz cell apparatus and controls were set up as described in chapter 7.4.1 and each test was repeated a minimum of six times.

Individual skin samples were subjected to five repeat insertions with either 300 μm length or 600 μm length MN arrays using thumb pressure application and then mounted onto the Franz cell. The Franz cell receptor volume was 4mls with an aperture surface area of 6.4mm². Next, 50 μl of 0.2mg/ml (2.5 $\mu\text{g/ml}$) calcein dissolved in dH₂O, was applied to the skin surface and 400 μl of the receptor fluid was withdrawn at various timepoints (described in chapter 7.4.1). In order to quantify the concentration of calcein in varying skin sections, each skin sample was tape stripped and homogenised using papain for 2 hours. The calcein concentration was analysed using a FLUOstar Omega spectrophotometer at excitation and emission wavelengths 485-12nm and 520nm respectively and the degree of fluorescence was compared to a calibration curve ($R = <0.98$).

The statistical significance was measured with $P < 0.05$ and a one-tailed T-test was performed for direct data comparison; multiple groups were compared using a one-way ANOVA with Tukey HSD *post hoc* test. Data analysis was performed using Microsoft Excel and SPSS software.

18.4 Results

To assess the capability of in-plane MNs to facilitate transdermal drug delivery, a small (622.5 Da) model compound, calcein, was chosen for its ease of detection through fluorescence spectroscopy and its low logP of -5.02 [311] rendering it hydrophilic and therefore, unable to cross the lipophilic SC barrier unaided. The two MN heights of 300 μm and 600 μm were verified in OCT analysis (see chapter 14.4.3), to penetrate the skin to approximately microchannel depths of 218 μm and 394 μm , respectively. These differences in depth were analysed to observe how calcein partition in the skin.

Using the fluorescent standard curve, generated in figure 18.1, the quantity of calcein in the receptor chamber at each time point was plotted in figure 18.2. Initially, a high permeation rate was observed for both MNs, with flux measurements calculated as

1.08 $\mu\text{g}/\text{cm}^2/\text{h}$ and 1.17 $\mu\text{g}/\text{cm}^2/\text{h}$ for shorter and longer MNs, respectively. However, the rate for the 300 μm MNs reduces by approximately half until a plateau was reached at 4 hours to a final steady flux rate of 0.08 $\mu\text{g}/\text{cm}^2/\text{h}$, resulting in an overall maximum cumulative concentration of 0.2 $\mu\text{g}/\text{ml}$ (8% of the original dosage).

The longer MNs showed an overall higher sustained flux, that reached a plateau at 6 hours at a flux rate of 0.10 $\mu\text{g}/\text{cm}^2/\text{h}$, which is still statistically higher ($P < 0.01$) than the shorter MNs. The final cumulative concentration for the longer MNs calculated as 0.7 $\mu\text{g}/\text{ml}$ (28% of the original dosage). The control demonstrated that without any MN treatment calcein cannot be detected in the Franz cell receptor. The SD error bars for the 6 data sets did not overlap and demonstrated good reproducibility.

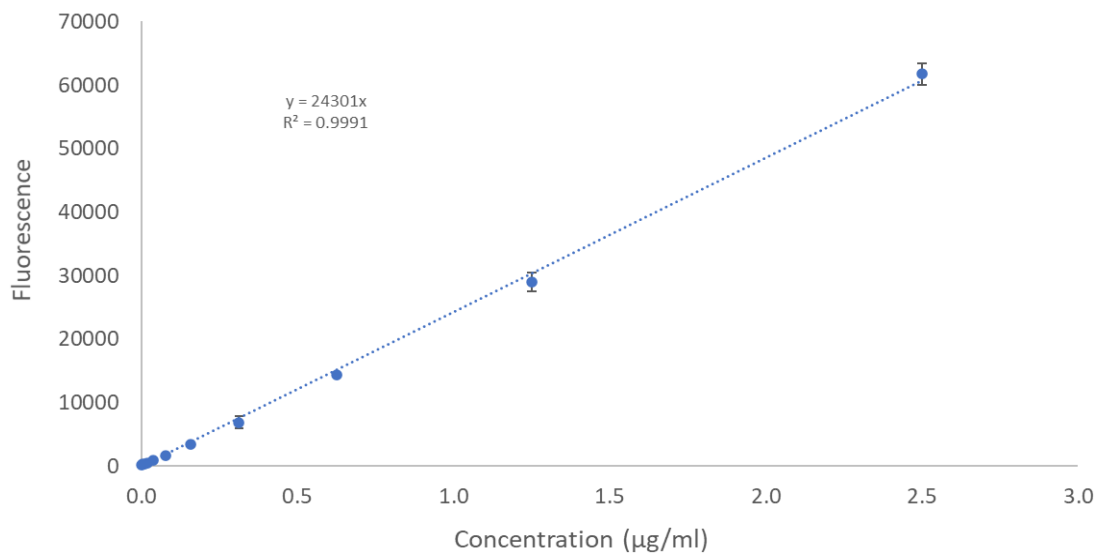


Figure 18.1 Exemplar standard curve used in quantitative analysis of calcein permeation (n=3)

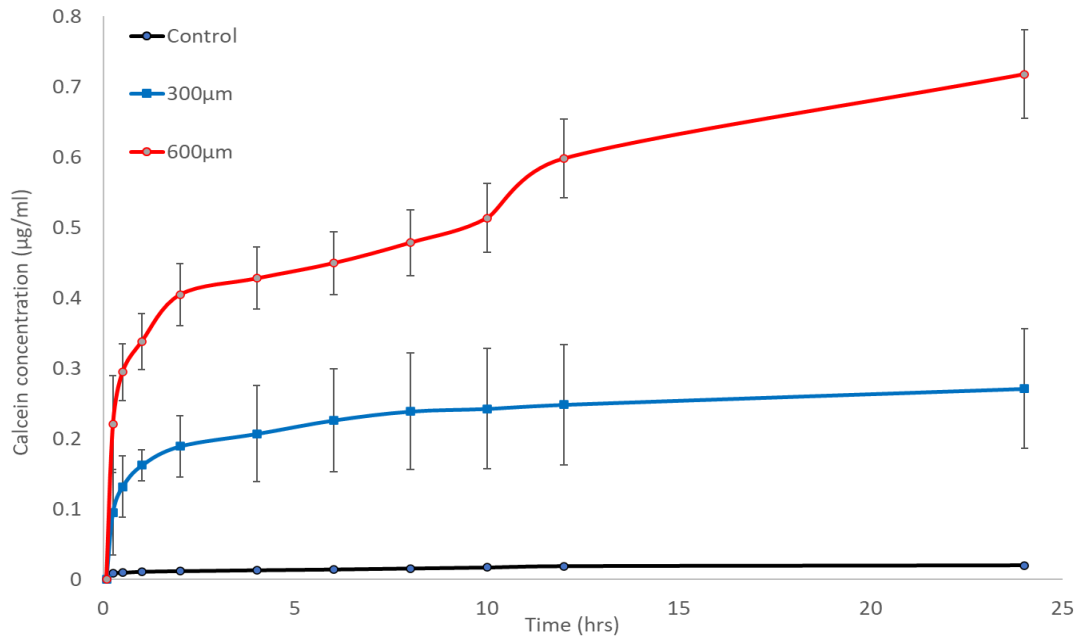


Figure 18.2 Cumulative concentration of calcein permeated through porcine skin without MN treatment control (black) and with treatment of MNs with varying heights of either 300µm (blue) or 600µm (red).

Both sets of MNs saw a plateau in the graph where calcein was no longer penetrating into the Franz cell. As the maximum calcein concentration detected was 0.2µg/ml and 0.7µg/ml for the shorter and longer MN respectively, the original dosage of 2.5µg/ml was unaccounted for, meaning that the profile of how the drug permeated through the skin layers could not be identified from the cumulative graph alone. Therefore, to quantify and visualise how calcein has partitioned through the skin and to account for the remaining calcein, tape stripping and homogenisation procedures were performed, and the results shown in figure 18.3.

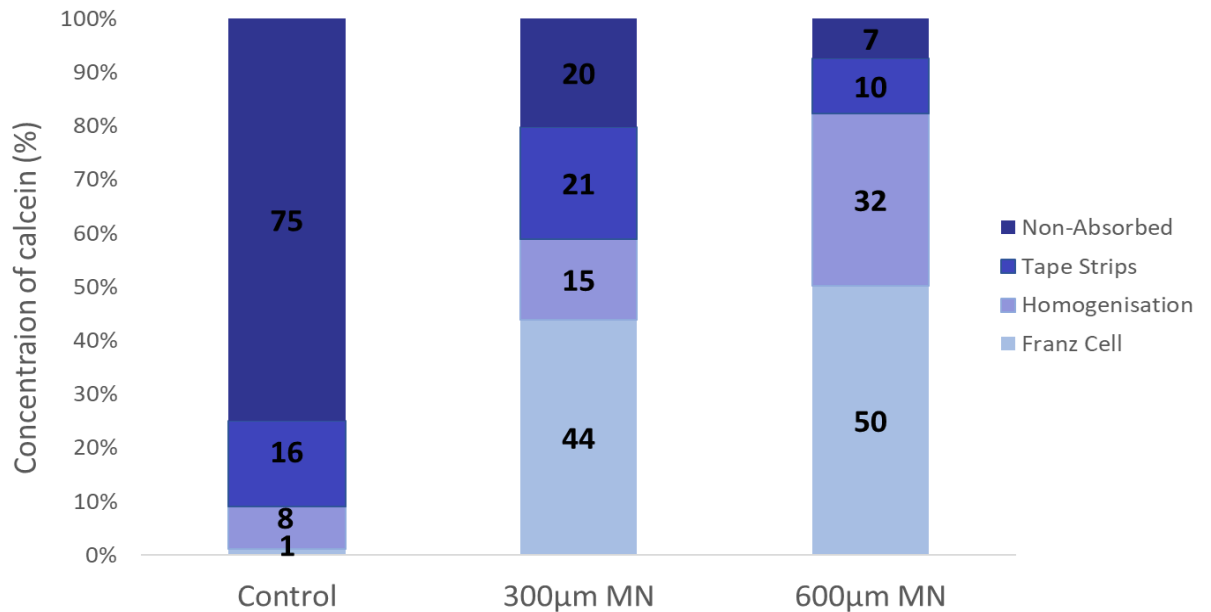


Figure 18.3 stacked bar graph showing the calcein permeation profile through porcine skin with and without MN treatments of 300 and 600µm in length.

As discussed in section 17.8, each section of the stacked bar graph indicates the percentage of calcein found in each layer of the skin i.e. the first tape strip accounts for the concentration not absorbed through the skin (darkest blue), while consecutive tape strips calculate the concentration of calcein which has partitioned into the SC. Homogenisation degrades any skin left to release the calcein retained within the epidermis, while the Franz cell (lightest blue) signifies the calcein concentration that has fully penetrated through the skin. The control study of no MN treatment calculated a total calcein recovery of 1.87µg/ml, in which 75% was retained on the first tape strip and had not diffused into the skin. Additionally, only 16% of the calcein (0.3µg/ml) was found to partition and diffuse through the SC towards the epidermal layers. This demonstrated that 91% of the calcein recovered had not significantly diffused into the skin.

In comparison, skin samples that received MN treatments demonstrated a reversal in results. Results obtained for the longer 600µm length MNs recovered in total 1.43µg/ml from the original 2.5µg/ml dosage, where the deeper skin layers received the highest concentration of calcein, as the Franz cell receptor equated 50% (0.72µg/ml) of the recovered calcein. The second highest concentration of 32% (0.46µg/ml) was located in

the homogenisation, while 17% (0.26µg/ml) of the calcein recovered remained in the top two sections and had not sufficiently permeated.

However, the total recovered calcein concentration for the 300µm length MNs was 0.47µg/ml, only 19% of the original 2.5µg/ml dosage. Of the recovered total 44% had permeated into the Franz cell receptor. The remaining layers all observed an approximate equal calcein concentration resulting in 20%, 21% and 15% (0.09µg/ml, 0.1µg/ml and 0.07µg/ml) respectively.

Overall, longer MNs recovered a calcein total concentration of 1.43µg/ml, while only 0.47µg/ml of this was recovered with the short MN designs. It is believed that due to the shorter microchannel created from the shorter MNs, the flow of calcein into the skin was limited and thus remained on the skins surface for longer, making it more susceptible to atmospheric evaporation due to the 32°C heat pad beneath the Franz cell. Although significantly less than the longer MN's, the shorter MNs still enabled more calcein to permeate the skin in relation to the control.

18.5 Conclusion

These results confirm that skin samples treated with in-plane MNs successfully enable hydrophilic calcein to be delivered through the lipid SC barrier and through the skin layers into the Franz cell receptor below with a total dosage recovery of 1.43µg/ml and 0.47µg/ml for long and short MNs respectively. In comparison, the control with no MN treatment recovered 1.87µg/ml, in which 75% of was found in the first tape strip and 91% recovered in all tape strips, meaning only 9% could effectively penetrate through the SC.

The two different MN lengths tested successfully delivered calcein into different skin depths, confirming that the MN length can influence the level at which calcein is partitioned within the skin to facilitate customised applications. Through OCT analysis the 600µm longer MNs had proven to penetrate to a depth of 420µm, while the shorter 300µm MN penetrated to a depth 250µm, creating a microchannel difference of 170µm. This difference enabled 82% and 59% of calcein to penetrate into therapeutic regions of the skin for long and short MNs respectively, with more of the calcein being retained within the tissue for the shorter MN and a higher percentage recovered in the Franz cell

with longer MN application. Customising the penetration depth is beneficial to enable the drug to be directly delivered to the active site, which consequently improve the therapeutic response to that drug. Shorter MNs are likely to prove advantageous for local skin applications such as, cosmetics or vaccines, while a longer MN is more suited to deliver medicinal compounds to deeper regions and direct them into the systemic circulation for a wider anatomical application, such as, insulin delivery.

Chapter 19

Transdermal delivery of Insulin and Hyaluronic acid

19.1 Introduction

The previous chapter (18) demonstrated the importance of MN length on delivery depth and how this can be modified to complement the application requirements. To investigate this further each MN length, 300 μ m and 600 μ m, will be assigned a therapeutic compound to deliver their respective active sites. The results of this chapter have been approved for publication in the journal of pharmaceuticals and biopharmaceutics.

Cosmetic products including botulinum toxin (Botox) and hyaluronic acid (HA) are popular treatments for the improvement of crow's feet wrinkles around the eye [312]. A hypodermic needle is the conventional method of application to inject the solutions into the muscle of the face, however, this is generally painful and is likely to cause swelling and bruising. Alternative applications, such as, topical creams, are available for local treatment of wrinkles and scars, however these are reported to have a low bioavailability at the intended target site limiting the therapeutic effect as only 10-20% of the drug permeates through the skin [313]. The results from chapter 18 concluded that the 300 μ m MNs demonstrated the ability to facilitate local delivery into the higher epidermal layers; utilising this would avoid deep painful muscular injection and improve bioavailability.

HA is a large homogenous polysaccharide found naturally in the extracellular matrix of human tissues with a wide range of molecular weights (MW), due to the high *in vivo* turnover [314]; because of this, the logP of HA is inconsistent but still has a strong water-binding capacity [314]. Therapeutics with a low MW of <500Da can easily penetrate the skin [315], however, the MW of fluorescein-HA used in this study measures ~800,000Da (as purchased from Sigma), and therefore when compared to the calcein study in chapter 18, fluorescein-HA is 12,851 times greater. Although both molecules are hydrophilic the size of fluorescein-HA could restrict its passive transport through the stratum corneum.

Diabetes is a chronic disease in which the glucose in the blood cannot be broken down by the pancreatic hormone insulin, either from insufficient insulin production (type 1) or defective insulin molecules (type 2) [316]. Worldwide, diabetes affects approximately 415 million people which is believed to increase to 642 million by 2040. The management of diabetes currently includes either daily injections of insulin units into the subcutaneous tissue or oral agents. However, variation in insulin pharmacokinetics and bioavailability [317] combined with painful and frequent dosing with hypodermic needles, [318] presents major drawbacks in insulin therapy such as scarring and low patient compliance. Alternative delivery routes include, intramuscular, whereby insulin injected into the muscular layers results in the insulin potentially being absorption too quickly and consequently the glucose concentration falls too quickly, rendering the patient hypoglycaemic. The oral route of administration although the most convenient, observes multiple physical, chemical, and biological challenges throughout the digestive tract, thereby, reducing the bioavailability of insulin. The low acidic pH of the stomach, the digestive enzymes located in the intestines and the intestine mucosal barrier contribute to reduce effectiveness [319], [320]. Thus, MN delivery offers an improved alternative due to its ability to by-pass hepatic first-pass metabolism to prevent insulin degradation, improving systemic bioavailability and improving the rate at which insulin can be released, reducing the risk of side-effects associated with the concentration [321]. The aim of injection is to deliver insulin into the systemic circulation, and, as demonstrated in the previous chapter, utilising the longer 600 μ m MN to deliver calcein into the Franz cell receptor, seems to be the most effective approach. However, in comparison to calcein at 622.5 Da, insulin has a larger MW of 5,808Da, therefore, this research will additionally investigate the 600 μ m length MN's ability to deliver larger molecules through the skin and into the Franz cell receptor to target the delivery to the receptor fluid which represents the systemic circulation.

19.2 Aims and objectives

1. To demonstrate that 300 μ m and 600 μ m length in-plane MNs can deliver, (a) HA to the primary layers of skin and (b) Insulin into the Franz cell receptor through porcine skin.

2. To compare the ability of MNs to deliver large molecular weight molecules in comparison to calcein in chapter 18.

19.3 Methods

The *in vitro* Franz cell preparation and MN application methods described in chapter 18 were adopted for this study. The 300µm MN length was tested to deliver FITC-HA, while the 600µm MN length was tested to deliver FITC-insulin. Both molecules were purchased from Sigma with fluorescent tags for ease of quantification using the FLUOstar Omega spectrophotometer.

FITC-HA was made up to 1mg/ml in cold dH₂O and left overnight in a dark fridge at 2-8°C to fully dissolve, in line with the Sigma instructions. FITC-insulin was dissolved in 0.01M HCl to a final concentration of 0.1mg/ml, which is equivalent to a clinical concentration of 2.8 units. For each experiment 200µl of FITC-HA or 350µl FITC-insulin was applied to the surface of the skin and left to permeate for 24hrs. The statistical significance was measured with $P < 0.05$ and a one-tailed T-test was performed for direct data comparison.

19.4 Results

19.4.1 Hyaluronic acid

To assess the ability of a 300µm in-plane MN to target delivery of a large molecule to the top layers of the epidermis, FITC-HA measuring ~800,000Da was studied by applying the solution to the skins surface post MN treatment. As FITC-HA is water-soluble it cannot bypass the lipophilic SC independently. The fluorescent standard curve, figure 19.1, was used to quantify the concentration of FITC-HA (figure 19.2) in the receptor chamber through permeation.

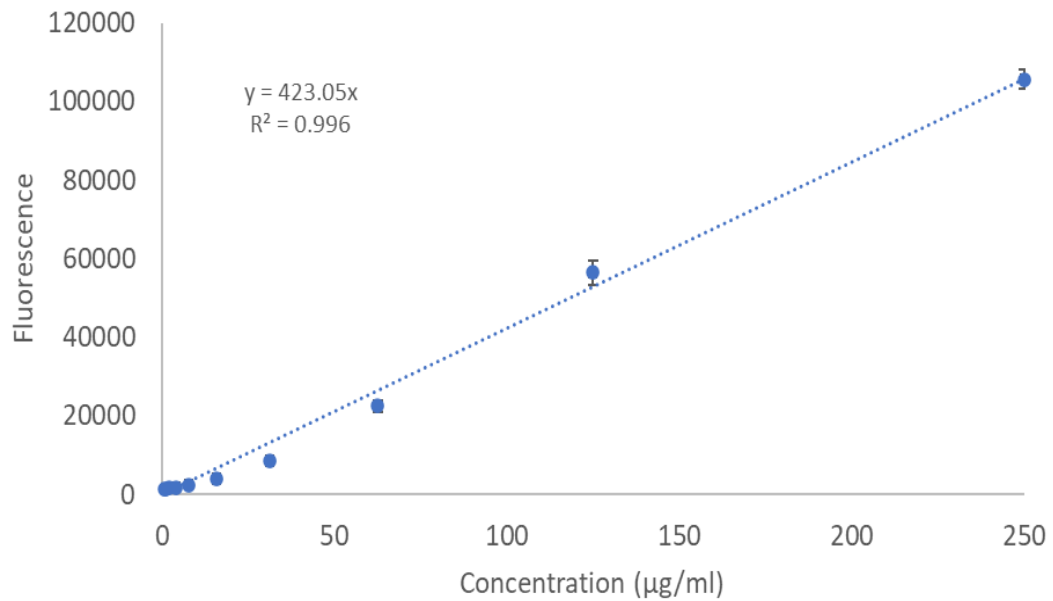


Figure 19.1 Standard curve used in quantitative analysis of FITC-HA permeation (n=3)

At the start of the experiment a large permeation flux of FITC-HA was observed calculating at $59.59\mu\text{g}/\text{cm}^2/\text{h}$, due to the freshly created micro-channels achieving their maximum opening dimensions to allow FITC-HA to flow through. From this point the flux began to drastically fall by approximately halve until a steady rate of $4.98\mu\text{g}/\text{cm}^2/\text{h}$ was reached at 6 hours; this is shown by the plateau in figure 19.2, equating to a final cumulative concentration of $25.03\mu\text{g}/\text{ml}$. In comparison, the highest flux rate observed with the control was $3.3\mu\text{g}/\text{cm}^2/\text{h}$ but remained stable between $1.7\mu\text{g}/\text{cm}^2/\text{h}$ and $0.5\mu\text{g}/\text{cm}^2/\text{h}$ providing a final cumulative concentration of $4.2\mu\text{g}/\text{ml}$. This fluorescence could be due to skin influences within the receptor, but overall, the control concentration remained low, where the standard deviations did not overlap to demonstrate a statistical difference of $P=<0.000006$.

In comparison, the calcein cumulative graph in 18.2, demonstrated that 8% of the overall calcein dosage had permeated into the receptor fluid, whereas 13% of the total FITC-HA data was detected in the receptor of this study. As there is no significant difference between the cumulative concentrations for large or smaller molecules with a $300\mu\text{m}$ MN, a potential difference could be sought in the permeation profiles and how FITC-HA distributes throughout the skin. However, so far, the results look optimistic in terms of targeted delivery as it would be expected to find a lower concentration of FITC-HA in the receptor fluid than the skin layers.

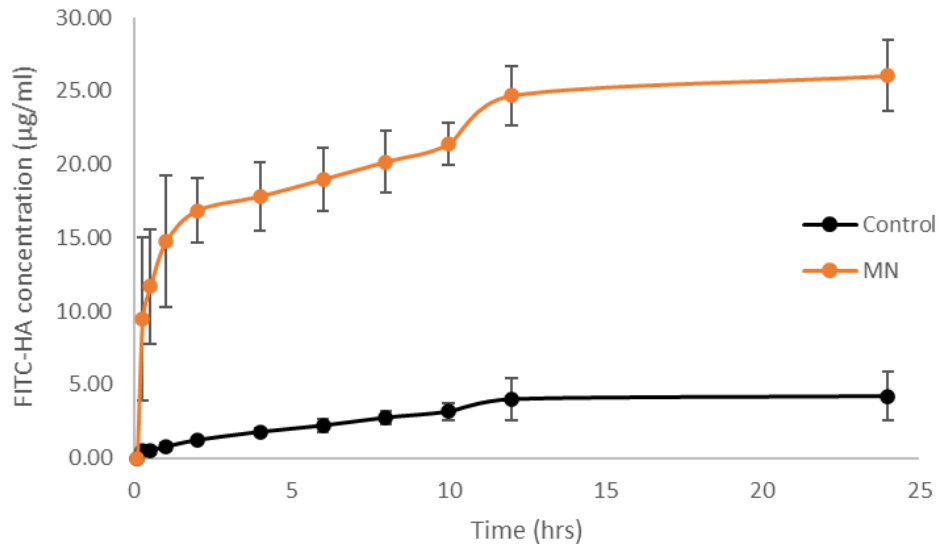


Figure 19.2 Cumulative concentration of FITC-HA permeated through porcine skin without MN treatment control (black) and with MN treatment (orange)

The stacked bar graph in figure 19.3 demonstrates the percentage of FITC-HA calculated from each skin treatment i.e., the tape strips and homogenisation. The darkest blue indicates the amount retained on the skin, while the colour gradient illustrates that the FITC-HA is partitioning deeper through the skin, until the receptor is reached (lightest blue), described in more detail in subchapter 17.8.

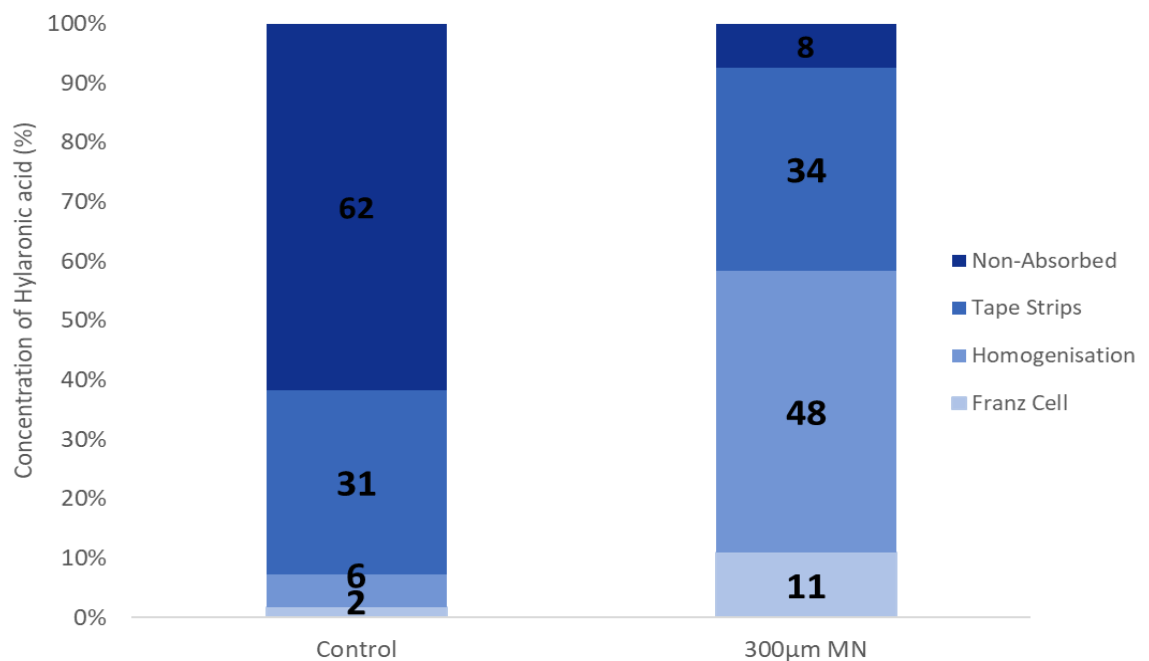


Figure 19.3 stacked bar graph showing the FITC-HA permeation profile through porcine skin with and without MN treatment.

The control profile reveals that 62% (153.16 $\mu\text{g/ml}$) of the FITC-HA is retained unabsorbed on top of the skin and 31% (77.31 $\mu\text{g/ml}$) had partitioned into the SC, calculating a combined non-delivered total of 93%. This confirms that FITC-HA cannot penetrate through porcine skin independently.

In comparison, the MN treated skin observed that 8% (17.93 $\mu\text{g/ml}$) of the FITC-HA remained unabsorbed on the skin, while 34% (81.31 $\mu\text{g/ml}$) partitioned into the SC, calculating a lower non-delivered total of 42%. However, the largest FITC-HA percentage recovered was calculated as 48% (113.57 $\mu\text{g/ml}$) found within the homogenisation. Combining this to the concentration found in the receptor fluid, (26.03 $\mu\text{g/ml}$) equates an overall successful permeation concentration of 139.60 $\mu\text{g/ml}$ (59%). These results demonstrate that FITC-HA resides mainly in the epidermal region of the skin, rendering it available for local skin treatments.

To evaluate the effect of the molecular weight of compounds administered, the stacked bar graphs of calcein (18.3) and FITC-HA, (figure 19.3) are compared. Both skin samples have undergone treatment with a 300 μm length MN but show significantly different results. The first noticeable observation is the difference in the percentage concentration of the homogenisation and receptor, measuring at 15% and 44% vs 48% and 11% for the calcein and FITC-HA delivery, respectively. The reversal in concentration demonstrates that the smaller molecule, calcein, was able to partition further through the skin into the receptor fluid, while the large molecule was retained within the top layer of the skin. It is believed that the smaller size of the calcein molecule enabled it to move between the cells of the skin layers easier than the larger molecule. Additionally, a difference is observed with the tape strip measurements where calcein had partitioned equally between the first tape strip and the combined ten consecutive tape strips to equate to 20% and 21% respectively, while FITC-HA partitioned into 8% and 34%. Although perhaps it would be thought that the FITC-HA results would be the other way around and reflect the partitioning effect previously discussed, overall, both molecules demonstrated unsuccessful permeation percentage totals of 41% and 42%.

This study discovered that both smaller calcein molecules and larger FITC-HA compounds can successfully penetrate the skin using 300 μm MN's. This provides a

potential superior method over traditional hypodermic needles and emollients to deliver compounds to their optimal regions for desirable and improved therapeutic outcomes.

19.4.2 Insulin

To examine the skin permeation of FITC-insulin with 600 μ m length MNs, the fluorescent standard curve $R^2=0.99$, produced in figure 19.4 was used to calculate the cumulative concentration curve from samples of the Franz cell receptor at various time points, figure 19.5.

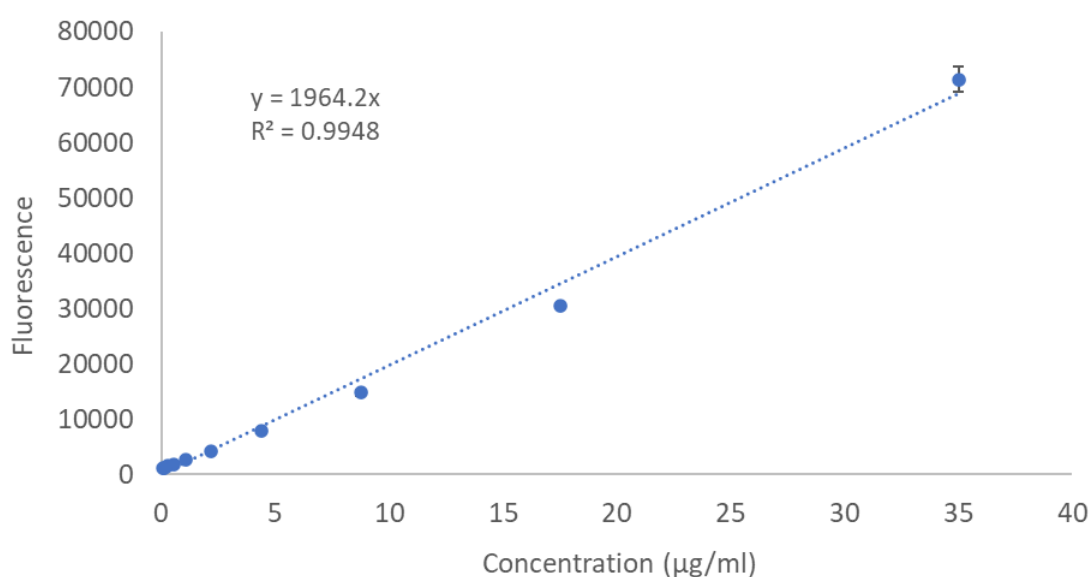


Figure 19.4 Standard curve used in quantitative analysis of FITC-Insulin permeation

Initial cumulative flux rates measured 1.41 μ g/cm²/h and 1.13 μ g/cm²/h for the control and MN treated skin, respectively. This rate steadily diminished to 0.02 μ g/cm²/h and 0.09 μ g/cm²/h after 24 hours once the MN channels had closed or the insulin dosage had totally permeated. At the 1-hour time point the curves started to separate as the MN treated skin enabled more FITC-insulin to be detected in the Franz Cell. The control sample demonstrated that overall 0.35 μ g/ml, 0.01% of the starting dosage, had permeated into the receptor fluid, while the MN treated sample shows that 1.19 μ g/ml has permeated into the receptor fluid. Although there is a significant statistical difference of $P=0.00318$ between the samples, the overall total recovered was only 3.4% of the original dosage (35 μ g/ml).

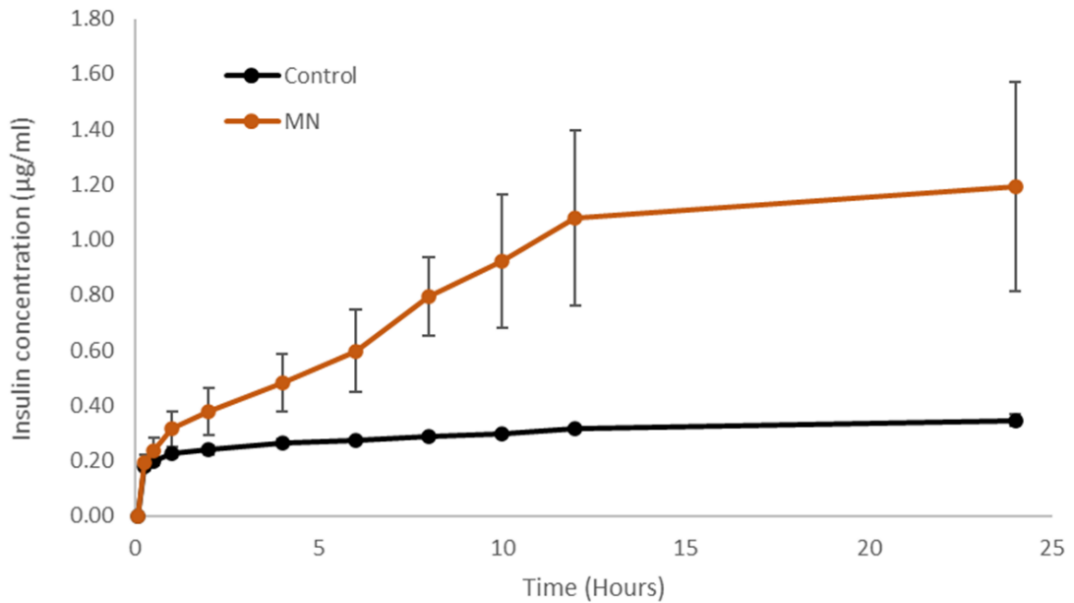


Figure 19.5 Cumulative concentration of FITC-insulin permeated through porcine skin without MN treatment control (black) and with MN treatment (orange)

To investigate the results further, the FITC-insulin concentration quantified in the tape strips and homogenisation were compared (figure 19.6). The total FITC-Insulin recovered for the control and MN treatment sample were 15.54µg/ml and 17.20µg/ml, equating to 44% and 49% of the original dosage. As approximately half of the sample was missing, this could be down to two factors:

1. The low flux rate into the skin means more FITC-insulin is retained on the surface and is susceptible to environmental factors such as evaporation due to the 32°C heat pad beneath
2. User error while pipetting, creating dilutions etc.

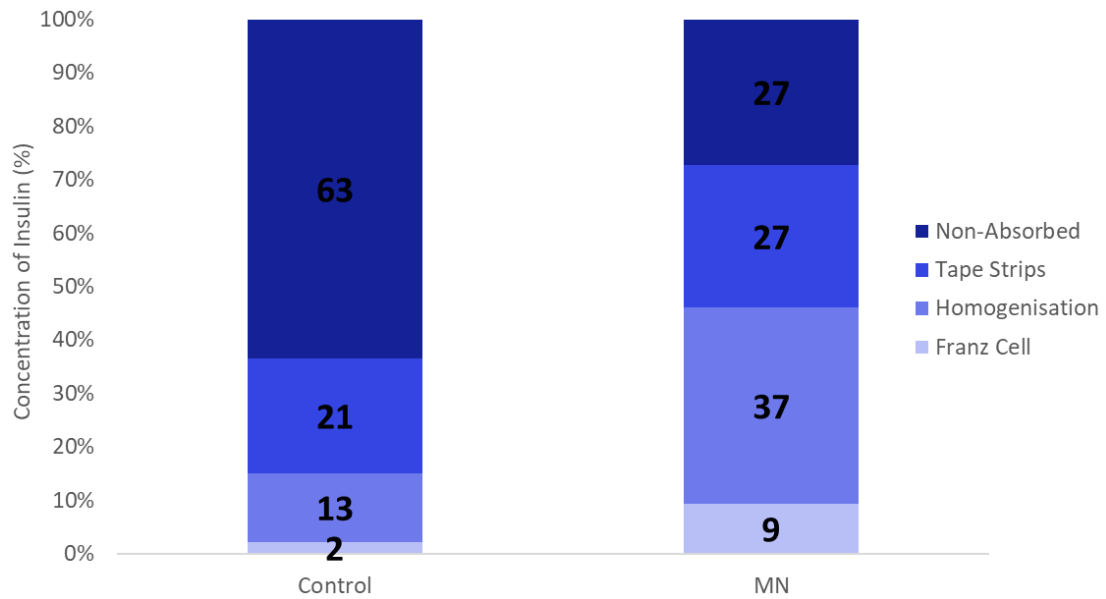


Figure 19.6 stacked bar graph showing the FITC-insulin permeation profile through porcine skin with and without MN treatment.

Analysing the percentage of FITC-insulin that did penetrate through the SC showed that with MN application only 9% made it into the receptor fluid, while other layers held concentrations of 27%, 27% and 37% respectively. The homogenisation layer received the largest concentration of 4.6 μ g/ml, demonstrating that when combined with the Franz cell receptor, 46% of the recovered dosage successfully penetrated the skin.

The control sample results showed that 63% (9.86 μ g/ml) of the FITC-insulin remained on the surface of the skin, while only 21% partitioned into the SC, confirming that FITC-insulin cannot penetrate through the skin unaided.

To compare if deeper skin penetration is attainable with a 600 μ m MN length, the smaller molecule calcein tested in figure 18.3, demonstrated that 82% of its recovered total had successfully penetrated the epidermis and receptor fluid, which is 36% more than FITC-insulin (46%). This demonstrates that smaller molecules can manoeuvre through the skin layers easier than larger molecules.

The aim of this study was to examine whether FITC-insulin could permeate into the epidermal homogenisation and the Franz cell receptor to target systemic delivery. Although some successful penetration was observed, a larger percentage of FITC-insulin remained on the top of the SC or partitioned into it, rendering it unavailable to

the systemic circulation. Insulin not only has a larger MW, but lower a solubility at physiological pH of 7.4 [322], adding another challenge to delivery. It is generally accepted that a non-ionised species of an acidic or basic molecule is more permeable across the skin barrier than the ionised form. Thus, penetration across the SC is affected by the physiochemical properties of the drug and the degree of ionisation. However, the SC is composed of an acidic pH for protection against biochemical processes such as pigmentation, ion homeostasis and epidermal cell behaviours. The pH ranges from 4.5 to 5.0 in the outer SC layers, termed the “acid mantle” and approaches a neutral pH in the lower layers and the epidermis [323]–[326]. As insulin is soluble in an acidic pH [327], the acidic nature of the SC could be beneficial to facilitate insulin permeation and provide a possible reason for the higher percentage, 57%, of FITC-insulin being recovered on the skins surface or partitioned into the SC. Whilst in addition to the large MW, the increasing pH gradient could be preventing it from penetrating further.

To improve the delivery of insulin, further enhancements could be used, such as, modifying insulin itself or encapsulating it in a different vehicle that has more attractive properties for transdermal delivery. In addition, other types of MNs, such as hollow or dissolvable enable a greater targeted penetration to directly inject into the skin and active site directly, rather than relying solely on passive diffusion.

19.5 Conclusion

Therapeutic molecules with low molecular weight (<500Da) can easily penetrate through the skin without the addition of enhancers; the molecules investigated in this study all carry a higher MW which significantly restricts their movement [315]. However, the 300µm MN demonstrated that it could successfully deliver both calcein and FITC-HA to the shallower epidermis to facilitate targeted local delivery. The longer MN length of 600µm also saw successful deeper penetration by creating a longer microchannel to enable calcein to permeate into the receptor fluid. However, attempts to deliver insulin into the receptor chamber were not as fruitful, due to the combined challenges of a larger MW and an acidic solubility. Traditionally, insulin is injected into the subcutaneous tissue through various processes such as a syringe, pen or pump. The insulin formulation injected includes excipients, such as, preservatives used for stability or altering the pH, which aid the absorption of insulin through the various tissues and into the systemic circulation. However, as the above experiment used pure insulin,

bound to a FITC fluorescent marker, without the enhancers this may have contributed to the lack of absorption results. Thus, for future studies either a chemical or physical enhancer will need to be explored.

Chapter 20

Conclusions and future work

The work throughout this thesis describes the fabrication and characterisation of two novel MNs fabricated from silicon wafers, through either DRIE or wet etching. Each MN successfully demonstrated the ability to penetrate through the SC and deliver substances into the skin to facilitate drug delivery. Both in-plane and OOP hollow MNs fabricated offer significant advantages over other injection methods currently available e.g., hypodermic needles, as the sub-millimetre lengths limits the risk of injury and reduces pain in patients, potentially counteracting patient phobia of hypodermic needle use.

The OOP microneedles were fabricated from a 3-step plasma etch method to create a MN with an adjustable tip angle and a closed central bore. Injection through the bore allows for controlled fluid volume delivery, whilst the sharp bevelled tip limits pain for patients by reducing insertion force.

Novel in-plane MNs were fabricated from simultaneous front and back side etching of a (100) silicon wafer in KOH solution, utilising the characteristic (110) and (111) 54.7° angled planes to create the MN tip. This fabrication method has also been used to demonstrate different aspect ratio MNs which enable targeted drug delivery depths. By utilising KOH etching, the fabrication process is low-cost and scalable.

Through mechanical testing it was established that the primary mechanism of failure for both MNs was compression at the tip of the MN causing it to crumble, chip or blunt.

The in-plane MN demonstrated that without the support of a wider MN, application of higher forces saw longer MNs ultimately fracture at the shaft and at their base.

However, all OOP and in-plane MN geometries were mechanically strong enough to withstand at least 10N of force; equivalent to thumb pressure insertion into skin. The characterisation of different in-plane MN geometries confirmed that MNs measuring >66µm in height and <460µm in width are suitable for effective skin penetration.

To demonstrate the ability of hollow MNs to deliver substances across the skin, histological sections were produced for both MNs. The OOP MNs successfully demonstrated delivery of a fluorescent marker into the skin, where a high concentration

of the marker situated at the base of the microchannel. In addition, two in-plane hollow MNs with open and closed bored also demonstrated successful delivery of FITC-insulin into the skin, again observing a higher concentration of fluorescence at the base of the microchannel. Future hollow MN injection experiments will analysis the maximal volume and maximal flow rates for injection to improve delivery aspects.

Varying the length of the MN may allow for targeted, application-dependent drug delivery to specific skin depths. In-plane MNs of different heights were used for testing the delivery of two large molecular weight molecules, HA and insulin, into porcine skin *in vitro* following solid MN application. MN heights measuring 300 μ m successfully delivered FITC-HA to the shallower epidermis to facilitate targeted local delivery, suitable for cosmetic applications. While longer, 600 μ m MNs, were used to deliver insulin into the deeper skin layers, with the assumption that the Franz cell receptor represents the systemic circulation. FITC-insulin delivery did not yield such a high degree of skin permeation into the Franz cell or the deeper epidermis as FITC-HA. This is suggested to be related to the larger MW and acidic solubility of insulin thus favouring the acidic SC and restricting the diffusion of insulin into the deeper skin layers. As these studies were completed with solid MNs, where the drug solution was applied to the surface of the skin after MN penetration, the majority of the overall concentration of each drug was unable to be quantified. Therefore, future studies will employ hollow MNs to directly inject substances into the deeper skin regions to facilitate a systemic uptake and avoid challenges with the upper layer possible restricting the molecules movements due to their physiological characteristics e.g., solubility in fats or water. In addition, the number of drugs tested will be expanded to understand how molecules of different molecular weights and solubilities are affected through both solid MN poke and patch administration and hollow MN poke and flow administration.

References

- [1] R. Liuzzi, A. Carciati, S. Guido, and S. Caserta, “Transport efficiency in transdermal drug delivery: What is the role of fluid microstructure?,” *Colloids and Surfaces B: Biointerfaces*, vol. 139. Elsevier B.V., pp. 294–305, 01-Mar-2016.
- [2] B. Hodayun, X. Lin, and H.-J. Choi, “pharmaceutics Challenges and Recent Progress in Oral Drug Delivery Systems for Biopharmaceuticals,” 2019.
- [3] T. Doogue, Matthew. Polasek, *Therapeutic Advances in Drug Safety*, vol. 4, no. 1. 2012.
- [4] T. Lynch and A. Price, “The Effect of Cytochrome P450 Metabolism on Drug Response, Interactions, and Adverse Effects,” Aug. 2007.
- [5] M. P. Doogue and T. M. Polasek, “The ABCD of clinical pharmacokinetics,” *Therapeutic Advances in Drug Safety*, vol. 4, no. 1. SAGE Publications, pp. 5–7, 2013.
- [6] R. F. Donnelly, *Microneedles for Drug and Vaccine Delivery and Patient Monitoring*. John Wiley & Sons, Ltd, 2018.
- [7] A. Z. Alkilani, M. T. C. McCrudden, and R. F. Donnelly, “Transdermal drug delivery: Innovative pharmaceutical developments based on disruption of the barrier properties of the stratum corneum,” *Pharmaceutics*, vol. 7, no. 4. MDPI AG, pp. 438–470, 22-Oct-2015.
- [8] R. Donnelly, T. Singh, E. Larraneta, and M. McCrudden, “Microneedles for Drug and Vaccine Delivery and Patient Monitoring,” 2018, pp. 2–6.
- [9] E. D. Lephart, “Skin aging and oxidative stress: Equol’s anti-aging effects via biochemical and molecular mechanisms,” *Ageing Research Reviews*, 01-Nov-2016.
- [10] H. Suh, J. Shin, and Y.-C. Kim, “Microneedle patches for vaccine delivery,” *Clin. Exp. Vaccine Res.*, vol. 3, no. 1, p. 42, 2014.

- [11] S. Ali, M. Shabbir, and N. Shahid, "The structure of skin and transdermal drug delivery system - A review," *Research Journal of Pharmacy and Technology*, vol. 8, no. 2. Research Journal of Pharmacy and Technology, pp. 103–109, 01-Feb-2015.
- [12] "Layers of the Skin – Anatomy and Physiology," 2020. [Online]. Available: <https://opentextbc.ca/anatomyandphysiology/chapter/5-1-layers-of-the-skin/>. [Accessed: 05-Oct-2020].
- [13] A. Baroni, E. Buommino, V. De Gregorio, E. Ruocco, V. Ruocco, and R. Wolf, "Structure and function of the epidermis related to barrier properties," *Clin. Dermatol.*, vol. 30, no. 3, pp. 257–262, May 2012.
- [14] H. Yousef and S. Sharma, *Anatomy, Skin (Integument), Epidermis*. StatPearls Publishing, 2018.
- [15] M. B. Murphrey and P. M. Zito, *Histology, Stratum Corneum*. StatPearls Publishing, 2018.
- [16] A. Webb, A. Li, and P. Kaur, "Location and phenotype of human adult keratinocyte stem cells of the skin," *Differentiation*, vol. 72, no. 8, pp. 387–395, 2004.
- [17] D. D. N'Da, "Prodrug strategies for enhancing the percutaneous absorption of drugs," *Molecules*, vol. 19, no. 12, pp. 20780–20807, Dec. 2014.
- [18] S. M. Ali and G. Yosipovitch, "Skin pH: From basic science to basic skin care," *Acta Derm. Venereol.*, vol. 93, no. 3, pp. 261–267, Mar. 2013.
- [19] R. O. Potts, E. M. Buras, and D. A. Chrisman, "Changes with age in the moisture content of human skin," *J. Invest. Dermatol.*, vol. 82, no. 1, pp. 97–100, 1984.
- [20] A. Williams, "Transdermal and Topical Drug Delivery from Theory to Clinical Practice," in *Transdermal and Topical Drug Delivery from Theory to Clinical Practice*, Pharmaceutical press, 2003, pp. 1–242.
- [21] E. Berardesca, J. De Rigal, J. L. Leveque, and H. L. Maibach, "In vivo biophysical characterization of skin physiological differences in races,"

Dermatology, vol. 182, no. 2, pp. 89–93, 1991.

- [22] M. Angelbeck-Schulze, R. Mischke, K. Rohn, M. Hewicker-Trautwein, H. Y. Naim, and W. Bäumer, “Canine epidermal lipid sampling by skin scrub revealed variations between different body sites and normal and atopic dogs,” *BMC Vet. Res.*, vol. 10, Jul. 2014.
- [23] D. A. Weigand, C. Haygood, and J. R. Gaylor, “Cell layers and density of Negro and Caucasian stratum corneum,” *J. Invest. Dermatol.*, vol. 62, no. 6, pp. 563–568, 1974.
- [24] J. H. Wedig and H. I. Maibach, “Percutaneous penetration of dipyrithione in man: Effect of skin color (race),” *J. Am. Acad. Dermatol.*, vol. 5, no. 4, pp. 433–438, 1981.
- [25] R. Darlenski and J. W. Fluhr, “Influence of skin type, race, sex, and anatomic location on epidermal barrier function,” *Clin. Dermatol.*, vol. 30, no. 3, pp. 269–273, May 2012.
- [26] A. . B. P. and N. R. Einstein, “Pharmacology of the skin,” *Phys. Rev.*, vol. 47, pp. 777–780, 1935.
- [27] C. N. Washington and C. Wils, “Barriers to Drug Absorption,” *Physiol. Pharm.*, pp. 182–187, 2001.
- [28] I. Singh and A. Morris, “Performance of transdermal therapeutic systems: Effects of biological factors,” *Int. J. Pharm. Investig.*, vol. 1, no. 1, p. 4, 2011.
- [29] R. C. Wester and H. I. Maibach, “Percutaneous Absorption,” in *Topical Drug Bioavailability, Bioequivalence, and Penetration*, Boston, MA: Springer US, 1993, pp. 3–15.
- [30] L. Norlén, I. P. Gil, A. Simonsen, and P. Descouts, “Human stratum corneum lipid organization as observed by atomic force microscopy on Langmuir-Blodgett films,” *J. Struct. Biol.*, vol. 158, no. 3, pp. 386–400, Jun. 2007.
- [31] S. Farahmand and H. I. Maibach, “Transdermal drug pharmacokinetics in man: Interindividual variability and partial prediction,” *Int. J. Pharm.*, vol. 367, no. 1–

2, pp. 1–15, Feb. 2009.

- [32] A. Williams, “Transdermal and topical drug delivery: from theory to clinical practice,” 2003.
- [33] *The Sumerians: Their History, Culture, and Character - Samuel Noah Kramer - Google Books*. 1971.
- [34] M. N. Pastore, Y. N. Kalia, M. Horstmann, and M. S. Roberts, “Transdermal patches: History, development and pharmacology,” *British Journal of Pharmacology*, vol. 172, no. 9. John Wiley and Sons Inc., pp. 2179–2209, 05-Jan-2015.
- [35] H. A. E. Benson, J. E. Grice, Y. Mohammed, S. Namjoshi, and M. S. Roberts, “Topical and Transdermal Drug Delivery: From Simple Potions to Smart Technologies,” *Curr. Drug Deliv.*, vol. 16, no. 5, pp. 444–460, Feb. 2019.
- [36] S. Szunerits and R. Boukherroub, “Heat: A highly efficient skin enhancer for transdermal drug delivery,” *Frontiers in Bioengineering and Biotechnology*, vol. 6, no. FEB. Frontiers Media S.A., p. 15, 15-Feb-2018.
- [37] D. D. Buranova, “The value of Avicenna’s heritage in development of modern integrative medicine in Uzbekistan,” *Integr. Med. Res.*, vol. 4, no. 4, pp. 220–224, Dec. 2015.
- [38] C. R. Moore, J. K. Lamar, and N. Beck, “Cutaneous absorption of sex hormones,” *J. Am. Med. Assoc.*, vol. 111, no. 1, pp. 11–14, Jul. 1938.
- [39] B. Zondek, “CUTANEOUS APPLICATION OF FOLLICULAR HORMONE,” *Lancet*, vol. 231, no. 5985, pp. 1107–1110, May 1938.
- [40] F. Lund, “Percutaneous Nitroglycerin Treatment in Gases of Peripheral Circulatory Disorders, Especially Raynaud’s Disease,” *Acta Med. Scand.*, vol. 130, no. 206 S, pp. 196–206, 1948.
- [41] M. Kleckner, E. V. Allen, and K. G. Wakim, “The effect of local application of glyceryl trinitrate (nitroglycerine) on Raynaud’s disease and Raynaud’s phenomenon; studies on blood flow and clinical manifestations.,” *Circulation*,

vol. 3, no. 5, pp. 681–689, 1951.

- [42] “Global Transdermal Patch Market, Dosage, Price & Clinical Trials Insight 2026,” 2020. [Online]. Available: <https://www.prnewswire.co.uk/news-releases/global-transdermal-skin-patch-market-sales-size-opportunity-to-reach-us-18-billion-by-2026-with-100-skin-patches-in-clinical-pipeline-trials-845958545.html>. [Accessed: 05-Oct-2020].
- [43] M. R. Prausnitz and R. Langer, “Transdermal drug delivery,” *Nature Biotechnology*, vol. 26, no. 11. NIH Public Access, pp. 1261–1268, Nov-2008.
- [44] C. A. Lipinski, F. Lombardo, B. W. Dominy, and P. J. Feeney, “Experimental and computational approaches to estimate solubility and permeability in drug discovery and development settings,” *Adv. Drug Deliv. Rev.*, vol. 46, no. 1–3, pp. 3–26, Mar. 2001.
- [45] B. Chaulagain, A. Jain, A. Tiwari, A. Verma, and S. K. Jain, “Passive delivery of protein drugs through transdermal route,” *Artif. Cells, Nanomedicine Biotechnol.*, vol. 46, no. sup1, pp. 472–487, Oct. 2018.
- [46] R. H. Guy, “Transdermal drug delivery,” *Handbook of Experimental Pharmacology*, vol. 197, no. 197. Handb Exp Pharmacol, pp. 399–410, 2010.
- [47] C. M. Schoellhammer, D. Blankschtein, and R. Langer, “Skin permeabilization for transdermal drug delivery: Recent advances and future prospects,” *Expert Opinion on Drug Delivery*, vol. 11, no. 3. Expert Opin Drug Deliv, pp. 393–407, Mar-2014.
- [48] S. H. Bariya, M. C. Gohel, T. A. Mehta, and O. P. Sharma, “Microneedles: an emerging transdermal drug delivery system,” *J. Pharm. Pharmacol.*, vol. 64, no. 1, pp. 11–29, Jan. 2012.
- [49] K. Ita, “Transdermal delivery of drugs with microneedles—potential and challenges,” *Pharmaceutics*, vol. 7, no. 3, pp. 90–105, Jun. 2015.
- [50] J. J. Escobar-Chávez, D. Bonilla-Martínez, M. A. Villegas-González, E. Molina-Trinidad, N. Casas-Alancaster, and A. L. Revilla-Vázquez, “Microneedles: A

valuable physical enhancer to increase transdermal drug delivery,” *J. Clin. Pharmacol.*, vol. 51, no. 7, pp. 964–977, Jul. 2011.

- [51] J. Yang, X. Liu, Y. Fu, and Y. Song, “Recent advances of microneedles for biomedical applications: drug delivery and beyond,” *Acta Pharmaceutica Sinica B*, vol. 9, no. 3. Chinese Academy of Medical Sciences, pp. 469–483, 01-May-2019.
- [52] A. J. Guillot, A. S. Cordeiro, R. F. Donnelly, M. C. Montesinos, T. M. Garrigues, and A. Melero, “Microneedle-based delivery: An overview of current applications and trends,” *Pharmaceutics*, vol. 12, no. 6, pp. 1–28, Jun. 2020.
- [53] M. S. Gerstel and V. A. Place, “United States Paten Gerstel et al. DRUG DELIVERY DEVICE,” 1976.
- [54] M. R. Prausnitz, “Microneedles for transdermal drug delivery,” *Adv. Drug Deliv. Rev.*, vol. 56, pp. 581–587, 2004.
- [55] “Microfabricated Microneedles: A Novel Approach to Transdermal Drug Delivery,” *J. Pharm. Sci.*, vol. 87, no. 8, pp. 922–925, Aug. 1998.
- [56] J. Halder, S. Gupta, R. Kumari, G. Das Gupta, and V. Kumar Rai, “Microneedle Array: Applications, Recent Advances, and Clinical Pertinence in Transdermal Drug Delivery.”
- [57] M. Kirkby, A. R. J. Hutton, and R. F. Donnelly, “Microneedle Mediated Transdermal Delivery of Protein, Peptide and Antibody Based Therapeutics: Current Status and Future Considerations,” *Pharmaceutical Research*, vol. 37, no. 6. Springer, pp. 1–18, 01-Jun-2020.
- [58] A. J. Guillot, A. S. Cordeiro, R. F. Donnelly, M. C. Montesinos, T. M. Garrigues, and A. Melero, “Microneedle-Based Delivery: An Overview of Current Applications and Trends,” *Pharmaceutics*, vol. 12, no. 6, p. 569, Jun. 2020.
- [59] D. V. McAllister *et al.*, “Microfabricated needles for transdermal delivery of macromolecules and nanoparticles: Fabrication methods and transport studies,” *Proc. Natl. Acad. Sci. U. S. A.*, vol. 100, no. SUPPL. 2, pp. 13755–13760, Nov.

2003.

- [60] Y. H. Mohammed *et al.*, “Microneedle enhanced delivery of cosmeceutically relevant peptides in human skin,” *PLoS One*, vol. 9, no. 7, Jul. 2014.
- [61] Z. Hu, C. S. Meduri, R. S. J. Ingrole, H. S. Gill, and G. Kumar, “Solid and hollow metallic glass microneedles for transdermal drug-delivery,” *Appl. Phys. Lett*, vol. 116, p. 203703, 2020.
- [62] Z. Li, X. Yan, M. Hu, G. Tang, and Z. Li, “The Study on Fabrication of Solid Metal Microneedles Based on Optimized Process of Electrochemical Etching and Cutting,” in *2018 IEEE International Conference of Intelligent Robotic and Control Engineering, IRCE 2018*, 2018, pp. 218–222.
- [63] E. R. Parker, M. P. Rao, K. L. Turner, C. D. Meinhart, and N. C. MacDonald, “Bulk micromachined titanium microneedles,” *J. Microelectromechanical Syst.*, vol. 16, no. 2, pp. 289–295, Apr. 2007.
- [64] C. S. Kolli and A. K. Banga, “Characterization of solid maltose microneedles and their use for transdermal delivery,” *Pharm. Res.*, vol. 25, no. 1, pp. 104–113, Jan. 2008.
- [65] S. Han Lim, J. Yao Ng, and L. Kang, “Three-dimensional printing of a microneedle array on personalized curved surfaces for dual-pronged treatment of trigger finger,” *Biofabrication*, vol. 9, no. 1, p. 15010, Mar. 2017.
- [66] S. Sharma, A. Saeed, C. Johnson, N. Gadegaard, and A. E. Cass, “Rapid, low cost prototyping of transdermal devices for personal healthcare monitoring,” *Sens. Bio-Sensing Res.*, vol. 13, pp. 104–108, Apr. 2017.
- [67] Y. Wu, Y. Qiu, S. Zhang, G. Qin, and Y. Gao, “Microneedle-based drug delivery: Studies on delivery parameters and biocompatibility,” *Biomed. Microdevices*, vol. 10, no. 5, pp. 601–610, 2008.
- [68] Y. Xie, B. Xu, and Y. Gao, “Controlled transdermal delivery of model drug compounds by MEMS microneedle array,” *Nanomedicine Nanotechnology, Biol. Med.*, vol. 1, no. 2, pp. 184–190, Jun. 2005.

- [69] S. H. Baek, J. H. Shin, and Y. C. Kim, "Drug-coated microneedles for rapid and painless local anesthesia," *Biomed. Microdevices*, vol. 19, no. 1, Mar. 2017.
- [70] T. H. Lin and J. M. Jiang, "Fabrication of a pyramidal micro-needle array structure using 3D micro-lens mask lithography," *Microsyst. Technol.*, vol. 25, no. 12, pp. 4637–4643, Dec. 2019.
- [71] H. R. Nejad, A. Sadeqi, G. Kiaee, and S. Sonkusale, "Low-cost and cleanroom-free fabrication of microneedles," *Microsystems Nanoeng.*, vol. 4, no. 1, pp. 1–7, Apr. 2018.
- [72] Y. C. Kim, J. H. Park, and M. R. Prausnitz, "Microneedles for drug and vaccine delivery," *Adv. Drug Deliv. Rev.*, vol. 64, no. 14, pp. 1547–1568, Nov. 2012.
- [73] G. Yan, K. S. Warner, J. Zhang, S. Sharma, and B. K. Gale, "Evaluation needle length and density of microneedle arrays in the pretreatment of skin for transdermal drug delivery," *Int. J. Pharm.*, vol. 391, no. 1–2, pp. 7–12, May 2010.
- [74] D. P. Wermeling *et al.*, "Microneedles permit transdermal delivery of a skin-impermeant medication to humans," *Proc. Natl. Acad. Sci. U. S. A.*, vol. 105, no. 6, pp. 2058–2063, Feb. 2008.
- [75] J. Gupta, H. S. Gill, S. N. Andrews, and M. R. Prausnitz, "Kinetics of skin resealing after insertion of microneedles in human subjects," *J. Control. Release*, vol. 154, no. 2, pp. 148–155, Sep. 2011.
- [76] H. Kalluri and A. K. Banga, "Formation and closure of microchannels in skin following microporation," *Pharm. Res.*, vol. 28, no. 1, pp. 82–94, Jan. 2011.
- [77] R. F. Donnelly *et al.*, "Hydrogel-forming microneedle arrays exhibit antimicrobial properties: Potential for enhanced patient safety," *Int. J. Pharm.*, vol. 451, no. 1–2, pp. 76–91, 2013.
- [78] J. J. Escobar-Chávez, D. Bonilla-Martínez, M. A. Villegas-González, E. Molina-Trinidad, N. Casas-Alancaster, and A. L. Revilla-Vázquez, "Microneedles: A valuable physical enhancer to increase transdermal drug delivery," *Journal of*

Clinical Pharmacology, vol. 51, no. 7. *J Clin Pharmacol*, pp. 964–977, Jul-2011.

- [79] R. Haj-Ahmad *et al.*, “Microneedle coating techniques for transdermal drug delivery,” *Pharmaceutics*, vol. 7, no. 4. MDPI AG, pp. 486–502, 05-Nov-2015.
- [80] J. A. Matriano *et al.*, “Macroflux® microprojection array patch technology: A new and efficient approach for intracutaneous immunization,” *Pharm. Res.*, vol. 19, no. 1, pp. 63–70, 2002.
- [81] A. Z. Alkilani, M. T. C. McCrudden, and R. F. Donnelly, “Transdermal Drug Delivery: Innovative Pharmaceutical Developments Based on Disruption of the Barrier Properties of the stratum corneum,” *Pharmaceutics*, vol. 7, no. 4, p. 438, Oct. 2015.
- [82] D. G. Koutsonanos *et al.*, “Transdermal influenza immunization with vaccine-coated microneedle arrays,” *PLoS One*, vol. 4, no. 3, Mar. 2009.
- [83] “Zosano Pharma Completes Enrollment in Phase 1 Study for Microneedle Patch Delivery of Zolmitriptan for the Treatment of Migraine | Zosano Pharma Corporation.” [Online]. Available: <https://ir.zosanopharma.com/news-releases/news-release-details/zosano-pharma-completes-enrollment-phase-1-study-microneedle>. [Accessed: 12-Oct-2020].
- [84] P. E. Daddona, J. A. Matriano, J. Mandema, and Y. F. Maa, “Parathyroid hormone (1-34)-coated microneedle patch system: Clinical pharmacokinetics and pharmacodynamics for treatment of osteoporosis,” *Pharm. Res.*, vol. 28, no. 1, pp. 159–165, Jan. 2011.
- [85] M. Ameri, P. E. Daddona, and Y. F. Maa, “Demonstrated solid-state stability of parathyroid hormone PTH(1-34) coated on a novel transdermal microprojection delivery system,” *Pharm. Res.*, vol. 26, no. 11, pp. 2454–2463, Nov. 2009.
- [86] J. H. Park, M. G. Allen, and M. R. Prausnitz, “Polymer microneedles for controlled-release drug delivery,” *Pharm. Res.*, vol. 23, no. 5, pp. 1008–1019, May 2006.
- [87] S. P. Sullivan, N. Murthy, and M. R. Prausnitz, “Minimally invasive protein

- delivery with rapidly dissolving polymer microneedles.," *Adv. Mater.*, vol. 20, no. 5, pp. 933–938, Mar. 2008.
- [88] J. W. Lee, J. H. Park, and M. R. Prausnitz, "Dissolving microneedles for transdermal drug delivery," *Biomaterials*, vol. 29, no. 13, pp. 2113–2124, May 2008.
- [89] Y. Ito, J. I. Yoshimitsu, K. Shiroyama, N. Sugioka, and K. Takada, "Self-dissolving microneedles for the percutaneous absorption of EPO in mice," *J. Drug Target.*, vol. 14, no. 5, pp. 255–261, Jun. 2006.
- [90] R. F. Donnelly *et al.*, "Processing difficulties and instability of carbohydrate microneedle arrays," *Drug Dev. Ind. Pharm.*, vol. 35, no. 10, pp. 1242–1254, 2009.
- [91] J. W. Lee, J. H. Park, and M. R. Prausnitz, "Dissolving microneedles for transdermal drug delivery," *Biomaterials*, vol. 29, no. 13, pp. 2113–2124, May 2008.
- [92] R. F. Donnelly *et al.*, "Design, optimization and characterisation of polymeric microneedle arrays prepared by a novel laser-based micromoulding technique," *Pharm. Res.*, vol. 28, no. 1, pp. 41–57, Jan. 2011.
- [93] R. F. Donnelly *et al.*, "Optical coherence tomography is a valuable tool in the study of the effects of microneedle geometry on skin penetration characteristics and in-skin dissolution," *J. Control. Release*, vol. 147, no. 3, pp. 333–341, Nov. 2010.
- [94] M. J. Garland *et al.*, "Influence of skin model on in vitro performance of drug-loaded soluble microneedle arrays," *Int. J. Pharm.*, vol. 434, no. 1–2, pp. 80–89, Sep. 2012.
- [95] E. Caffarel-Salvador *et al.*, "Potential of hydrogel-forming and dissolving microneedles for use in paediatric populations," *Int. J. Pharm.*, vol. 489, no. 1–2, pp. 158–169, Jul. 2015.
- [96] K. Migalska, D. I. J. Morrow, M. J. Garland, R. Thakur, A. D. Woolfson, and R.

- F. Donnelly, “Laser-engineered dissolving microneedle arrays for transdermal macromolecular drug delivery,” *Pharm. Res.*, vol. 28, no. 8, pp. 1919–1930, Aug. 2011.
- [97] Ryan Donnelly, “Microneedles for Drug and Vaccine Delivery and Patient Monitoring,” in *Microneedles for Drug and Vaccine Delivery and Patient Monitoring*, F. D. Ryan, Ed. Chichester, UK: John Wiley & Sons, Ltd, 2018, pp. 78–80.
- [98] P. Griss and G. Stemme, “Side-opened out-of-plane microneedles for microfluidic transdermal liquid transfer,” *J. Microelectromechanical Syst.*, vol. 12, no. 3, pp. 296–301, Jun. 2003.
- [99] W. Martanto *et al.*, “Microinfusion using hollow microneedles,” *Pharm. Res.*, vol. 23, no. 1, pp. 104–113, Jan. 2006.
- [100] K. B. Vinayakumar *et al.*, “A hollow stainless steel microneedle array to deliver insulin to a diabetic rat,” *J. Micromechanics Microengineering*, vol. 26, no. 6, p. 065013, May 2016.
- [101] D. V. McAllister *et al.*, “Microfabricated needles for transdermal delivery of macromolecules and nanoparticles: Fabrication methods and transport studies,” *Proc. Natl. Acad. Sci. U. S. A.*, vol. 100, no. SUPPL. 2, pp. 13755–13760, Nov. 2003.
- [102] B. Pamornpathomkul, A. Wongkajornsilp, W. Laiwattanapaisal, T. Rojanarata, P. Opanasopit, and T. Ngawhirunpat, “A combined approach of hollow microneedles and nanocarriers for skin immunization with plasmid DNA encoding ovalbumin,” *Int. J. Nanomedicine*, vol. 12, pp. 885–898, Jan. 2017.
- [103] “Homepage - NanoPass Technologies Ltd.” [Online]. Available: <https://www.nanopass.com/>. [Accessed: 16-Oct-2020].
- [104] “3M Drug Delivery Innovation.” [Online]. Available: <https://multimedia.3m.com/mws/media/9966290/intradermal-delivery-hollow-microneedle-article-september-2014.pdf>. [Accessed: 16-Oct-2020].

- [105] “Radius Health Initiates Phase 3 wearABLE Study of Abaloparatide-Patch in Postmenopausal Osteoporosis Patients at High Risk for Fracture | Radius Health, Inc.” [Online]. Available: <https://ir.radiuspharm.com/news-releases/news-release-details/radius-health-initiates-phase-3-wearable-study-abaloparatide>. [Accessed: 16-Oct-2020].
- [106] “3M Drug Delivery Systems announces collaboration with Panacea Pharmaceuticals, Inc. on New Cancer Vaccine.” [Online]. Available: https://www.3m.com/3M/en_US/drug-delivery-systems-us/resources/news/news-detail/?storyid=a9d79d86-f599-45a9-85c6-235d5a9a34cf. [Accessed: 16-Oct-2020].
- [107] Y. C. Kim, C. Jarrahan, D. Zehring, S. Mitragotri, and M. R. Prausnitz, “Delivery systems for intradermal vaccination,” *Curr. Top. Microbiol. Immunol.*, vol. 351, no. 1, pp. 77–112, 2012.
- [108] “DebioJect Microneedle INtra-Dermal Injection.” [Online]. Available: https://www.ondrugdelivery.com/wp-content/uploads/2017/06/1050_GR_ONdrugDelivery-Issue-49-Transdermal-Microneedles_150_DPI.pdf. [Accessed: 16-Oct-2020].
- [109] R. F. Donnelly *et al.*, “Hydrogel-forming microneedle arrays for enhanced transdermal drug delivery,” *Adv. Funct. Mater.*, vol. 22, no. 23, pp. 4879–4890, Dec. 2012.
- [110] R. F. Donnelly *et al.*, “Hydrogel-forming microneedles prepared from ‘super swelling’ polymers combined with lyophilised wafers for transdermal drug delivery,” *PLoS One*, vol. 9, no. 10, Oct. 2014.
- [111] R. F. Donnelly *et al.*, “Hydrogel-forming and dissolving microneedles for enhanced delivery of photosensitizers and precursors,” *Photochem. Photobiol.*, vol. 90, no. 3, pp. 641–647, 2014.
- [112] S. Yang, Y. Feng, L. Zhang, N. Chen, W. Yuan, and T. Jin, “A scalable fabrication process of polymer microneedles,” *Int. J. Nanomedicine*, vol. 7, pp. 1415–1422, 2012.

- [113] I. A. Tekko *et al.*, “Development and characterisation of novel poly (vinyl alcohol)/poly (vinyl pyrrolidone)-based hydrogel-forming microneedle arrays for enhanced and sustained transdermal delivery of methotrexate,” *Int. J. Pharm.*, vol. 586, p. 119580, Aug. 2020.
- [114] A. J. Courtenay *et al.*, “Hydrogel-forming microneedle arrays as a therapeutic option for transdermal esketamine delivery,” *J. Control. Release*, vol. 322, pp. 177–186, Jun. 2020.
- [115] E. M. Migdadi *et al.*, “Hydrogel-forming microneedles enhance transdermal delivery of metformin hydrochloride,” *J. Control. Release*, vol. 285, pp. 142–151, Sep. 2018.
- [116] D. Ramadon *et al.*, “Development, Evaluation, and Pharmacokinetic Assessment of Polymeric Microarray Patches for Transdermal Delivery of Vancomycin Hydrochloride,” *Mol. Pharm.*, vol. 17, no. 9, pp. 3353–3368, Sep. 2020.
- [117] A. J. Courtenay, M. T. C. McCrudden, K. J. McAvoy, H. O. McCarthy, and R. F. Donnelly, “Microneedle-Mediated Transdermal Delivery of Bevacizumab,” *Mol. Pharm.*, vol. 15, no. 8, pp. 3545–3556, Aug. 2018.
- [118] X. He, J. Sun, J. Zhuang, H. Xu, Y. Liu, and D. Wu, “Microneedle System for Transdermal Drug and Vaccine Delivery: Devices, Safety, and Prospects,” *Dose-Response*, vol. 17, no. 4. SAGE Publications Inc., 2019.
- [119] J. H. Oh *et al.*, “Influence of the delivery systems using a microneedle array on the permeation of a hydrophilic molecule, calcein,” *Eur. J. Pharm. Biopharm.*, vol. 69, no. 3, pp. 1040–1045, Aug. 2008.
- [120] D. G. Koutsonanos *et al.*, “Transdermal Influenza Immunization with Vaccine-Coated Microneedle Arrays.”
- [121] S. J. Paik *et al.*, “In-plane single-crystal-silicon microneedles for minimally invasive microfluid systems,” *Sensors Actuators, A Phys.*, vol. 114, no. 2–3, pp. 276–284, Sep. 2004.
- [122] S. S. Yun, J. Y. An, S. H. Moon, and J. H. Lee, “In-plane microneedle chip

- fabricated by crystalline wet etching of (110) silicon wafer,” in *TRANSDUCERS 2009 - 15th International Conference on Solid-State Sensors, Actuators and Microsystems*, 2009, pp. 204–207.
- [123] M. Jung, D. Jeong, S. S. Yun, and J. H. Lee, “Fabrication of a 2-D in-plane micro needle array integrated with microfluidic components using crystalline wet etching of (110) silicon,” *Microsyst. Technol.*, vol. 22, no. 9, pp. 2287–2294, Sep. 2016.
- [124] Y. Li *et al.*, “In-plane silicon microneedles with open capillary microfluidic networks by deep reactive ion etching and sacrificial layer based sharpening,” *Sensors Actuators, A Phys.*, vol. 292, pp. 149–157, Jun. 2019.
- [125] L. Xie, H. Zeng, J. Sun, and W. Qian, “Engineering microneedles for therapy and diagnosis: A survey,” *Micromachines*, vol. 11, no. 3, Mar. 2020.
- [126] wwwMicroChemicalscom, “MicroChemicals ®-Fundamentals of Microstructuring CRYSTALLOGRAPHY OF SILICON.”
- [127] K. Andrew, U. Gonzales, and E. Fuchs, “Developmental Cell Review Skin and Its Regenerative Powers: An Alliance between Stem Cells and Their Niche,” 2017.
- [128] J. L. Lenhart *et al.*, “X-ray absorption spectroscopy to probe surface composition and surface deprotection in photoresist films,” *Langmuir*, vol. 21, no. 9, pp. 4007–4015, Apr. 2005.
- [129] “The Difference Between Positive and Negative Photoresist | Shin-Etsu MicroSi.” [Online]. Available: <https://www.microsi.com/the-difference-between-positive-and-negative-photoresist/>. [Accessed: 25-Oct-2020].
- [130] “Spin Coating: Complete Guide to Theory and Techniques | Ossila.” [Online]. Available: <https://www.ossila.com/pages/spin-coating>. [Accessed: 25-Oct-2020].
- [131] wwwMicroChemicals.com, “MicroChemicals ®-Fundamentals of Microstructuring SPRAY COATING.”
- [132] B. Banks, *Microengineering, MEMS, and Interfacing: A Practical Guide* . 2006.

- [133] O. O. Abegunde, E. T. Akinlabi, O. P. Oladijo, S. Akinlabi, and A. U. Ude, "Overview of thin film deposition techniques," 2019.
- [134] D. Wagner, "Isotropic and Anisotropic Silicon Wet Etching Processes," *ISOTROPIC AND ANISOTROPIC SILICON WET ETCHING PROCESSES*, 06-Aug-2019. [Online]. Available: <https://www.modutek.com/isotropic-and-anisotropic-silicon-wet-etching-processes/>. [Accessed: 25-Oct-2020].
- [135] "IntelliSense." [Online]. Available: <http://www.intellisense.com/product.aspx?id=39>. [Accessed: 26-Oct-2020].
- [136] S. Henry, D. McAllister, M. Allen, and M. Prausnitz, "Microfabricated microneedles: a novel approach to transdermal drug delivery," *J. Pharm. Sci.*, vol. 87, no. 8, 1998.
- [137] Y. Li *et al.*, "Fabrication of sharp silicon hollow microneedles by deep-reactive ion etching towards minimally invasive diagnostics," *Microsystems Nanoeng.*, vol. 5, no. 1, pp. 1–11, Dec. 2019.
- [138] N. Roxhed, P. Griss, and G. Stemme, "Membrane-sealed hollow microneedles and related administration schemes for transdermal drug delivery," *Biomed. Microdevices*, vol. 10, no. 2, pp. 271–279, Apr. 2008.
- [139] N. Roxhed, T. C. Gasser, P. Griss, G. A. Holzapfel, and G. Stemme, "Penetration-enhanced ultrasharp microneedles and prediction on skin interaction for efficient transdermal drug delivery," *J. Microelectromechanical Syst.*, vol. 16, no. 6, pp. 1429–1440, Dec. 2007.
- [140] N. Wilke, A. Mulcahy, S. R. Ye, and A. Morrissey, "Process optimization and characterization of silicon microneedles fabricated by wet etch technology," *Microelectronics J.*, vol. 36, no. 7, pp. 650–656, Jul. 2005.
- [141] B. A. Jana and A. D. Wadhvani, "Microneedle - Future prospect for efficient drug delivery in diabetes management," *Indian J. Pharmacol.*, vol. 51, no. 1, pp. 4–10, Jan. 2019.
- [142] J. Yang, X. Liu, Y. Fu, and Y. Song, "Recent advances of microneedles for

- biomedical applications: drug delivery and beyond,” *Acta Pharm. Sin. B*, vol. 9, no. 3, pp. 469–483, May 2019.
- [143] W. Martanto, S. P. Davis, N. R. Holiday, J. Wang, H. S. Gill, and M. R. Prausnitz, “Transdermal delivery of insulin using microneedles in vivo,” *Pharm. Res.*, vol. 21, no. 6, pp. 947–952, Jun. 2004.
- [144] C. H. Chen, V. B. H. Shyu, and C. T. Chen, “Dissolving microneedle patches for transdermal insulin delivery in diabetic mice: Potential for clinical applications,” *Materials (Basel)*, vol. 11, no. 9, Sep. 2018.
- [145] S. Davis, W. Martanto, M. Allen, and M. Prausnitz, “Hollow Metal Microneedles for Insulin Delivery in Diabetic Rats,” *IEEE Trans. Biomed. Eng.*, vol. 52, no. 5, May 2005.
- [146] N. Roxhed, B. Samel, L. Nordquist, P. Griss, and G. Stemme, “Painless drug delivery through microneedle-based transdermal patches featuring active infusion,” *IEEE Trans. Biomed. Eng.*, vol. 55, no. 3, pp. 1063–1071, Mar. 2008.
- [147] J. Gupta, E. I. Felner, and M. R. Prausnitz, “Minimally invasive insulin delivery in subjects with type 1 diabetes using hollow microneedles,” *Diabetes Technol. Ther.*, vol. 11, no. 6, pp. 329–337, Jun. 2009.
- [148] T. Waghule *et al.*, “Microneedles: A smart approach and increasing potential for transdermal drug delivery system,” *Biomed. Pharmacother.*, vol. 109, pp. 1249–1258, Jan. 2019.
- [149] J. Arya and M. R. Prausnitz, “Microneedle patches for vaccination in developing countries,” *J. Control. Release*, vol. 240, pp. 135–141, Oct. 2016.
- [150] E. Larrañeta, R. E. M. Lutton, A. D. Woolfson, and R. F. Donnelly, “Microneedle arrays as transdermal and intradermal drug delivery systems: Materials science, manufacture and commercial development,” *Mater. Sci. Eng. R Reports*, vol. 104, pp. 1–32, Jun. 2016.
- [151] S. P. Sullivan *et al.*, “Dissolving polymer microneedle patches for influenza vaccination,” *Nat. Med.*, vol. 16, no. 8, 2010.

- [152] K. Van Der Maaden *et al.*, “Novel hollow microneedle technology for depth-controlled microinjection-mediated dermal vaccination: A study with polio vaccine in rats,” *Pharm. Res.*, vol. 31, no. 7, pp. 1846–1854, 2014.
- [153] P. Schipper *et al.*, “Determination of Depth-Dependent Intradermal Immunogenicity of Adjuvanted Inactivated Polio Vaccine Delivered by Microinjections via Hollow Microneedles,” *Pharm. Res.*, vol. 33, no. 9, pp. 2269–2279, Sep. 2016.
- [154] P. Schipper *et al.*, “Repeated fractional intradermal dosing of an inactivated polio vaccine by a single hollow microneedle leads to superior immune responses,” *J. Control. Release*, vol. 242, pp. 141–147, Nov. 2016.
- [155] K. Siddhapura, H. Harde, and S. Jain, “Immunostimulatory effect of tetanus toxoid loaded chitosan nanoparticles following microneedles assisted immunization,” *Nanomedicine Nanotechnology, Biol. Med.*, vol. 12, no. 1, pp. 213–222, Jan. 2016.
- [156] E. Kim *et al.*, “Microneedle array delivered recombinant coronavirus vaccines: Immunogenicity and rapid translational development,” *EBioMedicine*, vol. 55, p. 102743, 2020.
- [157] “Covid: Swansea Uni develops ‘world’s first’ vaccine smart patch - BBC News.” [Online]. Available: <https://www.bbc.co.uk/news/uk-wales-55548670>. [Accessed: 20-Feb-2021].
- [158] A. F. Moreira, C. F. Rodrigues, T. A. Jacinto, S. P. Miguel, E. C. Costa, and I. J. Correia, “Microneedle-based delivery devices for cancer therapy: A review,” *Pharmacological Research*, vol. 148. Academic Press, p. 104438, 01-Oct-2019.
- [159] S. Bhatnagar, N. G. Bankar, M. V. Kulkarni, and V. V. K. Venuganti, “Dissolvable microneedle patch containing doxorubicin and docetaxel is effective in 4T1 xenografted breast cancer mouse model,” *Int. J. Pharm.*, vol. 556, pp. 263–275, Feb. 2019.
- [160] W. Qin *et al.*, “Dissolving microneedles with spatiotemporally controlled pulsatile release nanosystem for synergistic chemo-photothermal therapy of

- Melanoma,” *Theranostics*, vol. 10, no. 18, pp. 8179–8196, 2020.
- [161] Y. Zhang *et al.*, “Locally Induced Adipose Tissue Browning by Microneedle Patch for Obesity Treatment,” *ACS Nano*, vol. 11, no. 9, pp. 9223–9230, Sep. 2017.
- [162] A. Than *et al.*, “Transdermal Delivery of Anti-Obesity Compounds to Subcutaneous Adipose Tissue with Polymeric Microneedle Patches,” *Small Methods*, vol. 1, no. 11, p. 1700269, Nov. 2017.
- [163] U. B. Kompella, R. S. Kadam, and V. H. L. Lee, “Recent advances in ophthalmic drug delivery,” *Ther. Deliv.*, vol. 1, no. 3, pp. 435–456, Sep. 2010.
- [164] R. Edgar *et al.*, “LifeMap Discovery™: The Embryonic Development, Stem Cells, and Regenerative Medicine Research Portal,” *PLoS One*, vol. 8, no. 7, p. e66629, Jul. 2013.
- [165] A. G. Harris, C. Naidoo, and D. F. Murrell, “Skin needling as a treatment for acne scarring: An up-to-date review of the literature,” *Int. J. Women’s Dermatology*, vol. 1, no. 2, pp. 77–81, Jun. 2015.
- [166] F. D. Ryan, Ed., “Microneedles for Drug and Vaccine Delivery and Patient Monitoring,” in *Microneedles for Drug and Vaccine Delivery and Patient Monitoring*, Chichester, UK: John Wiley & Sons, Ltd, 2018, pp. 259–268.
- [167] M. El-Domyati, M. Barakat, S. Awad, W. Medhat, H. El-Fakahany, and H. Farag, “Microneedling Therapy for Atrophic Acne Scars: An Objective Evaluation,” *J. Clin. Aesthet. Dermatol.*, vol. 8, no. 7, pp. 36–42, Jul. 2015.
- [168] T. P. Afra, M. T. Razmi, T. Narang, S. Dogra, and A. Kumar, “Topical Tazarotene Gel, 0.1%, as a Novel Treatment Approach for Atrophic Postacne Scars: A Randomized Active-Controlled Clinical Trial,” *JAMA Facial Plast. Surg.*, vol. 21, no. 2, pp. 125–132, Mar. 2019.
- [169] M. Jang, S. Baek, G. Kang, H. Yang, S. Kim, and H. Jung, “Dissolving microneedle with high molecular weight hyaluronic acid to improve skin wrinkles, dermal density and elasticity,” *Int. J. Cosmet. Sci.*, vol. 42, no. 3, pp.

302–309, Jun. 2020.

- [170] M. Kim, H. Yang, H. Kim, H. Jung, and H. Jung, “Novel cosmetic patches for wrinkle improvement: Retinyl retinoate- and ascorbic acid-loaded dissolving microneedles,” *Int. J. Cosmet. Sci.*, vol. 36, no. 3, pp. 207–212, 2014.
- [171] A. Singh and S. Yadav, “Microneedling: Advances and widening horizons,” *Indian Dermatol. Online J.*, vol. 7, no. 4, p. 244, 2016.
- [172] E. Larrañeta *et al.*, “Microneedle arrays as transdermal and intradermal drug delivery systems: Materials science, manufacture and commercial development,” 2016.
- [173] P. M. Wang, M. Cornwell, and M. R. Prausnitz, “Minimally invasive extraction of dermal interstitial fluid for glucose monitoring using microneedles,” *Diabetes Technol. Ther.*, vol. 7, no. 1, pp. 131–141, Feb. 2005.
- [174] P. Bollella, S. Sharma, A. E. G. Cass, and R. Antiochia, “Microneedle-based biosensor for minimally-invasive lactate detection,” *Biosens. Bioelectron.*, vol. 123, pp. 152–159, Jan. 2019.
- [175] T. M. Rawson *et al.*, “Microneedle biosensors for real-time, minimally invasive drug monitoring of phenoxymethylpenicillin: a first-in-human evaluation in healthy volunteers,” *Lancet Digit. Heal.*, vol. 1, no. 7, pp. e335–e343, Nov. 2019.
- [176] O. Howells *et al.*, “Microneedle Array-Based Platforms for Future Theranostic Applications,” *ChemBioChem*, vol. 20, no. 17, pp. 2198–2202, Sep. 2019.
- [177] C. Prével *et al.*, “Fluorescent peptide biosensor for monitoring CDK4/cyclin D kinase activity in melanoma cell extracts, mouse xenografts and skin biopsies,” *Biosens. Bioelectron.*, vol. 85, pp. 371–380, Nov. 2016.
- [178] A. M. V. Mohan, J. R. Windmiller, R. K. Mishra, and J. Wang, “Continuous minimally-invasive alcohol monitoring using microneedle sensor arrays,” *Biosens. Bioelectron.*, vol. 91, pp. 574–579, May 2017.
- [179] W. Yuan *et al.*, “Theranostic OCT microneedle for fast ultrahigh-resolution deep-brain imaging and efficient laser ablation in vivo,” *Sci. Adv.*, vol. 6, no. 15, p.

eaaz9664, Apr. 2020.

- [180] R. Thakur, K. Donnelly, R. F. Mcmillian, and H. Jones, “Minimally invasive microneedles for ocular drug delivery,” *Expert Opin. Drug Deliv.*, vol. 14, no. 4, pp. 525–537, 2017.
- [181] J. Jiang *et al.*, “Coated microneedles for drug delivery to the eye,” *Investig. Ophthalmol. Vis. Sci.*, vol. 48, no. 9, pp. 4038–4043, Sep. 2007.
- [182] J. Jiang, J. S. Moore, H. F. Edelhauser, and M. R. Prausnitz, “Intrascleral Drug Delivery to the Eye Using Hollow Microneedles,” *Pharm. Res.*, vol. 26, no. 2, pp. 395–403, Feb. 2009.
- [183] S. R. Patel, A. S. P. Lin, H. F. Edelhauser, and M. R. Prausnitz, “Suprachoroidal drug delivery to the back of the eye using hollow microneedles,” *Pharm. Res.*, vol. 28, no. 1, pp. 166–176, Jan. 2011.
- [184] G. Traverso *et al.*, “Microneedles for drug delivery via the gastrointestinal tract,” *J. Pharm. Sci.*, vol. 104, no. 2, pp. 362–367, 2015.
- [185] A. Abramson *et al.*, “A luminal unfolding microneedle injector for oral delivery of macromolecules,” *Nat. Med.*, vol. 25, no. 10, pp. 1512–1518, Oct. 2019.
- [186] “Thermal Spray Coatings – Keepsake.” [Online]. Available: <https://www.keepsake.in/keepsake-services/thermal-spray-coatings/>. [Accessed: 29-Dec-2020].
- [187] “PECVD | SPTS,” 2020. [Online]. Available: <https://www.spts.com/categories/pecvd>. [Accessed: 04-Nov-2020].
- [188] “What is Ellipsometry? - J.A. Woollam.” [Online]. Available: <https://www.jawoollam.com/resources/ellipsometry-tutorial/what-is-ellipsometry>. [Accessed: 04-Nov-2020].
- [189] “Evaluation of materials using scanning electron microscope (SEM) | The global standard for mixing, defoaming, dispersing, and pulverizing THINKY CORPORATION.” [Online]. Available: <https://www.thinkymixer.com/en-gl/library/report/evaluation-of-materials-using-scanning-electron-microscope->

sem/. [Accessed: 29-Jan-2021].

- [190] “Flourescent peptide-stabilized silver-nanoclusters, a solid-phase approach for high-throughput ligand discovery.” [Online]. Available: https://www.researchgate.net/publication/323734514_Flourescent_peptide-stabilized_silver-nanoclusters_a_solid-phase_approach_for_high-throughput_ligand_discovery. [Accessed: 29-Jan-2021].
- [191] M. J. Gora and G. J. Tearney, “Enhanced Imaging of the Esophagus: Optical Coherence Tomography,” in *Barrett’s Esophagus: Emerging Evidence for Improved Clinical Practice*, Elsevier Inc., 2016, pp. 105–122.
- [192] “Papain | Sigma-Aldrich.” [Online]. Available: <https://www.sigmaaldrich.com/life-science/metabolomics/enzyme-explorer/analytical-enzymes/papain.html>. [Accessed: 10-Jun-2020].
- [193] H. S. Gill, D. D. Denson, B. A. Burris, and M. R. Prausnitz, “Effect of microneedle design on pain in human volunteers,” *Clin. J. Pain*, vol. 24, no. 7, pp. 585–594, 2008.
- [194] C. J. W. Bolton *et al.*, “Hollow silicon microneedle fabrication using advanced plasma etch technologies for applications in transdermal drug delivery,” *Lab Chip*, vol. 20, no. 15, pp. 2788–2795, Aug. 2020.
- [195] S. Franssila and L. Sainiemi, “Reactive Ion Etching (RIE),” in *Encyclopedia of Microfluidics and Nanofluidics*, 2013.
- [196] MicroChemicals, “Technical Datasheet AZ 125nXT Series,” 2016.
- [197] F. Laermer and A. Schilp, “US5501893A Method of anisotropically etching silicon,” Nov. 1994.
- [198] S. P. Davis, B. J. Landis, Z. H. Adams, M. G. Allen, and M. R. Prausnitz, “Insertion of microneedles into skin: Measurement and prediction of insertion force and needle fracture force,” *J. Biomech.*, vol. 37, no. 8, pp. 1155–1163, Aug. 2004.
- [199] MicroChemicals, “AZnLOF20xx Negative Resist complement information for

processing,” 2005.

- [200] wwwMicroChemicals.com, “MicroChemicals ®- Photolithography exposure.”
- [201] “Spray Coating Photoresist MicroChemicals, AZ 4999,” 2020. [Online]. Available:
https://www.microchemicals.com/products/photoresists/spray_coating_resist/az4999.html. [Accessed: 28-Sep-2020].
- [202] E. Larrañeta, R. E. M. Lutton, A. D. Woolfson, and R. F. Donnelly, “Microneedle arrays as transdermal and intradermal drug delivery systems: Materials science, manufacture and commercial development,” *Materials Science and Engineering R: Reports*, vol. 104. Elsevier Ltd, pp. 1–32, 01-Jun-2016.
- [203] N. Wilke, C. Hibert, J. O’Brien, and A. Morrissey, “Silicon microneedle electrode array with temperature monitoring for electroporation,” in *Sensors and Actuators, A: Physical*, 2005, vol. 123–124, pp. 319–325.
- [204] wwwMicroChemicalscom, “MicroChemicals-Fundamentals of Microstructuring CRYSTALLOGRAPHY OF SILICON.”
- [205] B. Z. Olshanetsky and V. I. Mashanov, “LEED studies of clean high Miller index surfaces of silicon,” *Surf. Sci.*, vol. 111, no. 3, pp. 414–428, Nov. 1981.
- [206] “Crystal Scientific.” [Online]. Available: http://www.crystal-scientific.com/xtal_orientation.html. [Accessed: 23-Jun-2020].
- [207] P. Pal and K. Sato, “A comprehensive review on convex and concave corners in silicon bulk micromachining based on anisotropic wet chemical etching,” *Micro and Nano Systems Letters*, vol. 3, no. 1. Society of Micro and Nano Systems, 01-Dec-2015.
- [208] A. V. N. Rao, V. Swarnalatha, and P. Pal, “Etching characteristics of Si{110} in 20 wt% KOH with addition of hydroxylamine for the fabrication of bulk micromachined MEMS,” *Micro Nano Syst. Lett.*, vol. 5, no. 1, pp. 1–9, Dec. 2017.
- [209] N. Wilke, A. Mulcahy, S. R. Ye, and A. Morrissey, “Process optimization and

- characterization of silicon microneedles fabricated by wet etch technology,” *Microelectronics J.*, vol. 36, no. 7, pp. 650–656, Jul. 2005.
- [210] wwwMicroChemicalscom, “Chapter 01 MicroChemicals ®-Fundamentals of Microstructuring WET-CHEMICAL ETCHING OF SILICON AND SIO 2.”
- [211] “KOH Etching | BYU Cleanroom,” 1990. [Online]. Available: <https://cleanroom.byu.edu/KOH>. [Accessed: 30-Mar-2020].
- [212] T. Waghule *et al.*, “Microneedles: A smart approach and increasing potential for transdermal drug delivery system,” *Biomed. Pharmacother.*, vol. 109, no. October 2018, pp. 1249–1258, 2019.
- [213] R. F. Donnelly, T. R. R. Singh, E. Larrañeta, and M. T. C. McCrudden, “Microneedles for drug and vaccine delivery and patient monitoring,” 2018, p. 178.
- [214] S. Damiani *et al.*, “Sensitivity Comparison of Macro-and Micro-electrochemical Biosensors for Human Chorionic Gonadotropin Biomarker Detection.”
- [215] A. M. Römgens, D. L. Bader, J. A. Bouwstra, F. P. T. Baaijens, and C. W. J. Oomens, “Monitoring the penetration process of single microneedles with varying tip diameters,” *J. Mech. Behav. Biomed. Mater.*, vol. 40, pp. 397–405, Dec. 2014.
- [216] K. A. Moga *et al.*, “Rapidly-dissolvable microneedle patches via a highly scalable and reproducible soft lithography approach,” *Adv. Mater.*, vol. 25, no. 36, pp. 5060–5066, Sep. 2013.
- [217] S. Bhansali and A. Vasudev, “Mems for Biomedical Applications,” 2012, p. 223.
- [218] H. L. Quinn and R. F. Donnelly, “Microneedle-mediated Drug Delivery,” in *Microneedles for Drug and Vaccine Delivery and Patient Monitoring*, John Wiley & Sons, Ltd, 2018, pp. 71–91.
- [219] “The 7th International Conference on Solid-State Sensors and Actuators.”
- [220] L. Lin and A. P. Pisano, “Silicon-processed microneedles,” *J.*

Microelectromechanical Syst., vol. 8, no. 1, pp. 78–84, Mar. 1999.

- [221] J. D. Zahn, N. H. Talbot, D. Liepmann, and A. P. Pisano, “Microfabricated Polysilicon Microneedles for Minimally Invasive Biomedical Devices,” 2000.
- [222] J. Brazzle, I. Papautsky, and A. B. Frazier, “Micromachined needle arrays for drug delivery or fluid extraction: Design and fabrication aspects of fluid coupled arrays of hollow metallic microneedles,” *IEEE Eng. Med. Biol. Mag.*, vol. 18, no. 6, pp. 53–58, Nov. 1999.
- [223] K. Oka, S. Aoyagi, Y. Arai, Y. Isono, G. Hashiguchi, and H. Fujita, “Fabrication of a micro needle for a trace blood test,” in *Sensors and Actuators, A: Physical*, 2002, vol. 97–98, pp. 478–485.
- [224] M. Ombaba, S. B. Inayat, and M. S. Islam, “Wet Chemical and Electrochemical Etching Processes,” in *Encyclopedia of Nanotechnology*, Springer Netherlands, 2015, pp. 1–9.
- [225] Y. Li *et al.*, “Fabrication of sharp silicon hollow microneedles by deep-reactive ion etching towards minimally invasive diagnostics,” *Microsystems Nanoeng.*, vol. 5, no. 1, pp. 1–11, Dec. 2019.
- [226] D. Bowen, “Patterning,” *J. Pract. Nurs.*, vol. 20, no. 4, pp. 42–45, Apr. 1970.
- [227] R. Dorey, “Microstructure–property relationships: How the microstructure of the film affects its properties,” *Ceram. Thick Film. MEMS Microdevices*, pp. 85–112, 2012.
- [228] M. Shimbo, K. Furukawa, K. Fukuda, and K. Tanzawa, “Silicon-to-silicon direct bonding method,” *J. Appl. Phys.*, vol. 60, no. 8, pp. 2987–2989, Oct. 1986.
- [229] J. B. Lasky, “Wafer bonding for silicon-on-insulator technologies,” *Appl. Phys. Lett.*, vol. 48, no. 1, pp. 78–80, Jan. 1986.
- [230] “Patented Technology by Nanopass | Microneedles for interdermal injection,” 2017. [Online]. Available: <https://www.nanopass.com/technology/>. [Accessed: 07-May-2020].

- [231] Y. C. Kim, J. H. Park, and M. R. Prausnitz, "Microneedles for drug and vaccine delivery," *Advanced Drug Delivery Reviews*, vol. 64, no. 14. NIH Public Access, pp. 1547–1568, Nov-2012.
- [232] T. Waghule *et al.*, "Microneedles: A smart approach and increasing potential for transdermal drug delivery system," *Biomedicine and Pharmacotherapy*, vol. 109. Elsevier Masson SAS, pp. 1249–1258, 01-Jan-2019.
- [233] K. A. Moga *et al.*, "Rapidly-Dissolvable Microneedle Patches Via a Highly Scalable and Reproducible Soft Lithography Approach NIH Public Access," *Adv Mater*, vol. 25, no. 36, pp. 5060–5066, 2013.
- [234] B. Ahn, "Optimal Microneedle Design for Drug Delivery Based on Insertion Force Experiments with Variable Geometry," *Int. J. Control. Autom. Syst.*, vol. 18, no. 1, pp. 143–149, Jan. 2020.
- [235] S. P. Davis, B. J. Landis, Z. H. Adams, M. G. Allen, and M. R. Prausnitz, "Insertion of microneedles into skin: Measurement and prediction of insertion force and needle fracture force," *J. Biomech.*, vol. 37, no. 8, pp. 1155–1163, Aug. 2004.
- [236] A. Ovsianikov, B. Chichkov, P. Mente, N. A. Monteiro-Riviere, A. Doraiswamy, and R. J. Narayan, "Two photon polymerization of polymer-ceramic hybrid materials for transdermal drug delivery," *Int. J. Appl. Ceram. Technol.*, vol. 4, no. 1, pp. 22–29, Jan. 2007.
- [237] J. H. Park, Y. K. Yoon, S. O. Choi, M. R. Prausnitz, and M. G. Allen, "Tapered conical polymer microneedles fabricated using an integrated lens technique for transdermal drug delivery," *IEEE Trans. Biomed. Eng.*, vol. 54, no. 5, pp. 903–913, May 2007.
- [238] H. S. Gill, D. D. Denson, B. A. Burris, and M. R. Prausnitz, "Effect of microneedle design on pain in human subjects."
- [239] A. Davidson, B. Al-Qallaf, and D. B. Das, "Transdermal drug delivery by coated microneedles: Geometry effects on effective skin thickness and drug permeability," *Chem. Eng. Res. Des.*, vol. 86, no. 11, pp. 1196–1206, Nov. 2008.

- [240] S. P. Davis, B. J. Landis, Z. H. Adams, M. G. Allen, and M. R. Prausnitz, "Insertion of microneedles into skin: Measurement and prediction of insertion force and needle fracture force," *J. Biomech.*, vol. 37, no. 8, pp. 1155–1163, Aug. 2004.
- [241] J.-H. Park, S.-O. Choi, S. Seo, Y. Bin Choy, and M. R. Prausnitz, "A microneedle roller for transdermal drug delivery," *Eur. J. Pharm. Biopharm.*, vol. 76, pp. 282–289, 2010.
- [242] J. S. Kochhar, W. J. Goh, S. Y. Chan, and L. Kang, "A simple method of microneedle array fabrication for transdermal drug delivery," *Drug Dev. Ind. Pharm.*, vol. 39, no. 2, pp. 299–309, Feb. 2013.
- [243] G. Li, A. Badkar, H. Kalluri, and A. K. Banga, "Microchannels created by sugar and metal microneedles: Characterization by microscopy, macromolecular flux and other techniques," *J. Pharm. Sci.*, vol. 99, no. 4, pp. 1931–1941, Apr. 2010.
- [244] K. Moronkeji, S. Todd, I. Dawidowska, S. D. Barrett, and R. Akhtar, "The role of subcutaneous tissue stiffness on microneedle performance in a representative in vitro model of skin," *J. Control. Release*, vol. 265, pp. 102–112, Nov. 2017.
- [245] S. D. Gittard *et al.*, "The Effects of Geometry on Skin Penetration and Failure of Polymer Microneedles."
- [246] K. van der Maaden, E. Sekerdag, W. Jiskoot, and J. Bouwstra, "Impact-Insertion Applicator Improves Reliability of Skin Penetration by Solid Microneedle Arrays," *AAPS J.*, vol. 16, no. 4, pp. 681–684, Jul. 2014.
- [247] M. Leone *et al.*, "Universal Applicator for Digitally-Controlled Pressing Force and Impact Velocity Insertion of Microneedles into Skin," *Pharmaceutics*, vol. 10, no. 4, p. 211, 2018.
- [248] S. A. Coulman *et al.*, "In vivo, in situ imaging of microneedle insertion into the skin of human volunteers using optical coherence tomography," *Pharm. Res.*, vol. 28, no. 1, pp. 66–81, Jan. 2011.
- [249] S. A. Coulman *et al.*, "In vivo, in situ imaging of microneedle insertion into the

skin of human volunteers using optical coherence tomography,” *Pharm. Res.*, vol. 28, no. 1, pp. 66–81, Jan. 2011.

- [250] W. Yuan *et al.*, “Theranostic OCT microneedle for fast ultrahigh-resolution deep-brain imaging and efficient laser ablation in vivo,” *Sci. Adv.*, vol. 6, no. 15, p. eaaz9664, Apr. 2020.
- [251] J. Enfield, M.-L. O’Connell, K. Lawlor, E. Jonathan, C. O’Mahony, and M. Leahy, “In-vivo dynamic characterization of microneedle skin penetration using optical coherence tomography,” *J. Biomed. Opt.*, vol. 15, no. 4, p. 046001, 2010.
- [252] J. D. Zahn, N. H. Talbot, D. Liepmann, and A. P. Pisano, “Microfabricated polysilicon microneedles for minimally invasive biomedical devices,” *Biomed. Microdevices*, vol. 2, no. 4, pp. 295–303, 2000.
- [253] P. Khanna, K. Luongo, J. A. Strom, and S. Bhansali, “Axial and shear fracture strength evaluation of silicon microneedles,” *Microsyst. Technol.*, vol. 16, no. 6, pp. 973–978, Jun. 2010.
- [254] Z. F. Rad *et al.*, “High-fidelity replication of thermoplastic microneedles with open microfluidic channels,” *Microsystems Nanoeng.*, vol. 3, no. 1, pp. 1–11, Oct. 2017.
- [255] R. Donnelly, “Microneedles for Drug and Vaccine Delivery and Patient Monitoring,” in *Microneedles for Drug and Vaccine Delivery and Patient Monitoring*, F. D. Ryan, Ed. Chichester, UK: John Wiley & Sons, Ltd, 2018, pp. 57–58.
- [256] J. H. Park, M. G. Allen, and M. R. Prausnitz, “Biodegradable polymer microneedles: Fabrication, mechanics and transdermal drug delivery,” in *Annual International Conference of the IEEE Engineering in Medicine and Biology - Proceedings*, 2004, vol. 26 IV, pp. 2654–2657.
- [257] Y. C. Kim, J. H. Park, and M. R. Prausnitz, “Microneedles for drug and vaccine delivery,” *Advanced Drug Delivery Reviews*, vol. 64, no. 14. Elsevier, pp. 1547–1568, 01-Nov-2012.

- [258] X. He, J. Sun, J. Zhuang, H. Xu, Y. Liu, and D. Wu, "Microneedle System for Transdermal Drug and Vaccine Delivery: Devices, Safety, and Prospects," *Nanotechnol. Microtechnology Drug Deliv. Syst.*, 2019.
- [259] R. Neupane, S. H. S. Boddu, J. Renukuntla, R. J. Babu, and A. K. Tiwari, "Alternatives to biological skin in permeation studies: Current trends and possibilities," *Pharmaceutics*, vol. 12, no. 2, Feb. 2020.
- [260] E. Abd *et al.*, "Skin models for the testing of transdermal drugs," *Clinical Pharmacology: Advances and Applications*, vol. 8. Dove Medical Press Ltd, pp. 163–176, 19-Oct-2016.
- [261] S. Zsikó, E. Csányi, A. Kovács, M. Budai-Szűcs, A. Gácsi, and S. Berkó, "Methods to evaluate skin penetration in vitro," *Sci. Pharm.*, vol. 87, no. 3, Sep. 2019.
- [262] E. Abd *et al.*, "Skin models for the testing of transdermal drugs," *Clin. Pharmacol. Adv. Appl.*, vol. 8, pp. 163–176, 2016.
- [263] L. Bartosova and J. Bajgar, "Transdermal Drug Delivery In Vitro Using Diffusion Cells," *Curr. Med. Chem.*, vol. 19, no. 27, pp. 4671–4677, Oct. 2012.
- [264] "Comparison of Human, Porcine & Rodent Wound Healing with New Miniature Swine Study Data," 2019. [Online]. Available: <https://sinclairresearch.com/scientific-posters/comparison-of-human-porcine-rodent-wound-healing-with-new-miniature-swine-study-data/>. [Accessed: 05-Jun-2020].
- [265] F. Cilurzo, P. Minghetti, and C. Sinico, "Newborn pig skin as model membrane in in vitro drug permeation studies: A technical note," *AAPS PharmSciTech*, vol. 8, no. 4, Nov. 2007.
- [266] L. A. Ahlstrom, S. E. Cross, and P. C. Mills, "The effects of freezing skin on transdermal drug penetration kinetics," *J. Vet. Pharmacol. Ther.*, vol. 30, no. 5, pp. 456–463, Oct. 2007.
- [267] R. Abdayem, L. Roussel, N. Zaman, F. Pirot, E. Gilbert, and M. Haftek,

- “Deleterious effects of skin freezing contribute to variable outcomes of the predictive drug permeation studies using hydrophilic molecules,” *Exp. Dermatol.*, 2015.
- [268] J. B. Nielsen, I. Plasencia, J. A. Sørensen, and L. A. Bagatolli, “Storage conditions of skin affect tissue structure and subsequent in vitro percutaneous penetration,” *Skin Pharmacol. Physiol.*, vol. 24, no. 2, pp. 93–102, Jan. 2011.
- [269] A. M. Barbero and H. F. Frasch, “Effect of Frozen Human Epidermis Storage Duration and Cryoprotectant on Barrier Function Using Two Model Compounds,” *Skin Pharmacol. Physiol.*, vol. 29, no. 1, pp. 31–40, Feb. 2016.
- [270] S. Kächler, K. Strüver, and W. Friess, “Reconstructed skin models as emerging tools for drug absorption studies,” *Expert Opin. Drug Metab. Toxicol.*, vol. 9, no. 10, pp. 1255–1263, Oct. 2013.
- [271] The Organisation for Economic Cooperation and Development, “OECD Guidance document for the conduct of skin absorption studies,” 2004.
- [272] G. HAWKINS, “Development of an in vitro model for determining the fate of chemicals applied to skin,” *Fundam. Appl. Toxicol.*, vol. 4, no. 2, pp. S133–S144, Apr. 1984.
- [273] J. Swarbrick, G. Lee, and J. Brom, “Drug permeation through human skin: I. Effect of storage conditions of skin,” *J. Invest. Dermatol.*, vol. 78, no. 1, pp. 63–66, 1982.
- [274] A. Gordon, “INTEGUMENTARY SYSTEM,” *Slide-share*, 2016. [Online]. Available: <https://slideplayer.com/slide/9224453/>. [Accessed: 19-Sep-2020].
- [275] H. X. Nguyen, A. Puri, S. A. Bhattacharjee, and A. K. Banga, “Qualitative and quantitative analysis of lateral diffusion of drugs in human skin,” *Int. J. Pharm.*, vol. 544, no. 1, pp. 62–74, Jun. 2018.
- [276] H. X. Nguyen and A. K. Banga, “Fabrication, characterization and application of sugar microneedles for transdermal drug delivery,” *Ther. Deliv.*, vol. 8, no. 5, pp. 249–264, Mar. 2017.

- [277] S. F. Lahiji, M. Dangol, and H. Jung, "A patchless dissolving microneedle delivery system enabling rapid and efficient transdermal drug delivery," *Sci. Rep.*, vol. 5, no. 1, pp. 1–7, Jan. 2015.
- [278] L. B. Davies, C. Gateley, P. Holland, S. A. Coulman, and J. C. Birchall, "Accelerating Topical Anaesthesia Using Microneedles," *Skin Pharmacol. Physiol.*, vol. 30, no. 6, pp. 277–283, Jan. 2018.
- [279] Y. H. Mohammed *et al.*, "Microneedle enhanced delivery of cosmeceutically relevant peptides in human skin," *PLoS One*, vol. 9, no. 7, Jul. 2014.
- [280] W. Zhang *et al.*, "Penetration and distribution of PLGA nanoparticles in the human skin treated with microneedles," *Int. J. Pharm.*, vol. 402, no. 1–2, pp. 205–212, Dec. 2010.
- [281] F. Chabri *et al.*, "Microfabricated silicon microneedles for nonviral cutaneous gene delivery," *Br. J. Dermatol.*, vol. 150, no. 5, pp. 869–877, May 2004.
- [282] B. Pamornpathomkul, A. Wongkajornsilp, W. Laiwattanapaisal, T. Rojanarata, P. Opanasopit, and T. Ngawhirunpat, "A combined approach of hollow microneedles and nanocarriers for skin immunization with plasmid DNA encoding ovalbumin," *Int. J. Nanomedicine*, vol. 12, pp. 885–898, Jan. 2017.
- [283] J. W. Lee, J. H. Park, and M. R. Prausnitz, "Dissolving microneedles for transdermal drug delivery," *Biomaterials*, vol. 29, no. 13, pp. 2113–2124, May 2008.
- [284] C. S. Kolli, J. Xiao, D. L. Parsons, and R. J. Babu, "Microneedle assisted iontophoretic transdermal delivery of prochlorperazine edisylate," *Drug Dev. Ind. Pharm.*, vol. 38, no. 5, pp. 571–576, May 2012.
- [285] R. F. Donnelly *et al.*, "Hydrogel-Forming Microneedles Prepared from 'Super Swelling' Polymers Combined with Lyophilised Wafers for Transdermal Drug Delivery," *PLoS One*, vol. 9, no. 10, p. e111547, Oct. 2014.
- [286] E. M. Migdadi *et al.*, "Hydrogel-forming microneedles enhance transdermal delivery of metformin hydrochloride," *J. Control. Release*, vol. 285, pp. 142–

151, Sep. 2018.

- [287] G. Nava, E. Piñón, L. Mendoza, N. Mendoza, D. Quintanar, and A. Ganem, "Formulation and in vitro, ex vivo and in vivo evaluation of elastic liposomes for transdermal delivery of ketorolac tromethamine," *Pharmaceutics*, vol. 3, no. 4, pp. 954–970, Dec. 2011.
- [288] M. Kaur, K. B. Ita, I. E. Popova, S. J. Parikh, and D. A. Bair, "Microneedle-assisted delivery of verapamil hydrochloride and amlodipine besylate," *Eur. J. Pharm. Biopharm.*, vol. 86, no. 2, pp. 284–291, 2014.
- [289] E. Luu, K. B. Ita, M. J. Morra, and I. E. Popova, "The Influence of Microneedles on the Percutaneous Penetration of Selected Antihypertensive Agents: Diltiazem Hydrochloride and Perindopril Erbumine," *Curr. Drug Deliv.*, vol. 15, no. 10, pp. 1449–1458, Oct. 2018.
- [290] S. Zhang, Y. Qiu, and Y. Gao, "Enhanced delivery of hydrophilic peptides in vitro by transdermal microneedle pretreatment," *Acta Pharm. Sin. B*, vol. 4, no. 1, pp. 100–104, Feb. 2014.
- [291] P. Ronnander, L. Simon, H. Spilgies, A. Koch, and S. Scherr, "Dissolving polyvinylpyrrolidone-based microneedle systems for in-vitro delivery of sumatriptan succinate," *Eur. J. Pharm. Sci.*, vol. 114, pp. 84–92, Mar. 2018.
- [292] S. R. Vučen, G. Vuleta, A. M. Crean, A. C. Moore, N. Ignjatovič, and D. Uskokovič, "Improved percutaneous delivery of ketoprofen using combined application of nanocarriers and silicon microneedles," *J. Pharm. Pharmacol.*, vol. 65, no. 10, pp. 1451–1462, Oct. 2013.
- [293] P. González-Vázquez *et al.*, "Transdermal delivery of gentamicin using dissolving microneedle arrays for potential treatment of neonatal sepsis," *J. Control. Release*, vol. 265, pp. 30–40, Nov. 2017.
- [294] M. C. Kearney, P. E. McKenna, H. L. Quinn, A. J. Courtenay, E. Larrañeta, and R. F. Donnelly, "Design and development of liquid drug reservoirs for microneedle delivery of poorly soluble drug molecules," *Pharmaceutics*, vol. 11, no. 11, Nov. 2019.

- [295] R. F. Donnelly *et al.*, “Hydrogel-forming microneedle arrays for enhanced transdermal drug delivery,” *Adv. Funct. Mater.*, vol. 22, no. 23, pp. 4879–4890, Dec. 2012.
- [296] J. Kielhorn, S. Melching-Kollmuß, and I. Mangelsdorf, “Environmental Health Criteria 235 DERMAL ABSORPTION First draft prepared by Drs,” 2006.
- [297] H. Osman-Ponchet, “Use of Microneedle Device to Enhance Dermal Absorption: Study on Ex Vivo Human Skin,” *J. Dermatology Cosmetol.*, vol. 2, no. 1, Jan. 2018.
- [298] S. Jansen van Rensburg, A. Franken, and J. L. Du Plessis, “Measurement of transepidermal water loss, stratum corneum hydration and skin surface pH in occupational settings: A review,” *Ski. Res. Technol.*, vol. 25, no. 5, pp. 595–605, Sep. 2019.
- [299] D. J. Davies, J. R. Heylings, T. J. McCarthy, and C. M. Correa, “Development of an in vitro model for studying the penetration of chemicals through compromised skin,” *Toxicol. Vitr.*, vol. 29, no. 1, pp. 176–181, Feb. 2015.
- [300] B. Srinivasan, A. R. Kolli, M. B. Esch, H. E. Abaci, M. L. Shuler, and J. J. Hickman, “TEER measurement techniques for in vitro barrier model systems.”
- [301] E. Abd *et al.*, “Skin models for the testing of transdermal drugs,” *Clin. Pharmacol. Adv. Appl.*, vol. 8, pp. 163–176, Oct. 2016.
- [302] E. Takach, *Tissue analysis for drug development*. Future Medicine Ltd., 2013.
- [303] C. Yu and L. Cohen, “Tissue-Sample Preparation- Not the same Old Grind,” Michigan USA, Feb. 2004.
- [304] E. Takach, *Tissue analysis for drug development*. Future Medicine Ltd., 2013.
- [305] “Tissue Dissociation Guide: Collagenase, Dispase, and Liberase Enzyme Types | Sigma-Aldrich.” [Online]. Available: <https://www.sigmaaldrich.com/life-science/metabolomics/enzyme-explorer/learning-center/collagenase-guide.html>. [Accessed: 10-Jun-2020].

- [306] R. Nirogi *et al.*, “Skin sample preparation by collagenase digestion for diclofenac quantification using LC-MS/MS after topical application,” *Bioanalysis*, vol. 8, no. 12, pp. 1251–1263, Jun. 2016.
- [307] A. R. R. Qin, X. Liang, Y. Deng, B. Dean, and S. K. Shahidi-Latham, “Collagenase as an effective tool for drug quantitation in tissues,” *Bioanalysis*, vol. 7, no. 9, pp. 1069–1079, May 2015.
- [308] J. H. Moy, “Papayas,” in *Encyclopedia of Food Sciences and Nutrition*, 2nd ed., L. Trugo and M. Fingls, P, Eds. Blatimore: Academic Press, 2003, pp. 4345–4351.
- [309] C. Stremnitzer *et al.*, “Papain Degrades Tight Junction Proteins of Human Keratinocytes In Vitro and Sensitizes C57BL/6 Mice via the Skin Independent of its Enzymatic Activity or TLR4 Activation Europe PMC Funders Group,” *J Invest Dermatol*, vol. 135, no. 7, pp. 1790–1800, 2015.
- [310] J. M. Anderson and C. M. Van Itallie, “Physiology and function of the tight junction.,” *Cold Spring Harbor perspectives in biology*, vol. 1, no. 2. Cold Spring Harbor Laboratory Press, 2009.
- [311] Jaspreet Singh Kochhar, Justin J. Y. Tan, Yee Chin Kwang, and Lifeng Kang, *Microneedles for Transdermal Drug Delivery* . Springer, 2019.
- [312] S. Y. Choi *et al.*, “Hyaluronic acid microneedle patch for the improvement of crow’s feet wrinkles,” *Dermatol. Ther.*, vol. 30, no. 6, p. e12546, Nov. 2017.
- [313] T. Waghule *et al.*, “Microneedles: A smart approach and increasing potential for transdermal drug delivery system,” *Biomedicine and Pharmacotherapy*, vol. 109. Elsevier Masson SAS, pp. 1249–1258, 2019.
- [314] Y.-H. Liao, S. A. Jones, B. Forbes, G. P. Martin, and M. B. Brown, “Hyaluronan: Pharmaceutical Characterization and Drug Delivery,” *Drug Deliv.*, vol. 12, no. 6, pp. 327–342, Jan. 2005.
- [315] Y. Zhang, J. Yu, A. R. Kahkoska, J. Wang, J. B. Buse, and Z. Gu, “Advances in Transdermal Insulin Delivery HHS Public Access,” *Adv. Drug Deliv. Rev.*, vol.

15, no. 139, pp. 51–70, 2019.

- [316] X. Jin, D. D. Zhu, B. Z. Chen, M. Ashfaq, and X. D. Guo, “Insulin delivery systems combined with microneedle technology,” *Adv. Drug Deliv. Rev.*, vol. 127, pp. 119–137, Mar. 2018.
- [317] C. H. Chen, V. B. H. Shyu, and C. T. Chen, “Dissolving microneedle patches for transdermal insulin delivery in diabetic mice: Potential for clinical applications,” *Materials (Basel)*, vol. 11, no. 9, Sep. 2018.
- [318] L. C. Ng and M. Gupta, “Transdermal drug delivery systems in diabetes management: A review,” *Asian J. Pharm. Sci.*, vol. 15, no. 1, pp. 13–25, Jan. 2020.
- [319] E. Czuba *et al.*, “Oral insulin delivery, the challenge to increase insulin bioavailability: Influence of surface charge in nanoparticle system,” *Int. J. Pharm.*, vol. 542, no. 1–2, pp. 47–55, May 2018.
- [320] X. Jin, D. D. Zhu, B. Z. Chen, M. Ashfaq, and X. D. Guo, “Insulin delivery systems combined with microneedle technology,” *Adv. Drug Deliv. Rev.*, vol. 127, pp. 119–137, Mar. 2018.
- [321] X. Jin, D. D. Zhu, B. Z. Chen, M. Ashfaq, and X. D. Guo, “Insulin delivery systems combined with microneedle technology,” *Adv. Drug Deliv. Rev.*, vol. 127, pp. 119–137, Mar. 2018.
- [322] E. Hopkins and S. Sharma, *Physiology, Acid Base Balance*. StatPearls Publishing, 2019.
- [323] N. Østergaard Knudsen and G. Pommegaard Pedersen, “pH and Drug Delivery,” in *Current Problems in Dermatology (Switzerland)*, vol. 54, S. Karger AG, 2018, pp. 143–151.
- [324] C. Surber, P. Humbert, C. Abels, and H. Maibach, “The Acid Mantle: A Myth or an Essential Part of Skin Health?,” *Current Problems in Dermatology (Switzerland)*, vol. 54, S. Karger AG, pp. 1–10, 2018.
- [325] M. R. Prausnitz *et al.*, “Skin Barrier and Transdermal Drug Delivery,” in *Medical*

Therapy, 2012, pp. 2065–2073.

- [326] J. W. Fluhr and P. M. Elias, “Stratum corneum pH: Formation and function of the ‘acid mantle,’” *Exogenous Dermatology*, vol. 1, no. 4, pp. 163–175, 2002.
- [327] K. Nadendla and S. H. Friedman, “Light Control of Protein Solubility Through Isoelectric Point Modulation Corresponding Author Prof HHS Public Access,” *J Am Chem Soc*, vol. 139, no. 49, pp. 17861–17869, 2017.